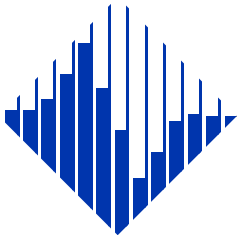

PACIFIC EARTHQUAKE ENGINEERING
RESEARCH CENTER

Hybrid Simulation of Seismic Isolation Systems Applied to an APR-1400 Nuclear Power Plant

Andreas H. Schellenberg
Pacific Earthquake Engineering Research Center
University of California, Berkeley

Alireza Sarebanha
Department of Structural Engineering
University of California, San Diego

Matthew J. Schoettler
Pacific Earthquake Engineering Research Center
University of California, Berkeley

Gilberto Mosqueda
Gianmario Benzoni
Department of Structural Engineering
University of California, San Diego

Stephen A. Mahin
Department of Civil and Environmental Engineering
University of California, Berkeley

PEER Report No. 2015/05
Pacific Earthquake Engineering Research Center
Headquarters at the University of California, Berkeley

PEER 2015/05
APRIL 2015

Disclaimer

The opinions, findings, and conclusions or recommendations expressed in this publication are those of the author(s) and do not necessarily reflect the views of the study sponsor(s) or the Pacific Earthquake Engineering Research Center.

Hybrid Simulation of Seismic Isolation Systems Applied to an APR-1400 Nuclear Power Plant

Andreas H. Schellenberg
Pacific Earthquake Engineering Research Center
University of California, Berkeley

Alireza Sarebanha
Department of Structural Engineering
University of California, San Diego

Matthew J. Schoettler
Pacific Earthquake Engineering Research Center
University of California, Berkeley

Gilberto Mosqueda
Gianmario Benzoni
Department of Structural Engineering
University of California, San Diego

Stephen A. Mahin
Department of Civil and Environmental Engineering
University of California, Berkeley

PEER Report No. 2015/05
Pacific Earthquake Engineering Research Center
Headquarters at the University of California, Berkeley

April 2015

ABSTRACT

Since the dynamic response of an isolated structure depends on the combined characteristics of the ground motion, bearings, and structure, standard isolator prototype component tests may not by themselves be sufficient to assess seismic performance and verify the adequacy of numerical models used for computer simulation. Thus, when assessing the applicability of seismic isolation to nuclear power facilities, tests that simulate dynamic response under realistic excitations are desired. However, available shaking tables have limits on the size, strength, and weight of the specimens they can test. Shaking table tests of reduced-scale test specimens introduce uncertainties about the realism of test results and complicate validation of numerical models since the properties of isolation bearings are likely sensitive to scale and rate-of-loading effects. Even where a relatively small number of full-scale bearings might be used in tests of simplified shaking table specimens, significant technical and economic challenges must be addressed in order to capture the stress and deformation conditions that would occur in bearings supporting large nuclear power plants (NPPs) subjected to gravity and three-dimensional seismic excitations. The best option for testing such large specimens may be through the use of "hybrid dynamic simulation."

Because laboratory facilities exist to test full-scale seismic isolation bearings under prescribed displacement or load protocols, and the supported structure is expected to remain essentially within the elastic range of response, hybrid simulation methods provide a unique opportunity to assess experimentally the dynamic behavior of base isolated NPPs using full-scale bearings. The adaptation of such a testing facility and the implementation of hybrid simulation using full-scale experimental bearings in a seismically isolated NPP model are described in this report.

The research program was able to confirm that hybrid simulation is indeed a viable and very promising testing method to experimentally assess the behavior of very large isolators in full-scale. It was confirmed that it is feasible and necessary to employ high-performance parallel computing analysis machines to perform hybrid simulations of large structures with several thousands of degrees of freedom, such as seismically isolated NPPs.

The primary objective of the research reported herein was to evaluate the dynamic response of an isolated NPP and assess key response parameters. A simplified, but realistic numerical model of an APR-1400 NPP designed by KEPCO Engineering and Construction (KEPCO E&C) was used as the basis of these studies. Two different types of isolation systems were considered: one based on lead plug rubber bearings, and the other based on friction bearings. Both have relatively high effective damping ratios. The isolation system was represented in the hybrid model by (a) a single test bearing representing all of the bearings supporting the plant, and (b) various combinations of numerically modeled and physically tested bearings. Ground motions used in the hybrid simulations were selected to represent situations that might be encountered in the design of NPPs in the U.S. or Europe for design-level events. Hybrid simulations were conducted considering one or two horizontal components of ground motion, as well as considering three components of excitation.

These hybrid simulations demonstrated the ability of the seismic isolation systems employed to perform well under design level conditions for the ground motions considered, and

to protect the supported structure and components from the intense vibrations that might be expected in a fixed-base plant. The hybrid tests showed that adding a second horizontal component of motion tended to narrow hysteretic loops and somewhat increase bearing displacements. It is believed that this is related in large part to the greater energy dissipated (and temperature rise) that occurs during two-dimensional motions because of the larger distance traveled compared to the one-dimensional excitation case. The tests also revealed that both of the bearing types tested showed substantial vertical–horizontal coupling. While this behavior had negligible effect on bearing displacement demands, it had a major effect on floor response spectra. For both of the relatively high-damping bearings considered, significantly amplified horizontal spectral ordinates were observed near the vertical natural frequencies of the isolated plant. This amplification was somewhat greater for cases with two horizontal components of excitation, and for cases using the friction isolation bearing. It is concluded that it is essential to include vertical ground motion input to accurately predict horizontal floor response spectra near the plant's fundamental vertical frequencies. Overturning moments had a negligible effect on the behavior of the isolators and resulted in relatively small increases in floor response spectra. For the friction-type isolators studied, the hybrid tests revealed some issues with breakaway and static frictions. True real-time hybrid simulations might alleviate such problems.

The study presented here investigated the behavior of seismically isolated NPPs for design-basis events. Future hybrid simulations should not only consider design-basis events but also investigate bearing behavior, moat wall impact, and possible bearing failure for beyond-design-level events. Additional development work that is needed to improve speed and performance of the hybrid test apparatus used in these tests is presented at the end of this report.

ACKNOWLEDGMENTS

This report summarizes results, observations and findings developed as part of a research project entitled, "Dynamic Testing of a Seismically Isolated APR-1400 Nuclear Power Plant Model Using Hybrid Simulation." This research was supported by Contract No. KCN04-13-73 from KEPCO Engineering and Construction Company, Inc., to the Pacific Earthquake Engineering Research Center (PEER). The authors are grateful for this financial support. In addition, the PEER research team appreciates greatly the advice and technical support provided by the engineering staff of the KEPCO Engineering and Construction Company, Inc., with special thanks to Mr. Chul Soon Choi, Dr. Sang-Hoon Lee, and Dr. Seung-Ryong Han. Their interest in and promotion of this research was invaluable.

This research is the result of collaboration between researchers at the University of California, Berkeley (UCB) and the University of California, San Diego (UCSD). The authors are grateful for the assistance of various experts on earthquake engineering at UCB, including Professor James M. Kelly and Dr. Frank McKenna. The success of this project was due in large part due to the skill and efforts of staff at the Structural Response Modification Device Laboratory at UCSD. The cooperation of staff members Mr. Danny Innamorato, Mr. Edward Stovin, Noemi Bonessio, and Giuseppe Lomiento was greatly appreciated.

The authors are grateful to those whose expertise helped improve the quality and outcomes of the research. Professor Jack Baker at Stanford University provided essential assistance in developing ground motions used in these studies. Testing was facilitated by the presence of knowledgeable engineers from Unison eTech and ESCO RTS. Technical insight was also provided by Jay Conklin from RJ Watson, Inc. A significant gain in hybrid test performance was obtained from the assistance of Brad Thoen from MTS Systems Corp.

Any opinions, findings, and conclusions or recommendations expressed in this report are those of the authors and do not necessarily reflect those of KEPCO Engineering and Construction, PEER, or the Regents of the University of California.

CONTENTS

LIST OF TABLES

LIST OF FIGURES

1 Introduction

Recent reports related to the feasibility of applying seismic isolation technology to nuclear power plants (NPPs) and related facilities have noted the lack of publicly available test data on the mechanical characteristics of large full-scale seismic isolation bearings, especially when subjected to realistic seismic loading conditions [Wong at al. 2012; Wong et al. 2013]. These reports underscored the need for component and structure system tests that consider different types of full-scale bearings in order to identify the influence of axial load intensity and history, lateral deformation history, and loading rates on seismic performance, and to evaluate and improve the reliability of numerical models and methods. Because the dynamic response of an isolated structure depends on the combined characteristics of the ground motion, bearings, and the superstructure, standard prototype tests may not by themselves be adequate for use in computer simulations. Thus, dynamic tests of isolated NPP models under more realistic excitations than provided by standard prototype tests are desired. Moreover, bearing properties and ultimate behavior likely depend on scale and rate-of-loading effects. Thus, the use of reduced-scale test specimens and quasi-static methods decreases the confidence that can be placed in a new technology. Uncertainties about the relevancy of prototype tests complicate validation of numerical models and understanding of the behavior of an isolated system under ultimate loading conditions.

Therefore, "hybrid dynamic simulations" may provide the best option for documenting both system and component response. This method combines in real time results from (a) test specimens representing critical components of a structure that exhibit uncertain nonlinear behavior; and (b) analytical models of the remainder of the structural system that exhibit behavior that can be predicted numerically with confidence. Because laboratory facilities exist to test full-scale seismic isolation bearings under prescribed displacement or load protocols, and the supported structure is expected to remain essentially within the elastic range of response, hybrid simulation methods provide a unique opportunity to assess experimentally the dynamic behavior of full-scale bearings for use in base isolated NPPs.

Adaptation of an existing laboratory's capabilities to perform these hybrid simulations is reported. The primary objective was to evaluate the dynamic response of an isolated NPP and assess key response parameters. A simplified, but realistic numerical model of an APR-1400 NPP designed by KEPCO Engineering and Construction was used as the basis of these studies. Two different types of isolation systems were considered; one based on lead plug rubber bearings (LRPBs), and the other based on friction bearings. The isolation system was represented in the hybrid model by (a) a single test bearing representing all of the bearings supporting the plant, and (b) various combinations of numerically modeled and physically tested bearings.

Ground motions used in the hybrid simulations were selected to represent situations that might be encountered in the design of NPPs in the U.S. or Europe for design-level events. To help understand the capabilities of the hybrid simulation method used, and the effect of ground motions on seismically isolated systems, hybrid simulations were conducted considering one or two components of ground motion, as well as considering three components of excitation.

For these studies, the key response parameters reported include bearing force, displacement and hysteretic response as well as superstructure floor response spectra. The following tasks were conducted for this study: characterization of the bearings, development of hybrid test capabilities, implementation and verification of this test methodology, and execution of the experimental tests.

Several improvements and additions, specifically developed for this project, were introduced to the OpenSees*SP* computational driver software and the OpenFresco middleware software. Both software frameworks are widely adopted to perform hybrid simulations. The research program confirmed that hybrid simulation is indeed a viable and very promising testing method to experimentally assess the behavior of large isolators in full scale. Rapid hybrid simulations, at or near-real-time conditions, were achieved, confirming that, when necessary, simulations can employ high-performance parallel computing analysis machines to perform hybrid simulations of large structures with several thousands of degrees of freedom (DOFs), such as seismically isolated NPPs. However, for cases where nonlinear numerical models of isolator behavior were included in the hybrid model, this study also determined that there is a need to improve the efficiency and fidelity of analytical models of isolators so that they can more closely capture the true behavior of a bearing in real time. Moreover, there is an overall need to streamline the transmission of command and feedback signals among the various equipment components used to implement the hybrid simulations, to tune the electronic system used to control the bearing test machine, and to investigate means to further increase computation speeds of such highly complex hybrid models in order to be able to perform near-real-time or real-time hybrid tests more reliably in the future.

This report is divided into four chapters. Following the brief introduction in Chapter 1, Chapter 2 describes the prototype structure considered in the hybrid simulations, and the two types of isolation bearings used. Chapter 3 is subdivided into five major parts: (i) description of the Seismic Response Modification Device (SMRD) Testing facility at UCSD that was used to conduct the hybrid simulations; (ii) description of the various electronic components and the software used to implement the hybrid test method on the SRMD testing facility; (iii) description of the test set up, including the numerical models used in the hybrid simulations, the instrumentation and data acquisition/processing procedures, and installation of the bearings in the test machine, (iv) the test protocol used, and (v) the test results. In addition to hybrid simulations, additional tests were carried out to characterize the mechanical behavior of the physical bearings. Observations, conclusions and recommendations regarding the response of the hybrid model of a seismically isolated NPP and the validity of the hybrid test method are summarized in Chapter 4. Detailed test results for the two types of bearings in the hybrid and characterization tests are provided in four appendices.

2 Prototype Structure and Bearing Designs

2.1 SEISMICALLY ISOLATED NUCLEAR POWER PLANT

The prototype structure was a seismically isolated APR-1400 power plant. The 1400 MW Advanced Power Reactor's seismic isolation system was designed by KEPCO E&C, composed of an isolation plane with 527 bearings that supported the superstructure. A carefully designed bearing layout produced a well-distributed axial load among the bearings. Considering this, an average design axial load was computed as 8663 kN. A total weight of 4572 MN would be isolated on a 103.6 m × 102.4 m upper mat, which includes the reactor, its containment building, and auxiliary buildings. Two bearing manufacturers produced full-scale test specimens based on this design parameter. The resulting specimens had significantly different design and ultimate displacement capacities.

Bearing manufacturers performed quality control tests on the test specimen before delivery. This data was utilized to create the analytical models used to predict seismic demands. Predicted demands were used to develop the test protocol described in Section 3.4.

2.2 UNISON BEARING

Three lead-plug rubber bearings (LPRB) produced by Unison eTech were designated as UET-1, UET-2, and UET-3. These bearings were 1500 mm in diameter and had a 320-mm-diameter lead core; see Figure 2.1. Thirty-two, 7-mm-thick rubber layers resulted in a total rubber thickness of 224 mm. These layers were sandwiched between 31, 7-mm-thick steel plates and 60-mm-thick end plates, resulting in a total bearing height of 527 mm.

A design shear strain of 100% produced a design displacement capacity of 224 mm. The zero-displacement force intercept, Q_d, was specified as 670 kN. Initial stiffness, K_1, and second slope stiffness, K_2, were calculated by Unison eTech to be 351 kN/mm and 3.4 kN/mm. These estimations agreed well with quality control test data provided by the manufacturer after the bearings were cycled three times to their design displacement; see Figure 2.2. The axial load applied during this test was 21,900 kN, a factor 2.5 times the design load. Results show a distinctly different initial quarter cycle force-displacement response; this cannot be analyzed using current models.

The measured axial force-displacement response is shown in Figure 2.3. This shows a nonlinear hardening response with minor hysteresis. Interestingly, the transition of the bilinear response occurs at the design axial load. This characteristic and the hysteretic damping are

important considerations for the axial load fluctuations caused by vertical excitation and overturning.

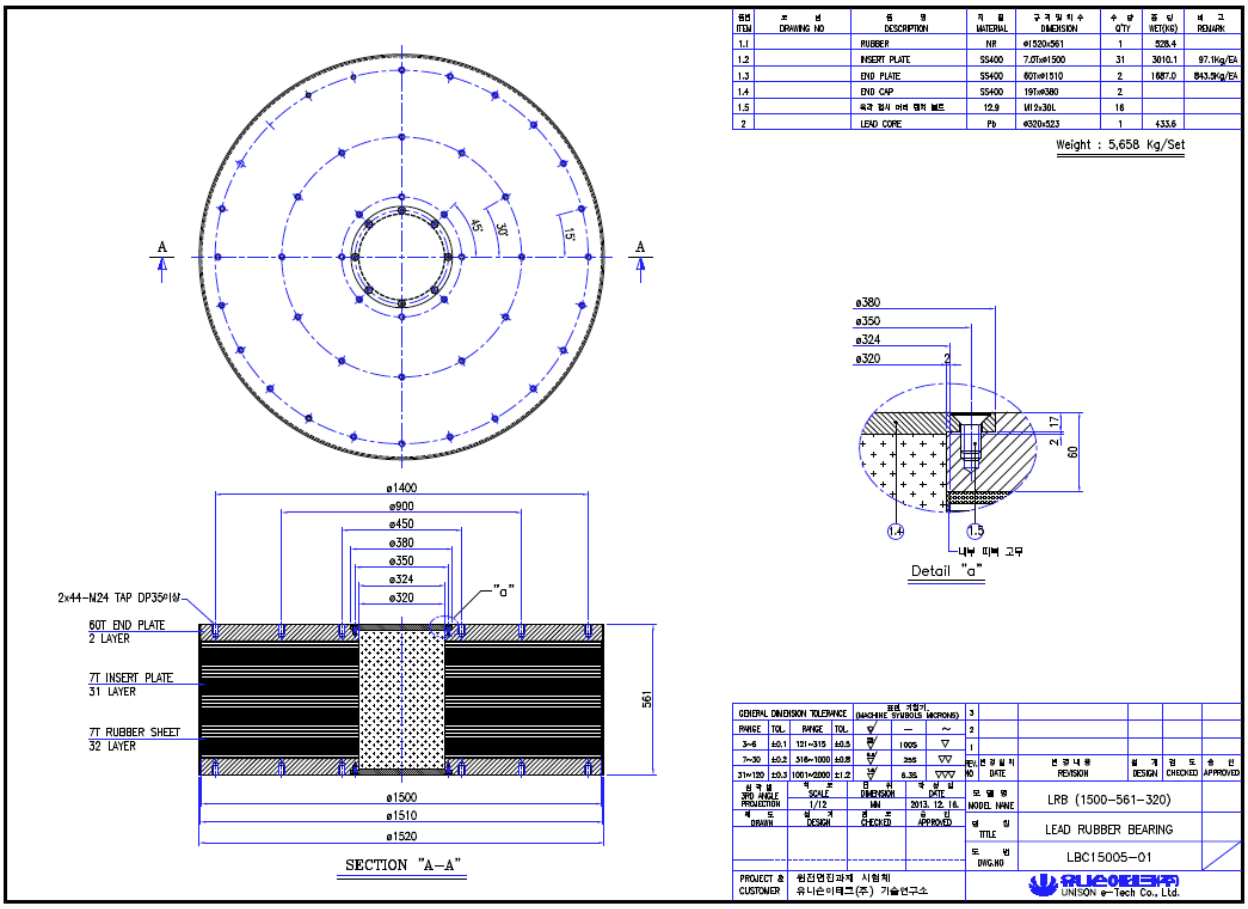

Figure 2.1 LPRB manufacturing specifications (courtesy of Unison eTech).

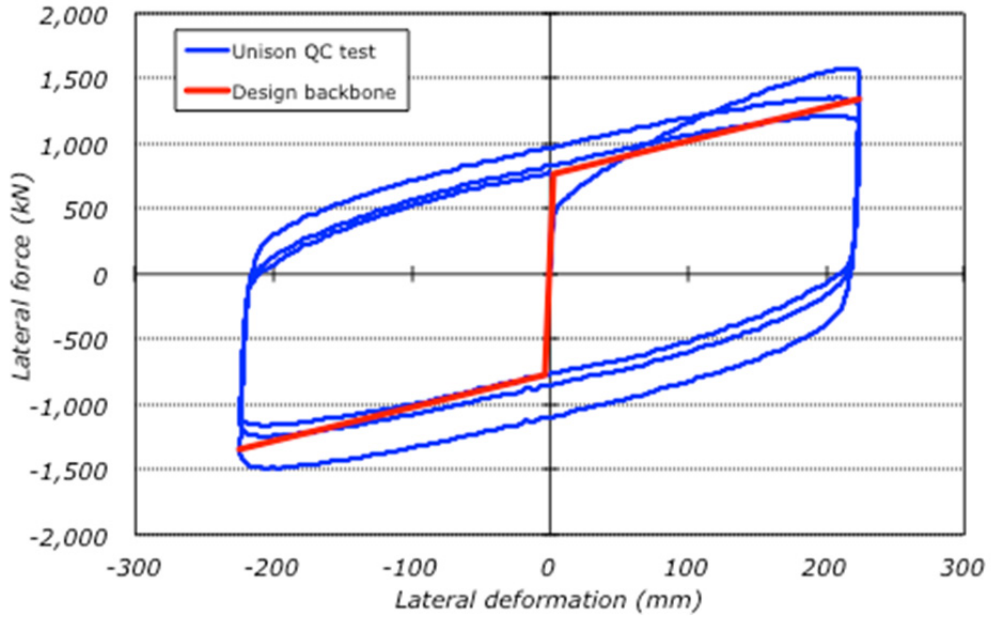

Figure 2.2 LPRB lateral quality-control test and design envelope.

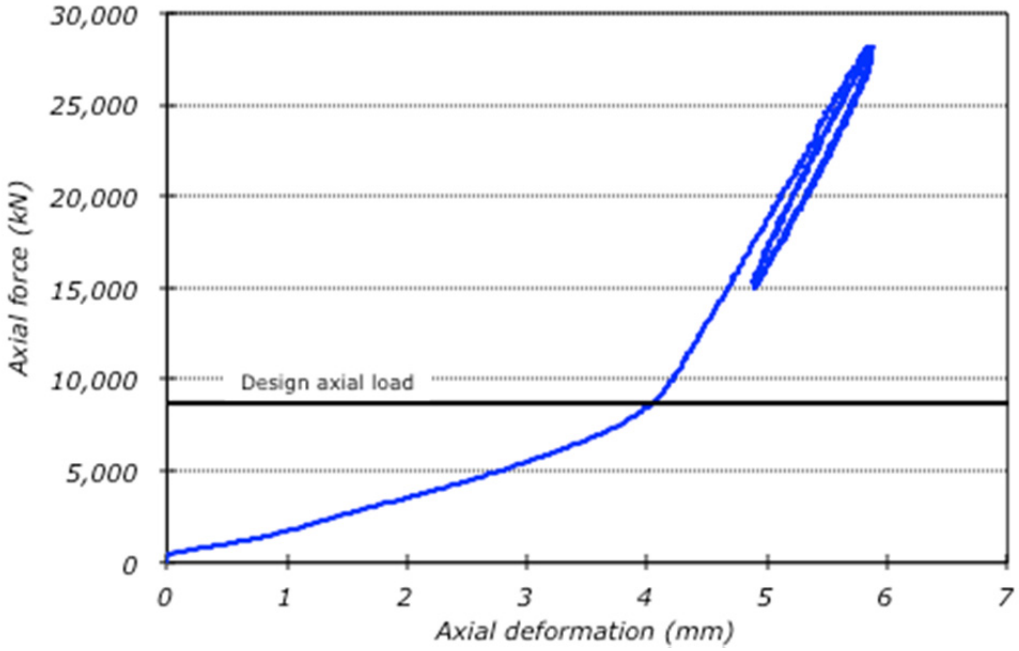

Figure 2.3 LPRB axial quality-control test.

2.3 ESCO RTS BEARING

Two bearings were provided by ESCO RTS for the test program. These bearings were EradiQuake System (EQS) isolators, that combine a flat slider with a restoring force generated by two horizontal, mass regulator (MER) compression springs; see Figure 2.4. The isolators had a low profile—only 474 mm high. The plan dimensions were 2110 mm × 2135 mm. The isolator consists of an upper sliding plate with stainless steel liner. A PTFE disk mates with the sliding

surface and sits in a recess of the middle plate. The middle plate is supported on a polytron disk that provides axial and rotational compliance. The polytron material behaves similar to rubber materials used in elastomeric bearing designs. Hence, derived mechanical properties can be calculated using a similar approach as is typical for elastomeric bearings. This disk sits on the lower plate that has a central shear key pin. The pin passes through a central hole in the polytron disk and locks the middle plate. The middle plate houses two guide rods per side that hold in place the MER springs. These compression springs react against vertical sliding plates attached to the upper plate. The vertical sliding plates are lined with stainless steel, and the ends of the MER springs have a PTFE liner to reduce lateral friction.

The manufacturer specified a nominally larger design axial load of 10,000 kN from the average axial load obtained from the seismic design. The design displacement specified by ESCO RTS was 120 mm. No axial quality control data was provided, but lateral characteristics were provided by the manufacturer, see Figure 2.5. The axial load applied during these tests was 10,000 kN. Response characteristics show the influence of stick-slip friction upon initial loading followed by a nonlinear hardening behavior due to the engagement of the springs. The spring stiffness exhibits hardening at about 60% of the design displacement. A peak force of 1120 kN was sustained before sliding initiated. After six cycles at the design displacement, the stabilized Q_d was approximately 620 kN, which is influenced by a dip in the force-displacement response as it crosses zero displacement. This is likely produced by the transition between compression springs on opposing sides. Pre-compression of the MER springs is not specified by the manufacturer, so unloaded springs disengage from their sliding surface. As they engage the sliding surface upon reloading, tolerances and the unloading strain rate of the MER spring on the opposite side are possible sources for this dip.

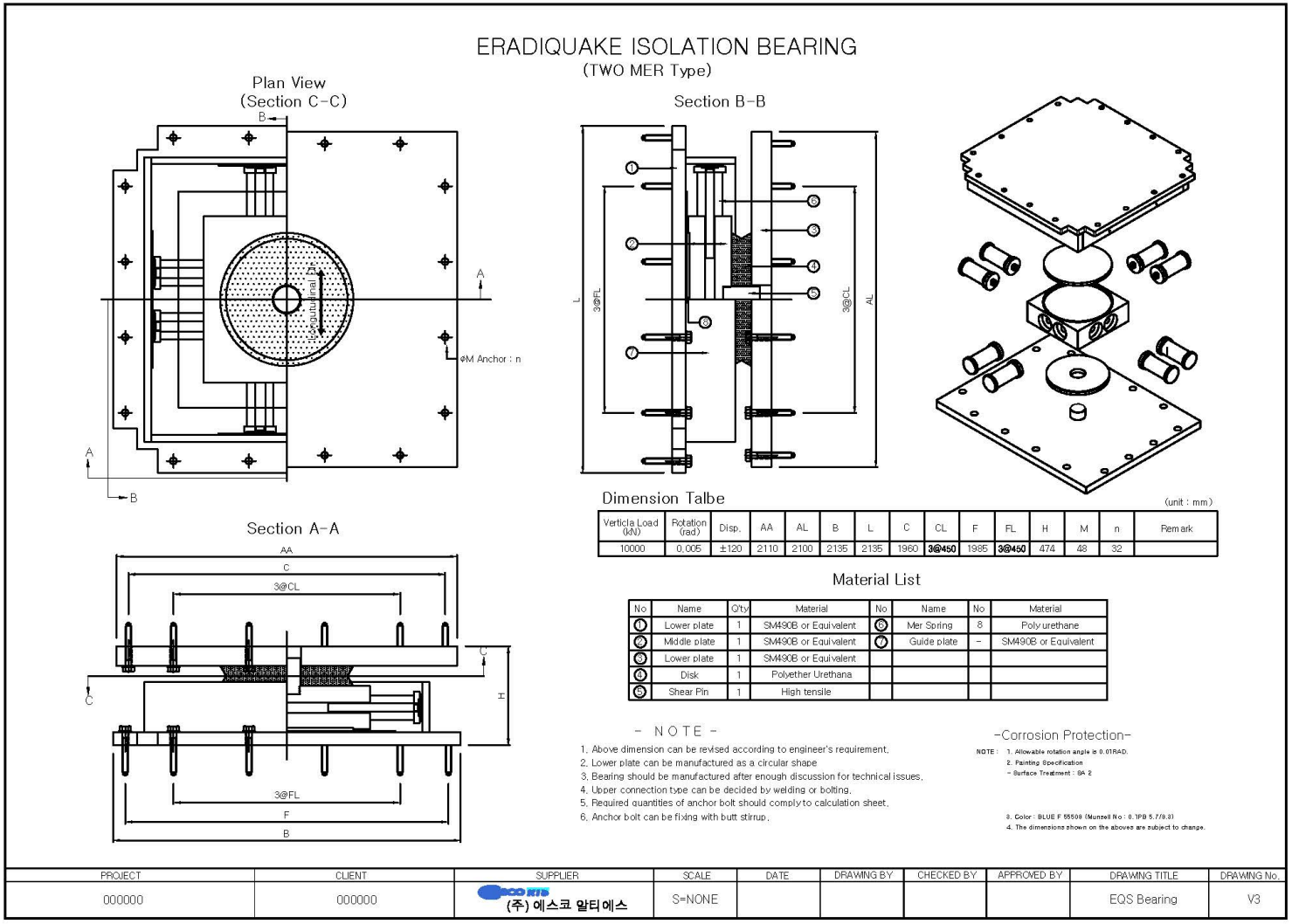

Verticla Load (kN)	Rotation (rad)	Disp.	AA	AL	B	L	C	CL	F	FL	H	M	n	Remark
10000	0.005	±120	2110	2100	2135	2135	1960	3@450	1985	3@450	474	48	32	

No.	Name	Q'ty	Material	No	Name	No	Material
①	Lower plate	1	SM490B or Equivalent	⑥	Mer Spring	8	Poly urethane
②	Middle plate	1	SM490B or Equivalent	⑦	Guide plate	-	SM490B or Equivalent
③	Lower plate	1	SM490B or Equivalent				
④	Disk	1	Polyether Urethana				
⑤	Shear Pin	1	High tensile				

PROJECT	CLIENT	SUPPLIER	SCALE	DATE	DRAWING BY	CHECKED BY	APPROVED BY	DRAWING TITLE	DRAWING No.
000000	000000	(주) 에스코 알티에스	S=NONE					EQS Bearing	V3

Figure 2.4 EQS bearing manufacturing specifications (courtesy of ESCO RTS).

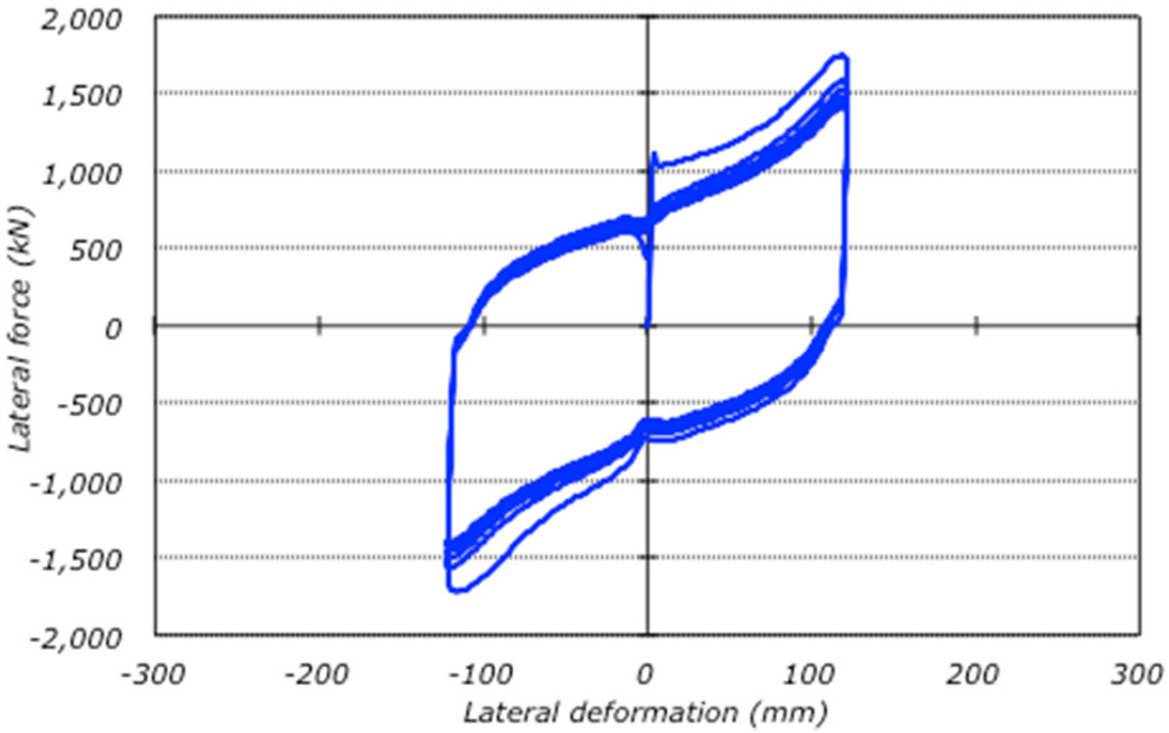

Figure 2.5 **EQS lateral quality control test.**

3 Experimental Tests

3.1 DESCRIPTION OF THE SRMD TESTING FACILITY

The Seismic Response Modification Device (SRMD) Testing facility at UCSD was designed for real-time six-DOF dynamic characterizations of full-scale bearing devices and dampers using predefined loading protocols; see Figure 3.1. The facility was developed jointly by the California Department of Transportation (Caltrans), the Department of Structural Engineering at UCSD, and MTS Corporation of Eden Prairie, Minnesota. Longitudinal and lateral displacement capacities of 1.219 m and 0.610 m, respectively, are more than 2.5 times the bearings' design displacements. The machine's axial load capacity, 53,400 kN, is well above the design gravity load and anticipated axial load demand induced by overturning moment. A summary of the machine's capacities is given in Table 3.1. testing facility

The testing system consists of a prestressed concrete reaction frame box surrounding a moving platen, connected by four horizontal actuators to the concrete box. The platen, 3.658 m wide × 4.750 m long, slides over four hydraulic hydrostatic low friction bearings attached to the floor of the concrete structure, see Figure 3.2. For improved stability, the platen also extends with four steel outrigger arms that support pairs (i.e., upper and lower) of low friction slide bearing actuators.

To expand the capabilities of the SRMD for the purpose of this project, the testing facility was adapted for hybrid simulation by utilizing existing, external command capabilities. For the project described herein, the SRMD was used for hybrid simulation of two types of large seismic isolators considered as an experimental substructure of a larger numerical model of a seismically isolated NPP.

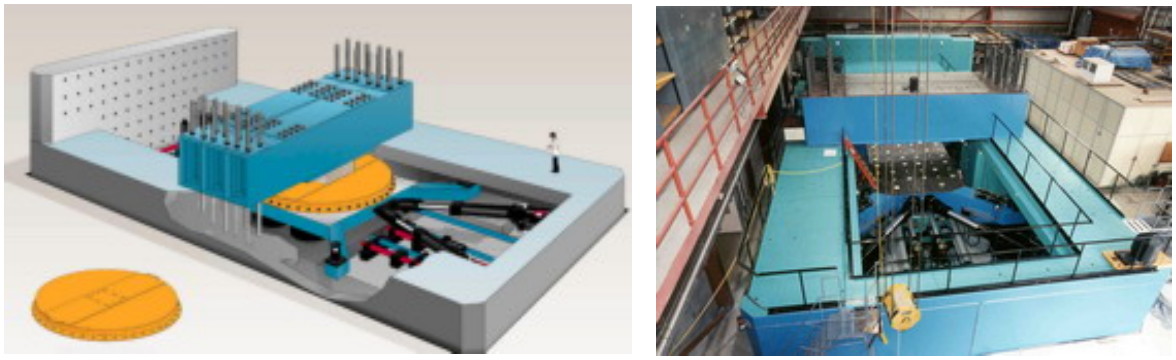

Figure 3.1 SRMD testing facility [UCSD 2014].

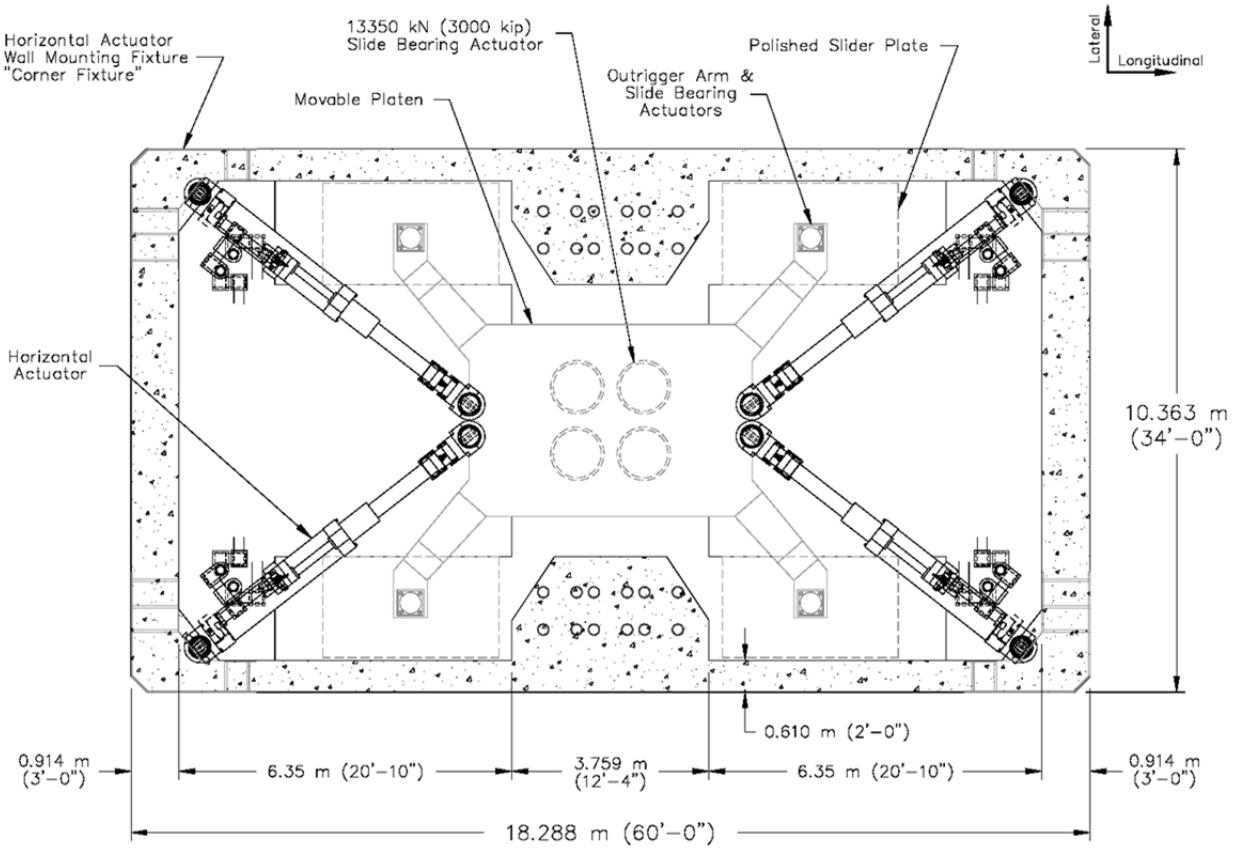

Figure 3.2 SRMD plan view.

Table 3.1 Testing machine technical specifications.

Component	Capacity	Accuracy of application	Accuracy of readout
Vertical force	53,400 kN	±5%	0.5% full range
Longitudinal force	8,900 kN		1.0% full range
Lateral force	4,450 kN		1.0% full range
Vertical displacement	±0.127 m	±2%	1.0% full range
Longitudinal displacement	±1.22 m	±2%	1.0% full range
Lateral displacement	±0.61 m	±2%	1.0% full range
Vertical velocity	±254 mm/sec	±10%	
Longitudinal velocity	±1,778 mm/sec	±10%	
Lateral velocity	±762 mm/sec	±10%	
Rotation (roll, pitch, and yaw)	±2°		

3.2 DEVELOPMENT OF HYBRID SIMULATION AT SRMD TESTING FACILITY

While the SRMD was not originally designed with the intent of conducting hybrid simulations, it includes different software and hardware components as well as communication links that allow for this adaptation. Each of these components needs to be fast, reliable, and able to communicate with each other and external hardware. Limitations in performance of the SRMD facility such as actuator delay and the speed of communication will determine the rate of testing that can be achieved.

In general, a hybrid simulation requires a computational driver to solve the equations of motion of the hybrid structural model, using time-stepping integration algorithms. The hybrid model needs to be linked to the experimental subassembly, which is loaded by the SRMD. Thus, the hybrid model needs to communicate with the SRMD control system in each integration time step. In order to achieve continuous communication with the SRMD controller, the architecture shown in Figure 3.3 was proposed that included a computational driver, the SRMD control system, and a real-time Digital Signal Processor (DSP) to communicate between the digital computers and the analog input/output of the SRMD control system. The different components of this hybrid simulation system are discussed in the following sections.

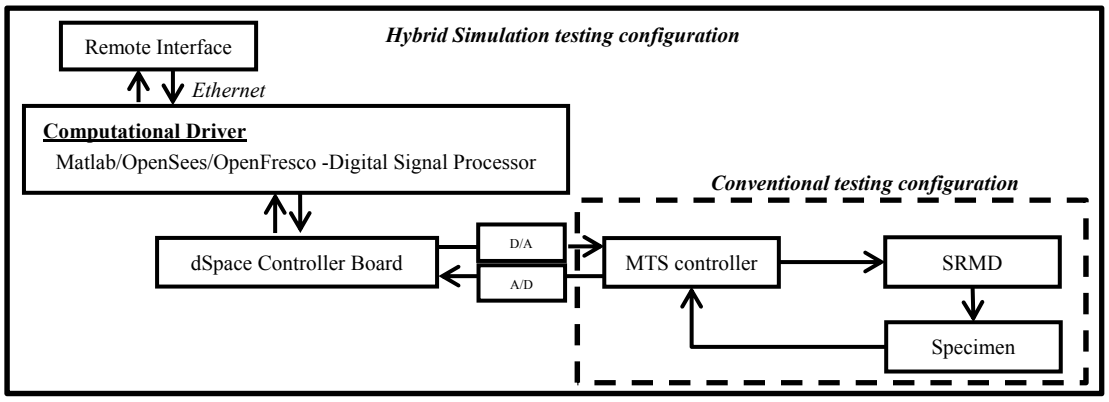

Figure 3.3 Hybrid simulation hardware configuration.

3.2.1 Hybrid Simulation Hardware Components

Hybrid simulation requires that customizable hardware components communicate between the computational driver, which solves the hybrid model consisting of numerical and experimental subassemblies, and the controller in the laboratory loading the experimental subassembly. Figure 3.4 illustrates the implementation of the hybrid set-up on top of the SRMD conventional configuration. The SRMD controller is used in a manner similar to conventional cyclic dynamic testing except that instead of providing a predefined loading signal, the longitudinal and lateral displacement commands and the vertical force command are external reference signals being computed as the simulation progresses.

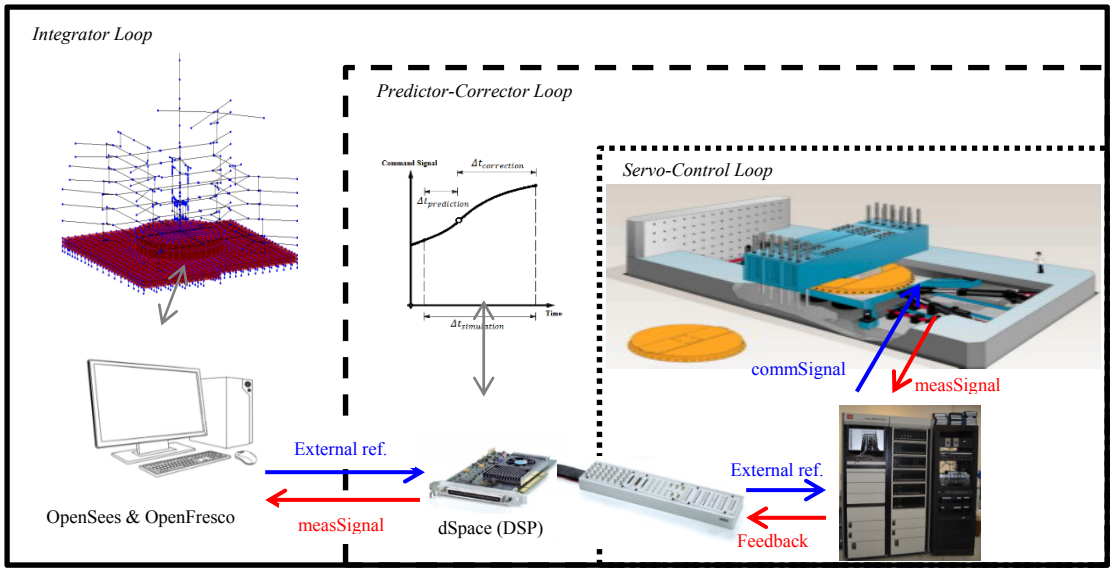

Figure 3.4 dSpace experimental control.

3.2.1.1 Digital Signal Processor for Real-Time Signal Generation

A real time digital signal processor (DSP) is used in the test set-up consisting of a dSpace ACE 1104 Hardware Kit [dSpace 2013]. The ACE 1104 Hardware Kit consists of a DSP processor on a PCI card with a Connector Panel with 16 BNC connectors. The connector panel has eight ADC inputs (Analog to Digital Converters), four with 16-bit resolution and four with 12-bit resolution, and eight DAC outputs (Digital to Analog Converters) with 16-bit resolution via BNC connectors. The dSpace DSP is used for signal generation; it sends commands and receives feedbacks at 1000 Hz (1 millisecond), which is identical to the rate of operation of the SRMD controller.

The dSpace command signals were calibrated to the same volt-displacement/force ratio as the command displacement/force of the SRMD facility for each DOF. In hybrid simulation, the digital control signals generated by the predictor-corrector algorithm running on the dSpace DSP are then converted to analog signals before transmitting them to the SRMD control system. With the Real-Time Interface (RTI) software, Simulink models can easily be run on the DS 1104 R&D Controller Board. Also, users are able to configure all I/O graphically, insert the blocks into a Simulink block diagram, and generate the model code via Simulink Coder (formerly Real-Time Workshop). The real-time model is then compiled, downloaded, and started automatically, thus reducing implementation time to a minimum.

3.2.1.2 MTS Controller for SRMD Machine

The SRMD is a six-DOF table system governed by movements of its collective actuators. This facility was primarily designed to have large displacement capacity with relatively high velocity as well as high load capacity. Each actuator is controlled using multi-stage closed-loop control principles, where the inner loop controls the poppet valves and the outer loop controls actuator displacements. Four-stage poppet valve assemblies are used in place of more traditional multi-stage servo-valves typically used in structural testing to provide the high volume of oil needed to facilitate movement of these actuators at the expense of more accurate control.

Each actuator in the SRMD test system is controlled using a Proportional and Integral (PI) closed-loop displacement controller. In addition, the digital real-time controller provides overall closed-loop control of the six degree-of-freedom system motion (DOF control). The controller also provides programming and feedback summing capabilities to guarantee an accurate reproduction of the desired waveform on top of the platen surface. The control hardware architecture is based on Digital Signal Processing technology that optimizes the performance of embedded control system, and allows for implementation of advance control and data filtering operation. The digital controller provides the following features: DOF control, displacement control, and force balance.

There are six controllable DOFs: vertical, lateral, longitudinal, yaw, pitch and roll. In addition, because there are eight actuators being controlled, there are two "internal" DOFs designed to maintain control of the system. The vertical force on a test bearing is controlled through a cascade control loop. The primary vertical control mode is displacement, while force is applied and controlled through an integrator dominated control loop.

3.2.1.3 Signal Conditioner

Sending feedback from the SRMD to the computational driver requires extracting signals in analog form using D/A (digital to analog) converters that are built into the SRMD. This D/A conversion introduced noise spikes in the feedback signal received by dSpace, which was resolved by adding signal conditioners (analog conditioning); see Figure 3.5. These spikes in the feedback signals were also observed through an oscilloscope, which was used to verify that the analog output was noisy and related to the output generated by the SRMD; see Figure 3.6. Digital filtering was another option to remove those glitches in the feedback signal. Using Moving Median and Moving Average digital filters within the Simulink model helped but did not solve the problem completely.

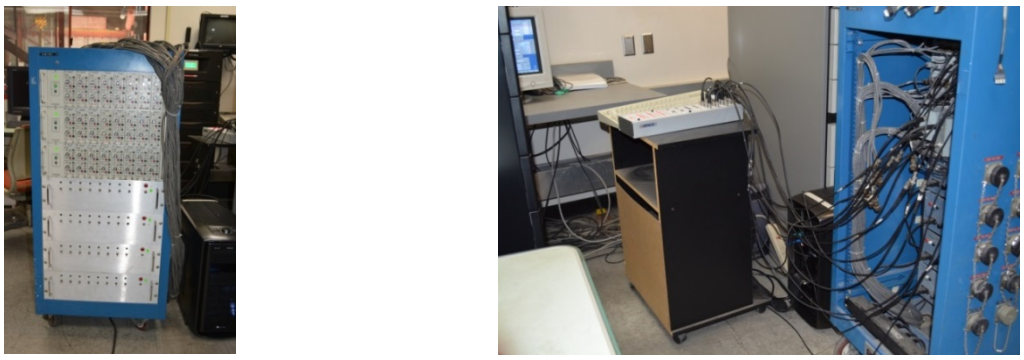

Figure 3.5 Analog signal conditioning for the feedback signal.

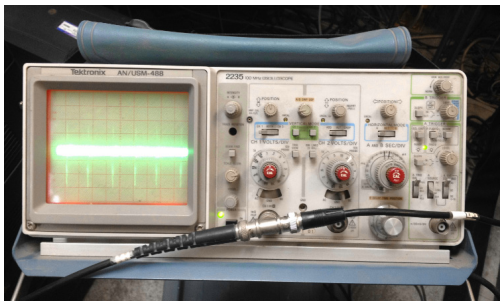

Figure 3.6 Noise in the feedback signal from the SRMD.

3.2.2 Hybrid Simulation Software Components

Integrated software and hardware is necessary to be able to conduct hybrid simulations in the laboratory. In general, a fast computational solver needs to communicate with the laboratory's controllers through a middleware that bridges numerical and physical portions of the hybrid simulation testing system. These software components need to communicate with each other throughout the test. The key software components for a hybrid simulation as implemented at the SRMD facility for this test series are described below.

3.2.2.1 OpenSees

OpenSees, the Open System for Earthquake Engineering Simulation, is a software framework for simulating applications in earthquake engineering using finite element methods, developed in 1997 by PEER. OpenSees has advanced capabilities for modeling and analyzing the nonlinear response of systems by using a wide range of material models, elements, and solution algorithms. OpenSees is an object-oriented software, implemented in C++ through an open-source development process; it is designed for parallel computing (OpenSees*SP*) to allow for scalable simulations on high-performance computing platforms or for parameter studies [OpenSees 2014]. Using OpenSees*SP* for hybrid simulation provides researchers with the ability to test the physical specimen in the laboratory, together with complex and nonlinear numerical models of structures with many DOFs at a faster rate. OpenSees is readily adaptable for hybrid simulation through a middleware component, OpenFresco.

3.2.2.2 OpenFresco

OpenFresco (the Open-source Framework for Experimental Setup and Control) is an environment-independent software framework that connects finite element models with control and data acquisition systems in laboratories to facilitate hybrid simulation of structural and geotechnical systems. OpenFresco standardizes the deployment of hybrid simulation and extends its capabilities to applications with advanced numerical techniques by providing an interface for different software and laboratory equipment [OpenFresco 2014].

3.2.2.3 Real-Time Predictor-Corrector

The SRMD control system runs at a rate of 1000 Hz, updating the actuator commands in each cycle at this rate. For smooth control and movement of the actuators, the commands to the actuators from the hybrid controller should be updated at the same exact rate. However, the numerical portion of the hybrid simulation may not be running in a real-time environment and

could require variable calculation times often exceeding the 0.001 sec/step to calculate the new target value for the control system. Therefore, a real-time Predictor-Corrector is needed to generate smooth signals updated at the same rate as the actuator controller while receiving displacement commands from the numerical model at a non-deterministic rate.

The Control Desk dSpace environment allows running real-time applications generated from Simulink and Stateflow models; see Figure 3.7. Simulink is a block library tool for modeling, simulating, and analyzing dynamic systems. Combined with Simulink Coder (formerly Real-Time Workshop) [Mathworks 2013] in the MATLAB environment it can generate C code for the real-time implementation of systems. Stateflow is an interactive design and simulation tool for event-driven systems. All these tools are used to create the event-driven real-time Predictor-Corrector algorithm used for continuous hybrid simulation. [Mosqueda et al. 2005; Schellenberg et al. 2009]. While receiving displacements from the numerical model, a polynomial is fitted to the displacement commands to generate a continuous command signal at the desired rate. The order of the fitted polynomial can simply be changed in the state-flow coder diagram (see Figure 3.7) before executing a hybrid test. For these simulations, first and second order polynomials were used.

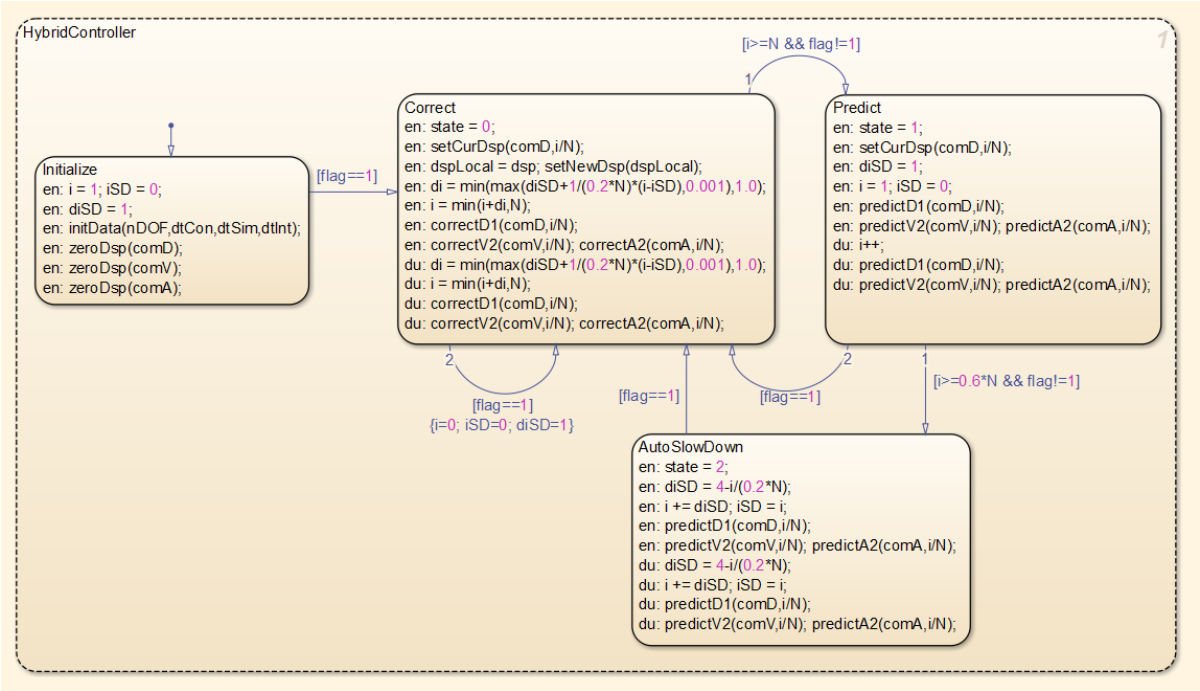

Figure 3.7 Predictor-corrector [Schellenberg et al. 2009].

3.2.3 Preparations for Hybrid Test

Before performing hybrid simulation in the laboratory, a few preliminary checks are required to make sure that different components are communicating properly and that the feedback signals to the numerical model are accurate. In this case, feedback signals consisted of the shear forces generated in the bearing.

3.2.3.1 Calibration

Numerical models calculate the command signals for the laboratory controller. These numerical values need to be converted to corresponding voltage through different gains based on the settings in the controller, shown schematically in Figure 3.8. The dSpace controller board (DS1104) has a ±10 volts input and output voltage range, which is the same as the MTS controller voltage range in the SRMD. Based on the output voltage and the resolution of each channel, the noise level for each DOF can be calculated. Table 3.2 shows D/A and A/D channels of the dSpace controller board connected to the MTS controller. The SRMD machine internal units are U.S. ton (ton short) for force, inches for displacement and degree for rotational DOF. Unit conversions from the hybrid model using [kip, ft, and rad] to the SRMD machine units of [ton, in., and] are performed through scale factors that can be specified for the experimental set-up in OpenFresco.

Signal calibration was based on a linear fit on each DOF calculated from Equation (3.1). This calibration, which did not need the machine hydraulics powered on, was done by comparing values for each DOF from the SRMD controller and the dSpace control desk experiment. Calibration points were selected at zero, ± half span and ± full span for longitudinal, lateral, roll, pitch, and yaw. For compression force, points were checked for five different values. Linear regression was applied and proper gain value [Equation (3.2)] and required offset voltage [Equation (3.3)] were added to command reference signals sent to and feedback coming from the MTS Controller. Table 3.3 is an example of the values obtained for the longitudinal displacement DOF.

$$\text{Linear Fit}: \; y = ax + b \tag{3.1}$$

where x and y are dSpace and SRMD readings; and

$$\text{Gain} = 1/a \tag{3.2}$$

$$\text{Offset} = -b/a * 10 \text{ volts} \tag{3.3}$$

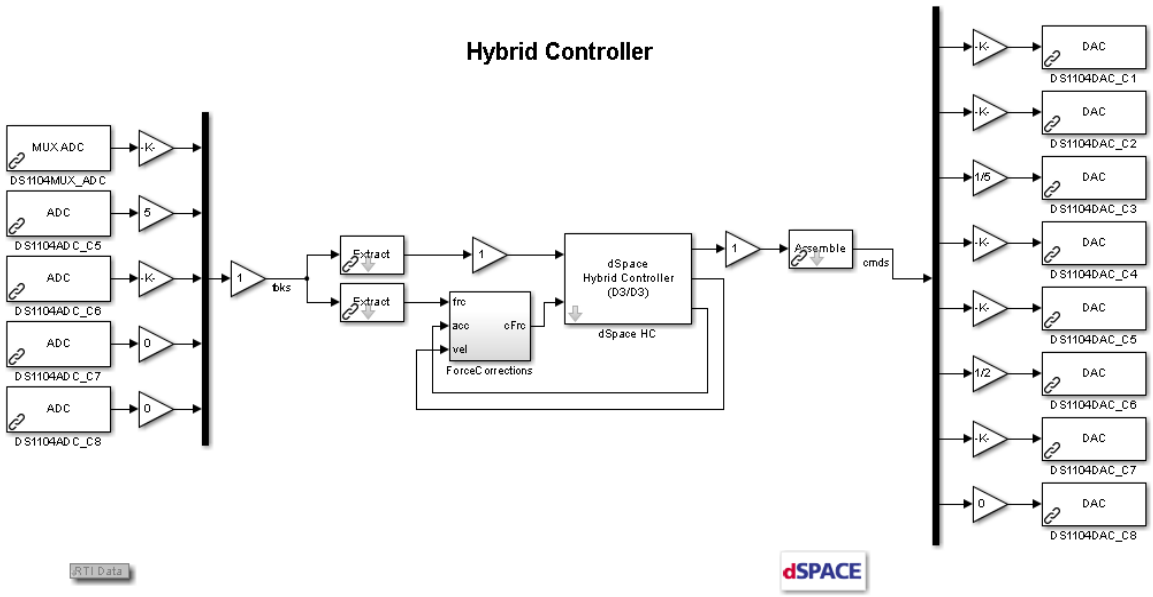

Figure 3.8 Hybrid controller configuration.

Table 3.2 Voltage conversion units for different channels.

Feedback (ADC)	Conversion	Reference (DAC)	Conversion
Longitudinal displacement (mm)	1219.2	Longitudinal displacement (mm)	1/1219.2
Longitudinal force (kN)	21016.8	Lateral displacement (mm)	1/609.6
Lateral displacement (mm)	609.6	Vertical displacement (mm)	1/127
Lateral force (kN)	16418.9	Roll (°)	1/2.25
Vertical displacement (mm)	127	Pitch (°)	1/2.25
Vertical force (kN)	70977.8	Yaw (°)	1/2
-	–	Vertical force (kN)	1/70977.8

Table 3.3 Signal calibration for longitudinal displacement.

Long. displacement (mm)				
Before calibration			After calibration	
SRMD	dSpace		SRMD	dSpace
-609.27	-609.85		-609.27	-609.35
-304.42	-304.55		-305.26	-305.44
-0.71	-0.51		-0.71	-0.79
303.91	304.29		303.56	303.86
608.46	609.60		609.02	608.89

offset	-0.00167
gain	0.998702

3.2.3.2 Limiter Settings for Magnitude and Rate

Magnitude limits (*magnlimits*) are set based on (1) the capacity of the machine; and (2) the limits that the SRMD machine operator has specified on the machine's control system to make sure that the command signals from the Simulink Predictor-Corrector model do not exceed certain values. This is necessary for safety reasons as both the equipment and the specimen can be damaged at certain levels. Typically, longitudinal and lateral displacement and vertical force are the DOFs that are controlled in a hybrid test of a bearing with the SRMD. The displacement and force limits were specified as shown in Table 3.4.

Velocity limits (*ratelimits*) are also important for the safety of the laboratory equipment, which caps the maximum rate at which the command signal is ramped to a certain values. If this rate cap is reached during the test, a command signal will continue to increase at the maximum allowable rate with constant velocity until it is able to catch up to the signal, which often occurs during load reversal. This value should be set slightly larger than the maximum expected velocity during the test, but can be an effective safety measure if the simulation becomes unstable and provides an excessively large command. The *ratelimits* set for the SRMD were as follows:

- Longitudinal displacement: 2540 mm/sec
- Lateral displacement: 2540 mm/sec
- Vertical force: 17,780 kN/sec

These *ratelimits* need to be modified when the testing rate (Simulation Time Step/Integration Time Step) is changed. Implementation of the magnitude and velocity limiters is schematically shown in Figure 3.9.

Table 3.4 Magnitude limits for different degrees of freedom.

	Full Stroke/Capacity	***magnlimit***
Longitudinal Displacement	±1219.2 mm	±787.4 mm
Lateral Displacement	±609.6 mm	±533.4 mm
Vertical Force	79476.6* kN	[+31,115 and -31.115] kN

* Compression is positive and tension is negative for the machine.

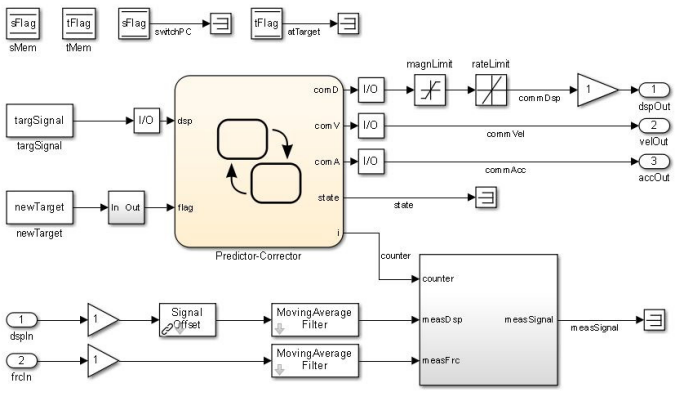

Figure 3.9 Applying the limits on the command signals.

3.2.3.3 Delay Check

Delay is another important parameter in hybrid simulation that needs to be considered. In general, delay is the time difference between the command signal from the real-time machine and what it measures as the response to that signal. The machine by itself has roughly 32 milliseconds of internal delay, but the built-in D/A converters introduce additional delays. By the time the measured signals are available in the dSpace Predictor-Corrector model, delays on the order of 100 milliseconds were observed. Implementing more advanced control strategies, such as adding feed-forward control, will help reduce this delay.

Different delay values for different DOFs

It is possible to have different delays for each DOF in multi-DOF systems. Compensating by a single time value for all DOFs may result in the actuators moving out of sync and exciting the higher modes in the system, especially in real-time testing and should be avoided. Also, in the SRMD facility, the vertical DOF is controlled in force control mode, while the other DOFs are controlled in displacement control mode. Thus, there can be large differences in the delay for the vertical DOF in comparison with the other two horizontal DOFs. Even the two horizontal displacement DOFs have been observed to have different delay times. Therefore, compensating for the proper delay in each DOF is necessary. A few changes have been made in the Simulink model to implement different delay values in the hybrid controller model, as shown in Figure 3.10.

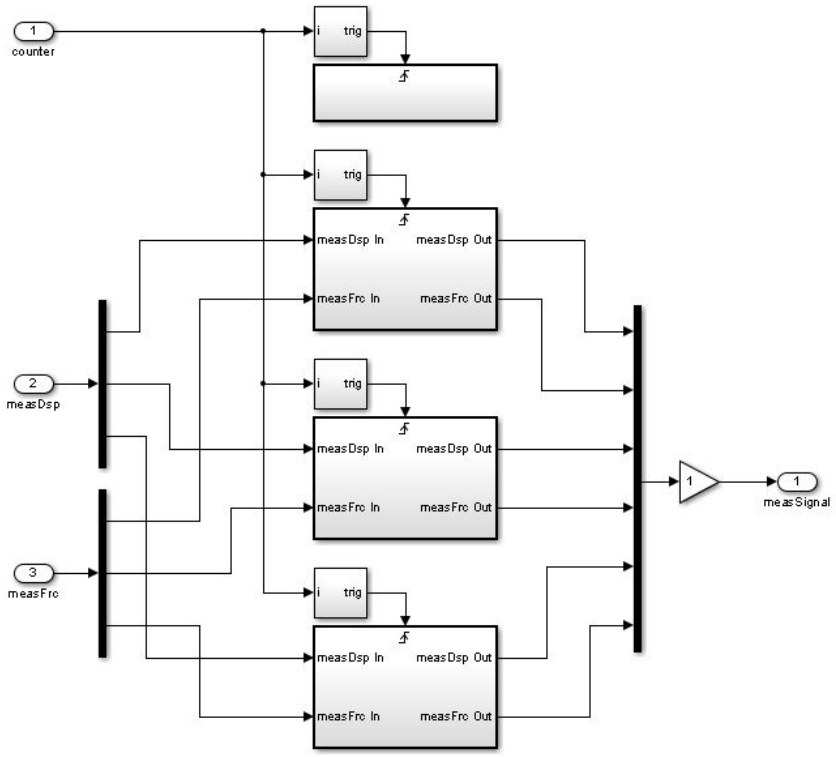

Figure 3.10 Delay model in simulink.

Feed-forward gain

Although the rate of testing for hybrid simulation is determined by different parameters, it is primarily governed by the computation time of the numerical model and the delay in the actuator system. One way to reduce the delay in the set-up is to use more advanced control strategies, such as adding an additional feed-forward gain control parameter. In the feed-forward control strategy, the derivative of the command signal is multiplied by the feed-forward gain and added directly to the servo-valve command signal. Basically, the command signal tries to predict the next value by using the current velocity, which can be problematic especially for higher frequency signals. Therefore, special caution is required when the controller uses this compensator.

The control system for the SRMD had this gain internally implemented, but because it was not useful for conventional testing, this feature had been deactivated on the operator interface to the system. Reintroducing this feature into the controller user-interface and tuning the system for feed-forward gain resulted in a significant improvement in performance; see Figure 3.11. The feedforward gain eliminated the delays in longitudinal and lateral DOFs, which were previously 110 and 105 milliseconds. With this improvement, the rate of testing was brought down from 25 times slower to five times slower than real time. The complexity of the numerical model required significant computational time to calculate the new target value and required substantial time to write results to the solid-state drive, which limited the rate of testing to five times slower than real time. Since the delay in the SRMD can be nearly reduced to zero, it is likely that real-time testing can be achieved for a simple computational model if the delays in the analog converters can be eliminated.

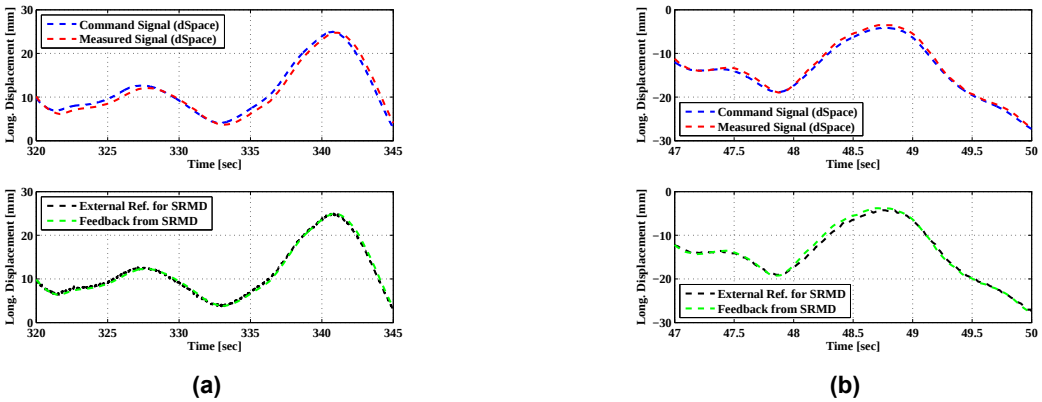

Figure 3.11 Tracking signal for delay: (a) no feed-forward and (b) with feed-forward.

Unfortunately, this feed-forward gain was not helpful in the vertical direction because the control system in the vertical direction is mainly in force control mode. Therefore, one-dimensional (1D) or two-dimensional (2D) hybrid testing (controlling translational DOFs in longitudinal and/or lateral direction) were conducted relatively quickly while three-dimensional (3D) hybrid tests (controlling the vertical force on the bearing as well as horizontal displacement DOFs) had to be run at a slower rate. Furthermore, the feed-forward gain was not implemented until late in the test program. Therefore, tests on the Unison bearings and the first ESCO RTS bearing did not take advantage of this important feature.

3.2.4 Compensation for Friction and Inertia Force

Feedback forces in the SRMD controller are obtained from load cells on the actuators. The measurements include not only the resisting forces in the bearing but also the friction and inertia forces of the table. Therefore, before sending back these feedback signals as restoring forces to OpenSees, some correction is required to remove these additional forces from the measured signal. In order to return a corrected value during the test, a model was developed in an effort to compensate for friction and inertia online (on-the-fly). In all previous cyclic testing of bearings on the SRMD, these effects are corrected during post-test analysis, often by subtracting the measured forces from an empty table run of the same motion. While an empty table run should ideally provide zero shear-force readings in the absence of friction and inertia, large forces on the order of 5 tons have been observed due mainly to friction by sliding on the vertical actuators and outrigger supports of the table, as well as inertial force of the table mass during fast tests with significant accelerations. The friction model, schematically shown in Figure 3.12, was calibrated by trying to reduce the measured force to zero during empty table runs.

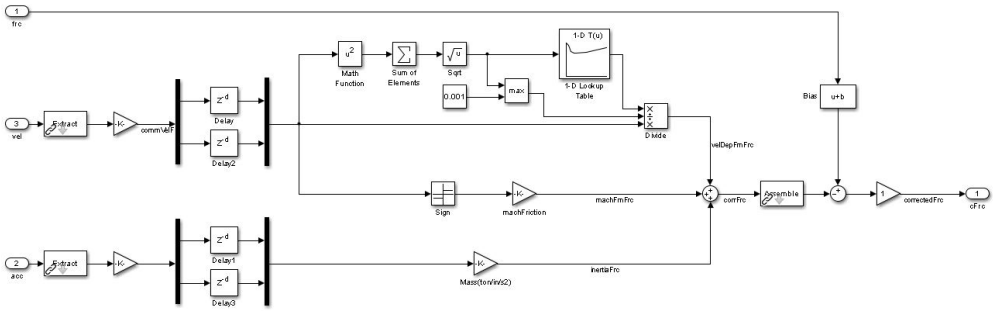

Figure 3.12 Model schematic to correct for friction, inertia and offset.

3.2.4.1 Friction Force Dependent on Velocity

Previous studies of the SRMD have identified the dependence of the friction force values with velocity as shown in Table 3.5 and Figure 3.13. In addition, the friction forces have been found to be dependent on the direction of sliding; e.g., the longitudinal and lateral directions indicate different friction values. Two different assumptions can be made to estimate the friction forces.

1. Use the square root of sums of squares (SRSS) of both (longitudinal and lateral direction) velocities to calculate the peak velocity dependent friction force and then distribute them based on their magnitude, neglecting the dependence on the direction; and
2. Calculating the corresponding friction force for each horizontal DOF based on its own velocity.

Based on several experiments, the second approach was found to be more appropriate in correcting for friction. Calculation of velocity and the application of any filter in displacement will add additional delays in the signal. It was first attempted to calculate velocity directly from the measured table displacements and/or accelerations, but the resulting signal turned out to have significant noise. Alternatively, the velocity was calculated based on the command signal sent to the controller from Simulink. However, the command is not guaranteed to be in phase with the actual motion of the table due to delays. To make sure that friction correction is applied with proper delay compensation, some empty table runs were first examined in the expected range of velocity. First, a few parameters were set, including the velocity at which to cap the maximum friction force. In order to simplify the model, a cap was assumed below a certain threshold velocity since the static friction force was not possible to capture. Also, to avoid big jumps in the force feedback, especially at displacement reversals when the velocity changes its sign, the friction force was set to zero below another threshold value. This is also beneficial during free vibration at the end of the experiment when the velocity is oscillating and large changes in the friction force would cause high-frequency noise in the measured signals sent back from Simulink to OpenSees.

Note that when one-directional testing is performed in the laboratory, velocity from the other DOF should be set to zero. The reason for this is because the noise in the calculated velocity can be very large even though the displacement is small. This large velocity noise in the perpendicular direction will change the calculation of the friction force, leading to erroneous compensation for friction due to the velocity. compensation for friction due to the velocity.

Table 3.5 Approximate friction force versus instantaneous velocity.

Instantaneous velocity (mm/sec)	Friction force (kN)
0.0	0.0
0.3	0.0
0.5	33.5
3.0	33.5
4.1	33.5
5.1	33.5
62.0	30.5
110.0	25.0
199.9	23.3
254.0	23.3
500.1	24.2
1000.0	28.3

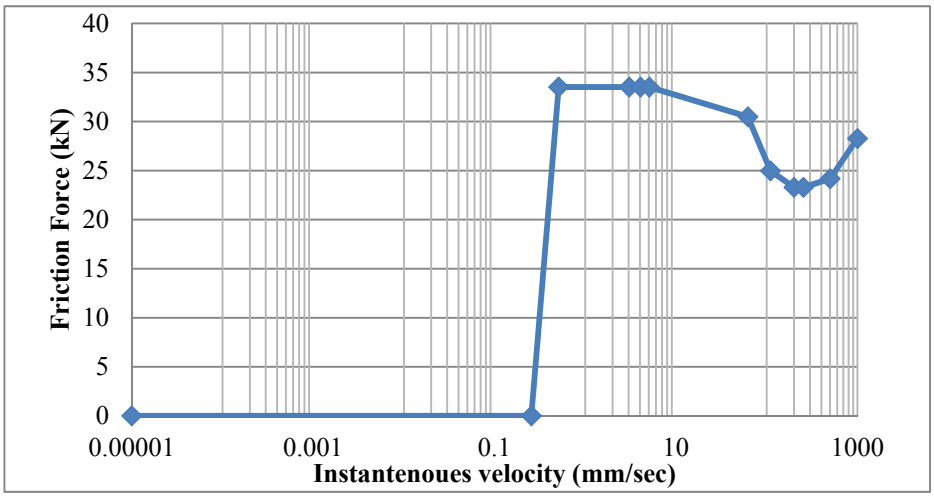

Figure 3.13 Friction force for different instantaneous velocity values.

3.2.4.2 Friction Force Dependency on the Vertical Load on the Table Support Bearings

A study by Spangler Shortreed et al. [2001] demonstrated that there is also another source for friction force, which depends on the vertical load in the machine. Movement of the platen will involve nine different friction surfaces, eight on outrigger actuator contact surfaces and one for the four vertical actuators beneath the table platen, see Figure 3.14.

This vertical load dependent friction force is a function of the direction of motion, outrigger forces, overall vertical load, and lift pressure. Based on the expected vertical load on the bearing during the hybrid simulations, constant single values can be calculated for different directions. If there had been enough channels available in the ADC controller board on the dSpace, this vertical load dependent friction force could have been calculated at each time step, and updated values could have been used for the correction; however, variations of this portion of the friction force were found to be negligible for these tests.

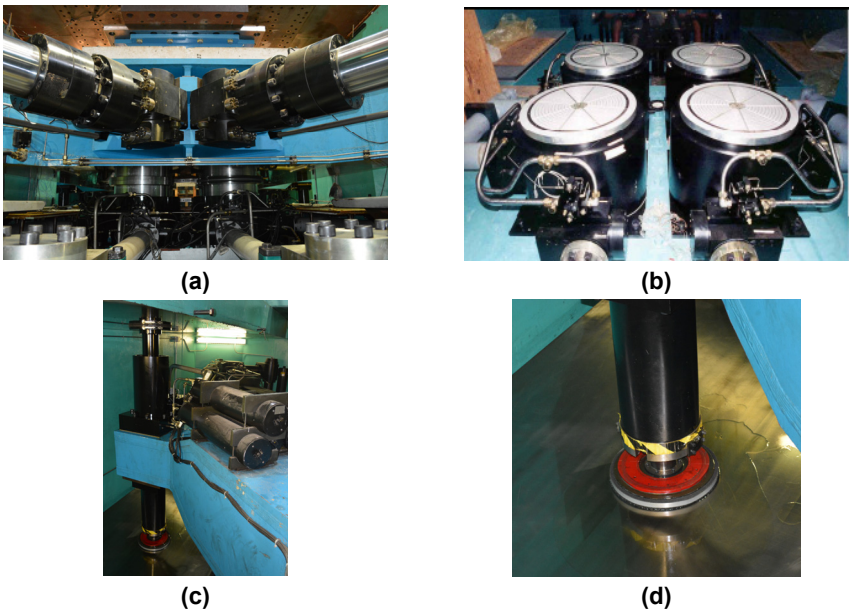

Figure 3.14 **Machine contact surfaces: (a) and (b) are he vertical actuators; (c) and (d) are the outriggers.**

3.2.4.3 Inertia Force

Inertia force also needs to be considered for fast hybrid testing. To calculate the inertia force, the effective mass of the set-up consisting of the weight of the specimen, platen and also the actuator pistons and the accelerations of the table in each direction are estimated. In these tests, accelerations were calculated through the Predictor-Corrector algorithm to obtain a smoother signal, similar to the calculation of velocities for the friction correction. The effective mass of the table can change for different set-ups and for different specimens. Bare weight of the machine for this specific test set-up was measured to be 1226.8 kN. Effective mass of the machine can also be estimated with system identification techniques discussed in the following section.

3.2.4.4 Initial Offset

Observations during testing with the SRMD found that there may be signal offsets in the measured forces by the controller. These offsets can be caused by drifts in the instrumentation with temperature or many other sources. There appears to be similar offsets in the measured raw data before correction is applied in all the tests performed in the SRMD laboratory. In order to resolve this issue, some maintenance or further calibration of the load cells may be required. Figure 3.15 shows the schematic of the SRMD for the calibration.

- General offset on the force
  - 11.55 kN in the longitudinal direction
  - 8 kN in the lateral direction

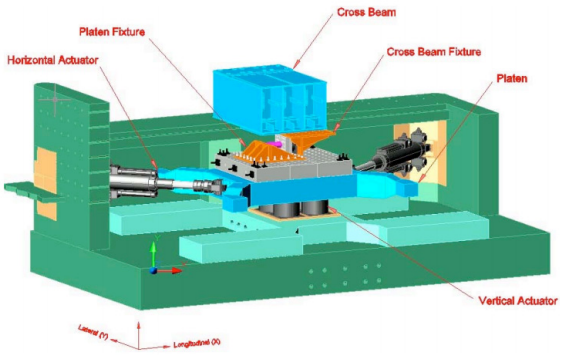

Figure 3.15 Schematic of SRMD machine for the calibration.

3.2.5 Pre-Test Checks

Pre-test checks required before hybrid simulations included:

- For a hybrid simulation in 1D:
  - Set the velocity for the other translational DOF to be zero. Otherwise this could cause high-frequency noise in the friction correction model creating incorrect and noisy compensation of the feedback signal, which in turn introduces spurious high-frequency noise in the numerical model.
- For a hybrid simulation in 2D:
  - Different delay values may need to be considered for each DOF based on the machine's controller settings as these affect table response performance.
- For a hybrid simulation in 3D:
  - The SRMD machine operates in force control mode for the vertical DOF. Delay compensation and control gains must be determined for the vertical force DOF.
  - Safe and appropriate rate limiter settings must be determined. Special consideration is given for the case that vertical ground motion is also applied.
- To prevent movement of the machine during gravity load application, the reference signal span needs to be set to zero until gravity is applied. Due to the gravity load in the model, a small deformation may result in either the lateral or longitudinal direction. This is within the noise level of the machine and can cause errors if the control system attempts to execute such low-level commands, so control of the machine should be taken after applying gravity.

- Any change in the machine settings (i.e., poppet-valve overlaps) will change the behavior of the machine, which means pre-test preparation such as delay calculation should be redone. Therefore, it is recommended to keep the same setting for the entire hybrid simulation test sequence.

3.3 TEST SET-UP

3.3.1 Hybrid Infrastructure

As described in the previous section, several components are necessary to conduct hybrid simulations with the SRMD. Figure 3.16 shows the different components and their line of communication with each other. The numerical model is programmed in OpenSees*SP* to solve the governing equations of motion at each integration time step for the hybrid model. OpenSees*SP* calculates new target displacement values for the next time step, and it sends these to all elements (including numerical elements and to OpenFresco, which is the link to the experimental subassembly). OpenFresco transforms the target signals to actuator DOFs and then communicates with the real-time DSP running the Simulink model of the hybrid controller. This Simulink model running on dSpace is able to generate smooth command signals by updating an analog output signal each 1 millisecond using a Predictor-Corrector algorithm within the simulation time step. The MTS SRMD real-time controller receives these command signals as external reference signals and moves the SRMD machine accordingly.

At the end of each simulation time step when the target displacement is reached by the SRMD, measurements of each desired DOF are recorded and then sent back to the numerical model. For a 2D hybrid simulation, the measurements are two horizontal displacements and their corresponding horizontal forces. Note that these feedback forces do not just consist of internal forces in the physical specimen; they are also contaminated with other forces such as inertia forces of the platen and friction forces of the table. These additional forces need to be subtracted from the feedback signals before sending them to the numerical model to apply the proper bearing restoring force. This correction of the feedback forces has been implemented within the Simulink real-time machine model described earlier. Once OpenSees*SP* receives the restoring forces from the numerical and experimental elements, the analysis can proceed to the next integration time step.

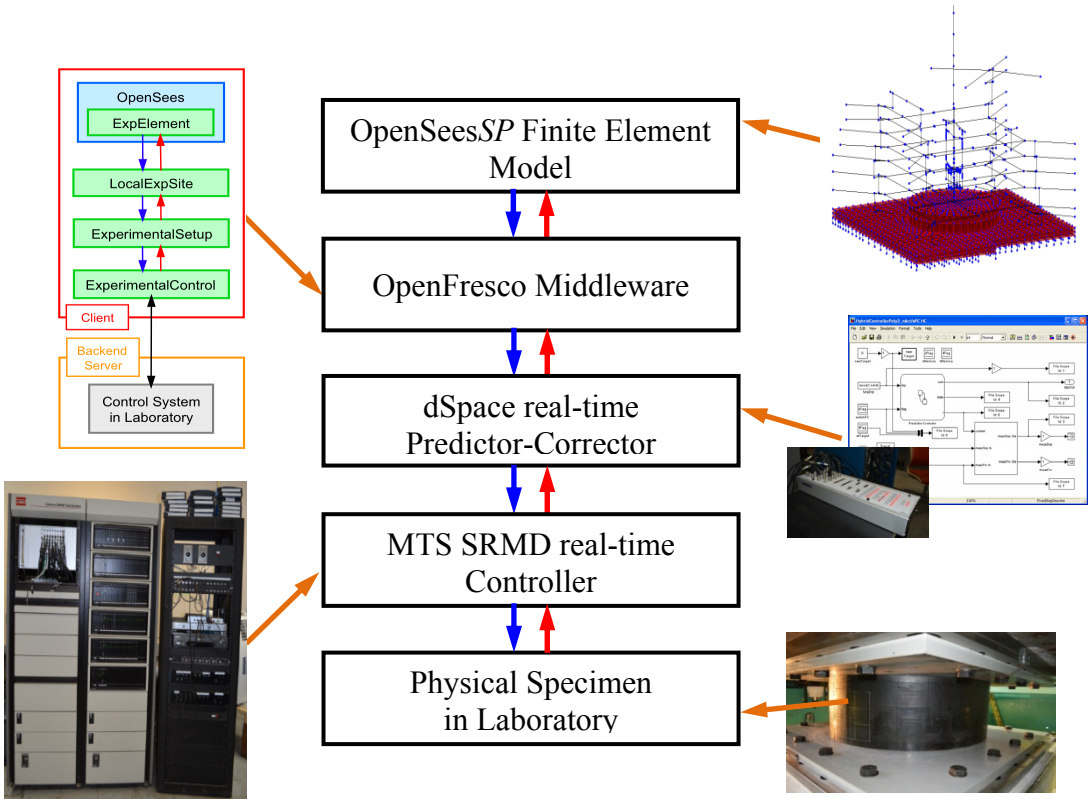

Figure 3.16 Schematic of the test set-up.

3.3.2 Analytical Model

KEPCO E&C provided an analytical model of the isolated NPP. Details of the analytical models can be found in an internal report by Schellenberg et al. [2014a]. Analytical bearing models in OpenSees included a newly developed Bouc-Wen model for a LPRB and a newly developed element for the EQS bearing.

To improve the hysteretic behavior of the elastomeric bearing [Schellenberg 2010], a new OpenSees element was developed based on the bidirectional coupled Bouc-Wen model [Casciati 1989]. This provides the capability to model hysteresis loops with rounded corners (see Figure 3.17), which more closely resemble the behavior of an elastomeric bearing than the bilinear behavior of the existing elastomeric element in OpenSees. In addition, the hardening behavior of the bearing was modified to be nonlinear and capture the stiffening effects that are observed at large shear strains in high-damping rubber bearings; see Figure 3.17. Ranges of possible hysteresis loops that can be generated with the new element are shown in Figure 3.18 below.

Another OpenSees bearing element was developed specifically for this project for the EQS isolator; see Figure 3.19. The EQS bearings consist of a flat PTFE-Stainless-Steel sliding interface and MER compression springs that provide restoring force capability. This element was specifically developed to address the unique combination of a circular yield surface with a post-

yield stiffness capable of deformation hardening; see Figure 3.20. Previous analytical software capabilities did not exist for this combination of hysteretic damping and nonlinear restoring force in a single element, and a special OpenSees element was developed specifically for this project to have this capability.

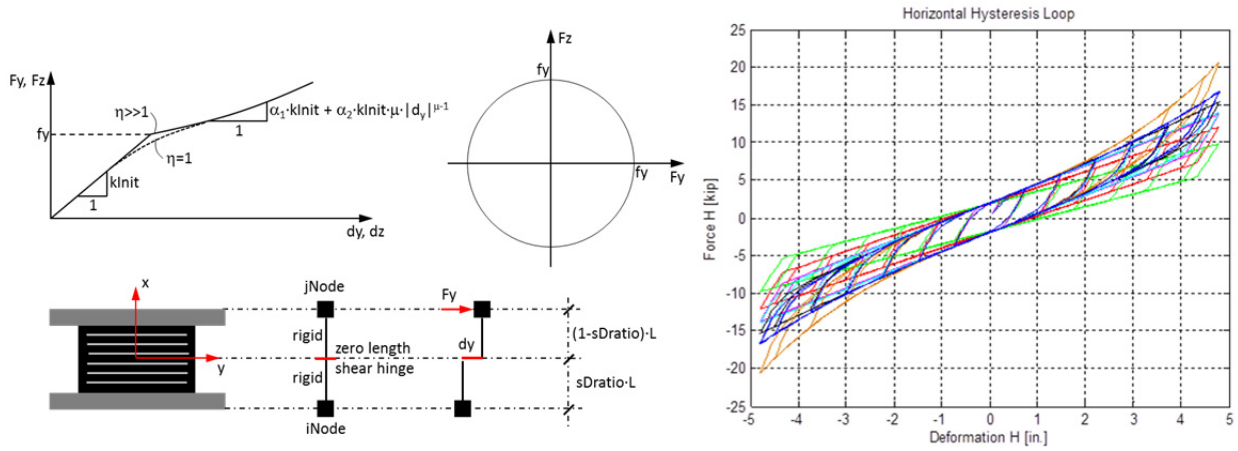

Figure 3.17 **New OpenSees elastomeric isolator based on enhanced Bouc-Wen material properties.**

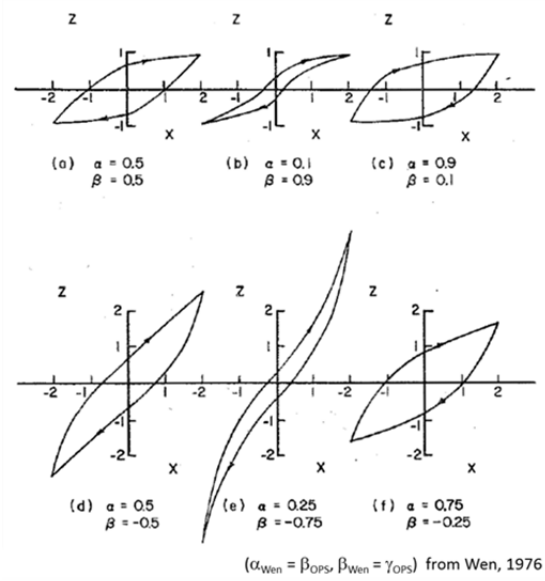

Figure 3.18 **Possible hysteresis loops for different Bouc-Wen model parameters.**

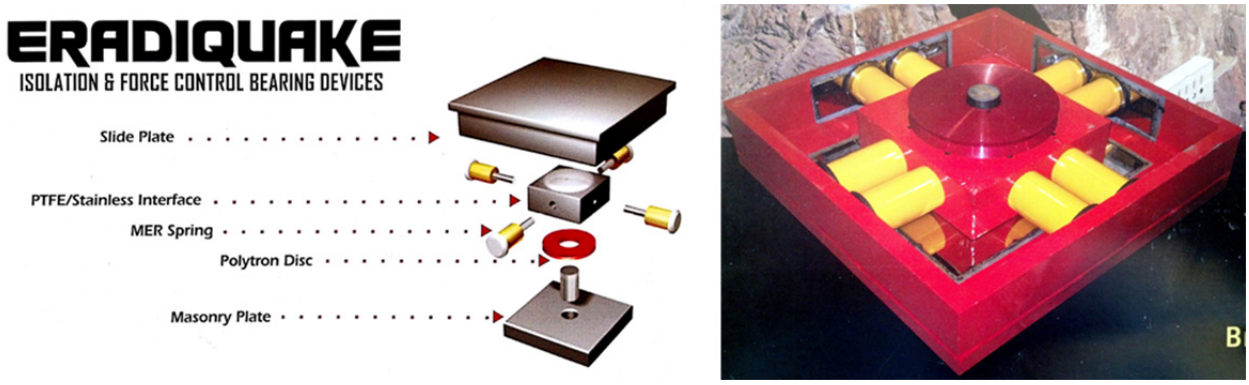

Figure 3.19 RJ-Watson EQS sliding isolator.

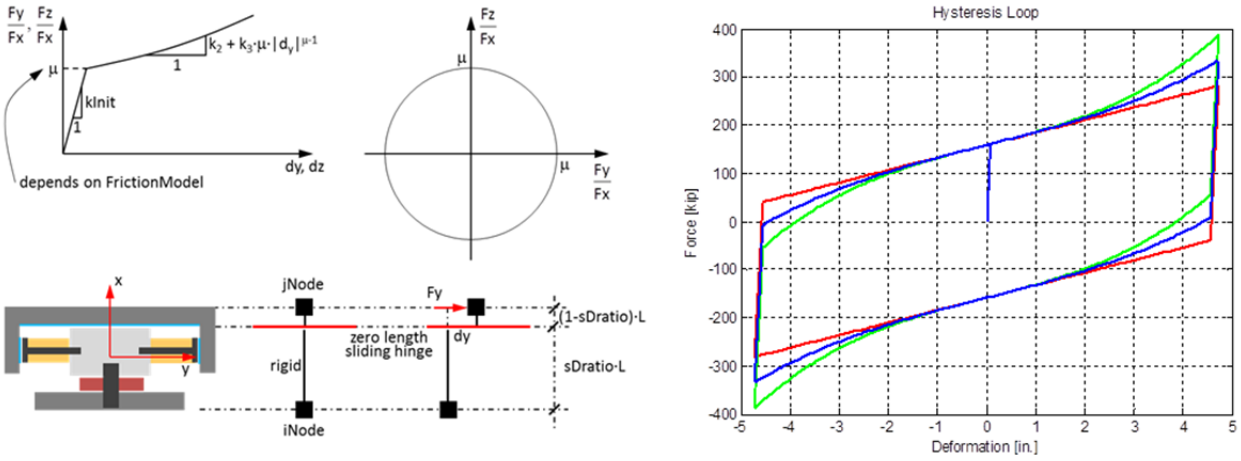

Figure 3.20 New EQS isolator element in OpenSees.

3.3.3 Experimental Set-Up

A system of concrete spacers blocks (bolted to the platen) and a system of steel spacers (bolted to the cross beam) were utilized to install the isolators into the test machine. The concrete spacer blocks were aligned, leveled, grouted, and then post-tensioned (through high-strength 38-mm-diameter threaded rods) to the platen. The steel spacers and upper adapting plate were aligned to the cross beam and bolted using high-strength 38-mm-diameter A325 bolts. The position of the lower adapting plate was established relative to the upper adapting plate assembly. The lower adapting plate was grouted and then post-tensioned (through high-strength 38-mm-diameter threaded rods) to the platen. An overview of the basic test set-up for this program is shown in Figure 3.21.

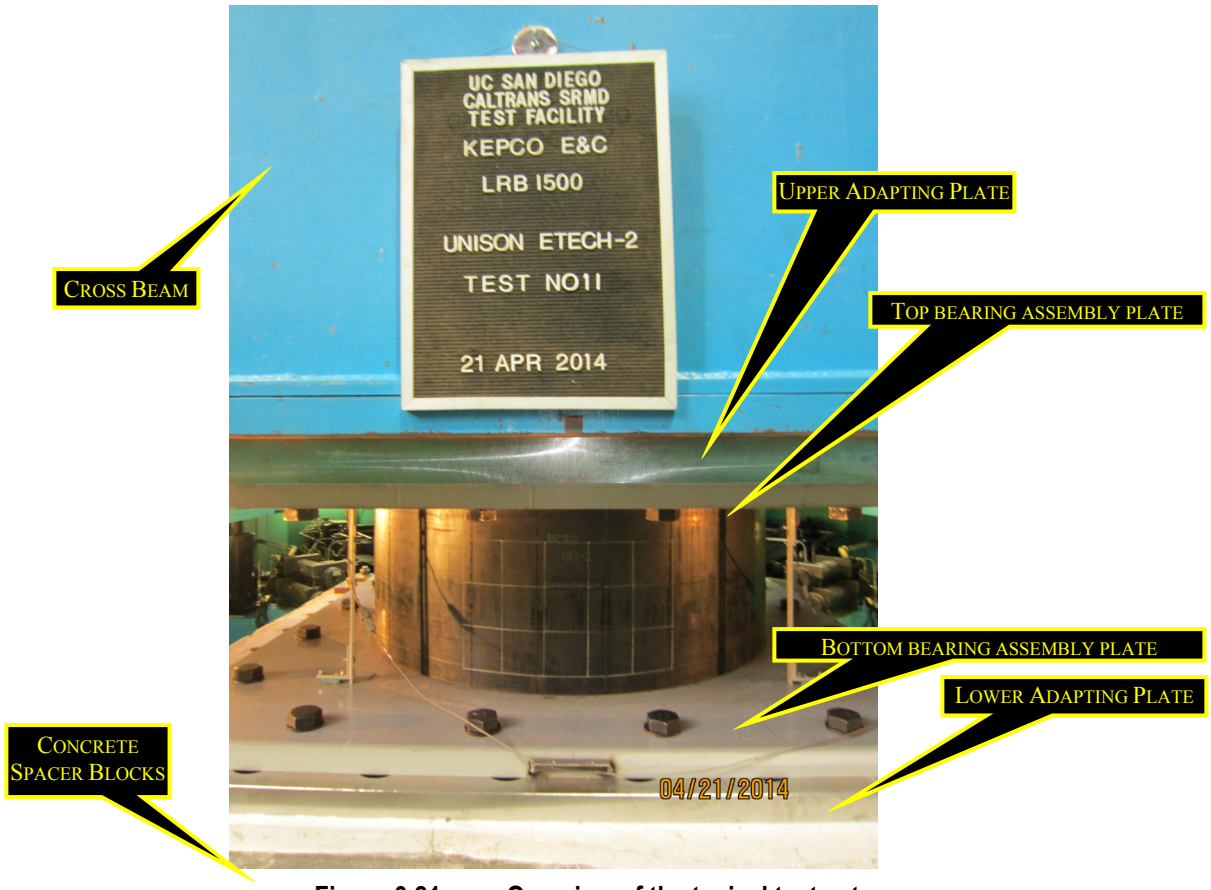

Figure 3.21 Overview of the typical test set-up.

3.3.4 Instrumentation

Horizontal force readouts on the SRMD test system are obtained by means of four load cells mounted at the interface between platen and horizontal actuators. Vertical force readouts are obtained by means of pressure cells on the four vertical actuators and the eight outrigger actuators. The position of the platen is measured using stroke transducers on the four horizontal actuators and the four vertical actuators. Each millisecond, the data recorders calculate the x, y, and z displacement components, and each force component is combined in order to provide three forces (longitudinal, lateral, and vertical) and three moments (roll, pitch, and yaw) acting on the platen. Accelerometers are installed on the platen, within the top surface plate for acceleration measurements in x, y, and z directions.

Each of the four horizontal load cells was calibrated in accordance with ASTM E4 on a test machine at McGill University, Montreal, Canada. Load cells were calibrated against a standard MTS cell calibrated by NIST. The twelve pressure cells were calibrated by means of a dead weight pressure standard. The force read-out from the load cells installed on each horizontal actuator contains a component of the frictional forces mainly generated at the sliding interfaces between reaction frame and vertical actuators as well as a component of the inertia forces caused by the platen mass. Sensors are calibrated yearly to be consistent with ASTM Standards.

The raw data provided by the machine and external sensors are stored for each test in binary format on a computer hard disk. The user is allowed to select the channels to be stored in a file, the sampling rate, starting delay and recording period, and the start recording trigger that can be either manual or synchronized with the run command. A typical list of channels recorded for tests on isolation bearings is provided in Table 3.6. Modifications to this list were introduced, for this project, based on the specific type of test and bearing.

Linear voltage displacement transducers (LVDTs) were used to measure vertical deformations of the bearing. Vertical displacement feedback of the table is not the same as vertical deformation of the bearing because of the flexibility of the cross beam, see Figure 3.22. Figure 3.23 shows the configuration for these LVDTs. The LVDTs for the Unison eTech bearings were placed in four corners as close as practical to the bearing. The LVDTs for the ESCO RTS bearing were placed internally between the middle and bottom plates to capture deformation of the polytron disk, and were left in place throughout testing. In order to obtain a more reliable measurement of the vertical deformation of the bearing—especially for calculation of the vertical stiffness of the bearings—average values of the four displacement transducers at each corner of the bearing were considered.

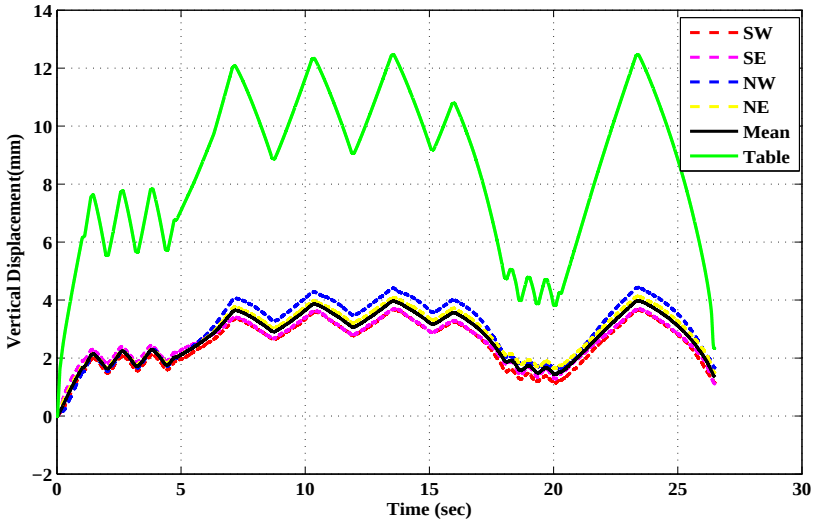

Figure 3.22 Vertical displacement of the SRMD and LVDTs.

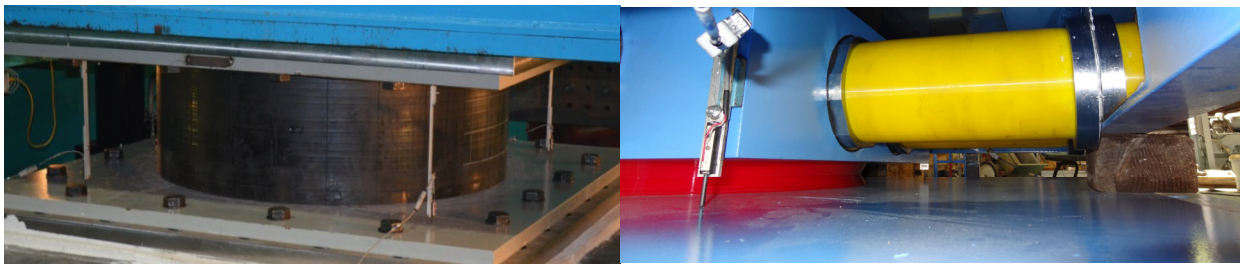

Figure 3.23 LVDTs used to measure vertical deformation of the bearings.

Table 3.6 Typically recorded channel list.

Channel number	Channel	Units
1	Long. reference	in.
2	Lat. eeference	in.
3	Long. feedback	in.
4	Lat. deedback	in.
5	Vert. feedback	in.
6	Roll feedback	°
7	Pitch feedback	°
8	Yaw feedback	°
9	Long. force fbk	U.S. ton
10	Lat. force fbk	U.S. ton
11	Vert. force fbk	U.S. ton
12	Roll force fbk	Ton-ft
13	Pitch force fbk	Ton-ft
14	Yaw force fbk	Ton-ft
15	Compression force fbk	U.S. ton
16	V-NE force fbk	U.S. ton
17	V-SE force fbk	U.S. ton
18	V-NW force fbk	U.S. ton
19	V-SW force fbk	U.S. ton
20	O-NE force fbk	U.S. ton
21	O-SE force fbk	U.S. ton
22	O-NW force fbk	U.S. ton
23	O-SW force fbk	U.S. ton
24	AXNE accel fbk	*g*
25	AYNE accel fbk	*g*
26	AYNW accel fbk	*g*
27	AZNE accel fbk	*g*
28	NE disp.	in.
29	SE disp.	in.
30	NW disp.	in.
31	SW disp.	in.

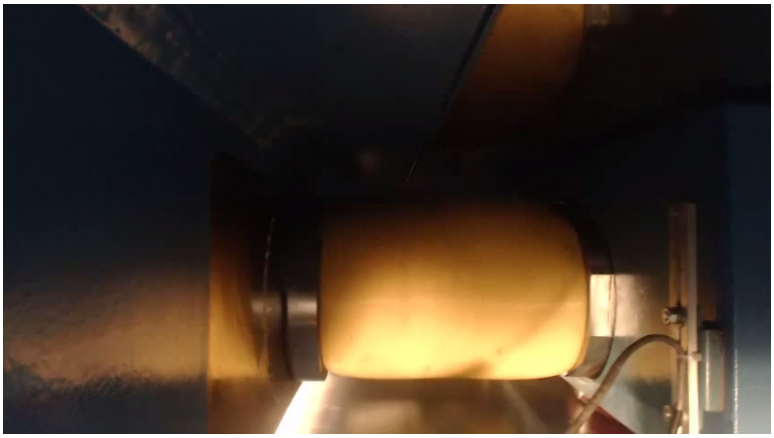

Figure 3.24 Snapshot from the camera mounted inside the EQS bearing. (courtesy of ESCO RTS).

Video and audio recordings were obtained of all testing stages via three color cameras. One other camera was installed inside the EQS bearings by ESCO RTS; see a video snapshot in Figure 3.24. Video captured through this camera helped to understand the behavior of the bearing, and in case of failure it helped identify the failure mechanism.

Thermocouples installed in the Unison eTech bearings were monitored by a separate data acquisition system. Synchronization of this system with the primary data acquisition system is achieved by comparison of a common signal recorded on both systems. Temperature monitoring of the EQS bearings by thermocouples was deemed impractical. Since heat generation and dissipation is a fairly slow process, temperature data was recorded at a low sampling rate of 1 Hz.

3.3.5 Data Reduction Procedure

Units reported in Table 3.6 are consistent with the units that are used in the machine operation. First, the data reduction process involves converting to the units requested by the client. Note that herein tons are English tons. The description of the physical quantities recorded reflects the classic control language. The Reference quantities (Channel #1 and #2) serve as the target signal used as input to the control; e.g., the signal histories of displacement components that the user requests the machine to perform. The corresponding feedback (fbk) readouts are the response histories of what the machine sensors detected. Note that the readout of forces and displacements in longitudinal, lateral, and vertical directions, (#3–#15) represent the results of computations by the control computer in order to combine the local readouts of the system sensors in the DOF directions.

In Table 3.6, vertical force (#11: Vert Force fbk) represents the net force exerted by the four vertical actuators mounted under the platen and the eight outrigger actuators. This vertical force takes into account all weights and external vertical loads applied to the platen and does not represent the vertical load applied to the test specimen. Instead, the Compression Force (#15 Compression Force fbk) is intended as the uncorrected vertical force applied to the specimen. The signals V-*xx* and O-*xx* (Channels #16 thru #23) indicate force readouts for vertical and outrigger actuators, respectively, at *xx* (e.g., NE=North-East etc.) location in the machine plan.

Channels #24–#27 are the acceleration readouts of the sensors installed within the top surface of the platen where X = Longitudinal, Y = Lateral, and NE = North East, and so on. The data from the displacement transducers utilized to measure the vertical deformation across the bearing were recorded in channels #28 through #31 when available.

As a general procedure adopted by the SRMD laboratory, the main objective of the data reduction process is to remove the components that are not directly applied to the test specimen from the measured forces; specifically the inertial and machine friction forces. This procedure required a theoretical and experimental phase of machine characterization and shake-down, mainly oriented to the assessment of the frictional and inertial characteristics of the system. Recorded forces are corrected based on the idealized horizontal equilibrium equation of the system:

Force readouts = Shear across the specimen + Inertial forces + Machine friction + Error.

Here, the error term takes into account all the uncertainties related to the readout and correction process. The inertia forces were estimated by means of the accelerometers mounted at the table top surface with longitudinal, lateral, and vertical orientation. The horizontal platen mass was assessed during high-speed tests at assigned frequency and amplitude, and calculated from actuator force-displacement hysteresis loops. Velocities and accelerations used for correction purposes can also be calculated as derivatives and double derivatives of the recorded displacements. In order to obtain smooth velocity and acceleration histories when derivatives are used in the reduction process, a preliminary smoothing procedure is applied to raw displacement data using a Savitzky-Golay (polynomial) smoothing filter.

In order to improve the assessment of the machine friction component independent of the applied vertical load, empty table runs were completed without the test specimen. These were conducted with displacement and velocities amplitudes identical to those previously applied to the isolators. The friction component obtained during these tests represents the most significant portion of the overall machine friction force. The friction component due to the instantaneously applied vertical load is later added to the frictional forces recorded during the runs without the test specimen since there was no vertical load on the platen during these runs. With this procedure, the forces recorded during the actual tests are corrected, point by point, by removing the overall friction forces generated by the test equipment. Data is presented in the form of "processed data" when data has been corrected with either of these processing protocols.

3.3.6 Pre-Test Bearing Condition

3.3.6.1 Unison Bearings

The Unison eTech bearings UET-1, UET-2, and UET-3 were received by UCSD, on April 4, 2014. Upon delivery to the SRMD laboratory, the LPRB bearings were inspected and found to be in poor condition. Lead-core cover plates were dislodged, which was caused by lead-core expansion and subsequent bolt failure, see Figures 3.25 and 3.26. The bolts, items 1.5 in “detail a” of Figure 2.1, failed in tension, presumably by differential creep of the pre-compressed lead core and surrounding bearing, which was compressed during lead installation. All three bearings had cover plate bolt fractures on either the top or bottom cover plate. Bolts continued to fracture after delivery. Prior to installation in the SRMD machine, the cover plates were compressed using the SRMD machine and spacer plates to install replacement bolts.

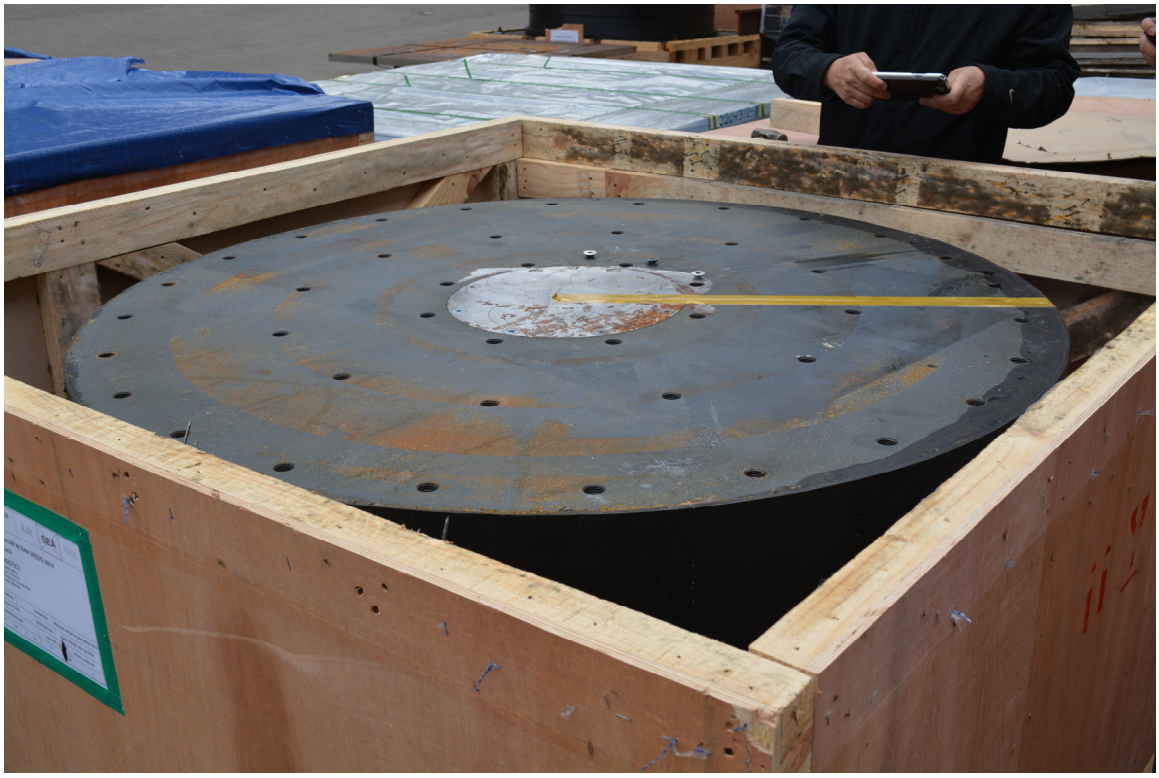

Figure 3.25 Unison bearing pre-test condition.

Figure 3.26 Unison bearing cover plate bolt failure.

Bearing end plates were bowed in a manner consistent with the lead core's pre-compression. The plates were convex, making installation of the adapter plates challenging. In order to close the millimeter-wide edge gaps between the bearing end plates and bearing adapter plates, the sandwiched bearings were loaded in the side of the machine and squeezed to enable the insertion of the bolts. The result was that the bearing adapter plates conformed to the bow of the bearing end plates.

Three thermocouples were installed in the lead core during production. One was installed near the top at an unspecified depth. The remaining two were installed next to each other down approximately one-third of the bearing height. Precise locations were not provided. In bearing UET-1, only one of the three thermocouples survived production and shipment. All three thermocouples in UET-2 were intact upon delivery. UET-3 was reserved as backup, and the thermocouples were not tested for continuity.

3.3.6.2 ESCO RTS Bearings

ESCO RTS bearings EQS-1 and EQS-2 were received by UCSD, on April 3, 2014. Upon delivery to the SRMD laboratory, the EQS bearings were in good condition; see Figure 3.27. They were delivered with the sliding plate on the bottom. However, installation of the asymmetric machine adapter plates required the sliding plate to be on top. The bearings were flipped to conform to this installation configuration and tested with the sliding plate on the top.

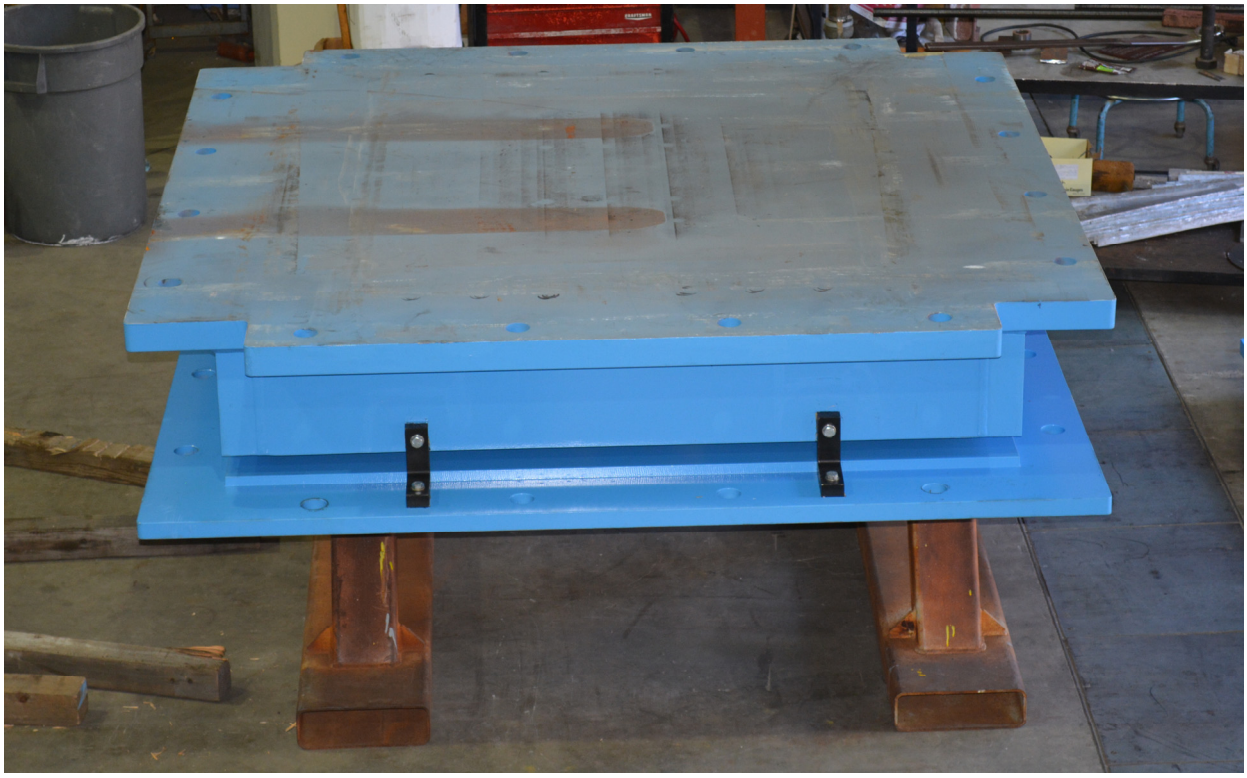

Figure 3.27 ESCO RTS bearing pre-test condition.

3.4 HYBRID SIMULATION TEST PROTOCOL

Hybrid simulations were conducted at hazards corresponding to a safe shutdown event according to EUR 2.4.6 and NRC RG1.60 specifications [EUR 2012; NRC 1973]. The hazards were each characterized with a set of twenty dispersion-appropriate three-component ground motions [Schellenberg et .al. 2014b]. The mean elastic response spectrum agreed well with the design spectrum, but significant deviations are present in individual records. Ground motions used in the hybrid tests were selected from both of these hazards.

A subset of ground motions was selected from the EUR and NRC sets of twenty records. The selection criteria were based on peak lateral displacement and axial force demands. These demands were analytical estimates obtained from nonlinear response history analyses conducted on bearing models calibrated against the manufacturer's quality control tests; see Sections 2.2 and 2.3. However, post-test comparisons showed these analytical estimates differed from results obtained in repeated manufacturer quality tests conducted at the SRMD. Ground motions that imposed a peak lateral displacement close to the median of the set were preferred. Attention was then directed towards motions that imposed large variations in axial force without producing uplift or tension in the isolators. For the LPRB isolator, the peak demands are provided in Figure 3.28 for lateral displacement and Figure 3.29 for axial force considering the EUR hazard, and considering the NRC hazard the demands are provided in Figure 3.30 for lateral displacement and Figure 3.31 for axial force. The resulting selections for the LPRB were Record #5 for the EUR hazard and Record #15 for the NRC hazard.

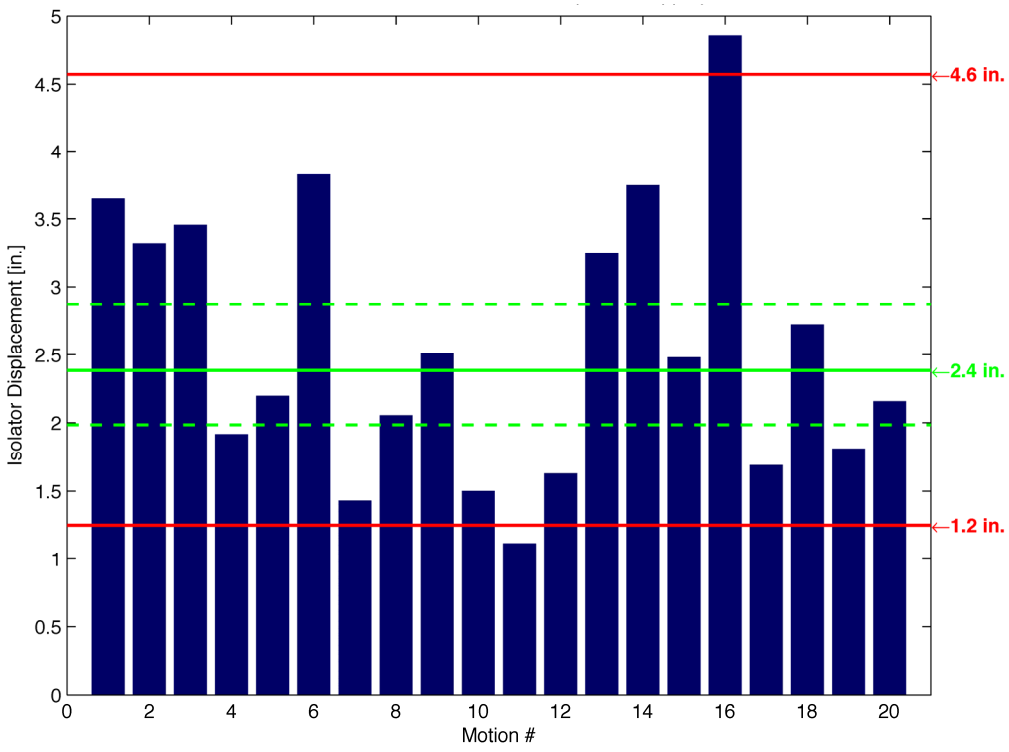

Figure 3.28 **Analytically determined peak lateral displacement demands per the EUR hazard level [2012] based on an LPRB isolator (green lines = median with 95% confidence interval, red lines = 5th and 95th percentile).**

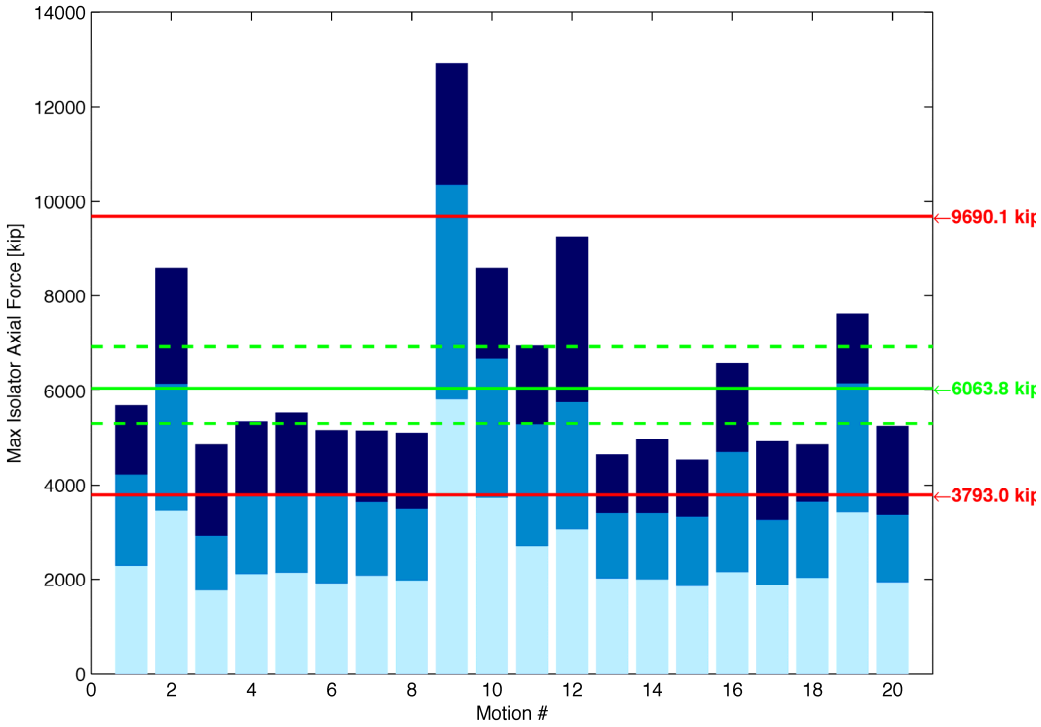

Figure 3.29 Analytically determined peak axial force demands for the EUR hazard level [2012] based on an LPRB isolator (green lines = median with 95% confidence interval, red lines = 5th and 95th percentile).

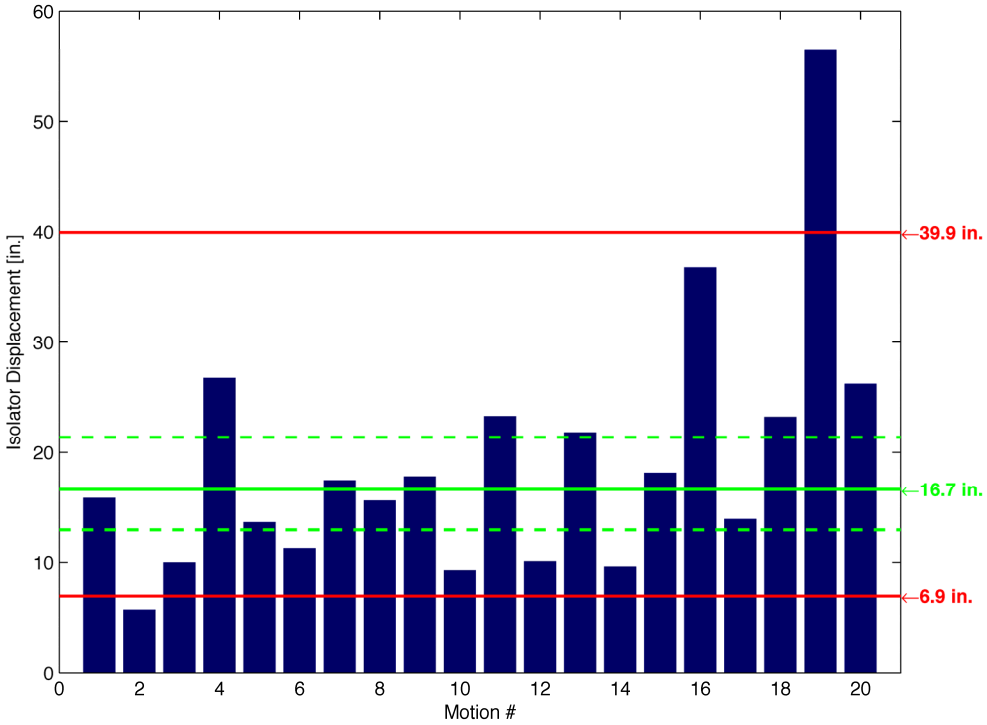

Figure 3.30 Analytically determined peak lateral displacement demands for the NRC hazard level [1973] based on an LPRB isolator (green lines = median with 95% confidence interval, red lines = 5th and 95th percentile).

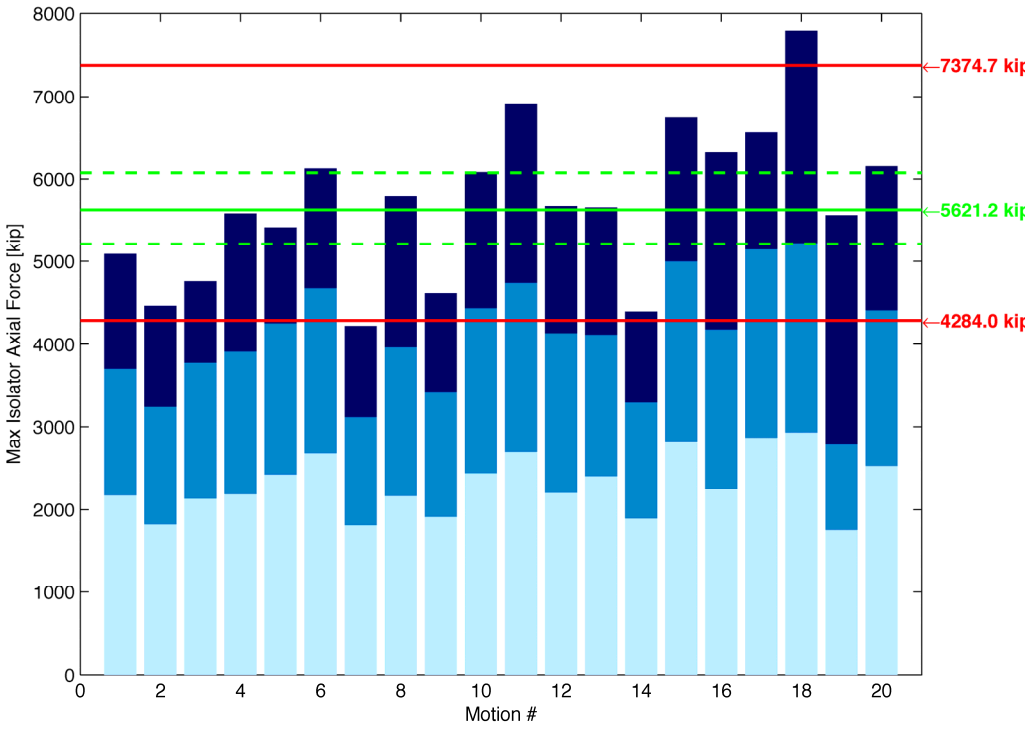

Figure 3.31 **Analytically based peak axial force demands for the NRC hazard level [1973] based on an LPRB isolator (green lines = median with 95% confidence interval, red lines = 5th and 95th percentile).**

For a FPSB isolator, the peak demands considering the EUR hazard are provided in Figure 3.32 for lateral displacement and Figure 3.33 for axial force, and considering the NRC hazard the peak demands are provided in Figure 3.34 for lateral displacement and Figure 3.35 for axial force. Selections for the EQS bearing were Record #5 for the EUR hazard and Record #2 and #10 for the NRC hazard.

The selection criteria resulted in ground motions designated as EUR5 and NRC15 for the LPRB bearing, and EUR5, NRC2, and NRC10 for the EQS bearing. These are characterized in terms of their horizontal and vertical response spectra in Figures 3.36–3.39. The set of hybrid simulation scenarios conducted on the LPRB using these records is summarized in Table 3.7. Hybrid simulation scenarios performed on the EQS bearing are summarized in Table 3.8. These tables contain the ground motion considered, ground motion components considered, model discretization, which bearing was tested, the test rate, and the test number. The test rate is the number of times slower than real time at which the test was conducted. The complete set of tests performed, including development tests and hybrid simulations, are provided in Appendix A for the LPRB bearing and Appendix C for the EQS bearing. Appendices B and D contain the full set of characterization tests conducted on the LPRB and EQS bearings, respectively.

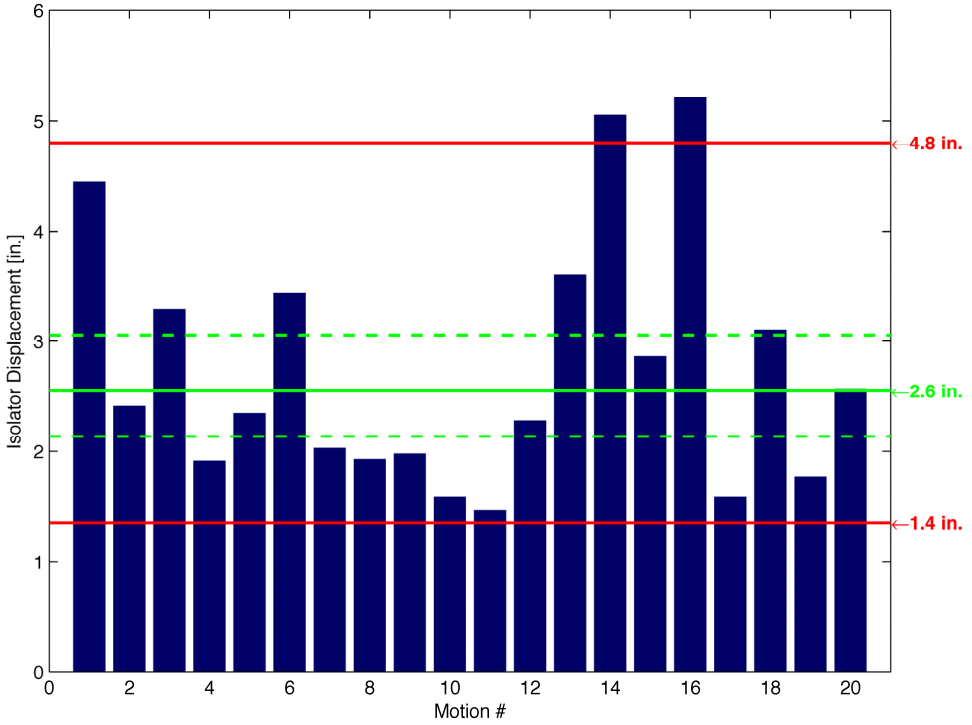

Figure 3.32 Analytically determined peak lateral displacement demands for the EUR hazard level [2012] based on an FPSB isolator (green lines = median with 95% confidence interval, red lines = 5th and 95th percentile).

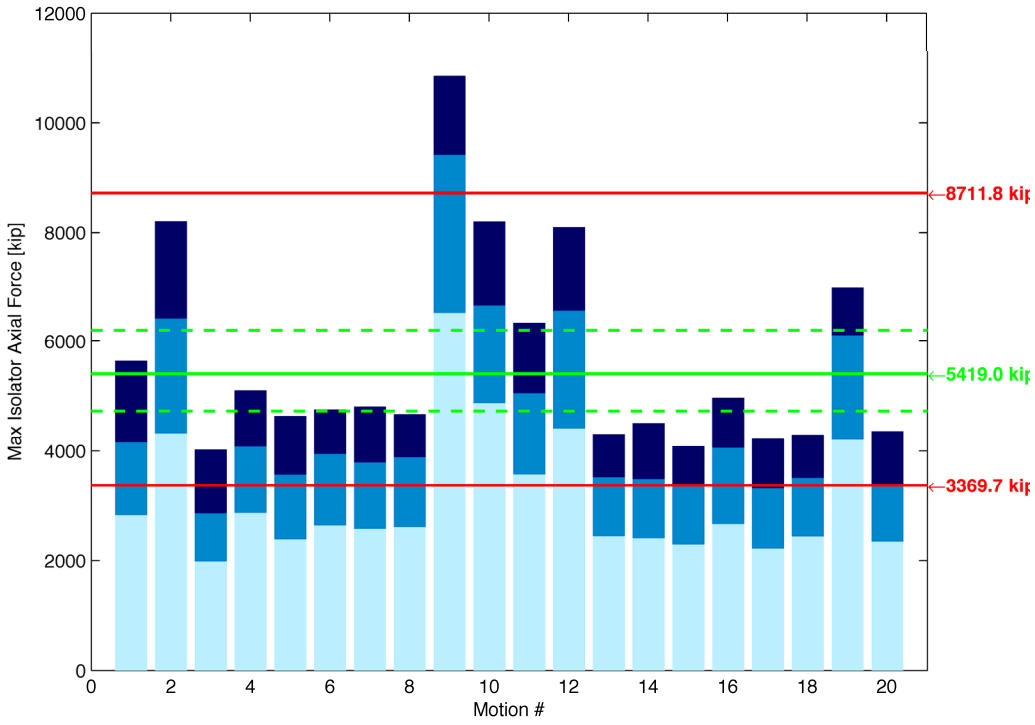

Figure 3.33 Analytically determined peak axial force demands for the EUR hazard level [2012] based on an FPSB isolator (green lines = median with 95% confidence interval, red lines = 5th and 95th percentile).

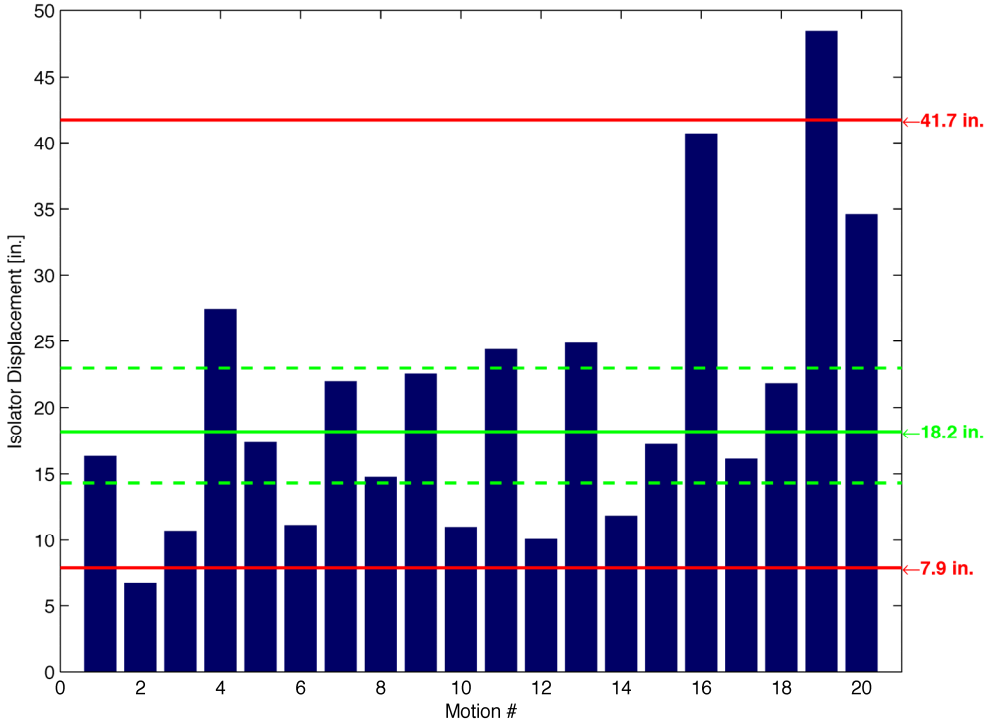

Figure 3.34 Analytically determined peak lateral displacement demands for the NRC hazard level [1973] based on an FPSB isolator (green lines = median with 95% confidence interval, red lines = 5th and 95th percentile).

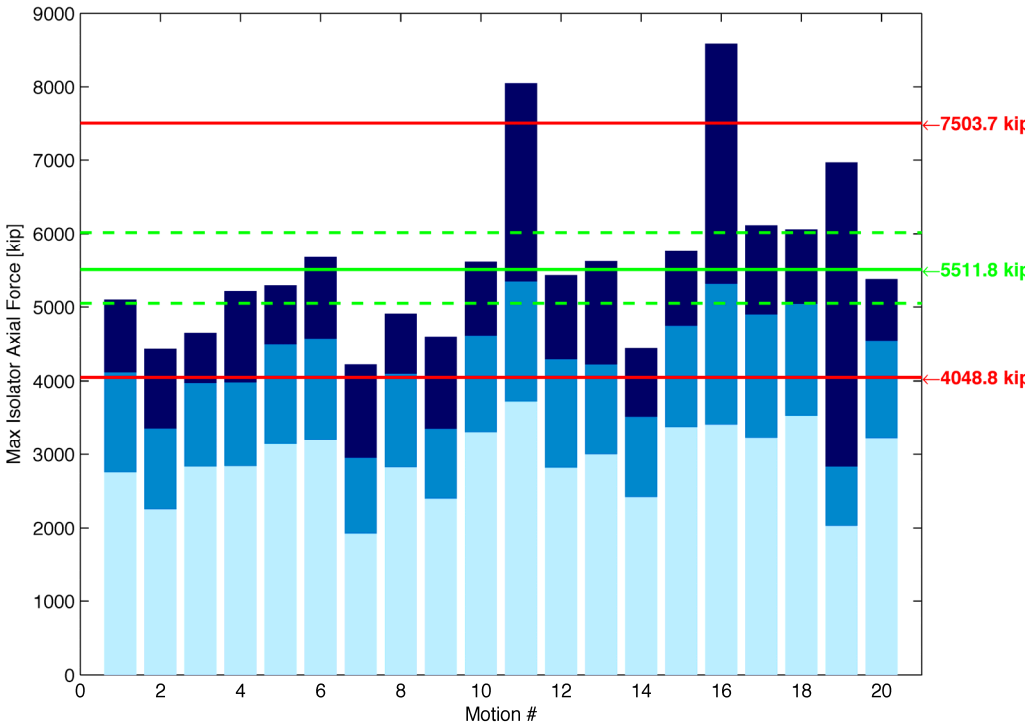

Figure 3.35 Analytically determined peak axial force demands for the NRC hazard level [1973] based on an FPSB isolator (green lines = median with 95% confidence interval, red lines = 5th and 95th percentile).

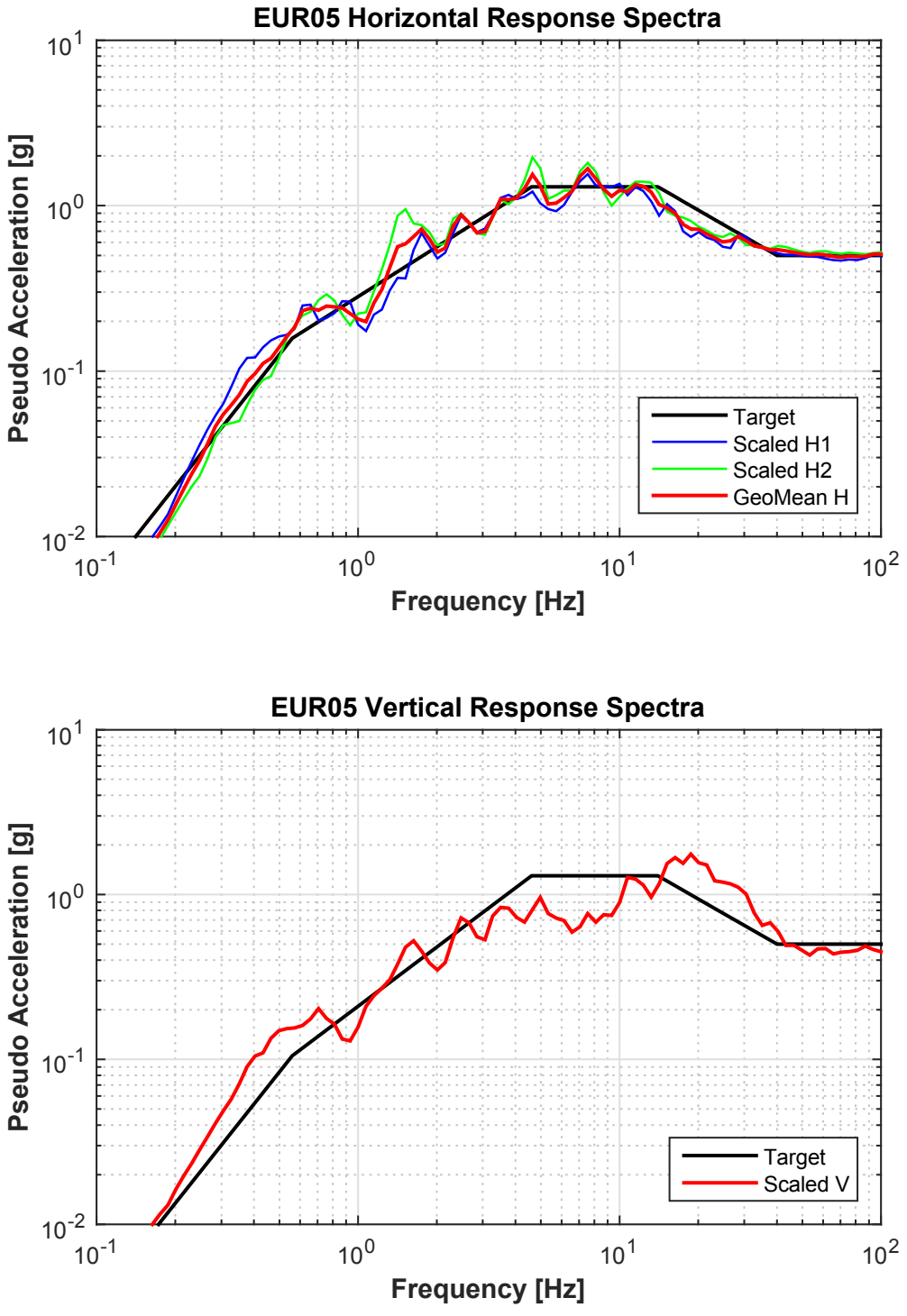

Figure 3.36 **Response spectra of the EUR05 ground motion characterizing the EUR hazard level [2012]**

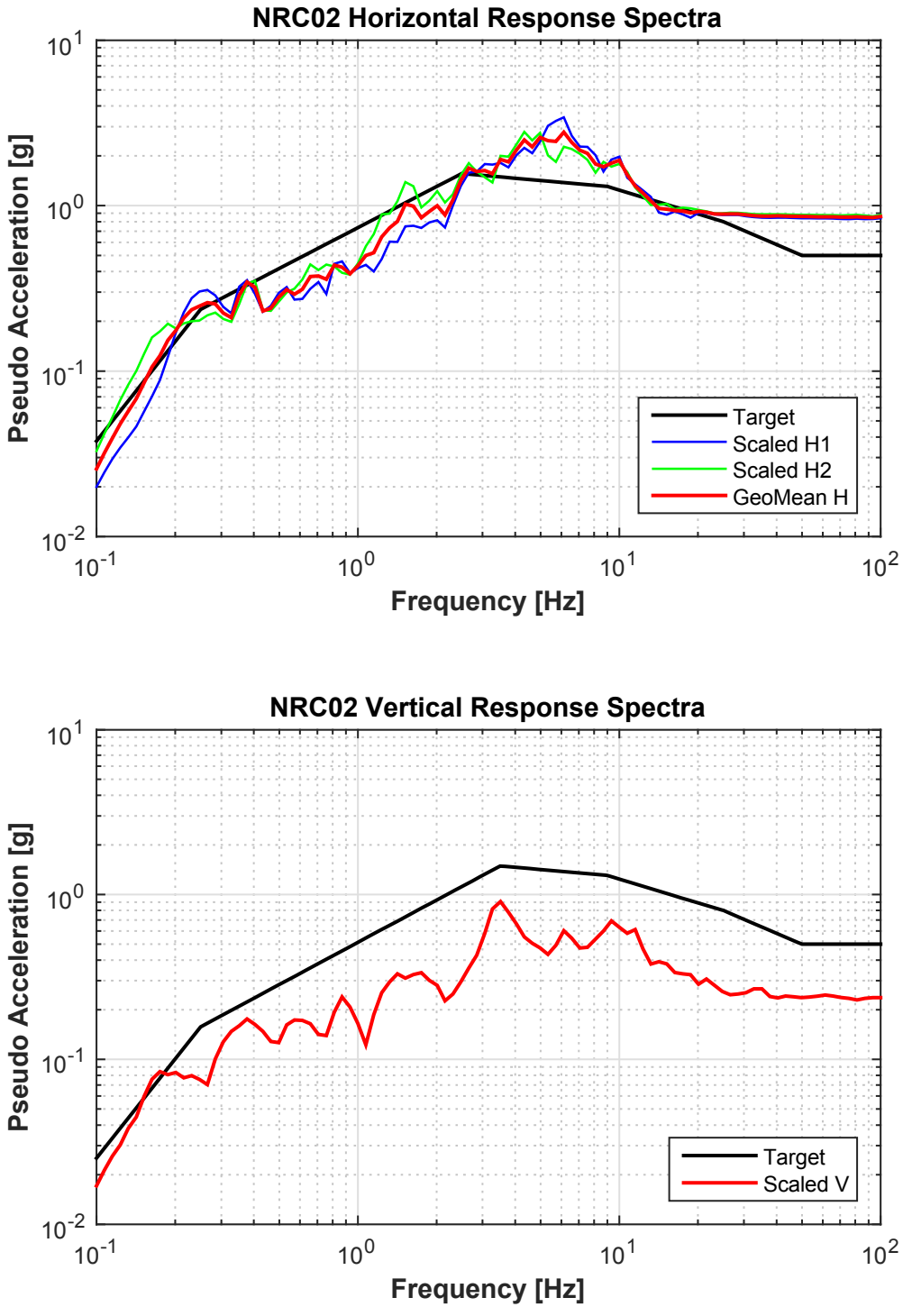

Figure 3.37 **Response spectra of the NRC02 ground motion characterizing the NRC hazard level [1973].**

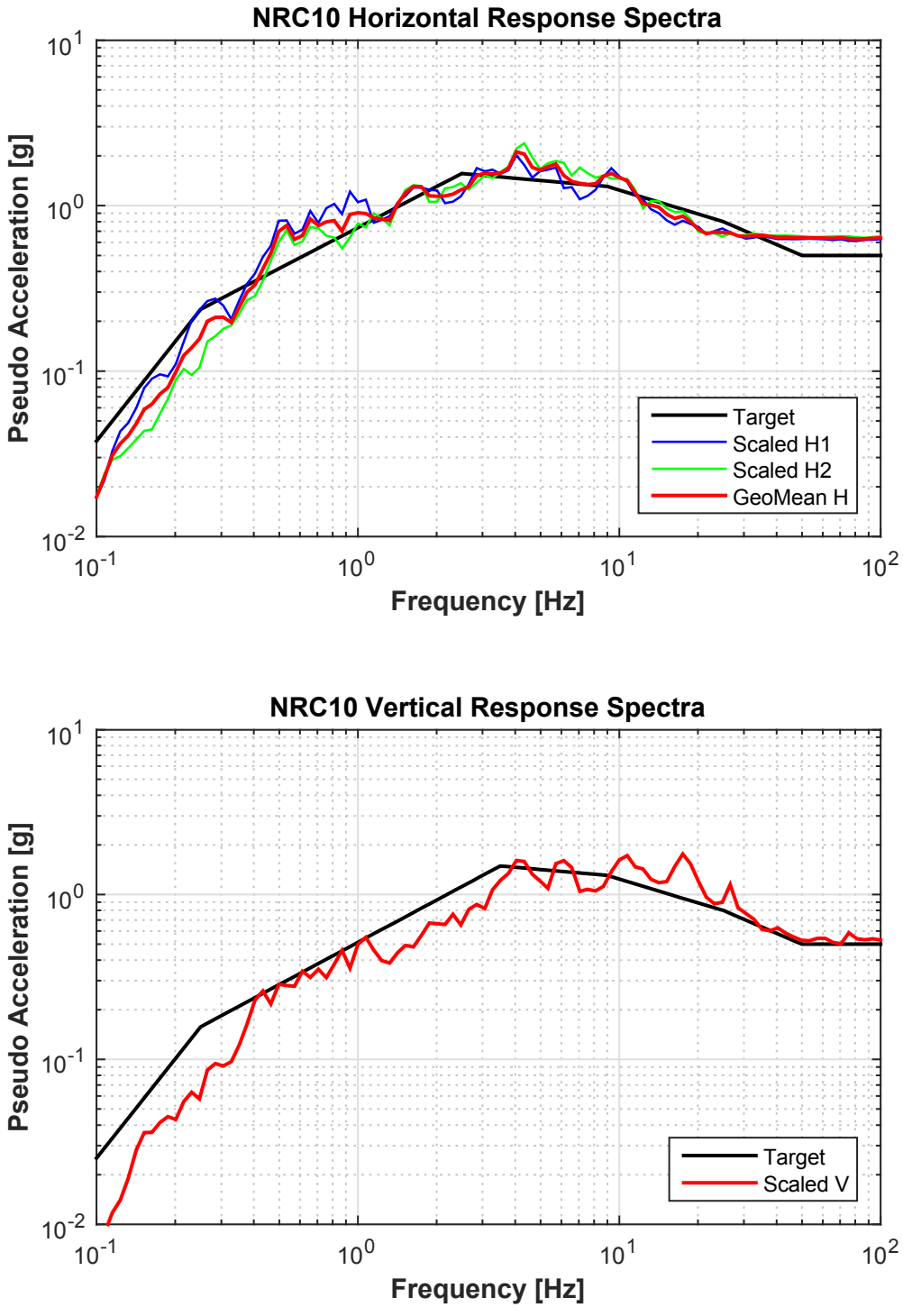

Figure 3.38 **Response spectra of the NRC10 ground motion characterizing the NRC hazard level [1973].**

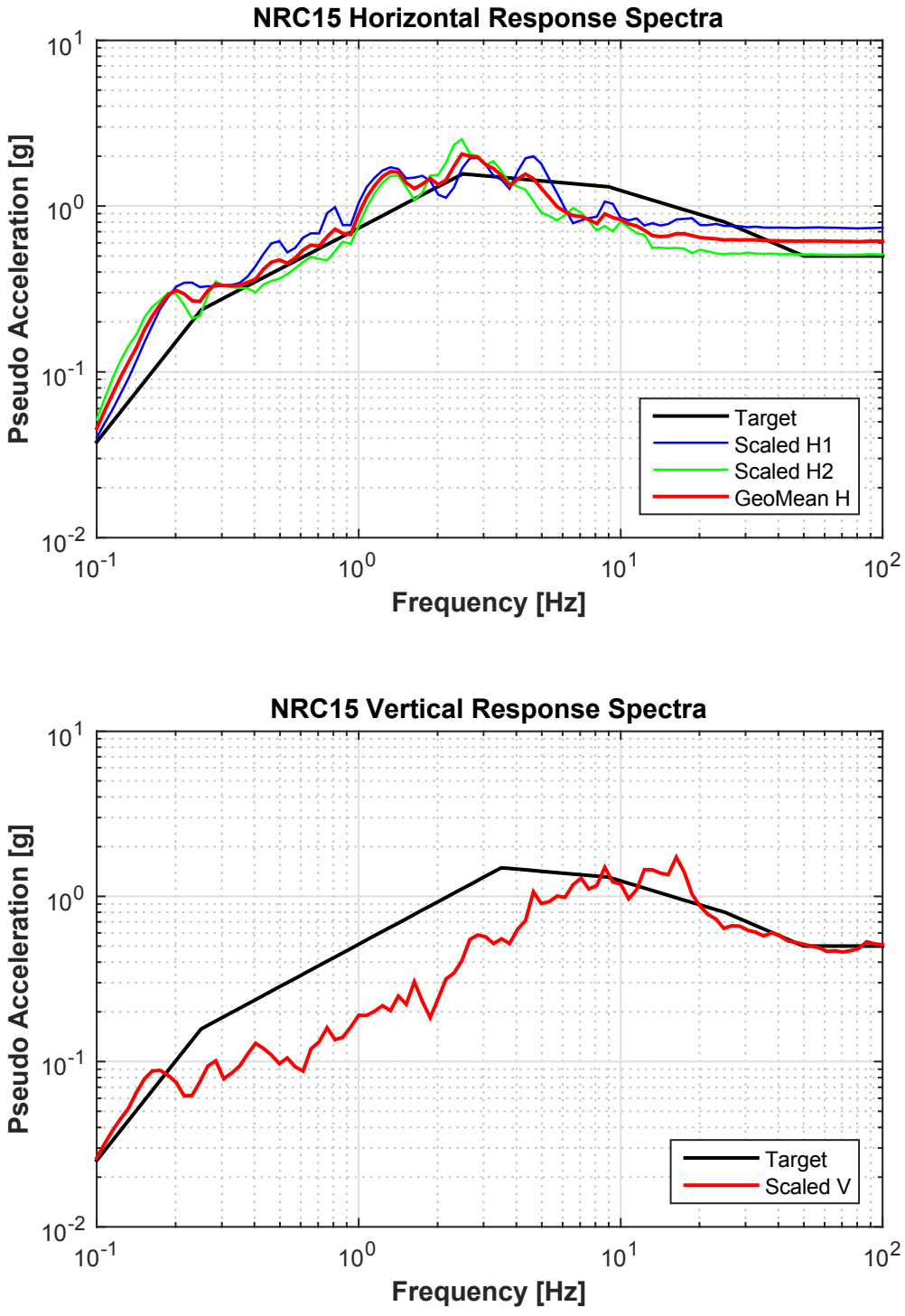

Figure 3.39 **Response spectra of the NRC15 ground motion characterizing the NRC hazard level [1973].**

Table 3.7 Hybrid tests conducted on the LPRB bearings.

Ground motion	Components	Model	Bearing	Test rate	LPRB test no.
EUR5	Longitudinal	Exp = All	UET-2	25	37
EUR5	Longitudinal	Exp = All	UET-2	25	44
EUR5	2D	Exp = All	UET-2	25	26
EUR5	2D	Exp = All	UET-2	25	45
EUR5	3D	Exp = All	UET-1	25	78
EUR5	3D	5 groups of bearings (Exp = Center)	UET-1	25	82
EUR5	3D	5 groups of bearings (Exp = Corner-No. 3)	UET-1	25	83
NRC15	Longitudinal	Exp = All	UET-2	25	47
NRC15	2D	Exp = All	UET-2	25	55
NRC15	2D	Exp = 1 of 527 bearings	UET-2	75	61
NRC15	2D	5 groups of bearings (Exp = Center)	UET-2	25	63
NRC15	3D	5 groups of bearing (Exp = Center)	UET-1	25	84
NRC15	3D	5 groups of bearing (Exp = Corner-No. 3)	UET-1	25	85
NRC15	3D with vertical	5 groups of bearings (Exp = Corner-No. 3)	UET-1	25	89

Table 3.8 Hybrid tests conducted on the EQS bearings.

Ground motion	Components	Model	Bearing	Test rate	EQS test no.
EUR5	Longitudinal	Exp = All	EQS-1	25	17
EUR5	Longitudinal	Exp = All	EQS-2	5	53
EUR5	2D	Exp = All	EQS-1	25	18
NRC2	2D	Exp = All	EQS-1	25	21
NRC2	Longitudinal	Exp = All	EQS-1	25	22
NRC2	2D	5 groups of bearings (Exp = Center)	EQS-2	5	43
NRC2	3D	5 groups of bearings (Exp = Center)	EQS-2	20	47
NRC2	3D	5 groups of bearings (Exp = Corner)	EQS-2	20	50
NRC2	3D with vertical motion	5 groups of bearings (Exp = Corner)	EQS-2	20	51
NRC2	Longitudinal	Exp = All	EQS-2	5	52
NRC2	2D	Exp = All	EQS-2	5	54
NRC10	2D	Exp = All	EQS-2	5	58

3.5 HYBRID SIMULATION TEST RESULTS

For all hybrid simulation tests, data was simultaneously recorded on four different machines that were part of the overall testing system. Nodal and element response quantities for the entire OpenSees model that was analyzed on a 12-core, high-performance computing machine were recorded there. Because the analysis model was a hybrid model consisting of numerical as well as an experimental element, measured response quantities included the experimental element. Furthermore, OpenFresco was deployed on the analysis machine, allowing control and data acquisition quantities to be recorded through the dSpace experimental control object. Response quantities in OpenSees and OpenFresco were recorded at the integration time step interval of 0.01 sec, providing a frequency resolution of up to 50 Hz. Secondly, data was recorded on the dSpace real-time digital signal processor board where the synchronization predictor-corrector algorithms were executed. All the commanded and measured data that passed through the predictor-corrector was recorded at the dSpace sampling rate of 1 kHz, which is identical to the MTS SRMD real-time digital controller sampling rate. In order to confirm the correct operation of the event-driven predictor-corrector and the real-time SRMD machine friction correction algorithm, it was necessary to record data at such a high sampling rate, even though the overall hybrid simulation was executed 25 times slower than real time for most of the tests. The third machine that recorded data during each hybrid simulation was the digital SRMD controller. For the majority of the hybrid tests, the data acquisition rate on the SRMD controller was set at 50

Hz. Command and measured signals for the six-DOFs table were recorded for most tests. The fourth data acquisition machine was the aforementioned standalone machine that monitored thermocouples.

Because the SRMD was not originally designed with the intent of conducting hybrid simulations it was necessary to determine and understand the limitations and difficulties arising from the many different testing components required to perform hybrid simulations. Hence, many of the hybrid simulation runs carried out over the five-week testing period were necessary to study, recalibrate, and ultimately improve the performance of the overall hybrid test system. These runs, which were crucial for the success of the test program, are considered developmental runs and their results are reported only in the appendices. Results that were recorded from the dSpace digital signal processor, the SRMD digital controller, and the independent DAQ system are also presented in the appendices of this report.

Results presented focus on the structural responses recorded by OpenSees and OpenFresco. A list of the hybrid simulation runs that are being discussed and compared is shown in Table 3.7 for the Unison eTech bearings and in Table 3.8 for the ESCO RTS bearings. For each comparison, the behavior of the experimentally tested isolator is presented in terms of displacement and force demands, and on the in-structure response in terms of floor response spectra. For the isolator specimen, hysteresis loops in longitudinal and lateral directions, the horizontal displacement orbit, and the shear-force interaction surface are provided. For the plant superstructure, floor response spectra at three different elevations along the height of the reactor containment building (RCB) and along the height of the primary shield wall (PSW) are provided. The response spectra for the input ground motion are included. The elastic response spectra were generated by analyzing 2 DOF linear-elastic systems with 5% damping; the reported spectral quantities are vector norms of the response quantities in the two horizontal directions.

3.5.1 Unison eTech: LPRB Test Results

3.5.1.1 Comparison of 1D and 2D Horizontal Inputs

Figure 3.40 presents a comparison of the hysteresis loops for a 1D longitudinal hybrid simulation (Run 44) with a 2D bidirectional hybrid simulation (Run 45). The hybrid model had one experimental bearing representing all the bearings and was analyzed for the EUR5 ground motion. As can be seen from the figure, the maximum longitudinal displacement demand from the 1D test is 61 mm, which is larger than the 54 mm demand from the 2D test. From the longitudinal hysteresis loop of the 2D test, shear-force fluctuations are obvious at around 40 mm, caused by the lateral deformation. Furthermore, the hysteresis loops of the 2D test become narrower a little more quickly compared to the 1D test. This reduction of the yield force over time is caused by the increase of the temperature in the lead core. In the 2D test the lead core heated up faster because of bidirectional motion, hence the observed narrowing of the hysteresis loops. However, for the very first few cycles, the hysteresis loop of the 2D test is wider than the 1D test, which ultimately caused the larger displacement demand seen in the 1D test. At this point it is not clear why this occurred. It is possibly the result of a small change made to the friction compensation model; further investigation is needed. Finally, the shear-force interaction surface was nearly circular, reaching a maximum shear force of 841 kN. The reason for the shear-force interaction surface being nearly circular is because the displacement demands caused

by the EUR5 ground motion were very small, and the LPRB responded primarily in its linear-elastic range, with only a few cycles exceeding the yield surface.

Figure 3.41 shows several floor response spectra for the RCB and PSW. Generally, the floor response spectra from the 1D and 2D test are nearly identical. Peaks can be identified in the spectra at several distinct frequencies. For the RCB, the largest spike in the floor spectra reaches 1.5*g* and occurs at ~3.7 Hz, which corresponds to the first horizontal mode of vibration of the RCB. A much lower spike of ~0.6*g* is observed between 7.5–10 Hz, which is due to the interaction of the RCB with the PSW and SSW. Similarly, in the floor response spectra of the PSW the main spike can be identified at ~9.5 Hz reaching a spectral acceleration of 2*g*. This spike corresponds to the first-mode frequency of the PSW. Finally, for all of the floor spectra for both substructures there is a small hump around 0.65 Hz, which corresponds to the isolation frequencies with the isolator responding somewhere in between the linear-elastic and nonlinear range.

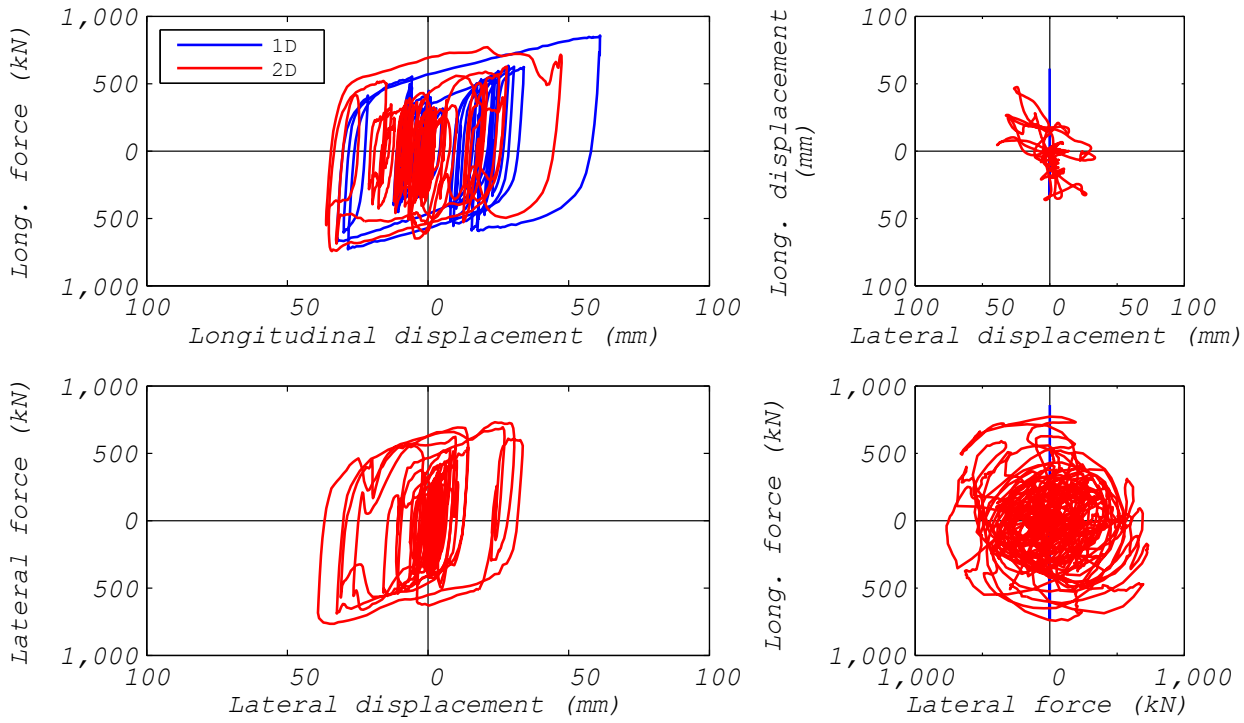

Figure 3.40 **LPRB bearing: comparison of bearing responses to ground motion EUR5 (1D and 2D analyses).**

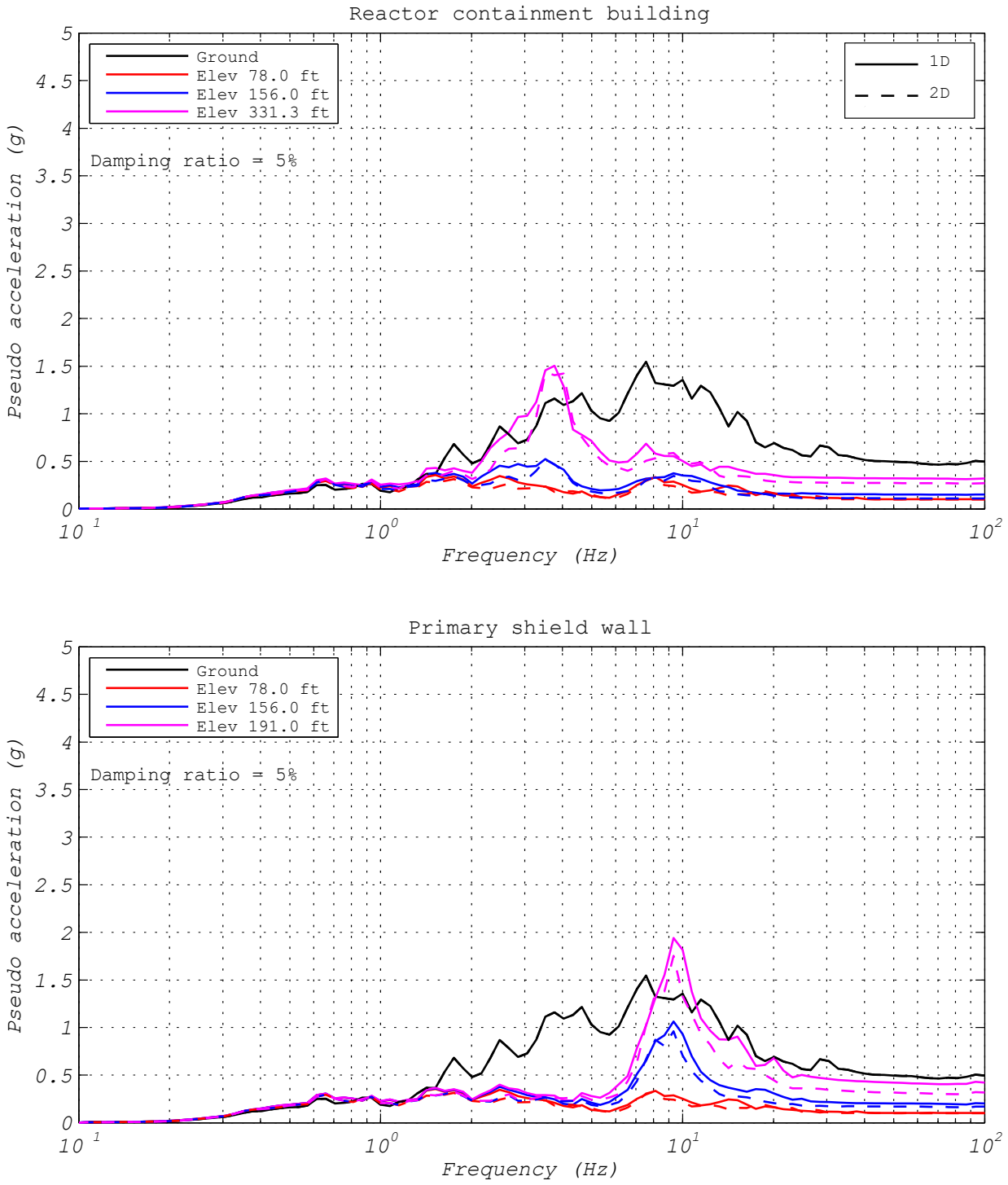

Figure 3.41 **LPRB bearing: response spectra comparison of response to ground motion EUR5 (1D and 2D analyses).**

Figures 3.42 and 3.43 compare the 1D (Run 47) to 2D (Run 55) results of the hybrid model with one experimental bearing representing all the bearings analyzed for the NRC15 ground motion. As can be seen in Figure 3.42, the maximum longitudinal displacement demand from the 1D test is 468 mm, which is smaller than the 531 mm demand obtained from the 2D test. Due to the faster and increased generation of heat in the lead core during bidirectional cycling in the 2D test as compared to the 1D test, the hysteresis loops of the 2D test became narrower much faster than the one of the 1D test. This effect is much more pronounced in these NRC15 tests with larger displacement demands than in the EUR5 tests. Because of this increased heat generation, bearing displacement demands from the 2D test were ultimately larger than the ones obtained from the 1D test. The shear-force fluctuations in the 2D test caused by perpendicular deformations were more pronounced in the NRC15 test than in the EUR5 test. This can be attributed to the almost ten times larger overall displacement demand in the NRC15 test. Finally, the shear-force interaction surface was no longer circular, and a maximum shear force of 1797 kN was reached. The shear-force interaction surface ceases to be circular because the displacement demands caused by the NRC5 ground motion are very large; therefore, the LPRB mostly responds in its post-yield range.

Figure 3.43 compares the floor response spectra for the NRC15 ground motion; note that there is a distinct difference in the size of the spectral acceleration spikes between the 1D and 2D tests. While the peaks occur around the same frequencies, the spectral accelerations from the 2D test are significantly smaller compared to the 1D test. For the 2D test the spectral amplitude at the first-mode frequency of the RCB is 0.6*g*, whereas the one from the 1D test is 1.0*g*. Similarly, the spectral amplitude at the first-mode frequency of the PSW is 0.8*g* for the 2D test and 1.7*g* for the 1D test. Less acceleration is transmitted to the superstructures in the 2D test as compared to the 1D test for two reasons:

1. As described earlier, the yield strength of the lead core reduces more and faster in the 2D test than the 1D test. A smaller characteristic strength of the isolator means that less shear force and hence less acceleration is being transmitted into the superstructure; and
2. The bidirectional movement in the 2D test produces more rounded hysteresis loops than the unidirectional movement in the 1D test. A more rounded hysteresis loop causes less abrupt changes in shear force; therefore, there are fewer acceleration spikes.

Note that all the spectral acceleration peaks computed from the recorded floor accelerations of the NRC15 tests are significantly smaller than the ones computed for the EUR5 tests. This improvement is attributed to the isolator mostly responding in its nonlinear range (low post-yield stiffness) for the NRC15 ground motion, whereas for the EUR5 ground motion the isolator mostly responds in its linear-elastic range (high initial stiffness). This same observation also explains the shift of the low-frequency spectral acceleration hump from 0.65 Hz for the EUR5 motion to ~0.25 Hz. This means the isolation period corresponding to the post-yield stiffness is somewhere around 4 sec. Finally, it is important to observe that for most elevations, the peak floor accelerations are around 0.25*g*, which is a reduction by almost a factor of three from the peak ground acceleration (PGA).

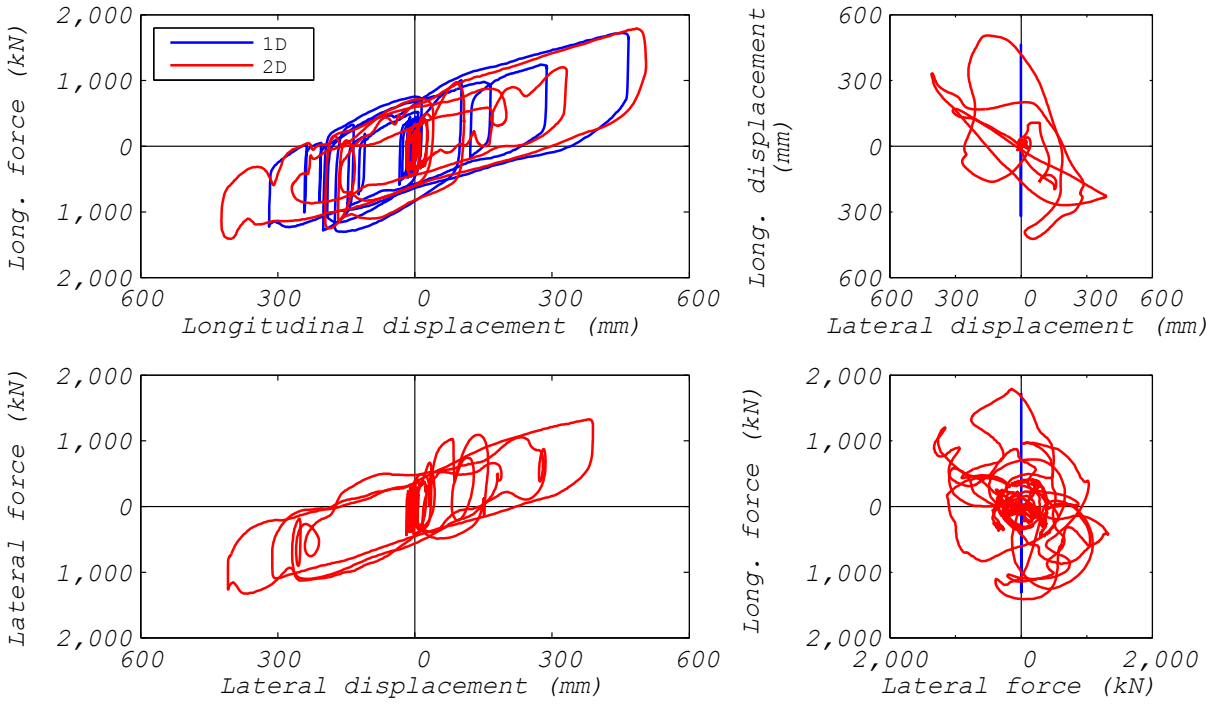

Figure 3.42 **LPRB bearing: comparison of bearing responses to ground motion NRC15 (1D and 2D analyses).**

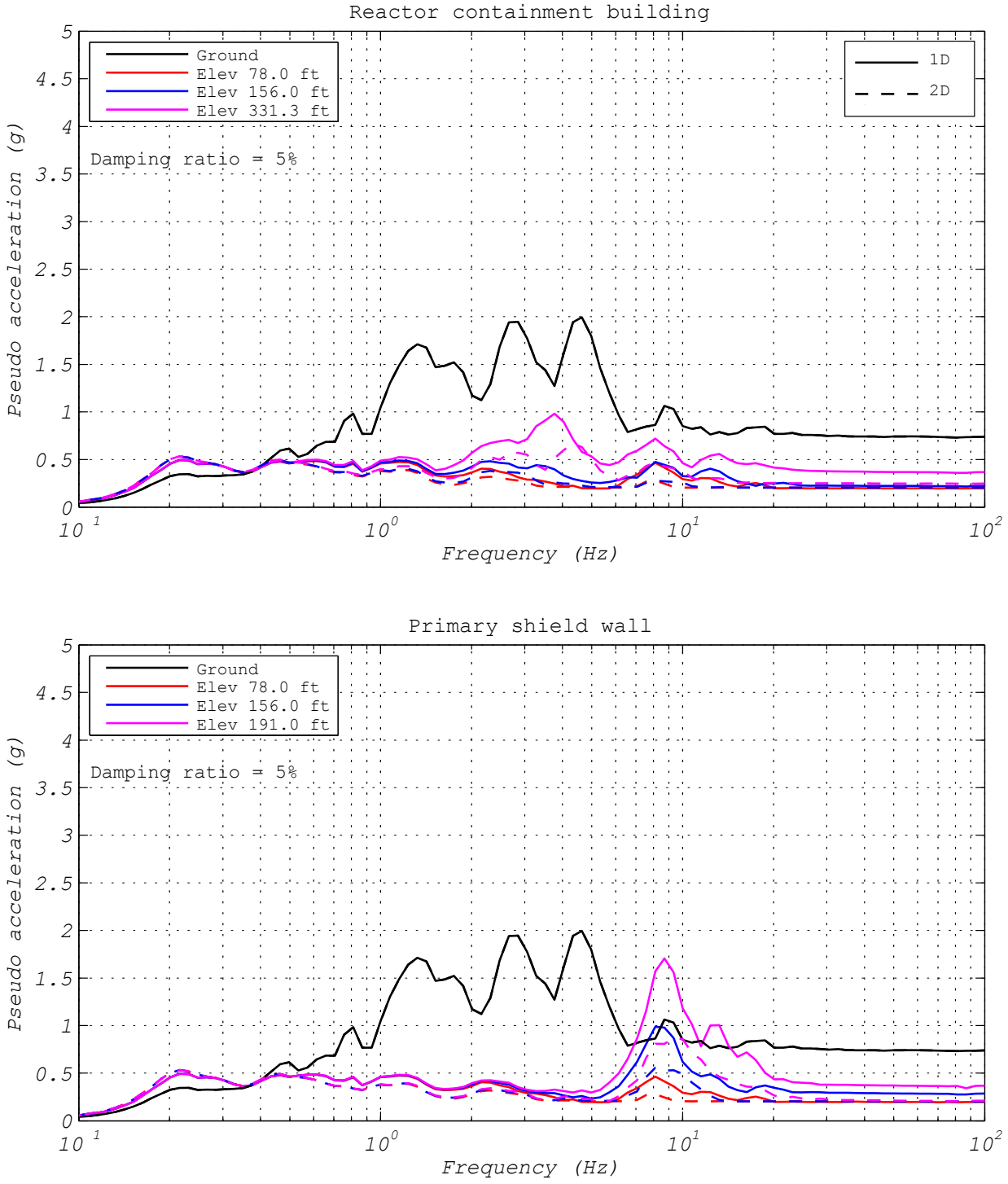

Figure 3.43 **LPRB bearing: response spectra comparison of responses to ground motion NRC15 (1D and 2D analyses).**

3.5.1.2 Influence of Vertical Excitation

Figure 3.44 compares the hysteresis loops obtained from a hybrid simulation without vertical excitation (Run 85) with a hybrid simulation including vertical excitation (Run 89). The hybrid model used for these tests had five equivalent bearings with one experimental bearing representing a group of 67 bearings under the south-west corner of the NPP, using the NRC15 ground motion. The hysteresis loops in longitudinal and lateral directions, the horizontal displacement orbits, and the shear-force interaction surfaces are nearly identical for the two tests. Close observation of the plots demonstrates that the results from the test including vertical excitation show small higher frequency (~10 Hz) shear-force oscillations that are not present in the results from the test without vertical excitation. The oscillations are most noticeable in the lateral hysteresis loop but can also be seen in the shear-force interaction diagram. It is apparent from the displacement orbit plot that these additional shear-force oscillations due to the vertical excitation have negligible effect on the bearing displacement demands. However, the shear-force oscillations clearly demonstrate the vertical–horizontal coupling that occurs in LPRBs. As the bearing displaces sideways in horizontal direction and the axial force fluctuates (between 2000 kN and 17,500 kN) due to the vertical ground motion input, the shear resistance of the bearing fluctuates as well.

Comparing the floor response spectra for the hybrid simulations with and without vertical excitation (see Figure 3.45), there is a very distinct difference in the size of the spectral acceleration spikes between the two tests. While the peaks occur around the same frequencies, the spectral accelerations from the test including vertical excitation are significantly larger. The differences are most pronounced for the PSW floor response spectra. As can be seen from the figure, the peak spectral acceleration for the test without vertical excitation is around 0.75*g*, whereas the one from the test including vertical acceleration spikes up to 4.2*g*. The spikes occur at a frequency of ~10 Hz, which is identified as the fundamental vertical frequency of the plant superstructure. As discussed in the previous section the LPRB exhibits vertical–horizontal coupling; this effect becomes most apparent in the floor response spectra, whereas it was barely noticeable in the hysteresis loop plots. Because the vertical frequency of oscillation is around 10 Hz, the shear-force oscillations caused by the coupling also occurred at around 10 Hz. The first-mode horizontal frequency of the PSW is around 8–10 Hz, which is very close to the vertical frequency of the superstructure. On the other hand, the first-mode frequency of the RCB at 3.7 Hz is well separated from the vertical frequency. Hence, the floor response spectra of the PSW are significantly affected by the vertical–horizontal coupling, while the floor response spectra of the RCB are much less influenced by this effect.

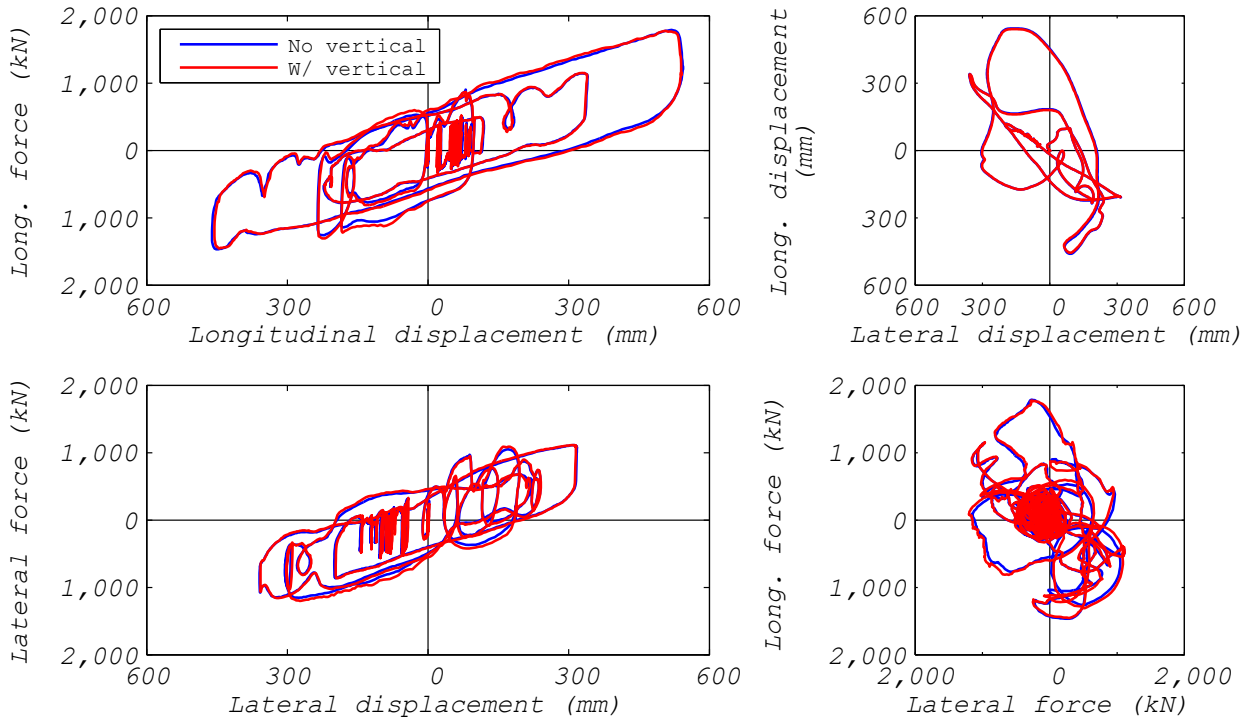

Figure 3.44 **LPRB bearing: comparison of bearing responses to a ground motion with and without vertical excitation (ground motion NRC15, 2D and 3D analyses).**

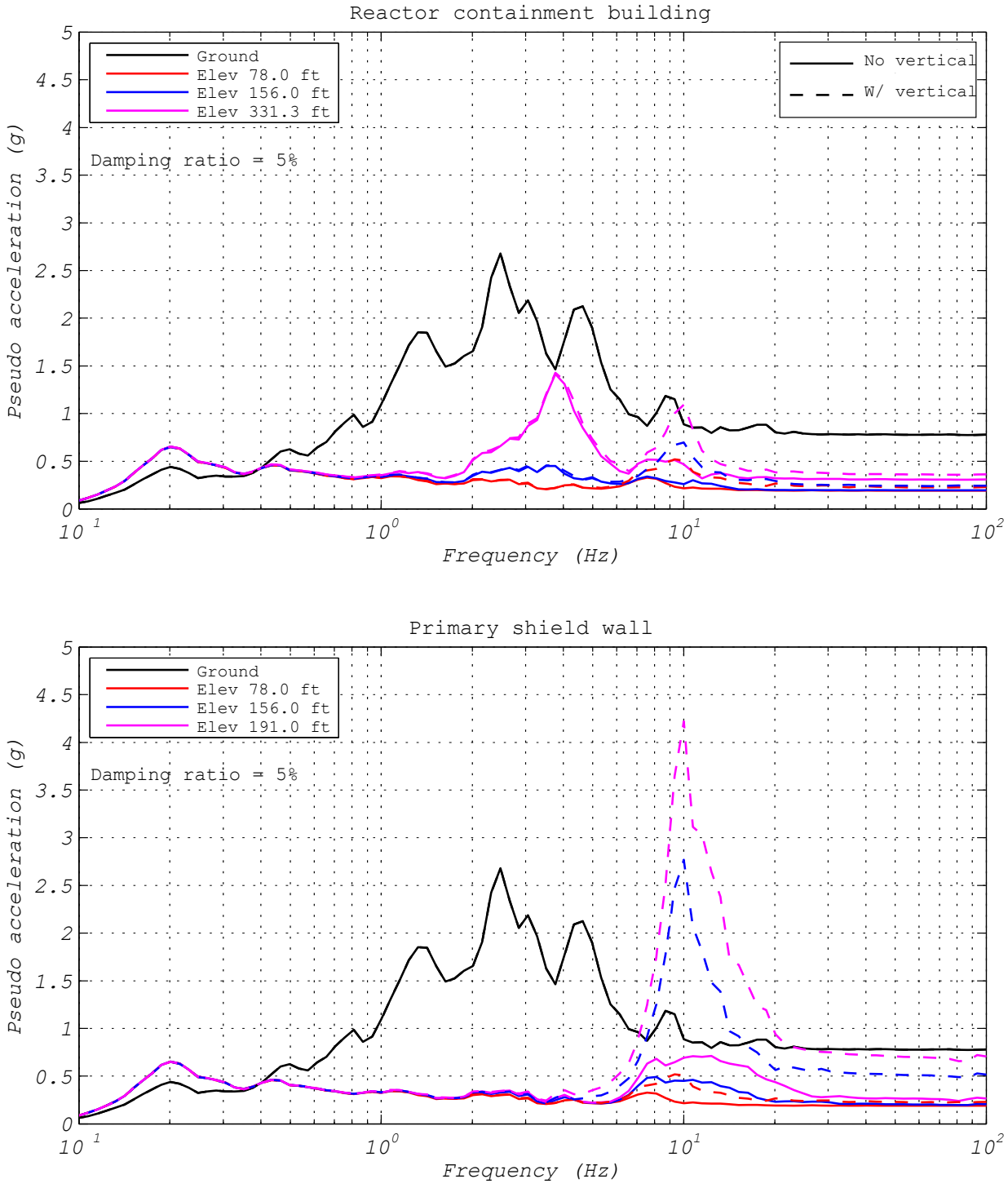

Figure 3.45 **LPRB bearing: response spectra comparison of responses to a ground motion with and without vertical excitation (ground motion NRC15, 2D and 3D analyses).**

3.5.1.3 Influence of Axial Load Variation due to Overturning

Figure 3.46 compares the hysteresis loops obtained from a hybrid simulation with the experimental bearing located in the center of the plant (Run 82) with a hybrid simulation where the experimental bearing is located in the south-west corner (Run 83). The hybrid model used for these tests had five equivalent bearings. The case with the experimental bearing in the center represents a group of 133 isolators, and the case with the experimental bearing in the south-west corner represents a group of 67 bearings. The EUR5 ground motion was used in these tests. The hysteresis loops in longitudinal and lateral directions, the horizontal displacement orbits, and the shear-force interaction surfaces were nearly identical for the two tests. It was concluded that the isolator location has a negligible influence on the response of the bearing for smaller shear strains demands, e.g., the ones caused by the EUR5 ground motion. It is also worth mentioning that the initial axial compression on the experimental bearing located in the center was 8357 kN and 8985 kN when it was located in the south-west corner.

Comparing the floor response spectra for the two hybrid simulations (see Figure 3.47), the spectral accelerations are almost identical. The hybrid test with the experimental bearing in the corner consistently produced slightly larger spectral accelerations at all frequencies and elevations than the hybrid test with the experimental bearing located in the center. This small increase in spectral accelerations is caused by the vertical–horizontal coupling characteristic of LPRBs. The vertical overturning force fluctuated between 6807 kN (24% below the initial axial force) and 11,364 kN (26% above the initial axial force). These fluctuations, which have similar frequency content as the bearing shear forces, influence the shear forces. This changes the transmissibility of the entire isolation system, and spectral accelerations in the plant superstructure were increased. This effect would be more pronounced if improved analytical bearing elements, capable of vertical–horizontal coupling, were available for the other three corners of the NPP.

Figure 3.48 compares the hysteresis loops obtained from a hybrid simulation with the experimental bearing located in the center of the plant versus a hybrid simulation where the experimental bearing was located in the south-west corner. The hybrid model used for these tests had five equivalent bearings. The case with the experimental bearing in the center represented a group of 133 isolators, and for the case with the experimental bearing in the south-west corner represented a group of 67 bearings. The NRC15 ground motion was used in these tests. The analytical bearing elements were changed from Bouc-Wen models (for the first test with the experimental bearing located in the center) to bi-linear plasticity models (for the second test with the experimental bearing in the south-west corner). This change makes comparisons of the two hybrid simulations very difficult because it is unclear if any of the differences in the results were caused by the change in bearing location or by the change of the analytical bearing models. It is again worth mentioning that the initial axial compression on the experimental bearing located in the center was 8357 kN and 8985 kN when it was located in the south-west corner.

That being said, the hysteresis loops, displacement orbits, and shear-force interaction diagram are almost identical between the two hybrid simulations; see Figure 3.48. However, the isolator post-yield stiffness for the test where the experimental bearing is located in the corner was slightly smaller than for the test where the experimental bearing was located in the center for the hysteresis loops in the longitudinal direction at very large displacements. This was more likely due to the change of the analytical bearing models than the location of the experimental

bearing. Had this difference been caused by the vertical force fluctuations due to overturning (which only affect the experimental bearing in the second test) the P-Δ effects would have been opposite to what was observed. Because the isolator was located in the negative longitudinal and lateral quadrant, a positive displacement should decrease the axial load, which should increase the shear stiffness; a negative displacement should increase the axial load, which should decrease the shear stiffness. This influence of the P-Δ effect is opposite to what is shown in the figure.

Comparing the floor response spectra for the two hybrid simulations (see Figure 3.49), the spectral accelerations are almost identical except for the spike at the fundamental frequency of the RCB, where the spectral acceleration from the center test is around 1.0g but from the corner test is around 1.5g. Again, it seems more likely that the larger spectral acceleration observed in the second test is caused by the change of the analytical bearing models rather than the change in the location of the experimental bearing.

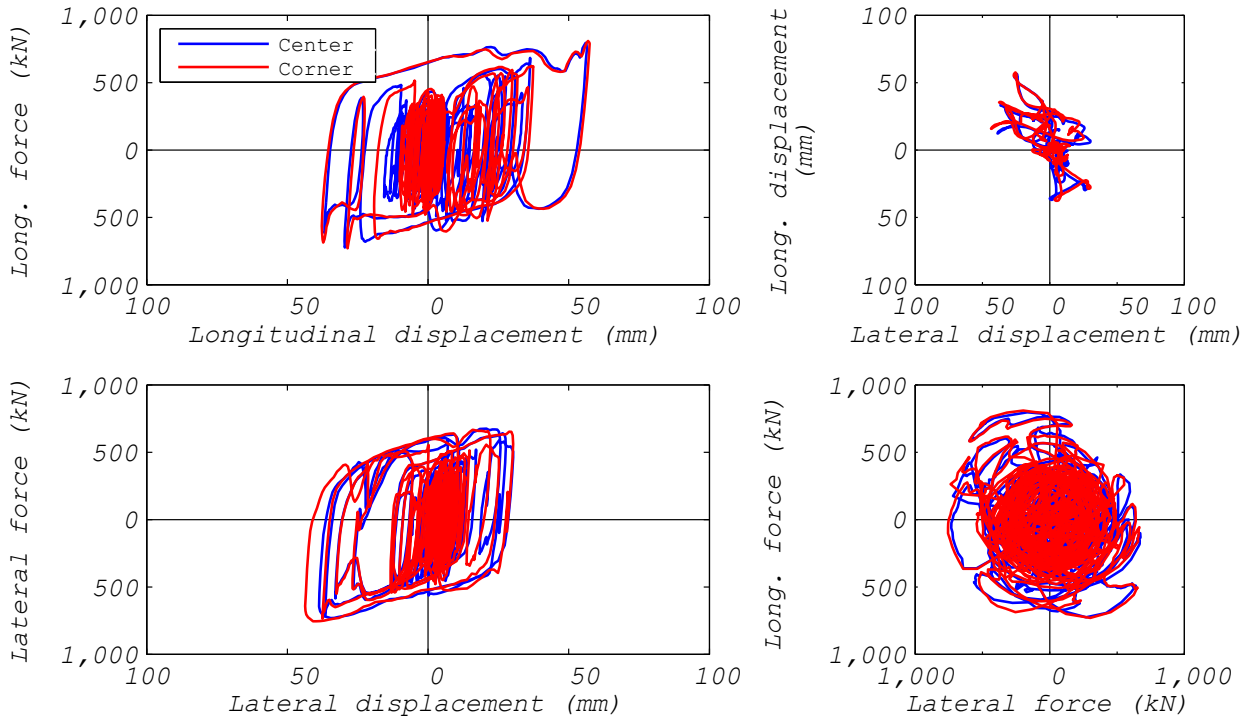

Figure 3.46 **LPRB bearing: comparison of bearing responses depending on the location of the bearing (ground motion EUR5, 3D analysis).**

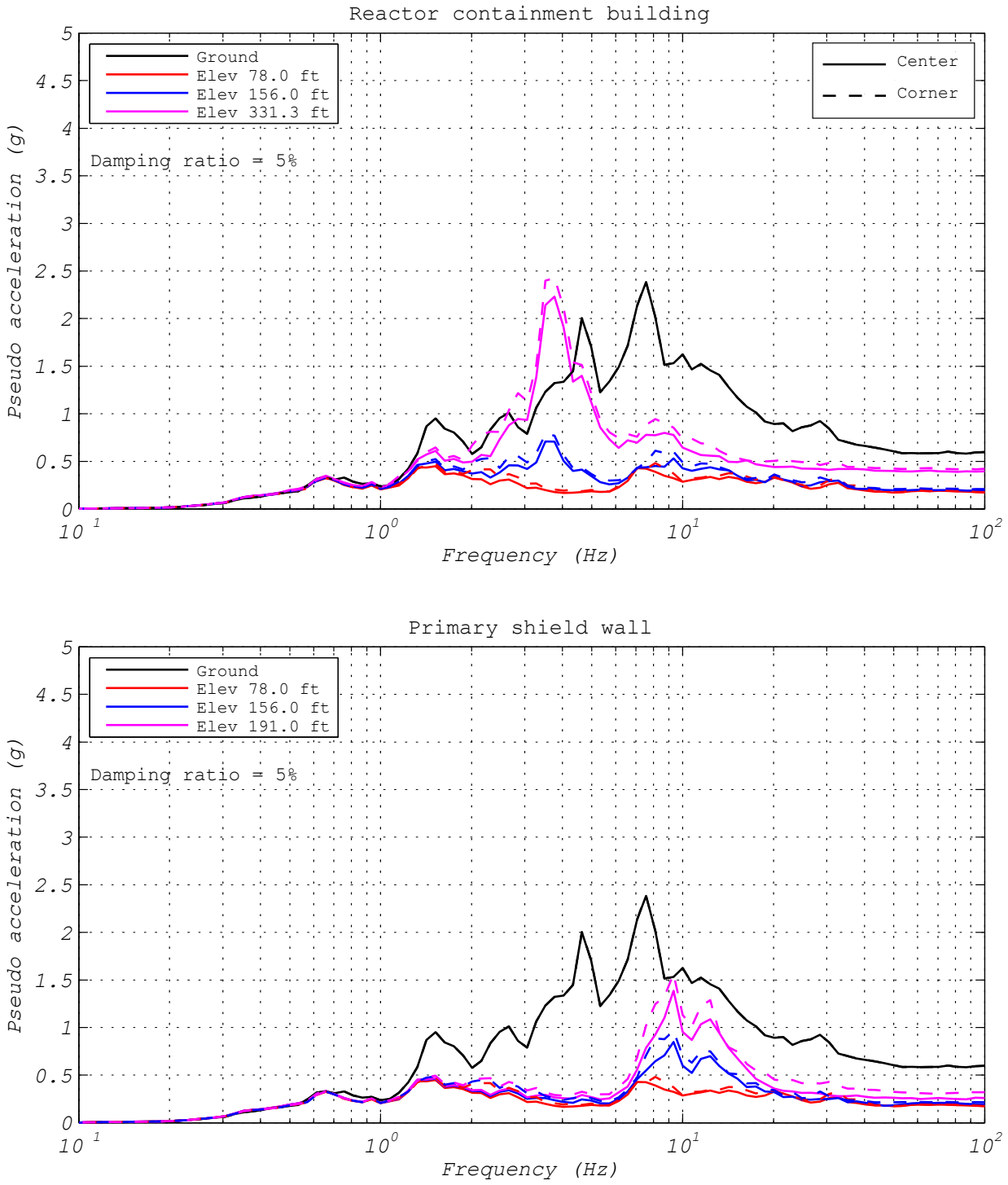

Figure 3.47 **LPRB bearing: response spectra comparison of responses depending on the location of the bearing (ground motion EUR5, 3D analysis).**

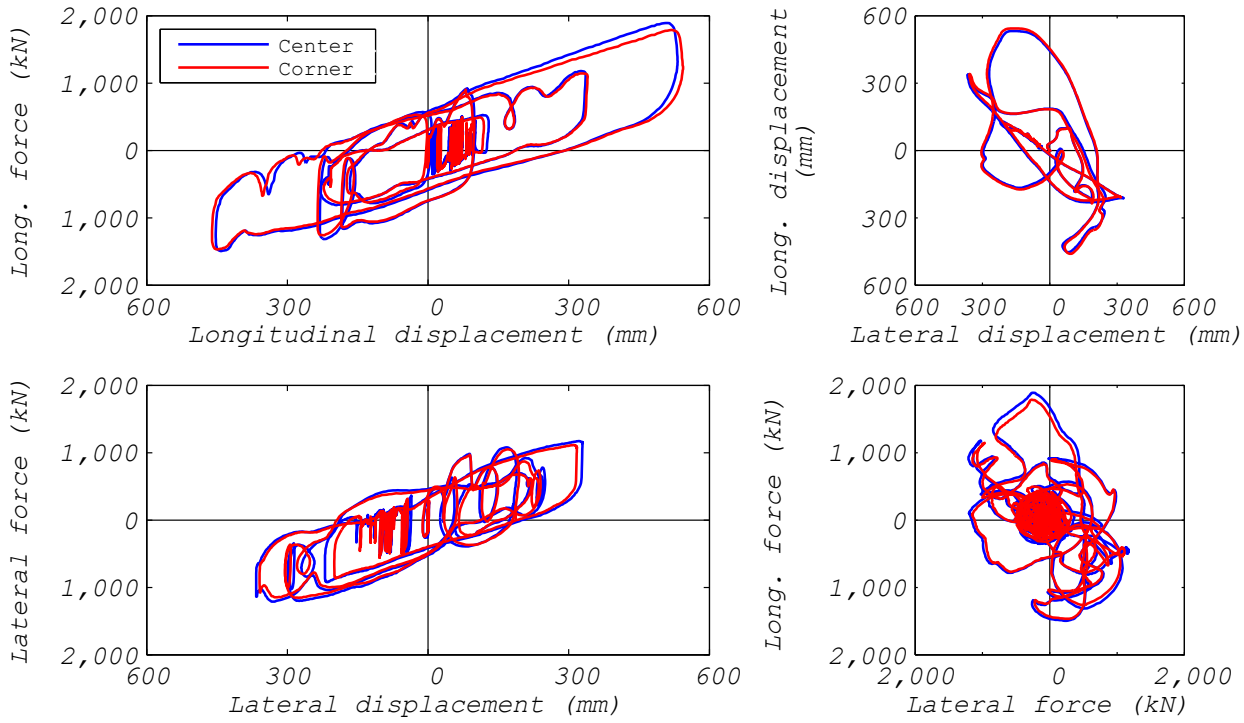

Figure 3.48 **LPRB bearing: comparison of bearing responses depending on the location of the bearing (ground motion NRC15, 3D analysis).**

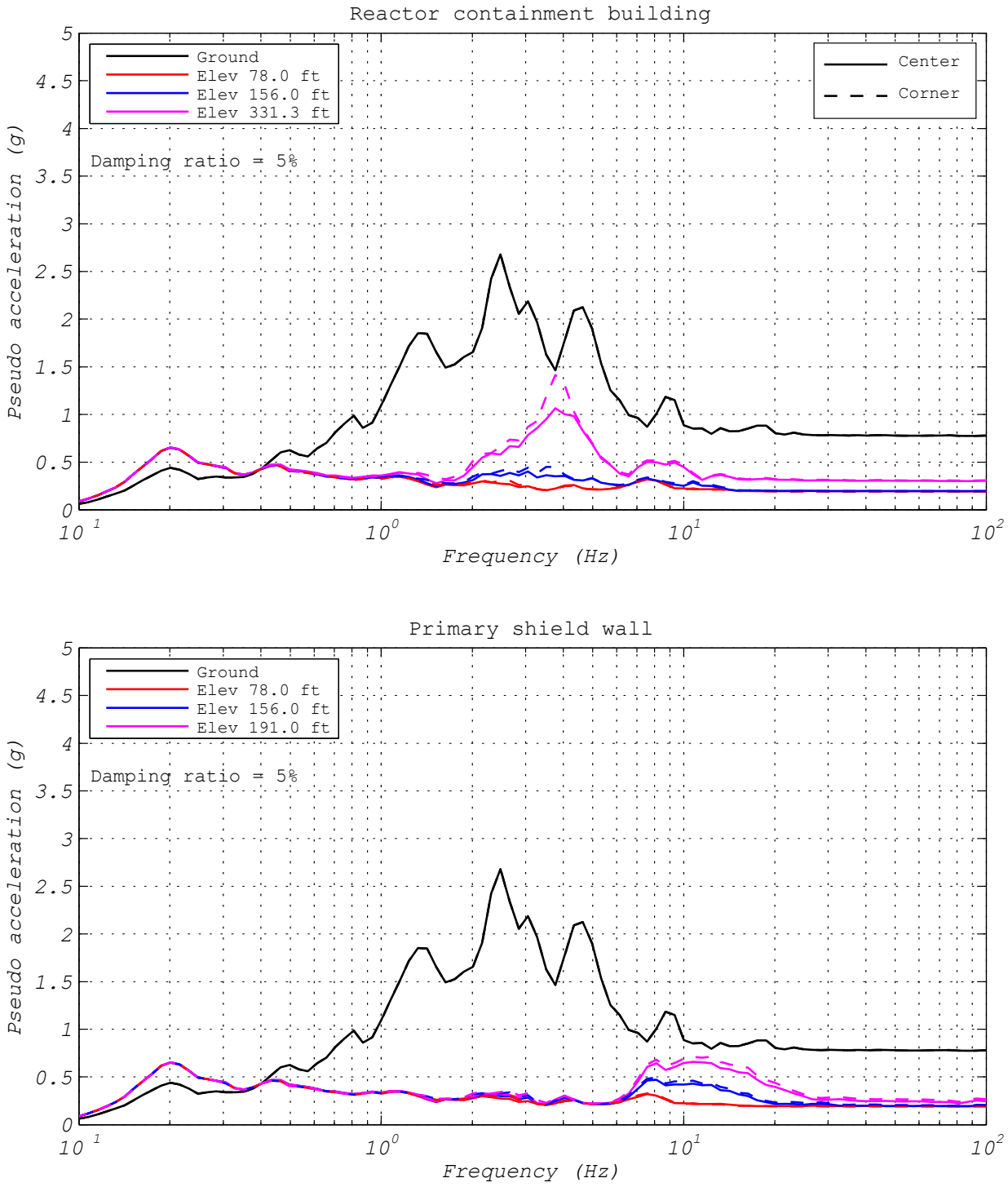

Figure 3.49 **LPRB bearing: response spectra comparison of responses depending on the location of the bearing (ground motion NRC15, 3D analysis).**

3.5.1.4 Variation due to Bearing Discretization Models

Figures 3.50 and 3.51 compare test results from three different hybrid models. In the first model, one experimental bearing represents all 527 bearings (Run 55); in the second model, one experimental bearing represents one of five bearing groups (Run 85); and lastly, in the third model the experimental bearing represents one individual bearing out of 527 (Run 61). All models were analyzed for the NRC15 ground motion. However, the hybrid simulations for the first two models were executed 25 times slower than real time, whereas the hybrid simulation for the third model had to be executed 300 times slower than real time due to the complexity of the model. These different execution speeds make it very difficult to compare the third model against the first two models. As observed in Figure 3.50, the hysteresis loops in longitudinal and lateral directions, the horizontal displacement orbits, and the shear-force interaction surfaces match fairly well for the first two models. The model where the experimental bearing represents one of five bearing groups predicts an overall slightly larger displacement demand of 561 mm than the model where one experimental bearing represents all bearings, which produces a displacement demand of 531 mm. Shear-force demands from those two models are very similar, reaching ~1.9 MN for the one bearing model and ~1.8 MN for the five bearing model. In contrast, the bearing response from the third model where the experimental bearing represents only one out of 527 bearings is very different from the first two models. It is obvious that the analytical isolator model used for the remaining 526 bearings was fairly inaccurate, and the response of the whole isolation system was dictated by the analytical bearings. It is concluded that for hybrid simulations where the experimental bearing represents only one bearing in the entire isolation system, improved analytical isolator models are necessary, and time is required during testing to iteratively tune the parameters of such improved analytical isolator models. Furthermore, means to increase computation speeds of such highly complex hybrid models are needed to perform near-real-time hybrid tests in the future.

Comparing the floor response spectra in Figure 3.51 results in similar conclusions to those drawn in the previous paragraph. The first two models produce spectral accelerations that match fairly well, while the ones from the third model—where the experimental bearing represents only one bearing—are quite different. As explained above, significant improvement in the spectral results would be expected if there had been time to better tune the analytical isolator models and/or improved analytical isolator elements had been available at the time of testing.

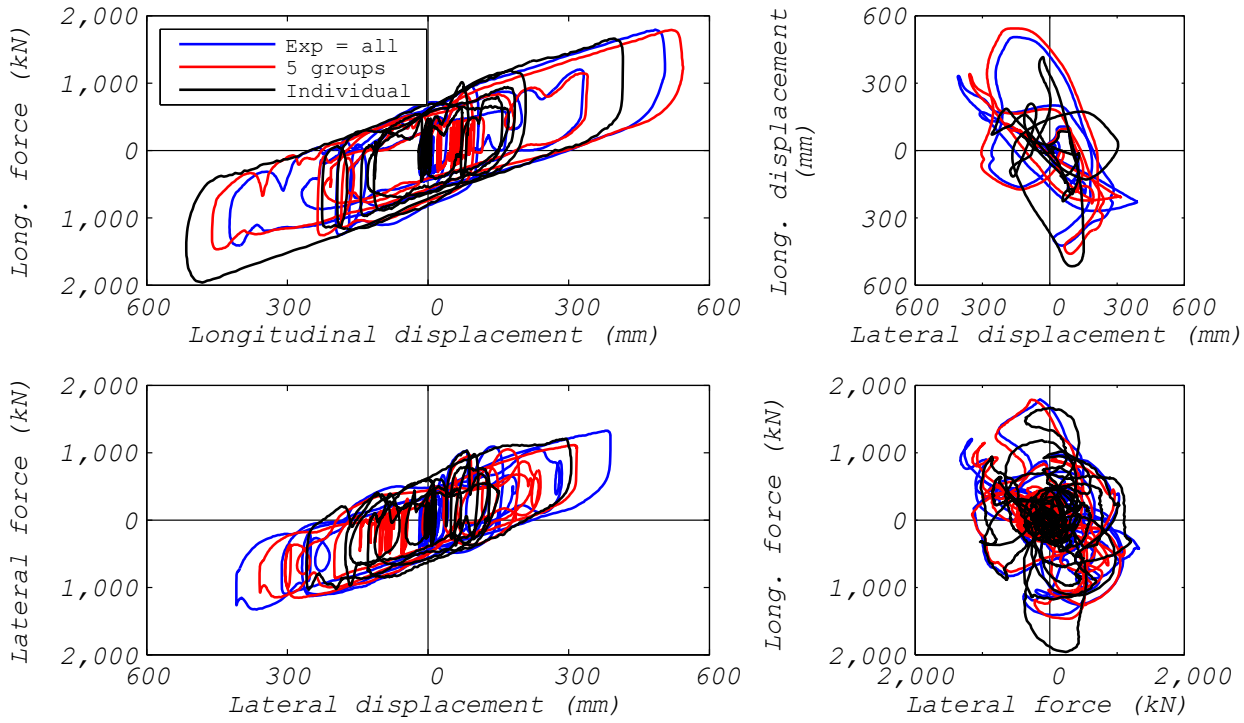

Figure 3.50 **LPRB bearing: comparison of bearing responses to bearing layout discretization (ground motion NRC15, 2D analysis).**

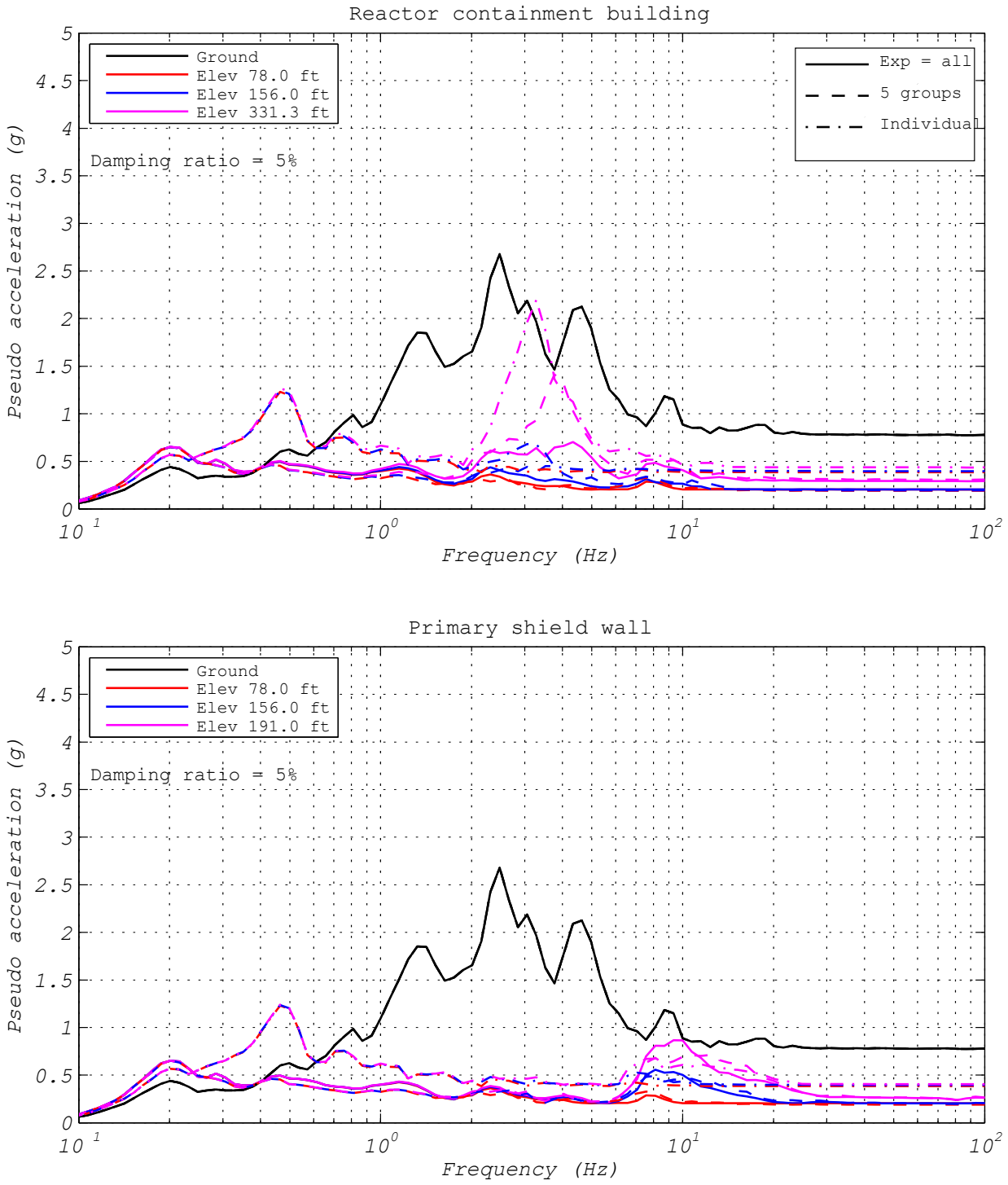

Figure 3.51 **LPRB bearing: response spectra comparison of responses to bearing layout discretization (ground motion NRC15, 2D analysis).**

3.5.1.5 Comparison Between Hybrid Simulation Tests and Analytical Estimation

Figures 3.52 and 3.53 compare an analytical simulation (Run 44A) and a hybrid simulation (Run 44) for the model with one experimental bearing representing all the bearings. Both models were analyzed for the EUR5 ground motion applied in longitudinal direction only. The analytical model utilized a bearing element based on the Bouc-Wen model with the following parameters: k_1 = 255 kN/mm, f_y = 578 kN, k_2 = 5.1 kN/mm, η = 0.75, $\beta = \gamma = 0.5$. These parameters were based on experimental results from the hybrid simulation. As can be seen from Figure 3.52, the maximum longitudinal displacement demand from the analytical simulation is 66 mm, which is a little larger than the 61 mm demand from the hybrid test. Comparing the two longitudinal hysteresis loops, it is obvious that the analytical bearing model captured the initial stiffness, the initial lead-core yield strength, and the post-yield stiffness quite well. In addition, it captured fairly well the rounded transition from the linear-elastic range into the nonlinear range. However, the analytical bearing model was not able to capture the change of the lead-core yield strength, which occurs as the bearing heats up. Furthermore, the analytical model cannot capture any short-term Mullins' effects or long-term scragging effects [Grant 2004].

A comparison of the floor response spectra presented in Figure 3.53 shows an excellent match between the analytical and hybrid simulation results. The simplified analytical model slightly overpredicts spectral accelerations at the first horizontal frequency of the RCB, and it slightly underpredicts spectral accelerations at the first horizontal frequency of the PSW. With the development of a more sophisticated model for LPRBs, the analytical predictions could be further improved.

Figures 3.54 and 3.55 compare an analytical simulation (Run 47A) and a hybrid simulation (Run 47) for the model with one experimental bearing representing all the bearings. Both models were analyzed for the NRC15 ground motion applied in longitudinal direction only. The analytical model utilized a bearing element based on the Bouc-Wen model with the following parameters: k_1 = 255 kN/mm, f_y = 672 kN, k_2 = 2.2 kN/mm, η = 0.55, $\beta = \gamma = 0.5$. These parameters were based on experimental results from the hybrid simulation. As can be seen in Figure 3.54, the maximum longitudinal displacement demand from the analytical simulation was 471 mm, which is almost identical to the 468 mm demand from the hybrid test. A comparison of the two longitudinal hysteresis loops shows that, again, the analytical bearing model captures quite well the initial stiffness, the initial lead-core yield strength, and the post-yield stiffness. However for the much larger shear strains caused by the NRC15 ground motion, the analytical model does not capture well the rounded transition from the linear-elastic range into the nonlinear range. As stated earlier, the analytical bearing model cannot capture the change of the lead-core yield strength, which occurs as the bearing heats up, or any of the more complicated phenomena, such as the short-term Mullins' effect or long-term scragging effects.

As shown in Figure 3.55, the simplified bearing model achieved an excellent match for all the floor response spectra. Once again, the analytical models slightly overpredicted spectral amplitudes for the RCB and underpredicted spectral amplitudes for the PSW; however, the differences in the spectral amplitude predictions obtained from the NRC15 ground motion are even smaller than for the previously presented results from the EUR5 motion.

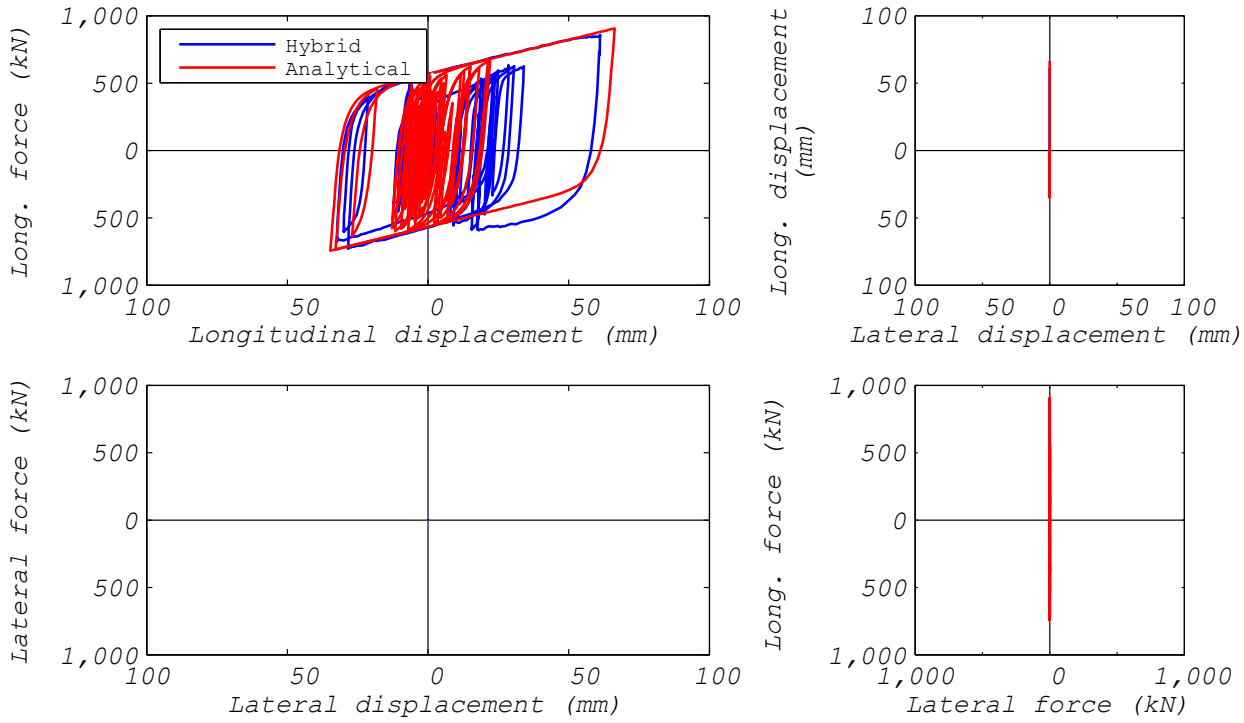

Figure 3.52 **LPRB bearing: comparison of hybrid simulation and analytical estimation bearing responses (ground motion EUR5, 1D analysis).**

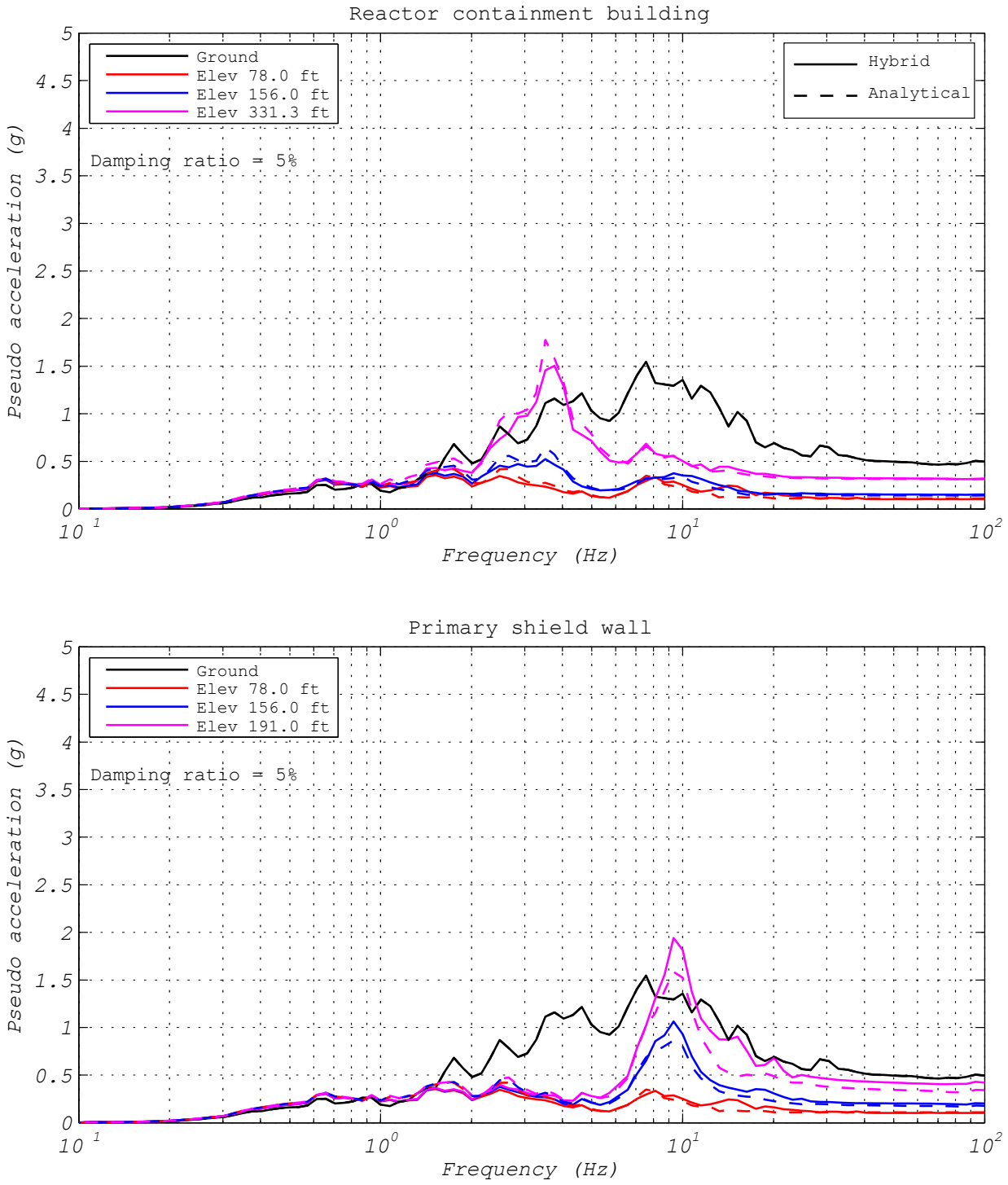

Figure 3.53 **LPRB bearing: response spectra comparison of hybrid simulation and analytical estimation responses (ground motion EUR5, 1D analysis).**

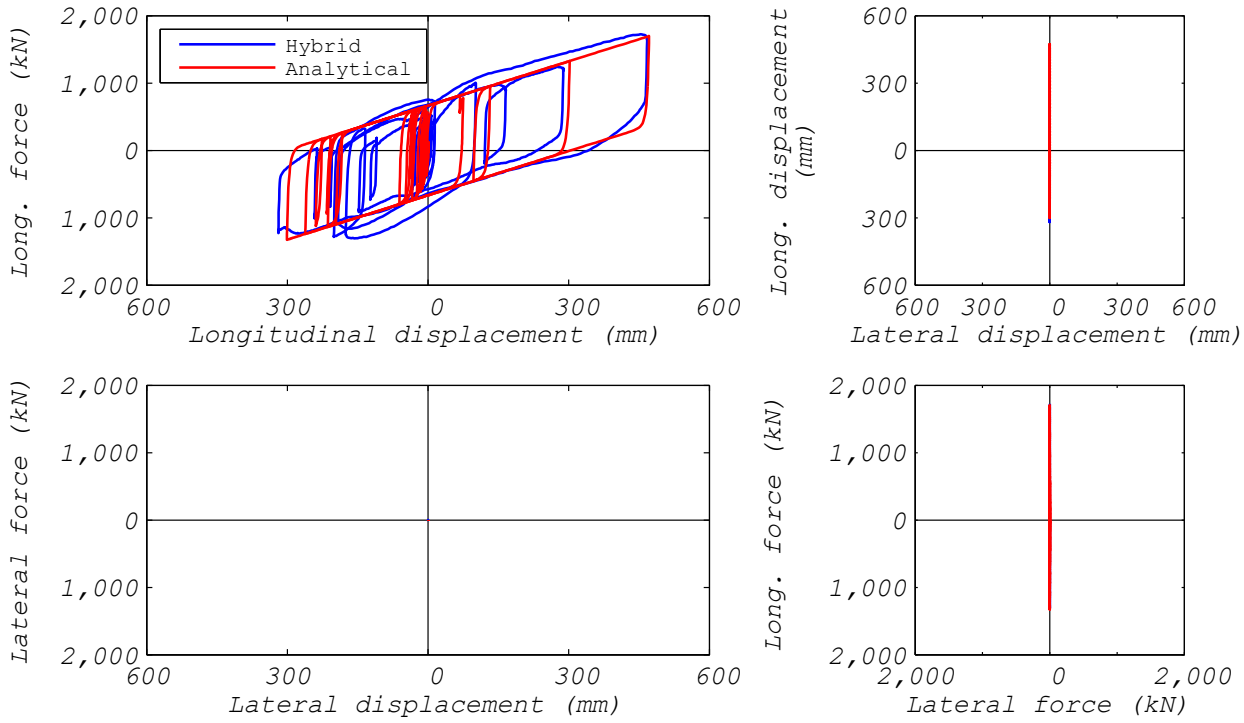

Figure 3.54 **LPRB bearing: comparison of hybrid simulation and analytical estimation bearing responses (ground motion NRC15, 1D analysis).**

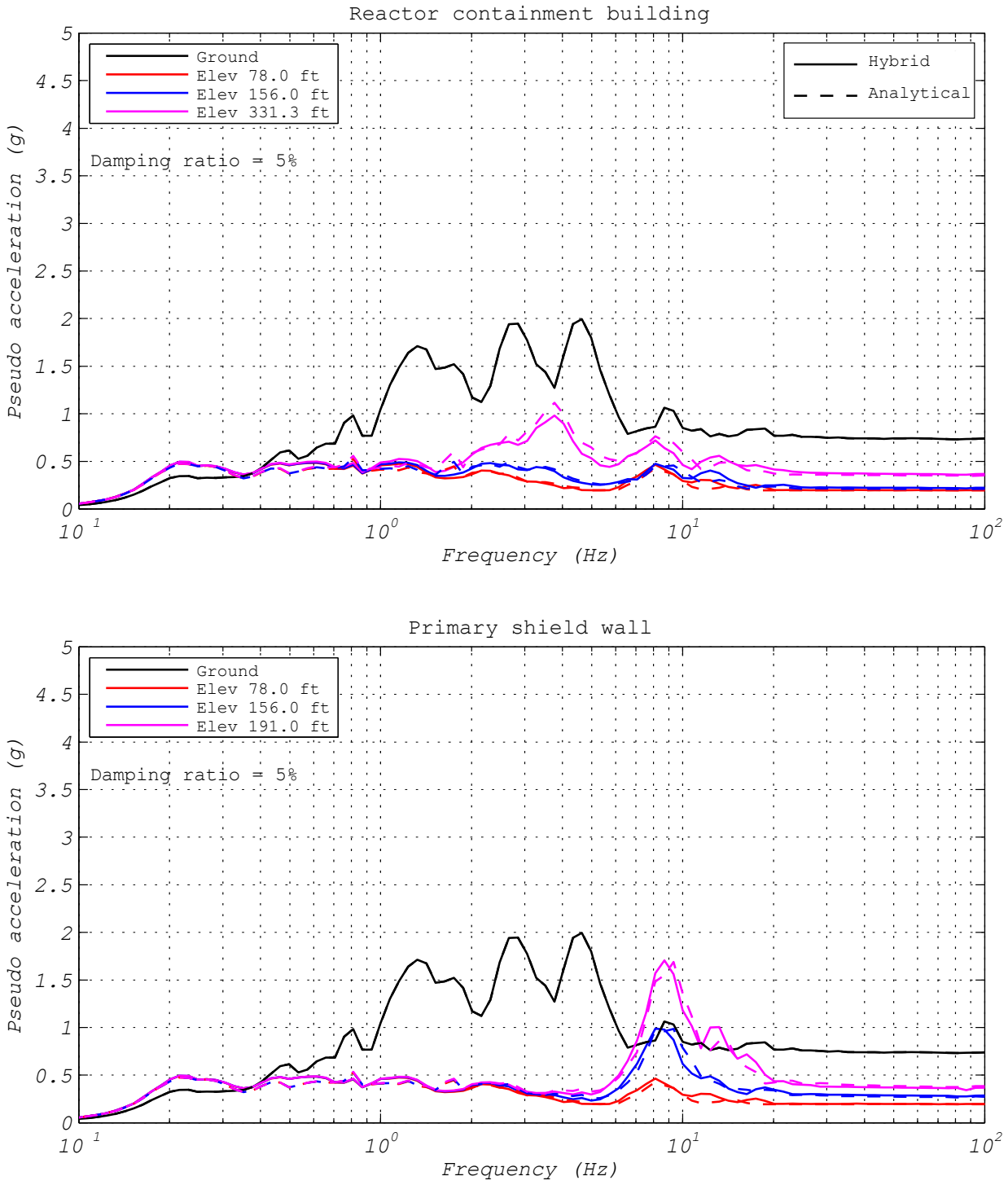

Figure 3.55 **LPRB bearing: response spectra comparison of hybrid simulation and analytical estimation responses (ground motion NRC15, 1D analysis).**

Figures 3.56 and 3.57 compare an analytical simulation (Run 45A) and a hybrid simulation (Run 45) for the model with one experimental bearing representing all the bearings. Both models were analyzed for the EUR5 ground motion applied in the two horizontal directions. The analytical model utilized a bearing element based on the Bouc-Wen model with the following parameters: k_1 = 255 kN/mm, f_y = 578 kN, k_2 = 5.1 kN/mm, $\eta = 0.75$, $\beta = \gamma = 0.5$. These parameters were based on experimental results from the hybrid simulation. The same unmodified parameters were used as for the unidirectional analysis presented above. As shown in Figure 3.56, the maximum bidirectional displacement demand from the analytical simulation was 68 mm, which is larger than the 54 mm demand obtained from the hybrid test. While a good match of the hysteresis loop in the lateral direction was achieved, the match in the longitudinal direction was not as good. Comparing the hysteresis loops in either direction, it is obvious that the analytical bearing model again captured quite well the initial stiffness, the initial lead-core yield strength, and the post-yield stiffness. As stated earlier, the analytical bearing model cannot capture the change of the lead-core yield strength, which occurs as the bearing heats up, or any of the more complicated phenomena, such as the short-term Mullins' effect or long-term scragging effect.

A comparison of the floor response spectra demonstrates an outstanding match between the analytical and hybrid simulation results, as shown in Figure 3.57.

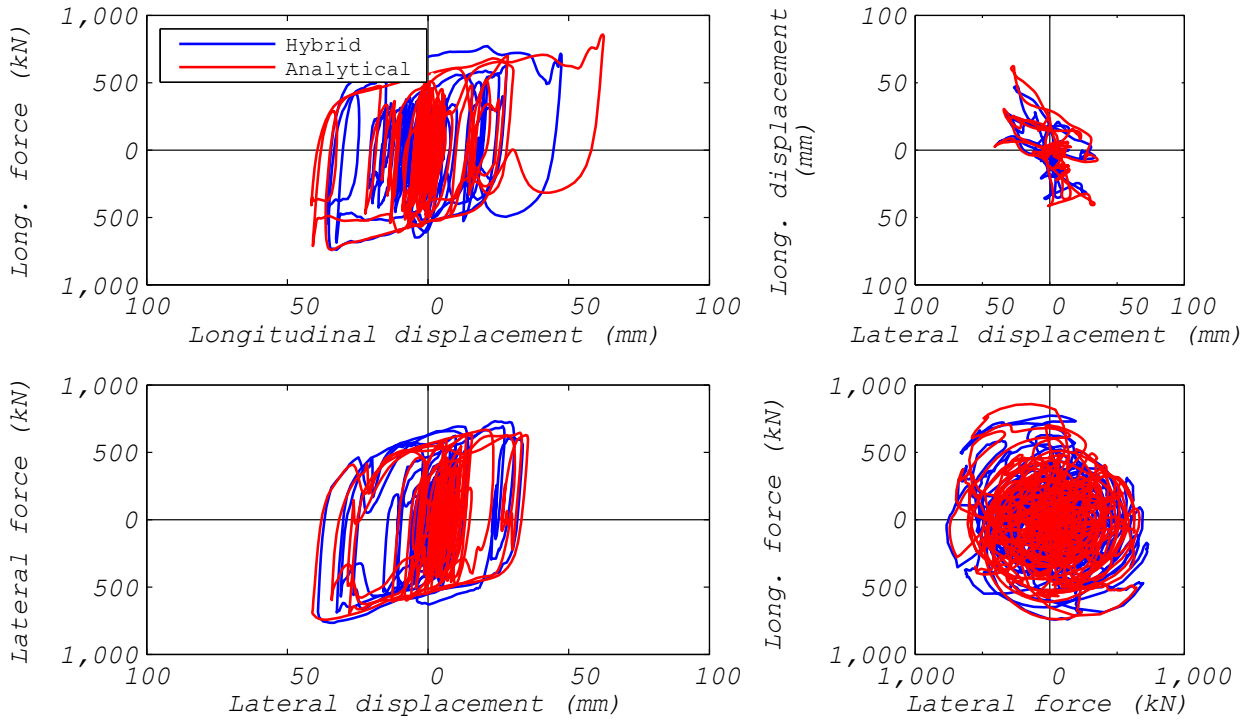

Figure 3.56 **LPRB bearing: comparison of hybrid simulation and analytical estimation bearing responses (ground motion EUR5, 2D analysis).**

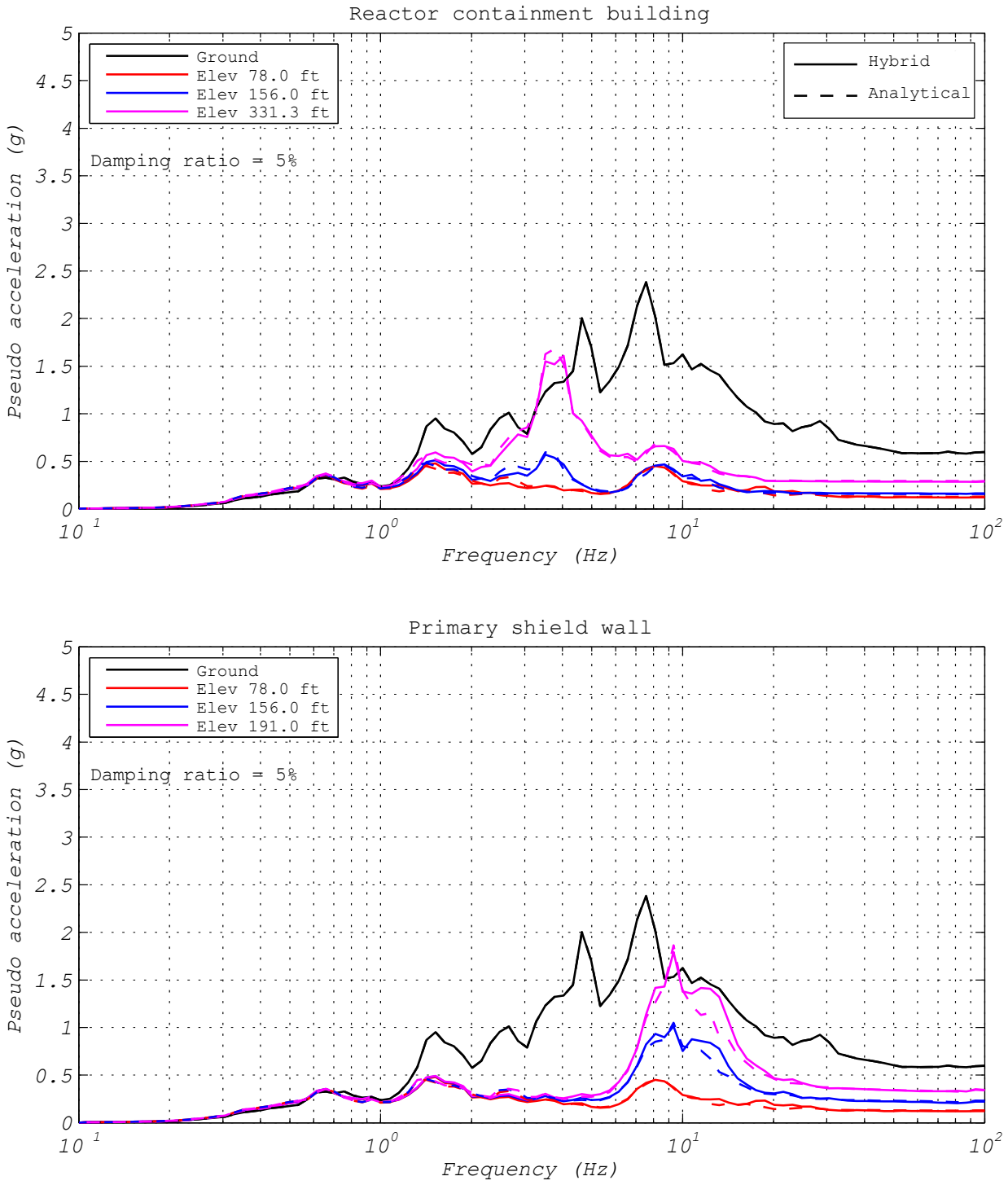

Figure 3.57 **LPRB bearing: response spectra comparison of hybrid simulation and analytical estimation responses (ground motion EUR5, 2D analysis).**

Figures 3.58 and 3.59 compare an analytical simulation and a hybrid simulation for the model with one experimental bearing representing all the bearings. Both models were analyzed for the NRC15 ground motion applied in the two horizontal directions. The analytical model utilized a bearing element based on the Bouc-Wen model with the following parameters: k_1 = 255 kN/mm, f_y = 672 kN, k_2 = 2.2 kN/mm, $\eta = 0.55$, $\beta = \gamma = 0.5$. These parameters were based on experimental results from the hybrid simulation. The same unmodified parameters were used as for the unidirectional analysis presented above. As shown in Figure 3.58, the maximum bidirectional displacement demand from the analytical simulation is 559 mm, which is larger than the 531 mm demand obtained from the hybrid test. While a decent match of the hysteresis loop in longitudinal direction was achieved, the match in lateral direction was not satisfactory. Comparing the hysteresis loops in either direction, it is obvious that the analytical bearing model again captures the initial stiffness, the initial lead-core yield strength and the post-yield stiffness quite well. For these large shear strains caused by the NRC15 ground motion, the analytical bearing model was not able to capture the roundedness of the hysteresis loops, the change of the lead-core yield strength, which occurs as the bearing heats up, or any of the more complicated phenomena, such as the short-term Mullins' effect or long-term scragging effect.

A comparison of the floor response spectra demonstrates a decent match between the analytical and hybrid simulation results; see Figure 3.59. Note that the analytical simulation consistently overpredicted spectral accelerations around the fundamental frequencies of the different parts of the superstructure.

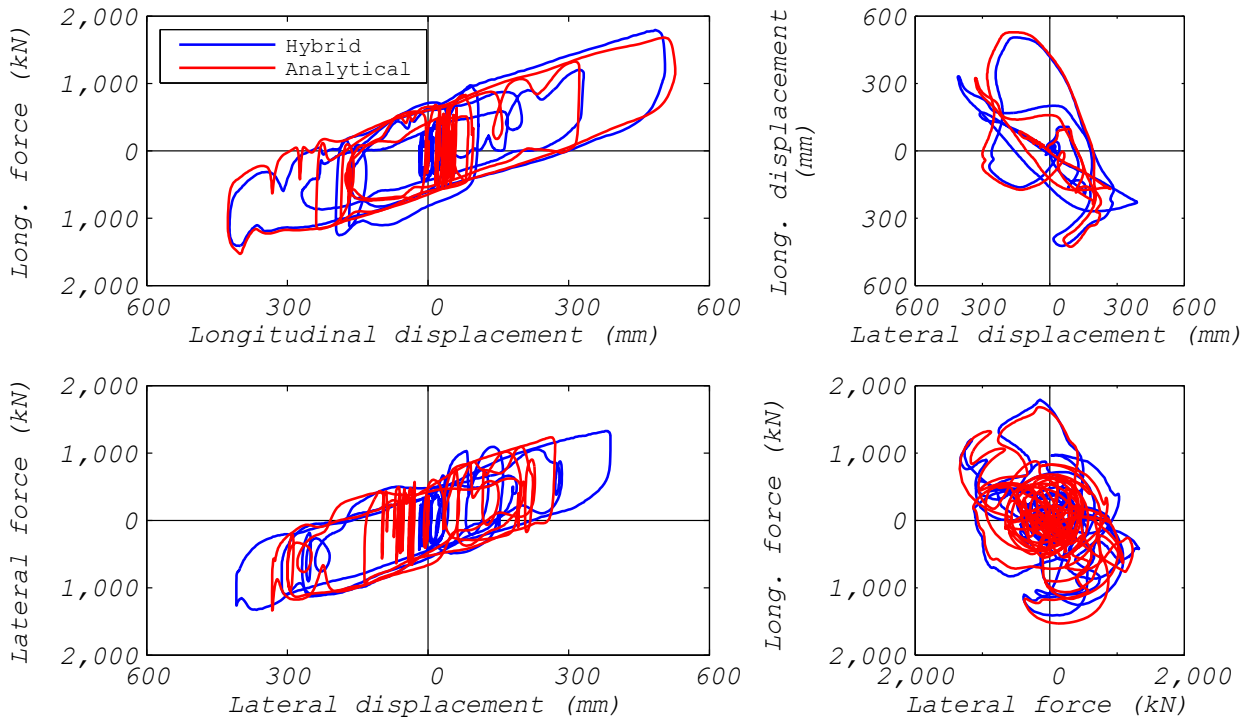

Figure 3.58 **LPRB bearing: comparison of hybrid simulation and analytical estimation bearing responses (ground motion NRC15, 2D analysis).**

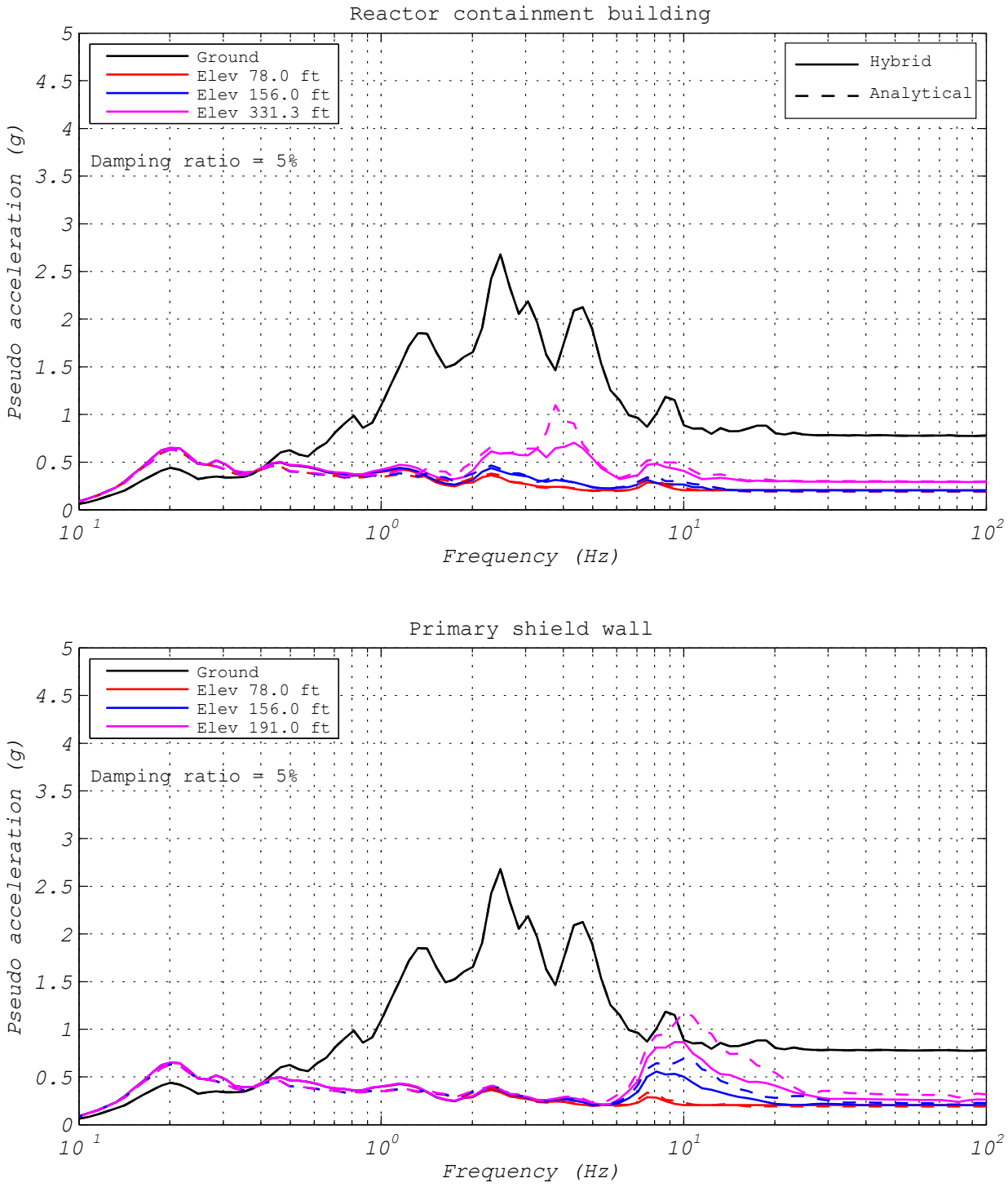

Figure 3.59 **LPRB bearing: response spectra comparison of hybrid simulation and analytical estimation responses (ground motion NRC15, 2D analysis).**

3.5.2 ESCO RTS: EQS Test Results

3.5.2.1 Comparison of 1D and 2D Horizontal Inputs

Figure 3.60 compares the hysteresis loops obtained for a 1D longitudinal hybrid simulation (Run 17) with a 2D bidirectional hybrid simulation (Run 18). The hybrid model had one experimental bearing representing all of the bearings and was analyzed for the EUR5 ground motion. Both tests were conducted 25 times slower than real time. As the figure shows, the 2D bidirectional test produces larger shear-force fluctuations and shear-force spikes compared to the 1D test. The shear-force spikes are caused by the static and breakaway friction characteristics of the EQS bearing when tested at slow speeds. Due to bidirectional excitation, more load reversals and therefore more shear-force oscillations and shear-force spikes occur in the 2D test compared to the 1D test. Most likely additional shear-force fluctuations were generated in the 2D test by sliding along the sidewalls of the EQS bearing. For the 1D test, the shear-force envelope reached 1300 kN, which corresponds to a static coefficient of friction of approximately 15%. For the 2D test, the shear-force interaction surface was almost circular, and its radius was close to the static friction of 1800 kN. This corresponds to a static coefficient of friction in the bearing of approximately 20%.

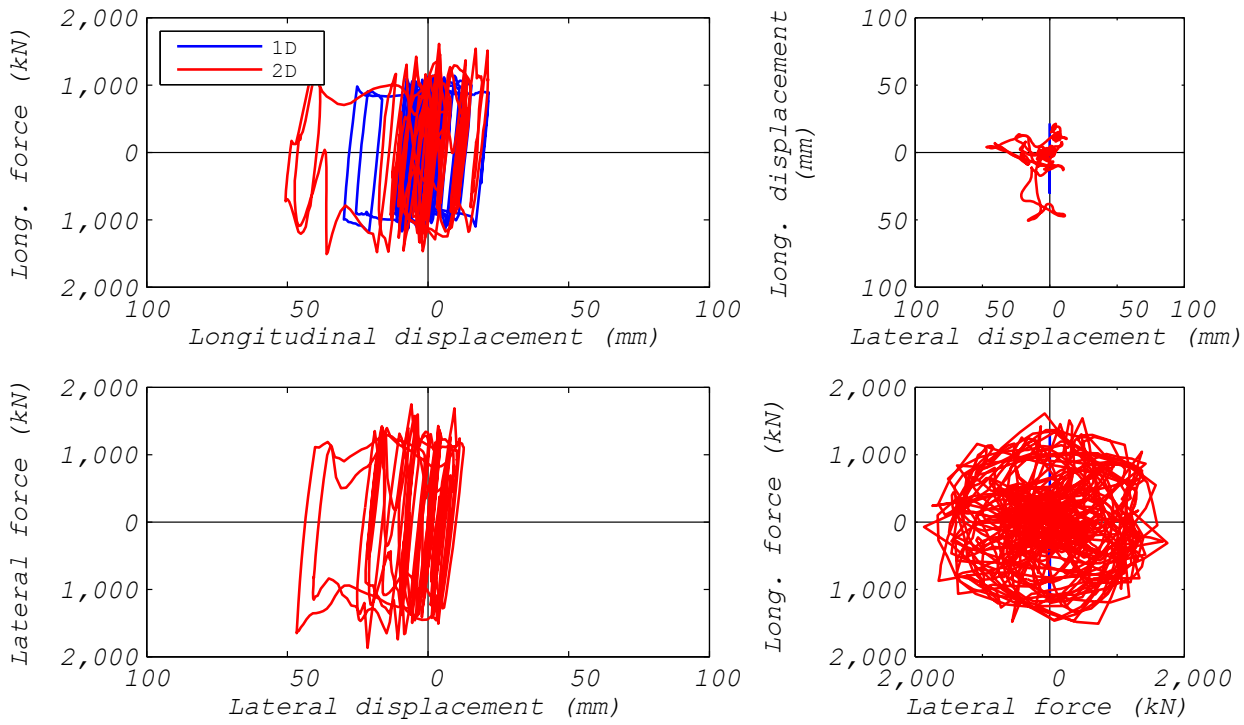

Figure 3.60 **EQS bearing: comparison of bearing responses to ground motion EUR5 executed 25 times slower than real time(1D and 2D analyses).**

Figure 3.61 shows several floor response spectra for the RCB and PSW. In general, the magnitudes of the spectral acceleration spikes are different in the 1D and 2D test, but they occur at the same frequencies. These peaks can be identified in the spectra at several distinct frequencies. For the RCB, the largest spike in the floor spectra reaches 4.2*g* and occurs at ~3.7 Hz, which corresponds to the first horizontal mode of vibration of the RCB. A lower spike of ~1.5*g* is observed between 7.5–10 Hz, which is due to the interaction of the RCB with the PSW and SSW. Similarly, in the floor response spectra of the PSW it is possible to identify the main spike at ~9.5 Hz, reaching a spectral acceleration of 4.8*g*. This spike corresponds to the first-mode frequency of the PSW. These large amplifications of the spectral accelerations at the fundamental frequencies of the RCB and PSW are caused by the very sudden and large change in stiffness that occurs when sliding commences, which is typical for isolators of the sliding friction type, especially if static and breakaway friction phenomena are present. Due to the larger shear-force oscillations in the 2D hybrid simulation floor spectral accelerations around the fundamental frequencies of the RCB and PSW are larger in the 2D test than in the 1D test. Note that at higher elevations, peak floor accelerations in both the RCB and PSW exceeded PGAs. For the PSW, the peak floor acceleration reached as high as 0.75*g*.

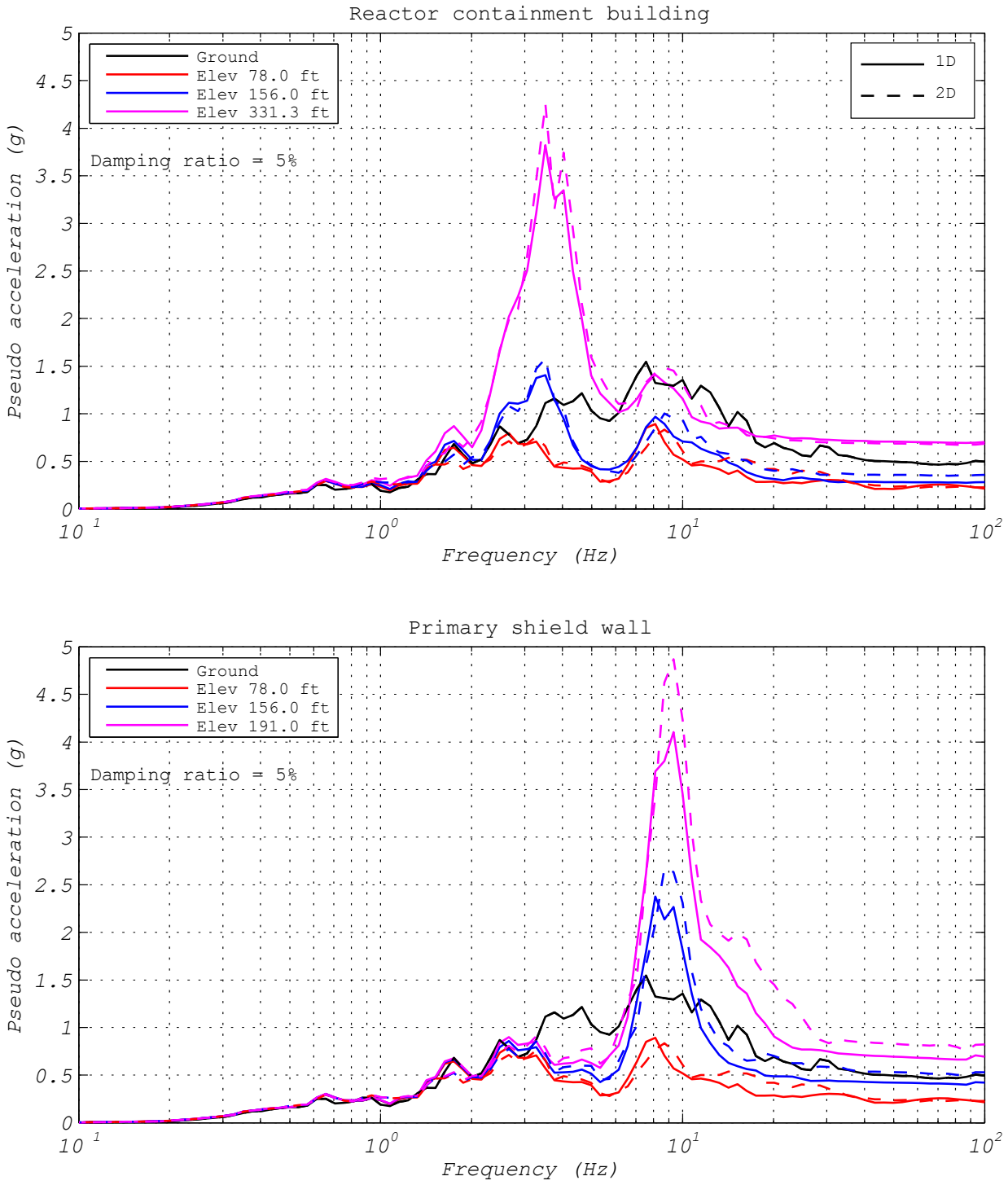

Figure 3.61 **EQS bearing: response spectra comparison of responses to ground motion EUR5 (1D and 2D analyses).**

Figure 3.62 compares 1D (Run 22) versus 2D (Run 21) test results of the hybrid model with one experimental bearing representing all the bearings analyzed for the NRC2 ground motion. Both of these hybrid tests were executed 25 times slower than real time. The maximum longitudinal displacement demand for the 1D test is 100 mm, which is smaller than the 125 mm obtained from the 2D test. The reduction in the shear resistance in one direction due to simultaneous movement in the perpendicular direction results in a 25% larger displacement demand from the 2D test. Once again, the 2D test seems to exhibit more fluctuation in the shear forces. As described earlier, these additional oscillations are most likely caused by the increase in the static and breakaway friction forces due to bidirectional motion, and the additional shear-force fluctuations that are generated by sliding along the sidewalls of the EQS bearing. For the 1D test, the shear-force envelope reached 1600 kN, which corresponds to a static coefficient of friction of approximately 18%. For the 2D test, the shear-force interaction surface was almost circular, and its radius is close to the static friction of 2000 kN. This corresponds to a static coefficient of friction in the bearing of approximately 23%. Both of these static coefficients of friction for the NRC2 ground motion input are 3% larger than those obtained in the previously described hybrid tests with the EUR5 ground motion input.

Figure 3.63 compares the floor response spectra for the NRC2 ground motion executed 25 times slower than real time. Note the large amplifications of the response at certain frequencies even though the magnitudes of these amplifications are different for 1D and 2D hybrid tests. The specific frequencies are ~3.7 Hz and 9.5 Hz, which correspond to the first horizontal mode of vibration of the RCB and the PSW, respectively. For the RCB, response spectra for the 1D and 2D tests are almost identical. However, for the PSW floor spectra the spectral accelerations around the fundamental frequency of the PSW are significantly larger for the 2D test compared to the 1D test. It can be concluded that the previously described high-frequency oscillations, which are larger in the 2D test than those obtained from the 1D test, are again the cause for the observed behavior. Finally, note that the small hump in the floor spectra at ~0.38 Hz, which corresponds to the first mode of vibration of the isolated structure at the post-yield stiffness of the EQS bearing.

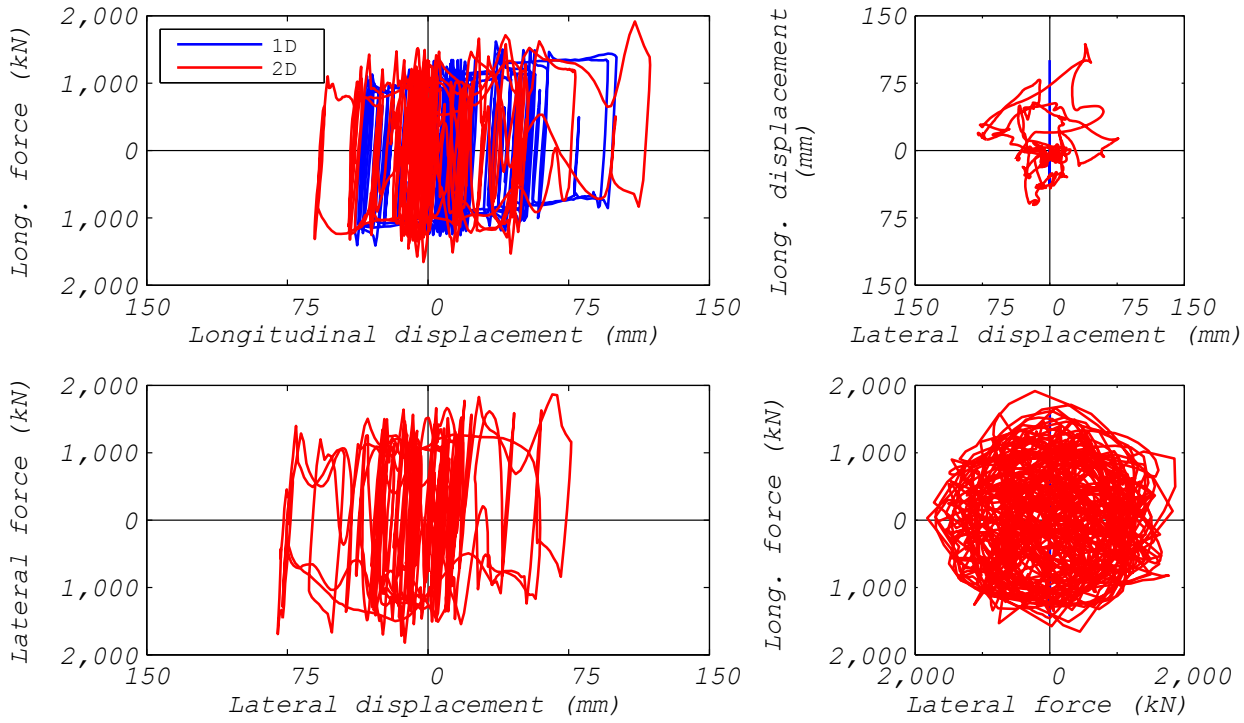

Figure 3.62 **EQS bearing: comparison of bearing responses to ground motion NRC2 executed 25 times slower than real time (1D and 2D analyses).**

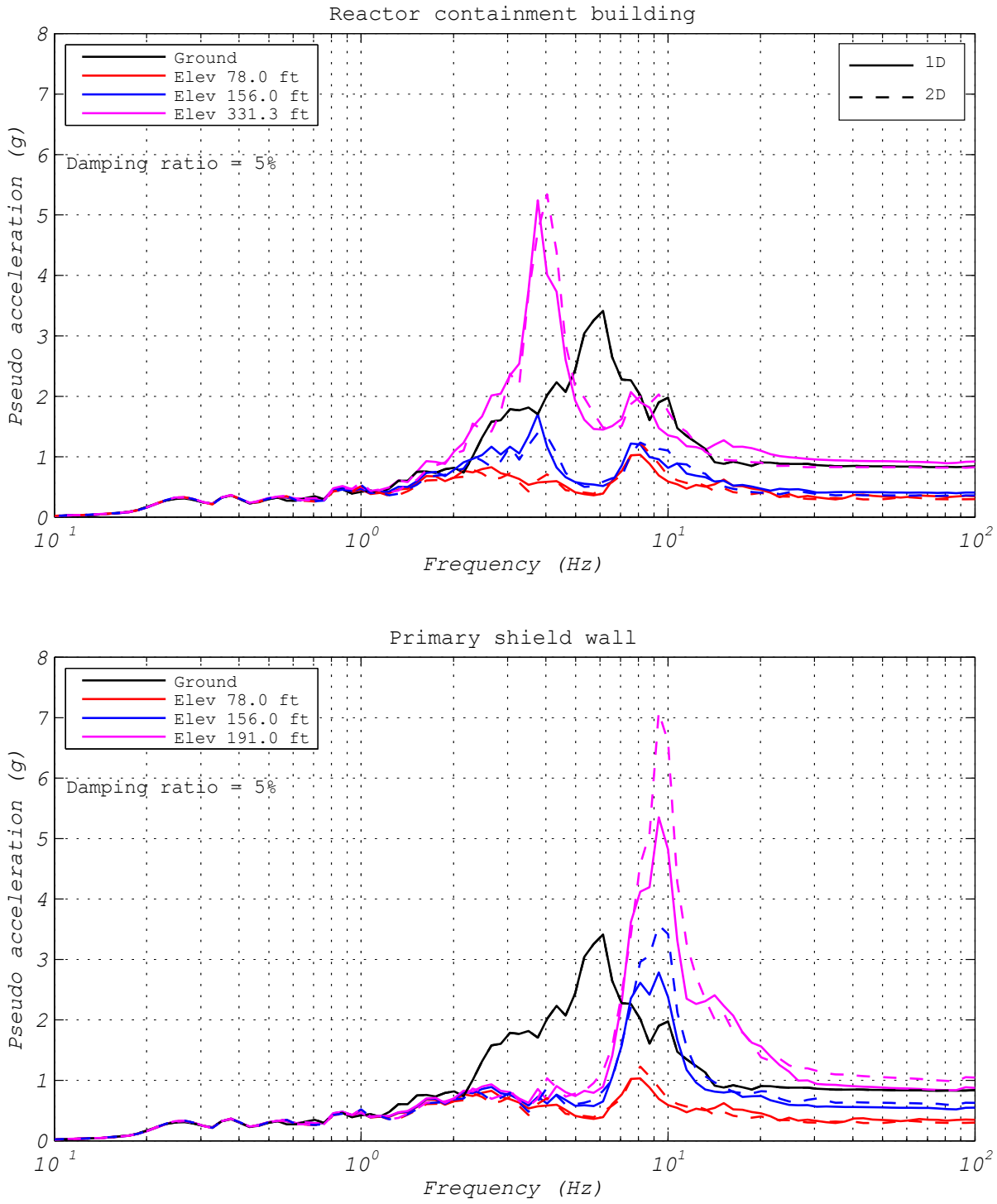

Figure 3.63 **EQS bearing: response spectra comparison of responses to ground motion NRC2 executed 25 times slower than real time (1D and 2D analyses).**

Figure 3.64 compares the test results of 1D (Run 52) versus 2D (Run 54) hybrid models with one experimental bearing representing all the bearings analyzed for the NRC2 ground motion. Both of these hybrid tests were executed five times slower than real time. The maximum longitudinal displacement demand for the 1D test is 92 mm, which is smaller than the 114 mm obtained from the 2D test. The reduction in the shear resistance in one direction due to simultaneous movement in the perpendicular direction results in a 25% larger displacement demand obtained from the 2D test. Heat generation on the sliding surface (due to rapid testing), as well as farther overall sliding due to bidirectional motion, might further reduce the shear resistance of the bearing as time elapses. Once again, the 2D test seems to exhibit more fluctuation in the shear forces. As described earlier, these additional oscillations are most likely caused by the increase in the static and breakaway friction forces due to bidirectional motion, and the additional shear-force fluctuations that are generated by sliding along the sidewalls of the EQS bearing.

Figure 3.65 compares the floor response spectra for the NRC2 ground motion executed five times slower than real time. Note the large amplifications of the response at certain frequencies even though the magnitudes of these amplifications are different for 1D and 2D hybrid tests. The specific frequencies are ~3.7 Hz and 9.5 Hz, which correspond to the first horizontal mode of vibration of the RCB and the PSW, respectively. For the RCB, response spectra for the 1D and 2D tests are almost identical. However, for the PSW floor spectra the spectral accelerations around the fundamental frequency of the PSW are significantly larger from the 2D test than those obtained from the 1D test. It can be concluded that the previously described high-frequency oscillations, which are larger in the 2D test than the 1D test, are again the cause for the observed behavior. Finally, note the small hump in the floor spectra at ~0.38 Hz, which corresponds to the first mode of vibration of the isolated structure at the post-yield stiffness of the EQS bearing.

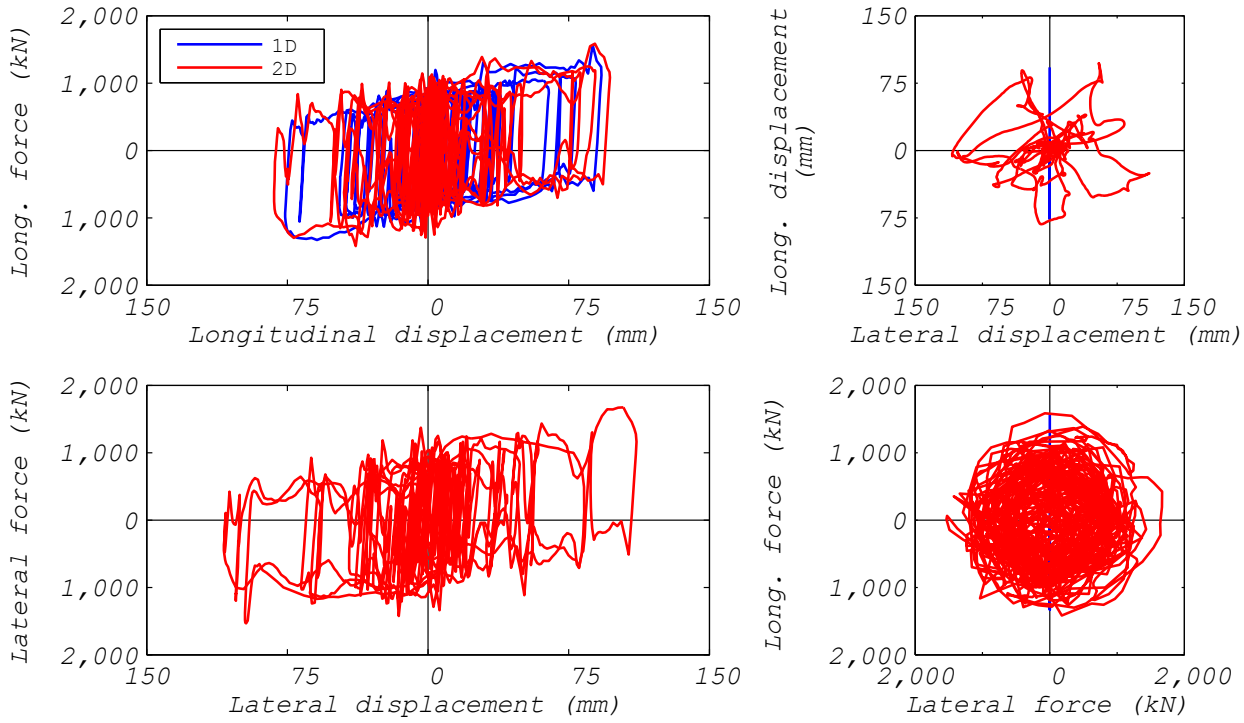

Figure 3.64 **EQS bearing: comparison of bearing responses to ground motion NRC2 executed five times slower than real time (1D and 2D analyses).**

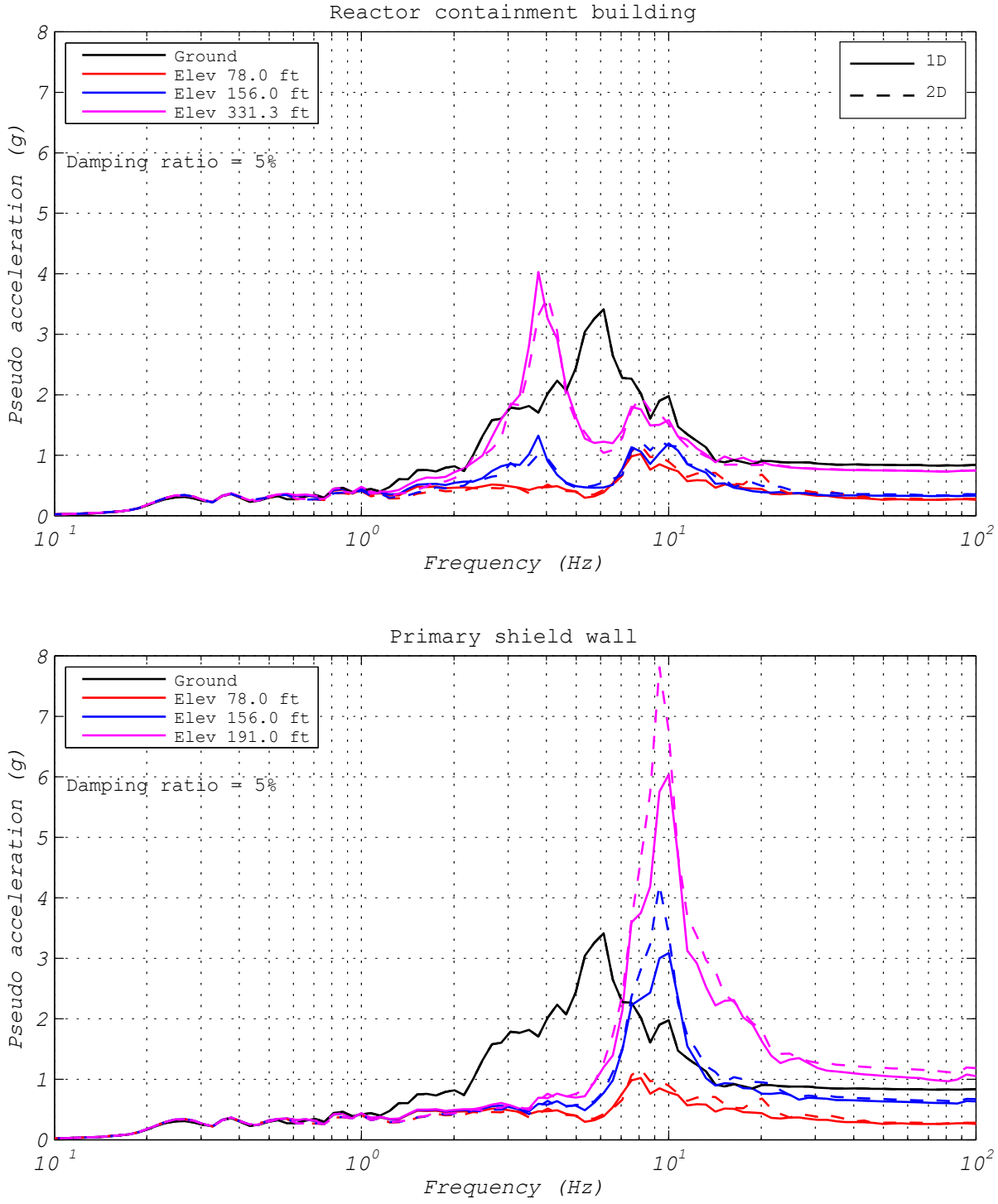

Figure 3.65 **EQS bearing: response spectra comparison of responses to ground motion NRC2 executed five-times slower than real time (1D and 2D analyses).**

3.5.2.2 Influence of Vertical Excitation

Figure 3.66 compares the hysteresis for a hybrid simulation without vertical excitation (Run 50) and a hybrid simulation including vertical excitation (Run 51). The hybrid model used for these tests had five equivalent bearings with one experimental bearing representing a group of 67 bearings under the south-west corner of the NPP. The NRC2 ground motion was used and both hybrid tests were executed 20 times slower than real time. As can be seen in the figure, the hysteresis loops in longitudinal and lateral directions, the horizontal displacement orbits and the shear-force interaction surfaces are nearly identical for the two tests. To investigate the influence of vertical excitation, comparison of the floor response spectra is necessary.

Figure 3.67 compares the floor response spectra for the hybrid simulations with and without vertical excitation; note that there is a distinct difference in the magnitude of the spectral acceleration spikes. While the peaks occur around the same frequencies, the spectral accelerations from the test including vertical excitation are larger than the test without vertical excitation. In general, the increase of the spectral accelerations due to vertical excitation are more pronounce at higher frequencies, and they are most pronounced around the first-mode frequency of the PSW. The peak spectral acceleration in the PSW for the test without vertical excitation was around 2.75*g*, whereas the one from the test including vertical acceleration reached 3.6*g*. This increase of the spectral accelerations is caused by the vertical–horizontal coupling behavior of the EQS bearing. As the vertical load on the EQS bearing fluctuates, the friction force and therefore the characteristic strength, Q_d, of the bearing keeps changing as well, which ultimately affects the shear resistance of the EQS bearing.

In the second test, the vertical ground motion input excites the vertical mode of vibration of the isolation system around 13 Hz as well as the first vertical mode of vibration of the plant superstructure around 10 Hz. Because the first-mode horizontal frequency of the PSW is around 8–10 Hz, which is very close to the vertical frequency of the superstructure, the effect of vertical excitation on the floor response spectra of the PSW is more pronounced. On the other hand, the first-mode frequency of the RCB at 3.7 Hz is well separated from the vertical frequency of the plant superstructure. Hence, the floor response spectra of the RCB are much less influenced by the vertical–horizontal coupling behavior of the EQS bearings. Finally, this effect is less pronounced in the EQS bearings as compared to the LPRB bearings because the spectral acceleration spikes generated by the EQS bearings without vertical excitation are already very large to begin with (see Section 3.5.2.1).

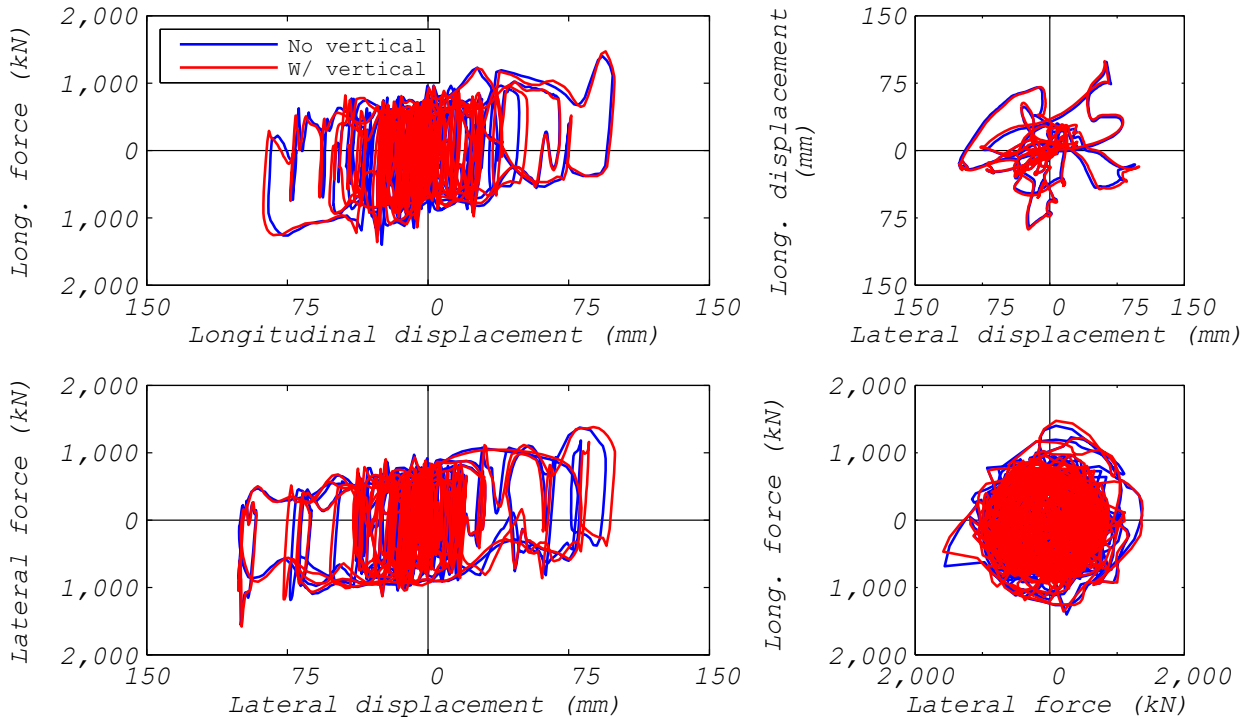

Figure 3.66 **EQS bearing: comparison of bearing responses to a ground motion with and without vertical excitation (ground motion NRC2, 2D and 3D analyses).**

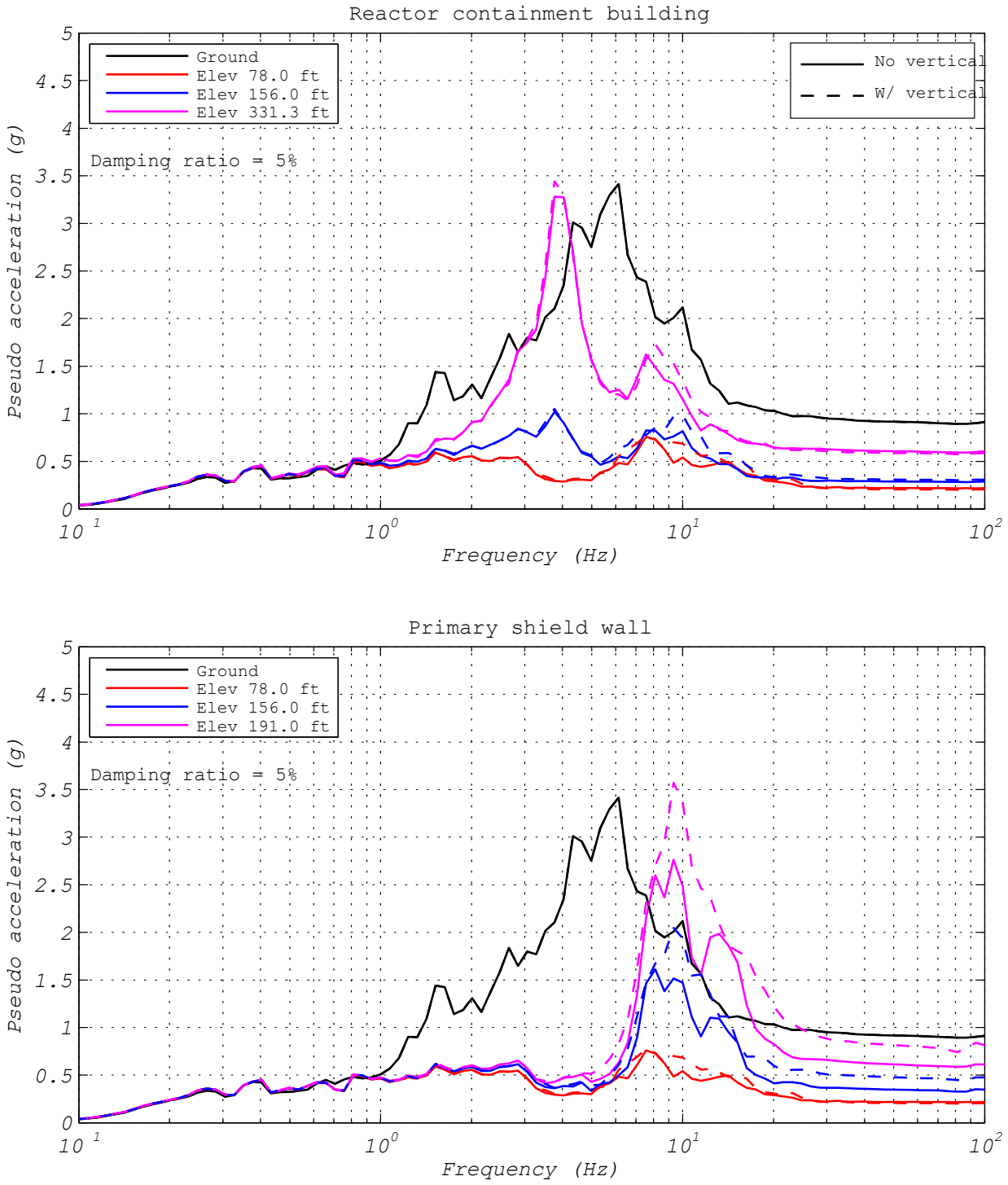

Figure 3.67 **EQS bearing: response spectra comparison of responses to a ground motion with and without vertical excitation (ground motion NRC2, 2D and 3D analyses).**

3.5.2.3 *Influence of Axial Load Variation due to Overturning*

Figures 3.68 and 3.69 compare the results from a hybrid simulation with the experimental bearing in the center of the plant (Run 47) versus one where the experimental bearing is located in the south-west corner of the plant (Run 50). The hybrid model used for these tests had five equivalent bearings and was executed 20 times slower than real time. The case with the experimental bearing located in the center represented a group of 133 isolators. The case with the experimental bearing in the south-west corner represented a group of 67 bearings. The NRC2 ground motion was used in these tests. As these figures show, the results for the two cases are almost identical despite axial force fluctuations between 6038 kN and 12,204 kN for the corner bearing case and for the middle bearing case a minimum and maximum axial forces of 8222 kN and 8500 kN, respectively. The only important difference can be observed in the floor response spectra of the PSW, where around 13 Hz, which corresponds to the vertical frequency of the isolation system, the spectral accelerations from the hybrid test with the experimental bearing located in the corner are slightly larger than the ones from the hybrid test with the experimental bearing located in the center. It can be concluded that the fluctuation of the axial load due to overturning has very little effect on the shear forces through the vertical–horizontal coupling behavior of the EQS bearings. In addition, the isolator location has negligible effect on the response of the EQS bearing.

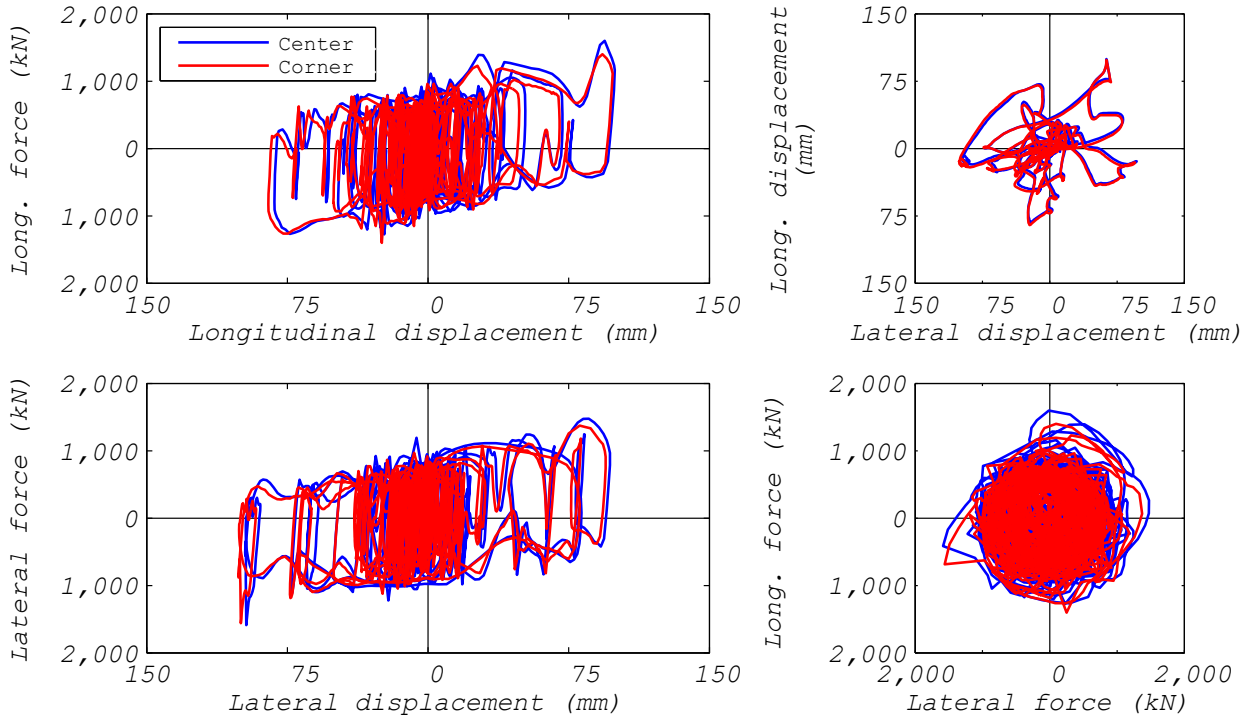

Figure 3.68 **EQS bearing: comparison of bearing responses depending on the location of the bearing (ground motion NRC2, 2D analysis).**

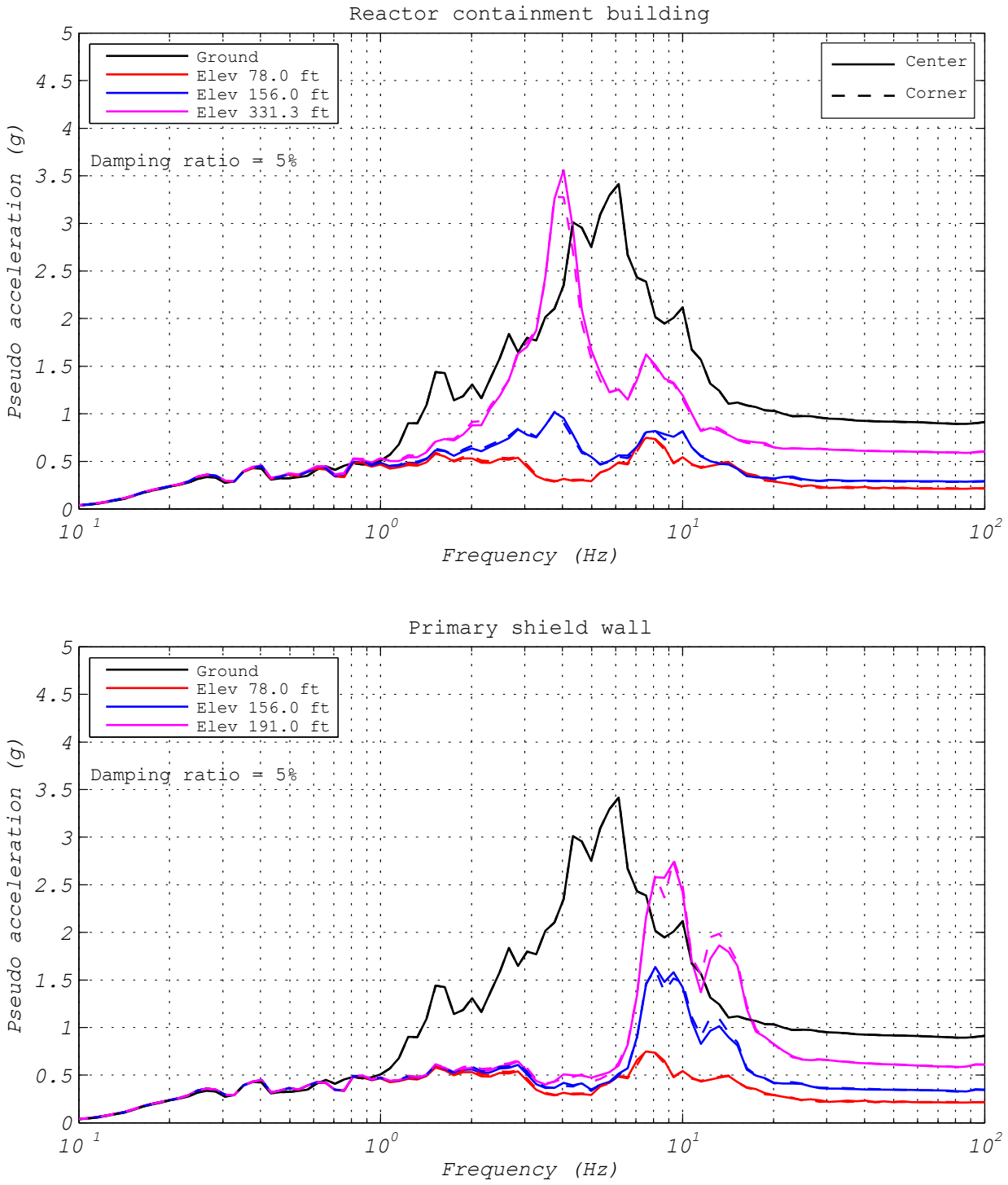

Figure 3.69 **EQS bearing: response spectra comparison of responses depending on the location of the bearing (ground motion NRC2, 2D analysis).**

3.5.2.4 Variation due to Bearing Layout Discretization Models

Figure 3.70 compares the hysteresis loops from two hybrid simulations with different hybrid models. In the first model, one experimental bearing represents all 527 bearings (Run 54) and in the second model one experimental bearing represents one of five-bearing groups (Run 43). Both models were analyzed for the NRC2 ground motion and were executed five times slower than real time. As the figure shows, the behavior of the experimental bearing is fairly similar in the two hybrid tests. However, there are more high-frequency oscillations in the shear forces for the case of one experimental bearing representing all 527 bearings because the hybrid model with five bearing groups (containing the four analytical isolators, which were incapable of modeling the breakaway and static friction forces) captured only one-fifth of the breakaway and static friction forces. In contrast, the hybrid model where one experimental bearing represents all 527 bearings, the entire isolation system experienced these phenomena.

Figure 3.71 shows several floor spectra for the RCB and PSW for the two different bearing layout discretizations. As described earlier, in the case of the five bearing model, only one bearing group used the experimental results and the other four groups were modeled with analytical isolator elements. The analytical isolator element was not able to capture the true behavior of the bearing, especially the breakaway friction; therefore, the amplification of the higher modes was significantly smaller in comparison to the case where all of the bearings were using the experimental results. This effect was again most pronounced for the floor response spectra of the PSW, where the peak spectral acceleration was only 3*g* for the five-bearing model but nearly 8*g* for the one-bearing model.

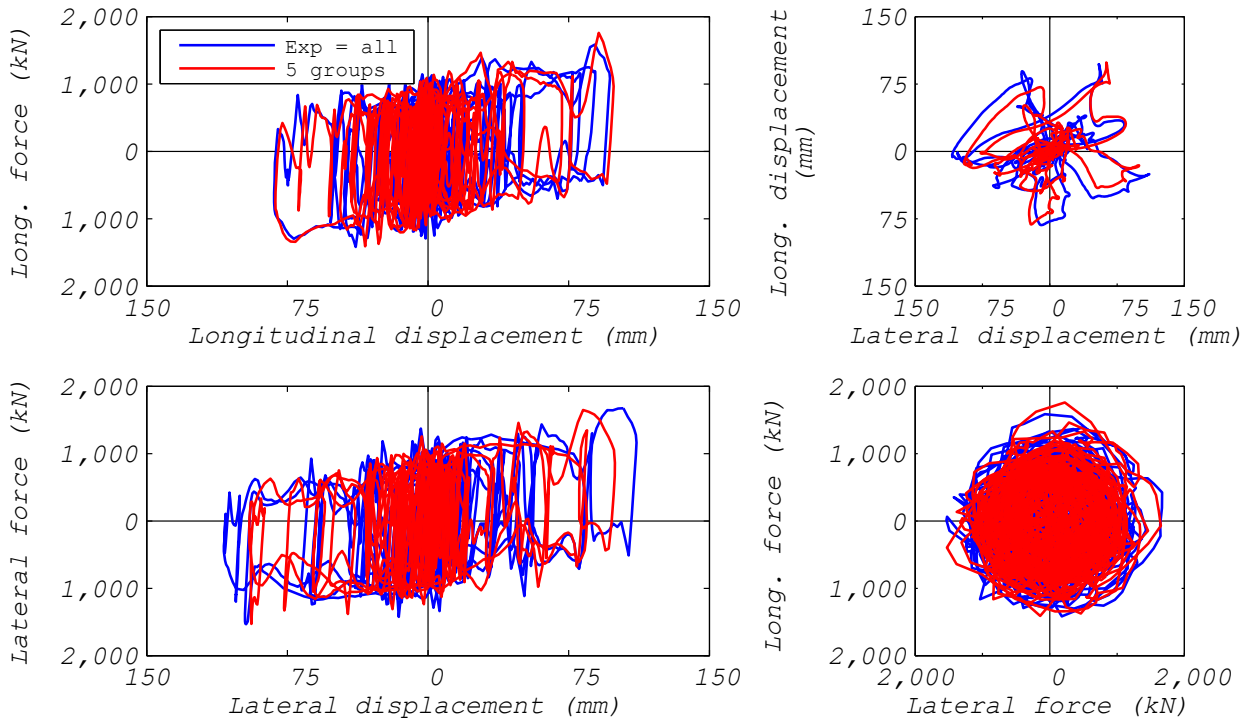

Figure 3.70 EQS bearing: comparison of bearing responses to bearing layout discretization (ground motion NRC2, 2D analysis).

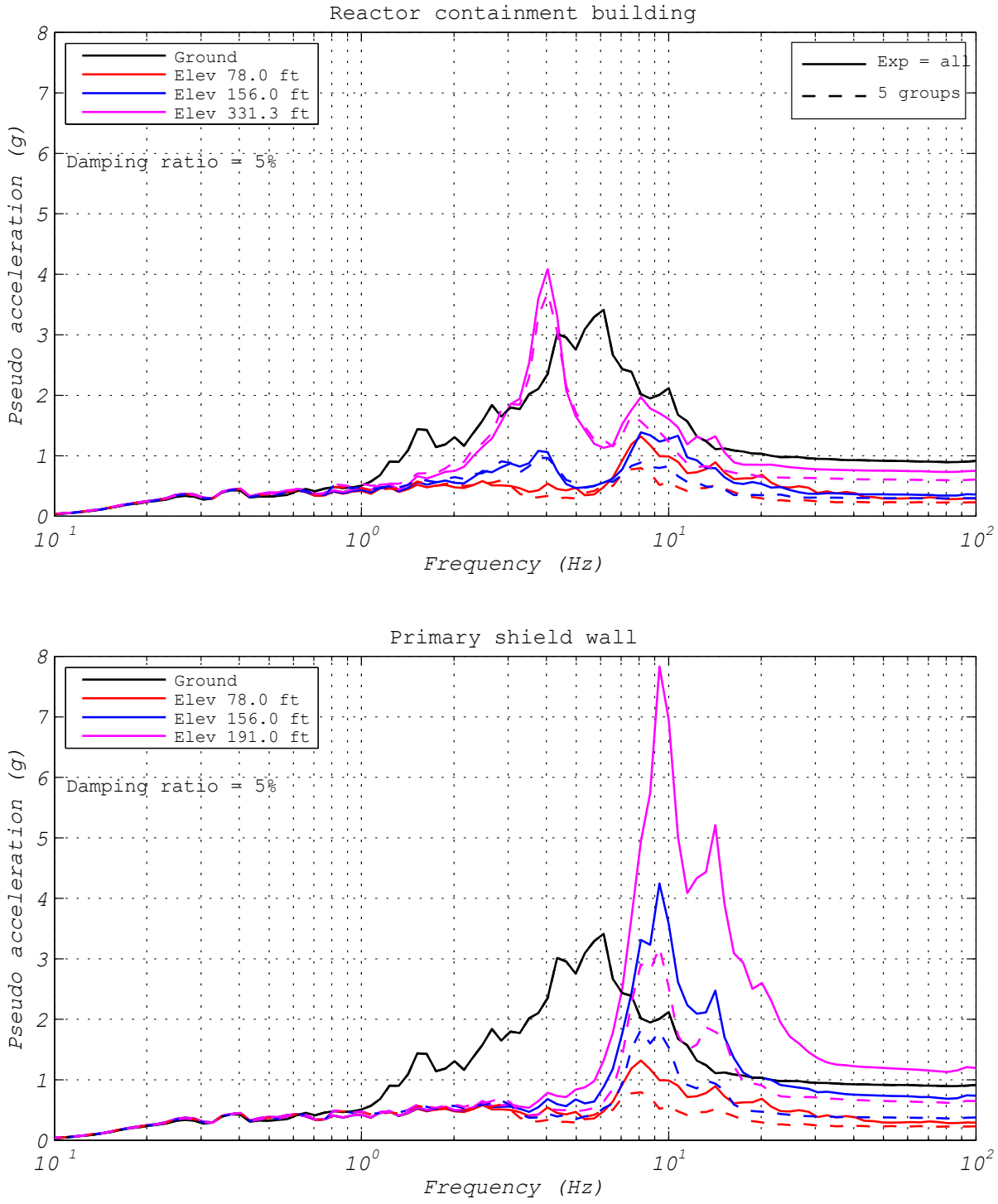

Figure 3.71 **EQS bearing: response spectra comparison of responses to bearing layout discretization (ground motion NRC2, 2D analysis).**

3.5.2.5 *Influence of Test Rate*

Figure 3.72 compares the hybrid test results for two different rates of testing. The hybrid model with one experimental bearing representing all of the bearings was tested 25 times (Run 17) and five times (Run 53) slower than real time. The EUR5 motion was applied in longitudinal direction in these tests. As the figure clearly shows, the test that was conducted 25 times slower has higher shear forces, which are caused by breakaway and static friction as a result of the five times lower velocities during the slower hybrid test. Also, the post-yield stiffness was nearly zero for these tests due to the small displacement demand (imposed by the EUR5 motion), which barley engages the MER spring restoring force mechanism.

Figure 3.73 compares the response spectra for the five times and 25 times slower than real-time hybrid tests. The response spectra for the RCB were almost identical from the two testing rates. For the response spectra of the PSW, however, the spectral accelerations from the rapid hybrid simulation were significantly greater than the ones from the slow hybrid simulation for frequencies above 7 Hz. The rapid hybrid simulation must have generated some high-frequency excitation that was transmitted through the EQS bearing but would be absent if the hybrid test was executed slowly. At present it is unclear if this effect was caused by suboptimal tracking performance of the test system when testing at faster rates or by the complex interaction between different friction forces on the various sliding surfaces in the EQS bearing. After comparing FFTs of the displacement errors and tracking indicators for the two test rates (see Appendix C), this behavior was most likely caused by poor tracking during the fast hybrid simulation in the lateral direction, perpendicular to the testing direction. Further investigation of this phenomenon is necessary to confirm this conclusion.

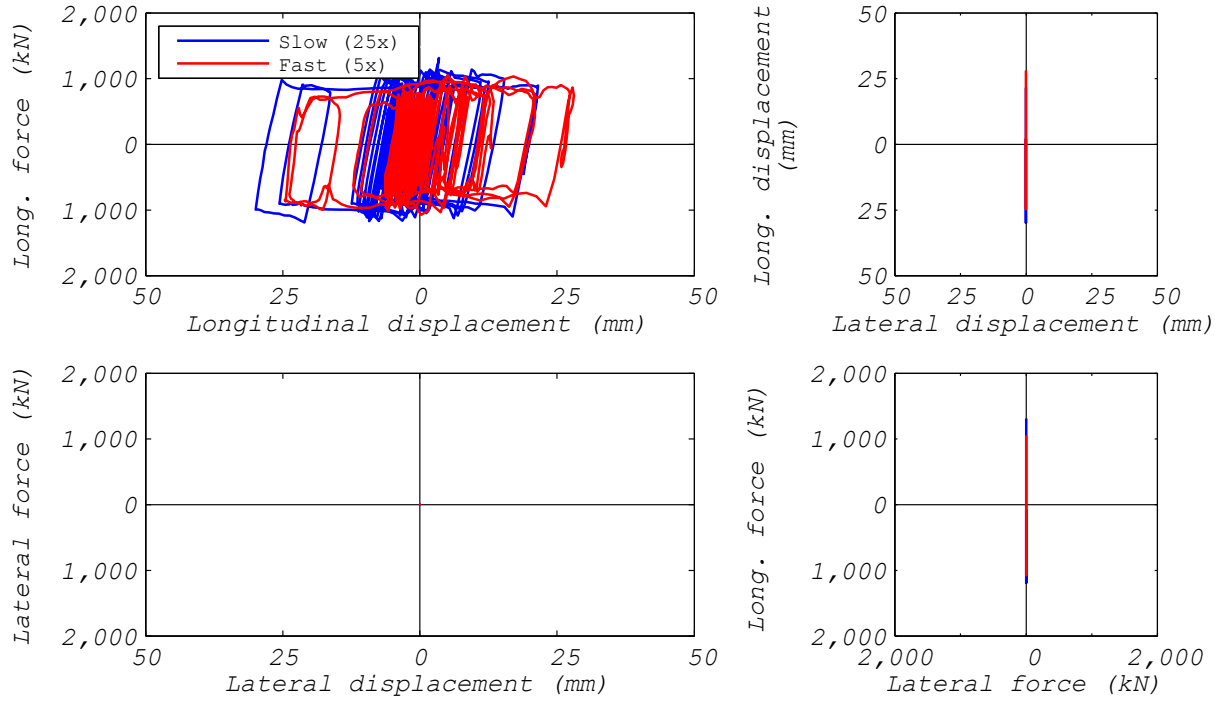

Figure 3.72 **EQS bearing: comparison of bearing responses to loading rates (ground motion EUR5, 1D analysis).**

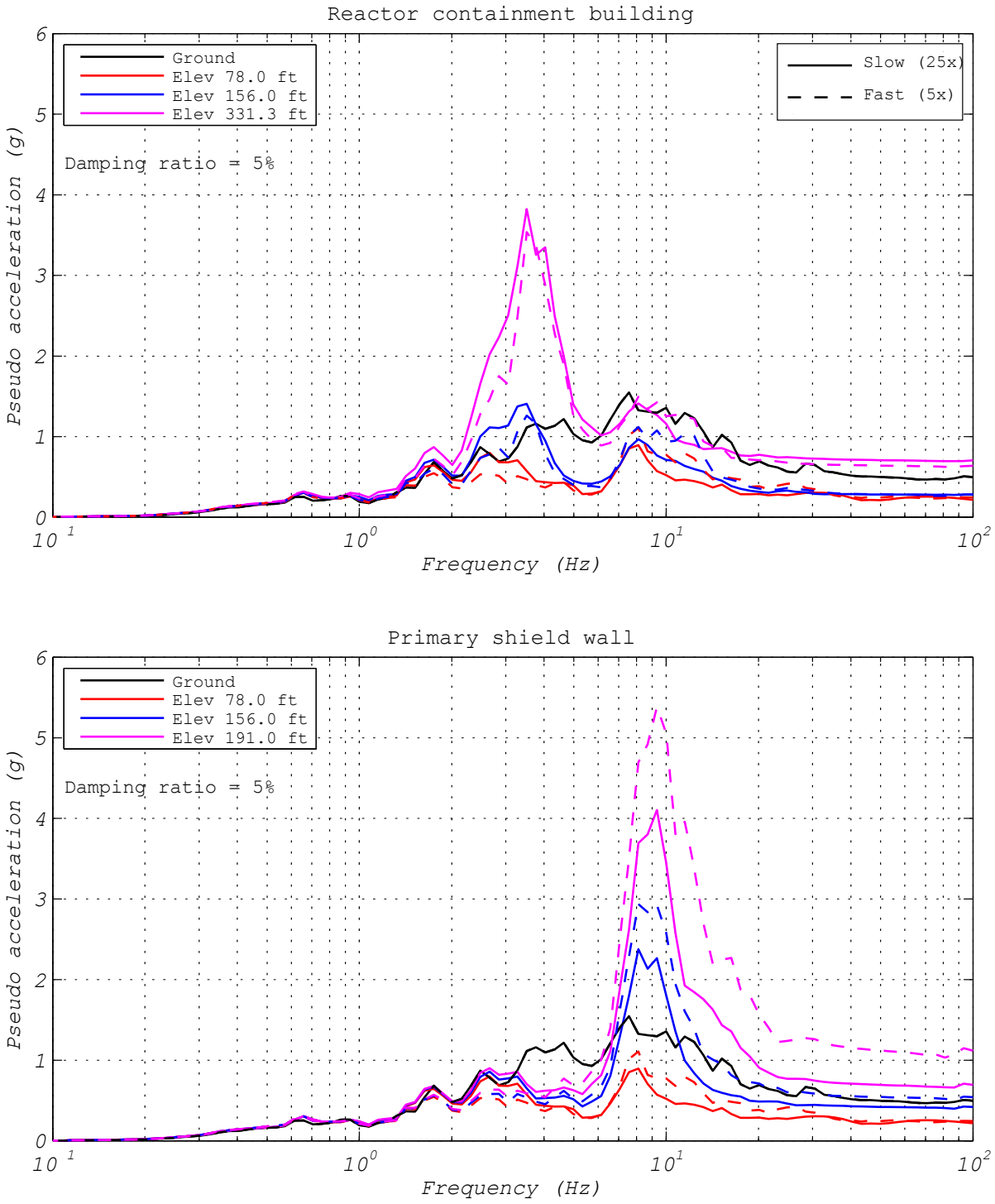

Figure 3.73 **EQS bearing: response spectra comparison of responses to loading rates (ground motion EUR5, 1D analysis).**

Figure 3.74 compares the hysteresis loops from two hybrid tests with different execution rates. As before, the hybrid model with one experimental bearing representing all of the bearings was executed 25 times (Run 22) and five times (Run 52) slower than real time. For these hybrid tests, the larger NRC2 motion was applied in longitudinal direction. As the figure shows, the test conducted 25 times slower has higher shear forces, which are caused by breakaway and static friction as a result of the five times lower velocities that occur during the slower hybrid test. In contrast to the previous results, the EQS bearing exhibited nearly four times larger displacements. The larger deformations engaged the MER spring restoring mechanism, which can be clearly identified from the positive post-yield stiffness.

Figure 3.75 compares the response spectra for the five times and 25 times slower than real-time hybrid tests. The response spectra for the RCB have somewhat smaller spectral accelerations for the rapid hybrid simulation as compared to the slow hybrid test. However, for the response spectra of the PSW, the spectral accelerations from the rapid hybrid simulation are slightly greater than the ones from the slow hybrid simulation. Comparing the tracking performance of the two hybrid simulations (see Appendix C) once again confirms that the tracking achieved during the rapid hybrid simulation was less accurate than during the slow hybrid test. However, tracking performance was better than the previously described rapid hybrid simulation with the EUR5 input motion. Hence, the spectral amplitudes for the PSW response spectra from the rapid test are only slightly larger than the ones obtained from the slow hybrid test. Tracking errors were once again mostly accumulated in the lateral direction, perpendicular to the direction of testing, demonstrating that experimental errors need to be minimized at all cost to obtain accurate and reliable results from hybrid simulation tests. The faster the hybrid test is executed, the more crucial this requirement becomes because the tracking performance of hydraulic systems deteriorates at high frequencies.

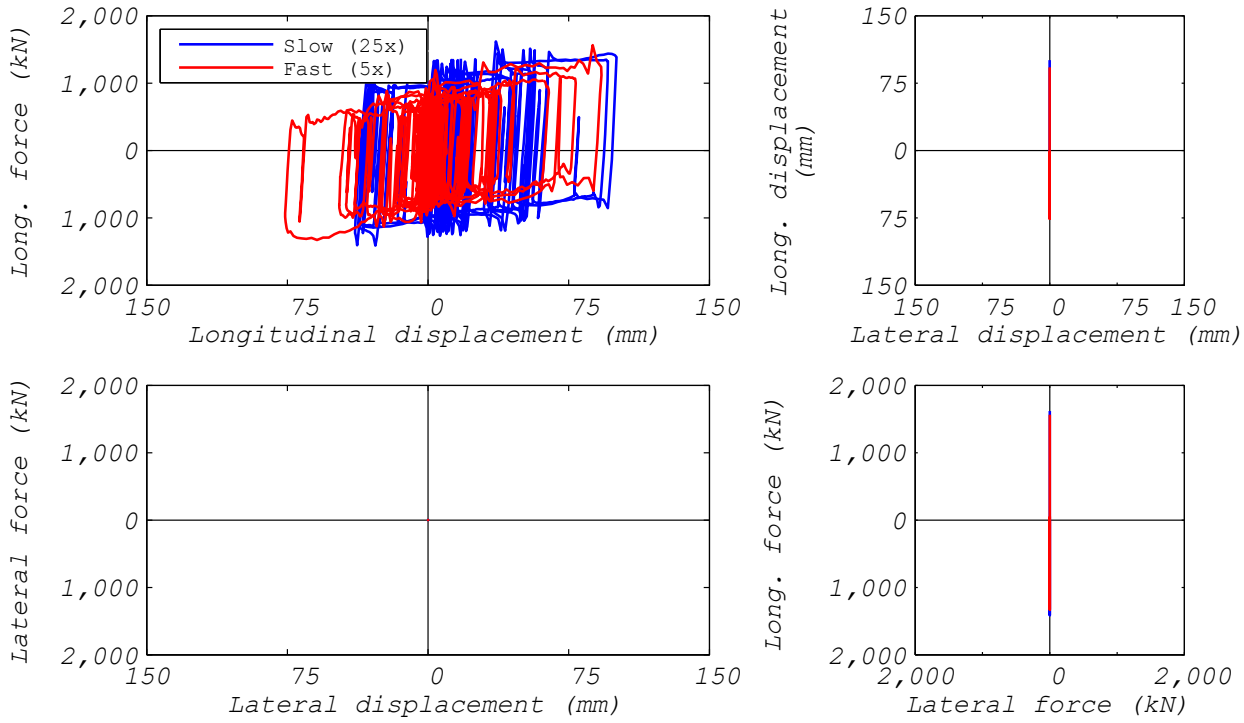

Figure 3.74 **EQS bearing: comparison of bearing responses to loading rates (ground motion NRC2, 1D analysis).**

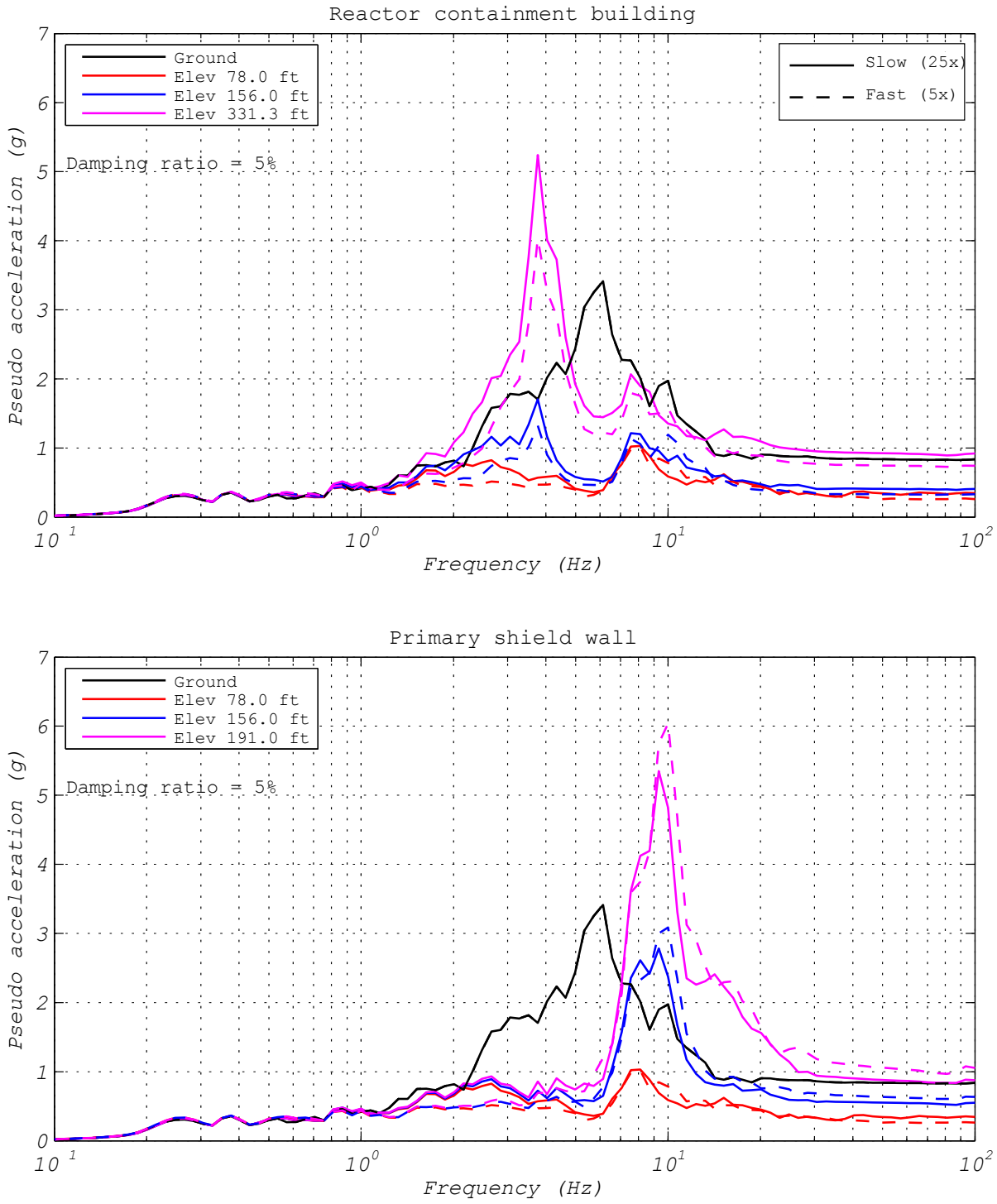

Figure 3.75 **EQS bearing: response spectra comparison of responses to loading rates (ground motion NRC2, 1D analysis).**

3.5.2.6 Comparison Between Hybrid Simulation Tests and Analytical Estimation

Figures 3.76 and 3.77 compare an analytical simulation (Run 53A) and a hybrid simulation (Run 53) for the model with one experimental bearing representing all the bearings. Both models were analyzed for the EUR5 ground motion applied in longitudinal direction only. The hybrid model was executed five times slower than real time. The analytical model utilized a bearing element based on the newly developed velocity-dependent OpenSees EQS bearing model (see Section 3.3.2) with the following parameters: k_1 = 511 kN/mm, μ_{Fast} = 0.10, μ_{Slow} = 0.08, k_2 = 4.4 kN/mm, k_3 = 0 kN/mm, η = 3. As shown in Figure 3.76, the maximum longitudinal displacement demand from the analytical simulation is 26 mm, which is almost identical to the 28 mm demand obtained from the hybrid test. Comparing the two longitudinal hysteresis loops demonstrates that the analytical bearing model captures quite well the initial stiffness, the dynamic friction yield strength, and the post-yield stiffness. However, the analytical bearing model was not able to capture the shear-force spikes due to the static and breakaway friction characteristics of the EQS bearing that occurred at every load reversal.

Comparison of the floor response spectra presented in Figure 3.77 reveals an excellent match of the spectral accelerations for frequencies below 6 Hz is obtained; see Figure 3.77. Above 6 Hz, however, the spectral accelerations from the hybrid simulation are substantially larger than the ones obtained from the numerical simulation. The reason for this behavior is twofold:

1. The analytical model cannot predict the shear-force oscillations due to the static and breakaway friction that occurs in the physical bearing; these oscillations increase spectral accelerations at higher frequencies; and
2. As mentioned earlier, the hybrid simulation Run 53 had some tracking performance issues. These systematic experimental errors excite higher mode effects and therefore amplify spectral accelerations at higher frequencies.

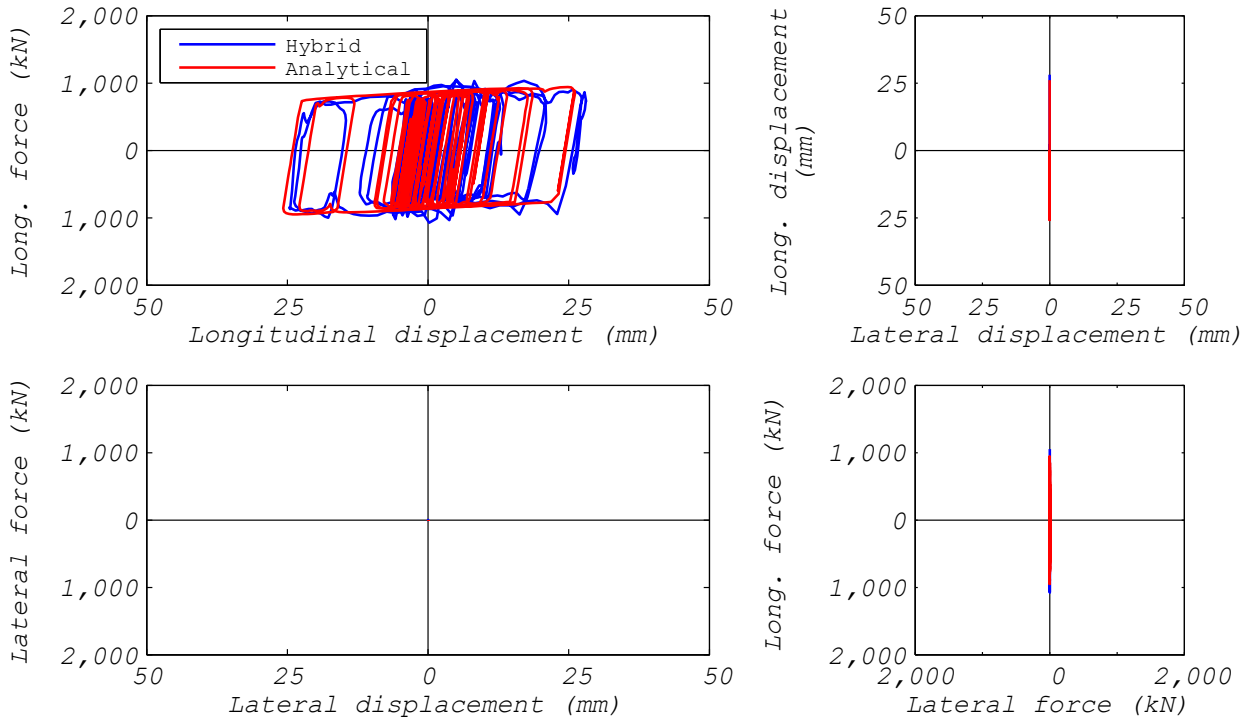

Figure 3.76 **EQS bearing: comparison of hybrid simulation and analytical estimation responses (ground motion EUR5, 1D analysis).**

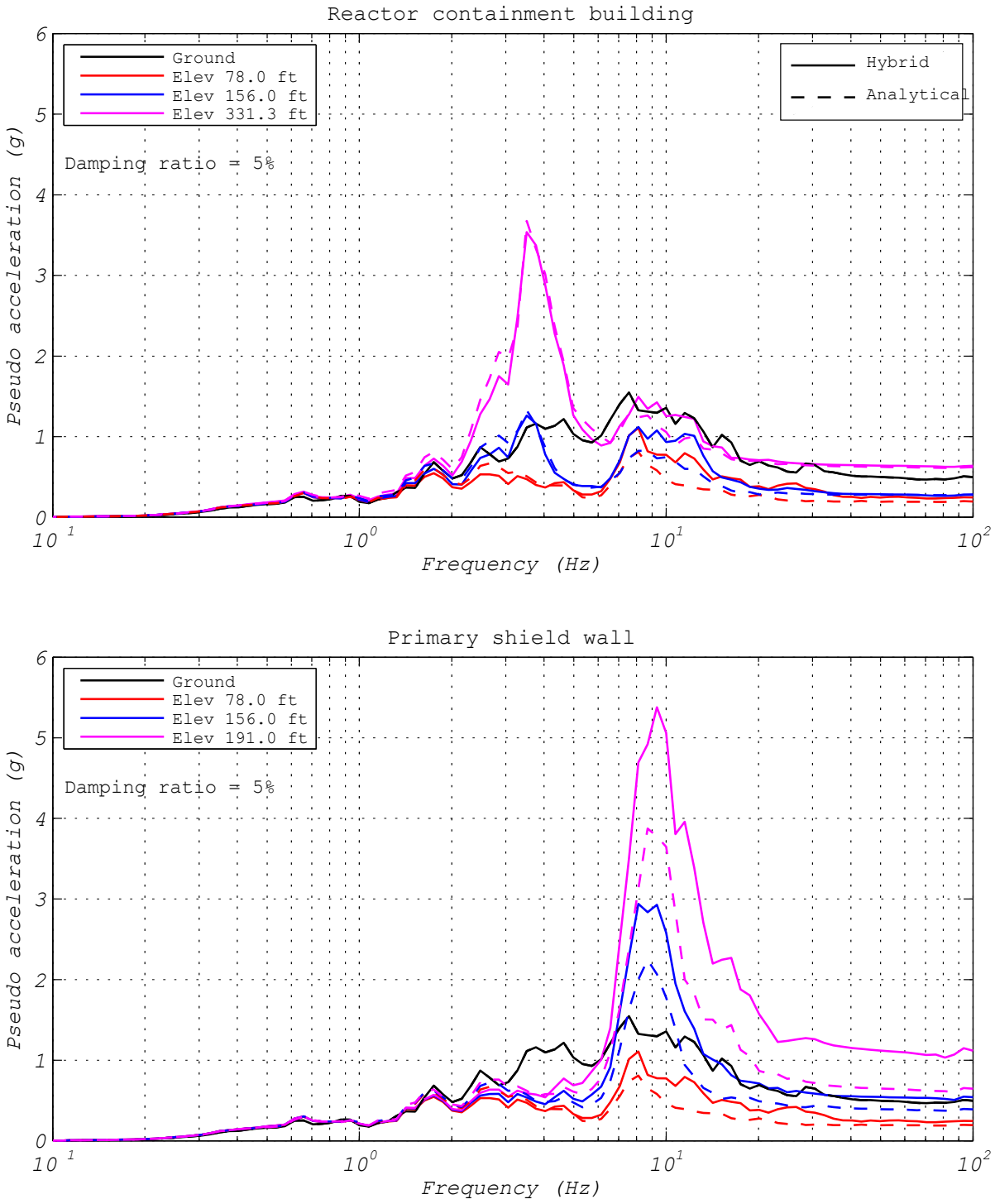

Figure 3.77 **EQS bearing: response spectra comparison of hybrid simulation and analytical estimation responses (ground motion EUR5, 1D analysis).**

Figures 3.78 and 3.79 compare an analytical simulation (Run 52A) and a hybrid simulation (Run 52) for the model with one experimental bearing representing all the bearings. Both models were analyzed for the NRC2 ground motion applied in longitudinal direction only. The hybrid model was executed five times slower than real time. The analytical model utilized a bearing element based on the newly developed velocity-dependent OpenSees EQS bearing model (see Section 3.3.2) with the following parameters: k_1 = 511 kN/mm, μ_{Fast} = 0.10, μ_{Slow} = 0.08, k_2 = 5.1 kN/mm, k_3 = 0 kN/mm, η = 3. As shown in Figure 3.78, the maximum longitudinal displacement demand from the analytical simulation is 93 mm, which is consistent with the 92 mm demand obtained from the hybrid test. Comparing the two longitudinal hysteresis loops demonstrates that once again the analytical bearing model captures quite well the initial stiffness, the dynamic friction yield strength, and the post-yield stiffness; however, as before, the analytical model was not able to capture the shear-force spikes and oscillations due to the static and breakaway friction behavior that is observed in the physical EQS isolator.

As shown in Figure 3.79, the simplified bearing model achieves an excellent match of the response spectra for the RCB; however, because the analytical model does not capture the shear-force oscillations and spikes due to static and breakaway friction, spectral amplitudes of the PSW at higher frequencies were underpredicted. Overall the floor response spectra match better because good tracking performance was achieved in hybrid test Run 52.

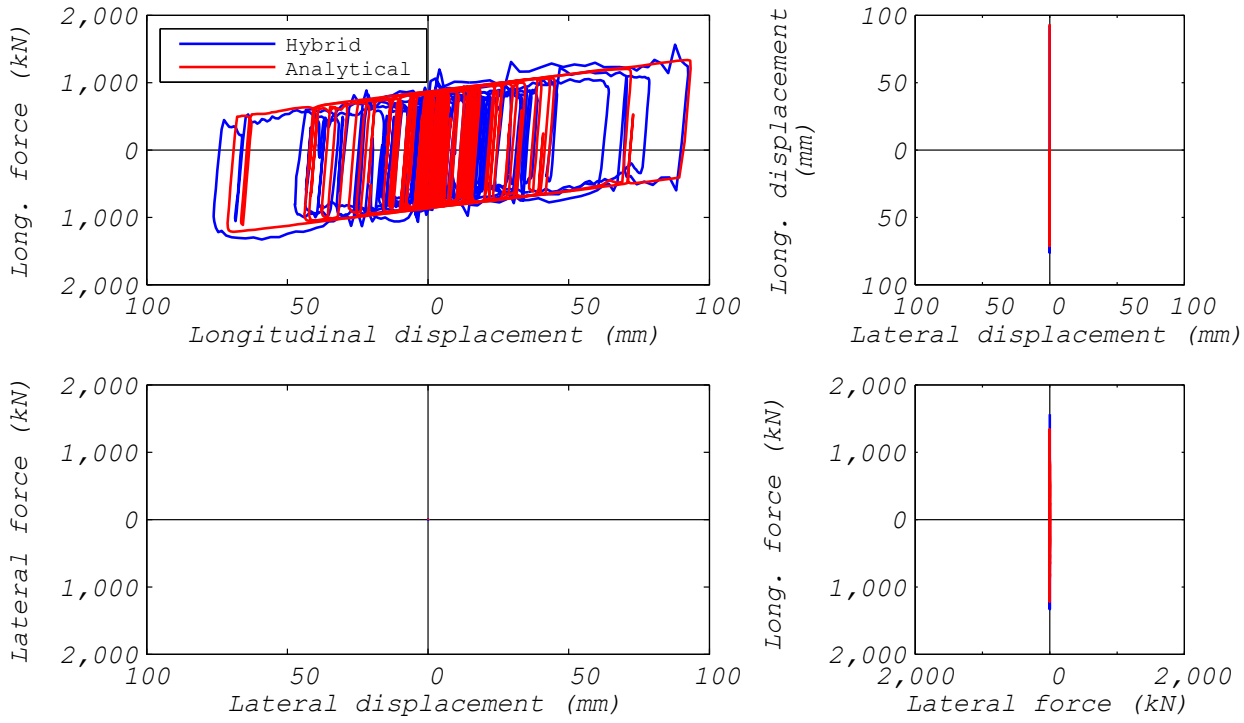

Figure 3.78 **EQS bearing: comparison of hybrid simulation and analytical estimation responses (ground motion NRC2, 1D analysis).**

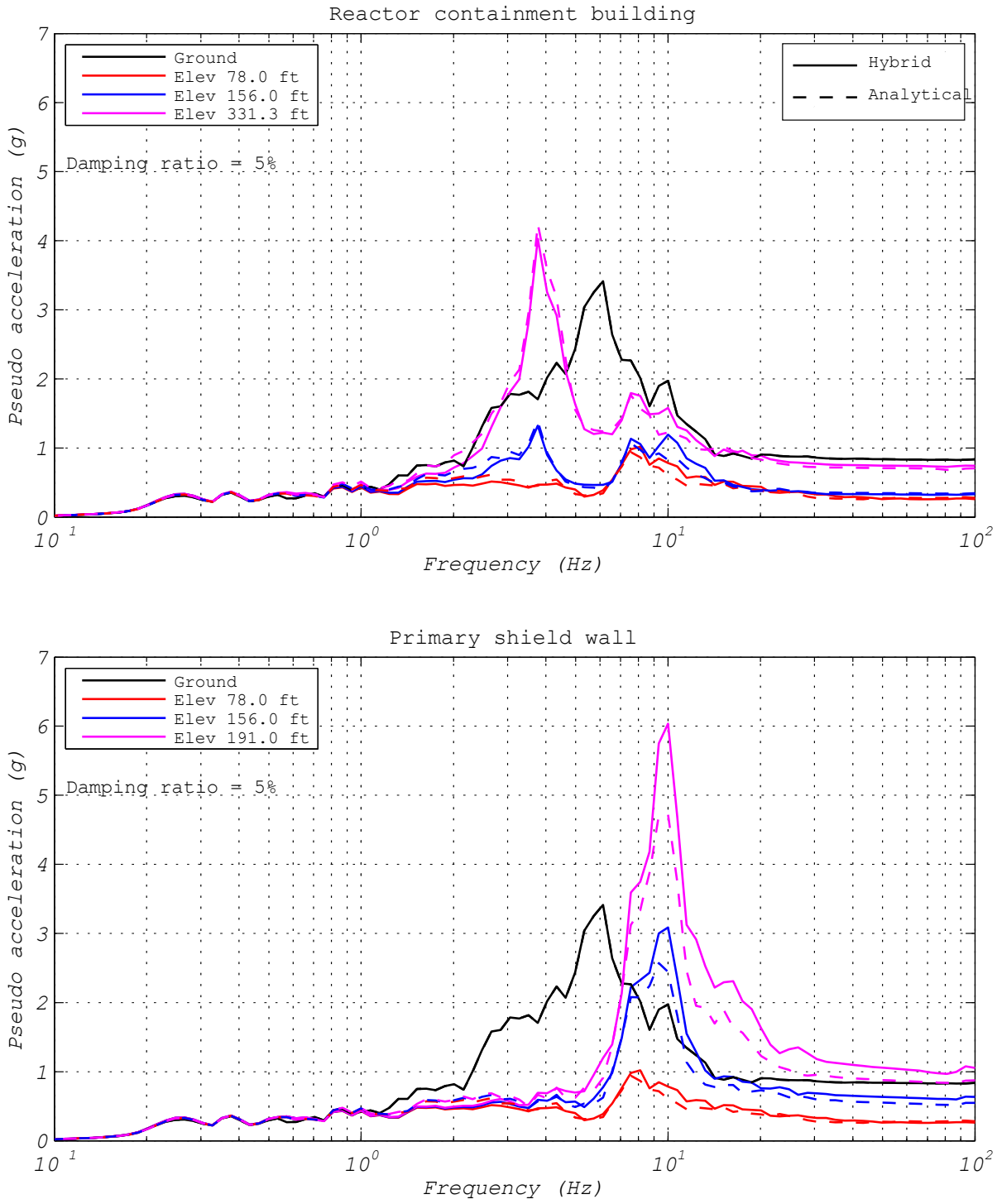

Figure 3.79 **EQS bearing: response spectra comparison of hybrid simulation and analytical estimation responses (ground motion NRC2, 1D analysis).**

Figures 3.80 and 3.81 compare an analytical simulation (Run 18A) and a hybrid simulation (Run 18) for the model with one experimental bearing representing all the bearings. Both models were analyzed for the EUR5 ground motion applied in the two horizontal directions. The hybrid model was executed 25 times slower than real time. The analytical model utilized a bearing element based on the newly developed velocity-dependent OpenSees EQS bearing model (see Section 3.3.2) with the following parameters: k_1 = 511 kN/mm, μ_{Fast} = 0.10, μ_{Slow} = 0.08, k_2 = 4.4 kN/mm, k_3 = 0 kN/mm, η = 3. As shown in Figure 3.81, the maximum longitudinal displacement demand from the analytical simulation is 40 mm, which is significantly smaller than the 53 mm demand obtained from the hybrid test. Comparing the two longitudinal hysteresis loops demonstrates that the analytical bearing model only captures the initial stiffness correctly. Because the hybrid simulation was executed 25 times slower than real time but the analytical isolator properties were calibrated based on Run 54, which was executed five times slower than real time, the width of the hysteresis loop (and hence the coefficient of friction) is greatly underestimated. In addition, the analytical bearing model is not able to capture the shear-force spikes due to the static and breakaway friction characteristics of the EQS bearing., which were very large in 25 times slower hybrid test.

Figure 3.81 compares the floor response spectra, demonstrating that the, spectral accelerations for frequencies above 1 Hz are greatly underestimated by the analytical model. As stated earlier, the excessive shear-force oscillations and spikes that occurred in the hybrid simulation were due to the slow testing rate. It is expected that if it had been possible to execute the hybrid simulation in real-time, static and breakaway friction problems would have been greatly reduced, with the results that the floor response spectra from the hybrid simulation would have been lower, thus matching better with the analytically predicted ones.

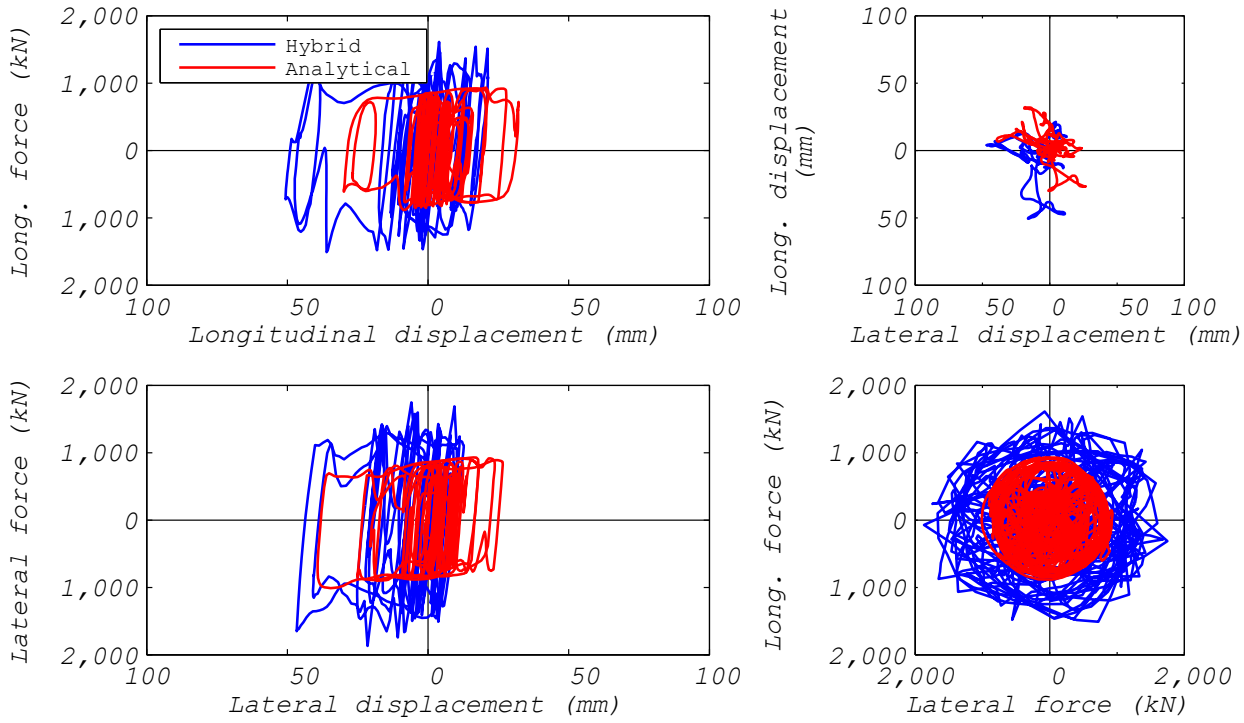

Figure 3.80 **EQS bearing: comparison of hybrid simulation and analytical estimation responses (ground motion EUR5, 2D analysis).**

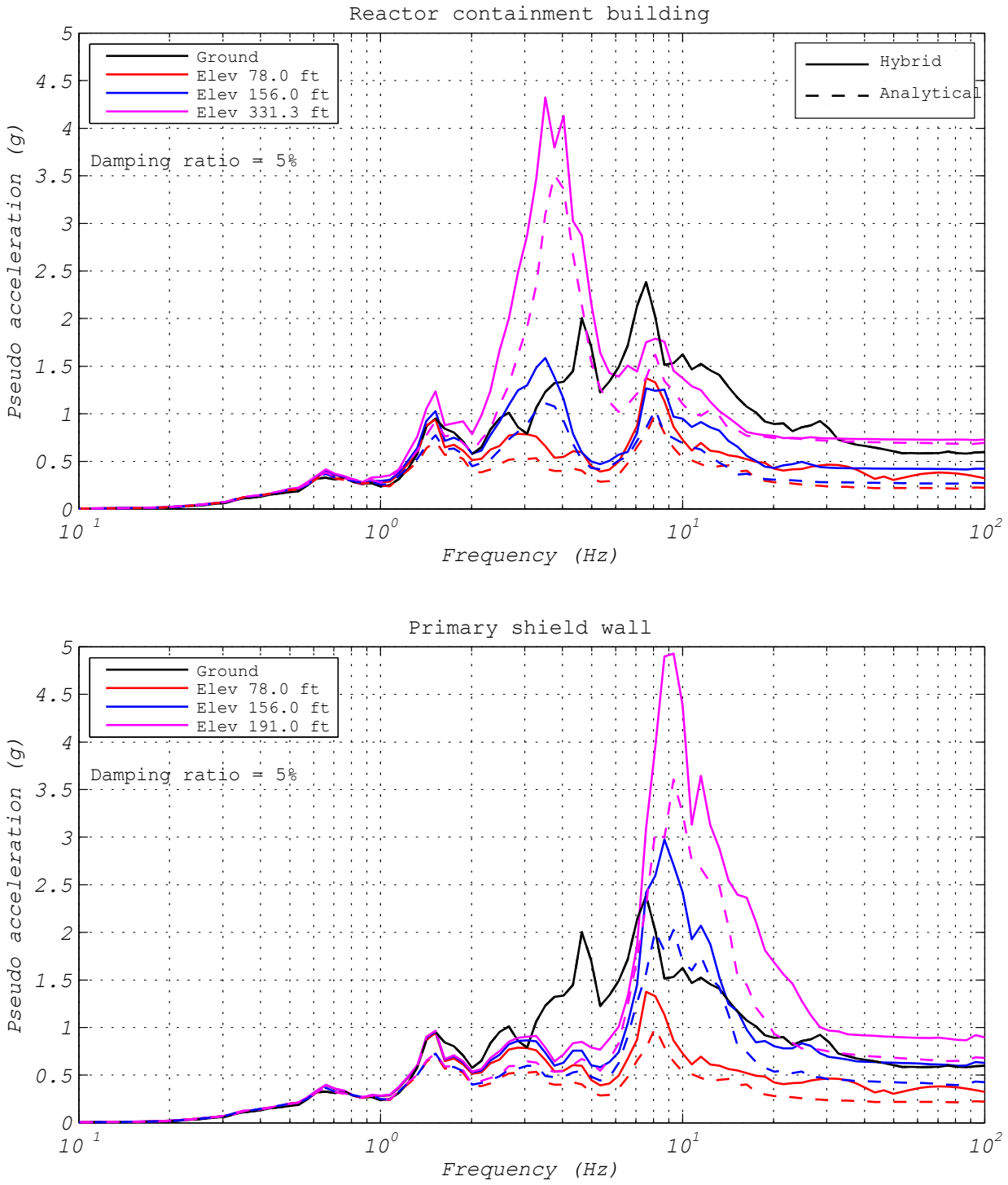

Figure 3.81 **EQS bearing: response spectra comparison of hybrid simulation and analytical estimation responses (ground motion EUR5, 2D analysis).**

Figures 3.82 and 3.83 compare an analytical simulation (Run 54A) and a hybrid simulation (Run 54) for the model with one experimental bearing representing all the bearings. Both models were analyzed for the NRC2 ground motion applied in the two horizontal directions. The hybrid model was executed five times slower than real time. The analytical model utilized a bearing element based on the newly developed velocity-dependent OpenSees EQS bearing model (see Section 3.3.2) with the following parameters: k_1 = 511 kN/mm, μ_{Fast} = 0.10, μ_{Slow} = 0.08, k_2 = 5.1 kN/mm, k_3 = 0 kN/mm, η = 3. As shown in Figure 3.82, the maximum longitudinal displacement demand from the analytical simulation is 120 mm, which is almost identical to the 114 mm demand obtained from the hybrid test. Comparing the two longitudinal hysteresis loops demonstrates that the analytical bearing model again captures quite well the initial stiffness, the dynamic friction yield strength, and the post-yield stiffness. However, as before, the analytical model was not able to capture the shear-force spikes and oscillations due to the static and breakaway friction behavior that is observed in the physical EQS isolator. Due to bidirectional excitation, more load reversals and therefore more shear-force oscillations and shear-force spikes occurred in the 2D test as compared to the 1D test described earlier.

Figure 3.83 shows that floor spectral accelerations for frequencies above 3 Hz were underestimated by the analytical model. Because the analytical model does not capture the large shear-force oscillations and spikes due to static and breakaway friction, spectral amplitudes of the RCB and PSW at higher frequencies were underpredicted. Overall, the floor response spectra from bidirectional excitation do not match as well as in the case of longitudinal excitation only.

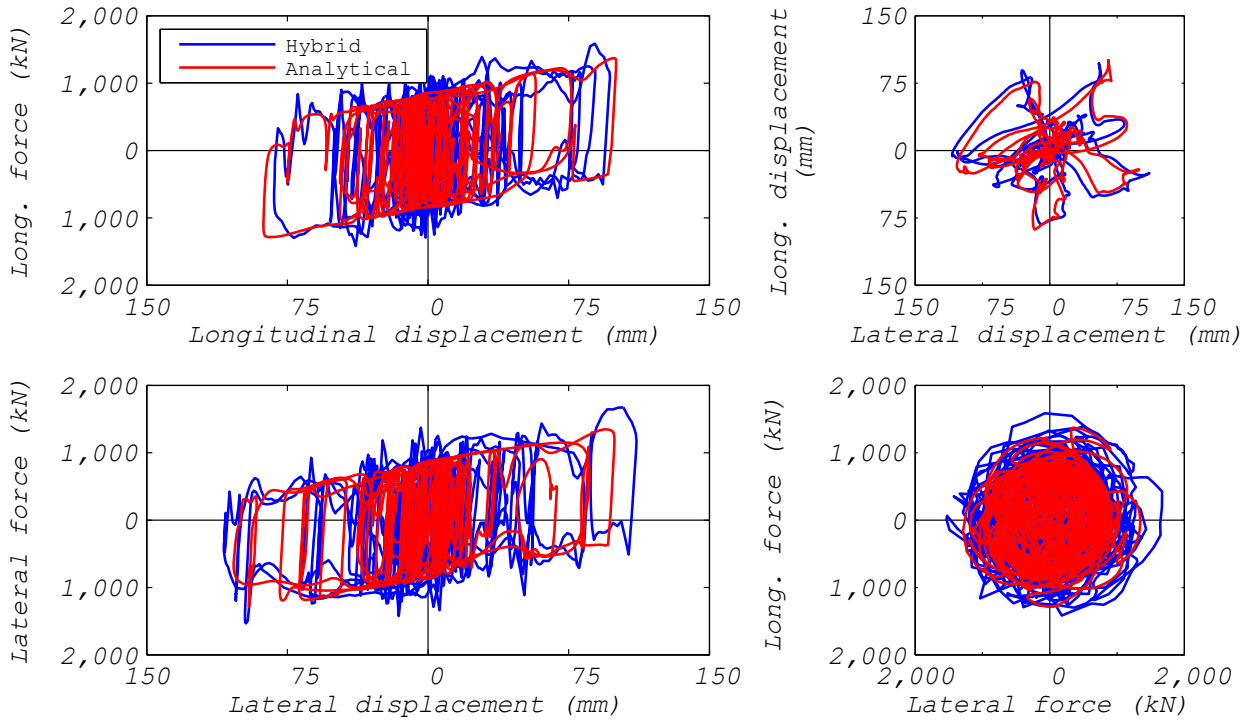

Figure 3.82 **EQS bearing: comparison of hybrid simulation and analytical estimation responses (ground motion NRC2, 2D analysis).**

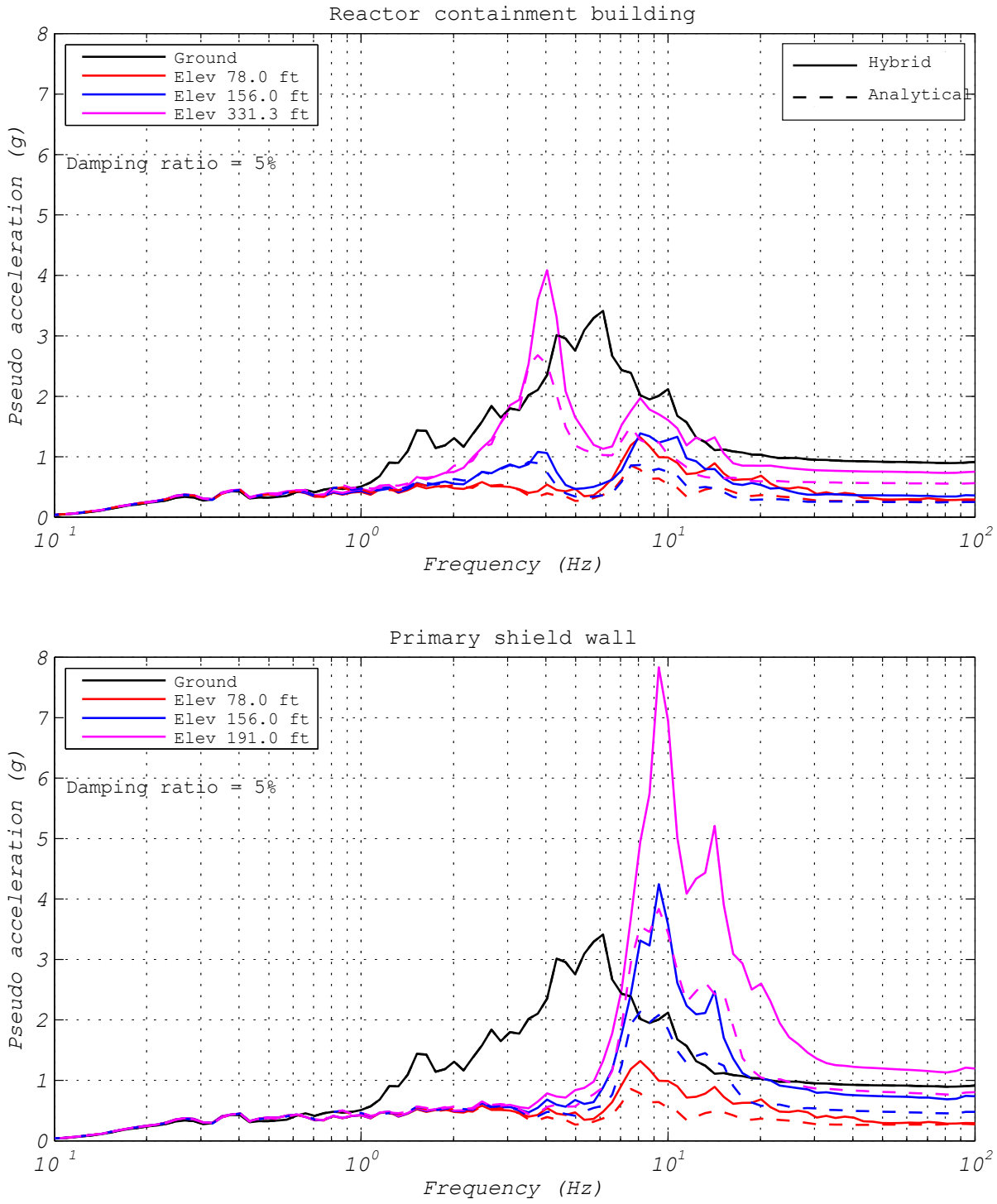

Figure 3.83 **EQS bearing: response spectra comparison of hybrid simulation and analytical estimation responses (ground motion NRC2, 2D analysis).**

3.6 CHARACTERIZATION TESTS

Characterization tests results are provided in Appendix B for the LPRB bearings and Appendix D for the EQS bearings. From the extensive set of tests conducted, two are highlighted because they induced bearing failure. While the LPRB failure test was intended in the loading protocol, the EQS bearing failed unexpectedly.

3.6.1 Unison eTech (LPRB) Failure Test

Test 66 was conducted in order to characterize the behavior of the LPRB for beyond-design-level response through an ellipse input motion for 500% shear strain in the bearing. The bearing failed at approximately 1092 mm longitudinal displacement. Therefore, the peak longitudinal shear strain was 488% at failure, which is 4.9 times the design shear strain. This failure was mainly due to bond failure between the rubber and steel shim (see Figure 3.84), as it was experiencing very large shear strain. Hysteretic response of the bearing is shown in Figure 3.85.

Figure 3.84 Failure of the LPRB (UET-2).

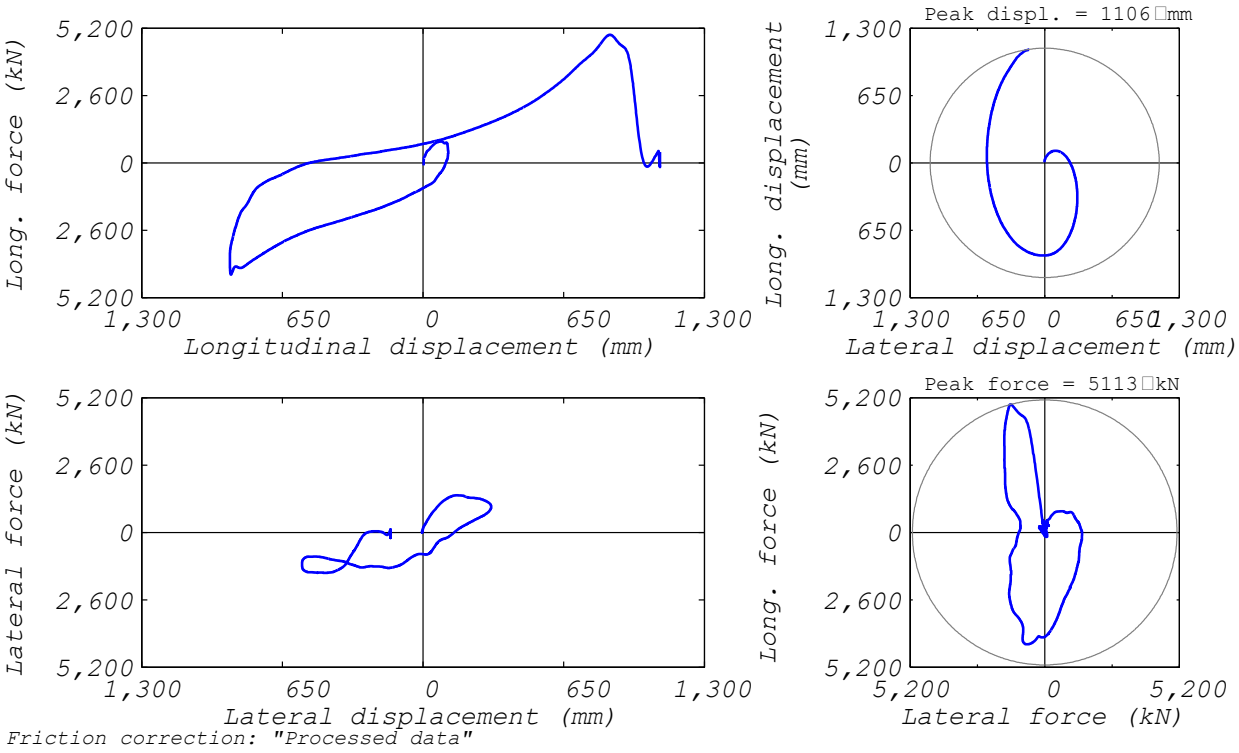

Figure 3.85 Bearing response during failure test (UET-2): Run 66 with 8663 kN axial load.

3.6.2 ESCO RTS (EQS) Failure Tests

As part of characterization tests on the EQS bearing, square orbit input motions were applied at different axial loads; see Figure 3.86. For the low axial load case (178 kN), the interior block (to which all of the springs are attached) started to rotate around the vertical axis of the bearing. This occurred during the last cycle at a displacement of 120 mm corresponding to the design displacement. The rotation completely misaligned the MER springs, which changed the properties of the bearing. The only two mechanisms that prevent rotation of the interior block are the reaction forces in the MER springs and frictional torque reacting on the surfaces between the interior block and upper and lower plates. This failure was caused by low axial load on the bearing (providing lower than design frictional torque) and sliding along one sidewall (with MER springs on the opposite side disengaged). The sidewall friction produced a torque larger than the frictional resistance of the interior block. Figure 3.87 shows the rotated interior block after the test. after the test.

The bearing was permanently damaged, which altered the response and caused disengagement of the MER springs. The permanent damage included permanent deformation in the MER springs, some residual bending in a spring, loss of a PTFE pad on one of the MER springs, and several nicks on the sliding surfaces of the sidewalls. The sidewall sliding surfaces were damaged by the tip of the MER springs; see the localized damage in Figure 3.88.

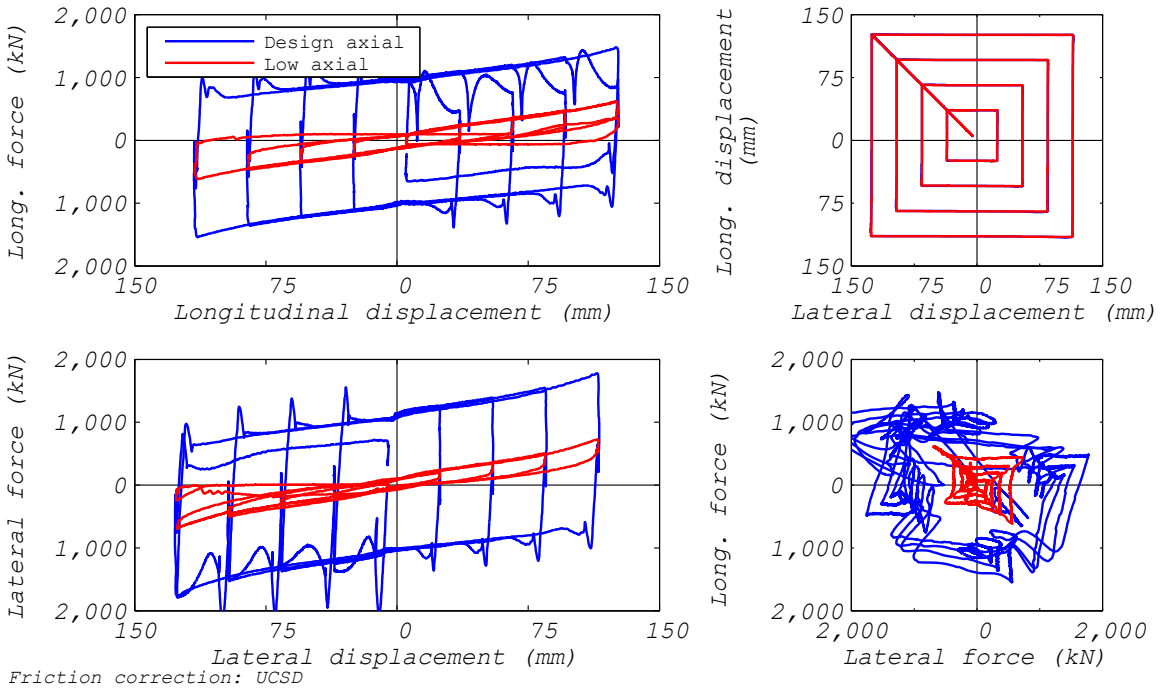

Figure 3.86 EQS-1 bearing response to square orbits.

Figure 3.87 Failure of the EQS-1 bearing.

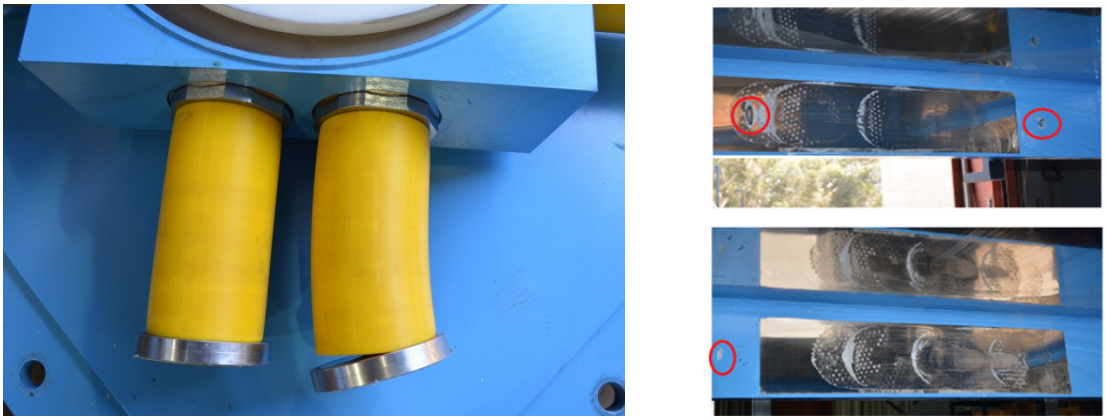

Figure 3.88 Localized damages in the failed EQS-1 bearing.

3.6.2.1 Beyond Design-Level Response

Another test that produced bearing failure was hybrid simulation Run 58, which was performed on bearing EQS-2 to evaluate beyond--design-level response. The NRC dispersion appropriate ground motion number 10 was used as it produced larger-than-design displacements in an analytical simulation. The input motion consisted of two horizontal components; the displacement demand was calculated to be around 190 mm, which is slightly larger than the manufacturer's specified 180-mm-maximum allowable displacement. As the bearing experienced large displacements, the MER springs experienced nonlinear deformation, causing permanent axial deformations and bending in the springs. Moreover, a bonding mechanism was observed between the sliding surface and the sliding pad. A significant increase in initial friction can be observed by comparing Run 30 with Run 59 in Figure 3.89, which were the first and last tests on bearing EQS-2. Figure 3.90 clearly shows that bonding formed, which can cause very large breakaway friction and potentially high-frequency excitation within the system. This bonding could only be confirmed at the conclusion of testing after the failure test, when the bearing was removed from the test machine and inspected.

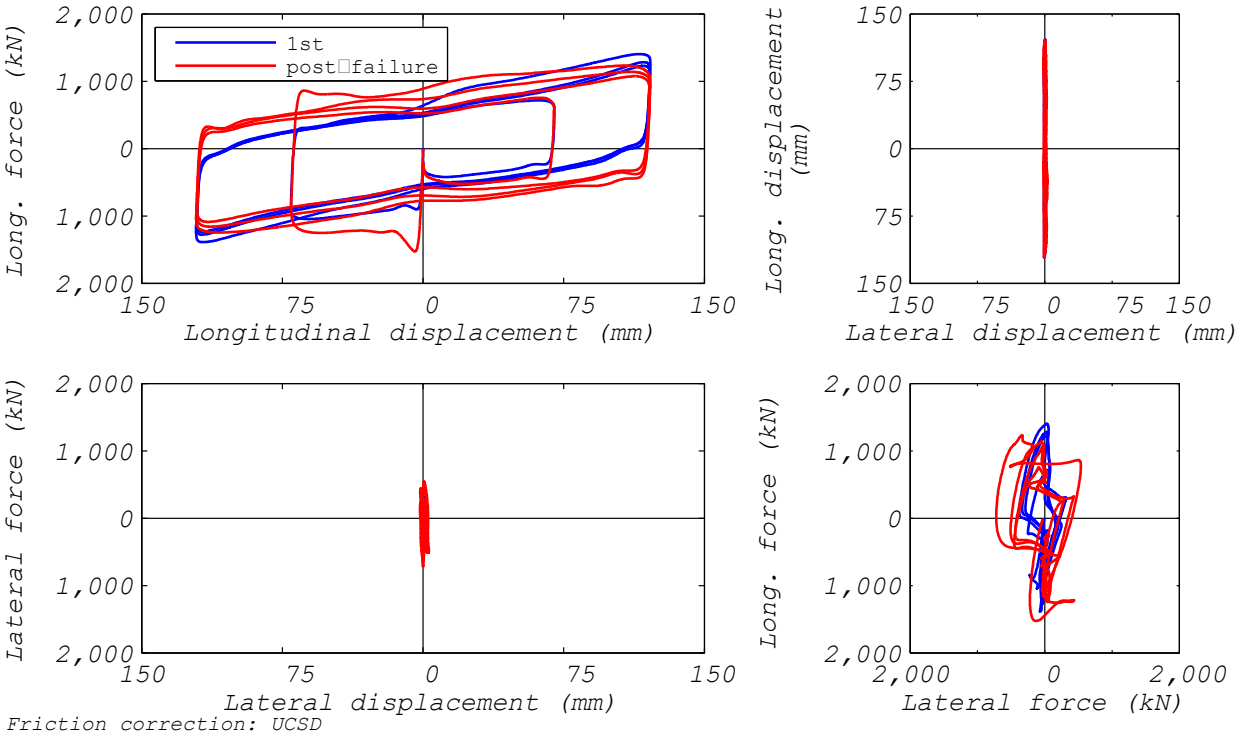

Figure 3.89 EQS-2 bearing response to longitudinal characterization tests.

Figure 3.90 **Bonding between sliding surface and sliding pad for EQS-2 bearing with a pry-bar unable to separate the two.**

4 Conclusions

Conclusions and recommendations related to hybrid simulation as a viable testing method for determining the mechanical influence of seismic isolators in NPPs is reported. Observations and conclusions related to the assessed behavior of the tested isolation systems and the numerically modeled plant superstructure follow:

With regards to the hybrid simulation testing method employed to experimentally test isolators in NPPs the following conclusions are drawn:

- This research program confirmed that hybrid simulation is indeed a viable testing method to experimentally assess the behavior of large isolators at full-scale.
- The SRMD bearing test machine was successfully converted to perform rapid (not real time) hybrid simulation tests for large hybrid models.
- Despite the lack of a load cell to measure directly the experimental bearing forces, reliable results were obtained by measuring forces from actuator load cells and correcting them on-the-fly for machine friction and inertia force effects.
- During the experimental test program the tracking performance (in terms of delays) was significantly improved by installing a feedforward-control software patch provided by MTS, which improved testing speeds from 25 times slower than real time to five times slower than real time.
- It was demonstrated that it is possible to use a high-performance computing platform with parallel processing capabilities (OpenSees*SP*) to perform hybrid simulations of large structures with many DOFs, such as NPPs.
- The performance and accuracy of several different hybrid models of the NPP structure were assessed. It is concluded that the hybrid model that used one experimental bearing to represent all the bearings under the plant performed very well in terms of execution speed and accurate results were obtained from 1D and 2D tests. However, the model was not able to simulate overturning from the plant superstructure or capture the resulting axial load fluctuations in the bearings.
- The hybrid model where one experimental bearing represents one of five bearing groups also performed very well in terms of execution speed. With this model it was possible to capture and study the effect of axial force fluctuations in the test bearing due to overturning. However, the accuracy of the response of this model is somewhat dependent

on the fidelity and accuracy of the analytical bearing elements used to represent the other four bearing groups.

- The efficacy of the hybrid model where the experimental bearing represents one individual bearing out of all the bearings in the isolation system was limited. The response of the overall isolation system was entirely dictated by the behavior of the analytical bearing elements. The ability to accurately calibrate the analytical bearing behavior to match the experimental bearing behavior was heavily dependent on the fidelity of the numerical model; in addition it was time consuming to run. Despite employing a high-performance computing platform, the hybrid model could not be analyzed in real time. The analytical model presented herein was the current speed limitation for this hybrid simulation. Model simplification or computational speed increases are feasible enhancements, but solid state drive write-time hampered execution speed for the model investigated and must be addressed.
- With respect to modeling for hybrid simulations where the experimental bearing represents only one bearing in the entire isolation system, improved analytical isolator models are necessary. Critical to this process is capturing the true behavior of the bearing under different loading conditions; time is required during testing to iteratively tune the parameters of such improved analytical isolator models. Furthermore, investigations are needed on developing strategies to increase computation speeds of such highly complex hybrid models in order to be able to perform near-real-time hybrid tests in the future. Improvements to the analytical model will foreseeably achieve faster execution time, so SRMD hardware limitations are likely to govern the speed of future tests.
- It is recommended to improve the tracking performance of the SRMD test system for any future hybrid simulations performed on this testing system. Because it is apparent that real-time or near-real-time hybrid simulations of seismic isolation systems can more closely capture the true behavior of the isolators, it is recommended that strategies be developed to determine how to reduce overall delays currently present in the system to an absolute minimum.

Conclusions regarding the behavior of the different isolation systems and the NPP superstructure response are as follows:

- Overall, the seismically isolated plant facilities behaved as expected. Base shears and floor accelerations were generally reduced substantially compared to what might be expected for a fixed-base structure (here observed by comparison of floor spectra). However, the tests were able to identify specific differences associated with different bearings, loading conditions, and earthquake excitations.
- Heat generation in the LPRB was larger during 2D testing than during 1D testing, causing the yield strength of the lead core to decrease faster, leading to larger displacement demands in the hybrid tests. At least 2D hybrid simulations should be performed to capture bearing demands accurately. Two-dimensional versus 1D testing also affected floor response spectra, with the 1D tests significantly overestimating spectral accelerations.

- The LPRB showed substantial vertical–horizontal coupling behavior. While this behavior did not affect bearing displacement demands, it had a major effect on floor response spectra. It is essential to include vertical ground motion input in hybrid testing to accurately predict floor response spectra. Neglecting vertical excitation can significantly underestimate horizontal spectral accelerations around the vertical frequency of the isolated plant.
- Vertical force fluctuations due to overturning effects did not influence significantly the behavior of the LPRB. However, a small increase in floor spectral accelerations was observed, which was attributed to the vertical–horizontal coupling of the LPRBs. In terms of overturning effects, net tension was not recorded in any of the bearings for the two selected ground motions with the specific NPP structure, its specified bearing layout, and the type of LPRB used in these hybrid simulations. Note that this conclusion only applies to the LPRBs with these specifications under these loading protocols, and the superstructure in question. This conclusion could well be different under different circumstances.
- For the modeling of the LPRB, a fairly simple analytical Bouc-Wen model captured floor response spectra quite accurately under 1D and 2D excitation. Softening of the lead core as heat was generated did not affect significantly floor response spectra, and a simple model that ignores this effect is sufficient. However, to accurately predict bearing displacement demands—especially for 2D and 3D excitation and to accurately predict floor response spectra for 3D excitation—it is important to develop an improved analytical model that more closely captures the true behavior of LPRBs.
- For the hybrid simulations on the EQS bearings, the breakaway and static frictions were more pronounced in the 25 times slower tests as compared to the five times slower tests. It is important to perform rapid hybrid simulation tests on this type of isolator to capture accurately the bearing behavior; it is recommended that real-time hybrid testing be performed on these isolators.
- The EQS bearings showed substantial vertical–horizontal coupling behavior. While this behavior did not affect bearing displacement demands, it had a major effect on floor response spectra. It is essential to include vertical ground motion input in hybrid testing to accurately predict floor response spectra. Neglecting vertical excitation can significantly underestimate horizontal spectral accelerations around the vertical frequency of the isolated plant.
- Vertical force fluctuations due to overturning effects did not influence to any significant degree the behavior of the EQS bearings. However, a small increase in floor spectral accelerations was observed, which was attributed to the vertical–horizontal coupling of the EQS bearings. In terms of overturning effects, uplift of the friction surface was not recorded in any of the bearings when tested for the selected ground motions and for the specific NPP structure, its specific bearing layout, and the EQS bearing type used in these hybrid simulations. Note that this conclusion only applies to the EQS bearing with these specifications under these loading protocols and the superstructure in question. This conclusion could well be different under different circumstances.

- For the modeling of the EQS bearing, more complex modeling is required to be able to accurately capture floor response spectra under 1D and 2D excitation. The breakaway friction force in these bearings greatly affects the floor response spectra and a simple velocity dependent friction model is not sufficient.

REFERENCES

Casciati F. (1989). Stochastic dynamics of hysteretic media, *Struct. Safety*, 6: 259–269.

EUR (2012). *European Utility Requirements for LWR Nuclear Power Plants, Revision D*, European Utility Requirements for LWR Nuclear Power Plants, available online at: *http://www.europeanutilityrequirements.org/Documentation/EURdocument.aspx*.

dSpace (2013). dSPACE GmbH, available from: *http://www.dspace.com*.

Grant D. (2004). *Bidirectional Modeling of High-Damping Rubber Bearings*, PhD dissertation, The Rose School, Pavia, Italy.

Mathworks (2013). MathWorks – Real-Time Workshop, available online at: *https://www.mathworks.com/matlabcentral/linkexchange/links/752-mathworks-real-time-workshop*.

Mosqueda G., Stojadinovic B., Mahin S.A. (2005). Implementation and accuracy of continuous hybrid simulation with geographically distributed substructures, *Report No. EERC 2005-02*, Earthquake Engineering Research Center, University of California, Berkeley, CA.

NRC (1973). *Regulatory Guide 1.60 (Rev. 1, December 1973), Design Response Spectra for Seismic Deign of Nuclear Power Plants*, U.S. Nuclear Regulatory Commission, NUREG-1.60, Washington, D.C.

OpenFresco (2014). *Open-Source Framework for Experimental Setup and Control* (Version 2.7) [computer software], available online at: *http://openfresco.berkeley.edu/*.

OpenSees (2014). *Open System for Earthquake Engineering Simulation* (Version 2.4.4) [computer software], available online at: *http://opensees.berkeley.edu/*.

Schellenberg A., Mahin S.A., Fenves G. (2009). Advanced implementation of hybrid simulation, *Report No. PEER 2009/104*, Pacific Earthquake Engineering Research Center, University of California, Berkeley, Berkeley, CA.

Schellenberg A., Drosos V., Mahin S.A., Sitar N. (2014a). Investigation of seismic isolation technology applied to the APR 1400 nuclear power plant: Review and improve numerical models, Vol. 1, *Project Report to KEPCO E&C,* Pacific Earthquake Engineering Research Center, University of California, Berkeley, CA.

Schellenberg A., Baker J., Mahin S.A., Sitar, N. (2014b). Investigation of seismic isolation technology applied to the APR 1400 nuclear power plant: Selection of ground motions, Vol. 2, *Project Report to KEPCO E&C*, Pacific Earthquake Engineering Research Center, University of California, Berkeley, CA.

Schellenberg A. (2010). Elastomeric bearing (Plasticity) element, available online at: *http://opensees.berkeley.edu/wiki/index.php/Elastomeric_Bearing_%28Plasticity%29_Element*.

Spangler Shortreed J., Seible F., Filiatrault A., Benzoni G. (2001). Characterization and testing of the Caltrans seismic response modification device test system, *Phil. Trans. R .Soc. A*, 359: 1829–1850.

UCSD (2014). Caltrans seismic response modification device (SRMD) test facility, University of California, San Diego, available online at: *http://structures.ucsd.edu/node/62*.

Wong J., Zhou Z., Mahin, S. (2012). On-going research activities for seismically isolated facilities at nuclear power stations, *Project Report on Task 1.3 to KEPCO E&C*, Seismic Isolation of Nuclear Power Plants (Phase 1), Pacific Earthquake Engineering Research Center, University of California, Berkeley, Berkeley, CA.

Wong J., Zhou Z., Mahin S. (2013). Seismic isolation of nuclear power plants, *Report 3002000561*, Electric Power Research Institute, Palo Alto, CA.

Appendix A: Hybrid Simulation Tests Conducted on Lead Plug Rubber Bearings

Hybrid tests listed in Table A.1 and Table A.2 were performed on the Unison eTech bearings UET-2 and UET-1, respectively. Detailed responses of these tests are shown in sections A.1 through A.30. For select tests, a corresponding analytical estimation was performed and included in this appendix. These are indicated by the letter *A* appending the run number.

Table A.1 Hybrid simulations and analyses conducted on lead plug rubber bearing UET-2

Section	Run	Ground motion	Model	Components	Test rate
A.1	24	EUR5	Exp = All	2D	25
A.2	25	EUR5	Exp = All	2D	25
A.3	26	EUR5	Exp = All	2D	25
A.4	37	EUR5	Exp = All	Longitudinal	25
A.5	38	Displacement from #26	Exp = All	2D	-
A.6	42	EUR5	Exp = All	Longitudinal	25
A.7	43	EUR5	Exp = All	Longitudinal	25
A.8	44	EUR5	Exp = All	Longitudinal	25
A.9	*44A*	*EUR5*	*Exp = All*	*Longitudinal*	-
A.9	45	EUR5	Exp = All	2D	25
A.11	*45A*	*EUR5*	*Exp = All*	*2D*	-
A.11	46	NRC15	Exp = All	2D	25
A.13	47	NRC15	Exp = All	Longitudinal	25
A.14	*47A*	*NRC15*	*Exp = All*	*Longitudinal*	-
A.14	55	NRC15	Exp = All	2D	25
A.16	*55A*	*NRC15*	*Exp = All*	*2D*	-
A.16	58	EUR5	Exp = 1 of 527	2D	25 with 4 iterations
A.18	60	EUR5	Exp = 1 of 527	2D	30 with 4 iterations
A.19	61	NRC15	Exp = 1 of 527	2D	75 with 4 iterations
A.20	63	NRC15	5 groups of bearings (Exp = Center)	2D	25

Table A.2 Hybrid simulations and analyses conducted on lead plug rubber bearing UET-1

Section	Run	Ground motion	Model	Components	Test rate
A.21	78	EUR5	Exp = All	3D	25
A.22	79	EUR5	5 groups of bearings (Exp = Center)	3D	25
A.23	80	EUR5	5 groups of bearings (Exp = Center)	3D	25
A.24	82	EUR5	5 groups of bearings (Exp = Center)	3D	25
A.25	83	EUR5	5 groups of bearings (Exp = Corner No. 3)	3D	25
A.26	84	NRC15	5 groups of bearings (Exp = Center)	3D	25
A.27	85	NRC15	5 groups of bearings (Exp = Corner No. 3)	3D	25
A.28	86	Displacement from #84	-	3D	-
A.29	88	NRC15	5 groups of bearings (Exp = Corner No. 3)	3D + Vertical	25
A.30	89	NRC15	5 groups of bearings (Exp = Corner No. 3)	3D + Vertical	25

A.1 DEVELOPMENT RUN 24

Development run 24 was a hybrid test of the EUR dispersion appropriate ground motion number five. The model consisted of a single experimental bearing representing all 527 bearings. Input motions consisted of two horizontal components and a constant axial load specified as the design axial load of 8,663 kN. The test was executed at a rate 25 times slower than real time to compensate for machine delays. Bearing UET-2 was used in this test. Figure A.1-1 shows the fidelity achieved in the hybrid test. Figures A.1-2 and A.1-3 contain bearing responses, and Figure A.1-4 depicts the resulting floor response spectra for select locations in two of the isolated structures.

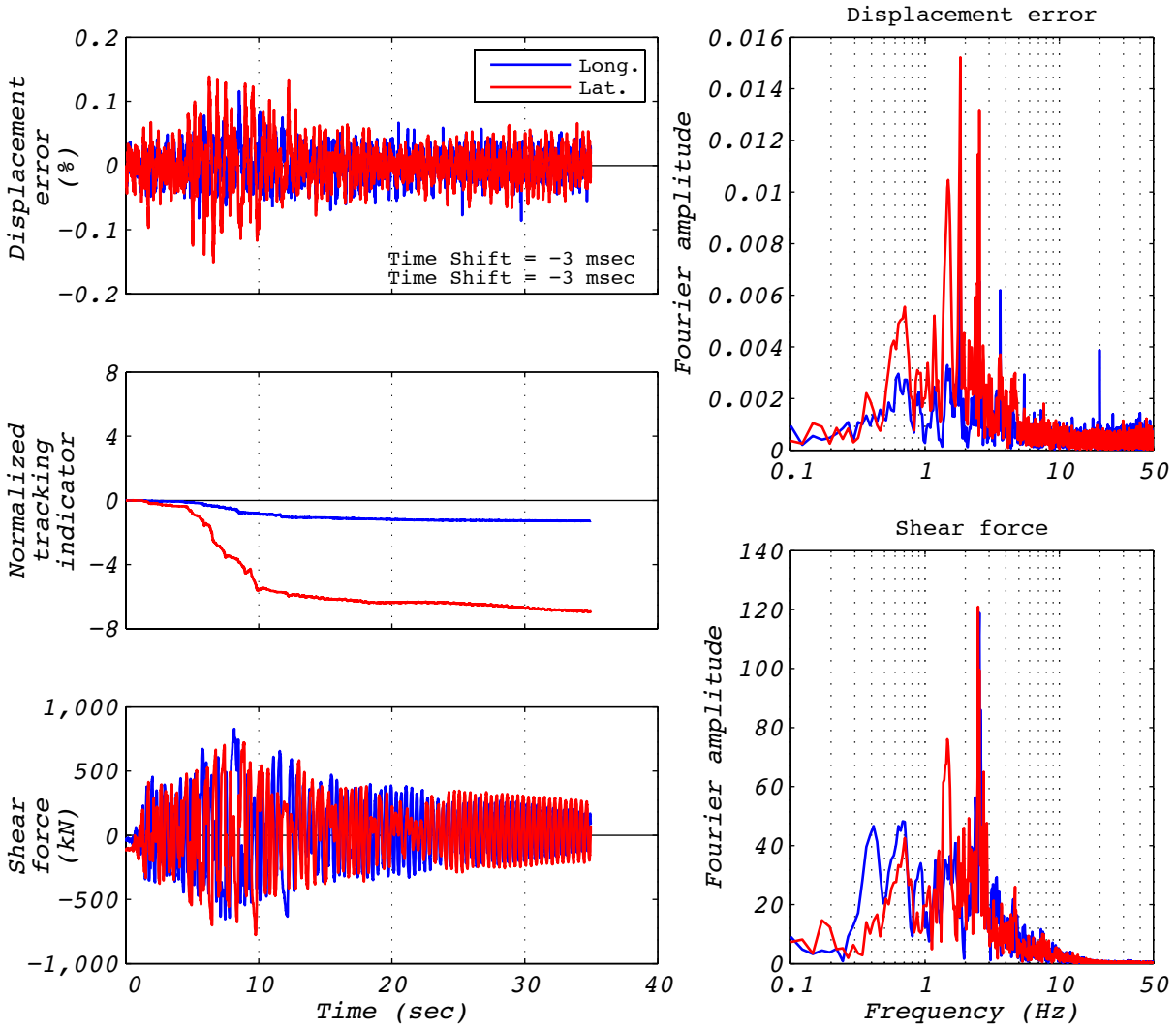

Figure A.1 Hybrid test performance metrics for run 24: EUR5, 2D with experimental bearing representing all bearings.

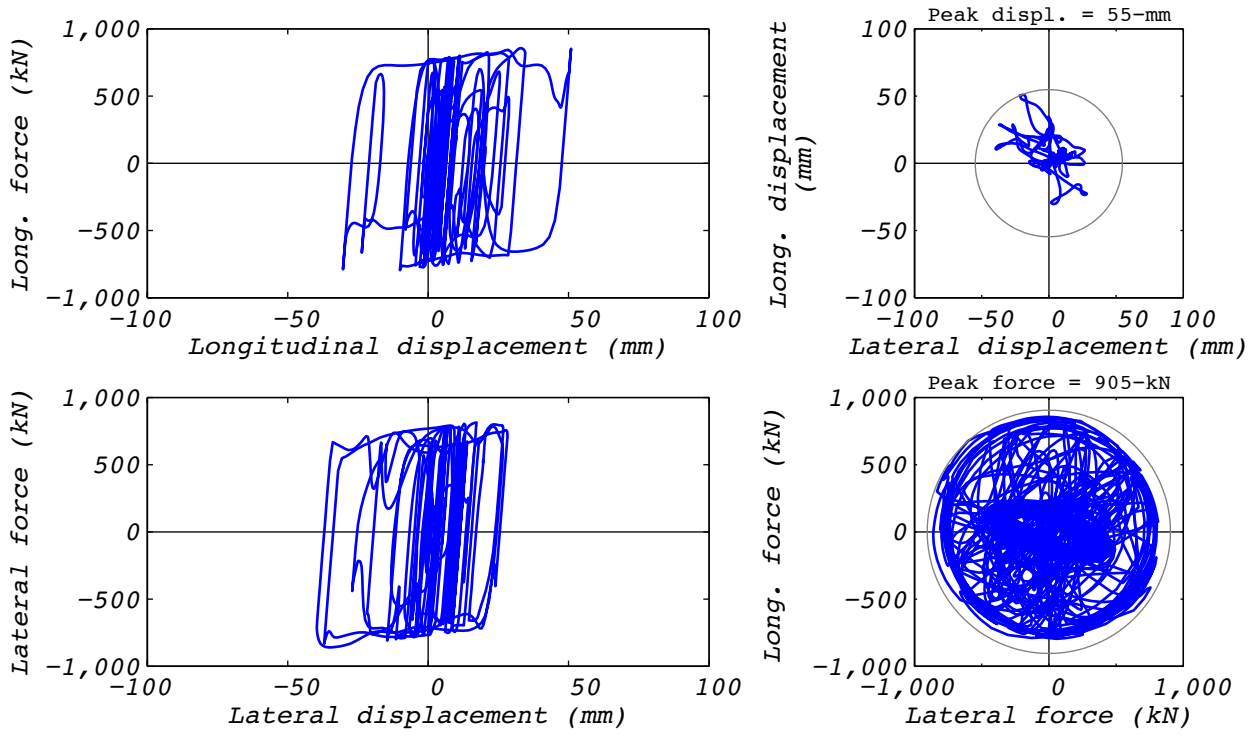

Figure A.2 Hybrid test bearing response for run 24: EUR5, 2D with experimental bearing representing all bearings.

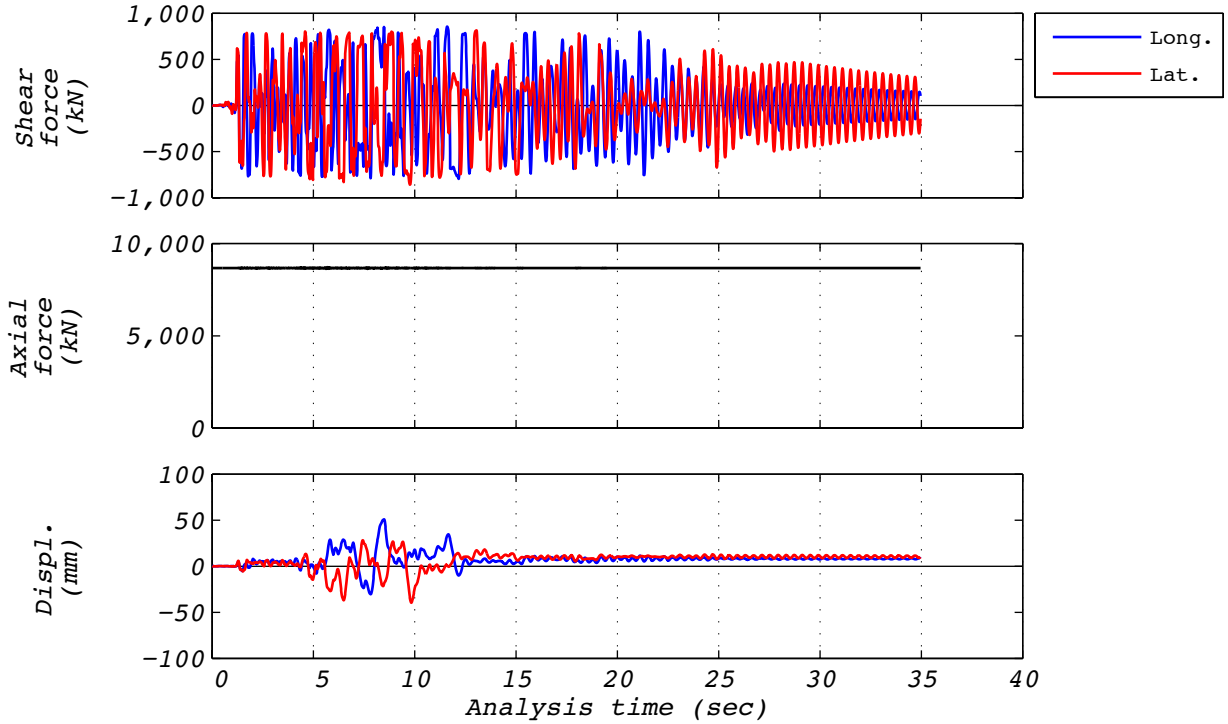

Figure A.3 Hybrid test time history responses for run 24: EUR5, 2D with experimental bearing representing all bearings.

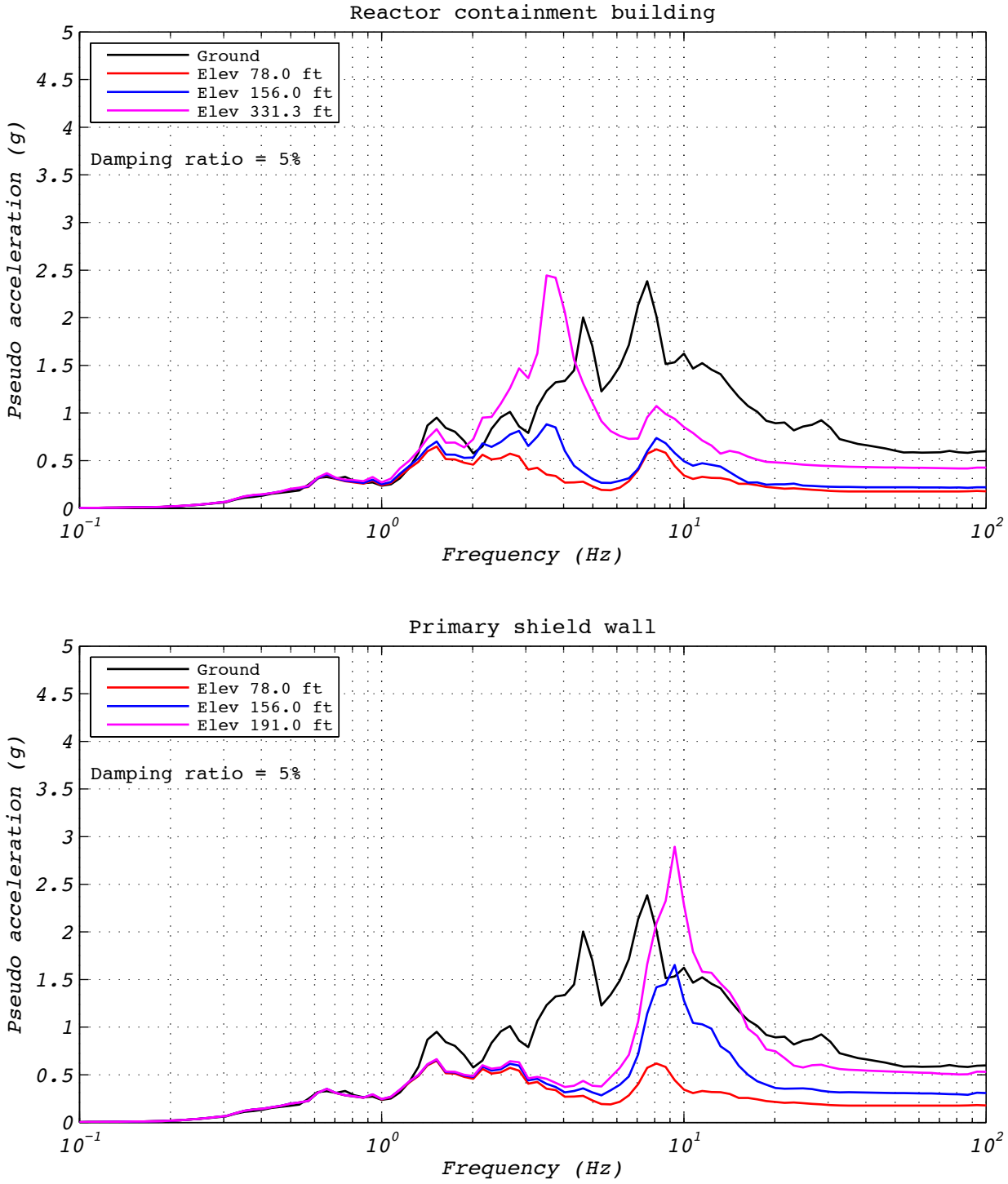

Figure A.4 Hybrid test floor spectra for run 24: EUR5, 2D with experimental bearing representing all bearings.

A.2 DEVELOPMENT RUN 25

Development run 25 was a hybrid test of the EUR dispersion appropriate ground motion number five. The model consisted of a single experimental bearing representing all 527 bearings. Input motions consisted of two horizontal components and a constant axial load specified as the design axial load of 8,663 kN. The test was executed at a rate 25 times slower than real time to compensate for machine delays. Bearing UET-2 was used in this test. Figure A.2-1 shows the fidelity achieved in the hybrid test. Figures A.2-2 and A.2-3 contain bearing responses, and Figure A.2-4 depicts the resulting floor response spectra for select locations in two of the isolated structures.

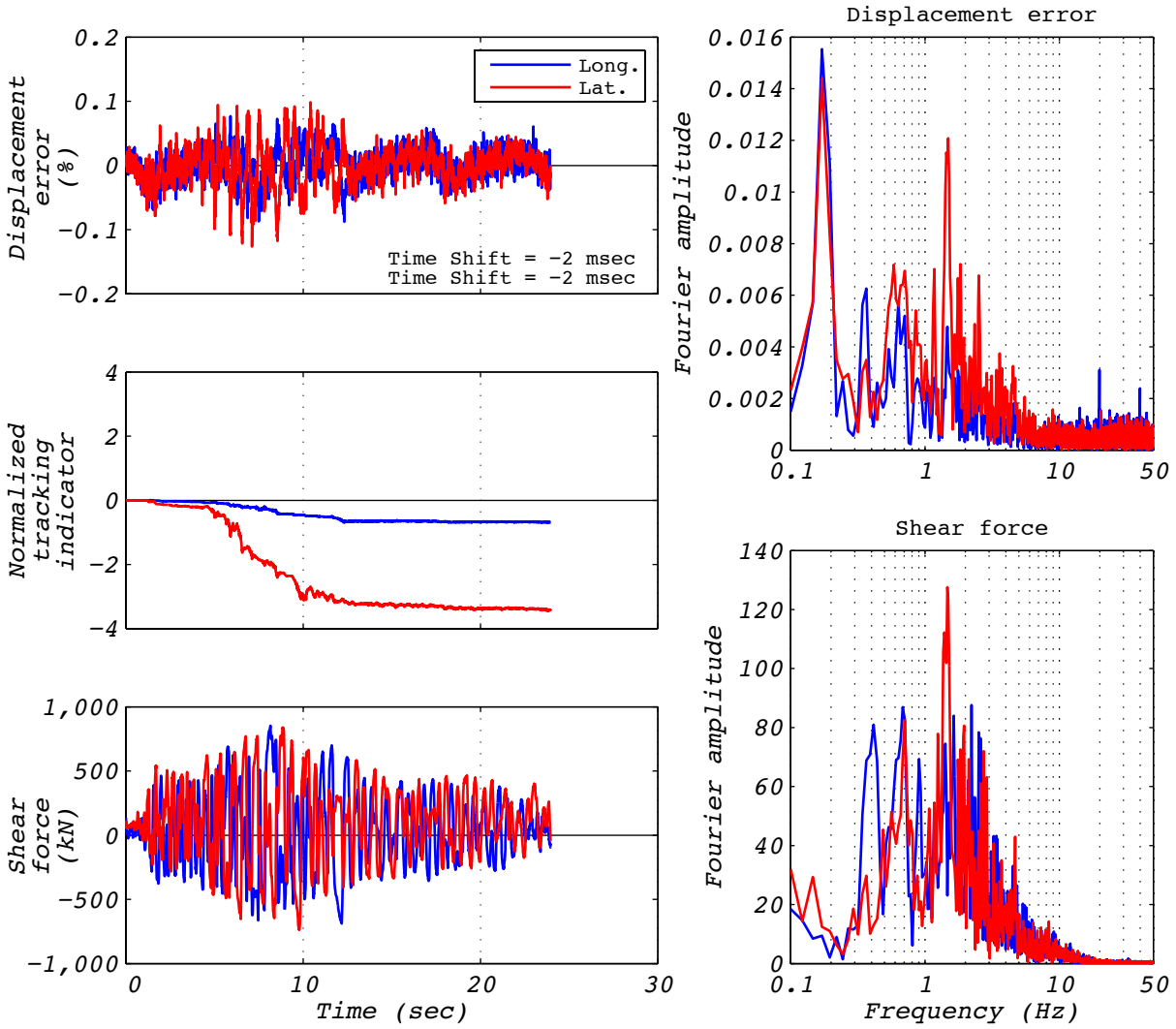

Figure A.2-1 Hybrid test performance metrics for run 25: EUR5, 2D with experimental bearing representing all bearings.

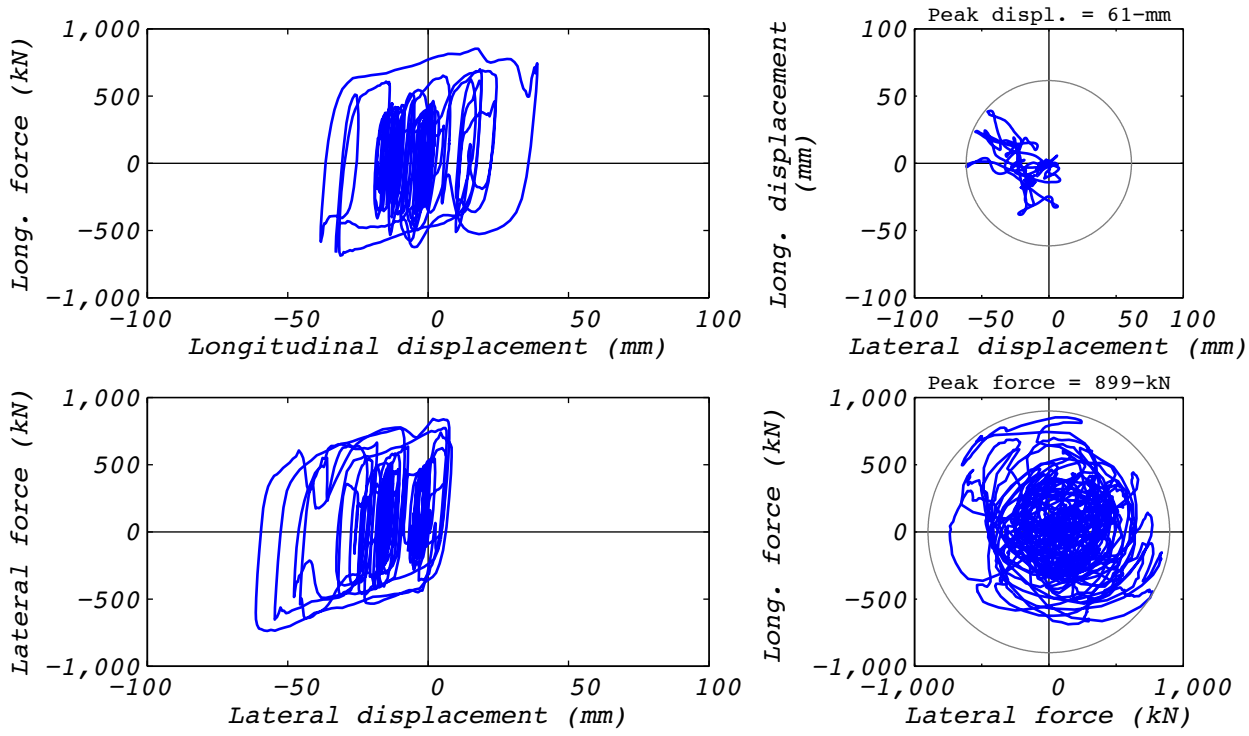

Figure A.2-2 Hybrid test bearing response for run 25: EUR5, 2D with experimental bearing representing all bearings.

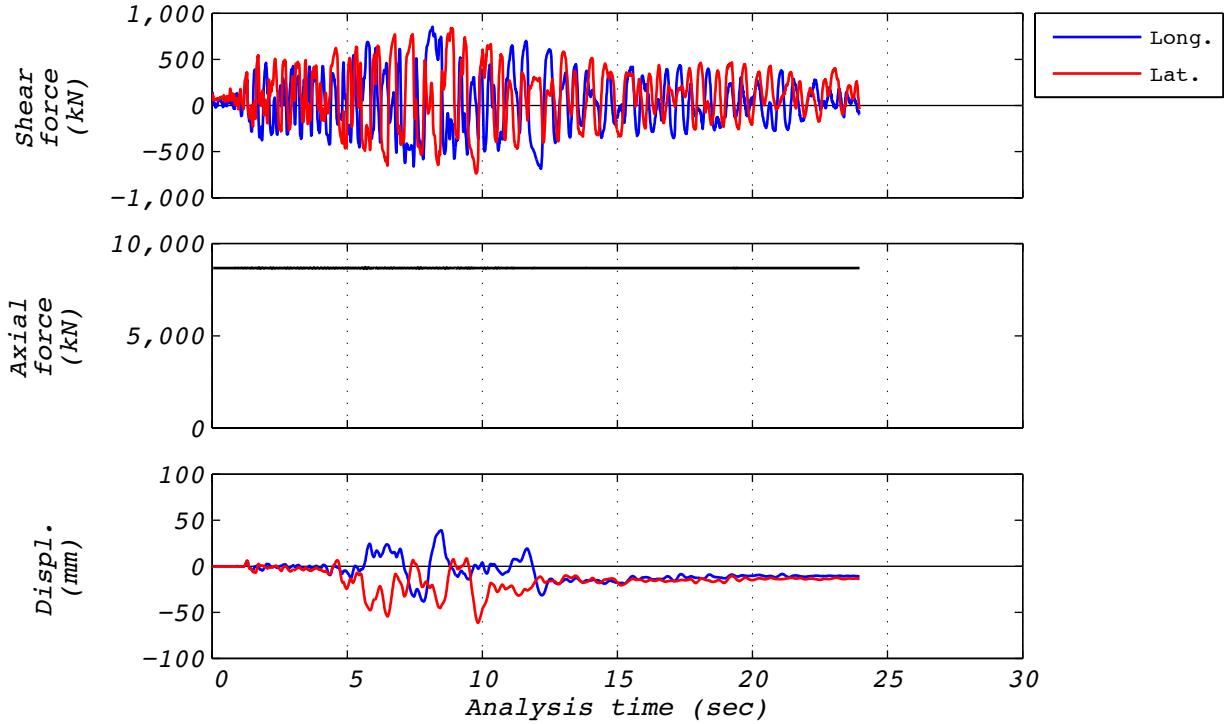

Figure A.2-3 Hybrid test time history responses for run 25: EUR5, 2D with experimental bearing representing all bearings.

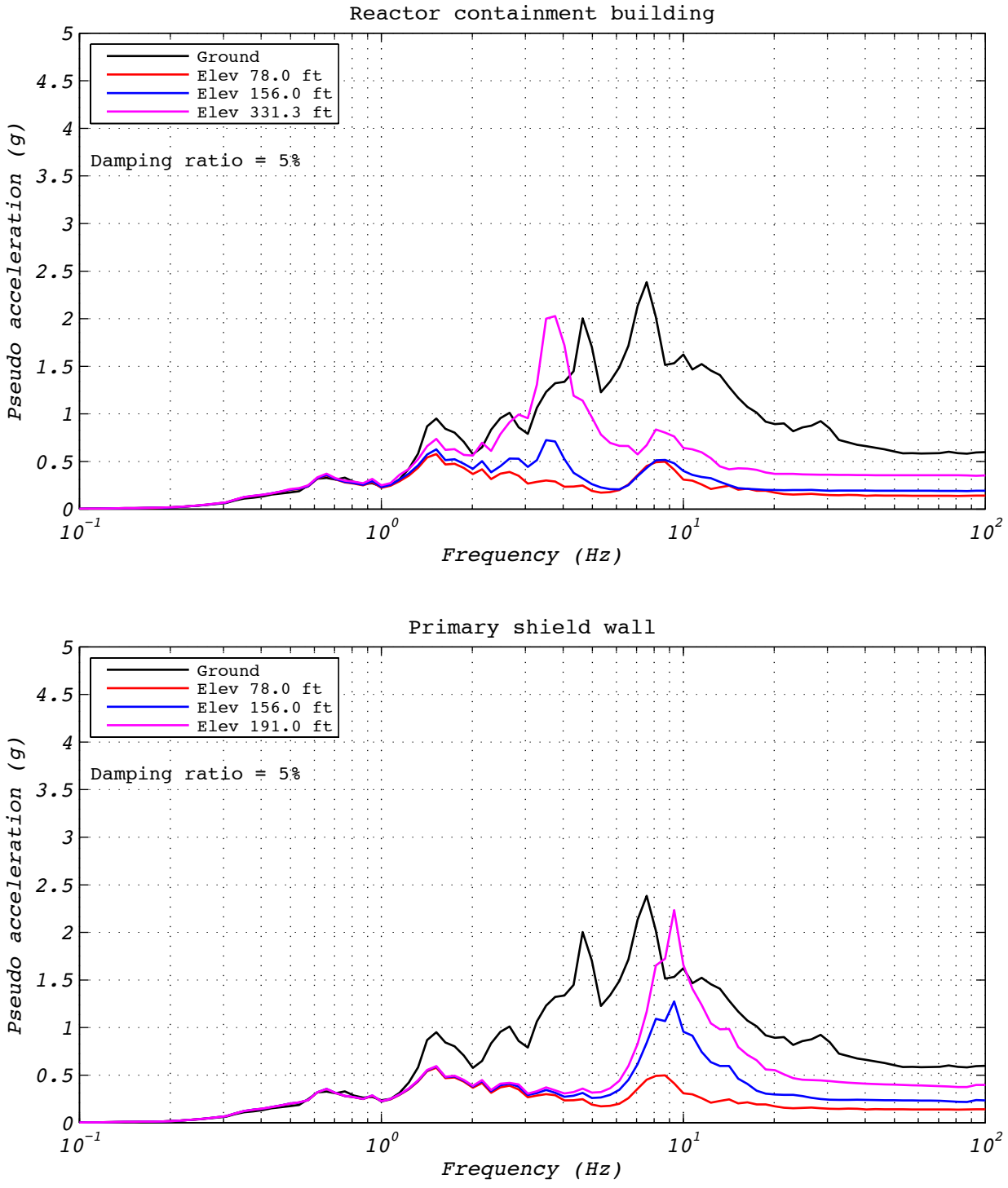

Figure A.2-4 Hybrid test floor spectra for run 25: EUR5, 2D with experimental bearing representing all bearings.

A.3 TEST RUN 26

Test run 26 was a hybrid test of the EUR dispersion appropriate ground motion number five. The model consisted of a single experimental bearing representing all 527 bearings. Input motions consisted of two horizontal components and a constant axial load specified as the design axial load of 8,663 kN. The test was executed at a rate 25 times slower than real time to compensate for machine delays. Bearing UET-2 was used in this test. Figure A.3-1 shows the fidelity achieved in the hybrid test. Figures A.3-2 and A.3-3 contain bearing responses, and Figure A.3-4 depicts the resulting floor response spectra for select locations in two of the isolated structures.

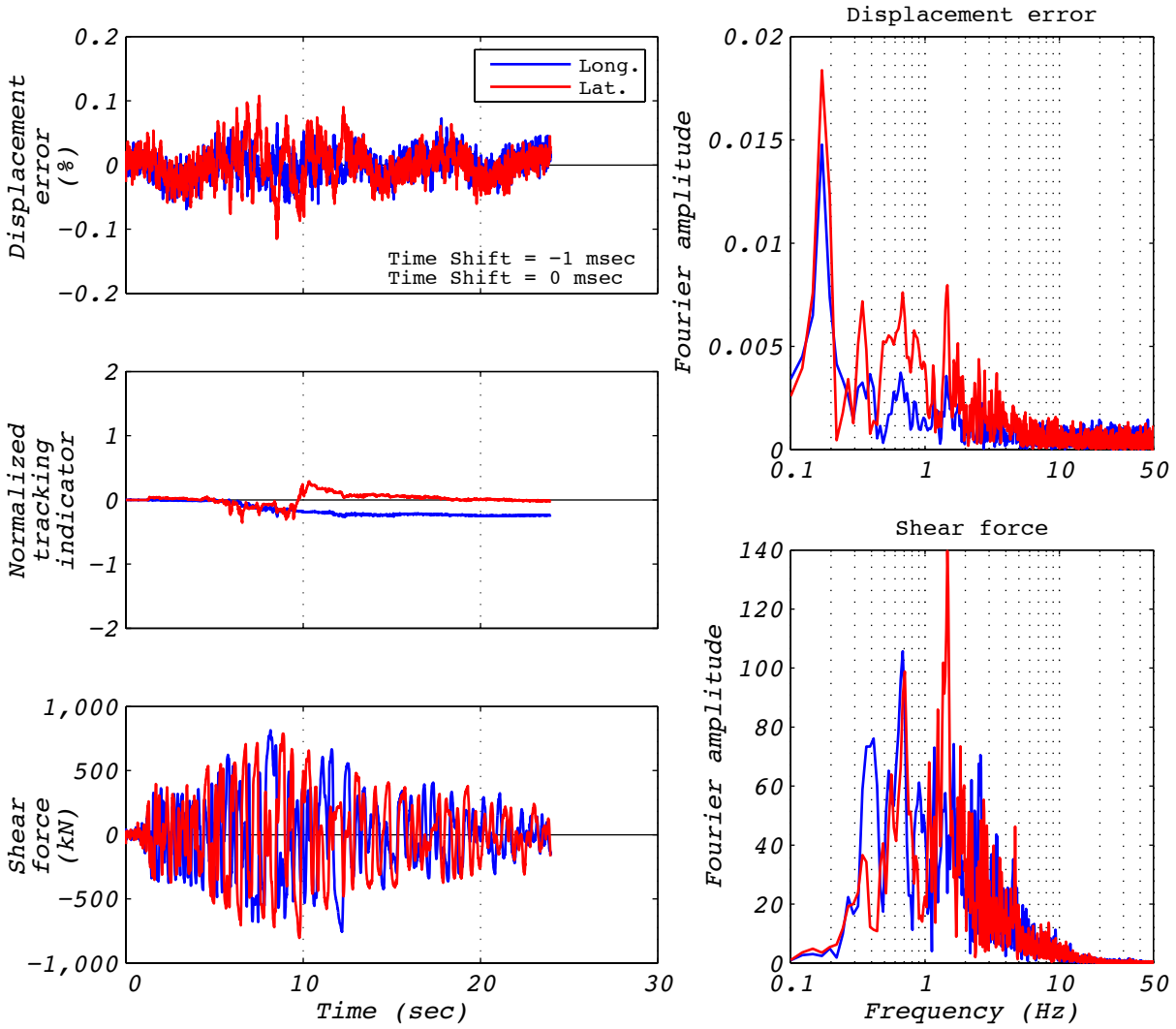

Figure A.3-1 Hybrid test performance metrics for run 26: EUR5, 2D with experimental bearing representing all bearings.

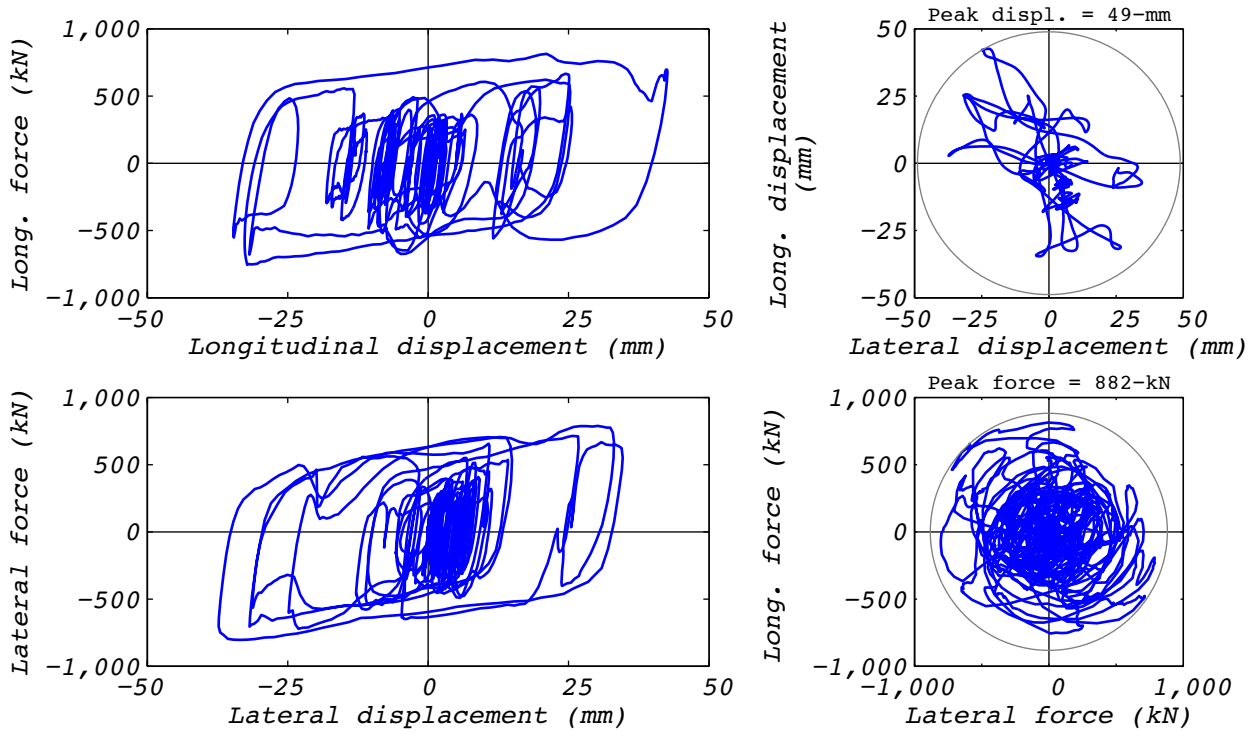

Figure A.3-2 Hybrid test bearing response for run 26: EUR5, 2D with experimental bearing representing all bearings.

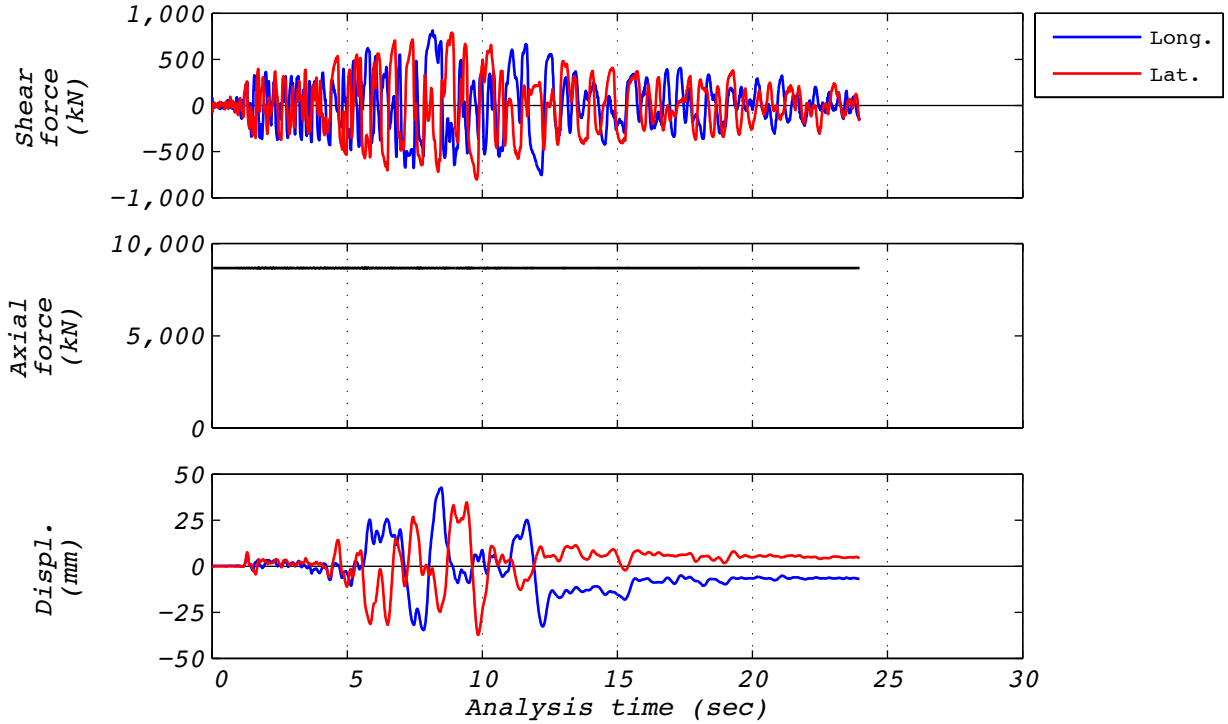

Figure A.3-3 Hybrid test time history responses for run 26: EUR5, 2D with experimental bearing representing all bearings.

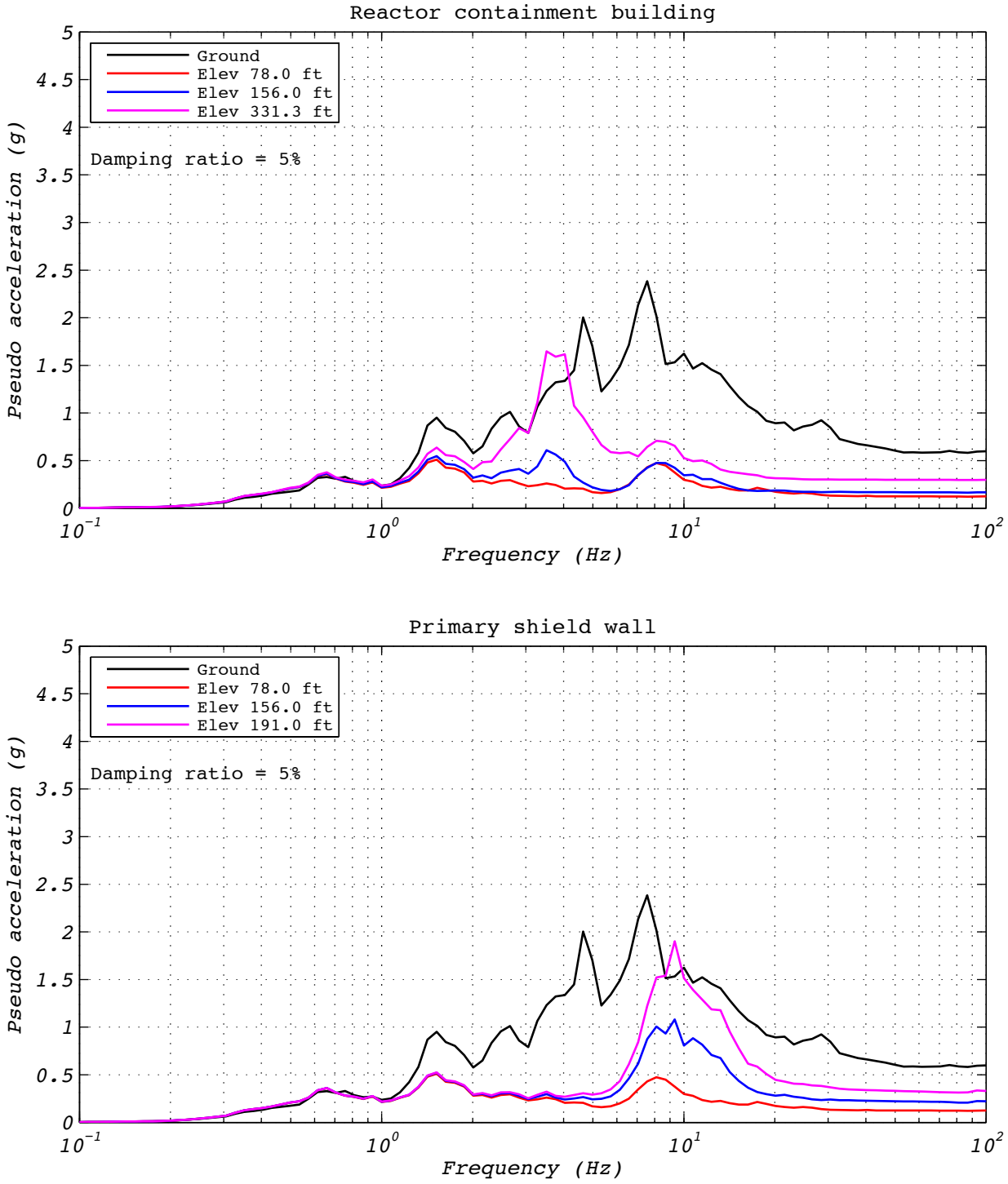

Figure A.3-4 Hybrid test floor spectra for run 26: EUR5, 2D with experimental bearing representing all bearings.

A.4 TEST RUN 37

Test run 37 was a hybrid test of the EUR dispersion appropriate ground motion number five. The model consisted of a single experimental bearing representing all 527 bearings. Input motions consisted of one horizontal component and a constant axial load specified as the design axial load of 8,663 kN. The test was executed at a rate 25 times slower than real time to compensate for machine delays. Bearing UET-2 was used in this test. Figure A.4-1 shows the fidelity achieved in the hybrid test. Figures A.4-2 and A.4-3 contain bearing responses, and Figure A.4-4 depicts the resulting floor response spectra for select locations in two of the isolated structures.

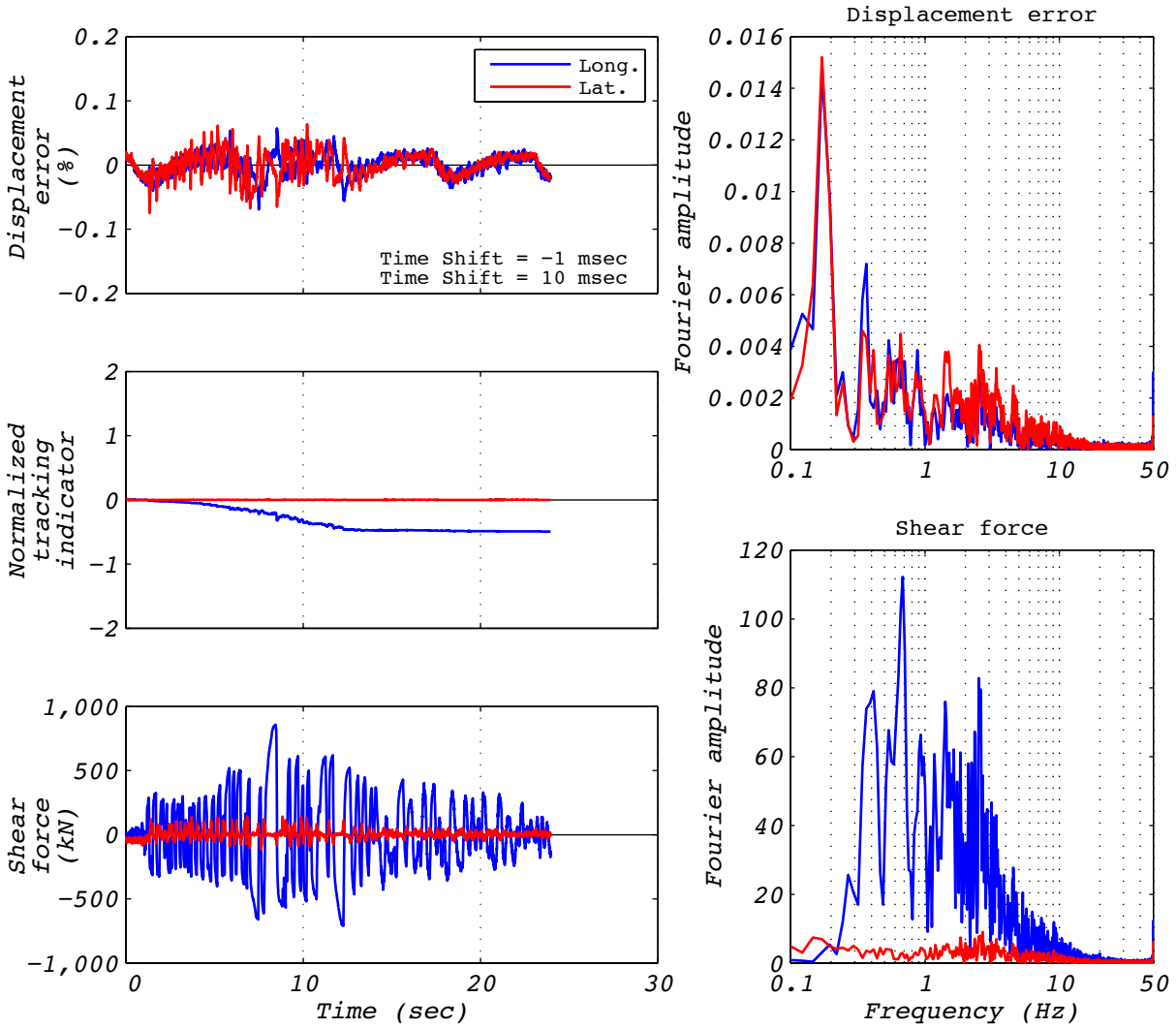

Figure A.4-1 Hybrid test performance metrics for run 37: EUR5, 1D with experimental bearing representing all bearings.

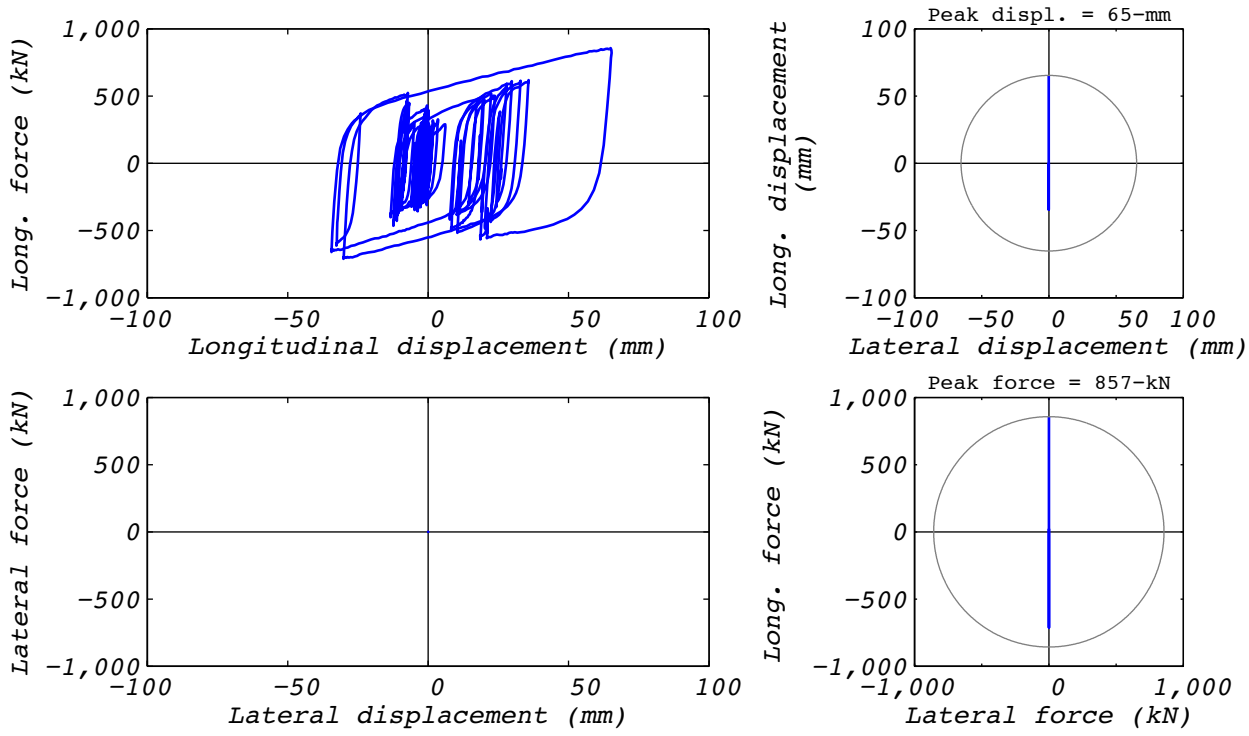

Figure A.4-2 Hybrid test structural response for run 37: EUR5, 1D with experimental bearing representing all bearings.

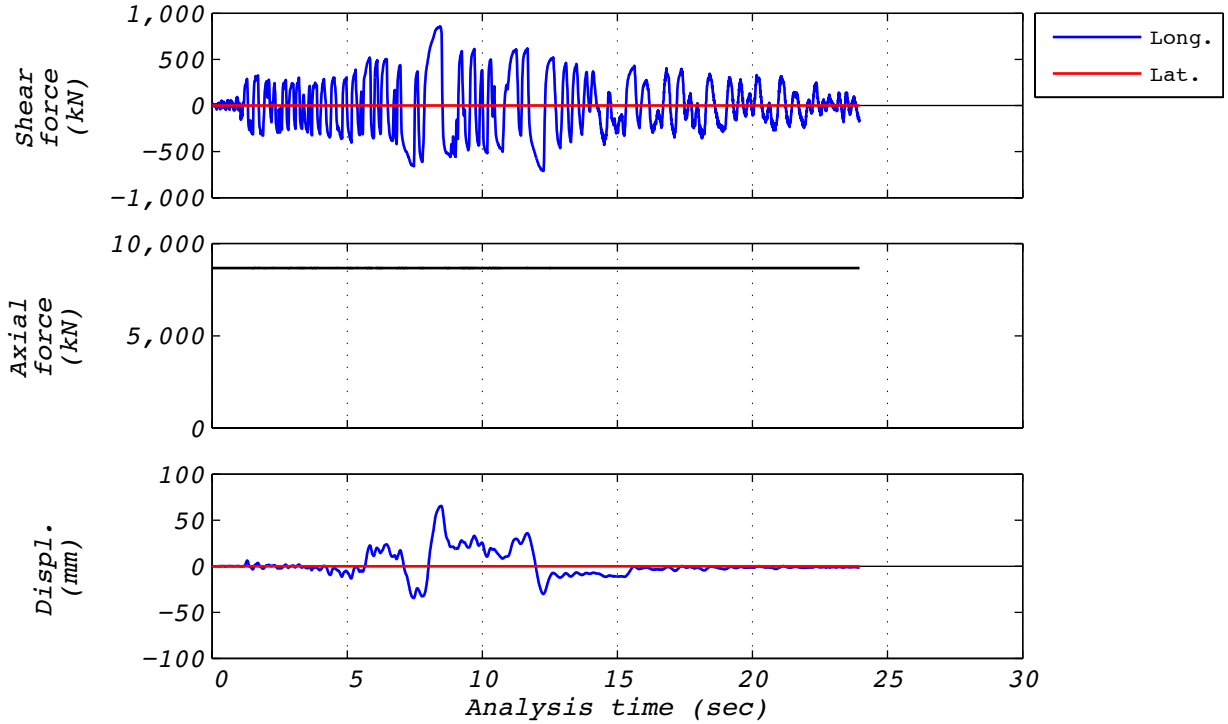

Figure A.4-3 Hybrid test bearing response for run 37: EUR5, 1D with experimental bearing representing all bearings.

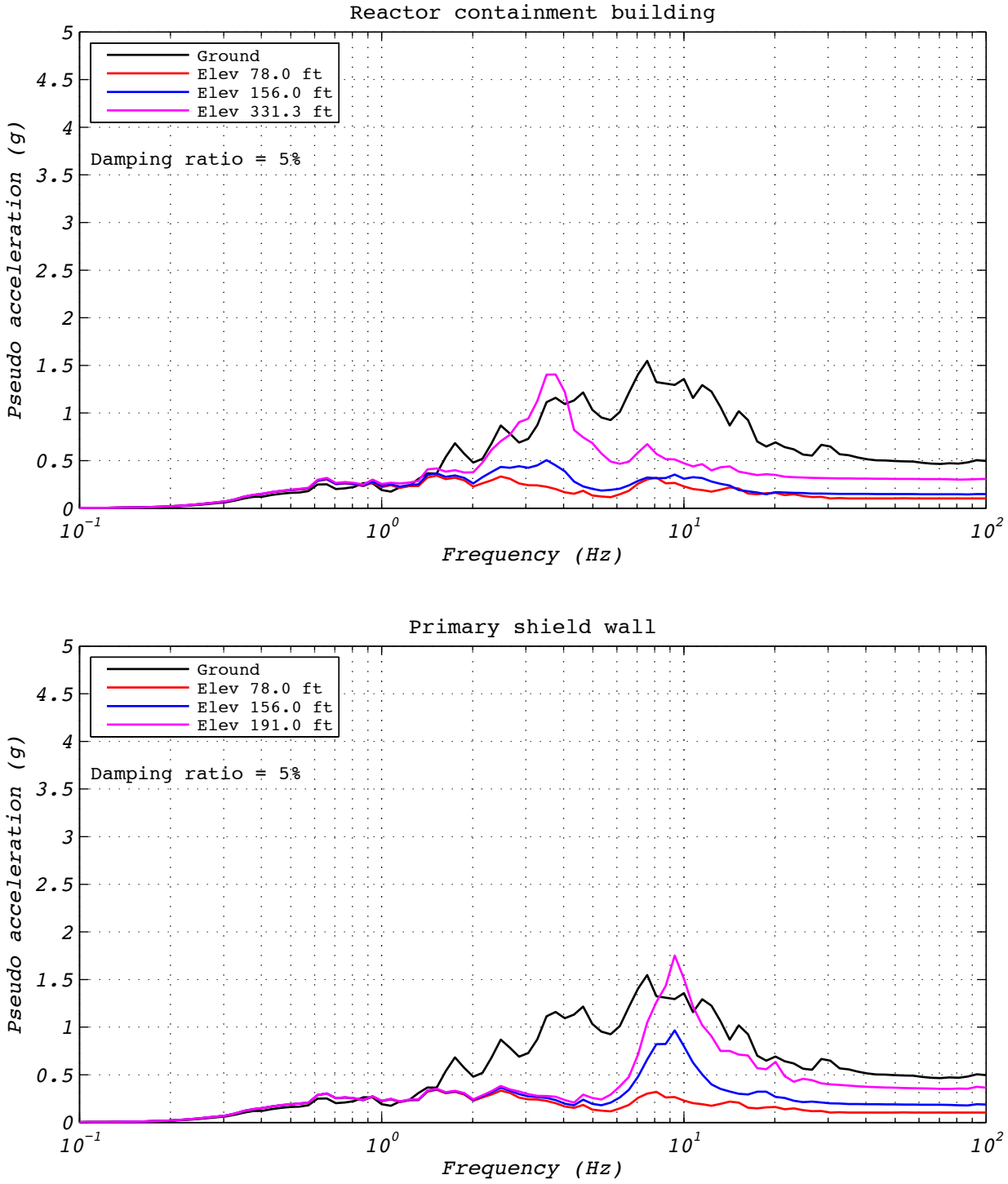

Figure A.4-4 Hybrid test floor spectra for run 37: EUR5, 1D with experimental bearing representing all bearings.

A.5 DISPLACEMENT RUN 38

Test run 38 was a real-time displacement history recorded from test run 26, which was a hybrid test of the EUR dispersion appropriate ground motion number five. Input motions consisted of two horizontal components and a constant axial load specified as the design axial load of 8,663 kN. The test was executed at a rate real time to investigate loading rate effects. Bearing UET-2 was used in this test. Figures A.5-1 and A.5-2 contain bearing responses.

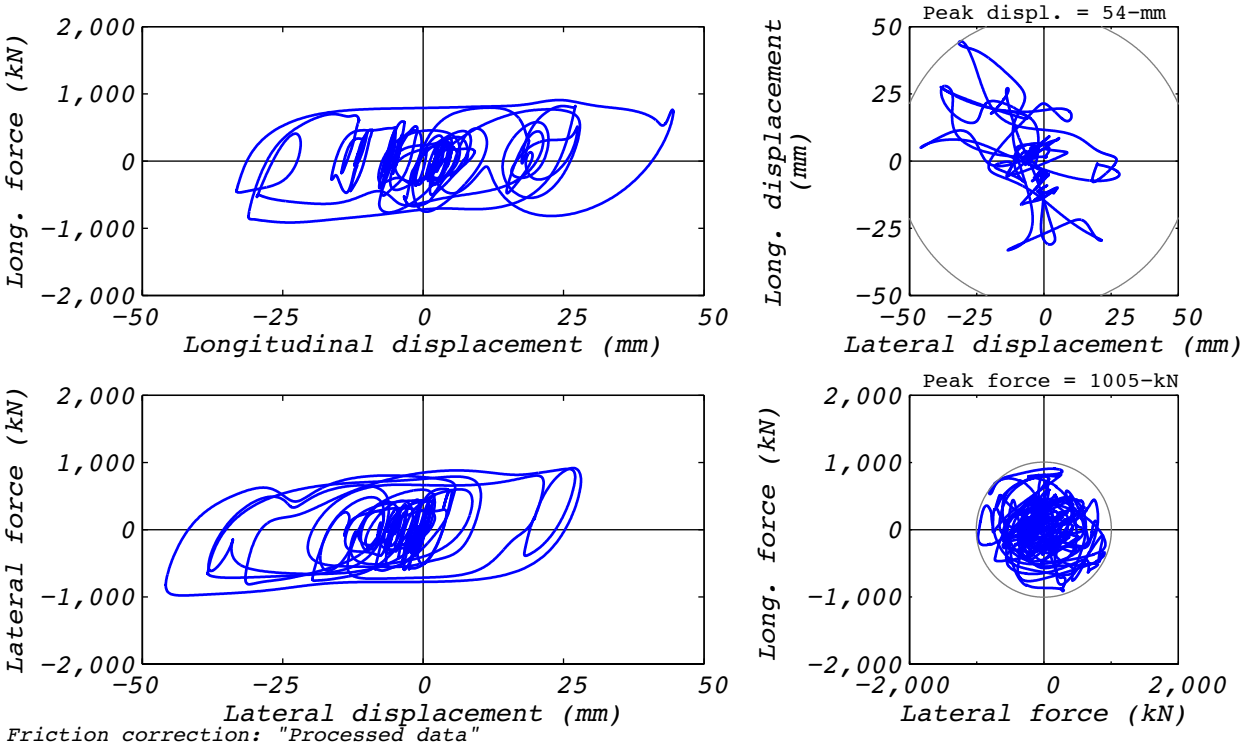

Figure A.5-1 Bearing response for real-time reproduction of hybrid test run 26: EUR5, 2D with experimental bearing representing all bearings.

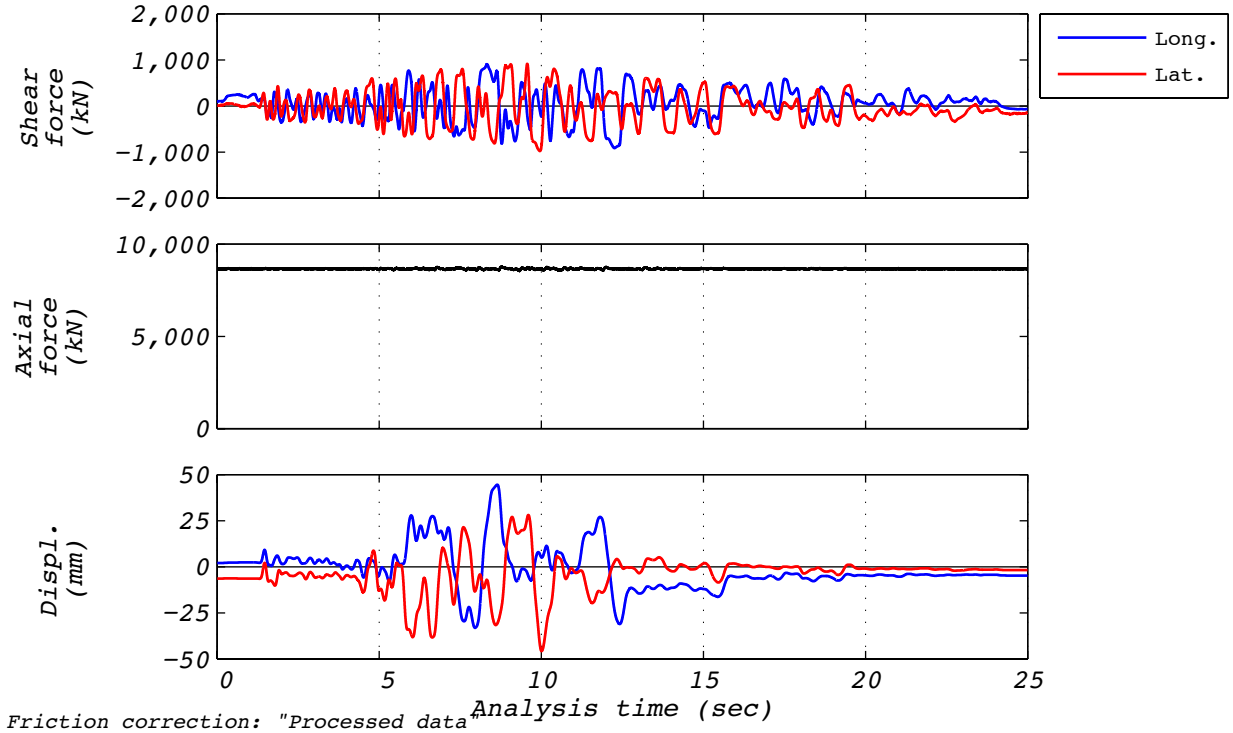

Figure A.5-2 Time history responses for real-time reproduction of hybrid test run 26: EUR5, 2D with experimental bearing representing all bearings.

A.6 DEVELOPMENT RUN 42

Development run 42 was a hybrid test of the EUR dispersion appropriate ground motion number five. The model consisted of a single experimental bearing representing all 527 bearings. Input motions consisted of one horizontal component and a constant axial load specified as the design axial load of 8,663 kN. The test was executed at a rate 25 times slower than real time to compensate for machine delays. Bearing UET-2 was used in this test. Figure A.6-1 shows the fidelity achieved in the hybrid test. Figures A.6-2 and A.6-3 contain bearing responses, and Figure A.6-4 depicts the resulting floor response spectra for select locations in two of the isolated structures.

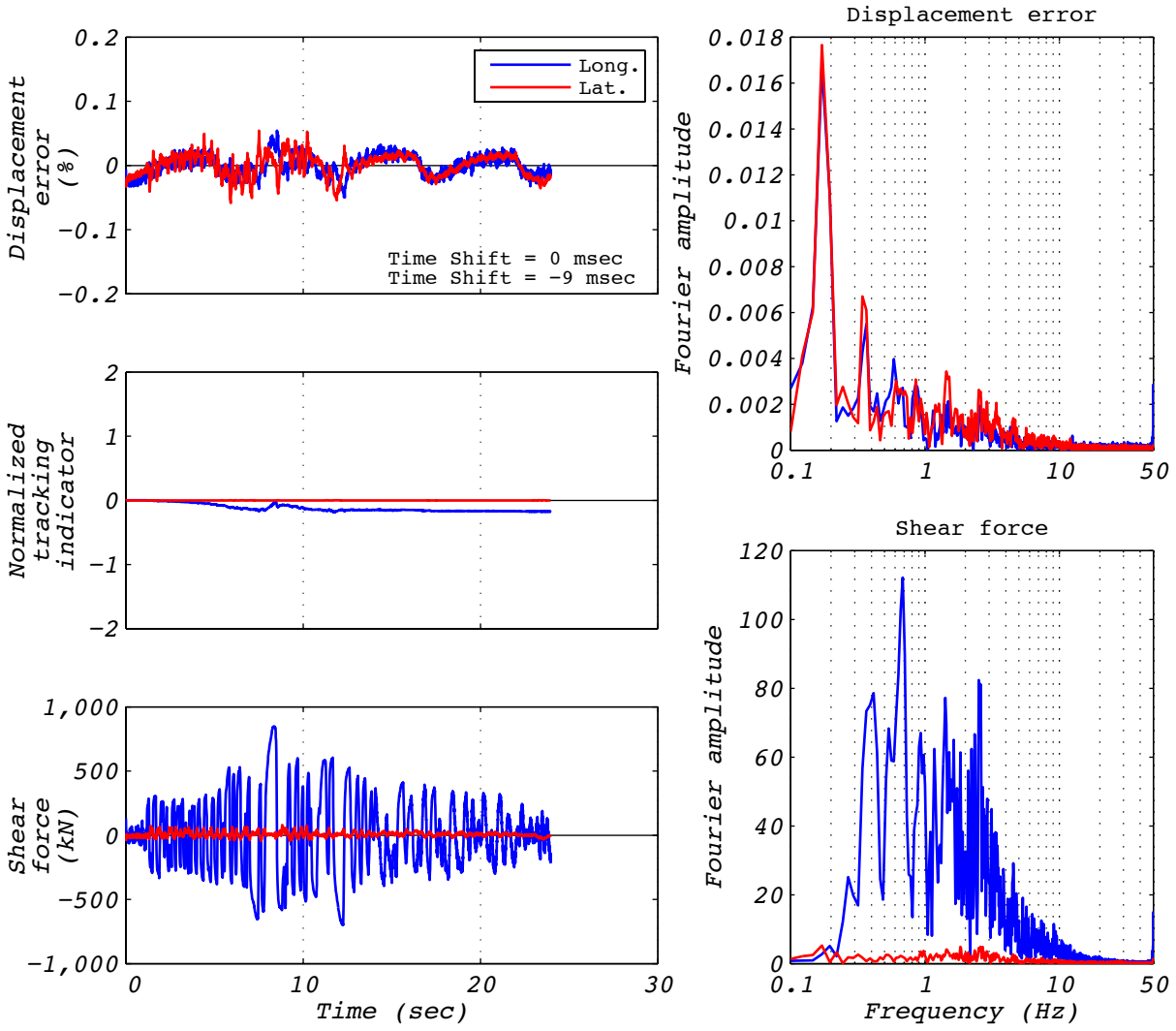

Figure A.6-1 Hybrid test performance metrics for run 42: EUR5, 1D with experimental bearing representing all bearings.

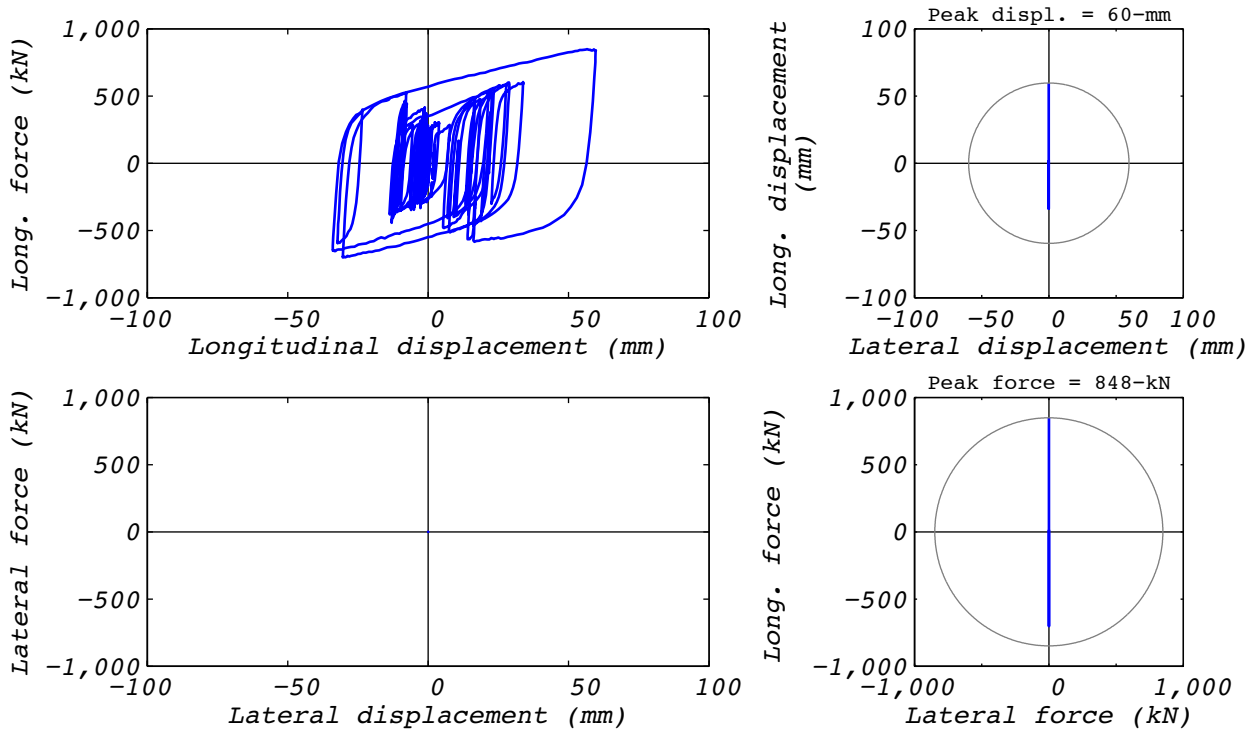

Figure A.6-2 Hybrid test bearing response for run 42: EUR5, 1D with experimental bearing representing all bearings.

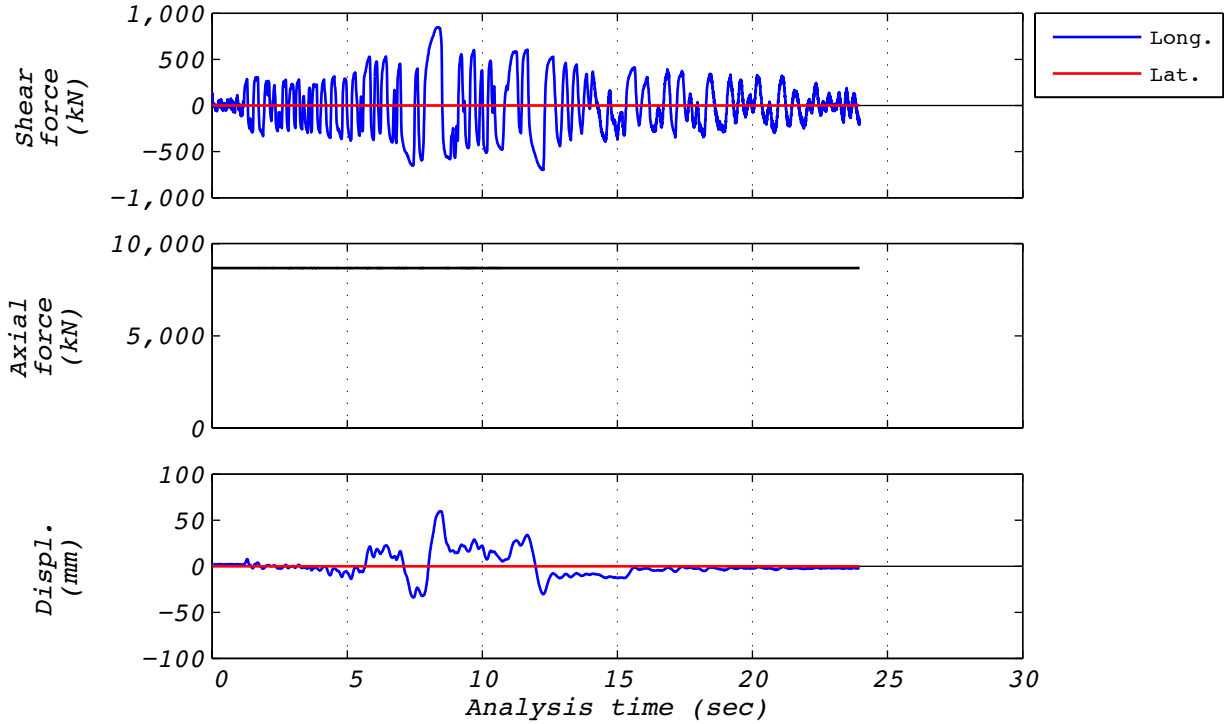

Figure A.6-3 Hybrid test time history responses for run 42: EUR5, 1D with experimental bearing representing all bearings.

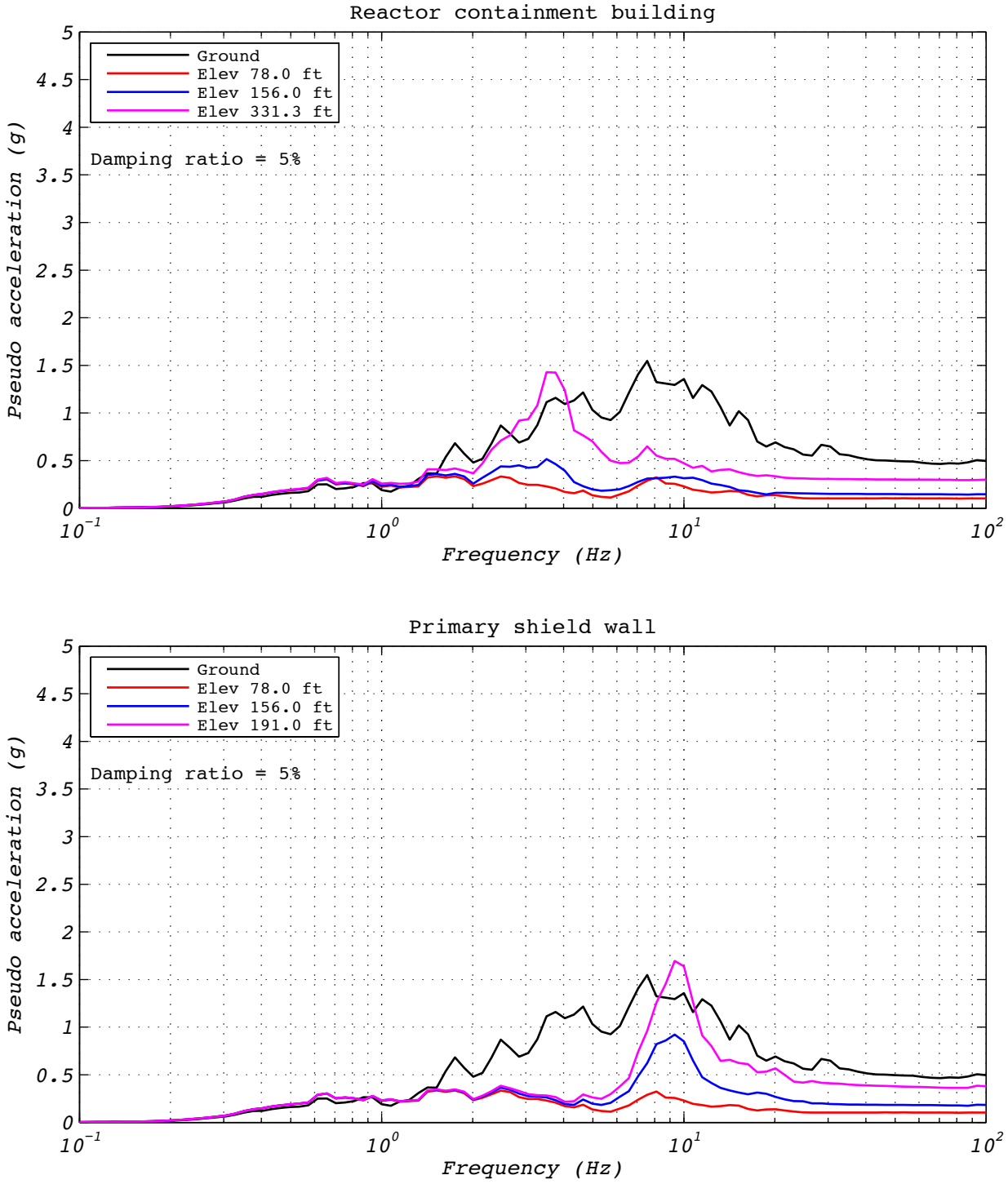

Figure A.6-4 Hybrid test floor spectra for run 42: EUR5, 1D with experimental bearing representing all bearings.

A.7 DEVELOPMENT RUN 43

Development run 43 was a hybrid test of the EUR dispersion appropriate ground motion number five. The model consisted of a single experimental bearing representing all 527 bearings. Input motions consisted of one horizontal component and a constant axial load specified as the design axial load of 8,663 kN. The test was executed at a rate 25 times slower than real time to compensate for machine delays. Bearing UET-2 was used in this test. Figure A.7-1 shows the fidelity achieved in the hybrid test. A.7-2 and A.7-3 contain bearing responses, and Figure A.7-4 depicts the resulting floor response spectra for select locations in two of the isolated structures.

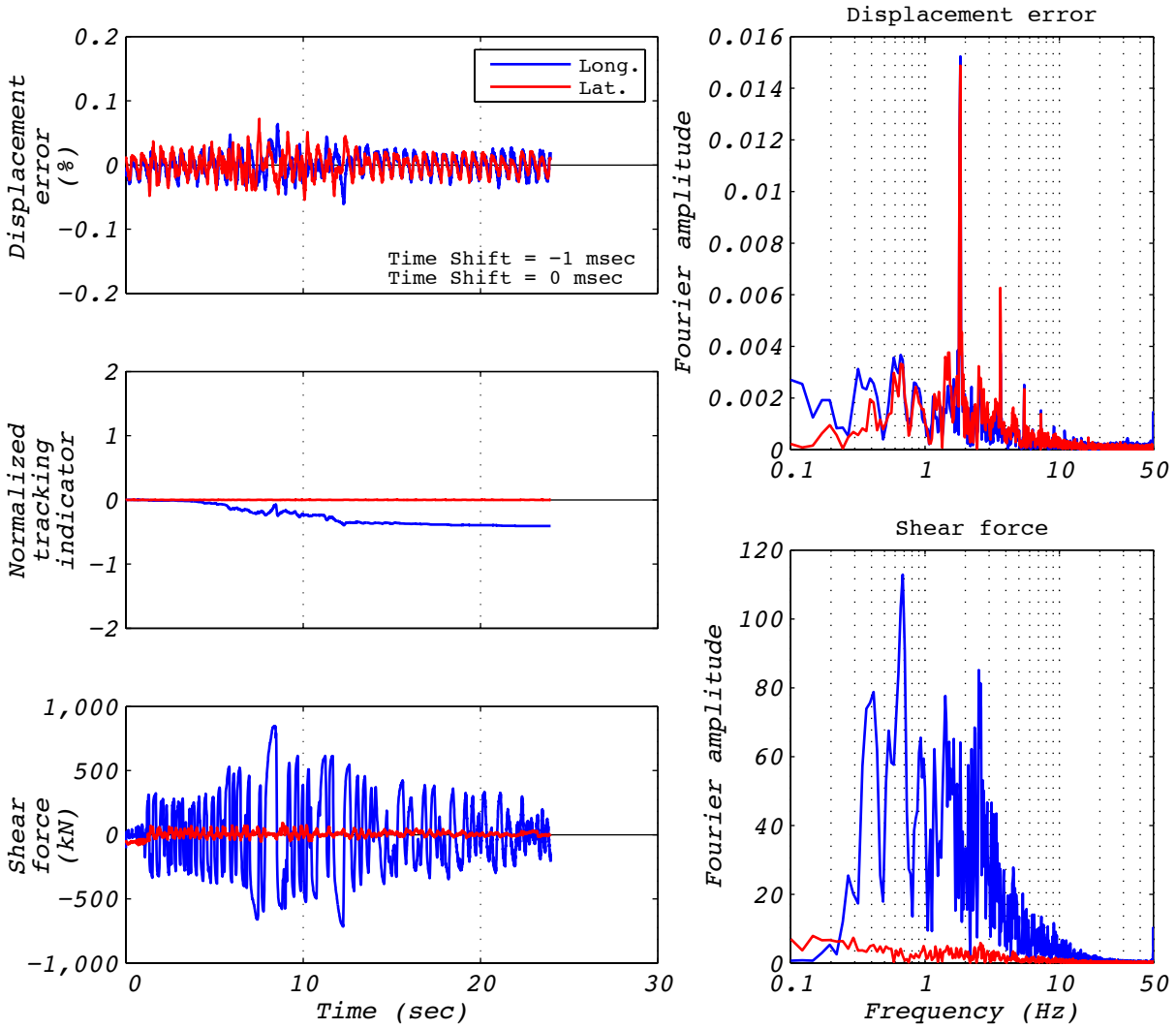

Figure A.7-1 Hybrid test performance metrics for run 43: EUR5, 1D with experimental bearing representing all bearings.

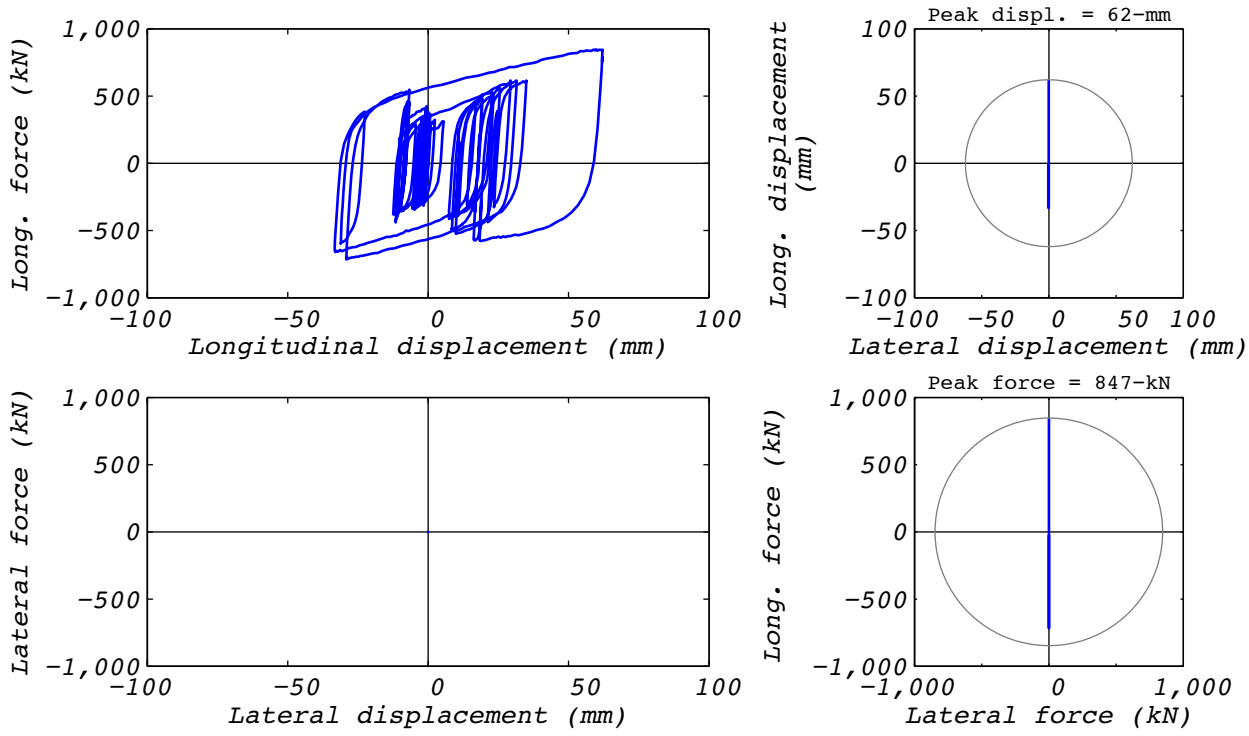

Figure A.7-2 Hybrid test bearing response for run 43: EUR5, 1D with experimental bearing representing all bearings.

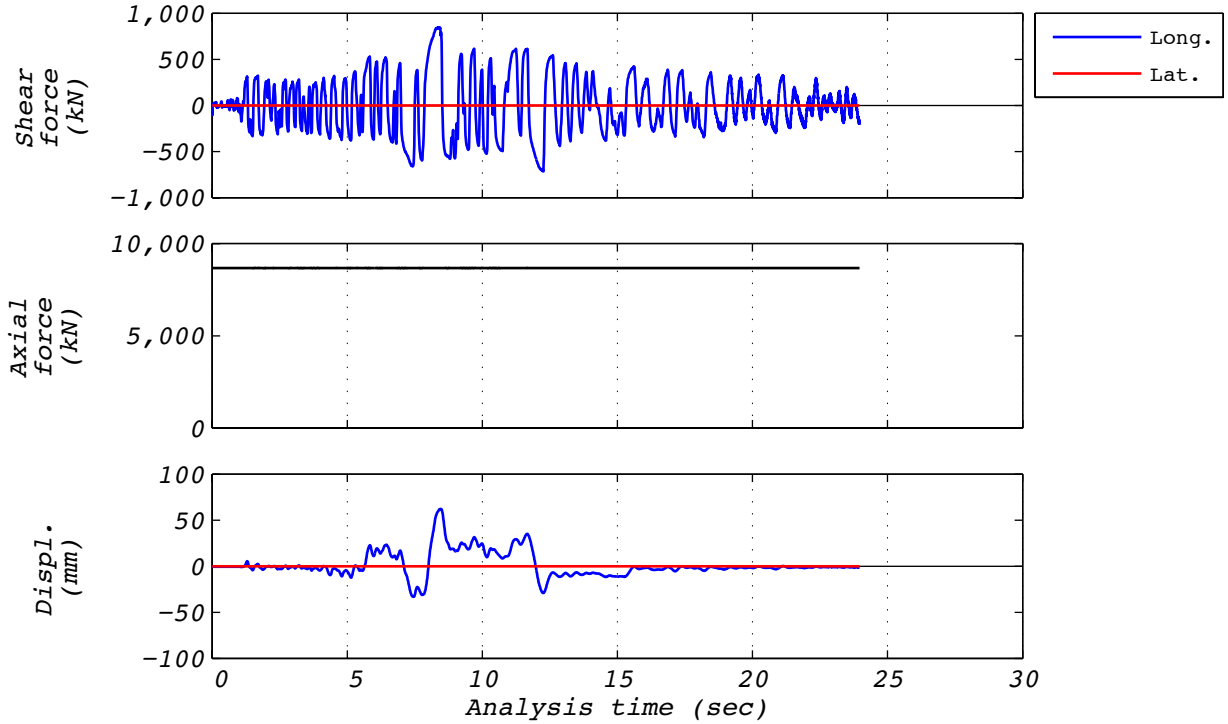

Figure A.7-3 Hybrid test time history responses for run 43: EUR5, 1D with experimental bearing representing all bearings.

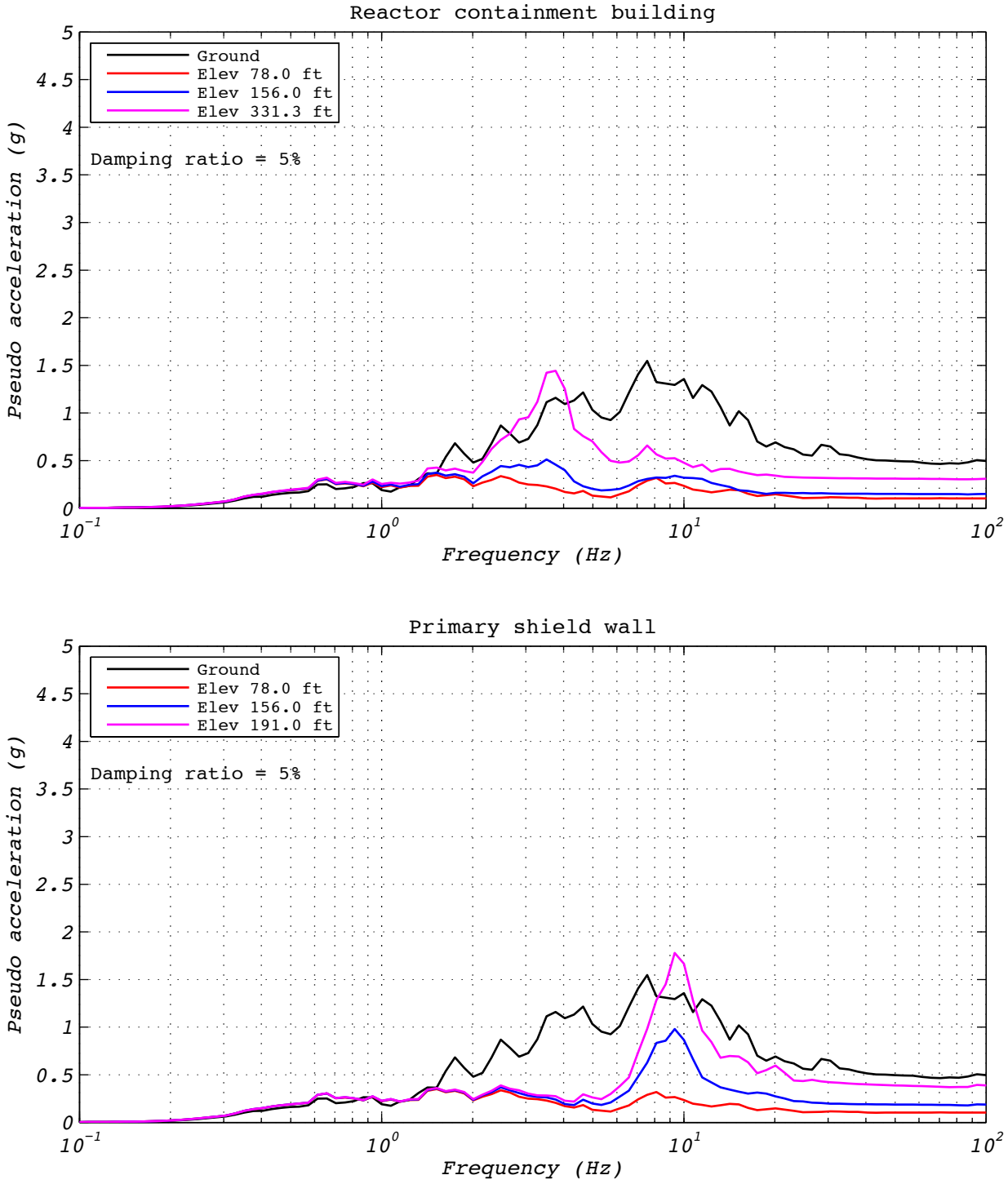

Figure A.7-4 Hybrid test floor spectra for run 43: EUR5, 1D with experimental bearing representing all bearings.

A.8 TEST RUN 44

Test run 44 was a hybrid test of the EUR dispersion appropriate ground motion number five. The model consisted of a single experimental bearing representing all 527 bearings. Input motions consisted of one horizontal component and a constant axial load specified as the design axial load of 8,663 kN. The test was executed at a rate 25 times slower than real time to compensate for machine delays. Bearing UET-2 was used in this test. Figure A.8-1 shows the fidelity achieved in the hybrid test. Figures A.8-2 and A.8-3 contain bearing responses, and Figure A.8-4 depicts the resulting floor response spectra for select locations in two of the isolated structures.

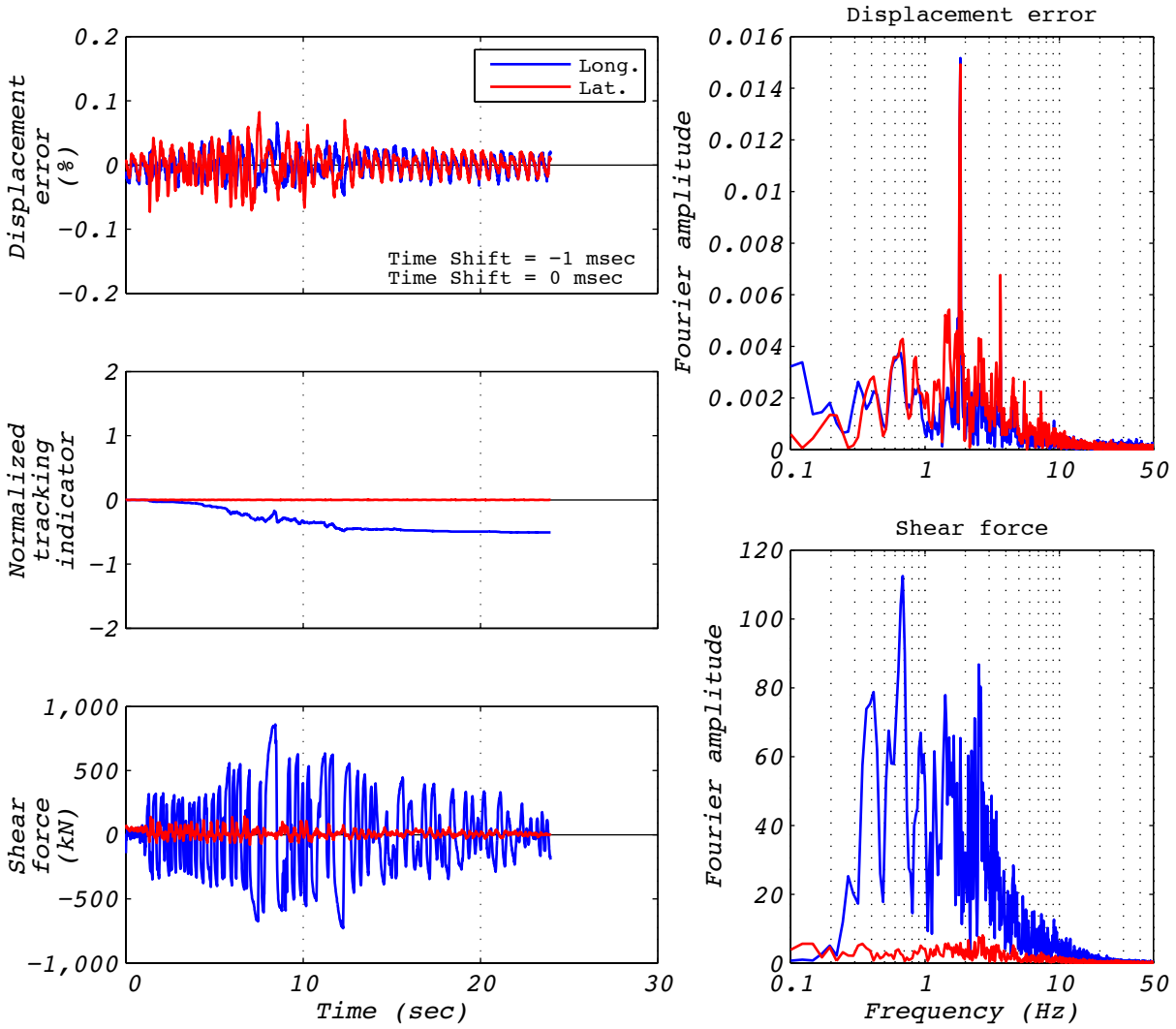

Figure A.8-1 Hybrid test performance metrics for run 44: EUR5, 1D with experimental bearing representing all bearings.

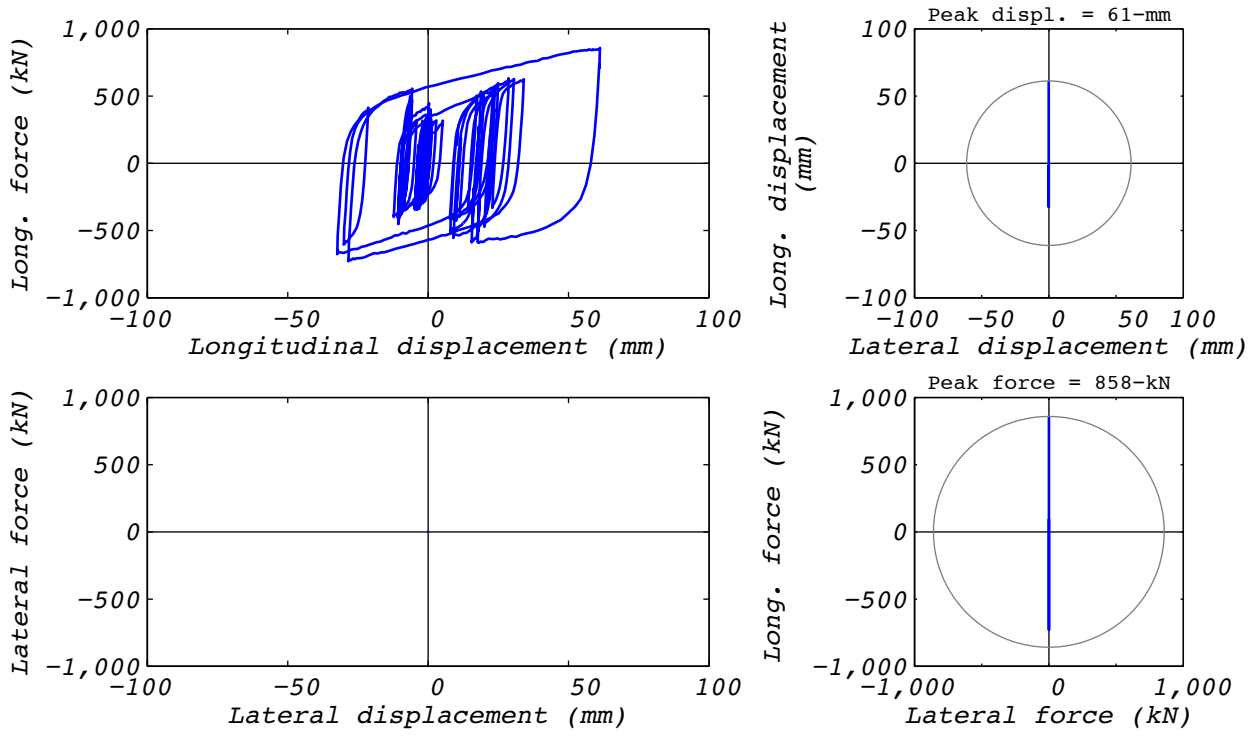

Figure A.8-2 Hybrid test bearing response for run 44: EUR5, 1D with experimental bearing representing all bearings.

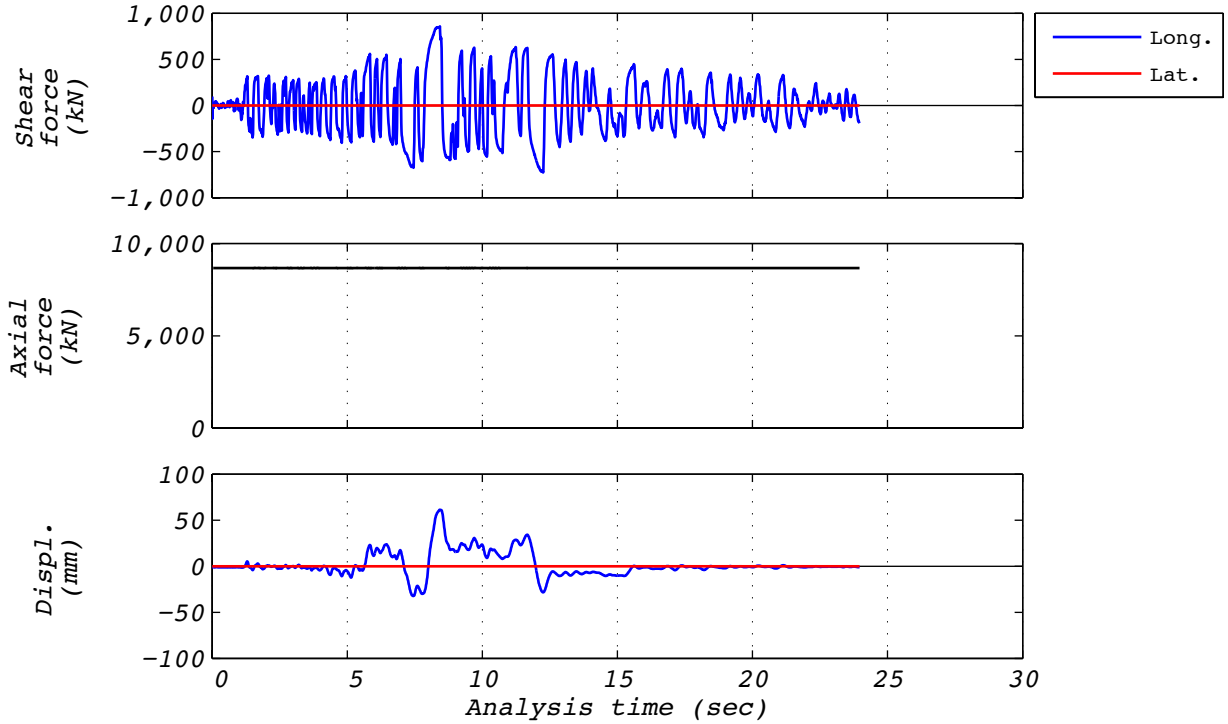

Figure A.8-3 Hybrid test time history responses for run 44: EUR5, 1D with experimental bearing representing all bearings.

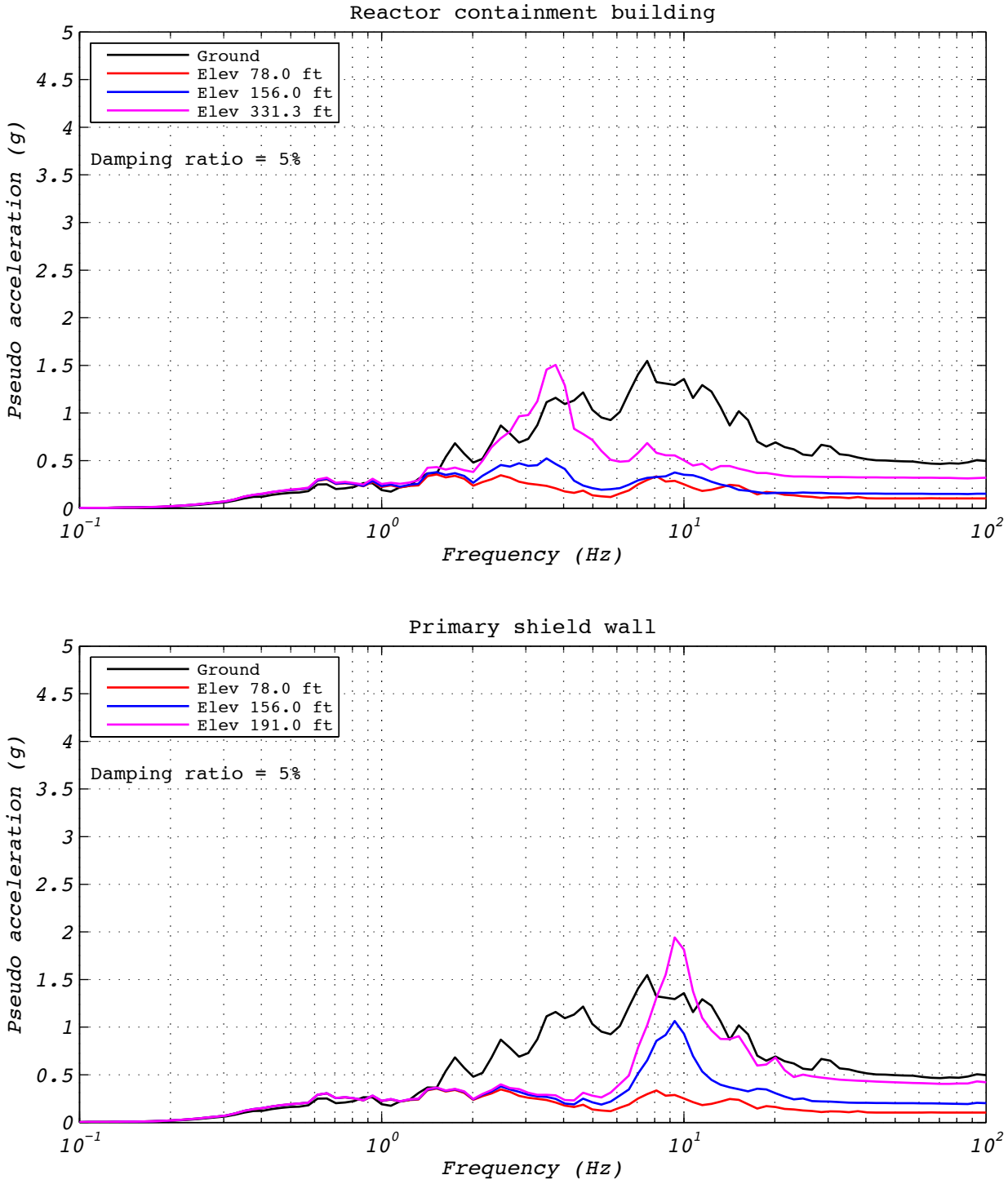

Figure A.8-4 Hybrid test floor spectra for run 44: EUR5, 1D with experimental bearing representing all bearings.

A.9 ANALYSIS RUN 44A

Analysis run 44A was an analytical estimation of the EUR dispersion appropriate ground motion number five. The model consisted of a single analytical bearing representing all 527 bearings. Input motions consisted of one horizontal component and a constant axial load specified as the design axial load of 8,663 kN. Figures A.9-1 and A.9-2 contain bearing responses, and Figure A.9-3 depicts the resulting floor response spectra for select locations in two of the isolated structures.

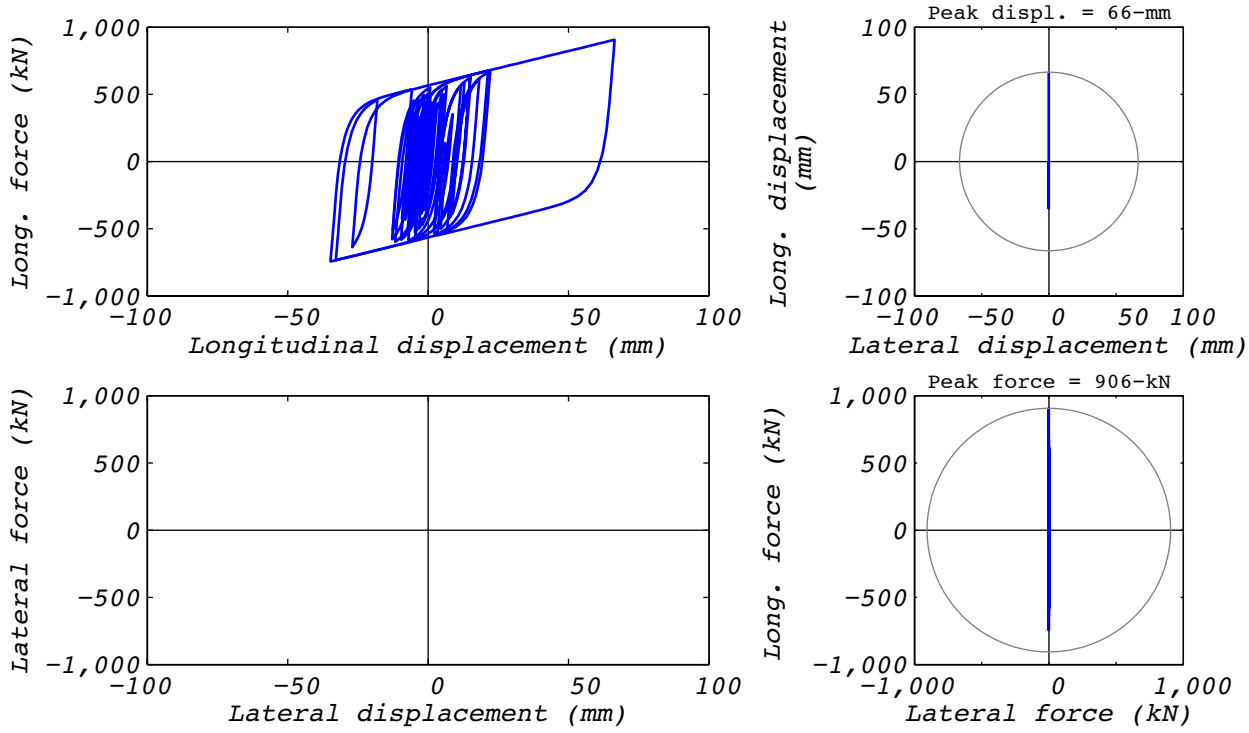

Figure A.9-1 Analytical bearing response for run 44A: EUR5, 1D with a single analytical bearing.

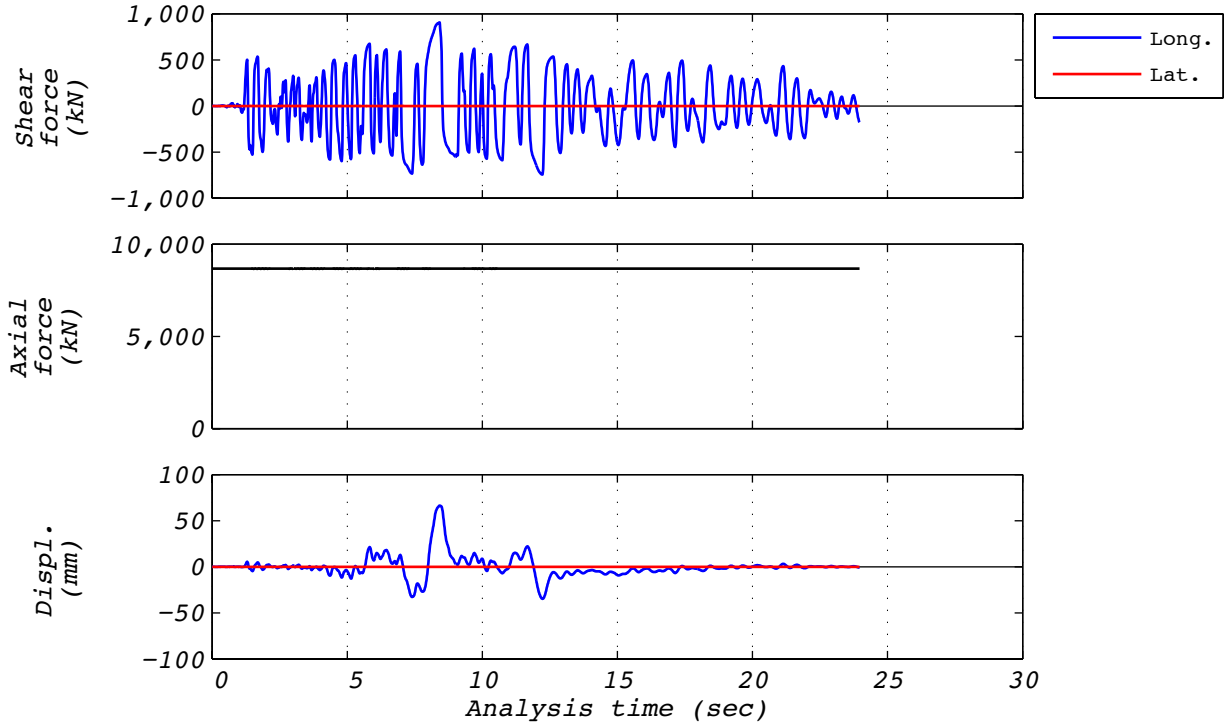

Figure A.9-2 Analytical time history responses for run 44A: EUR5, 1D with a single analytical bearing.

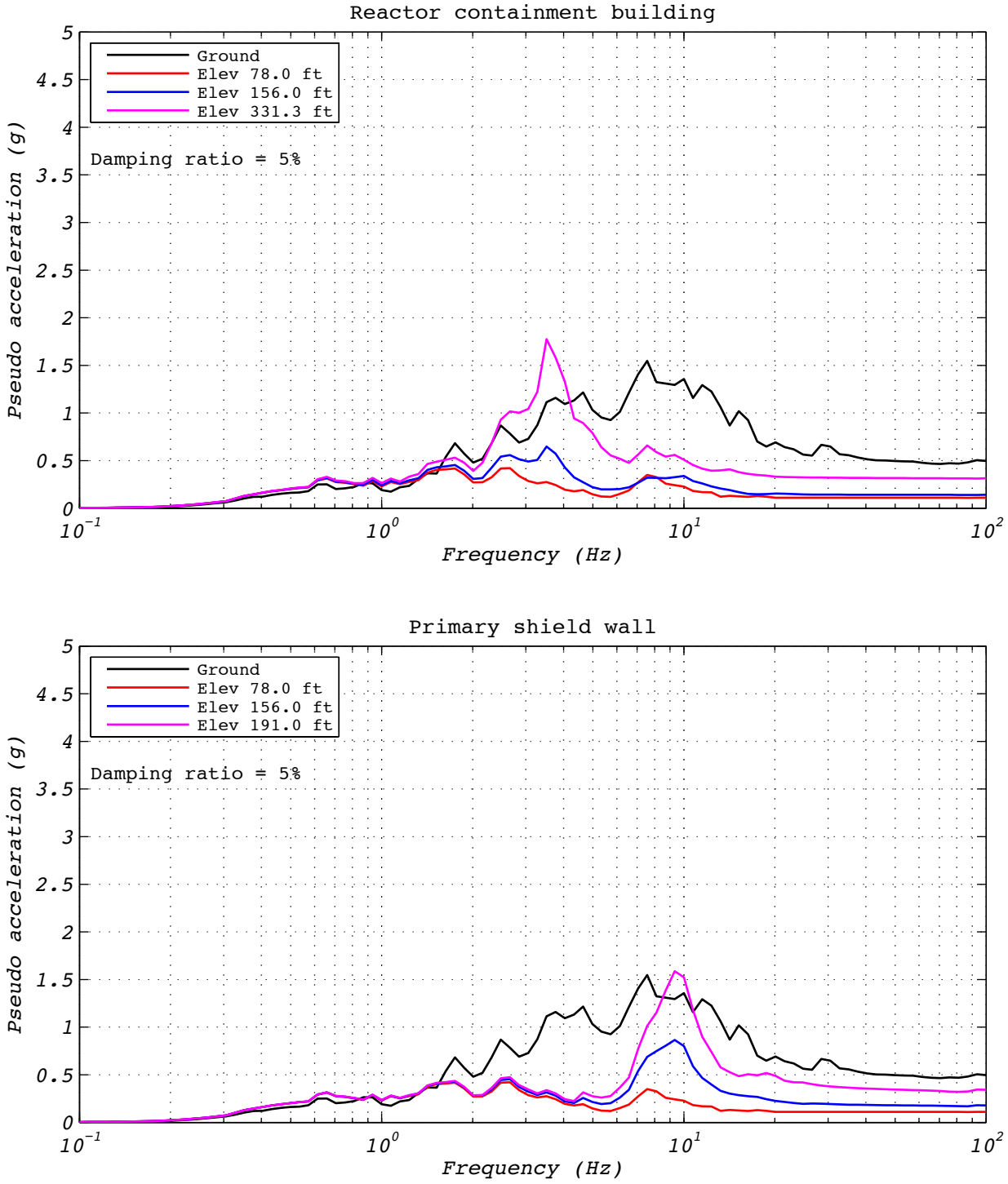

Figure A.9-3 Floor spectra for analytical run 44A: EUR5, 1D with a single analytical bearing.

A.10 TEST RUN 45

Test run 45 was a hybrid test of the EUR dispersion appropriate ground motion number five. The model consisted of a single experimental bearing representing all 527 bearings. Input motions consisted of two horizontal components and a constant axial load specified as the design axial load of 8,663 kN. The test was executed at a rate 25 times slower than real time to compensate for machine delays. Bearing UET-2 was used in this test. Figure A.9-1 shows the fidelity achieved in the hybrid test. Figures A.9-2 and A.9-3 contain bearing responses, and Figure A.9-4 depicts the resulting floor response spectra for select locations in two of the isolated structures.

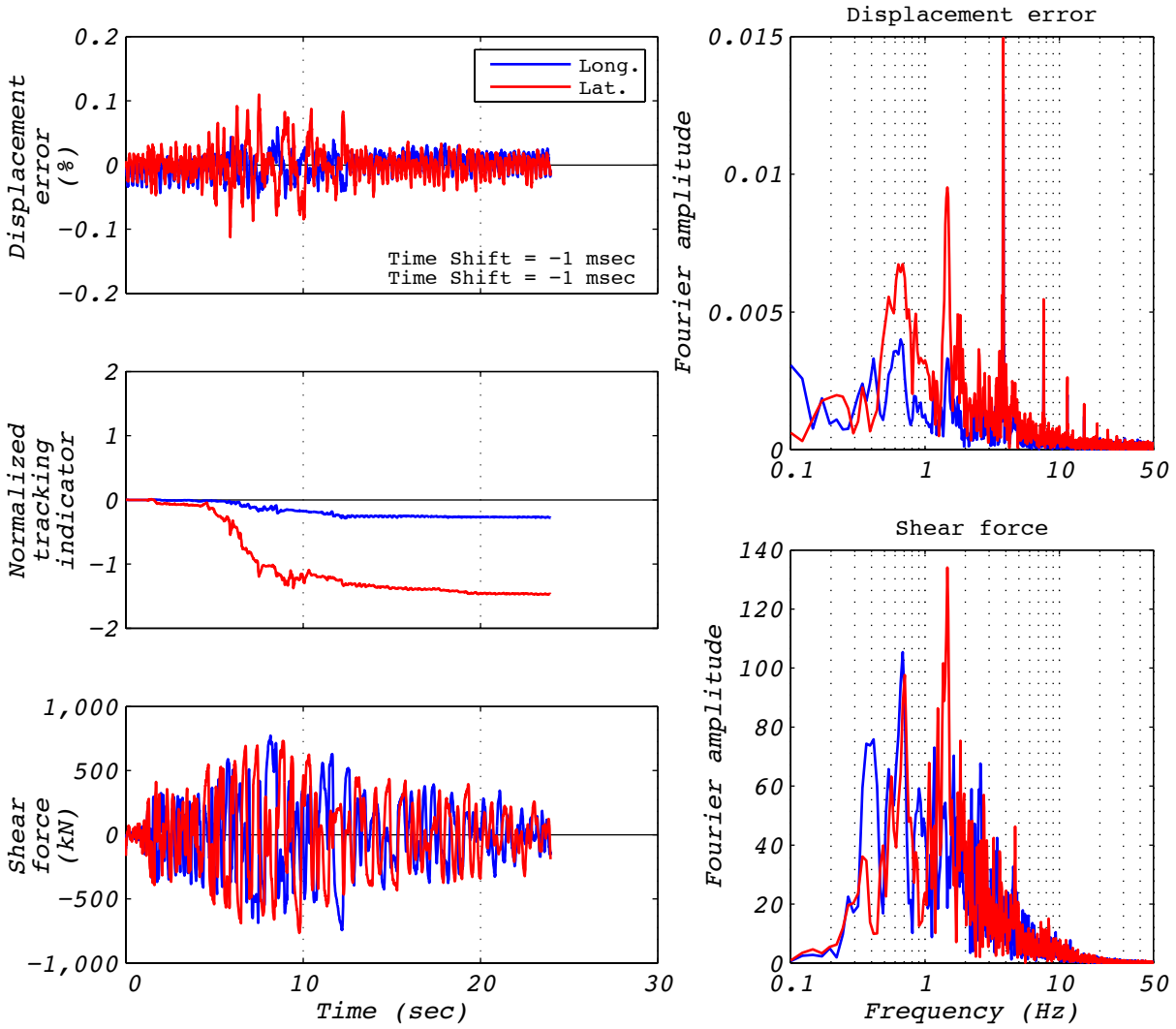

Figure A.10-1 Hybrid test performance metrics for run 45: EUR5, 2D with experimental bearing representing all bearings.

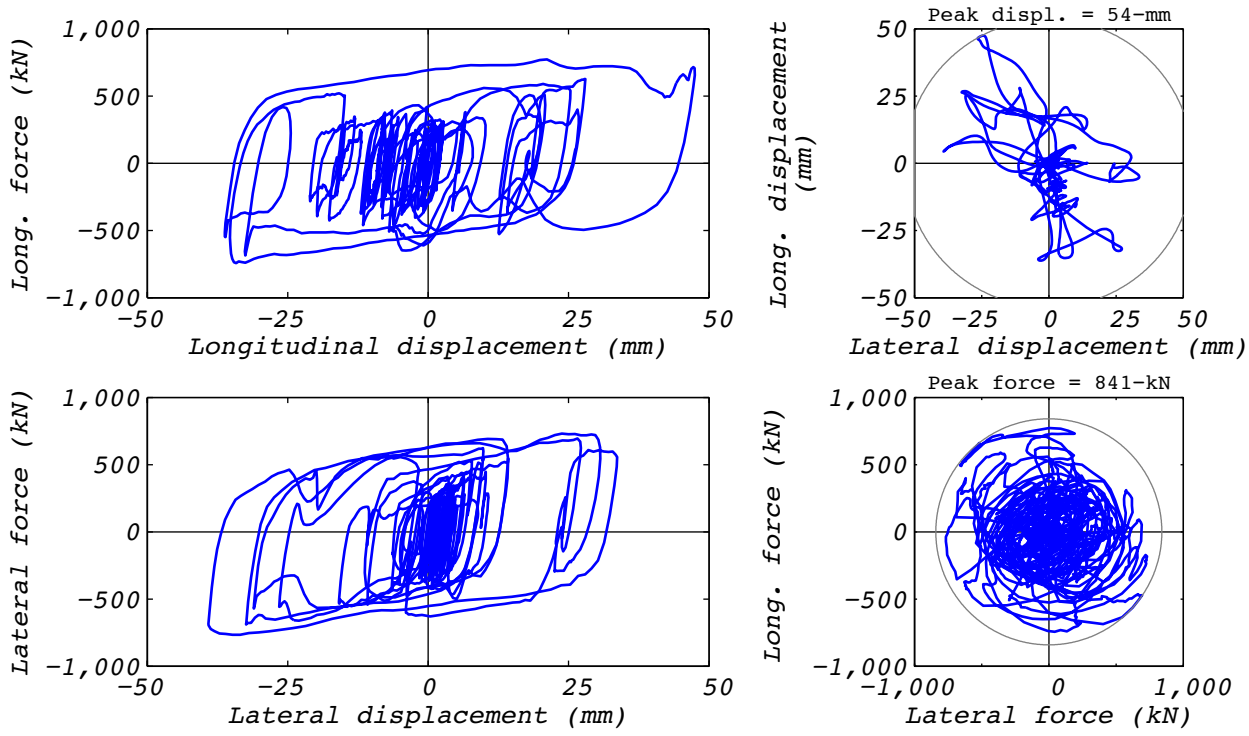

Figure A.10-2 Hybrid test bearing response for run 45: EUR5, 2D with experimental bearing representing all bearings.

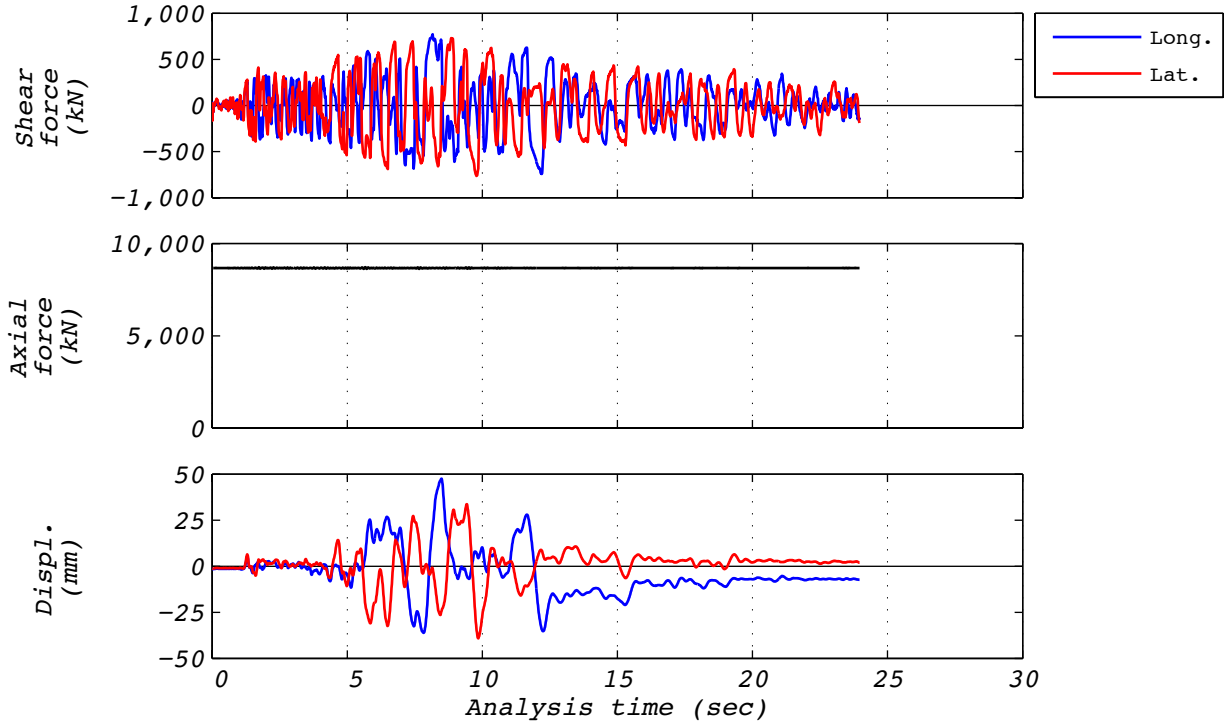

Figure A.10-3 Hybrid test time history responses for run 45: EUR5, 2D with experimental bearing representing all bearings.

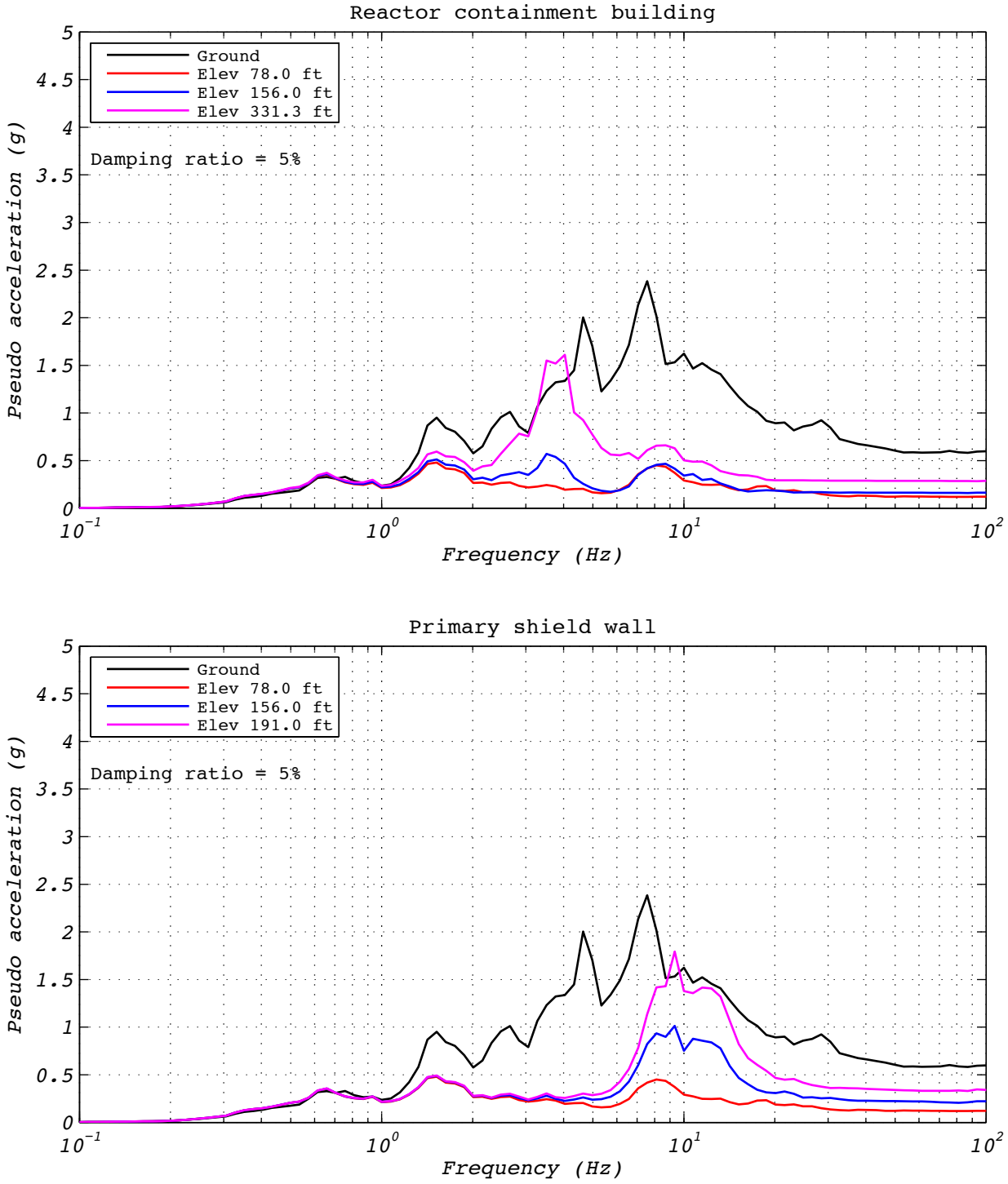

Figure A.10-4 Hybrid test floor spectra for run 45: EUR5, 2D with experimental bearing representing all bearings.

A.11 ANALYSIS RUN 45A

Analysis run 45A was an analytical estimation of the EUR dispersion appropriate ground motion number five. The model consisted of a single analytical bearing representing all 527 bearings. Input motions consisted of two horizontal components and a constant axial load specified as the design axial load of 8,663 kN. Figures A.11-1 and A.11-2 contain bearing responses, and Figure A.11-3 depicts the resulting floor response spectra for select locations in two of the isolated structures.

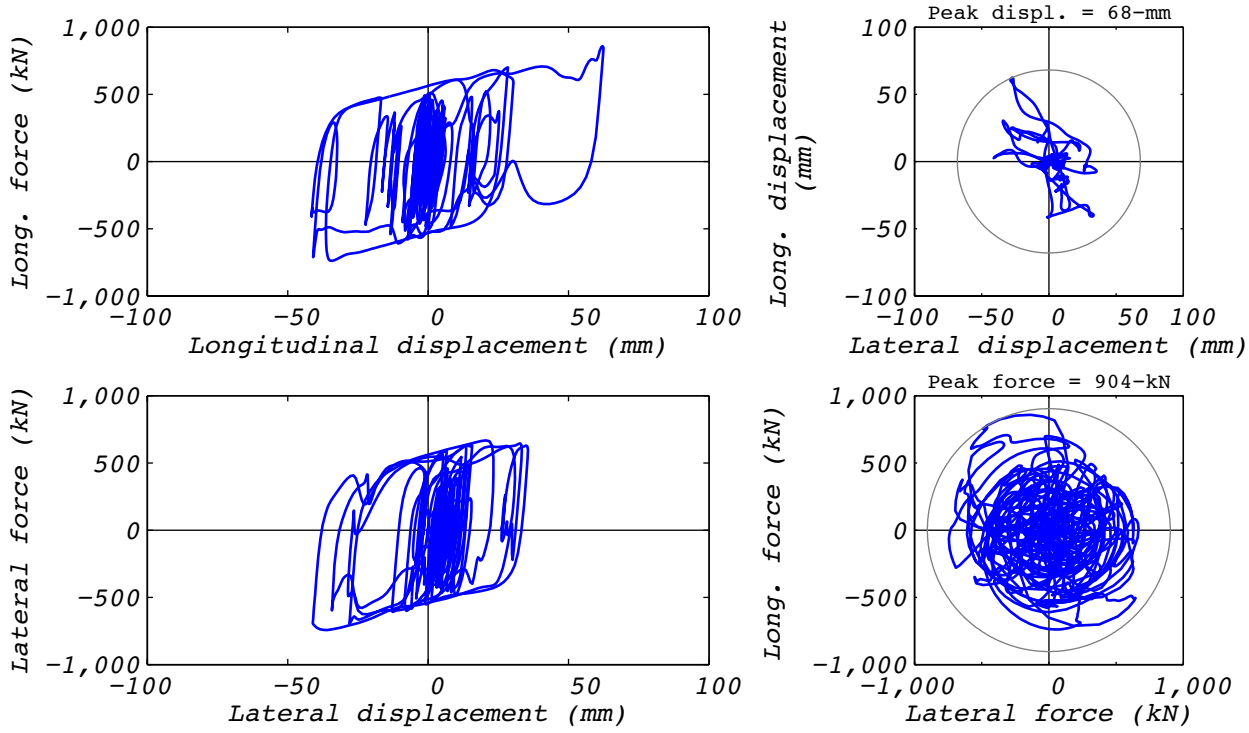

Figure A.11-1 Analytical bearing response for run 45A: EUR5, 2D with a single analytical bearing.

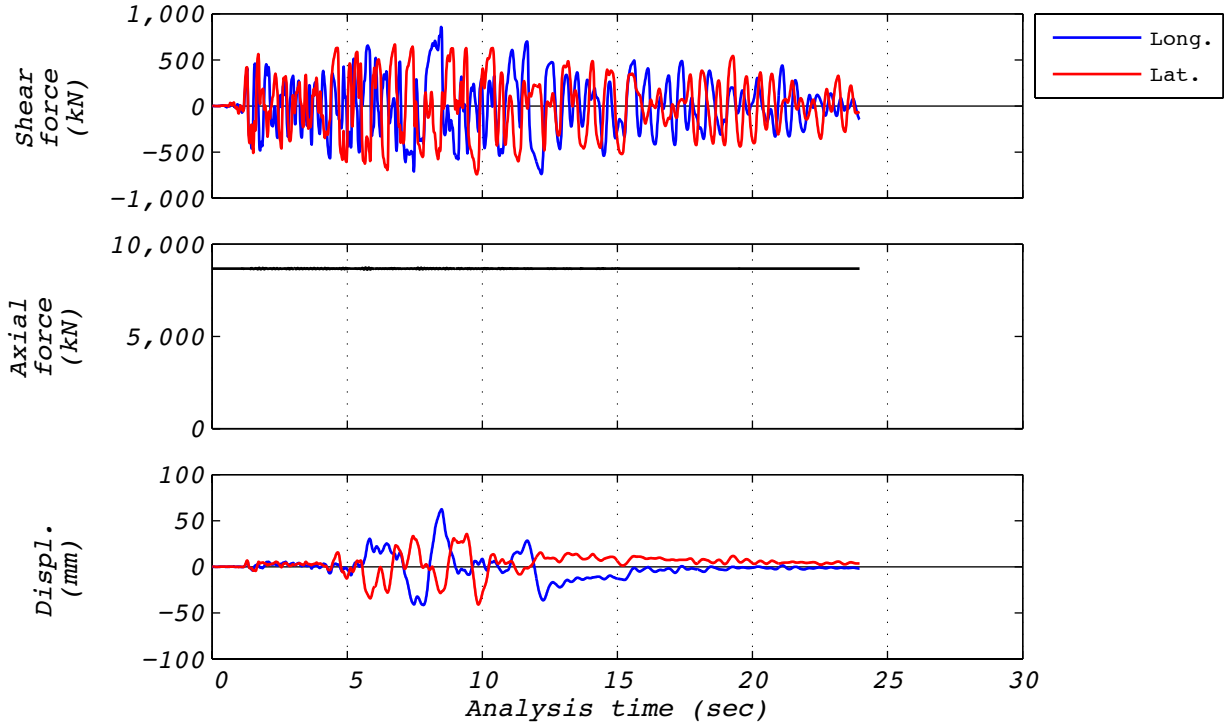

Figure A.11-2 Analytical time history responses for run 45A: EUR5, 2D with a single analytical bearing.

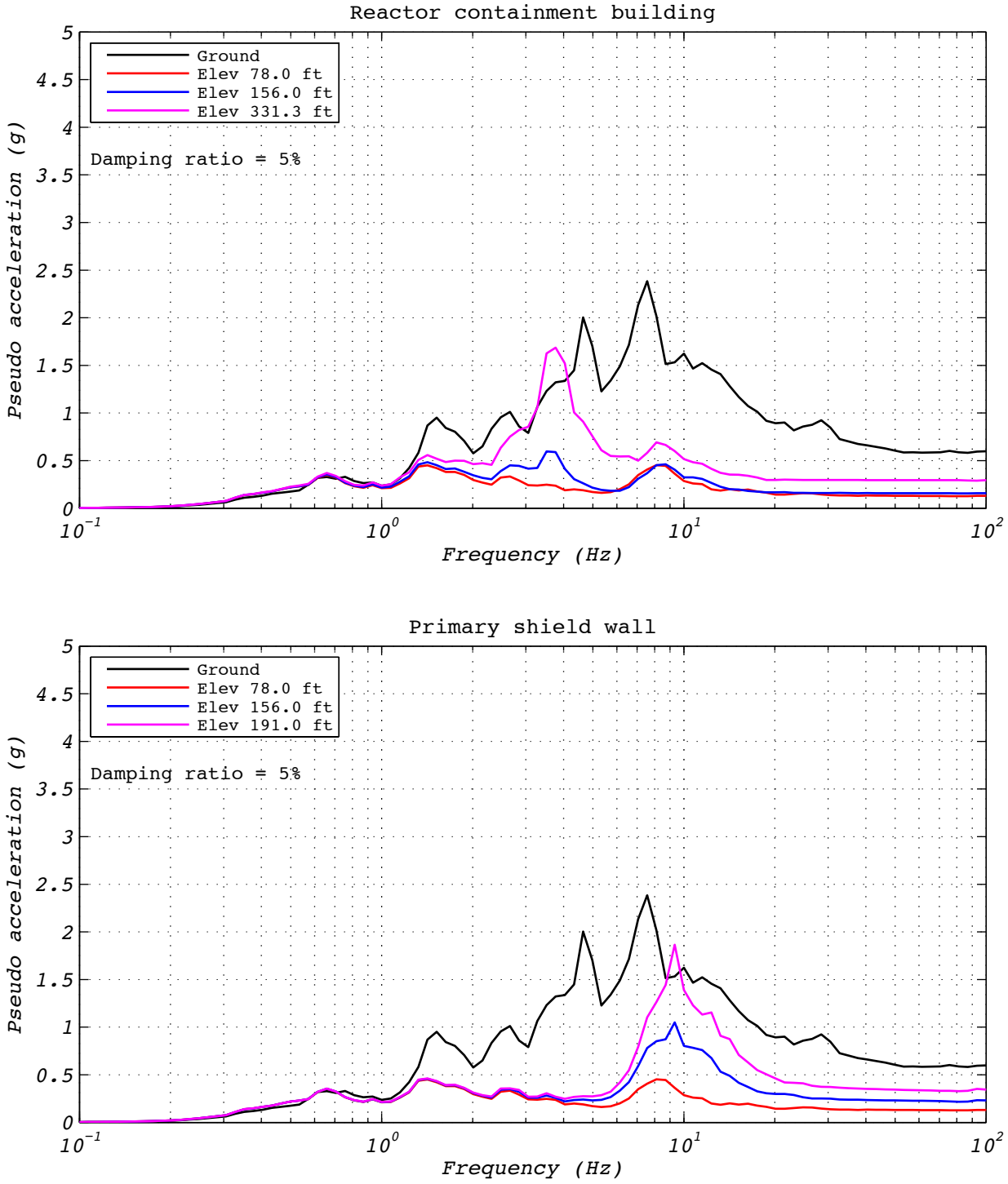

Figure A.11-3 Floor spectra for analytical run 45A: EUR5, 2D with a single analytical bearing.

A.12 DEVELOPMENT RUN 46

Development run 46 was a hybrid test of the NRC dispersion appropriate ground motion number 15. The model consisted of a single experimental bearing representing all 527 bearings. Input motions consisted of two horizontal components and a constant axial load specified as the design axial load of 8,663 kN. The test was executed at a rate 25 times slower than real time to compensate for machine delays. Bearing UET-2 was used in this test. Figure A.11-1 shows the fidelity achieved in the hybrid test. Figures A.11-2 and A.11-3 contain bearing responses, and Figure A.11-4 depicts the resulting floor response spectra for select locations in two of the isolated structures.

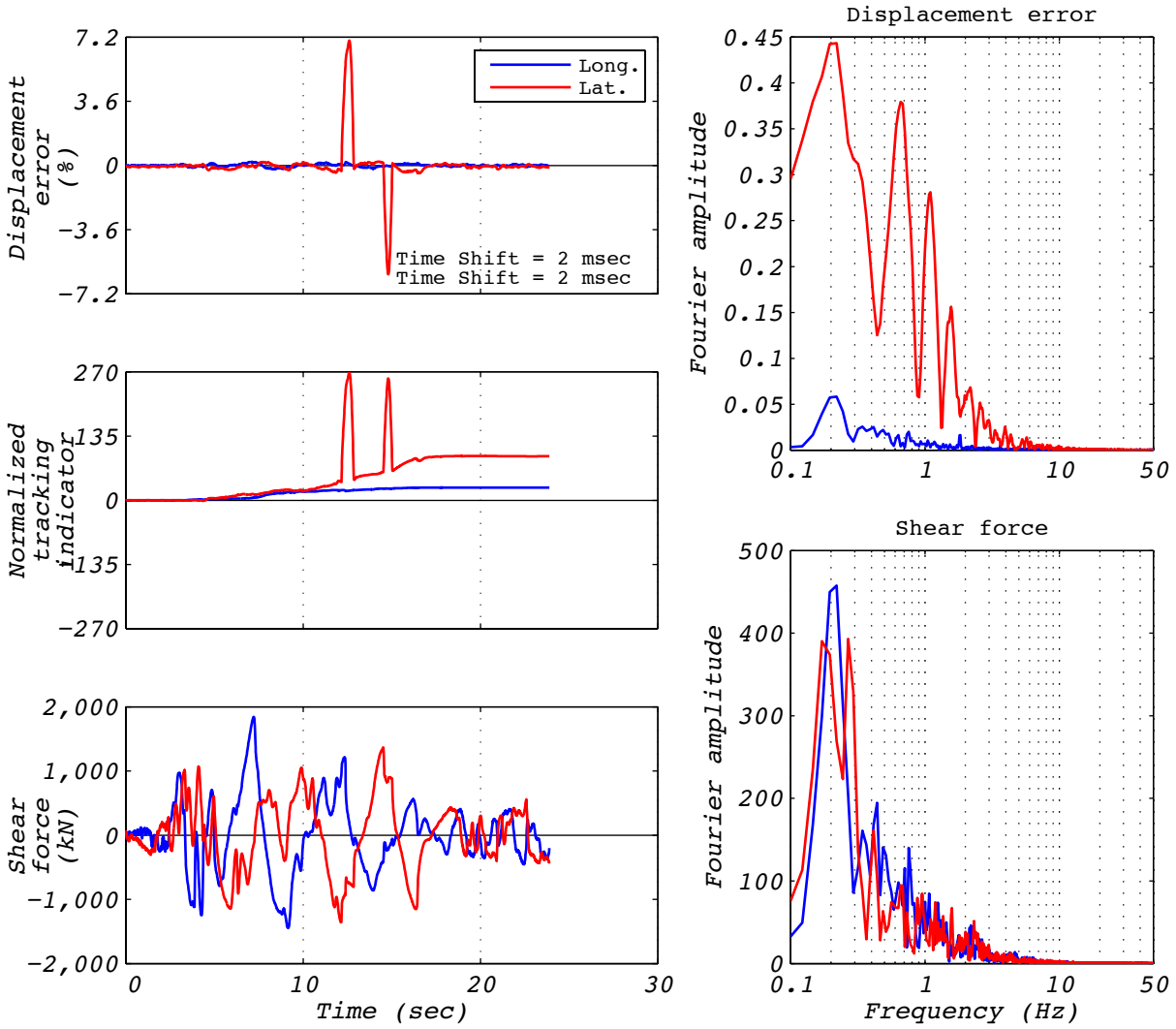

Figure A.12-1 Hybrid test performance metrics for run 46: NRC15, 2D with experimental bearing representing all bearings.

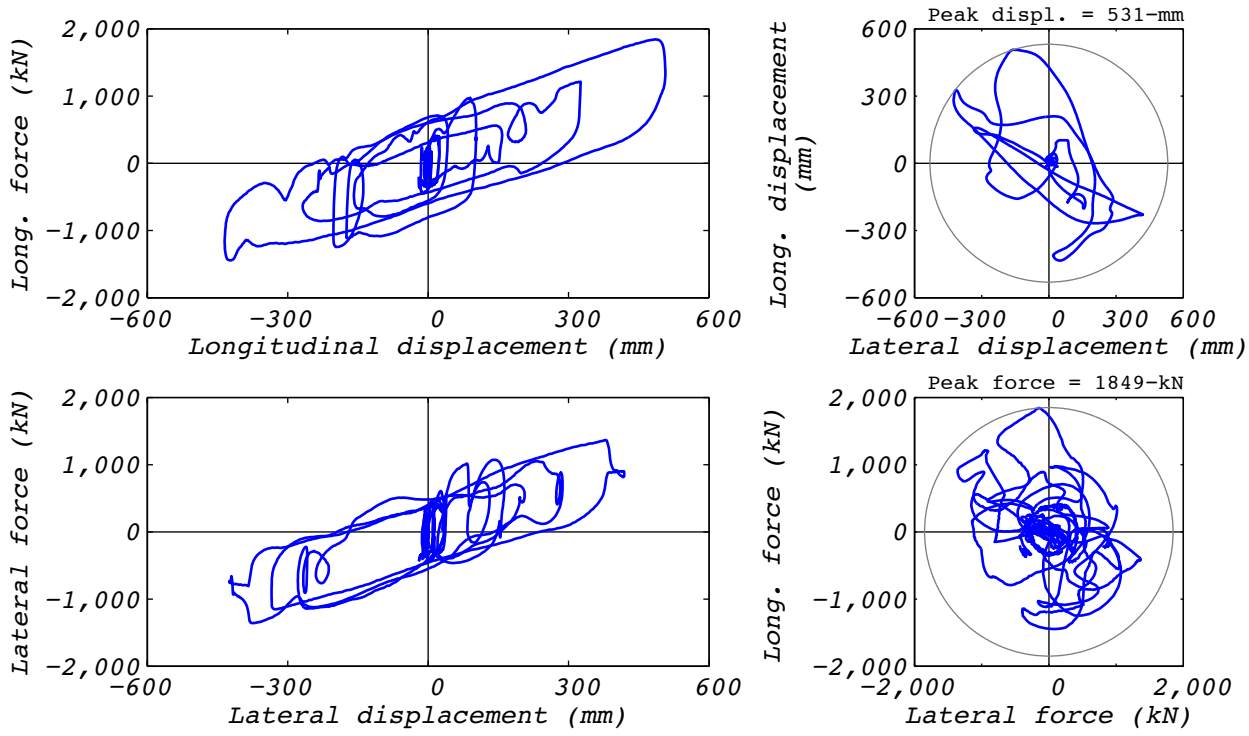

Figure A.12-2 Hybrid test bearing response for run 46: NRC15, 2D with experimental bearing representing all bearings.

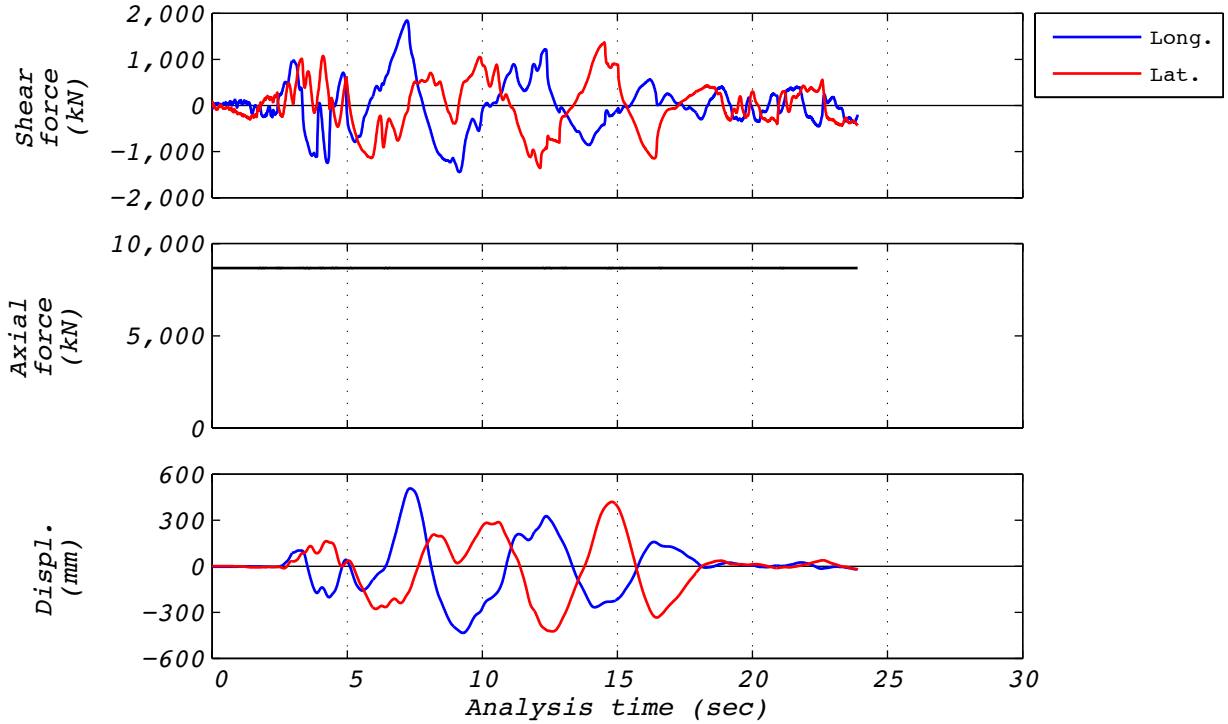

Figure A.12-3 Hybrid test time history responses for run 46: NRC15, 2D with experimental bearing representing all bearings.

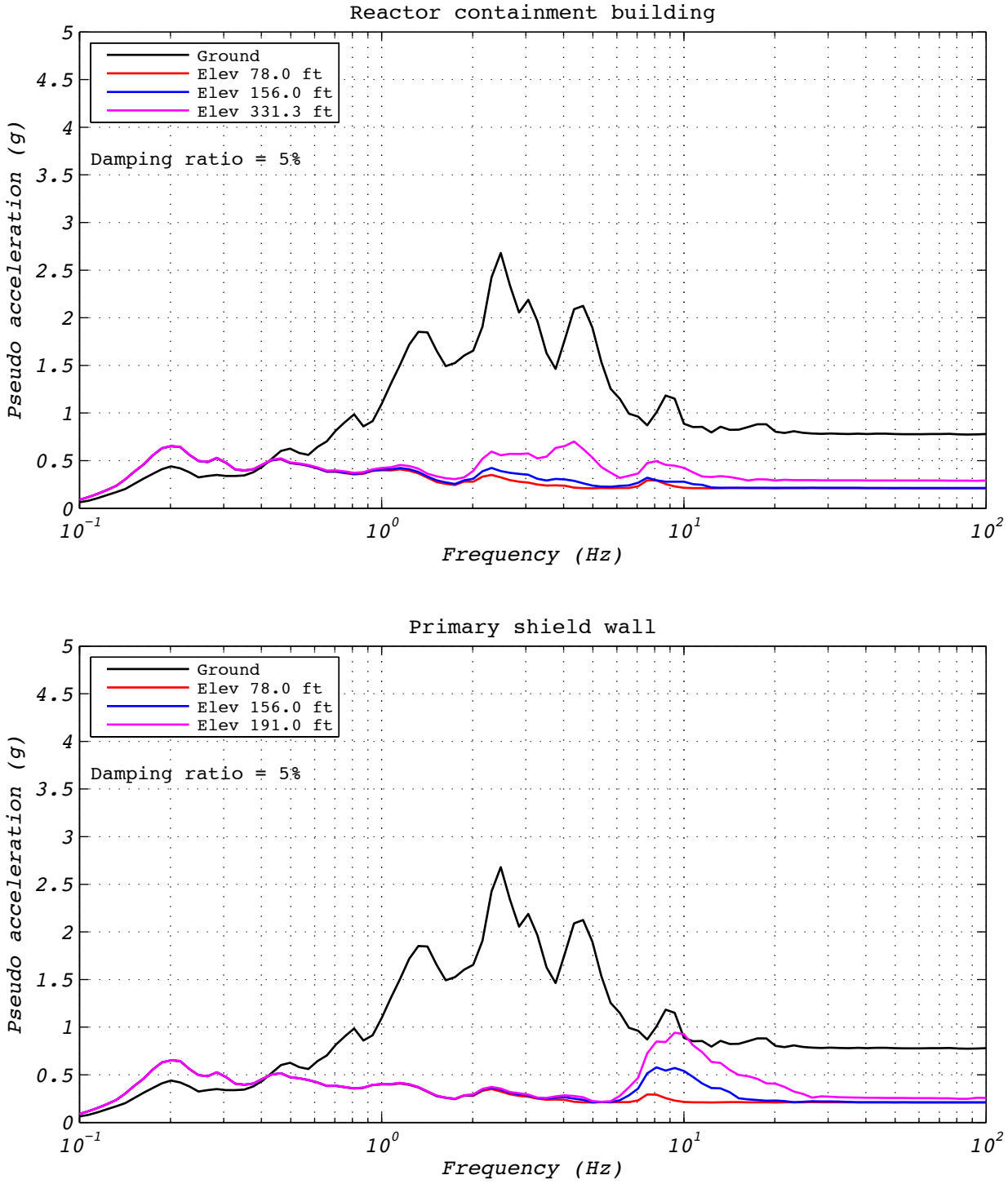

Figure A.12-4 Hybrid test floor spectra for run 46: NRC15, 2D with experimental bearing representing all bearings.

A.13 TEST RUN 47

Test run 47 was a hybrid test of the NRC dispersion appropriate ground motion number 15. The model consisted of a single experimental bearing representing all 527 bearings. Input motions consisted of one horizontal component and a constant axial load specified as the design axial load of 8,663 kN. The test was executed at a rate 25 times slower than real time to compensate for machine delays. Bearing UET-2 was used in this test. Figure A.13-1 shows the fidelity achieved in the hybrid test. Figures A.13-2 and A.13-3 contain bearing responses, and Figure A.13-4 depicts the resulting floor response spectra for select locations in two of the isolated structures.

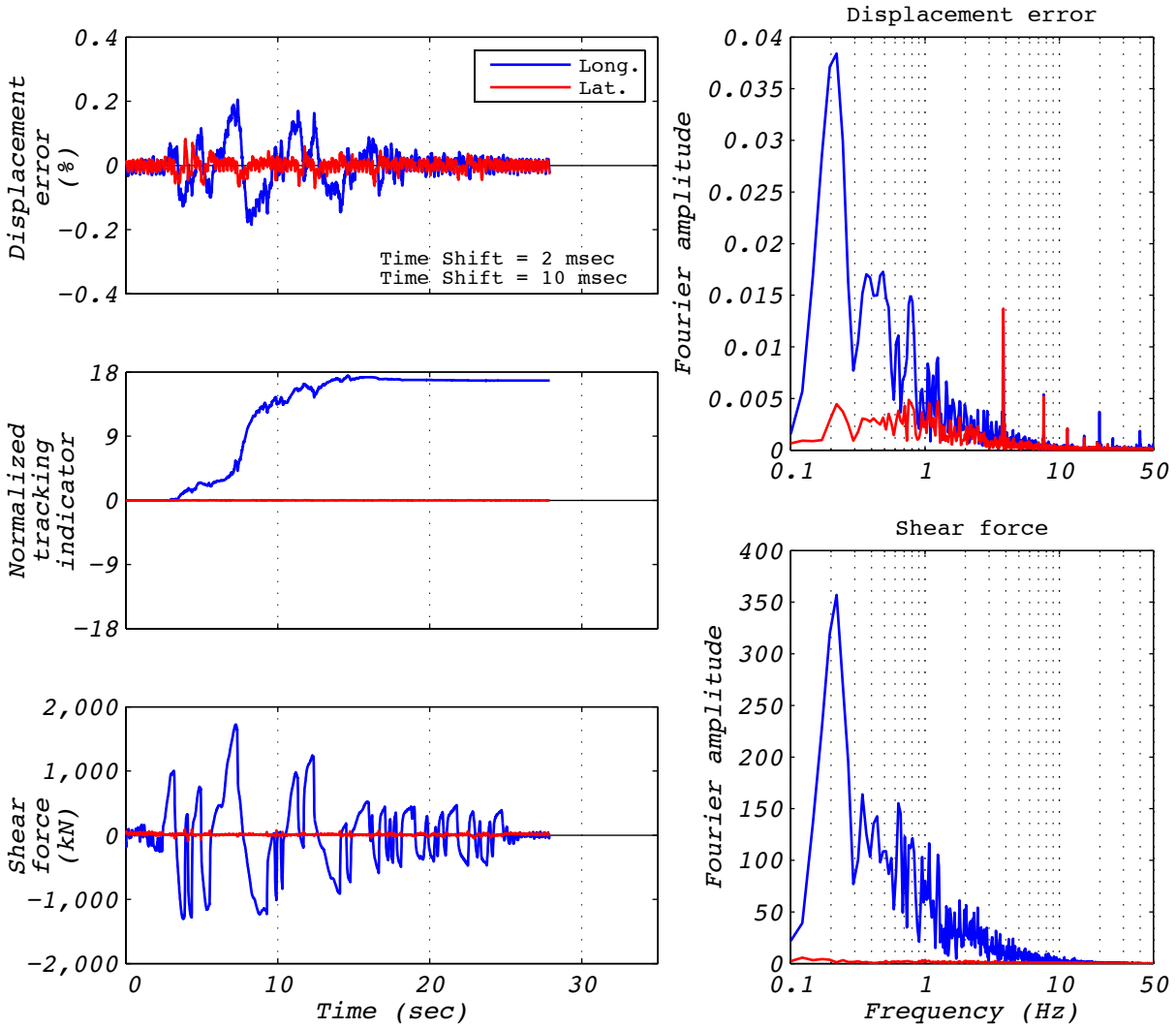

Figure A.13-1 Hybrid test performance metrics for run 47: NRC15, 1D with experimental bearing representing all bearings.

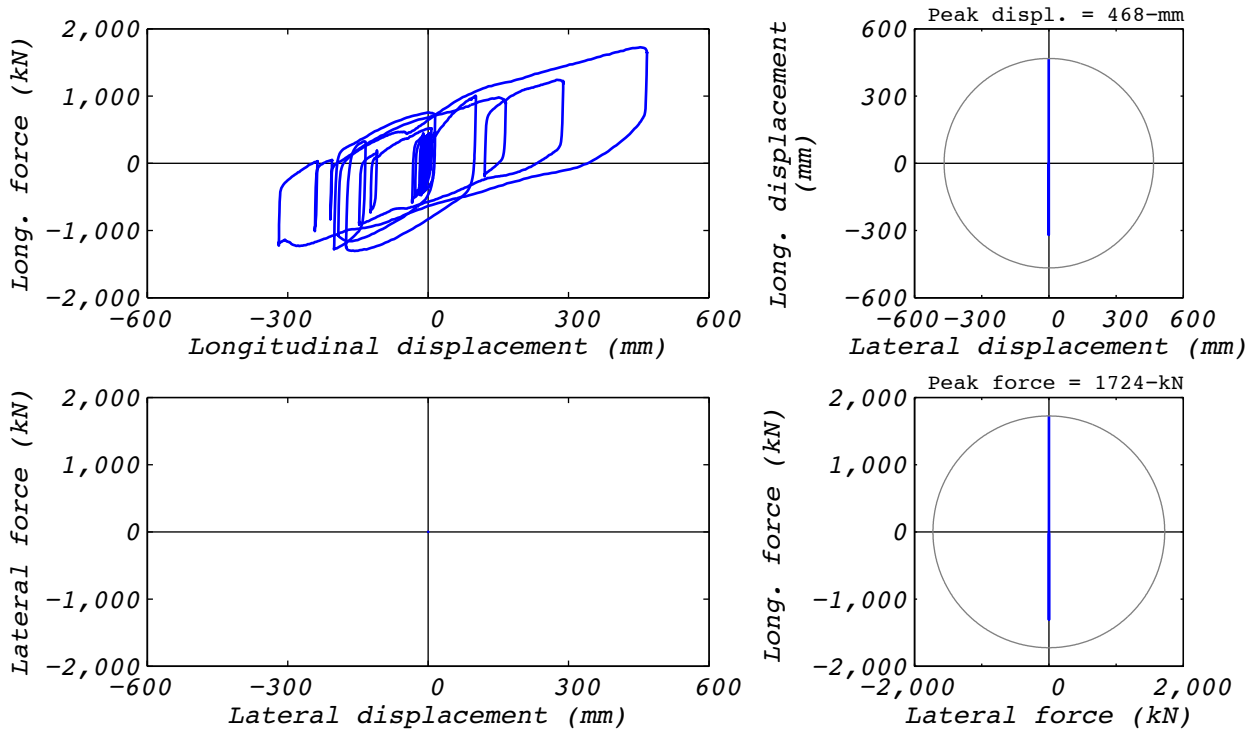

Figure A.13-2 Hybrid test bearing response for run 47: NRC15, 1D with experimental bearing representing all bearings.

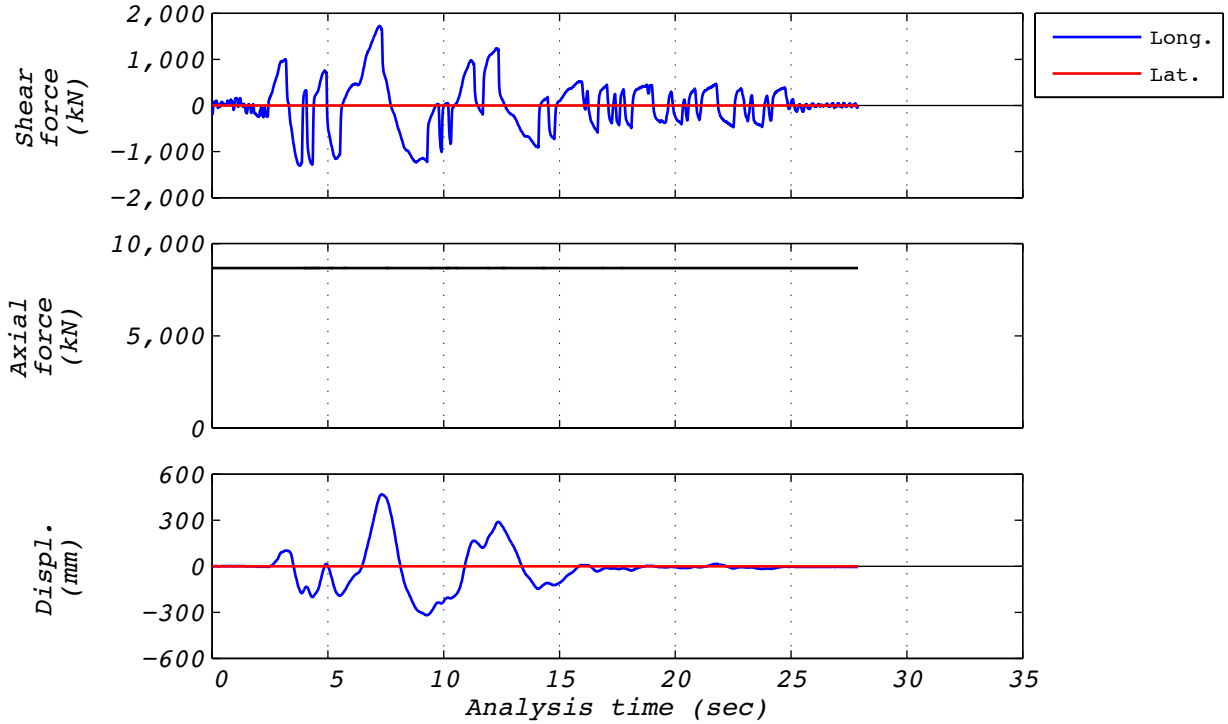

Figure A.13-3 Hybrid test time history responses for run 47: NRC15, 1D with experimental bearing representing all bearings.

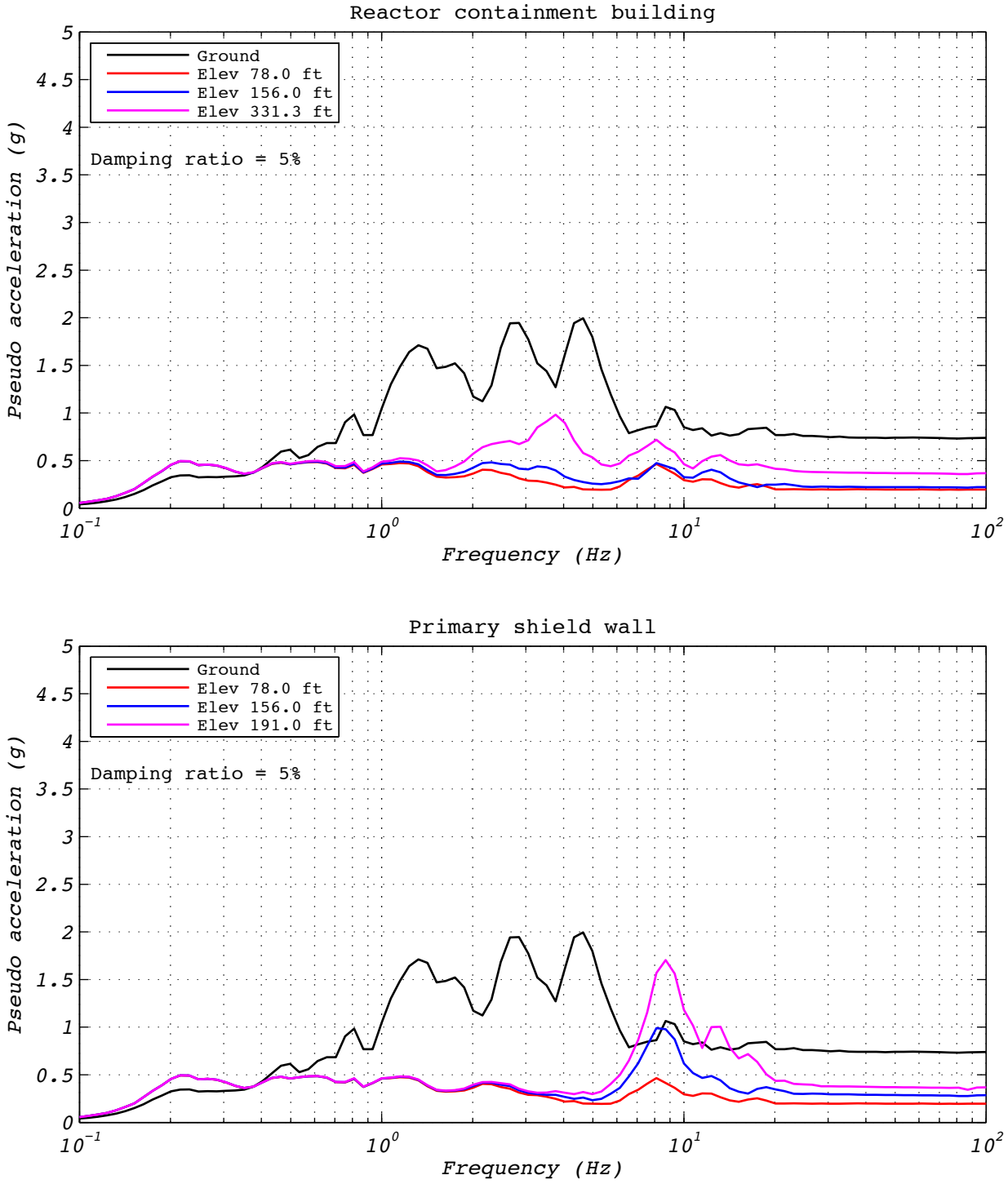

Figure A.13-4 Hybrid test floor spectra for run 47: NRC15, 1D with experimental bearing representing all bearings.

A.14 ANALYSIS RUN 47A

Analysis run 47A was an analytical estimation of the NRC dispersion appropriate ground motion number 15. The model consisted of a single analytical bearing representing all 527 bearings. Input motions consisted of a single horizontal component and a constant axial load specified as the design axial load of 8,663 kN. Figures A.14-1 and A.14-2 contain bearing responses, and Figure A.14-3 depicts the resulting floor response spectra for select locations in two of the isolated structures.

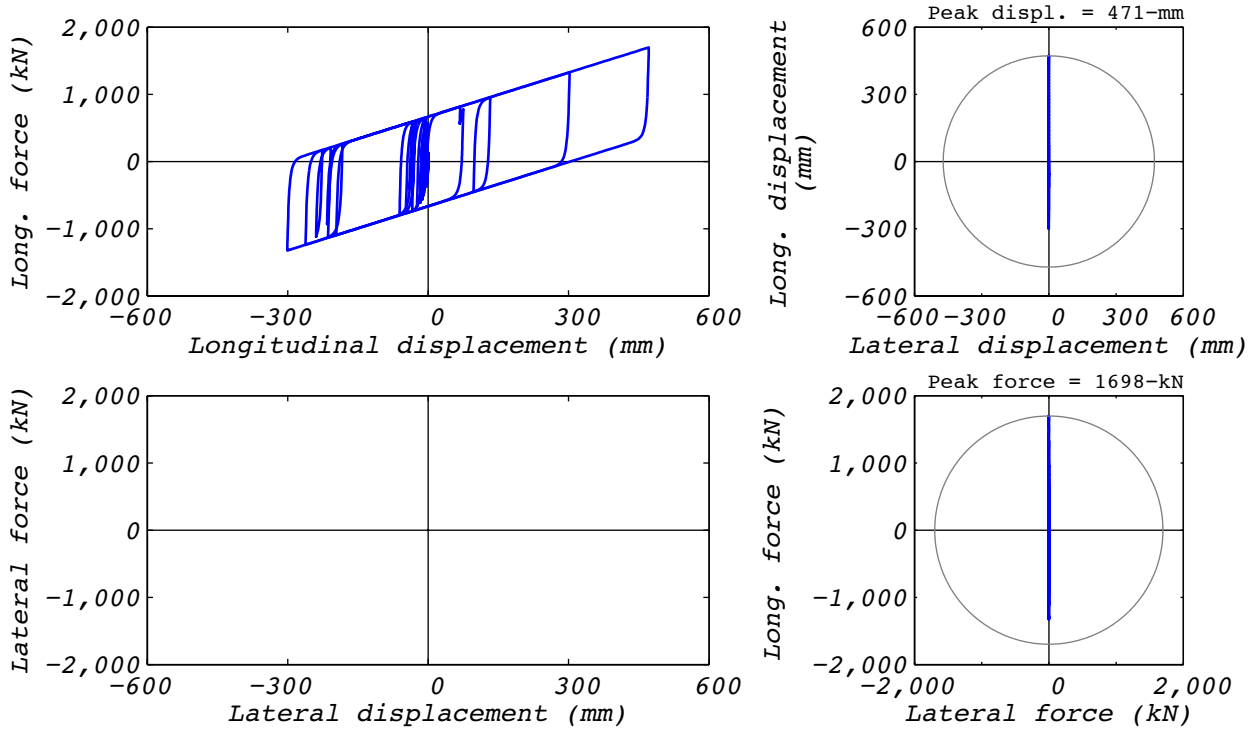

Figure A.14-1 Analytical bearing response for run 47A: NRC15, 1D with a single analytical bearing.

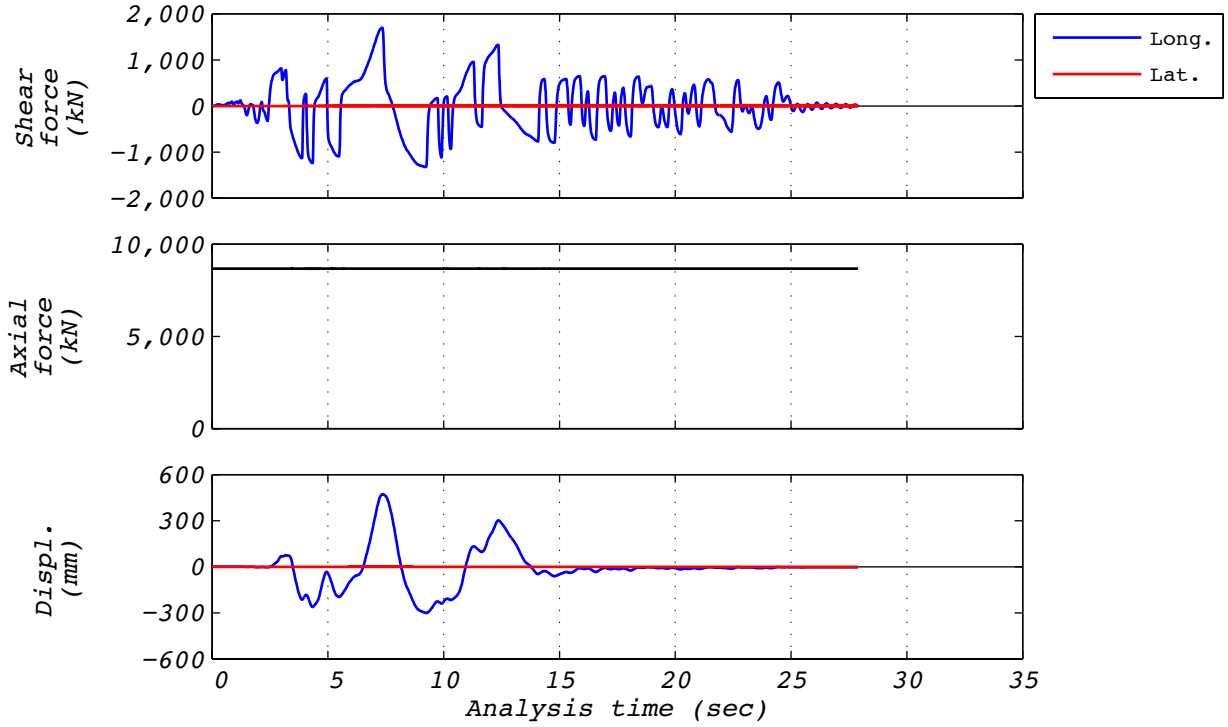

Figure A.14-2 Analytical time history responses for run 47A: NRC15, 1D with a single analytical bearing.

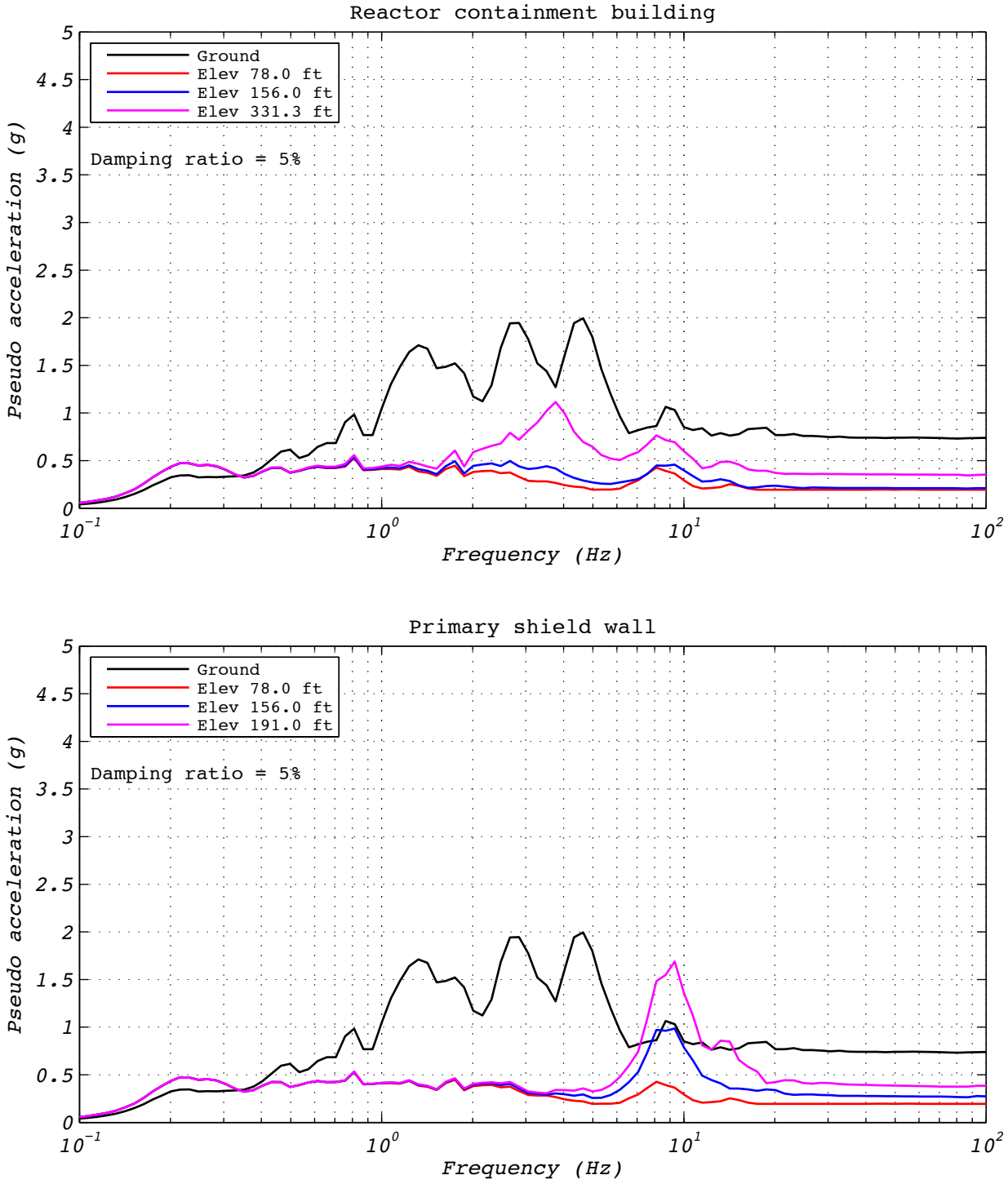

Figure A.14-3 Floor spectra for analytical run 47A: NRC15, 1D with a single analytical bearing.

A.15 TEST RUN 55

Test run 55 was a hybrid test of the NRC dispersion appropriate ground motion number 15. The model consisted of a single experimental bearing representing all 527 bearings. Input motions consisted of two horizontal components and a constant axial load specified as the design axial load of 8,663 kN. The test was executed at a rate 25 times slower than real time to compensate for machine delays. Bearing UET-2 was used in this test. Figure A.14-1 shows the fidelity achieved in the hybrid test. Figures A.14-2 and A.14-3 contains bearing responses, and Figure A.14-4 depicts the resulting floor response spectra for select locations in two of the isolated structures.

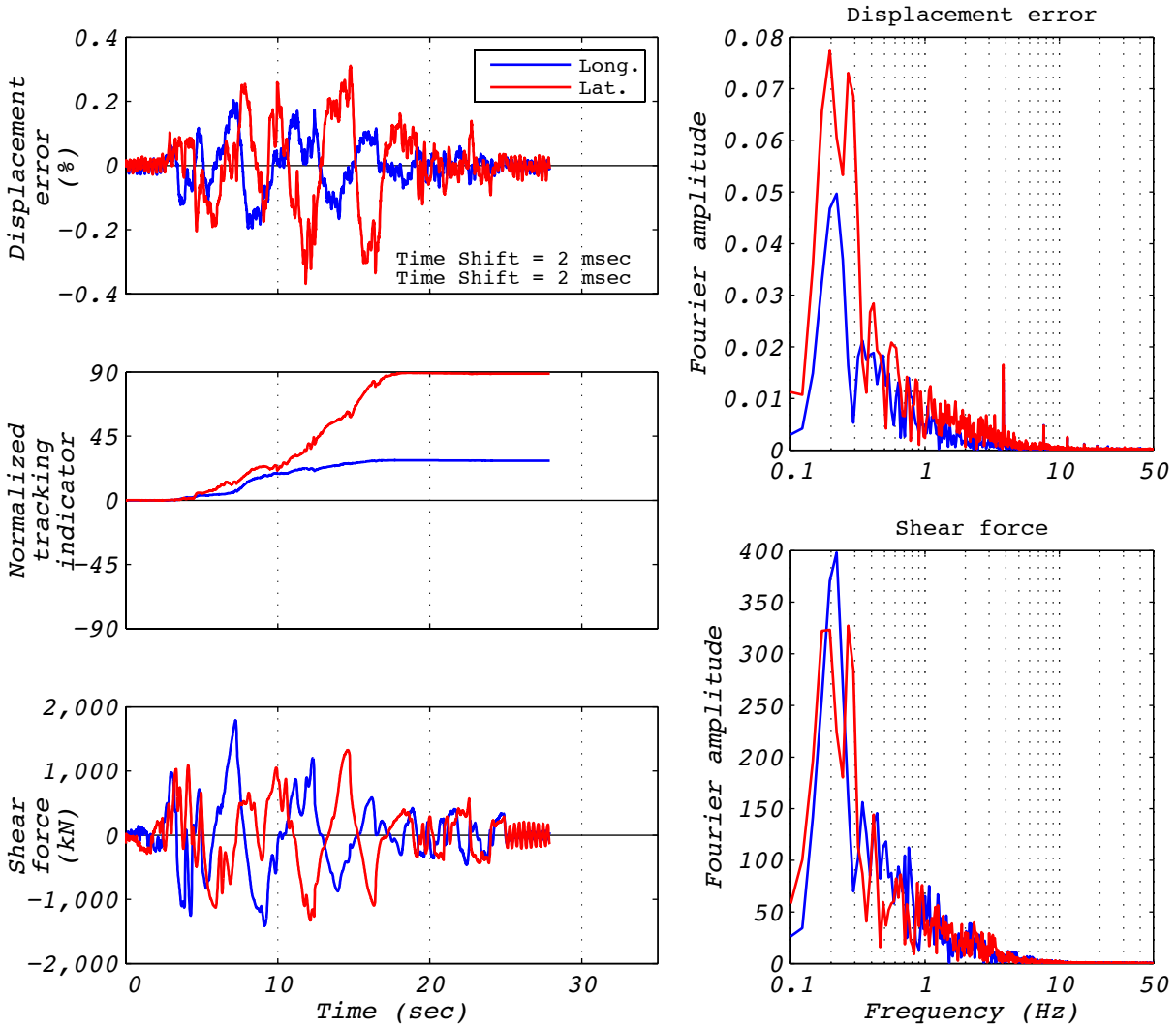

Figure A.15-1 Hybrid test performance metrics for run 55: NRC15, 2D with experimental bearing representing all bearings.

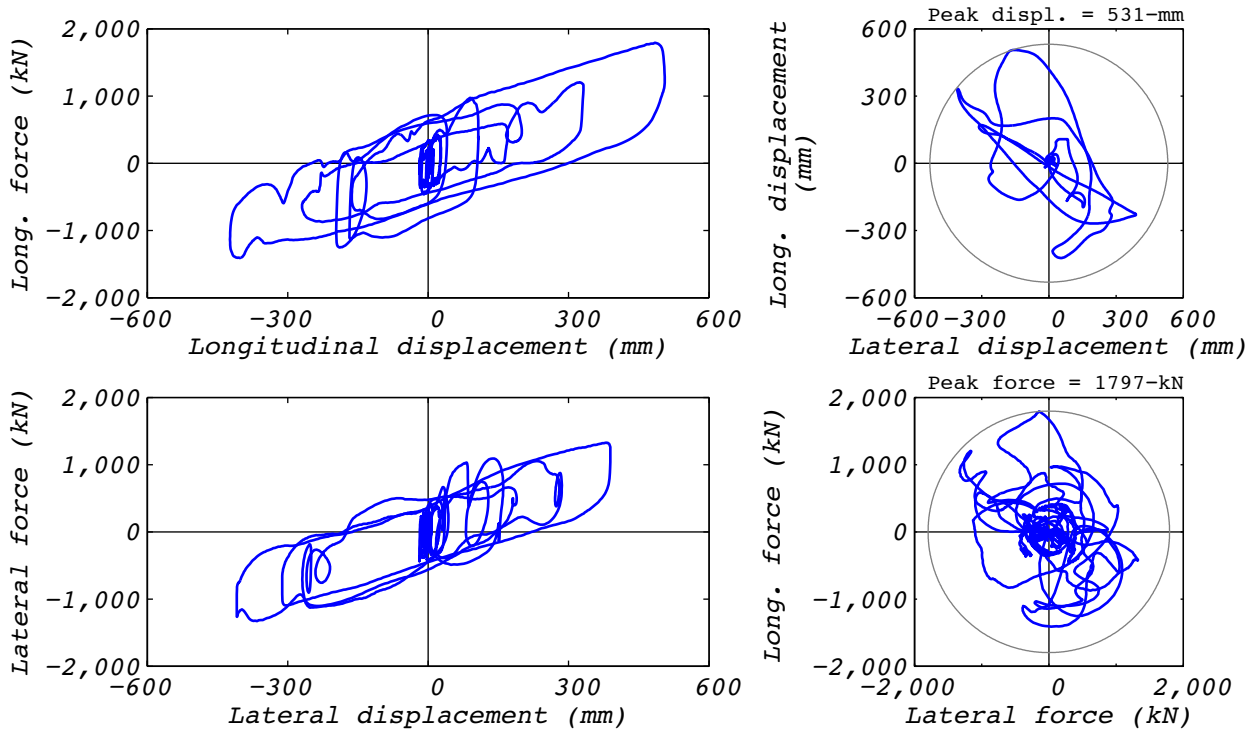

Figure A.15-2 Hybrid test bearing response for run 55: NRC15, 2D with experimental bearing representing all bearings.

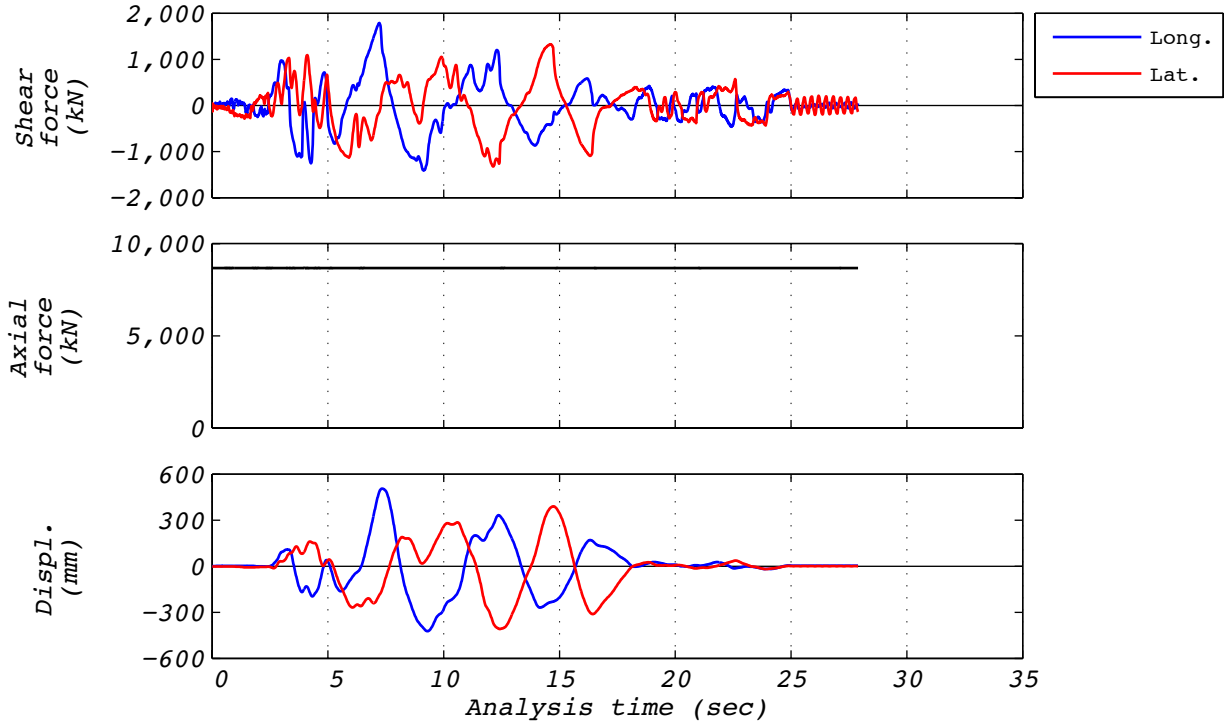

Figure A.15-3 Hybrid test time history responses for run 55: NRC15, 2D with experimental bearing representing all bearings.

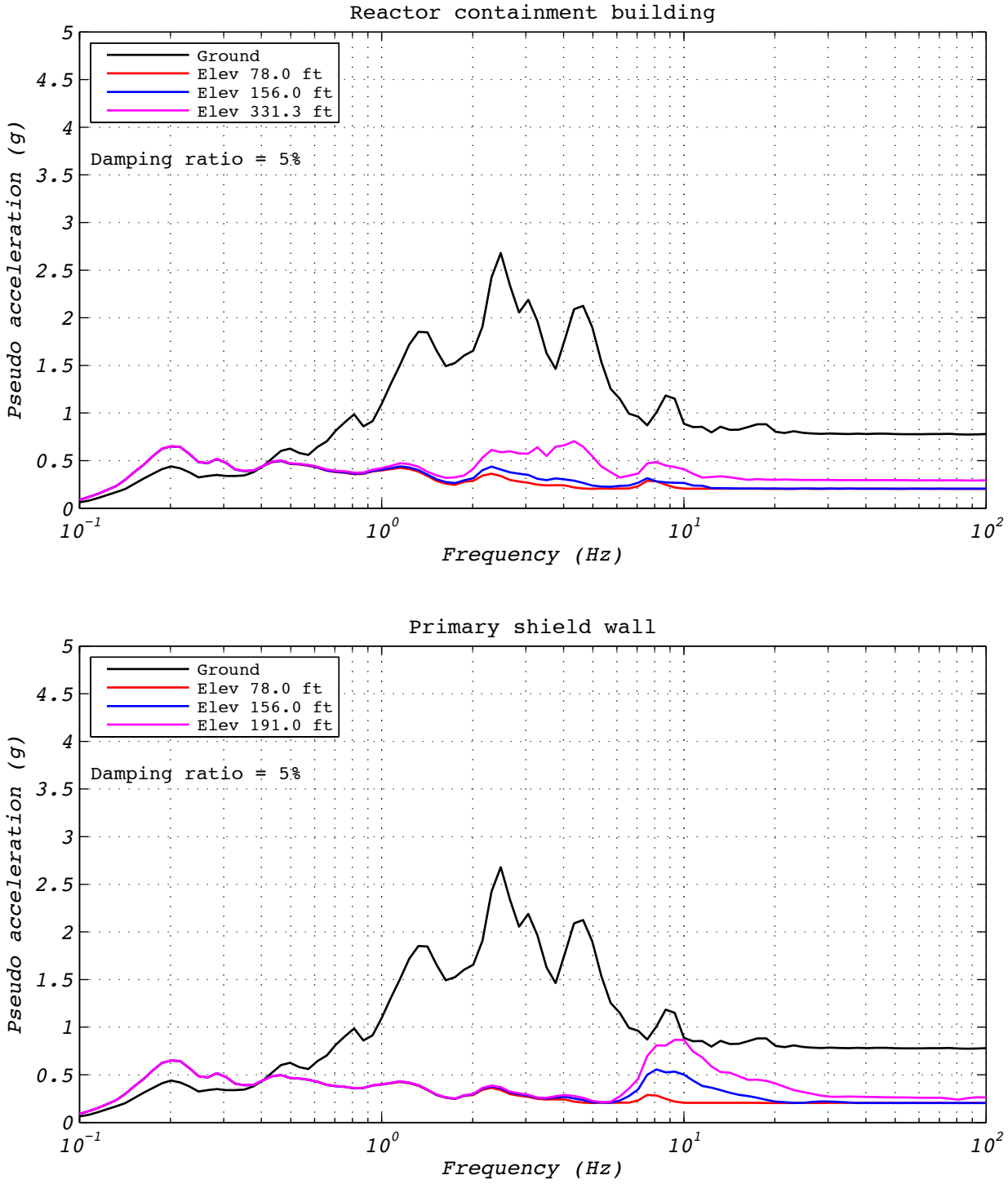

Figure A.15-4 Hybrid test floor spectra for run 55: NRC15, 2D with experimental bearing representing all bearings.

A.16 ANALYSIS RUN 55A

Analysis run 55A was an analytical estimation of the NRC dispersion appropriate ground motion number 15. The model consisted of a single analytical bearing representing all 527 bearings. Input motions consisted of two horizontal components and a constant axial load specified as the design axial load of 8,663 kN. Figures A.16-1 and A.16-2 contain bearing responses, and Figure A.16-3 depicts the resulting floor response spectra for select locations in two of the isolated structures.

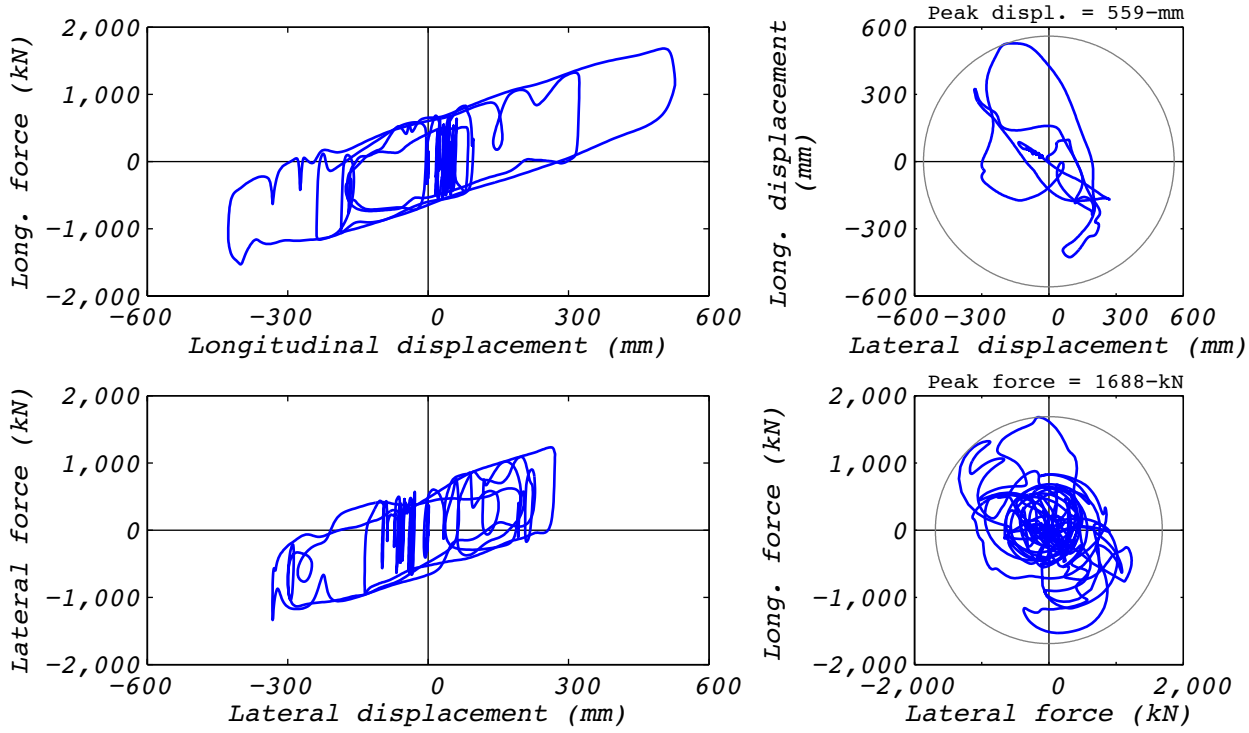

Figure A.16-1 Analytical bearing response for run 55A: NRC15, 2D with a single analytical bearing.

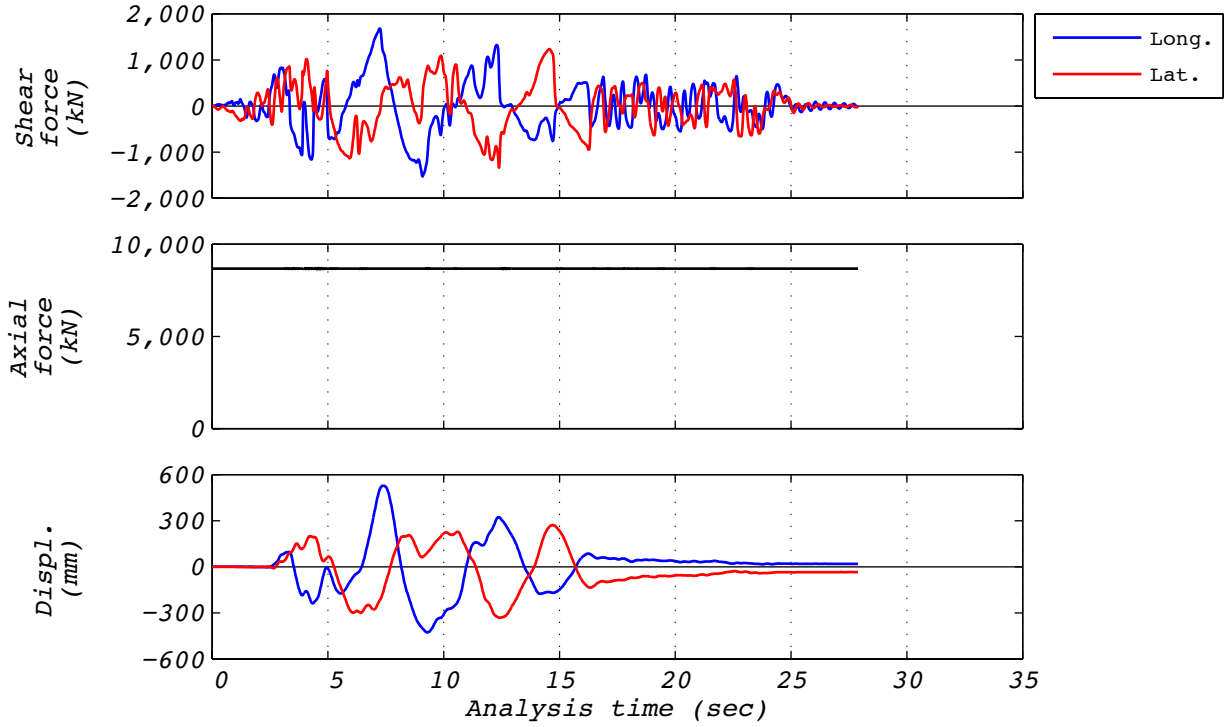

Figure A.16-2 Analytical time history responses for run 55A: NRC15, 2D with a single analytical bearing.

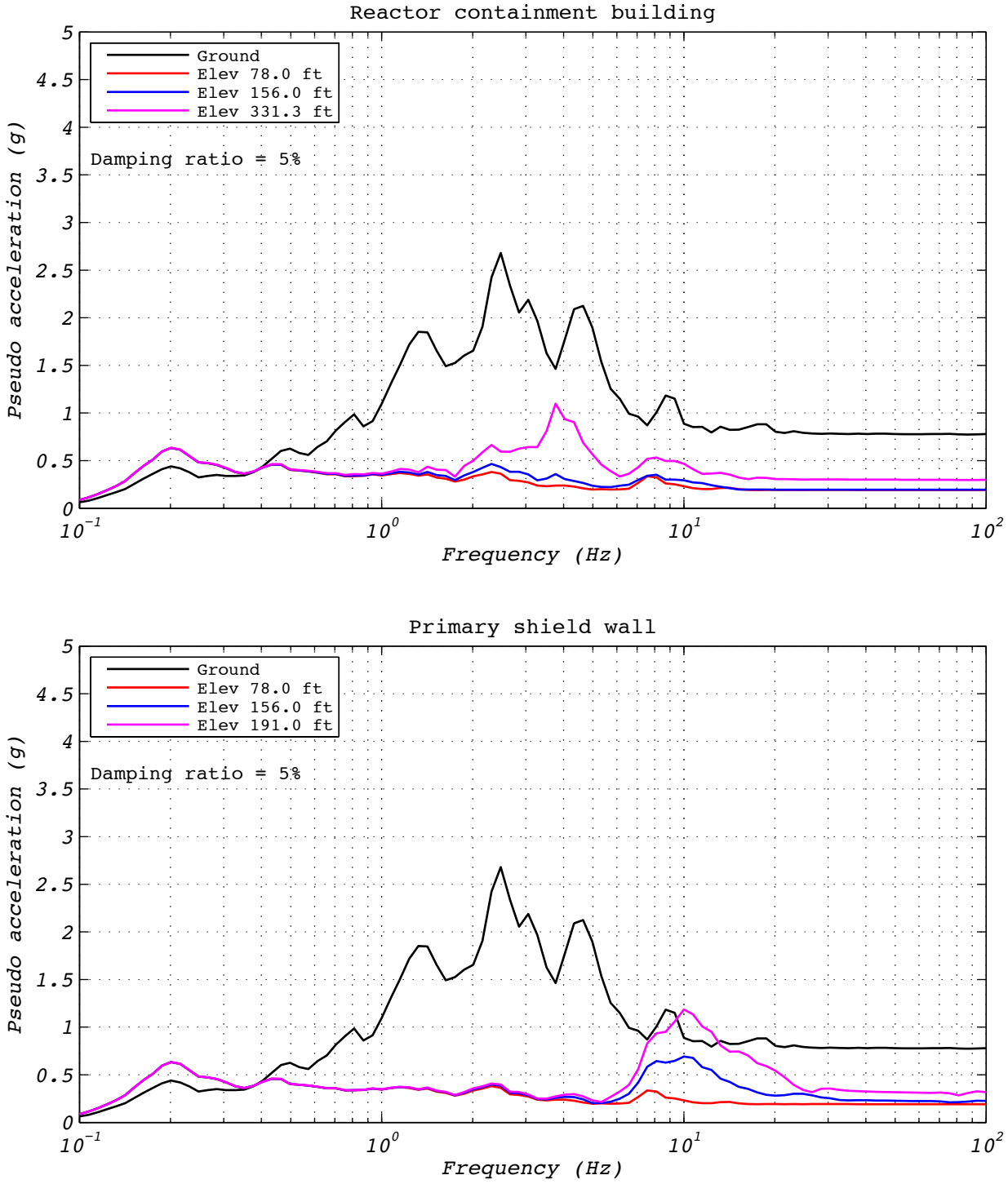

Figure A.16-3 Floor spectra for analytical run 55A: NRC15, 2D with a single analytical bearing.

A.17 DEVELOPMENT RUN 58

Development run 58 was a hybrid test of the EUR dispersion appropriate ground motion number five. The model consisted of 526 analytical bearings and the experimental bearing centrally located in the layout. Input motions consisted of two horizontal components and a constant axial load specified as the design axial load of 8,663 kN. The test was executed at a rate 25 times slower than real time to compensate for machine delays and the analytical model iterations required for the complex model. Bearing UET-2 was used in this test. Figure A.16-1 shows the fidelity achieved in the hybrid test. Figures A.16-2 and A.16-3 contain bearing responses, and Figure A.16-4 depicts the resulting floor response spectra for select locations in two of the isolated structures.

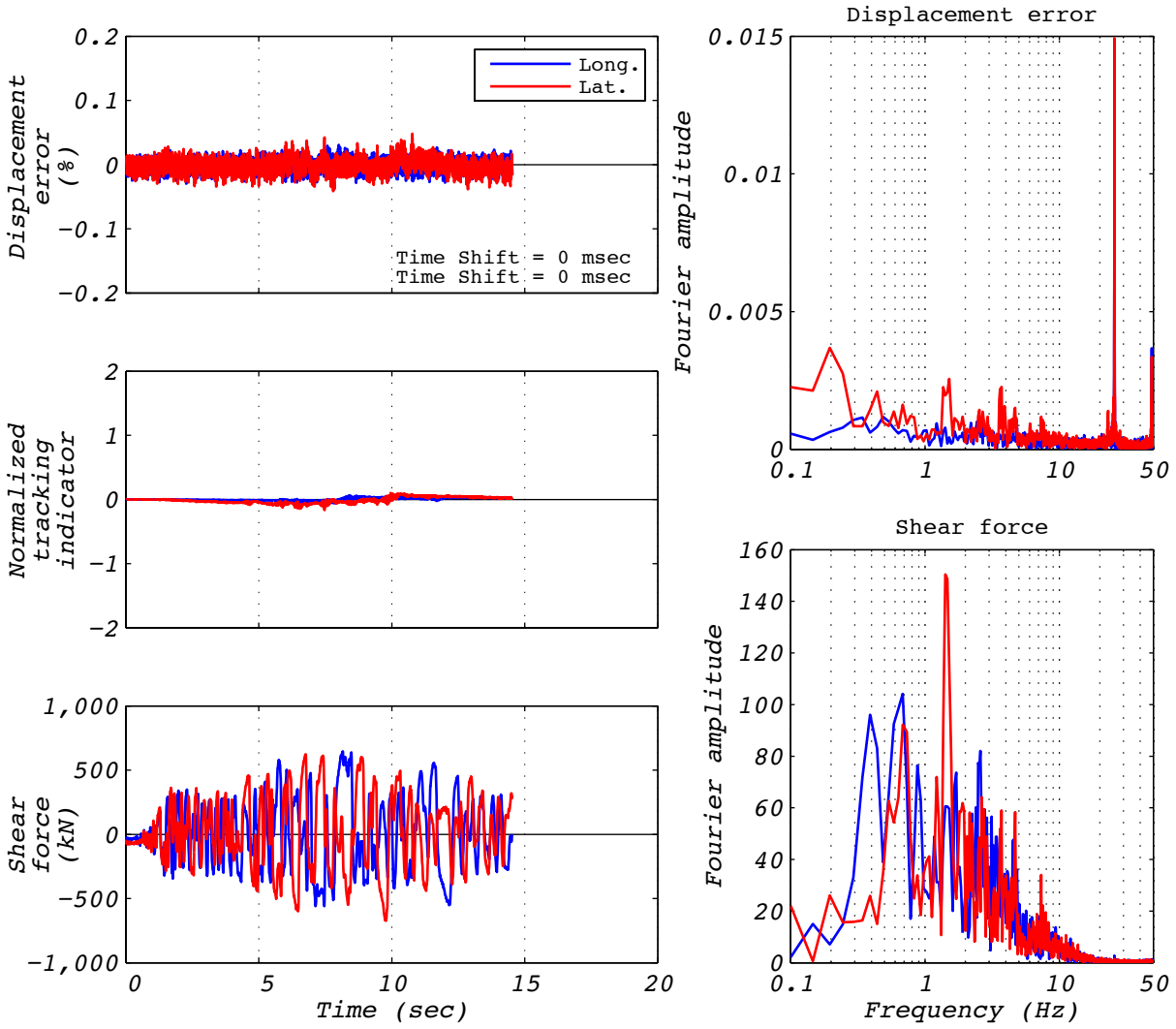

Figure A.17-1 Hybrid test performance metrics for run 58: EUR5, 2D with experimental bearing representing one of 527 bearings.

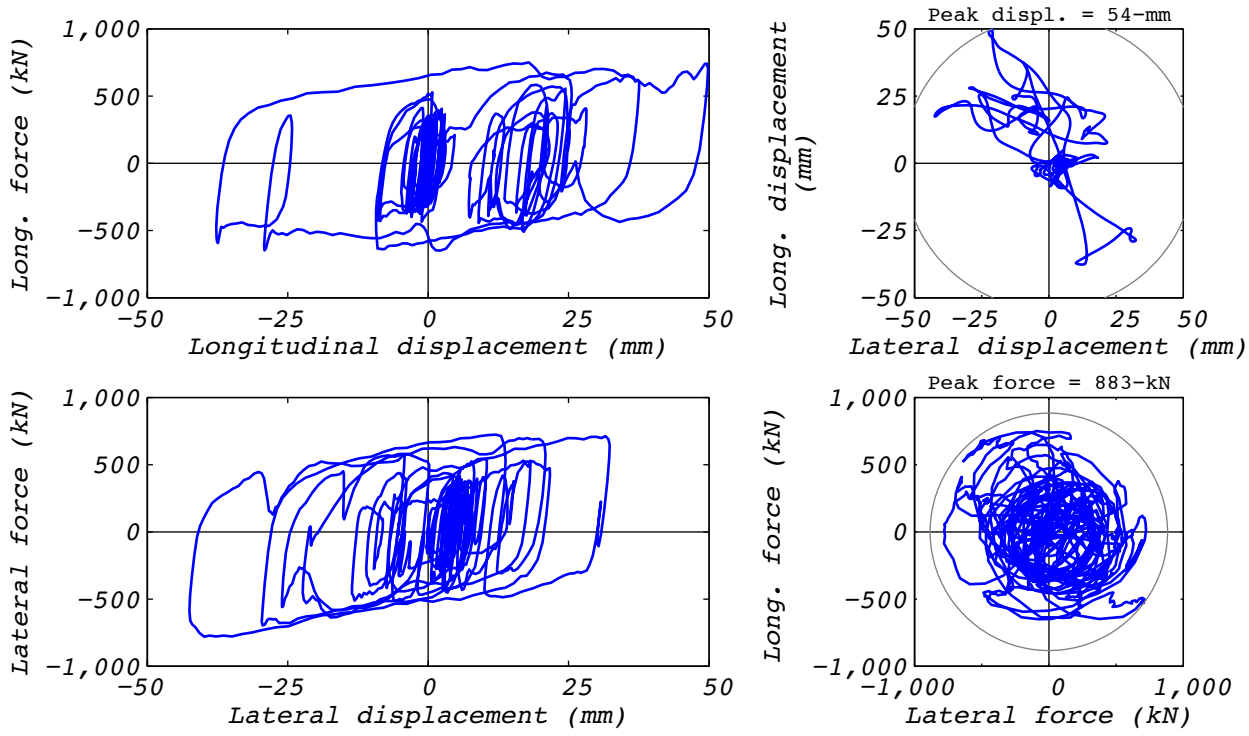

Figure A.17-2 Hybrid test bearing response for run 58: EUR5, 2D with experimental bearing representing one of 527 bearings.

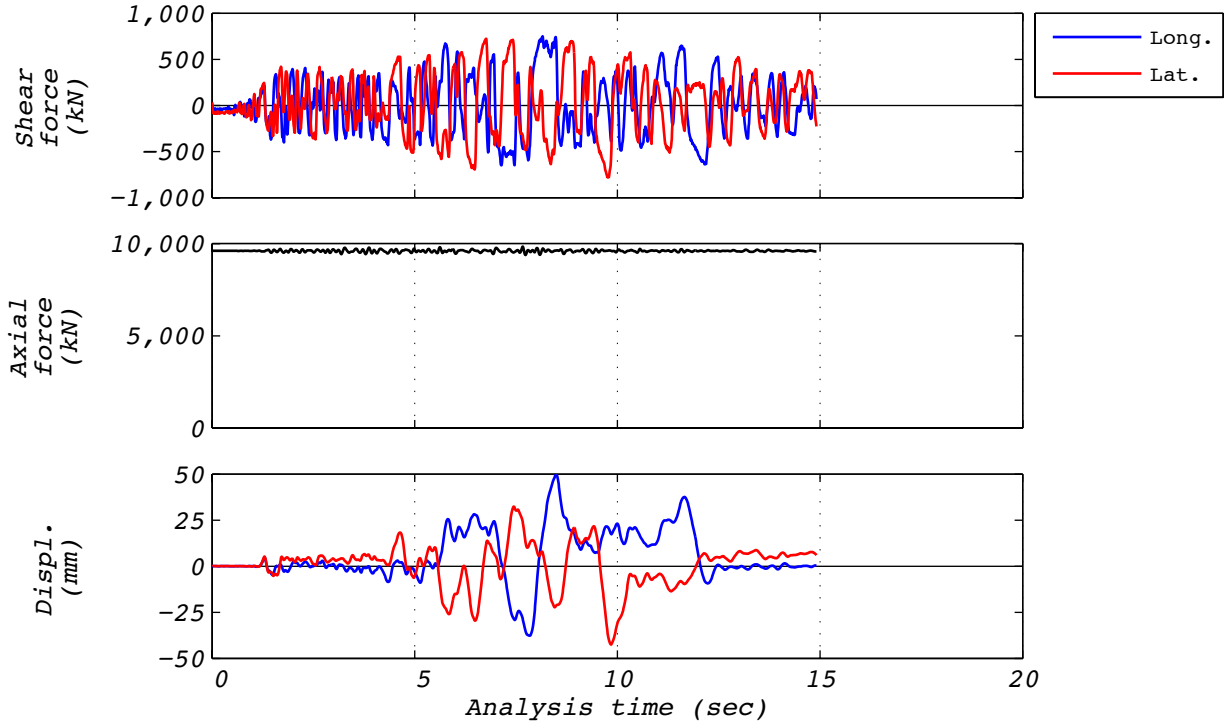

Figure A.17-3 Hybrid test time history responses for run 58: EUR5, 2D with experimental bearing representing one of 527 bearings.

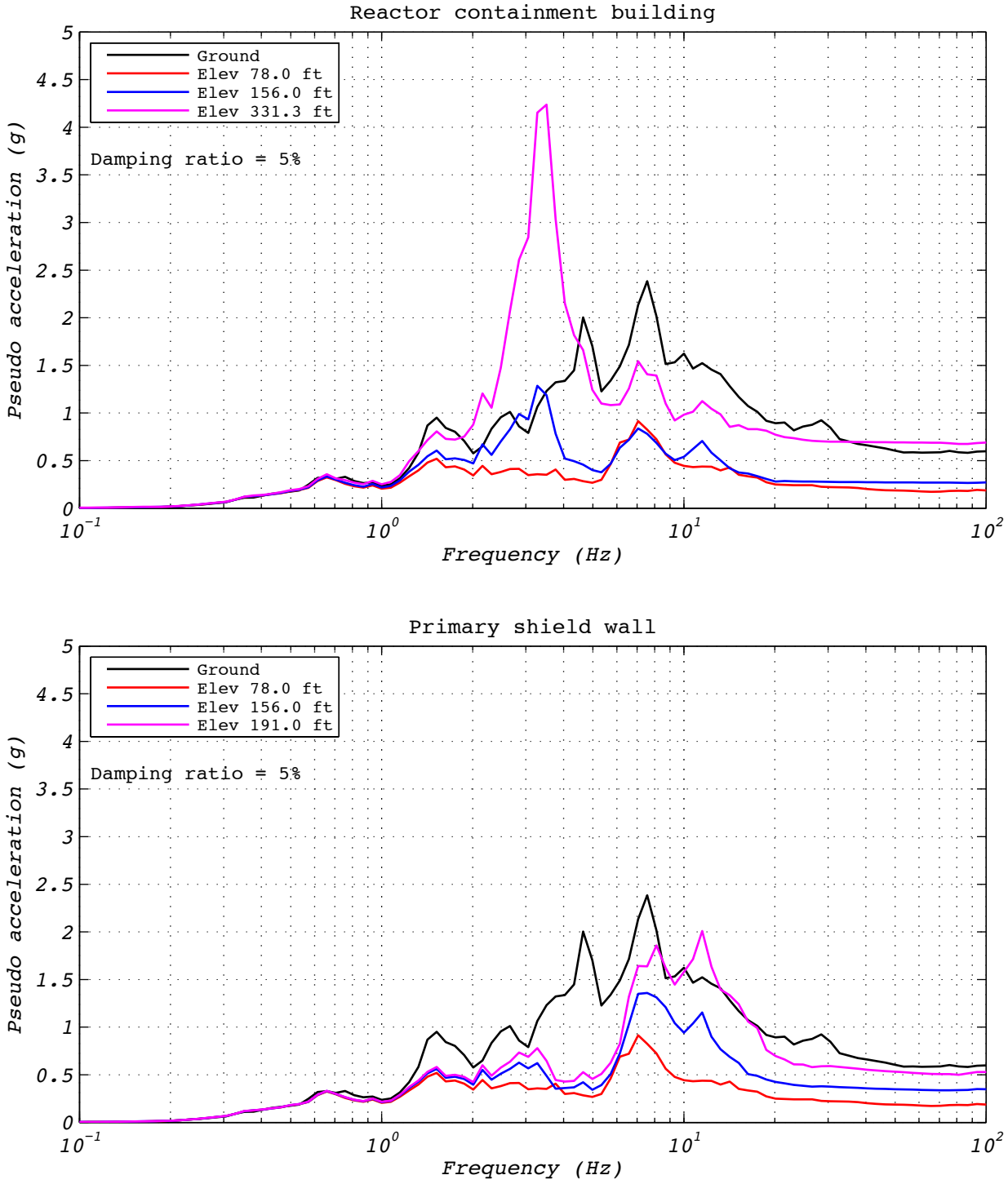

Figure A.17-4 Hybrid test floor spectra for run 58: EUR5, 2D with experimental bearing representing one of 527 bearings.

A.18 DEVELOPMENT RUN 60

Development run 60 was a hybrid test of the EUR dispersion appropriate ground motion number five. The model consisted of 526 analytical bearings and the experimental bearing centrally located in the layout. Input motions consisted of two horizontal components and a constant axial load specified as the design axial load of 8,663 kN. The test was executed at a rate 30 times slower than real time to compensate for machine delays and the analytical model iterations required for the complex model. Bearing UET-2 was used in this test. Figure A.18-1 shows the fidelity achieved in the hybrid test. Figures A.18-2 and A.18-3 contain bearing responses, and Figure A.18-4 depicts the resulting floor response spectra for select locations in two of the isolated structures.

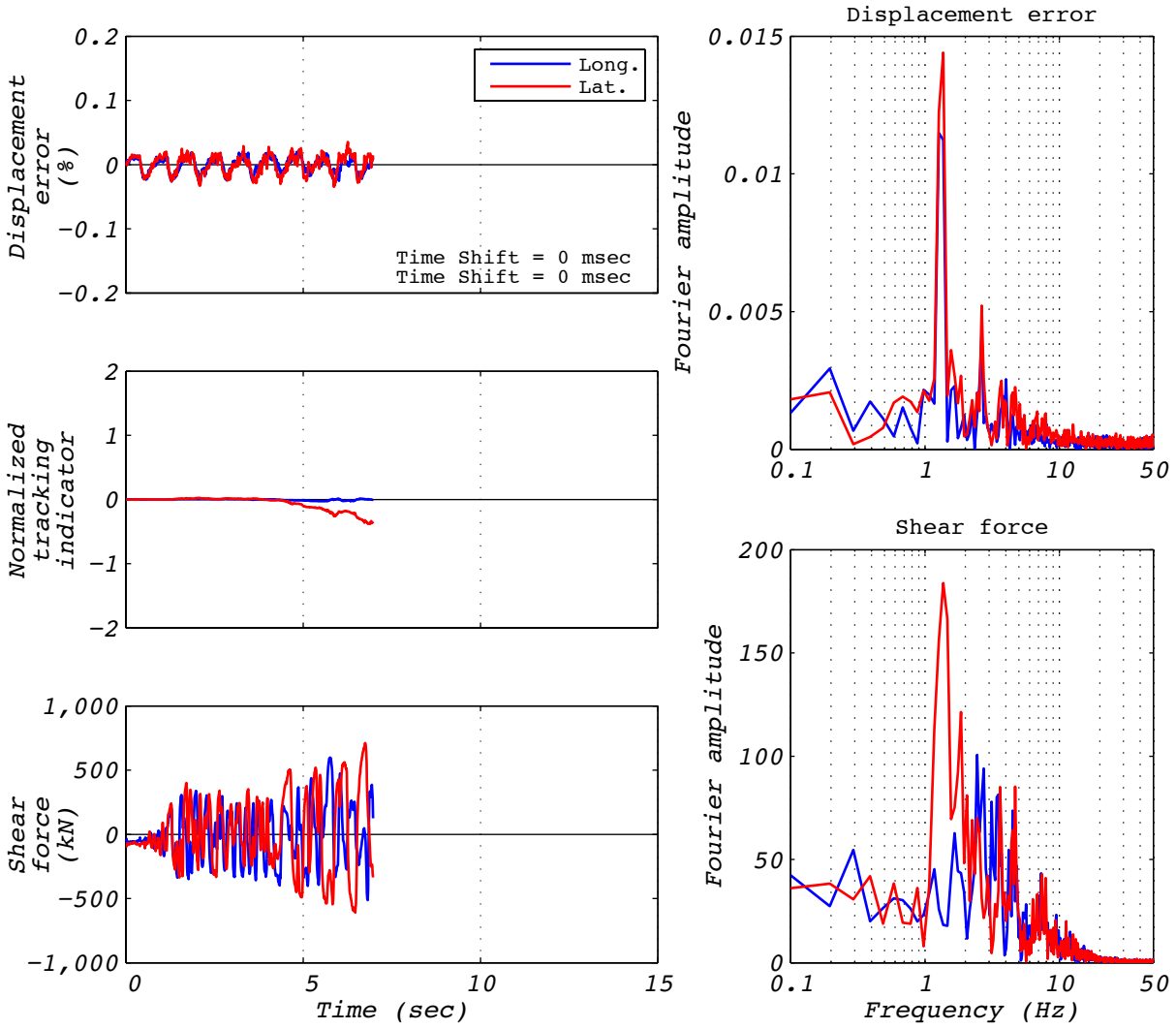

Figure A.18-1 Hybrid test performance metrics for run 60: EUR5, 2D with experimental bearing representing one of 527 bearings.

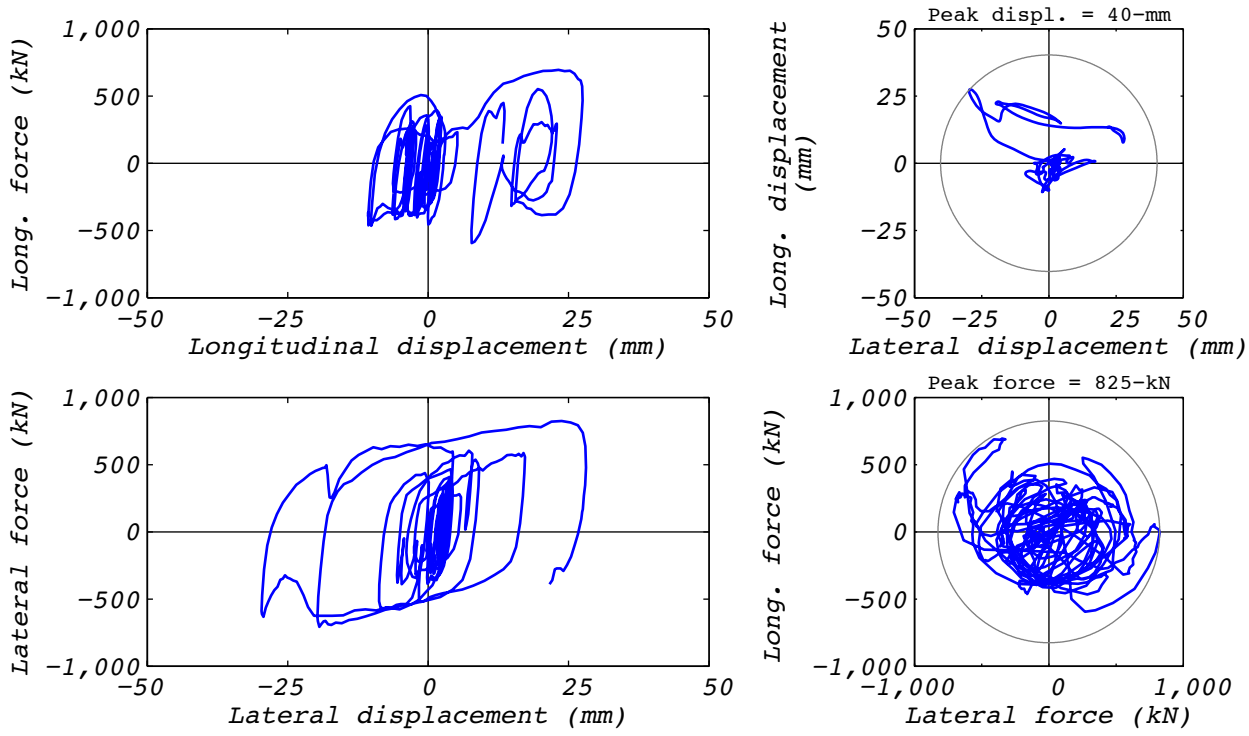

Figure A.18-2 Hybrid test bearing response for run 60: EUR5, 2D with experimental bearing representing one of 527 bearings.

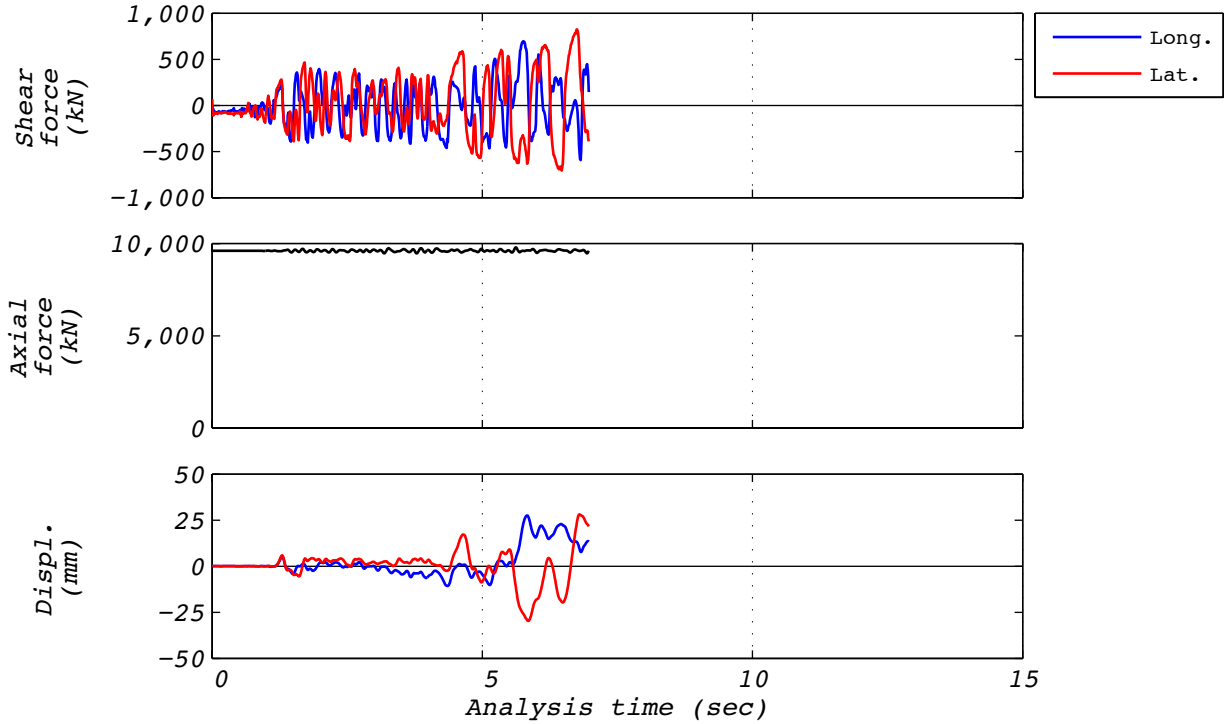

Figure A.18-3 Hybrid test time history responses for run 60: EUR5, 2D with experimental bearing representing one of 527 bearings.

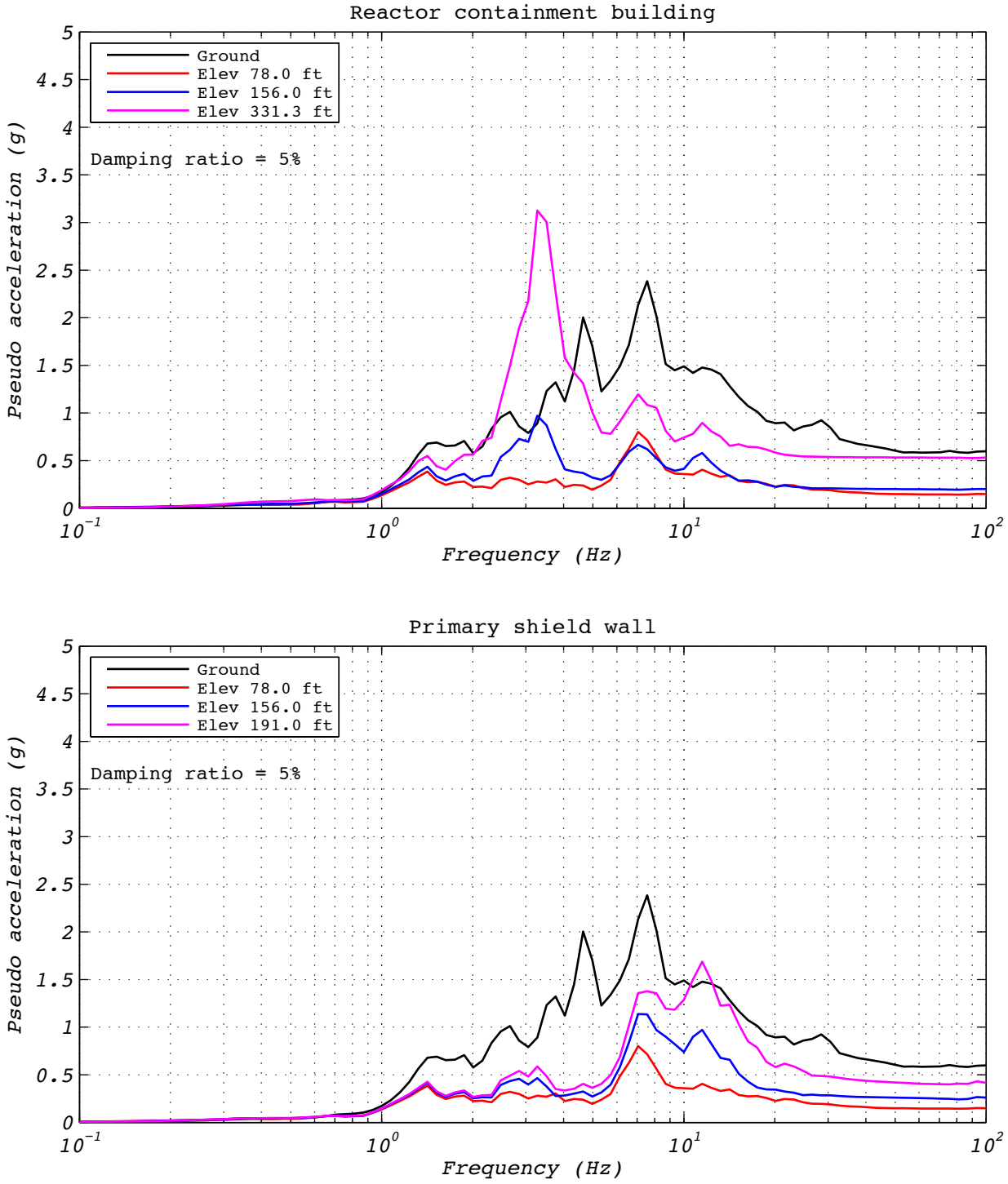

Figure A.18-4 Hybrid test floor spectra for run 60: EUR5, 2D with experimental bearing representing one of 527 bearings.

A.19 TEST RUN 61

Test run 61 was a hybrid test of the NRC dispersion appropriate ground motion number 15. The model consisted of 526 analytical bearings and the experimental bearing centrally located in the layout. Input motions consisted of two horizontal components and a constant axial load specified as the design axial load of 8,663 kN. The test was executed at a rate 75 times slower than real time to compensate for machine delays and the analytical model iterations required for the complex model. Bearing UET-2 was used in this test. Figure A.19-1 shows the fidelity achieved in the hybrid test. Figures A.19-2 and A.19-3 contain bearing responses, and Figure A.19-4 depicts the resulting floor response spectra for select locations in two of the isolated structures.

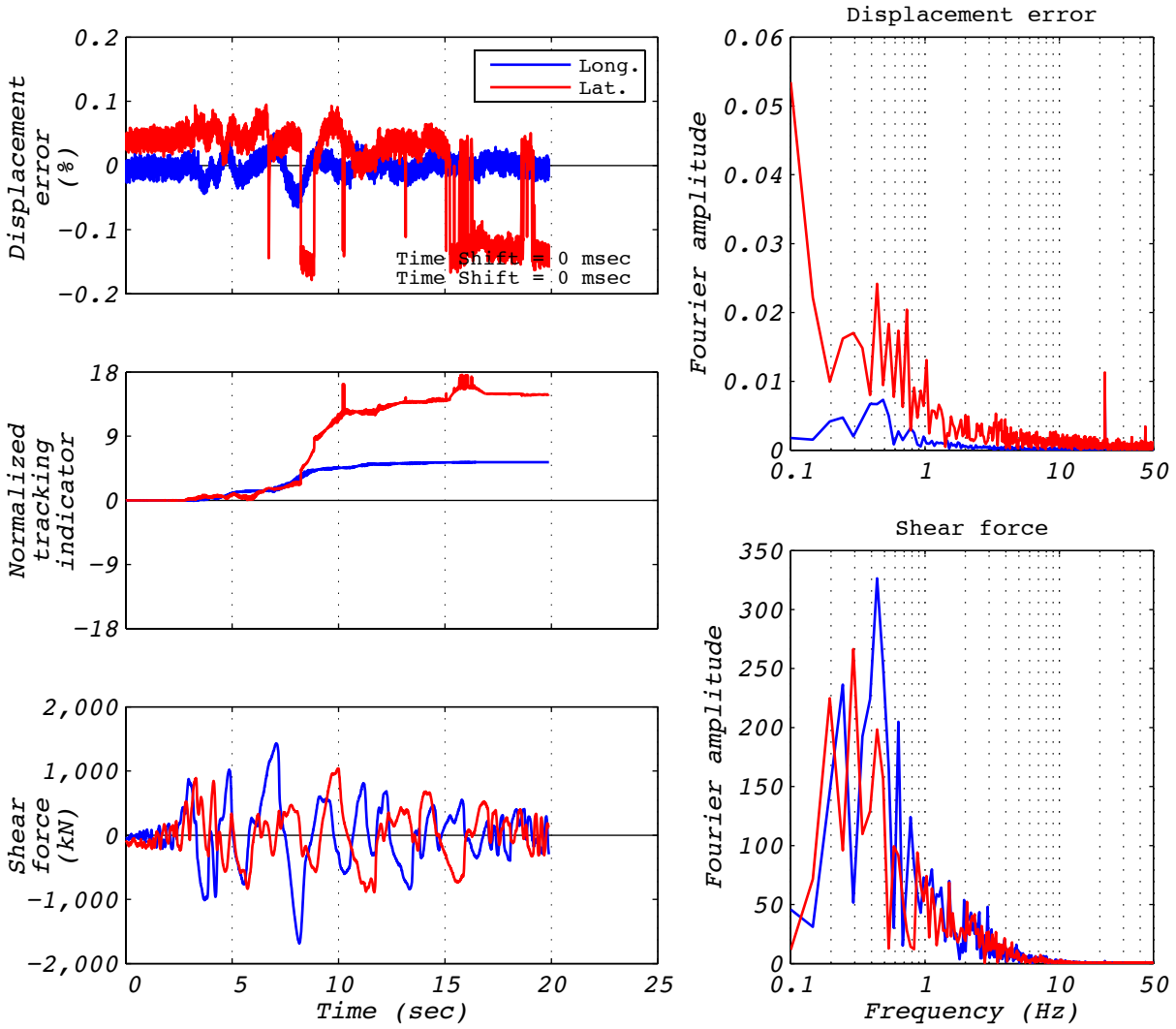

Figure A.19-1 Hybrid test performance metrics for run 61: NRC15, 2D with experimental bearing representing one of 527.

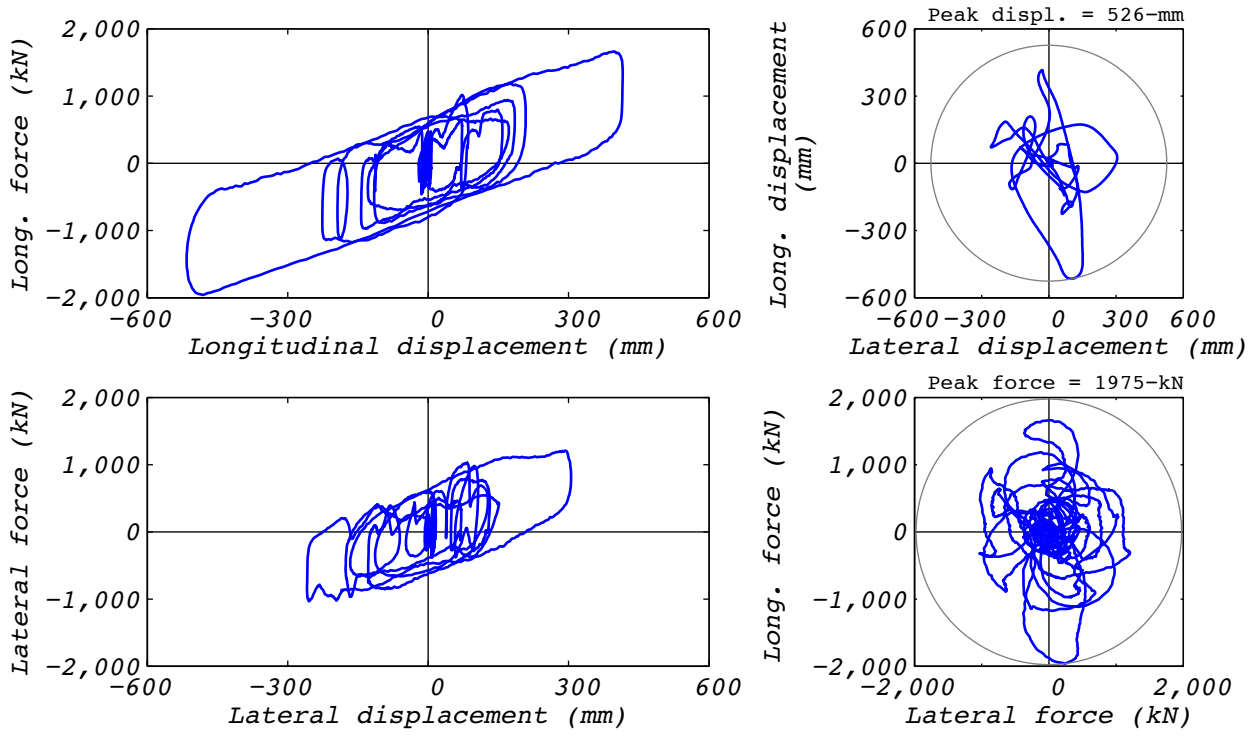

Figure A.19-2 Hybrid test bearing response for run 61: NRC15, 2D with experimental bearing representing one of 527.

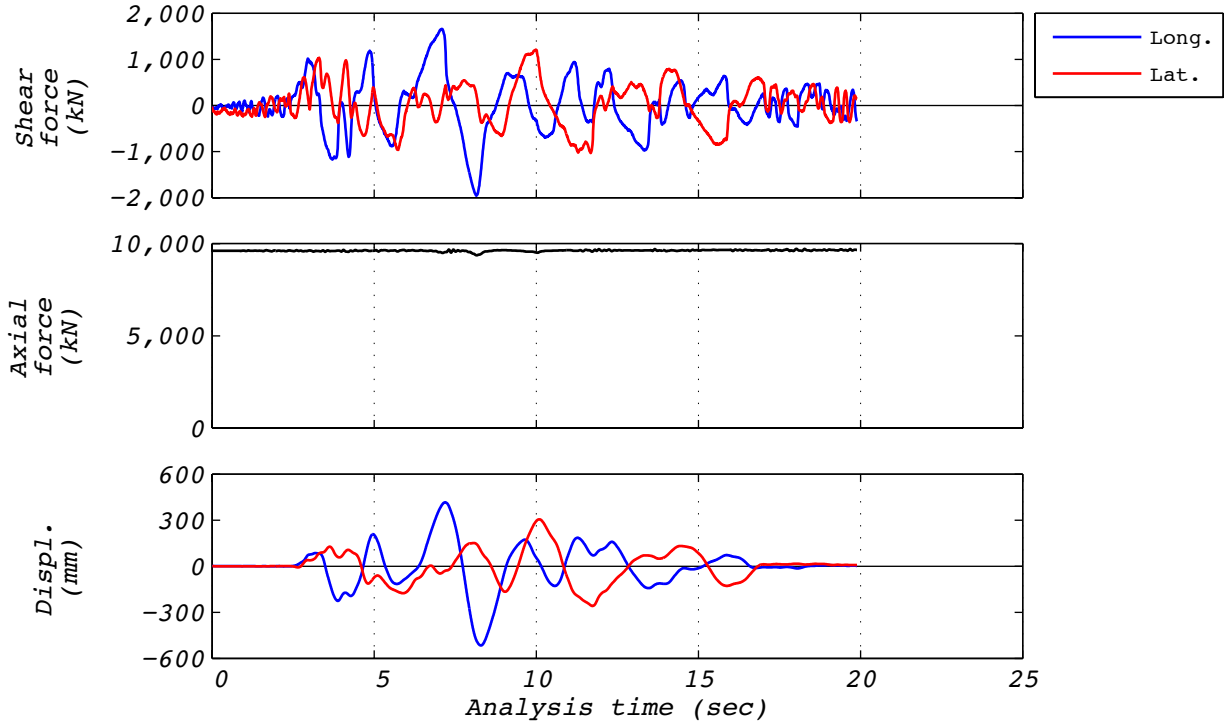

Figure A.19-3 Hybrid test time history responses for run 61: NRC15, 2D with experimental bearing representing one of 527.

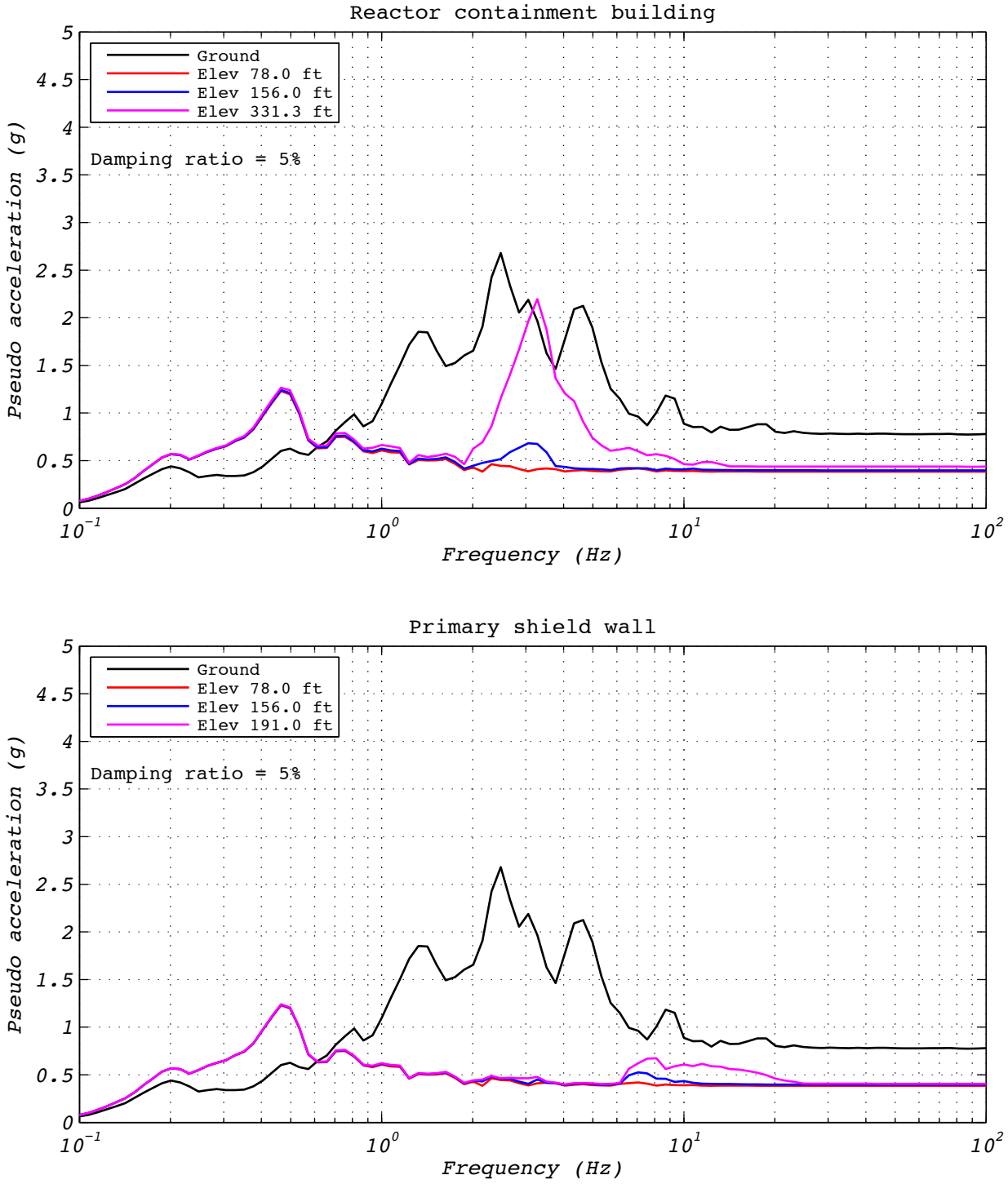

Figure A.19-4 Hybrid test floor spectra for run 61: NRC15, 2D with experimental bearing representing one of 527.

A.20 TEST RUN 63

Test run 63 was a hybrid test of the NRC dispersion appropriate ground motion number 15. The model consisted of five groups of bearings. The experimental bearing was centrally located in the layout. Input motions consisted of two horizontal components and a constant axial load specified as the design axial load of 8,663 kN. The test was executed at a rate 25 times slower than real time to compensate for machine delays. Bearing UET-2 was used in this test. Figure A.20-1 shows the fidelity achieved in the hybrid test. Figures A.20-2 and A.20-3 contain bearing responses, and Figure A.20-4 depicts the resulting floor response spectra for select locations in two of the isolated structures.

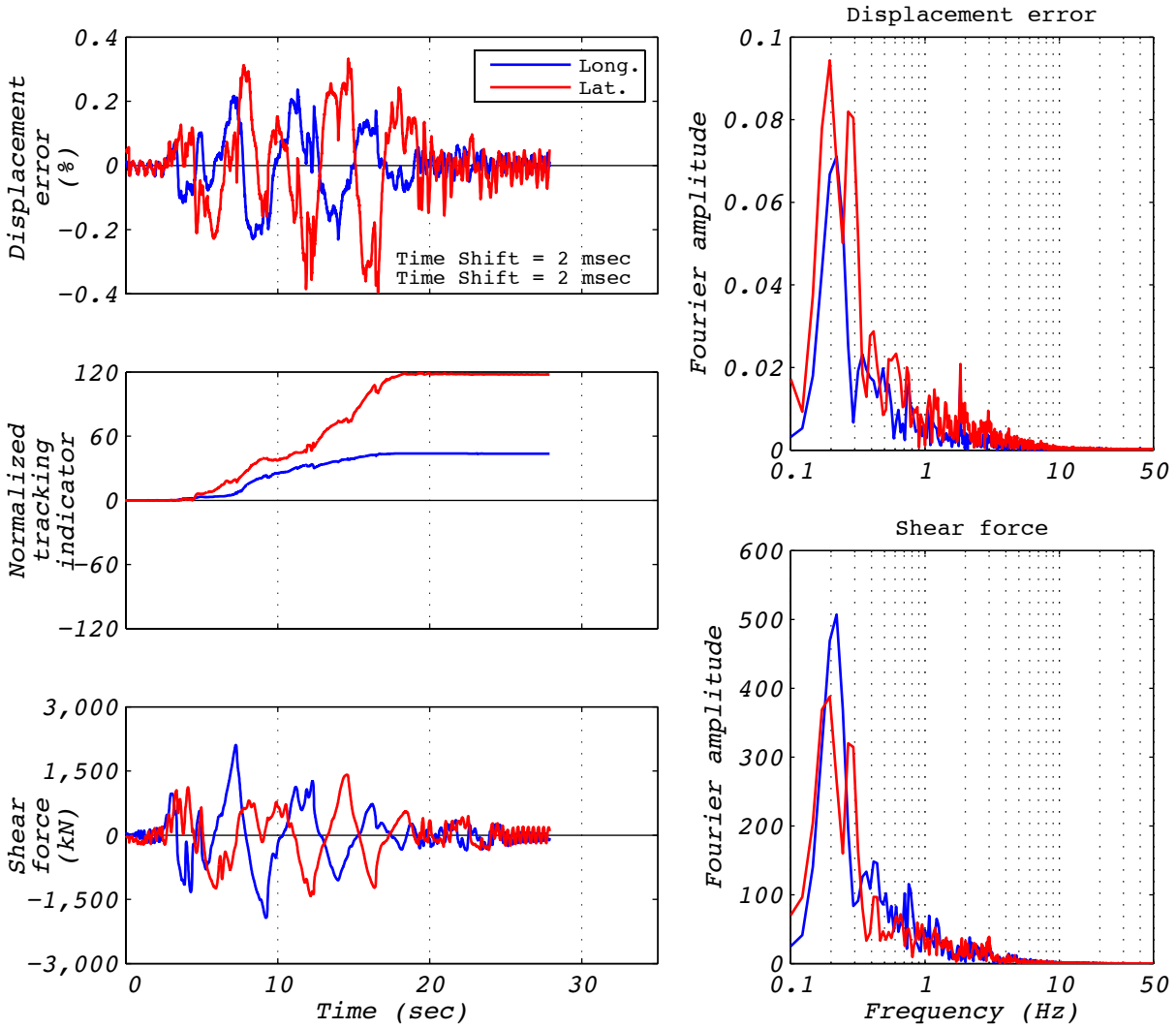

Figure A.20-1 Hybrid test performance metrics for run 63: NRC15, 2D with five groups of bearings.

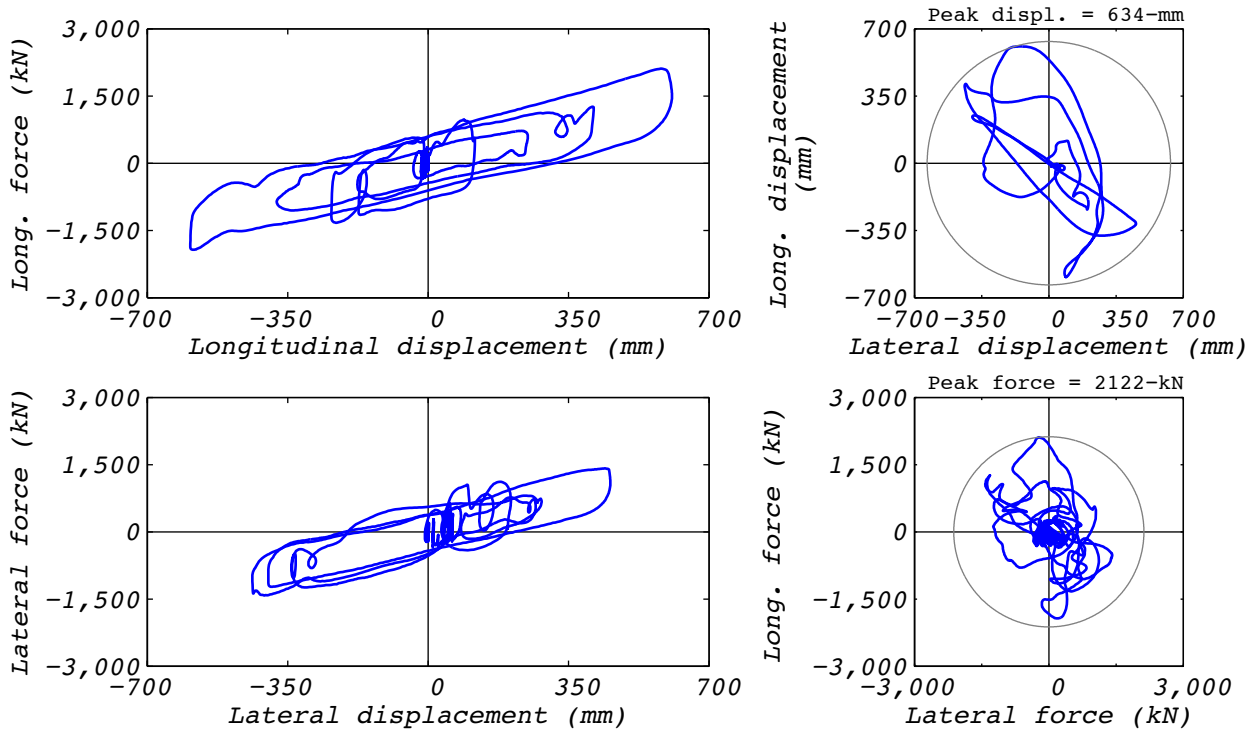

Figure A.20-2 Hybrid test bearing response for run 63: NRC15, 2D with five groups of bearings.

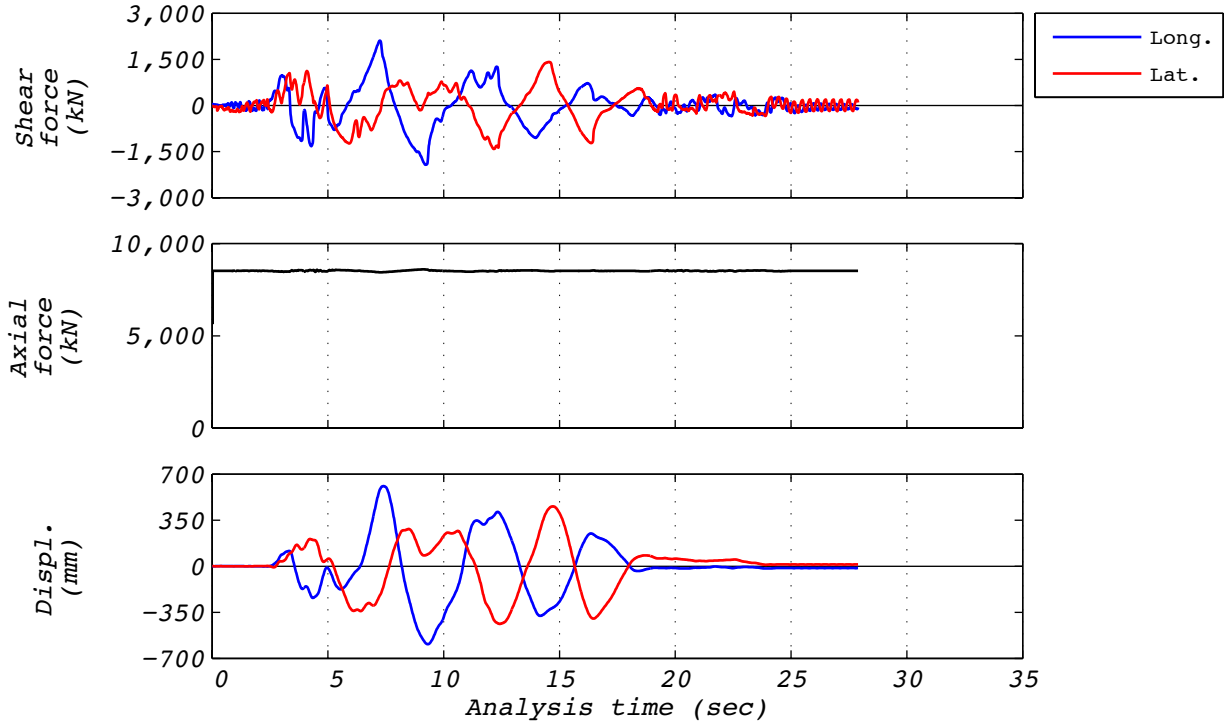

Figure A.20-3 Hybrid test time history responses for run 63: NRC15, 2D with five groups of bearings.

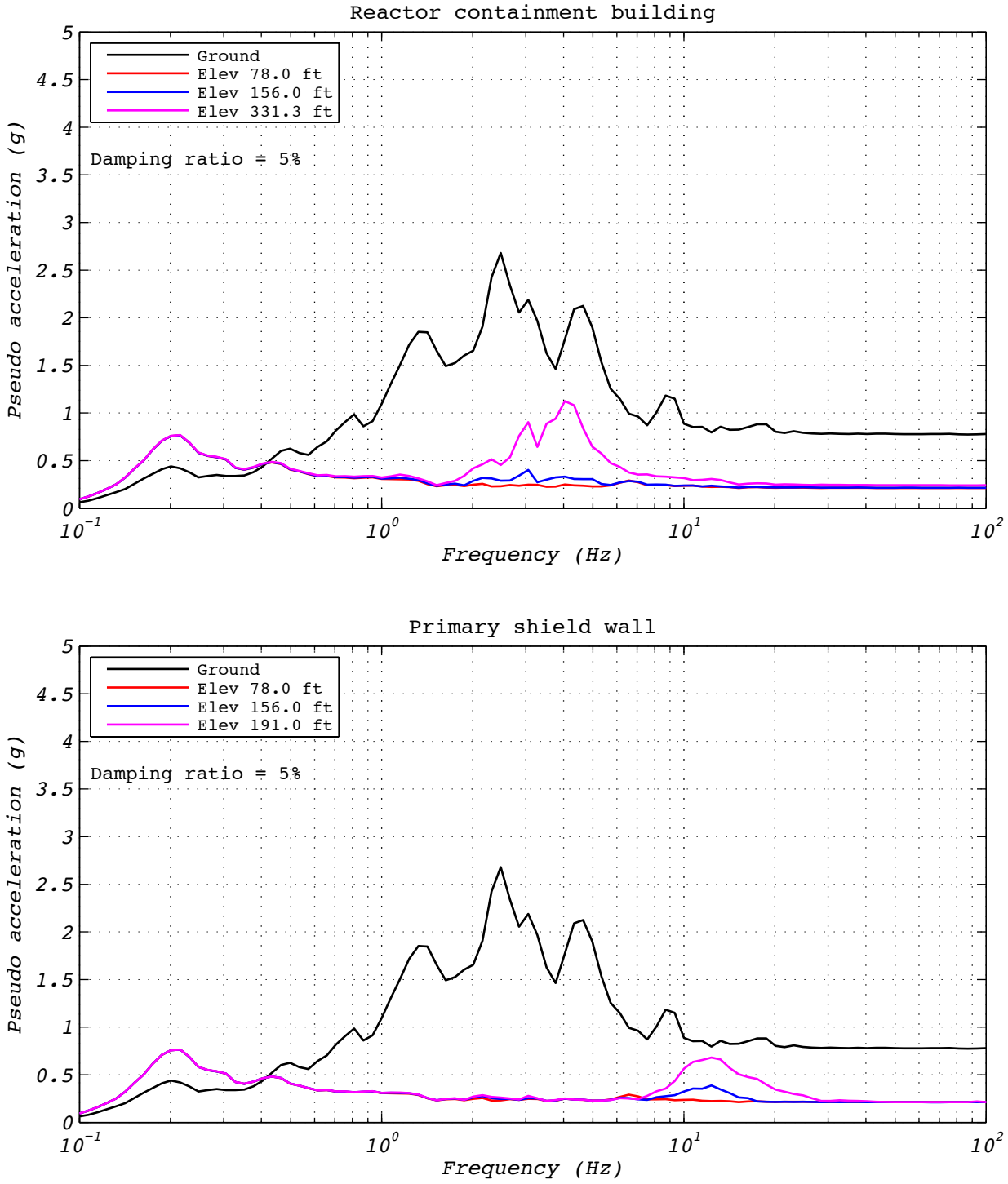

Figure A.20-4 Hybrid test floor spectra for run 63: NRC15, 2D with five groups of bearings.

A.21 TEST RUN 78

Test run 78 was a hybrid test of the EUR dispersion appropriate ground motion number five. The model consisted of a single experimental bearing representing all 527 bearings. Input motions consisted of two horizontal components. The axial load was specified as the design axial load of 8,663 kN. The test was executed at a rate 25 times slower than real time to compensate for machine delays. Bearing UET-1 was used in this test. Figure A.21-1 shows the fidelity achieved in the hybrid test. Figures A.21-2 and A.21-3 contain bearing responses, and Figure A.21-4 depicts the resulting floor response spectra for select locations in two of the isolated structures.

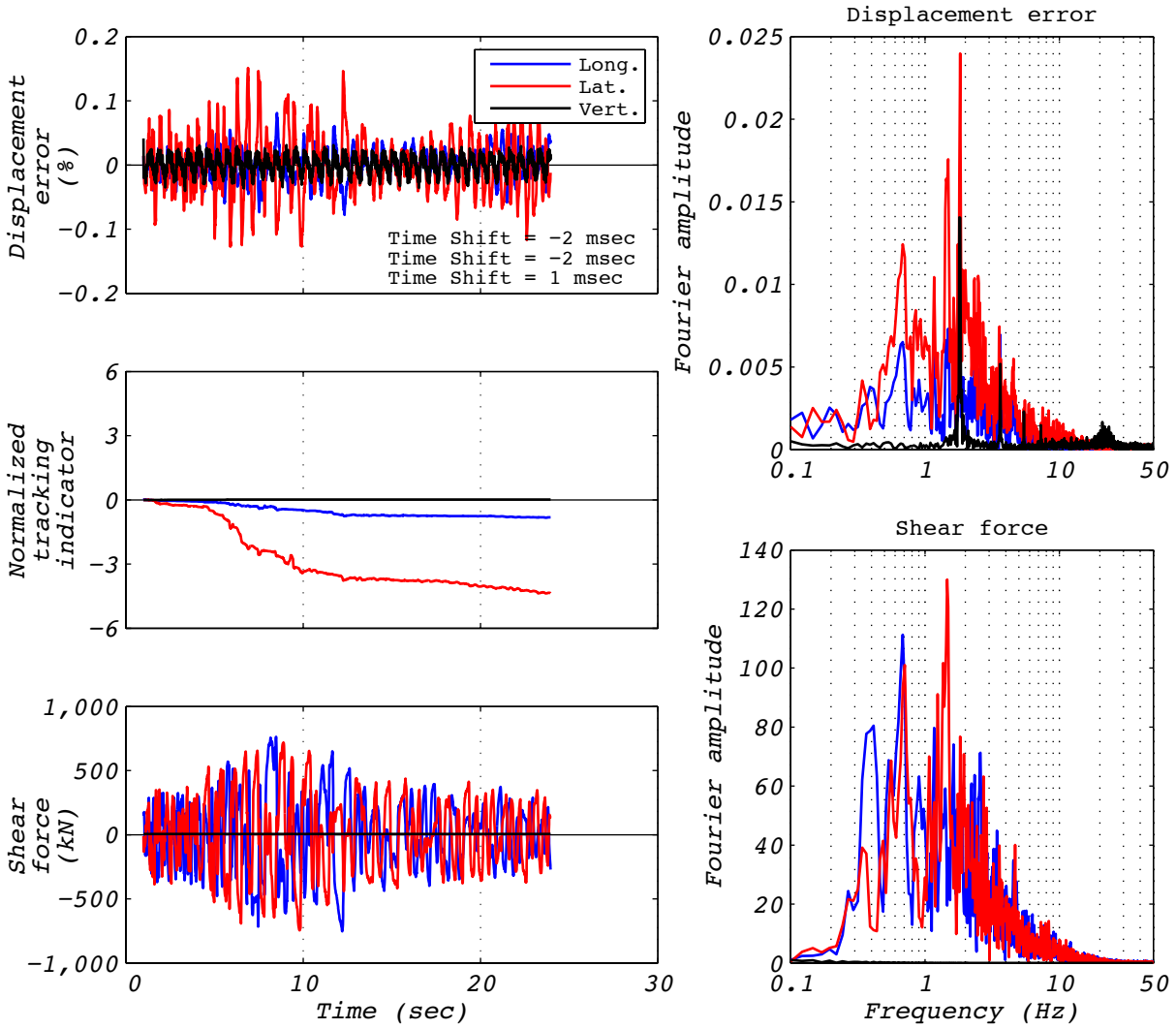

Figure A.21-1 Hybrid test performance metrics for run 78: EUR5, 3D with experimental bearing representing all bearings.

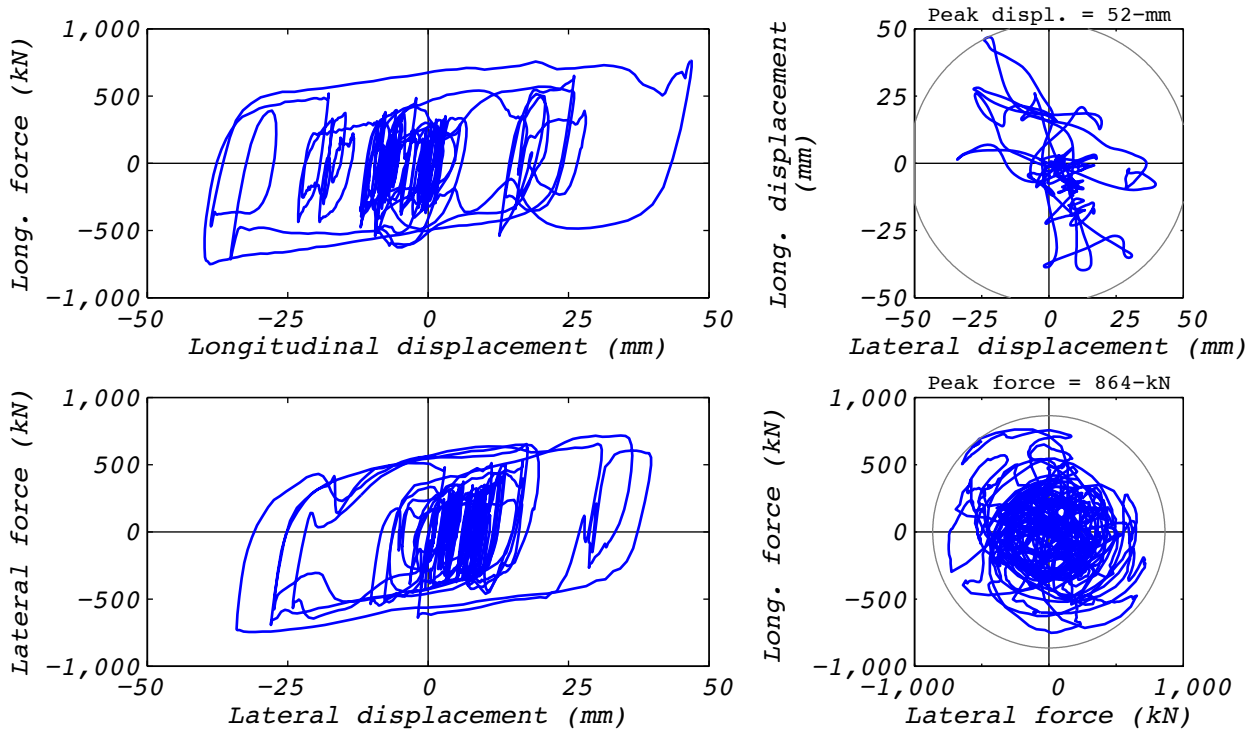

Figure A.21-2 Hybrid test bearing response for run 78: EUR5, 3D with experimental bearing representing all bearings.

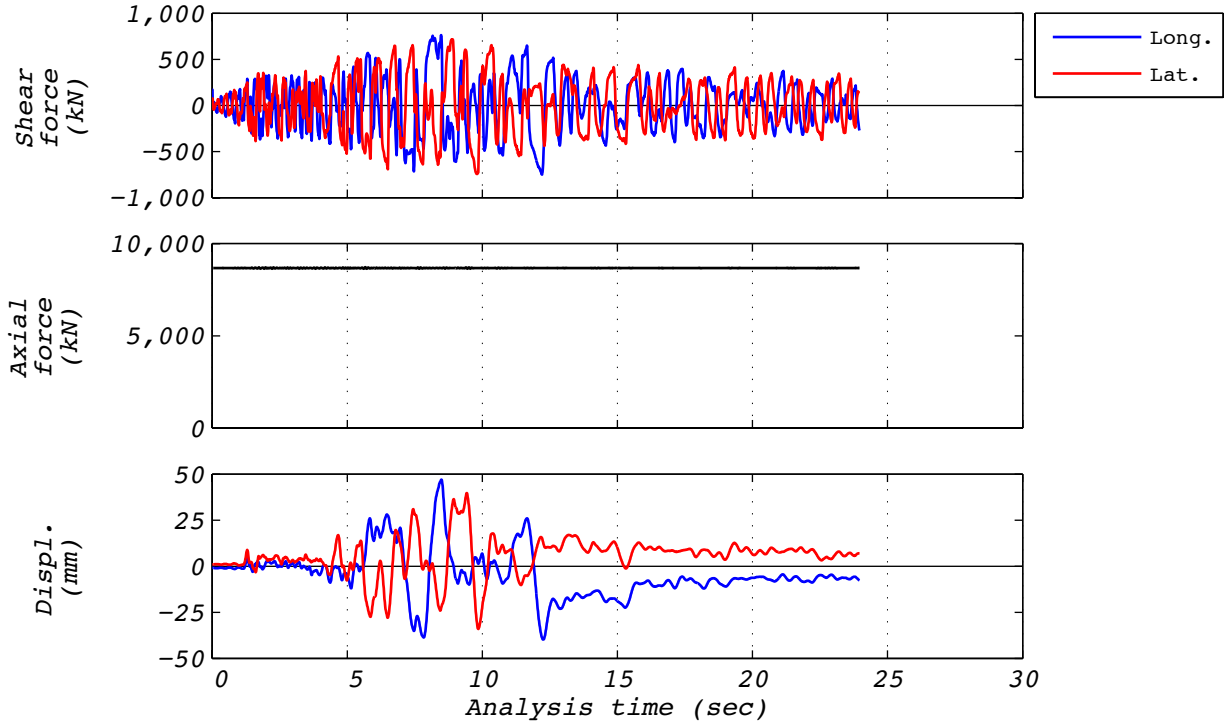

Figure A.21-3 Hybrid test time history responses for run 78: EUR5, 3D with experimental bearing representing all bearings.

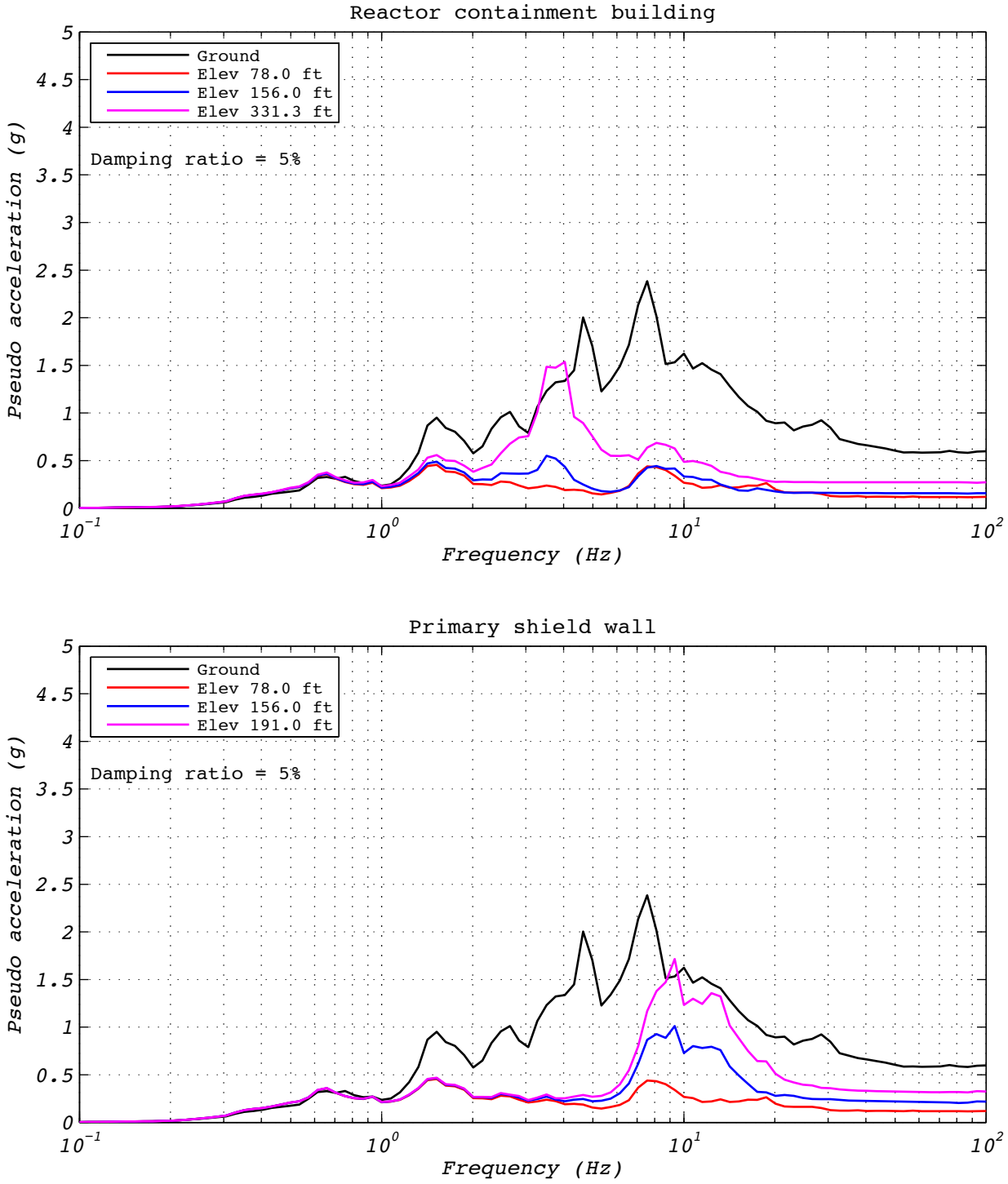

Figure A.21-4 Hybrid test floor spectra for run 78: EUR5, 3D with experimental bearing representing all bearings.

A.22 DEVELOPMENT RUN 79

Development run 79 was a hybrid test of the EUR dispersion appropriate ground motion number five. The model consisted of five groups of bearings. The experimental bearing's group was centrally located in the layout. Input motions consisted of two horizontal components. The axial load specified was the design axial load of 8,663 kN, but this dof command was included during the test. The test was executed at a rate 25 times slower than real time to compensate for machine delays. Bearing UET-1 was used in this test. Figure A.22-1 shows the fidelity achieved in the hybrid test. Figures A.22-2 and A.22-3 contain bearing responses, and Figure A.22-4 depicts the resulting floor response spectra for select locations in two of the isolated structures.

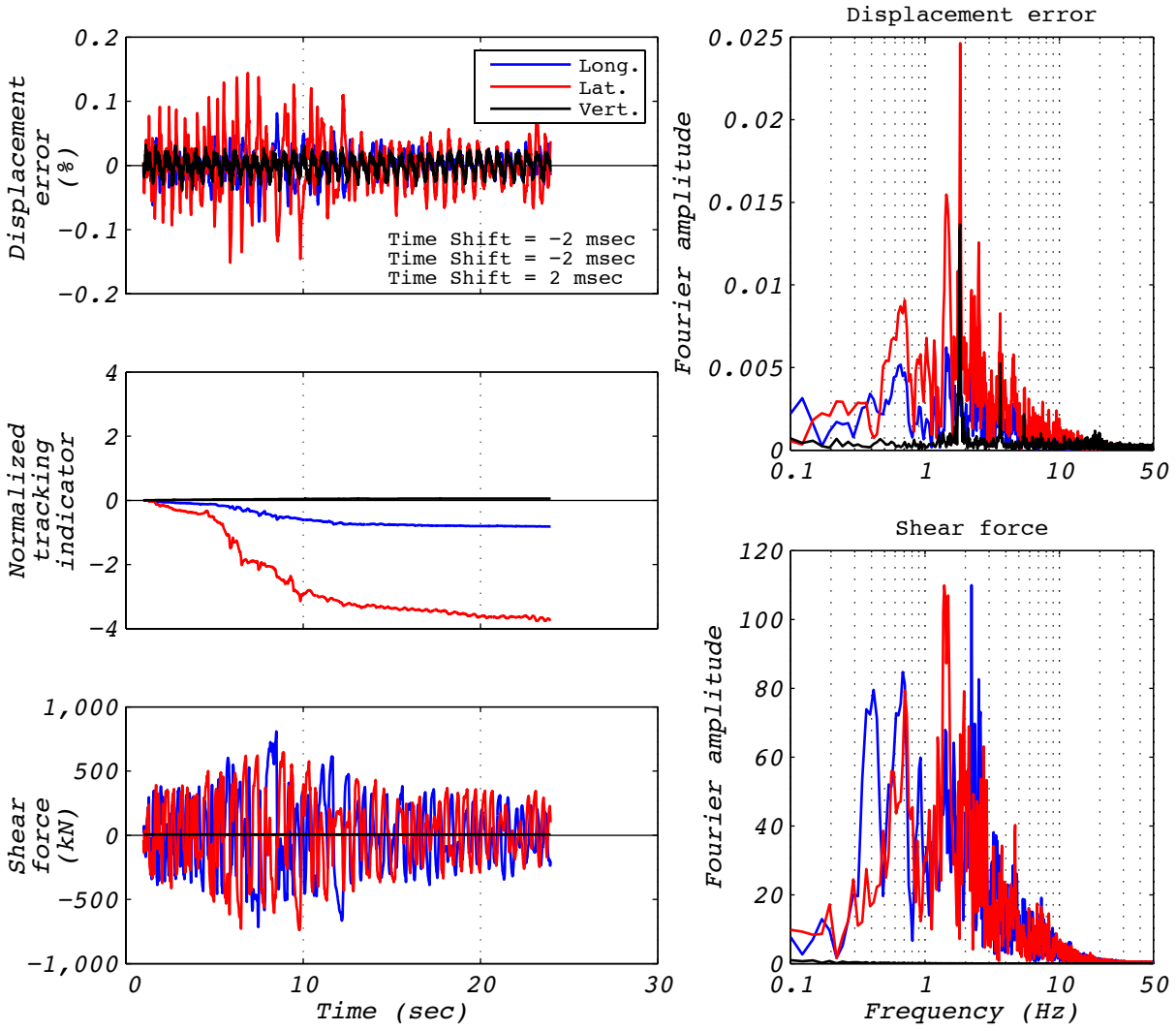

Figure A.22-1 Hybrid test performance metrics for run 79: EUR5, 3D with 5 groups of bearings and the experimental bearing representing the center group.

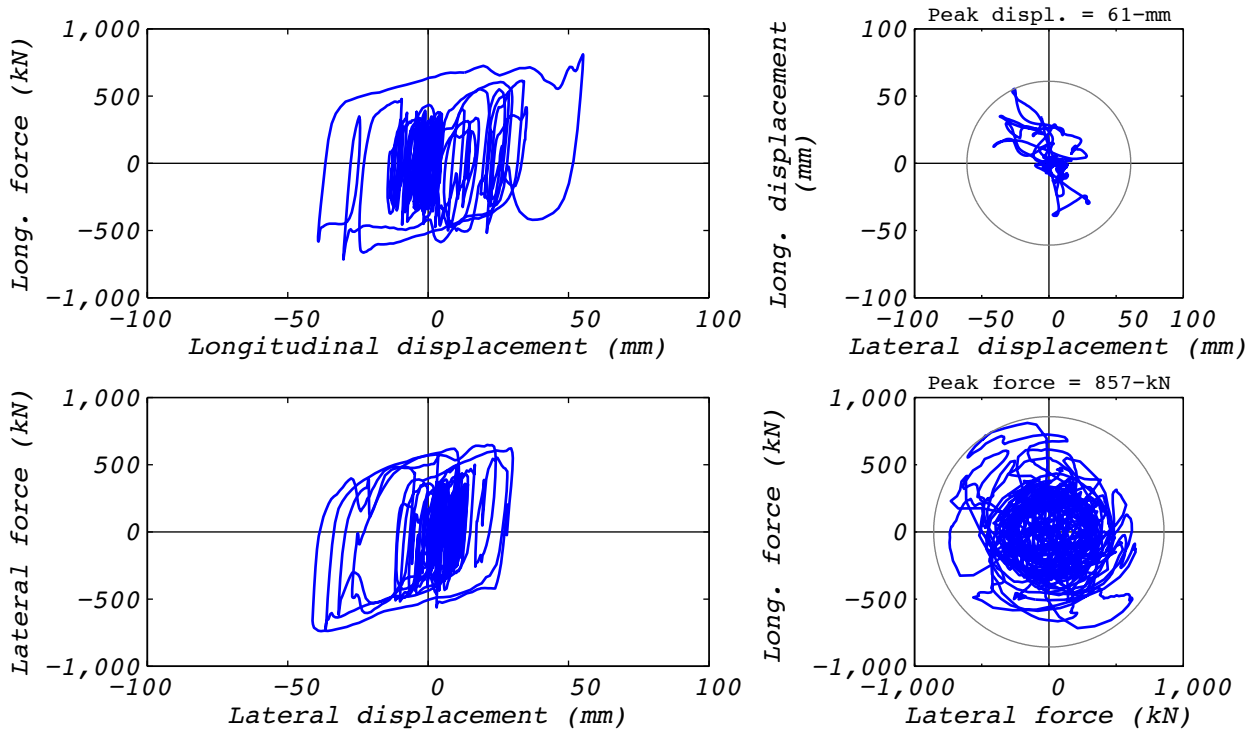

Figure A.22-2 Hybrid test bearing response for run 79: EUR5, 3D with 5 groups of bearings and the experimental bearing representing the center group.

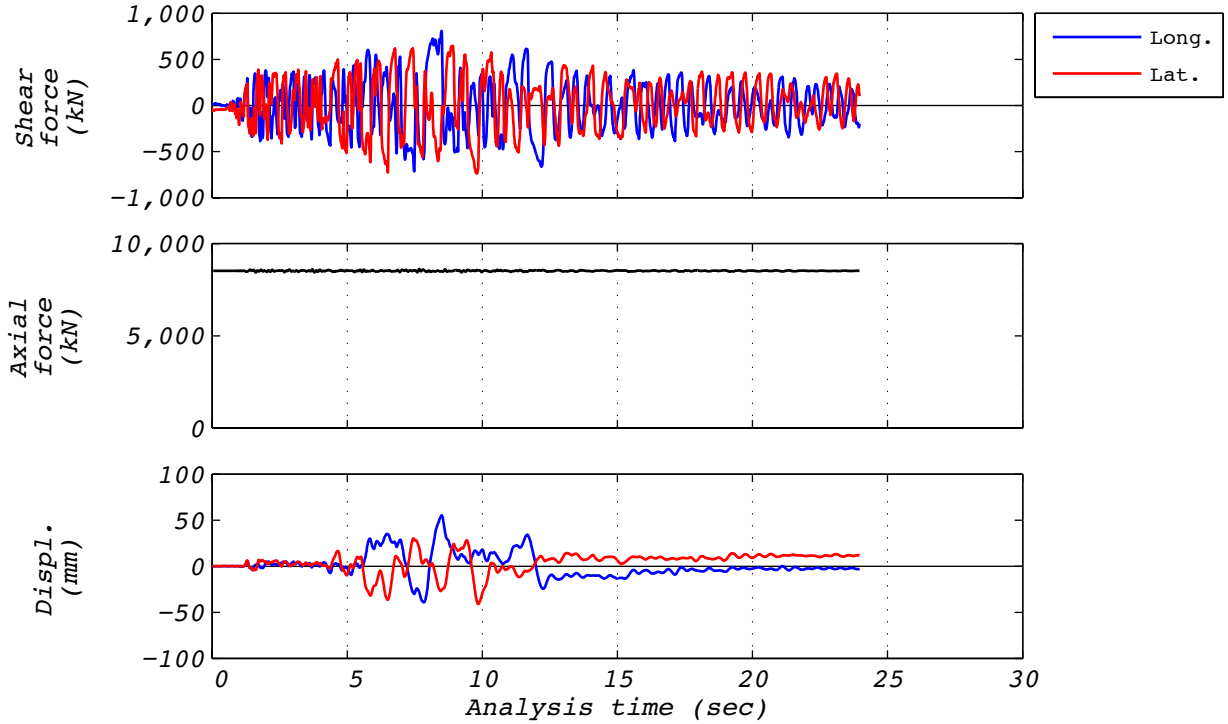

Figure A.22-3 Hybrid test time history responses for run 79: EUR5, 3D with 5 groups of bearings and the experimental bearing representing the center group.

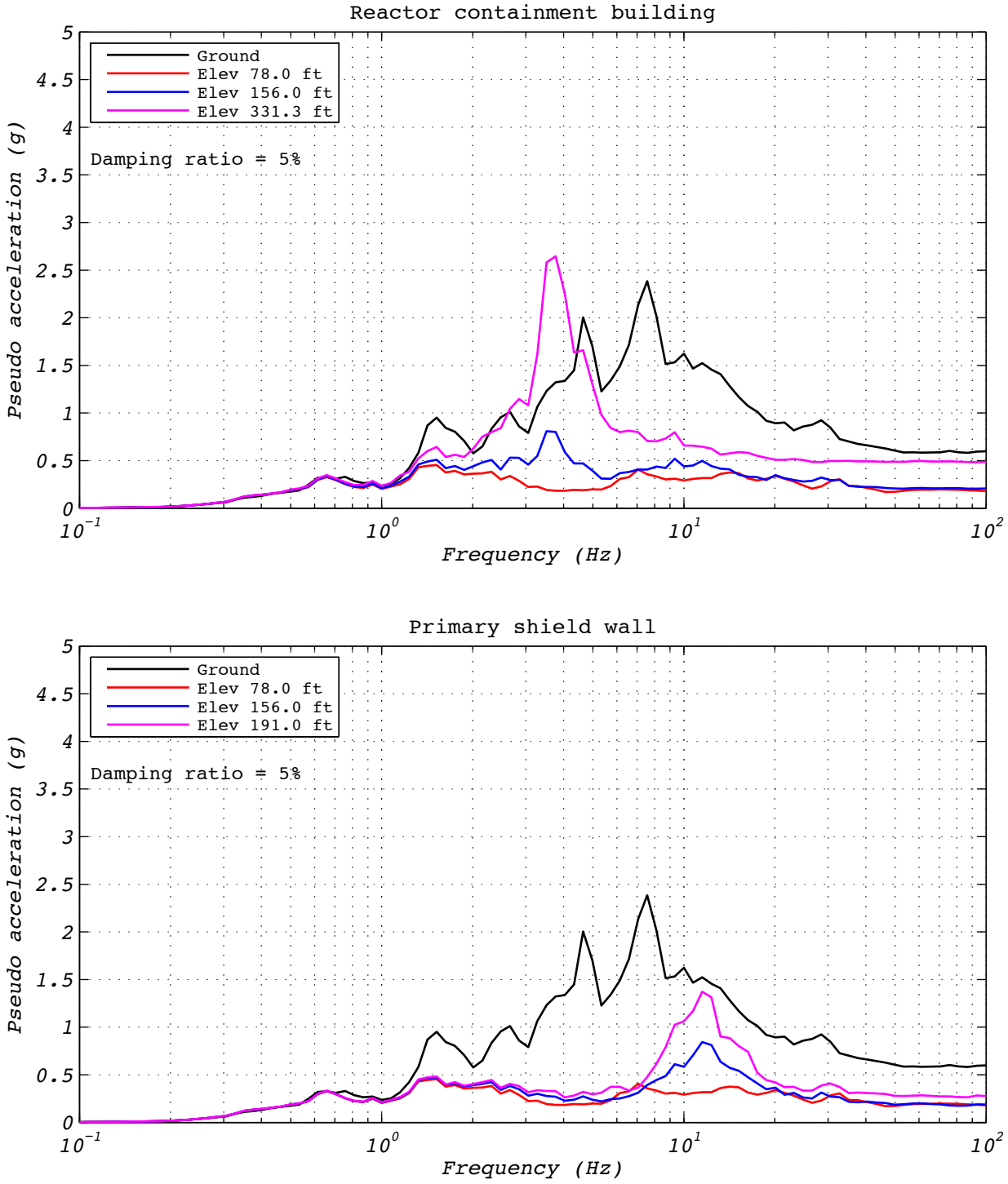

Figure A.22-4 Hybrid test floor spectra for run 79: EUR5, 3D with 5 groups of bearings and the experimental bearing representing the center group.

A.23 DEVELOPMENT RUN 80

Development run 80 was a hybrid test of the EUR dispersion appropriate ground motion number five. The model consisted of five groups of bearings. The experimental bearing's group was centrally located in the layout. Input motions consisted of two horizontal components. The axial load specified was the design axial load of 8,663 kN, but this dof command was included during the test. The test was executed at a rate 25 times slower than real time to compensate for machine delays. Bearing UET-1 was used in this test. Figure A.23-1 shows the fidelity achieved in the hybrid test. Figures A.23-2 and A.23-3 contain bearing responses, and Figure A.23-4 depicts the resulting floor response spectra for select locations in two of the isolated structures.

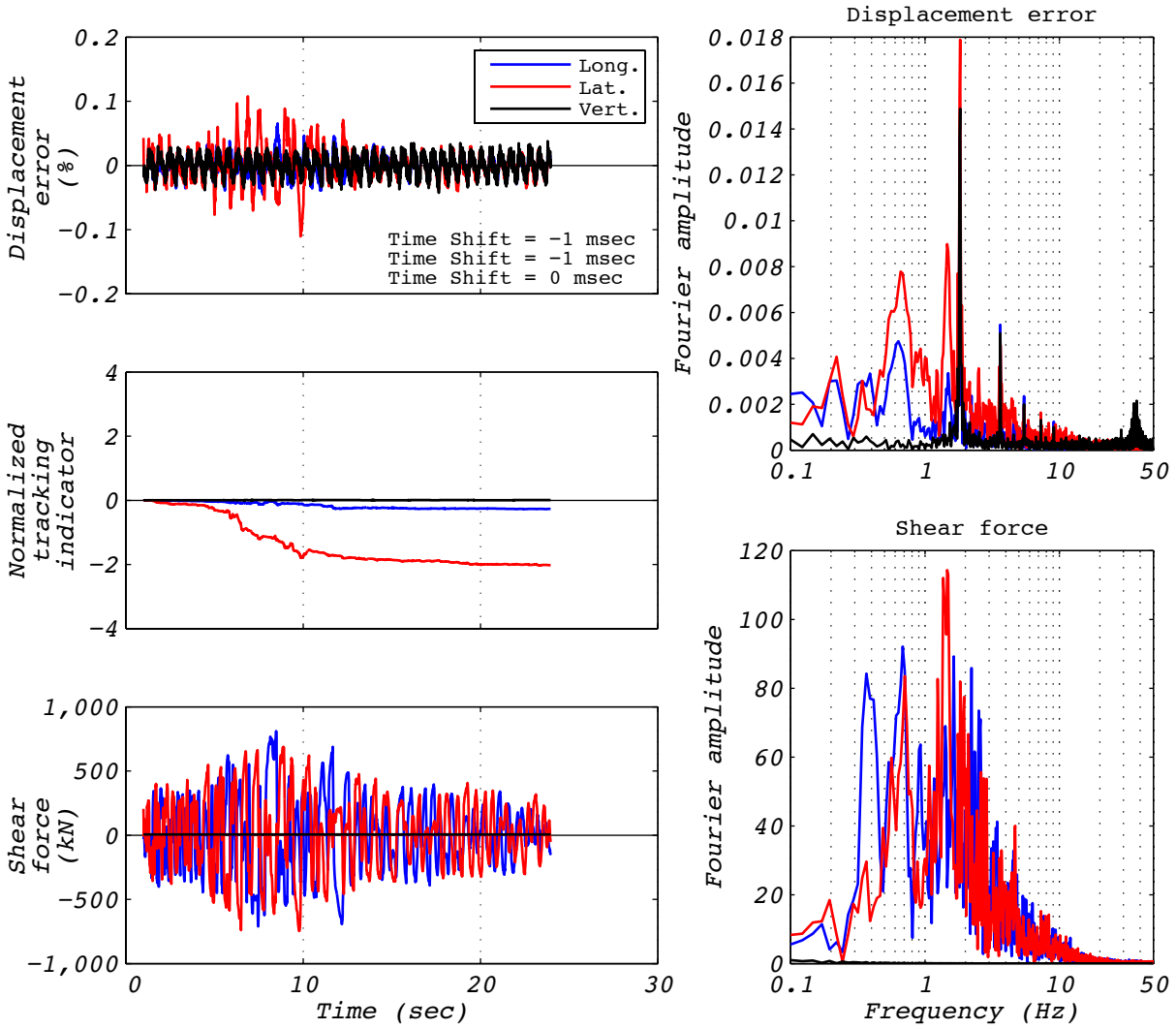

Figure A.23-1 Hybrid test performance metrics for run 80: EUR5, 3D with 5 groups of bearings and the experimental bearing representing the center group.

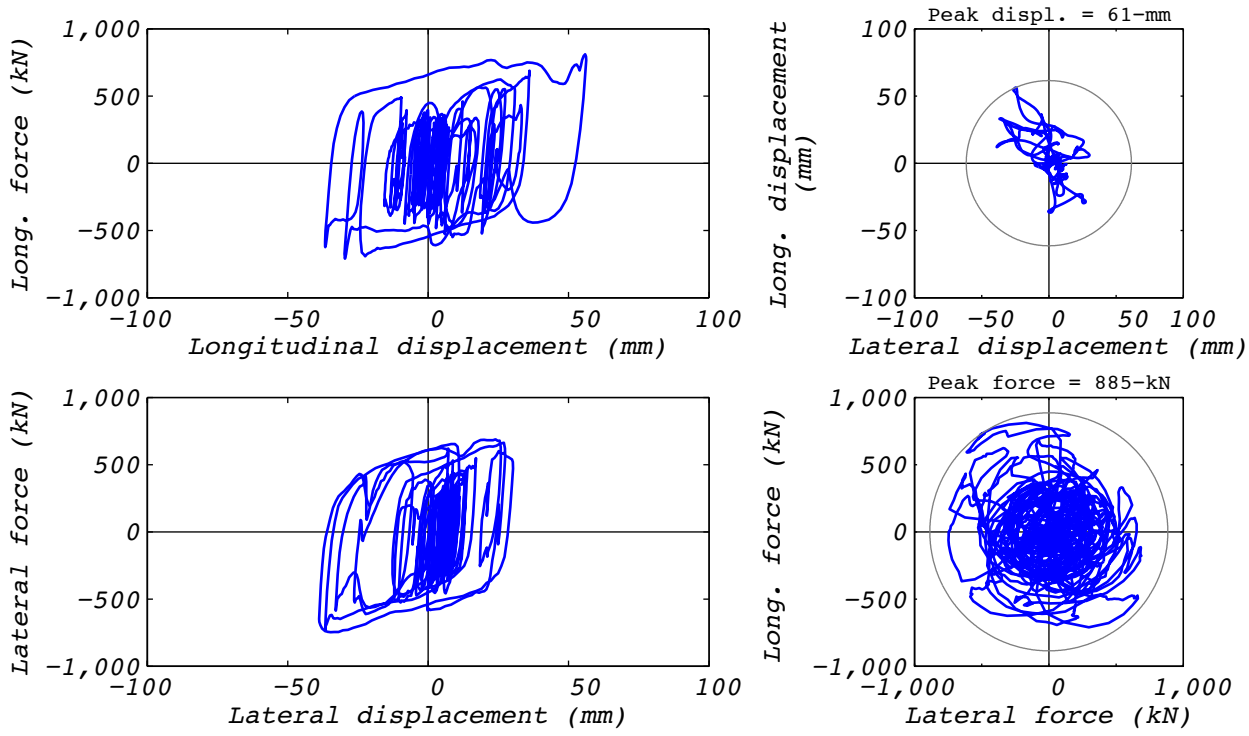

Figure A.23-2 Hybrid test bearing response for run 80: EUR5, 3D with 5 groups of bearings and the experimental bearing representing the center group.

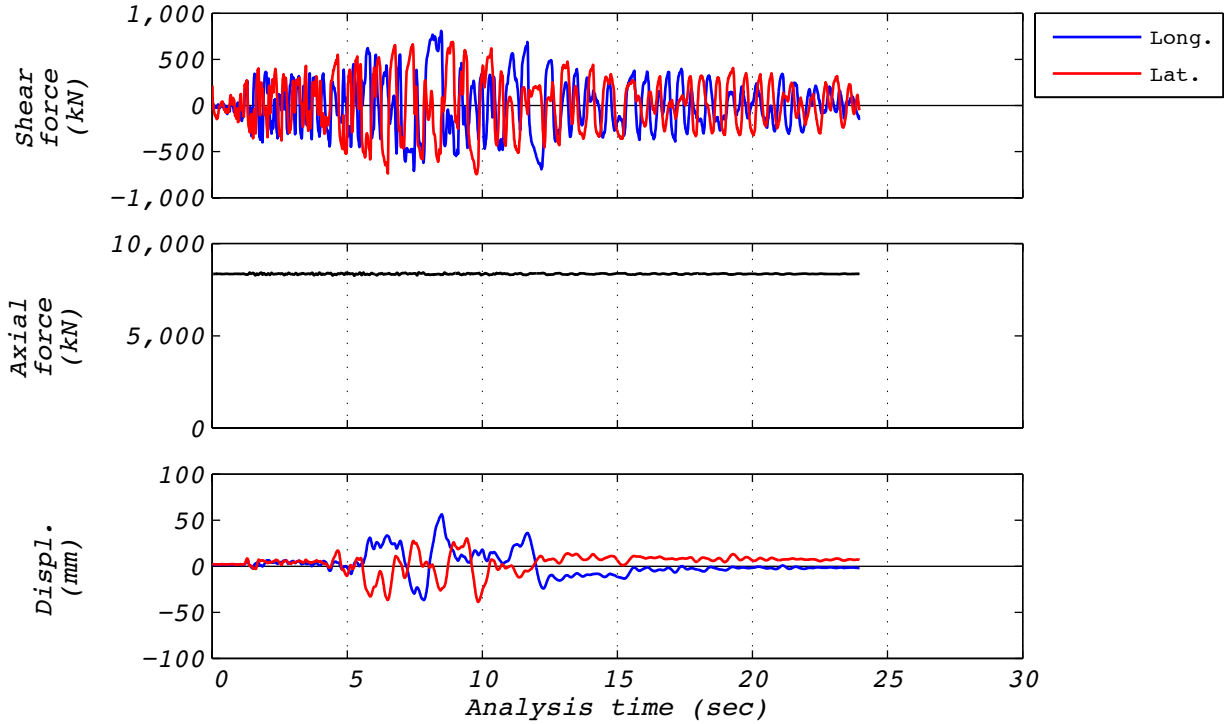

Figure A.23-3 Hybrid test time history responses for run 80: EUR5, 3D with 5 groups of bearings and the experimental bearing representing the center group.

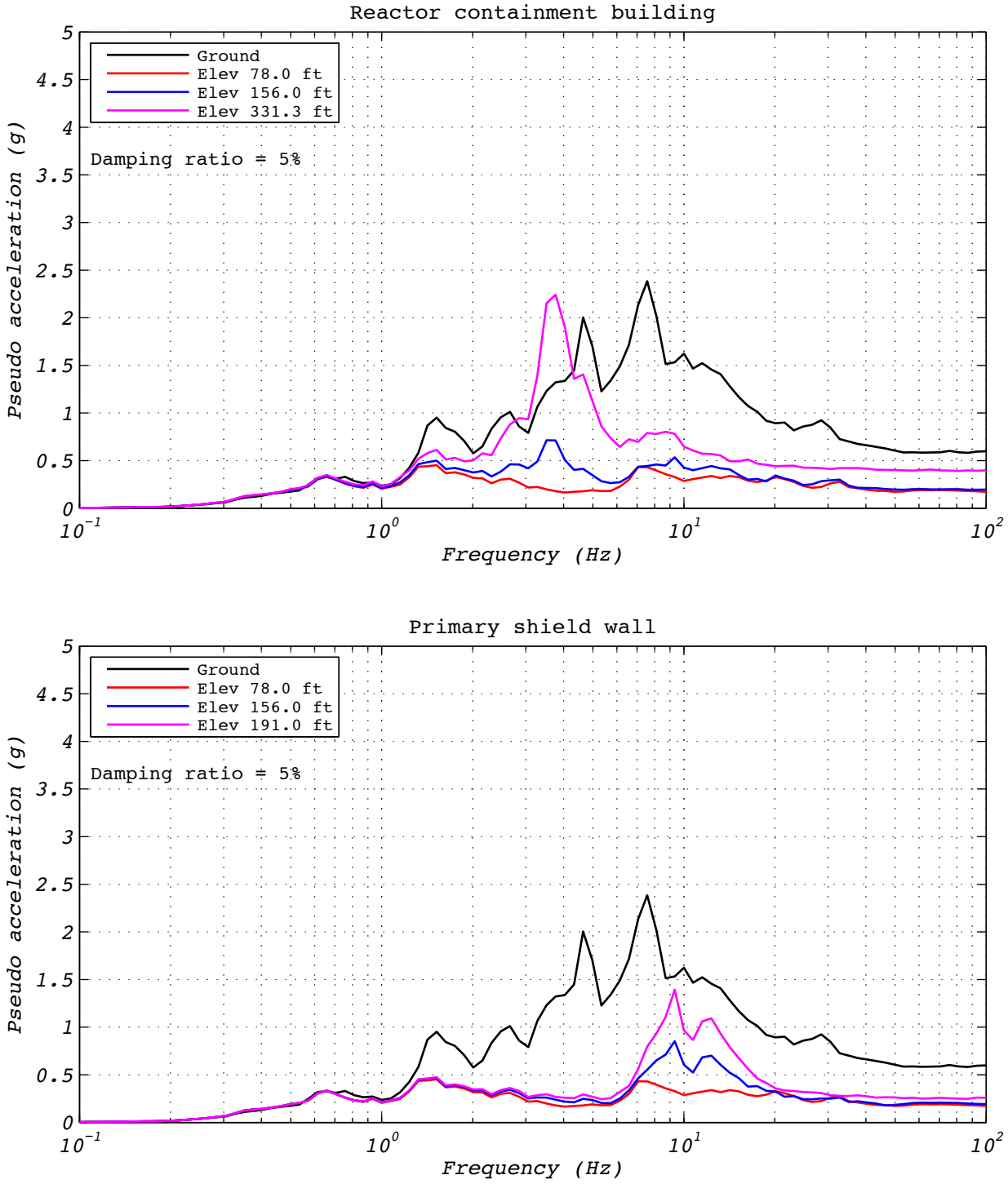

Figure A.23-4 Hybrid test floor spectra for run 80: EUR5, 3D with 5 groups of bearings and the experimental bearing representing the center group.

A.24 TEST RUN 82

Test run 82 was a hybrid test of the EUR dispersion appropriate ground motion number five. The model consisted of five groups of bearings. The experimental bearing's group was centrally located in the layout. Input motions consisted of two horizontal components. The axial load was specified as the design axial load of 8,663 kN, but this dof command was included during the test. The test was executed at a rate 25 times slower than real time to compensate for machine delays. Bearing UET-1 was used in this test. Figure A.24-1 shows the fidelity achieved in the hybrid test. Figures A.24-2 and A.24-3 contain bearing responses, and Figure A.24-4 depicts the resulting floor response spectra for select locations in two of the isolated structures.

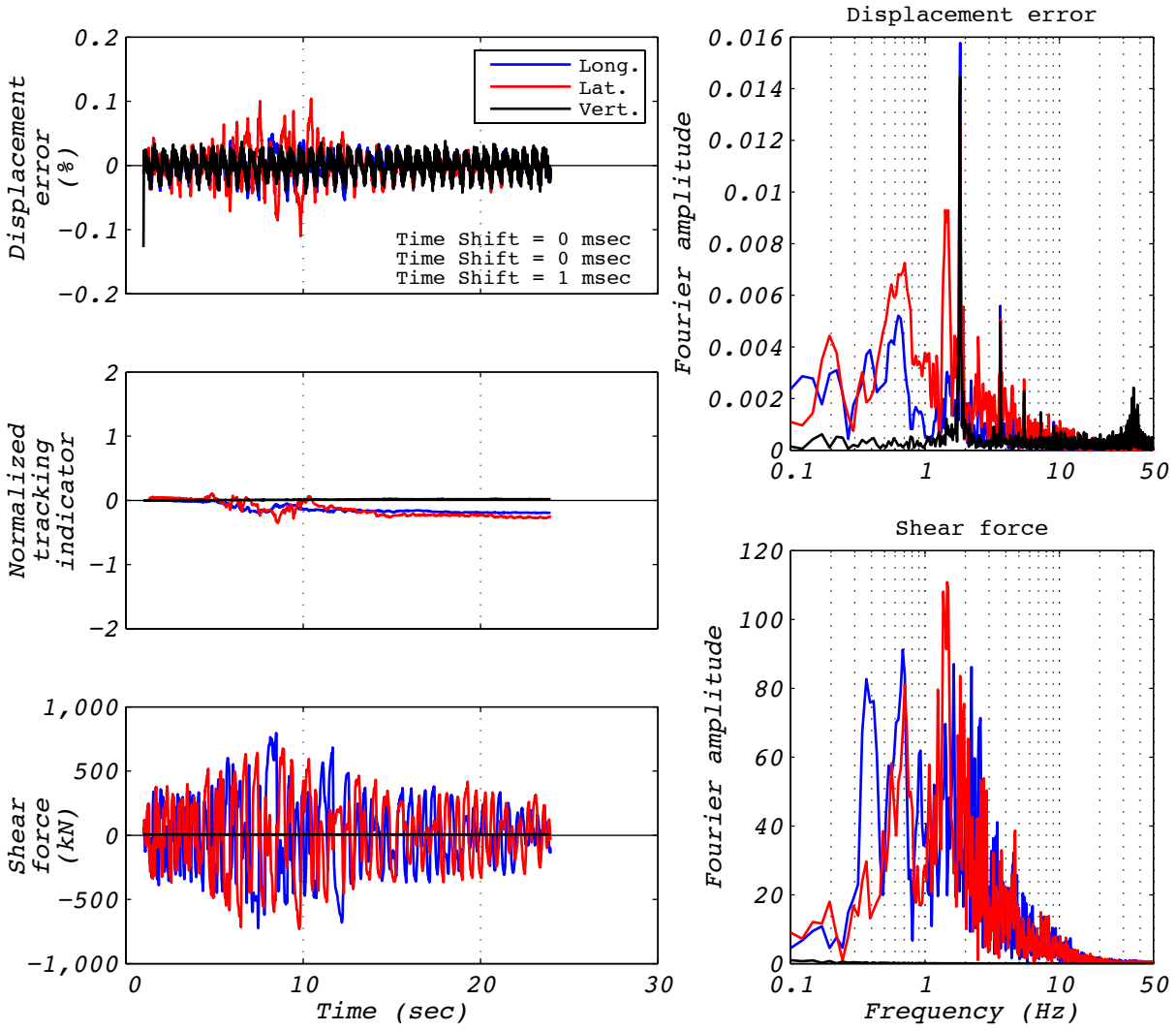

Figure A.24-1 Hybrid test performance metrics for run 82: EUR5, 3D with 5 groups of bearings and the experimental bearing representing the center group.

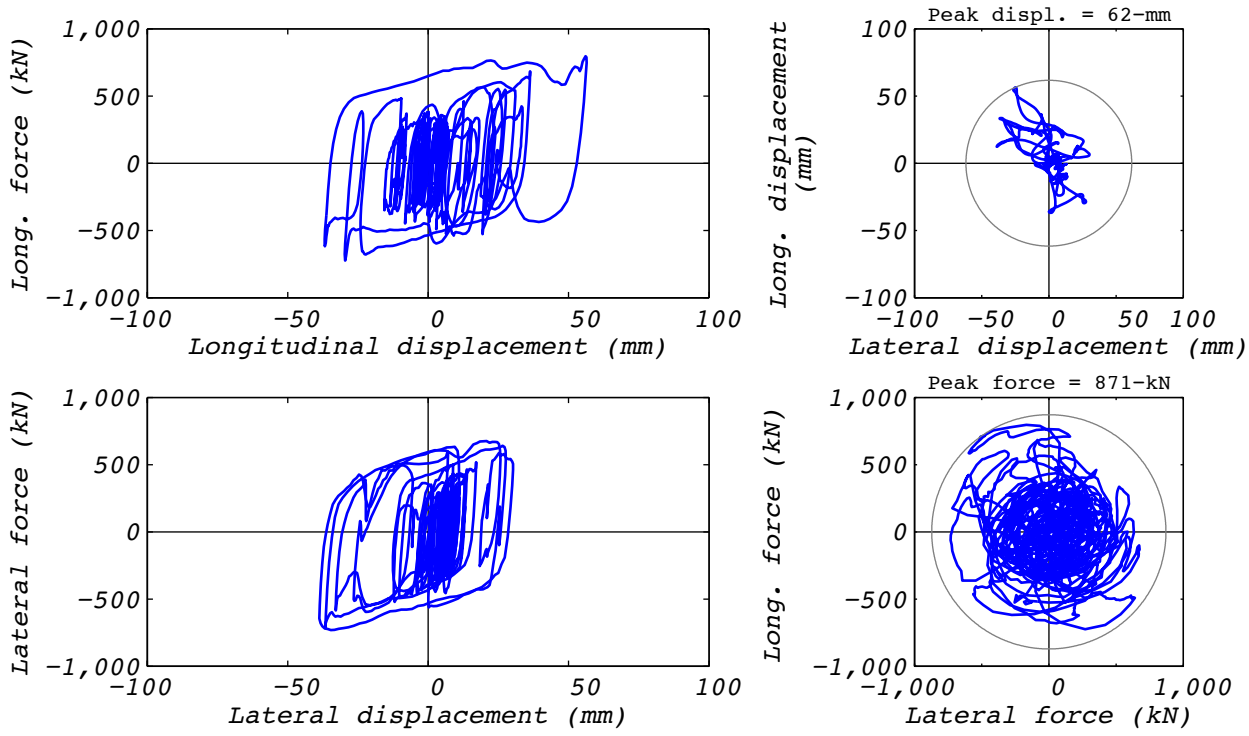

Figure A.24-2 Hybrid test bearing response for run 82: EUR5, 3D with 5 groups of bearings and the experimental bearing representing the center group.

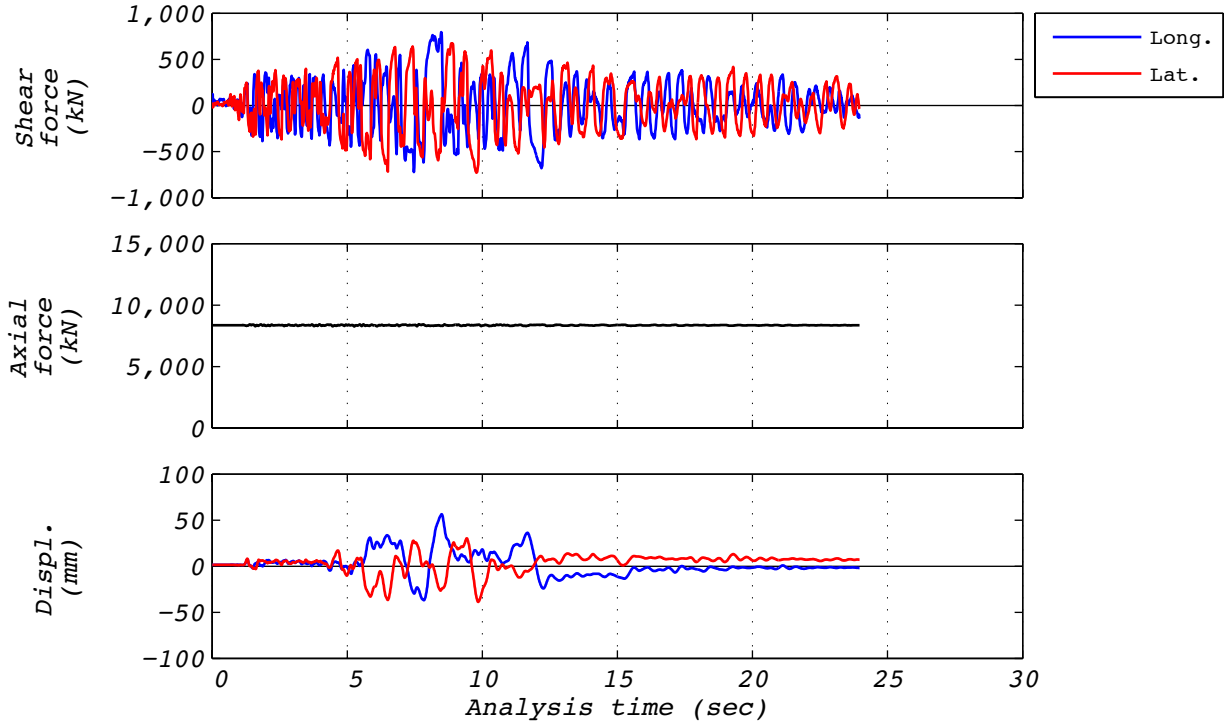

Figure A.24-3 Hybrid test time history responses for run 82: EUR5, 3D with 5 groups of bearings and the experimental bearing representing the center group.

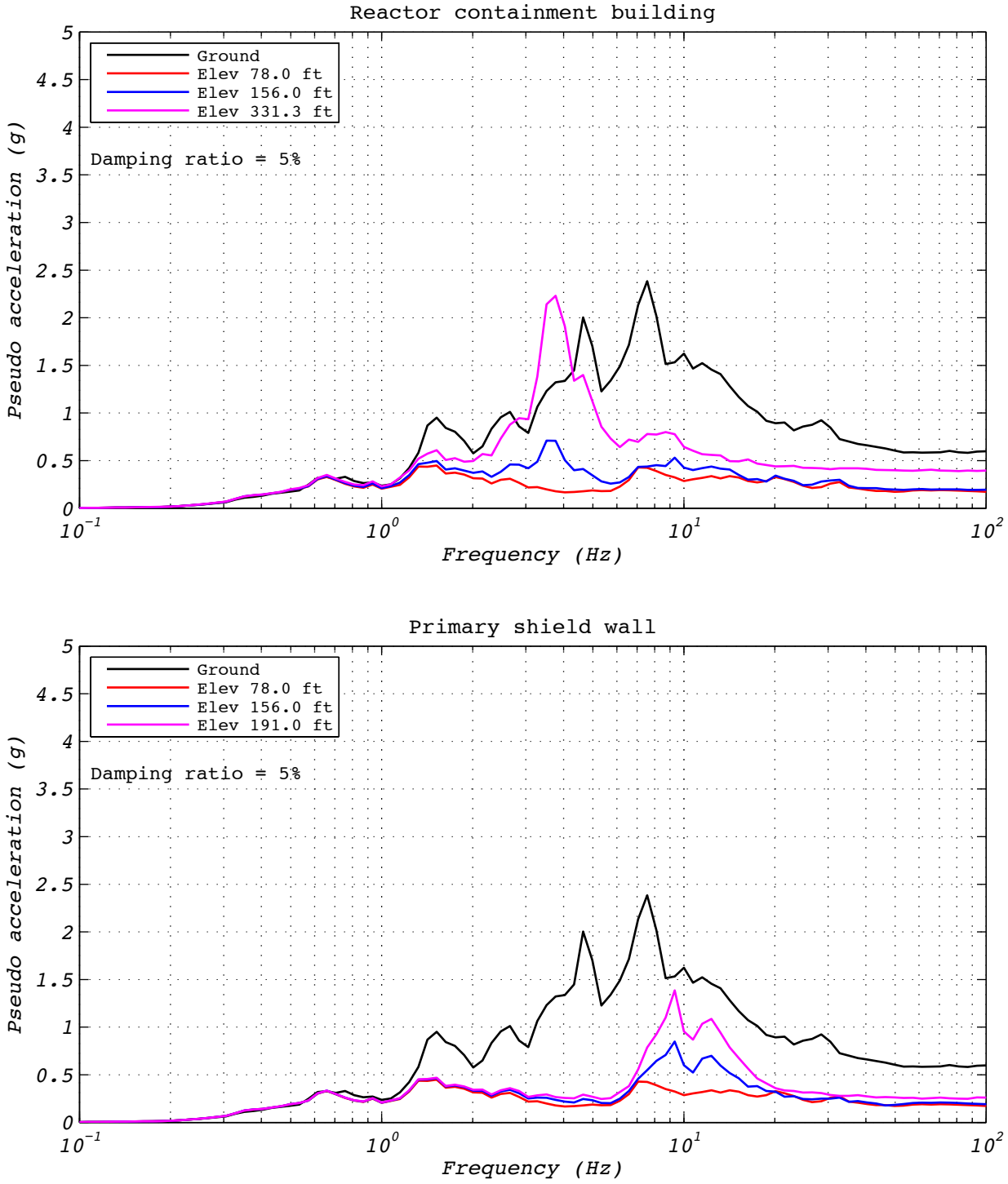

Figure A.24-4 Hybrid test floor spectra for run 82: EUR5, 3D with 5 groups of bearings and the experimental bearing representing the center group.

A.25 TEST RUN 83

Test run 83 was a hybrid test of the EUR dispersion appropriate ground motion number five. The model consisted of five groups of bearings. The experimental bearing's group was located in corner number 3 of the layout. Input motions consisted of two horizontal components. The axial load was specified as the design axial load of 8,663 kN, but this dof command was included during the test. The test was executed at a rate 25 times slower than real time to compensate for machine delays. Bearing UET-1 was used in this test. Figure A.25-1 shows the fidelity achieved in the hybrid test. Figures A.25-2 and A.25-3 contain bearing responses, and Figure A.25-4 depicts the resulting floor response spectra for select locations in two of the isolated structures.

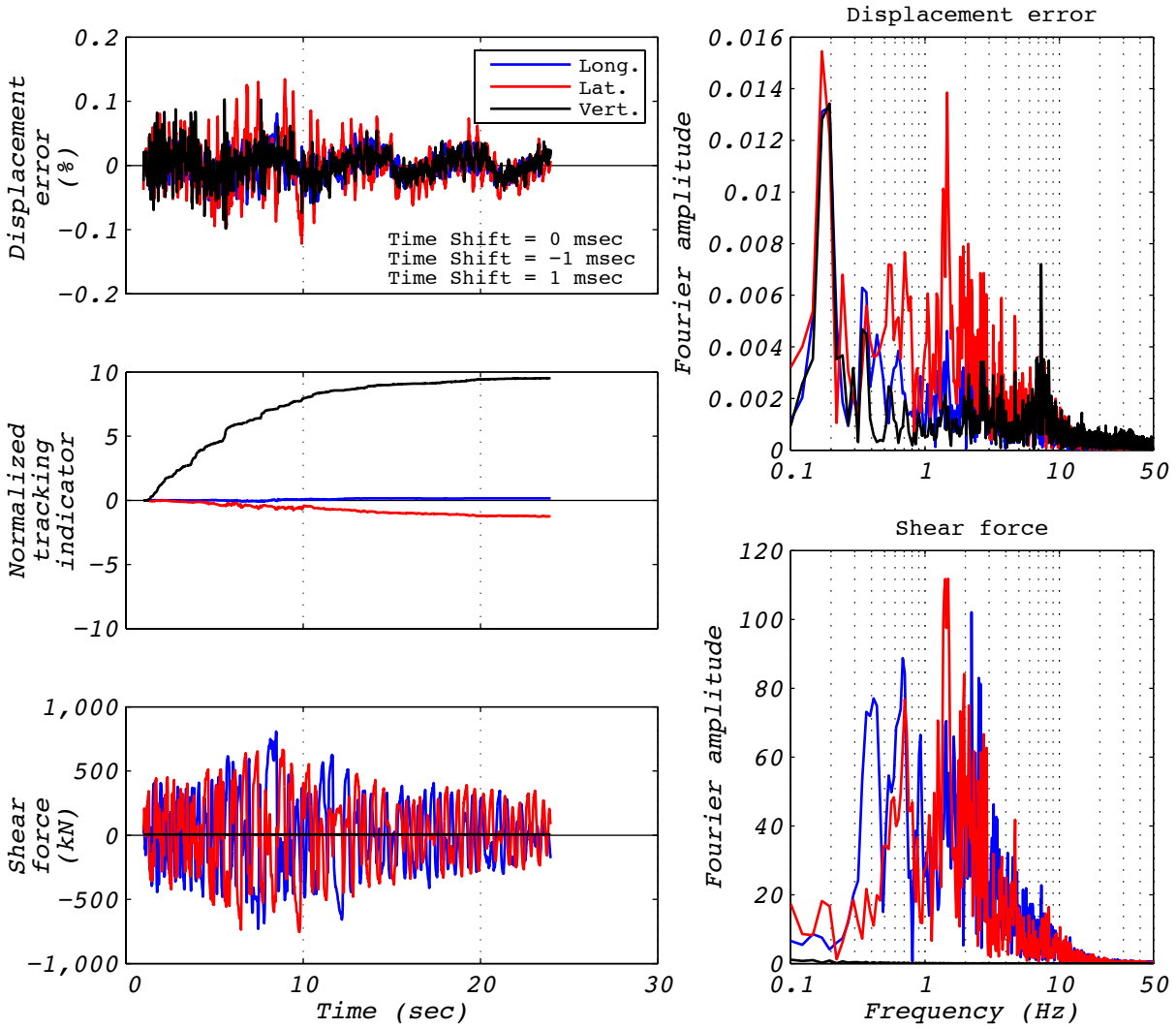

Figure A.25-1 Hybrid test performance metrics for run 83: EUR5, 3D with 5 groups of bearings and the experimental bearing representing the no. 3 corner group.

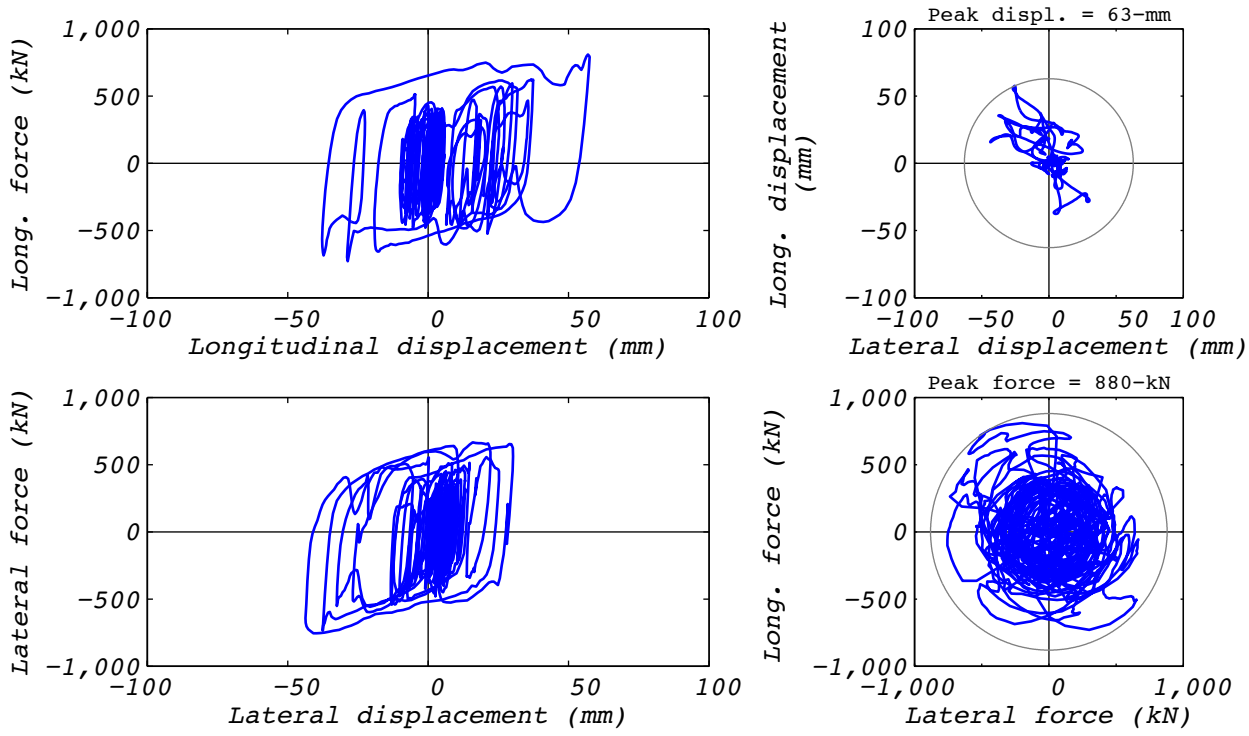

Figure A.25-2 Hybrid test bearing response for run 83: EUR5, 3D with 5 groups and the experimental bearing representing the no. 3 corner group.

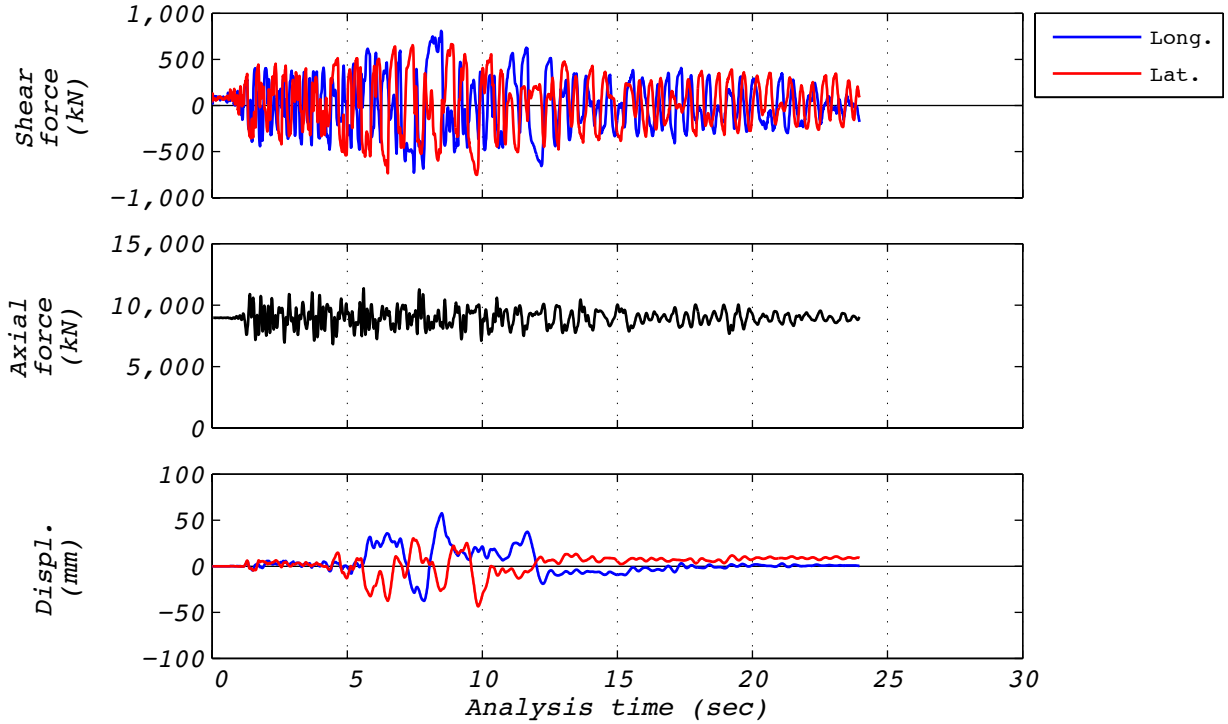

Figure A.25-3 Hybrid test time history responses for run 83: EUR5, 3D with 5 groups and the experimental bearing representing the no. 3 corner group.

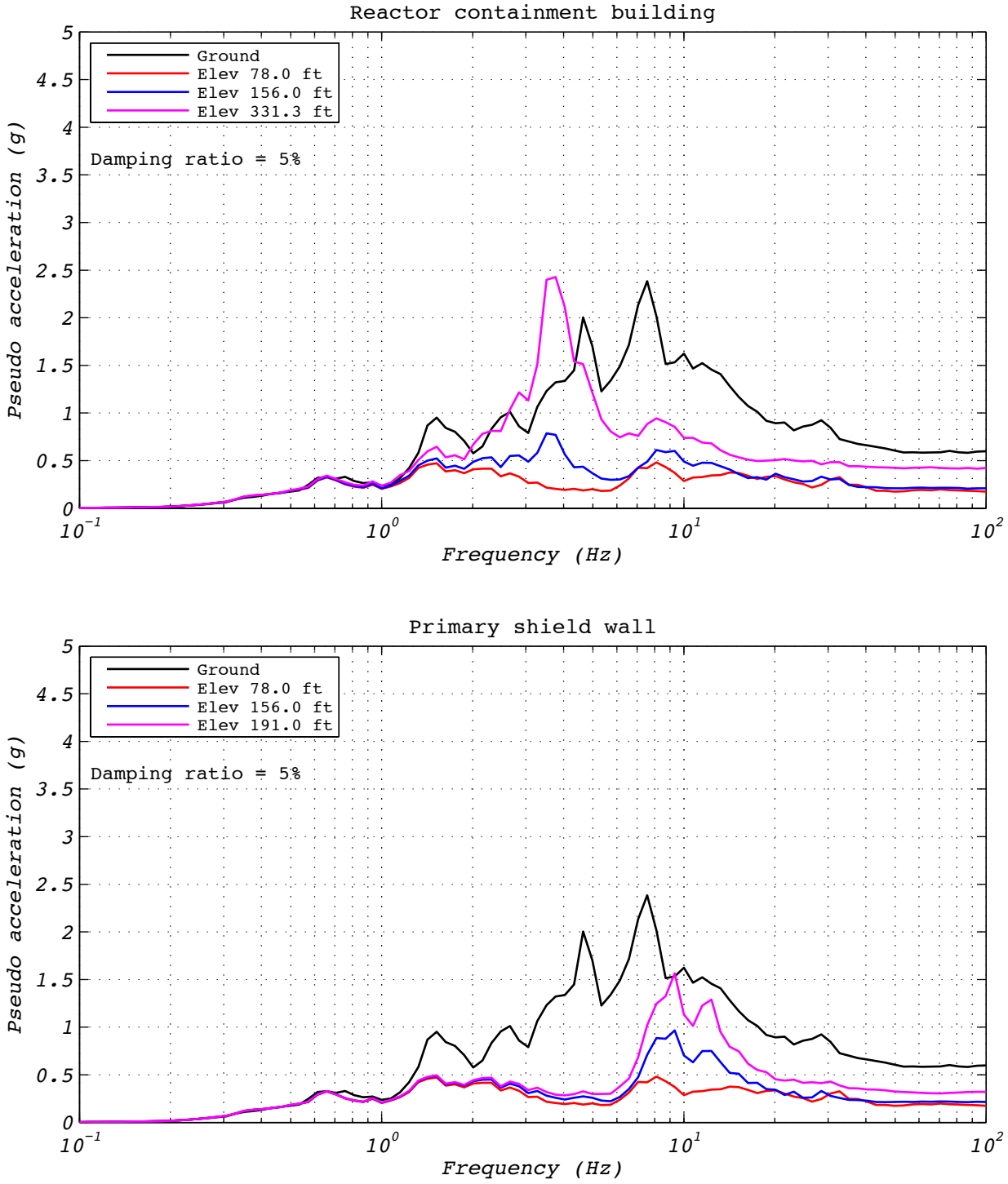

Figure A.25-4 Hybrid test floor spectra for run 83: EUR5, 3D with 5 groups of bearings and the experimental bearing representing the no. 3 corner group.

A.26 TEST RUN 84

Test run 84 was a hybrid test of the NRC dispersion appropriate ground motion number 15. The model consisted of five groups of bearings. The experimental bearing's group was centrally located in the layout. Input motions consisted of two horizontal components. The axial load was specified as the design axial load of 8,663 kN, but this dof command was included during the test. The test was executed at a rate 25 times slower than real time to compensate for machine delays. Bearing UET-1 was used in this test. Figure A.26-1 shows the fidelity achieved in the hybrid test. Figures A.26-2 and A.26-3 contain bearing responses, and Figure A.26-4 depicts the resulting floor response spectra for select locations in two of the isolated structures.

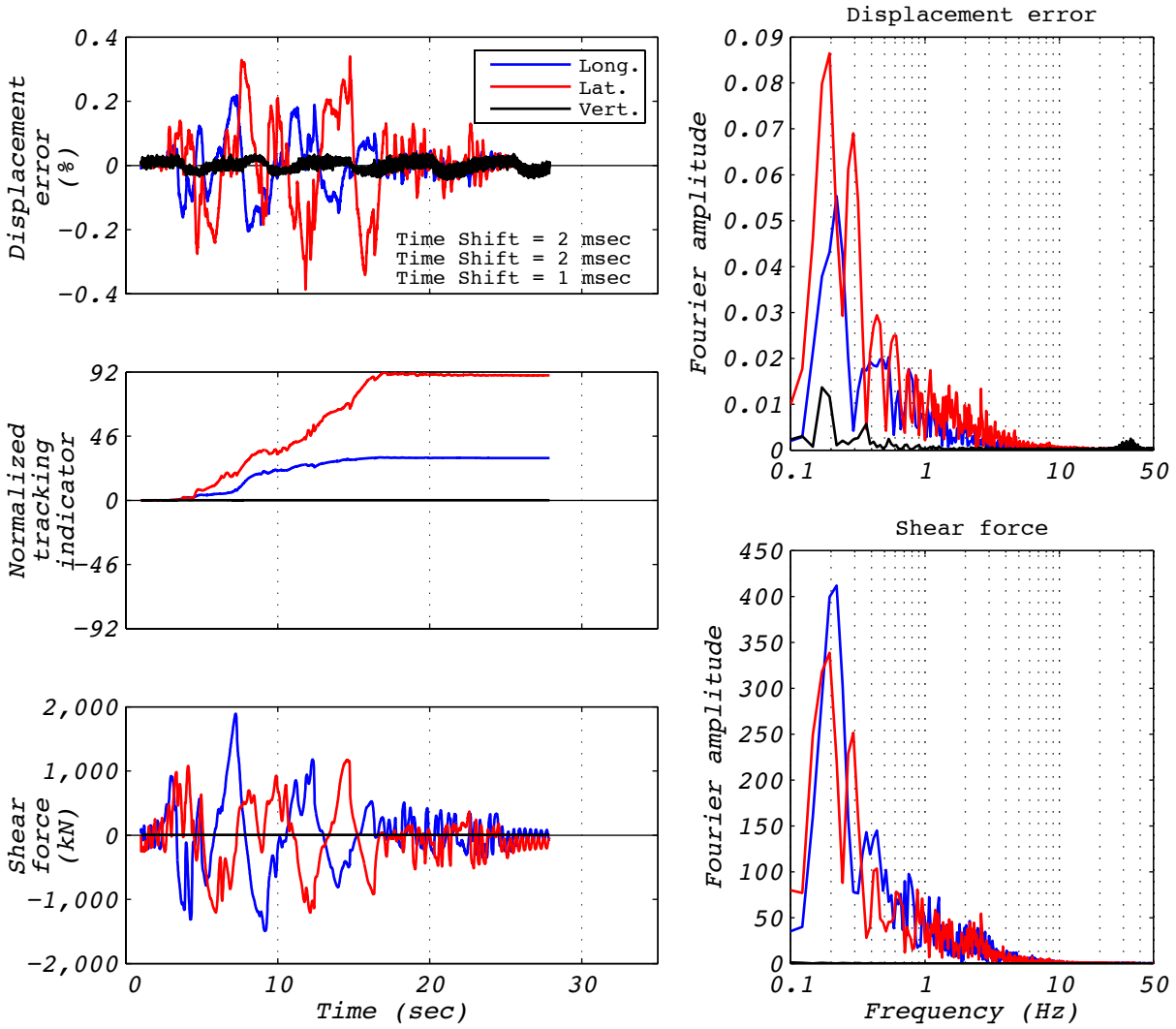

Figure A.26-1 Hybrid test performance metrics for run 84: NRC15, 3D with 5 groups of bearings and the experimental bearing representing the center group.

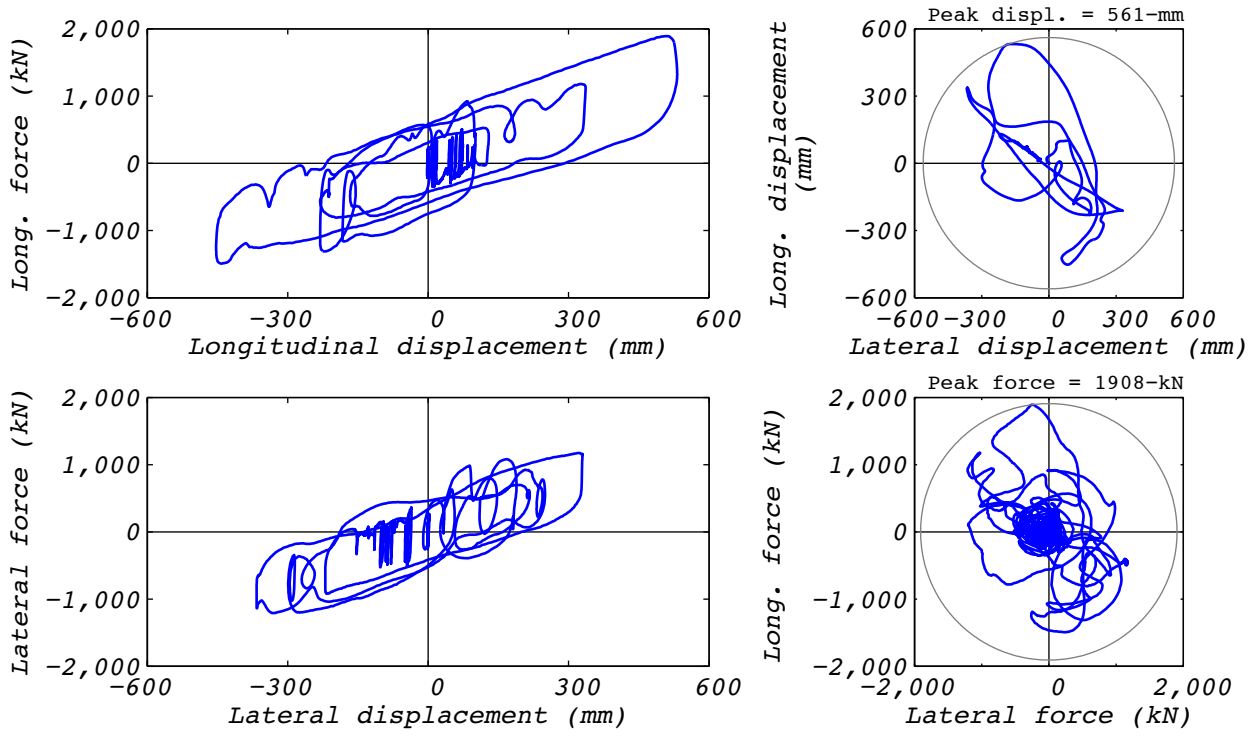

Figure A.26-2 Hybrid test bearing response for run 84: NRC15, 3D with 5 groups of bearings and the experimental bearing representing the center group.

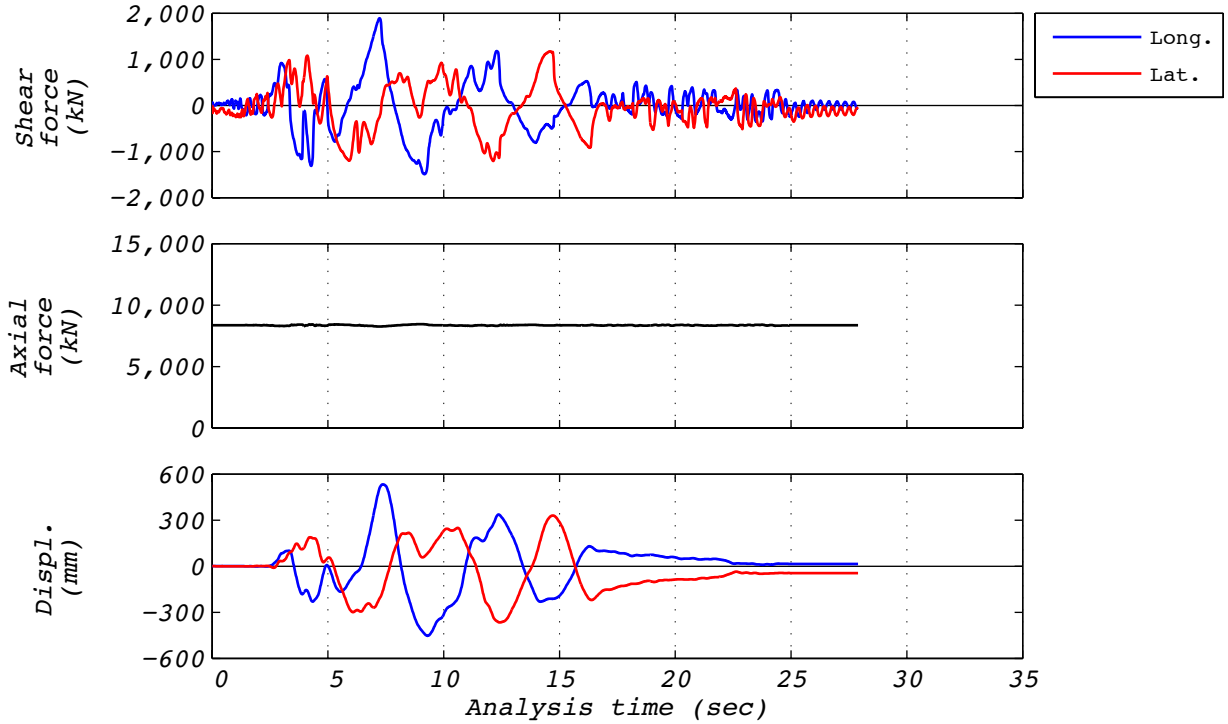

Figure A.26-3 Hybrid test time history responses for run 84: NRC15, 3D with 5 groups of bearings and the experimental bearing representing the center group.

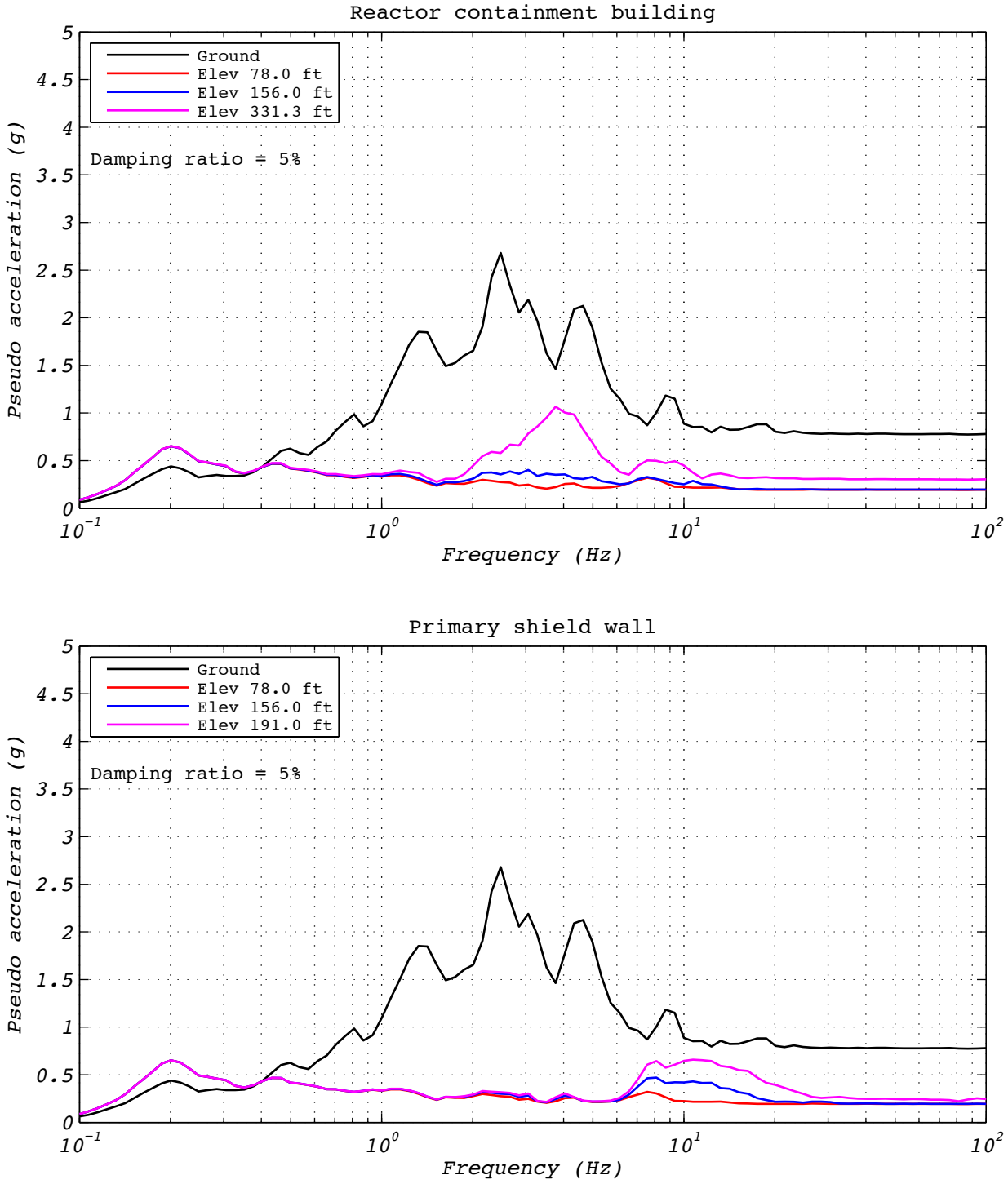

Figure A.26-4 Hybrid test floor spectra for run 84: NRC15, 3D with 5 groups of bearings and the experimental bearing representing the center group.

A.27 TEST RUN 85

Test run 85 was a hybrid test of the NRC dispersion appropriate ground motion number 15. The model consisted of five groups of bearings. The experimental bearing's group was located in corner number 3 of the layout. Input motions consisted of two horizontal components. The axial load was specified as the design axial load of 8,663 kN, but this dof command was included during the test. The test was executed at a rate 25 times slower than real time to compensate for machine delays. Bearing UET-1 was used in this test. Figure A.27-1 shows the fidelity achieved in the hybrid test. Figures A.27-2 and A.27-3 contain bearing responses, and Figure A.27-4 depicts the resulting floor response spectra for select locations in two of the isolated structures.

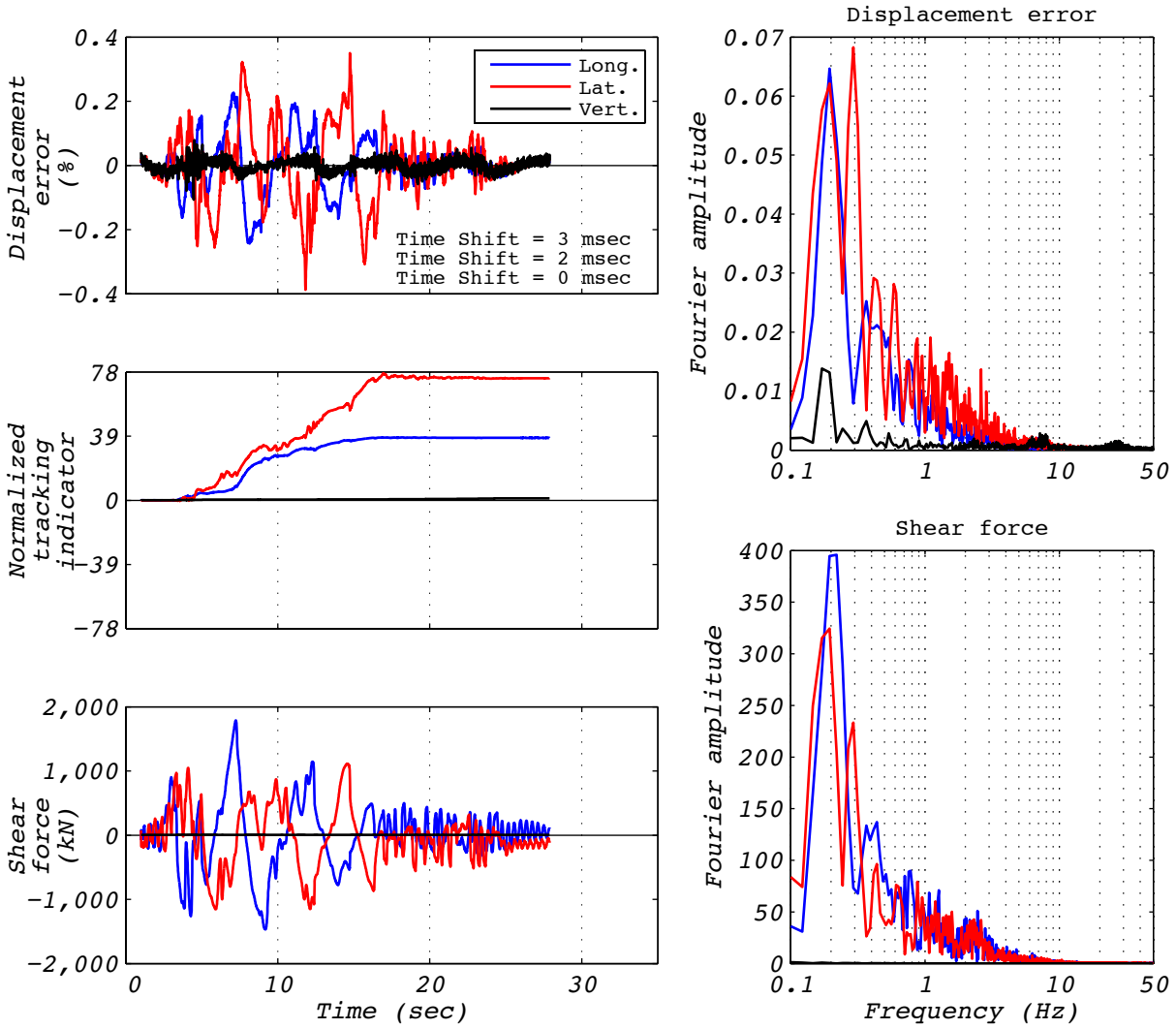

Figure A.27-1 Hybrid test performance metrics for run 85: NRC15, 3D with 5 groups of bearings and the experimental bearing representing the no. 3 corner group.

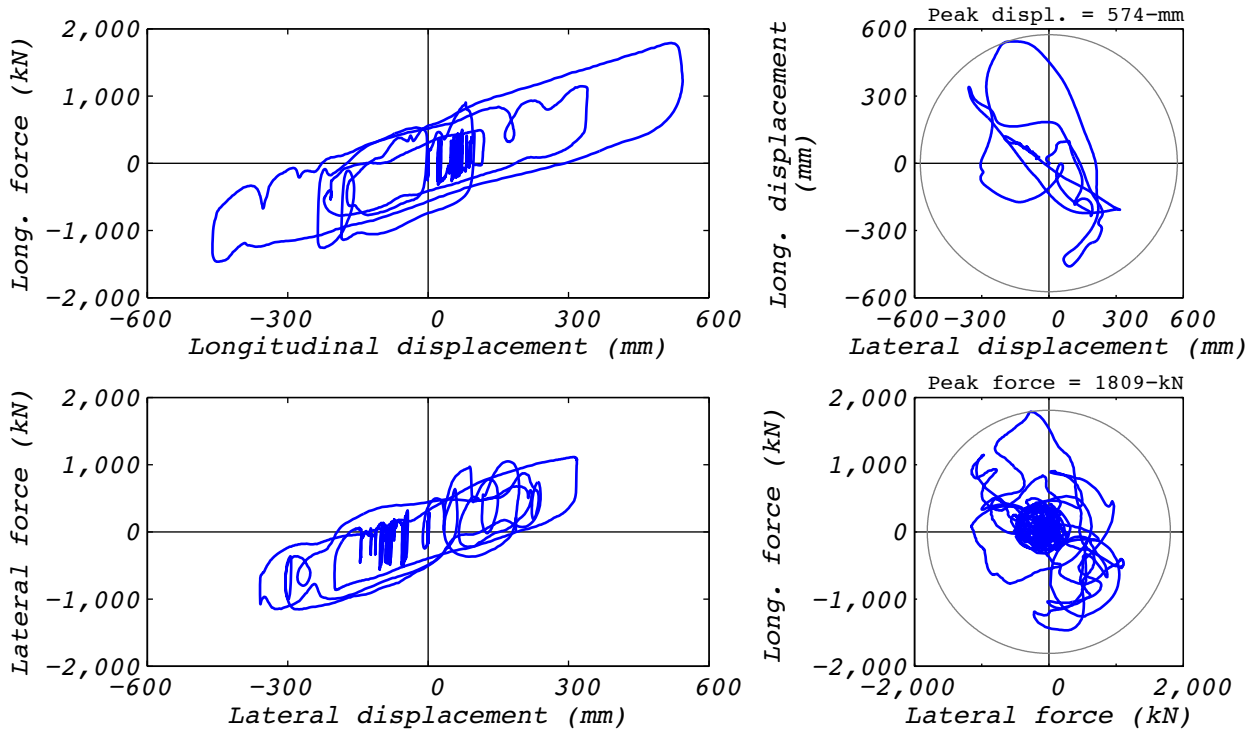

Figure A.27-2 Hybrid test bearing response for run 85: NRC15, 3D with 5 groups and the experimental bearing representing the no. 3 corner group.

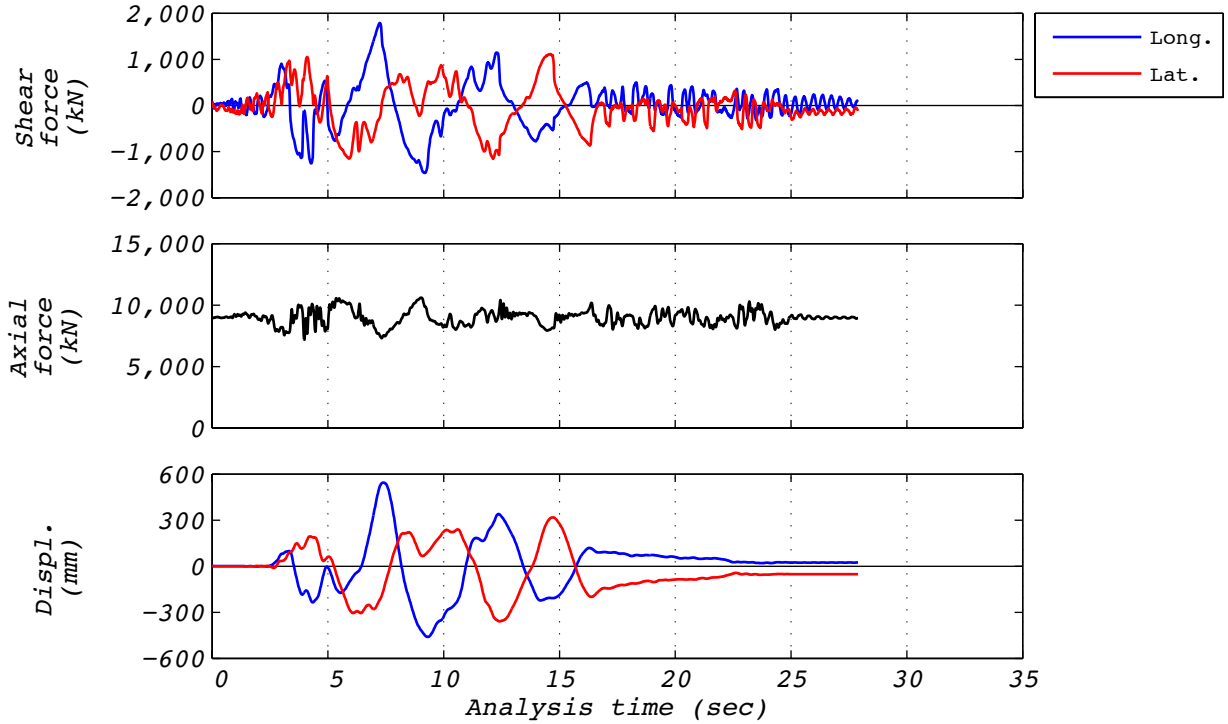

Figure A.27-3 Hybrid test time history responses for run 85: NRC15, 3D with 5 groups and the experimental bearing representing the no. 3 corner group.

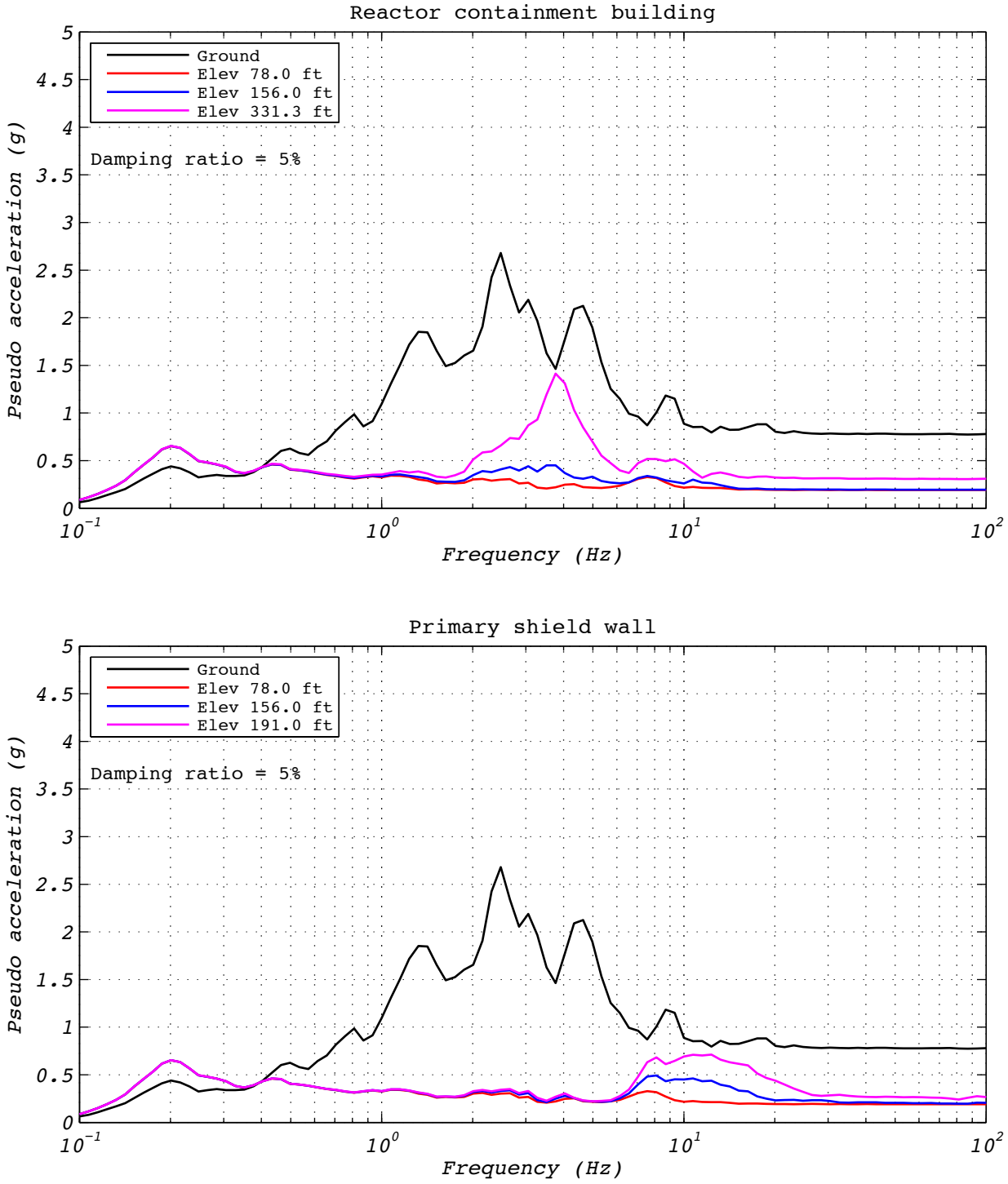

Figure A.27-4 Hybrid test floor spectra for run 85: NRC15, 3D with 5 groups of bearings and the experimental bearing representing the no. 3 corner group.

A.28 DISPLACEMENT RUN 86

Test run 86 was a repeat of the displacement history resulting from run 84 executed at real time. Run 84 was a hybrid test of the NRC dispersion appropriate ground motion number 15. The model consisted of five groups of bearings. The experimental bearing's group was located in the center of the layout. Input motions consisted of two horizontal components and a constant axial load specified as the design axial load of 8,663 kN. Bearing UET-1 was used in this test. Figures A.28-1 and A.28-2 contain bearing responses.

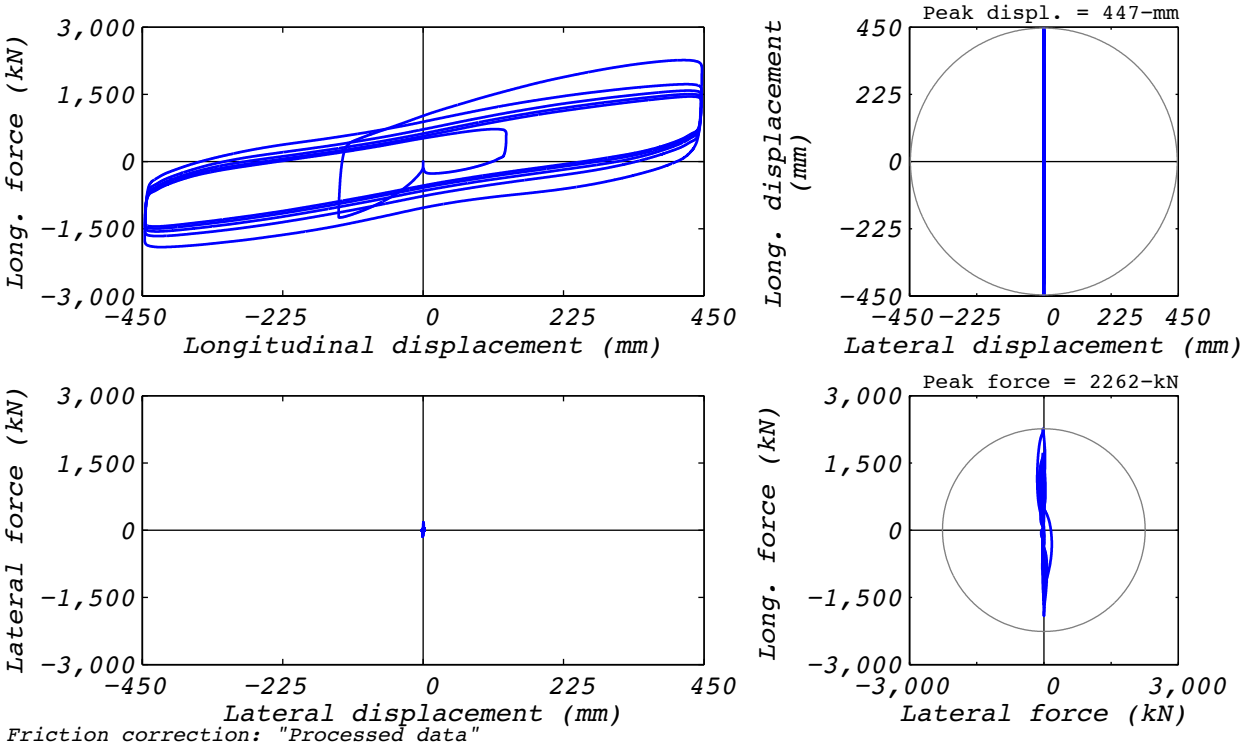

Figure A.28-1 Bearing response for real-time displacement history from hybrid test run 84: NRC15, 3D with 5 groups of bearings and the experimental bearing representing the center group.

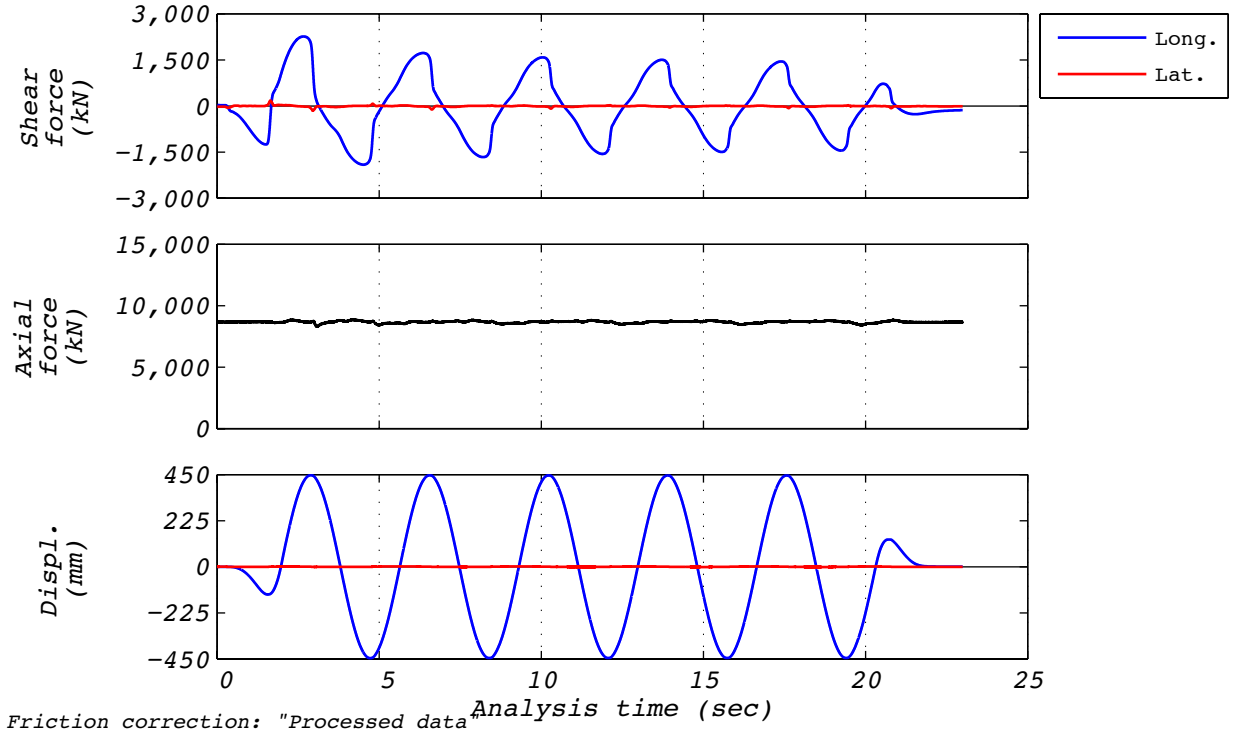

Figure A.28-2 Time history responses for real-time displacement history from hybrid test run 84: NRC15, 3D with 5 groups of bearings and the experimental bearing representing the center group.

A.29 DEVELOPMENT RUN 88

Development run 88 was a hybrid test of the NRC dispersion appropriate ground motion number 15. The model consisted of five groups of bearings. The experimental bearing's group was located in corner number 3 of the layout. Input motions consisted of three horizontal components. The initial axial load was solved for during the simulation. The test was executed at a rate 25 times slower than real time to compensate for machine delays. Bearing UET-1 was used in this test. Figure A.29-1 shows the fidelity achieved in the hybrid test. Figures A.29-2 and A.29-3 contain bearing responses, and Figure A.29-4 depicts the resulting floor response spectra for select locations in two of the isolated sructures.

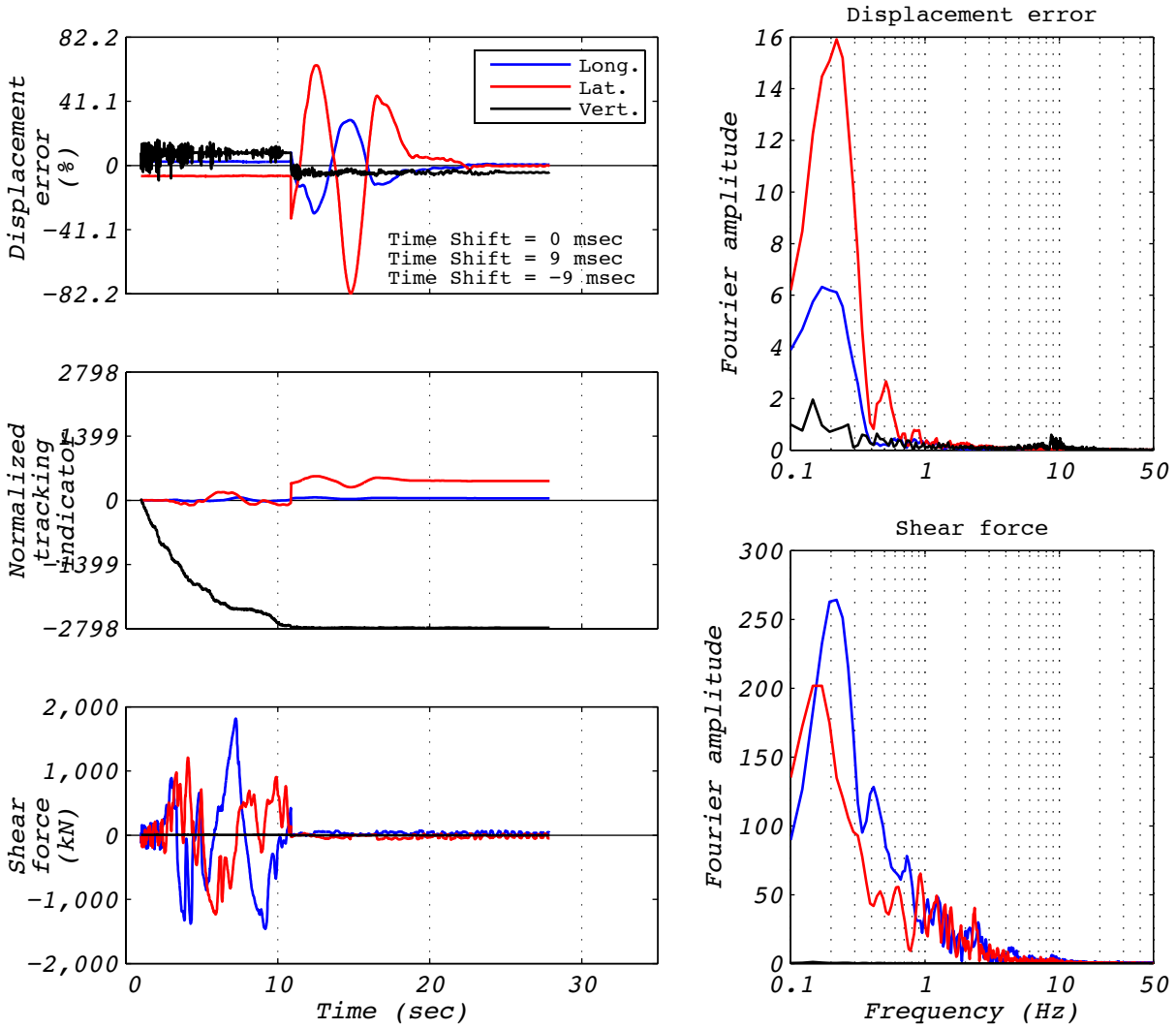

Figure A.29-1 Hybrid test performance metrics for run 88: NRC15, 3D with 5 groups of bearings and the experimental bearing representing the no. 3 corner group.

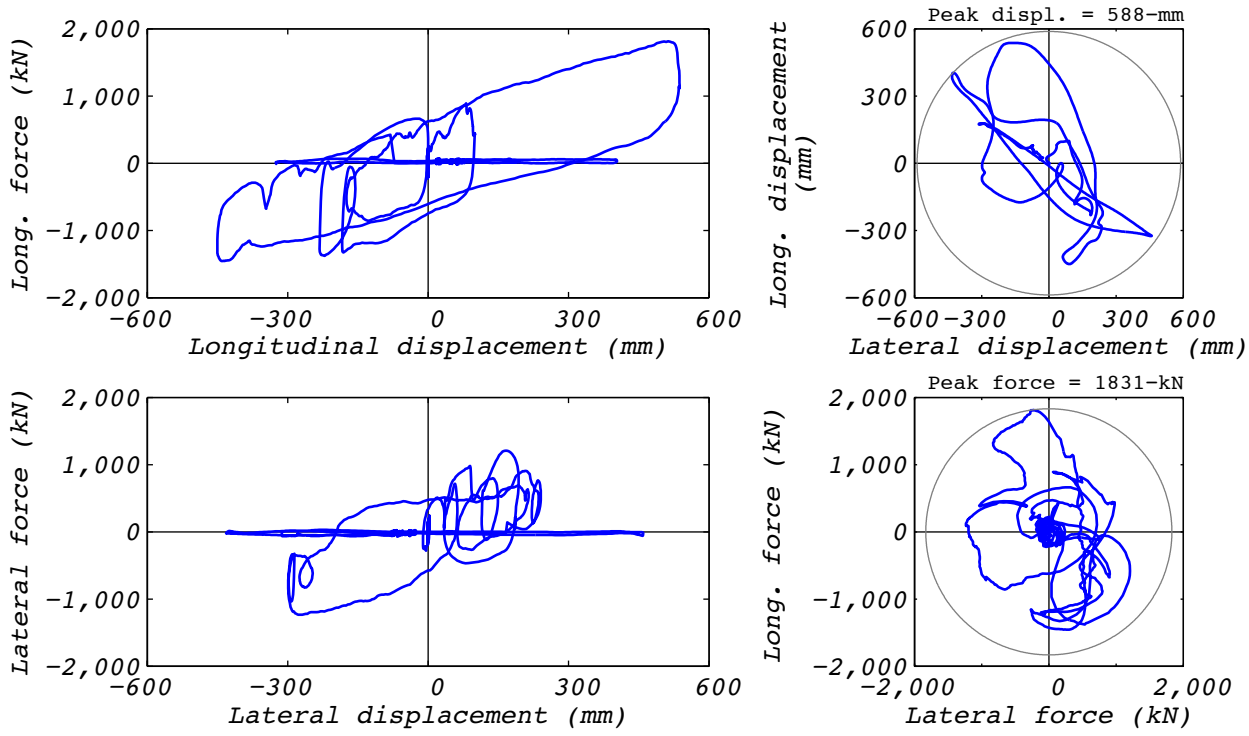

Figure A.29-2 Hybrid test bearing response for run 88: NRC15, 3D with 5 groups and the experimental bearing representing the no. 3 corner group.

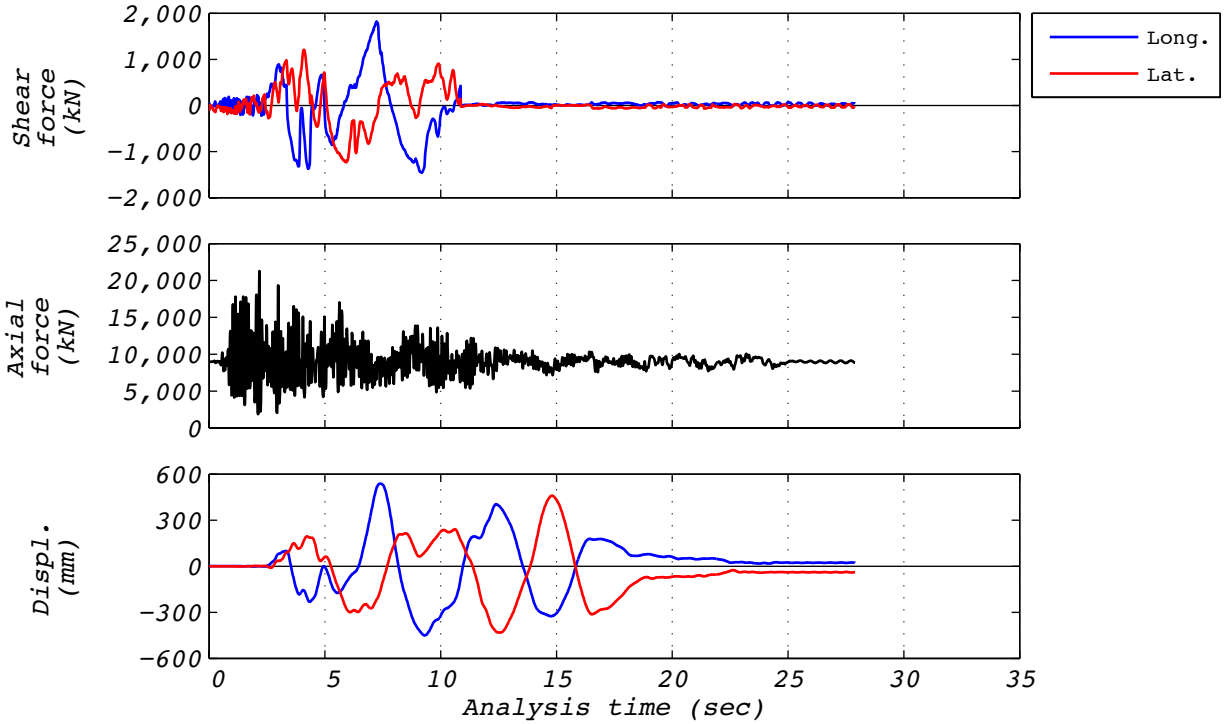

Figure A.29-3 Hybrid test time history responses for run 88: NRC15, 3D with 5 groups and the experimental bearing representing the no. 3 corner group.

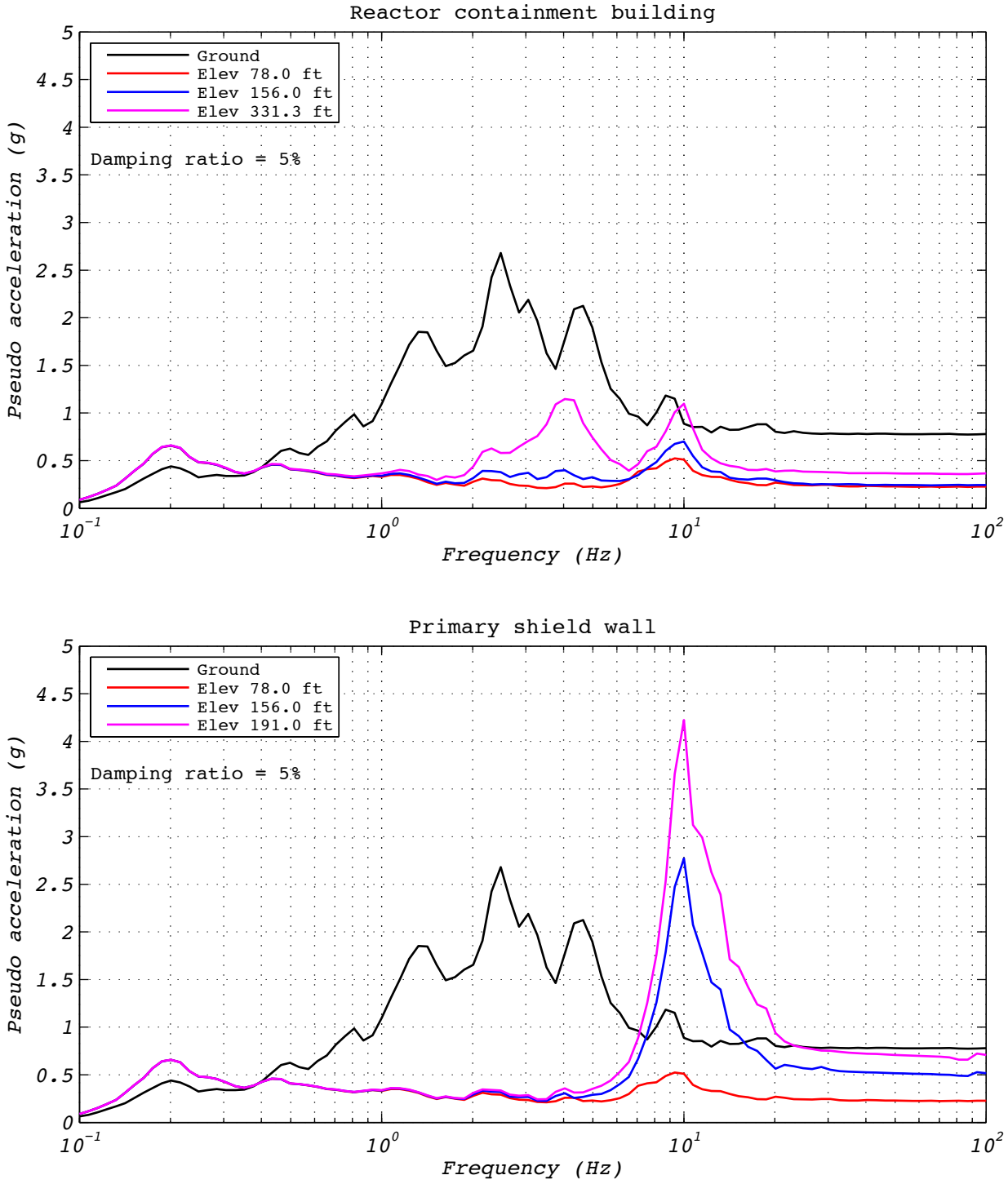

Figure A.29-4 Hybrid test floor spectra for run 88: NRC15, 3D with 5 groups of bearings and the experimental bearing representing the no. 3 corner group.

A.30 TEST RUN 89

Test run 89 was a hybrid test of the NRC dispersion appropriate ground motion number 15. The model consisted of five groups of bearings. The experimental bearing's group was located in corner number 3 of the layout. Input motions consisted of three horizontal components. The initial axial load was solved for during the simulation. The test was executed at a rate 25 times slower than real time to compensate for machine delays. Bearing UET-1 was used in this test. Figure A.30-1 shows the fidelity achieved in the hybrid test. Figures A.30-2 and A.30-3 contain bearing responses, and Figure A.30-4 depicts the resulting floor response spectra for select locations in two of the isolated structures.

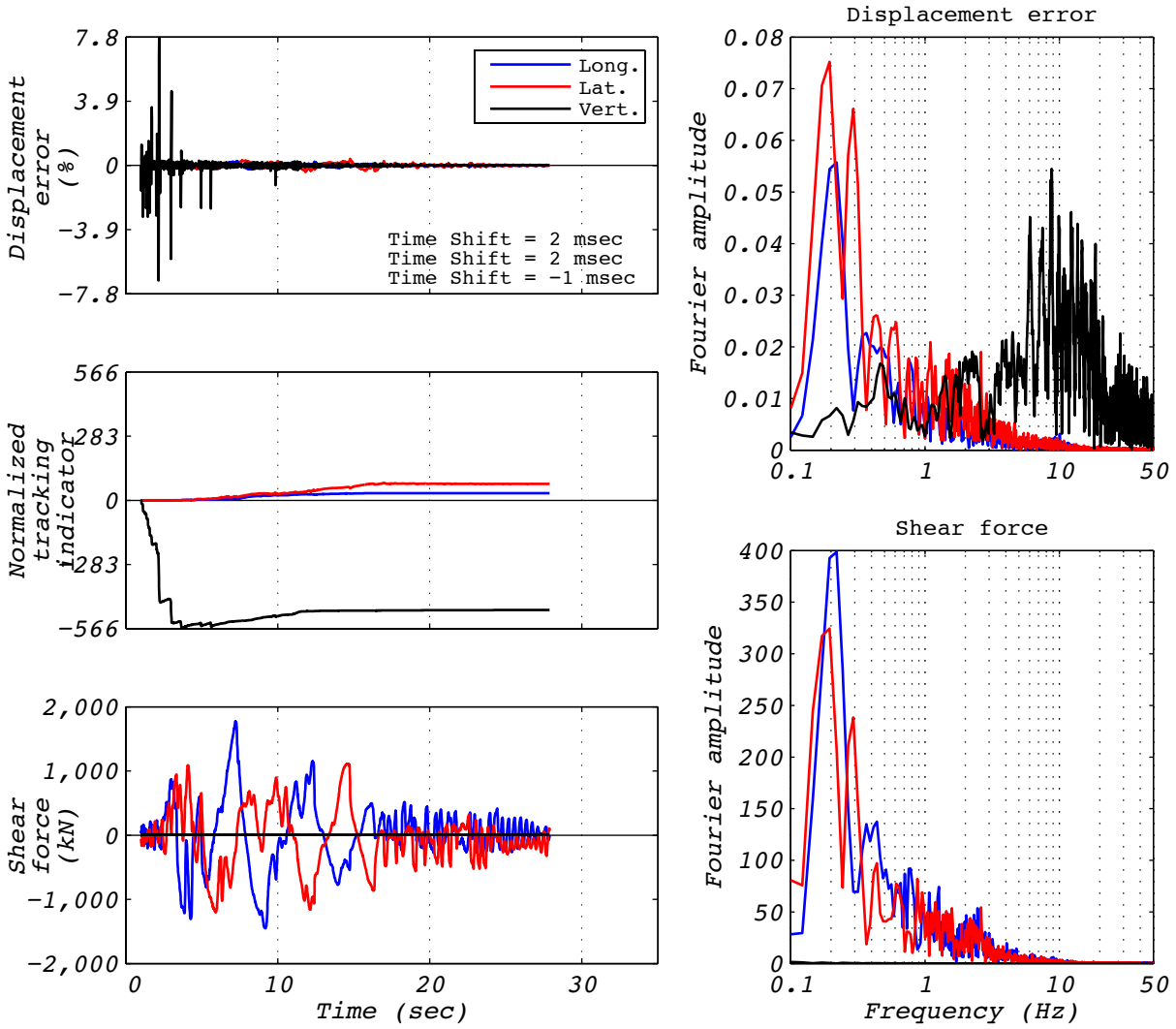

Figure A.30-1 Hybrid test performance metrics for run 89: NRC15, 3D with 5 groups of bearings and the experimental bearing representing the no. 3 corner group.

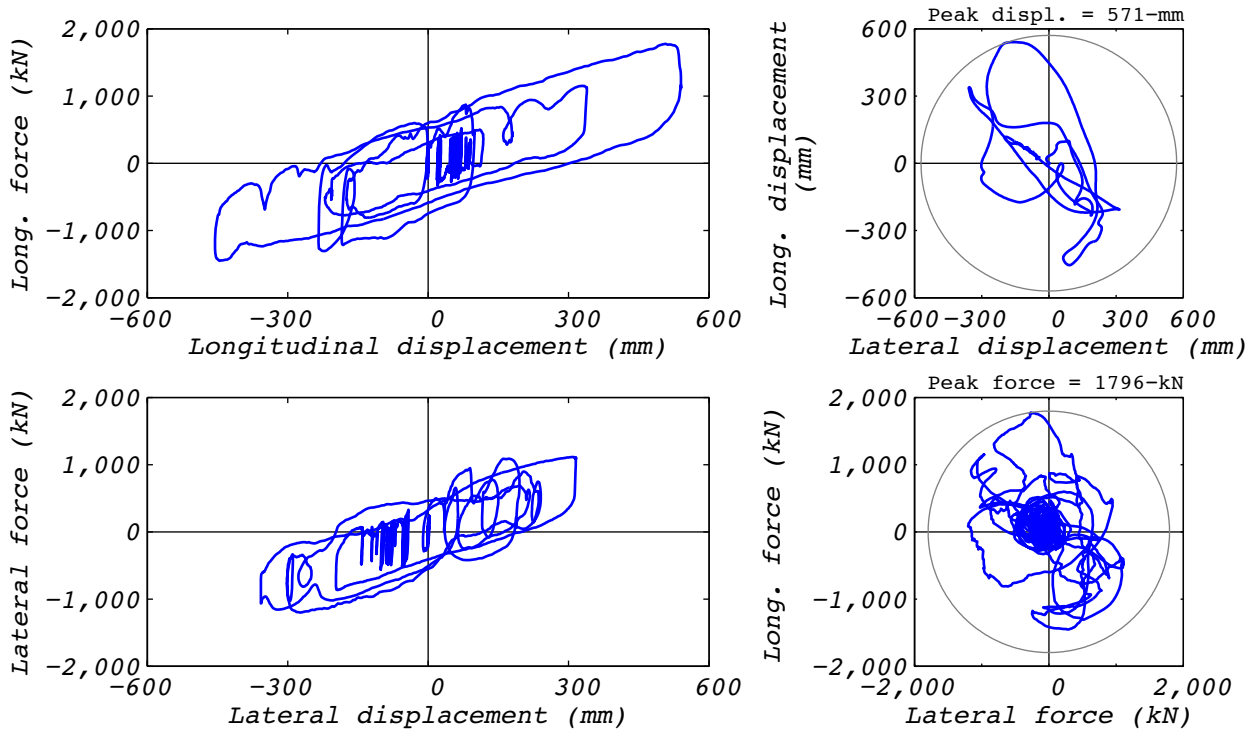

Figure A.30-2 Hybrid test bearing response for run 89: NRC15, 3D with 5 groups and the experimental bearing representing the no. 3 corner group.

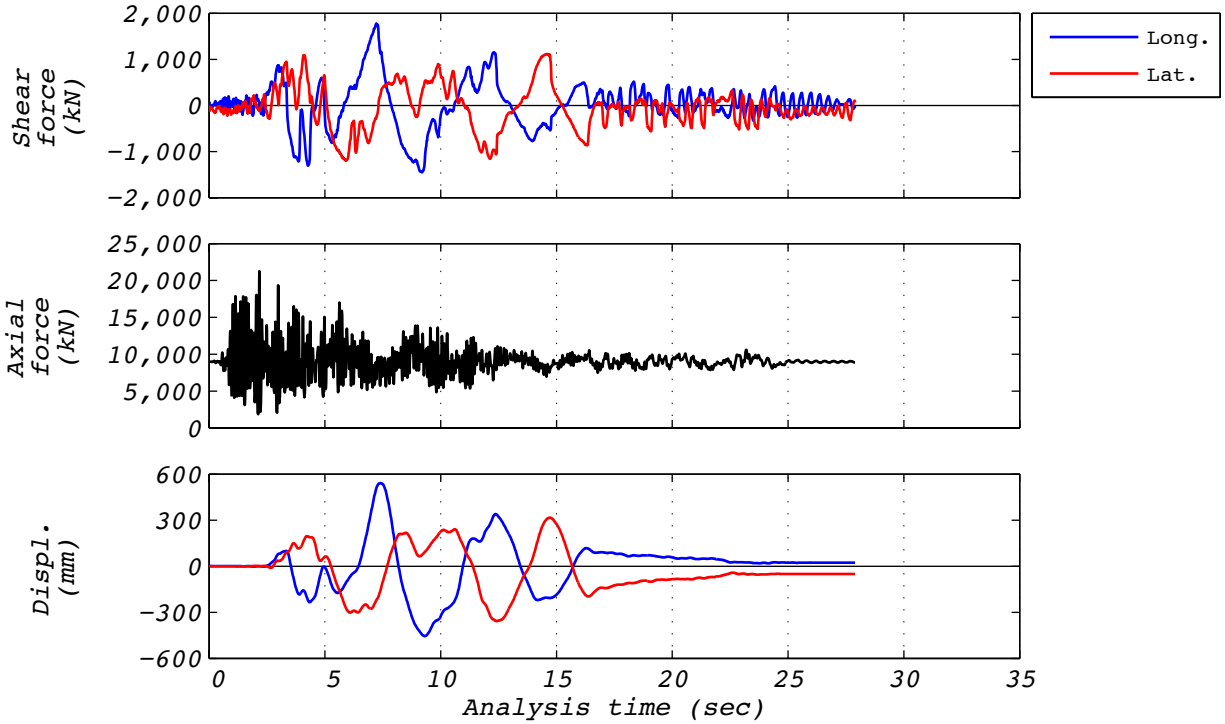

Figure A.30-3 Hybrid test time history responses for run 89: NRC15, 3D with 5 groups and the experimental bearing representing the no. 3 corner group.

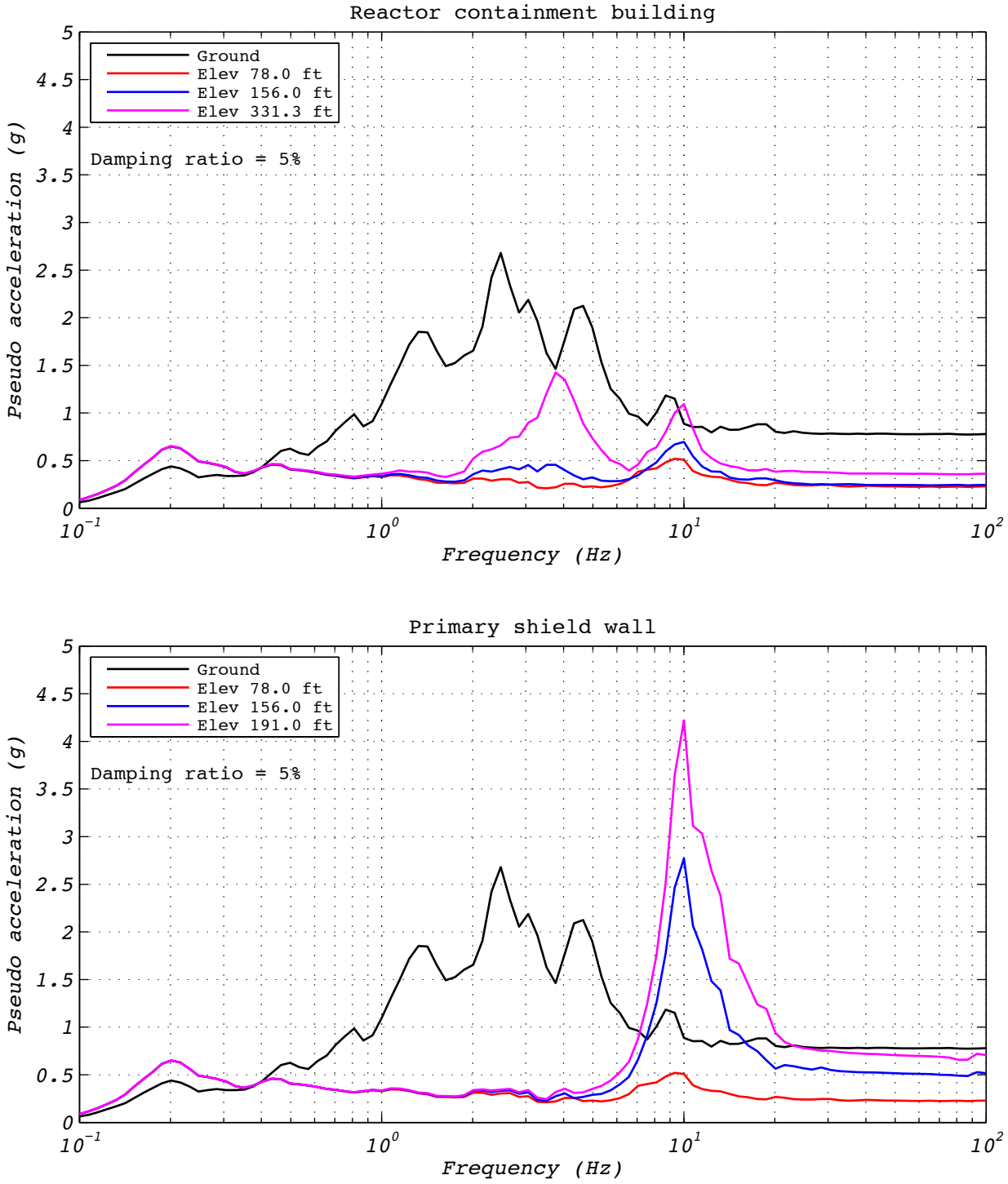

Figure A.30-4 Hybrid test floor spectra for run 89: NRC15, 3D with 5 groups of bearings and the experimental bearing representing the no. 3 corner group.

Appendix B: Characterization Tests Conducted on Lead Plug Rubber Bearings

Characterization tests listed in Table B.1 and Table B.2 were performed on the Unison eTech bearings UET-2 and UET-1, respectively.

Table B.1 Characterization tests conducted on lead plug rubber bearing UET-2.

Section	Run	Components	Number of cycles	Displ. amplitude* (mm)	Axial load* (kN)	Velocity* (mm/s)	Wave form
B.1	8	Axial	9	0	Varies	-	Ramp and sine
B.2	9	Longitudinal	3	224	8,663	586	Sine
B.3	12	Longitudinal	3	224	21,927	7	Sine
B.4	13	Axial	3	0	Varies	-	Ramp and sine
B.5	14	Axial	9	0	Tension	-	Ramp and sine
B.6	15	Axial	9	56	Varies	-	Ramp and sine
B.7	16	Axial	9	112	Varies	-	Ramp and sine
B.8	17	Axial	9	224	Varies	-	Ramp and sine
B.9	18	Axial	9	336	Varies	-	Ramp and sine
B.10	23	Transverse	3	224	8,663	586	Sine
B.11	35	Longitudinal	3	224	8,663	586	Sine
B.12	41	Longitudinal	3	224	8,663	7	Sine
B.13	51	Trans. Rot.	2	0	8,663	-	Sine
B.14	52	Long. Rot.	2	0	8,663	-	Sine
B.15	53	Twist	9	0	8,663	-	Sine
B.16	54	Longitudinal	3	224	8,663	586	Sine
B.17	56	Longitudinal	3	224	8,663	7	Sine
B.18	57	Bidirectional	2	224	8,663	Varies	Sines
B.19	59	Longitudinal	3	224	8,663	586	Sine

* Target values

Table B.1 (Continued) Characterization tests conducted on lead plug rubber bearing UET-2.

Section	Run	Components	Number of cycles	Displ. amplitude* (mm)	Axial load* (kN)	Velocity* (mm/s)	Wave form
B.20	62	Bidirectional	3	224	8,663	28	Sine
B.21	64	Longitudinal	3	448	8,663	28	Sine
B.22	65	Longitudinal	3	896	8,663	56	Sine
B.23	66	Bidirectional	-	To failure	8,663	-	Elipse

* Target values

Table B.2 Characterization tests conducted on lead plug rubber bearing UET-1

Section	Run	Components	Number of cycles	Displ. amplitude* (mm)	Axial load* (kN)	Velocity* (mm/s)	Wave form
B.24	67	Longitudinal	3	224	8,663	586	Sine
B.25	68	Axial	3	0	Varies	-	Ramp and sine
B.26	69	Longitudinal	3	224	21,927	7	Sine
B.27	70	Transverse	3	224	8,663	586	Sine
B.28	71	Longitudinal	5	224	8,663	373	Triangle
B.29	72	Longitudinal	4	224	8,663	9	Triangle
B.30	73	Longitudinal	4	224	8,663	1,173	Sine
B.31	74	Longitudinal	3	224	21,927	7	Sine
B.32	75	Longitudinal	4	224	25,002	373	Triangle
B.33	76	Longitudinal	4	224	2,807	373	Triangle
B.34	81	Longitudinal	20	13	8,663	4	Sine
B.35	87	Longitudinal	5	444	8,663	485	Sine

B.1 TEST RUN 8

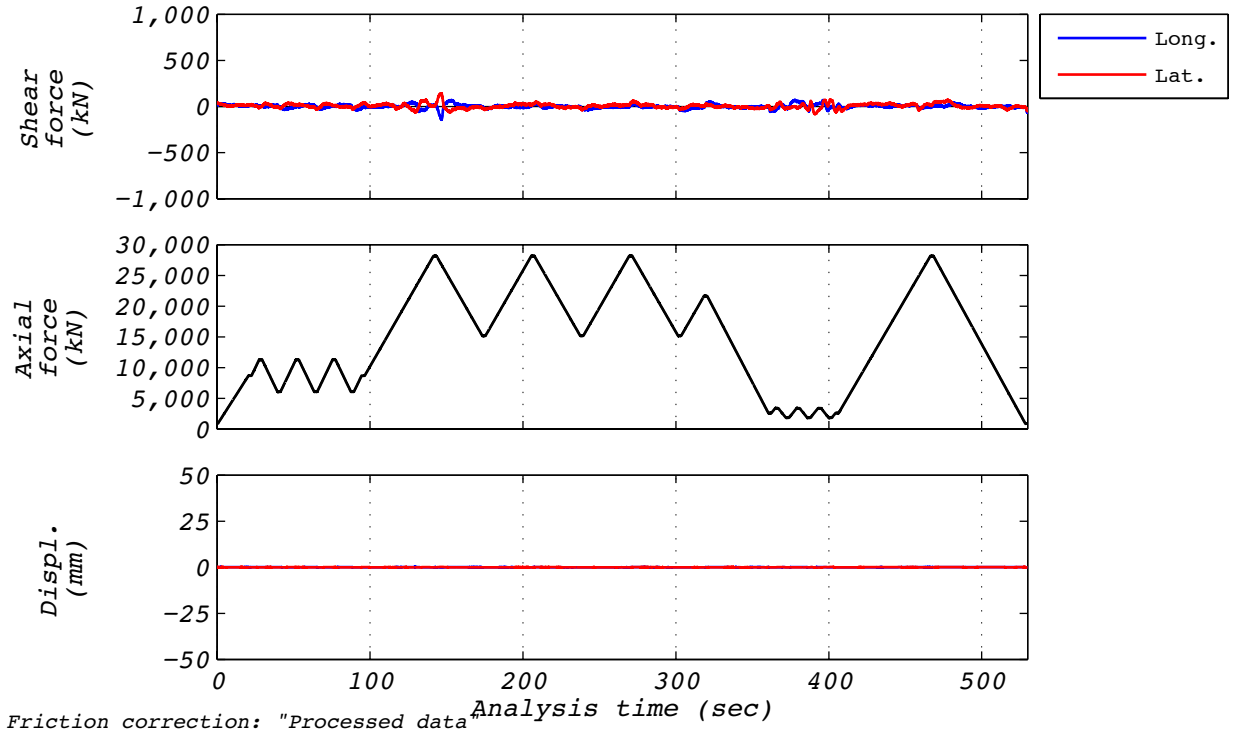

Figure B.1-1 Test run no. 8 time history: Axial compression (0 mm amplitude and varying axial load).

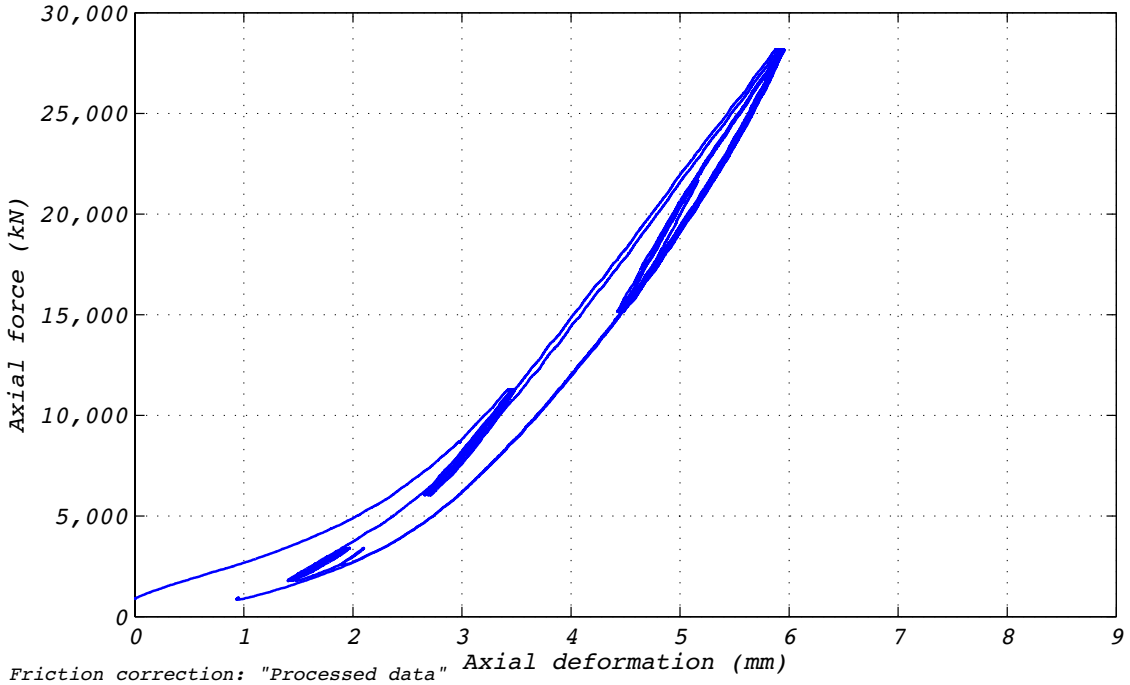

Figure B.1-2 Test run no. 8 hysteresis: Axial compression (0 mm amplitude and varying axial load).

B.2 TEST RUN 9

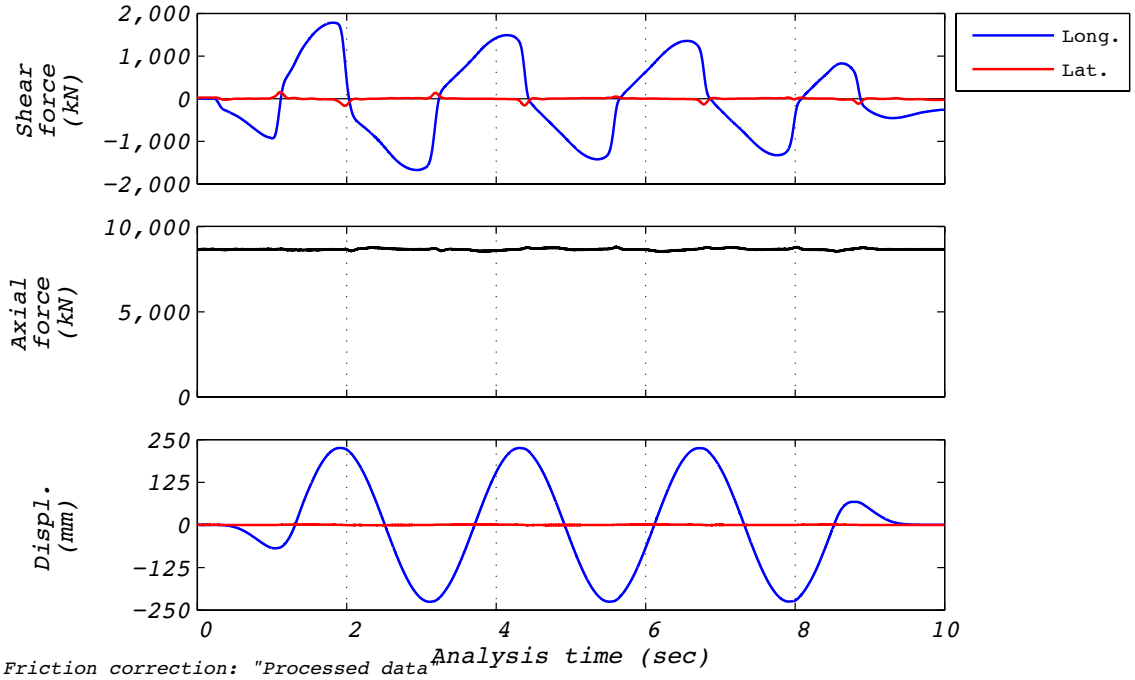

Figure B.2-1 Test run no. 9 time history: Longitudinal (224 mm amplitude, 8,663 kN axial load, and 586 mm/s velocity).

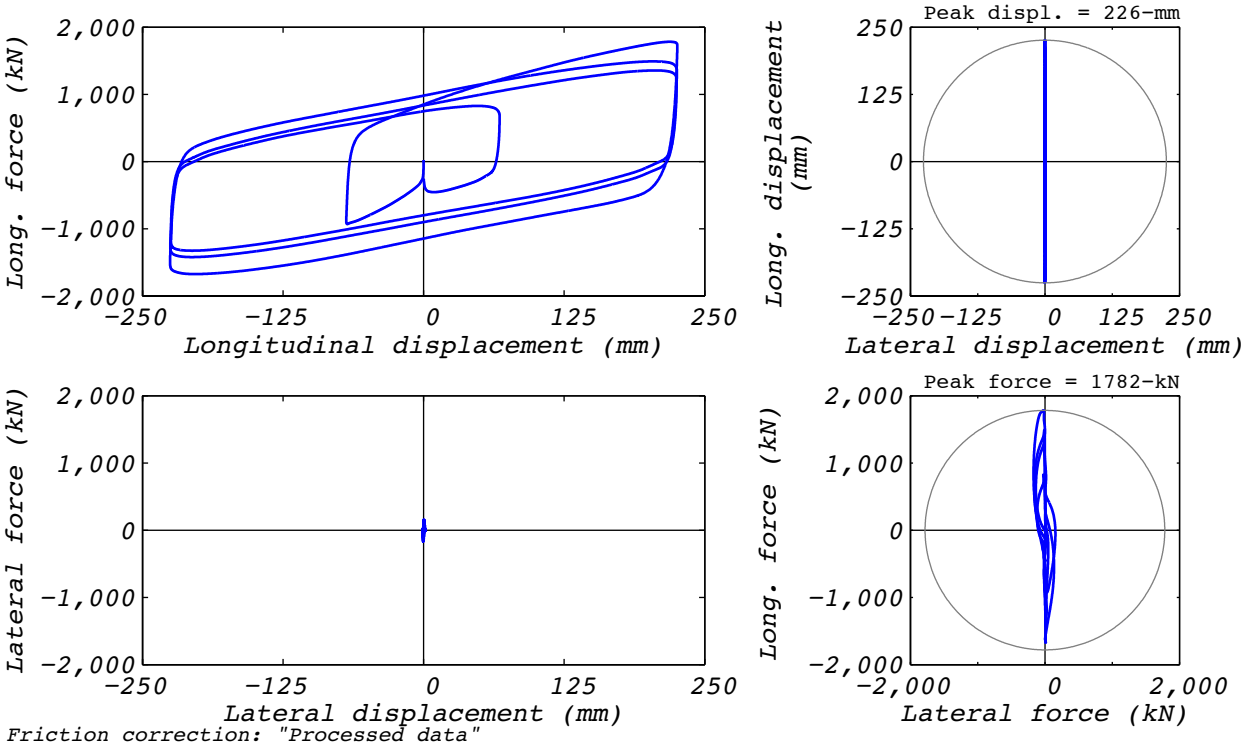

Figure B.2-2 Test run no. 9 hysteresis: Longitudinal (224 mm amplitude, 8,663 kN axial load, and 586 mm/s velocity).

B.3 TEST RUN 12

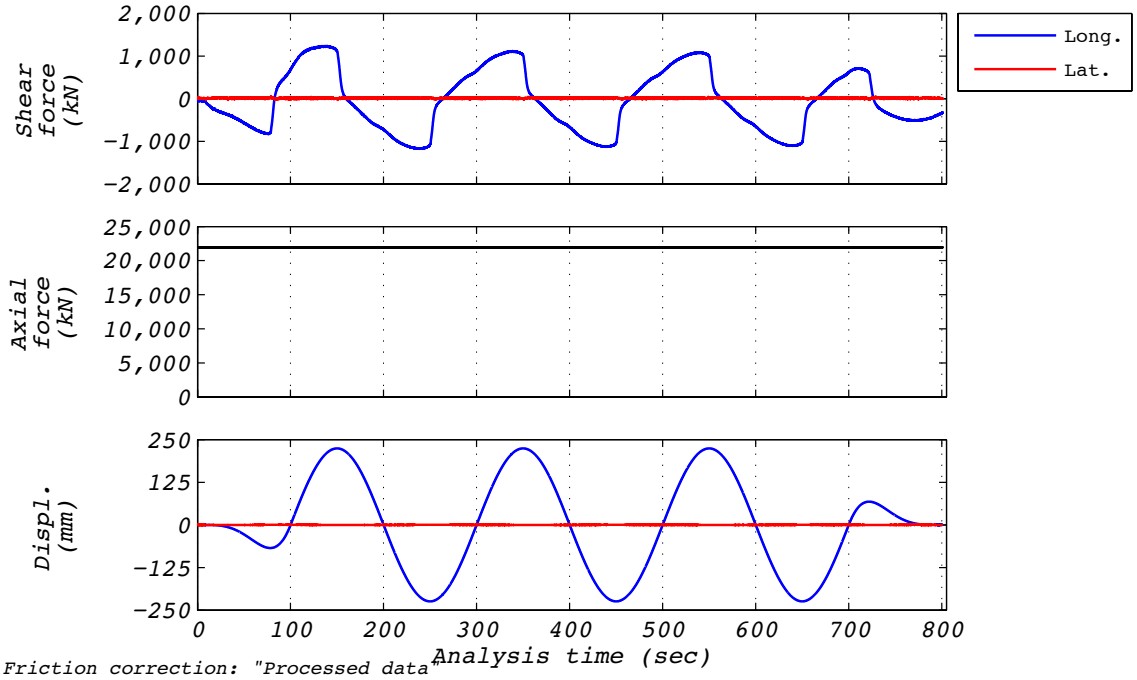

Figure B.3-1 Test run no. 12 time history: Longitudinal (224 mm amplitude, 21,927 kN axial load, and 7 mm/s velocity).

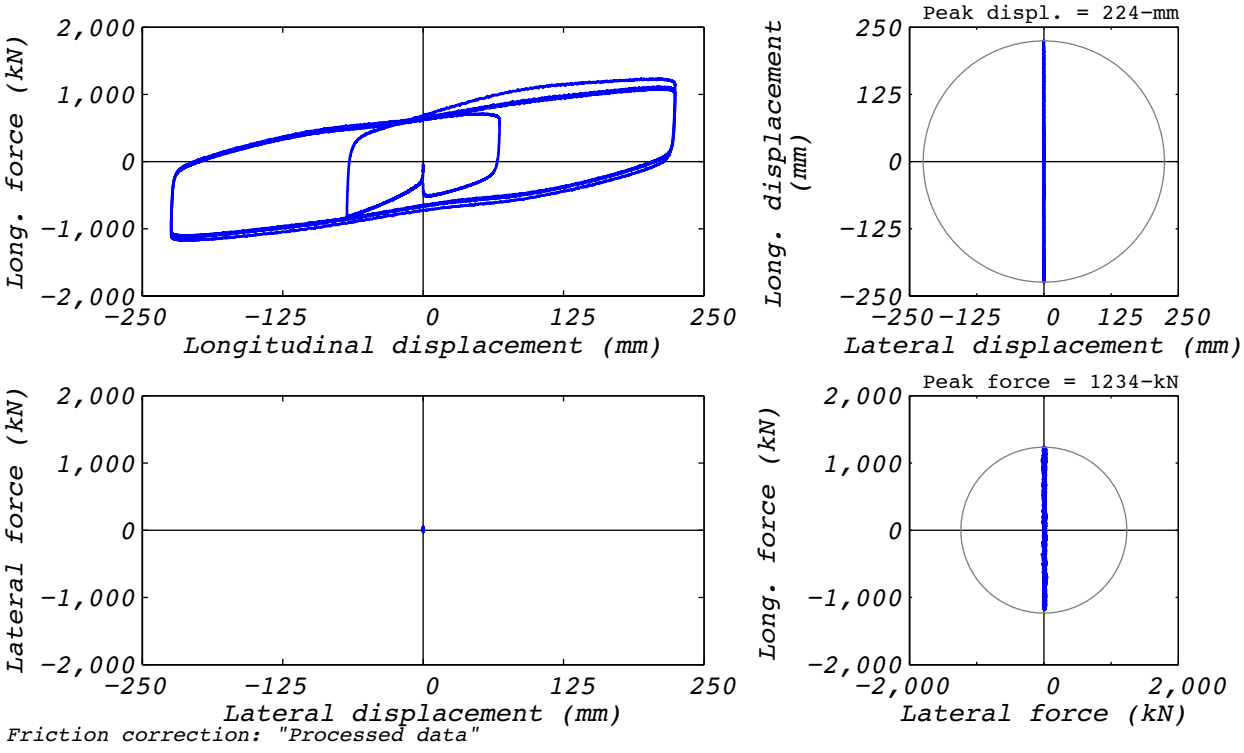

Figure B.3-2 Test run no. 12 hysteresis: Longitudinal (224 mm amplitude, 21,927 kN axial load, and 7 mm/s velocity).

B.4 TEST RUN 13

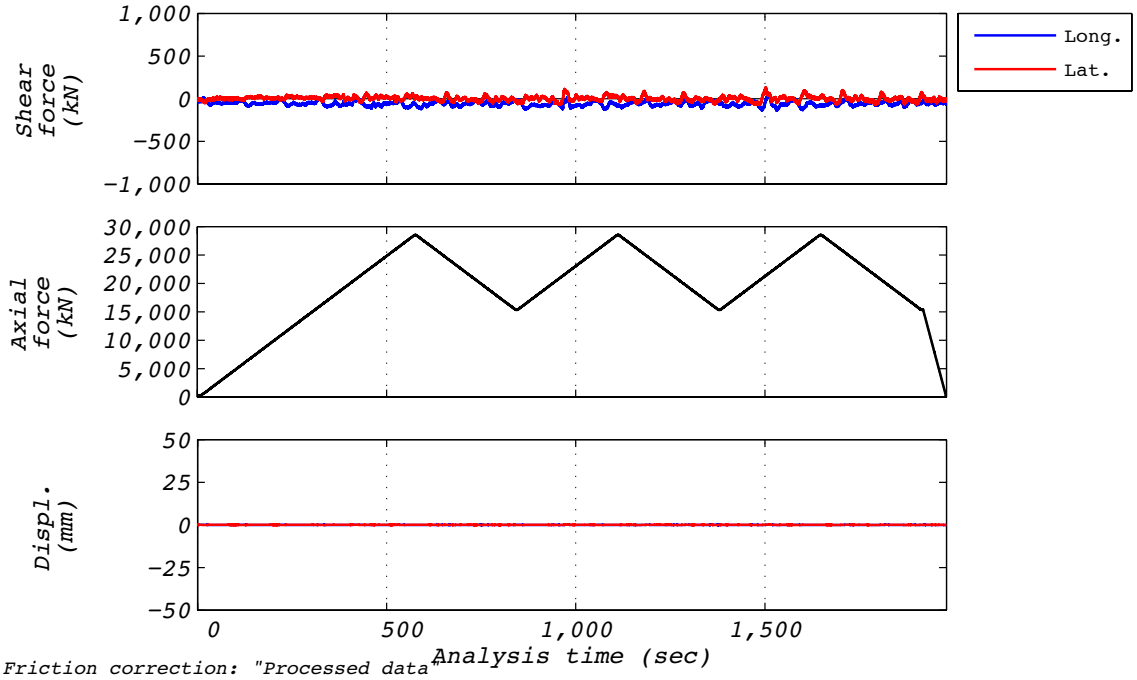

Figure B.4-1 Test run no. 13 time history: Axial (0 mm amplitude and varying axial load).

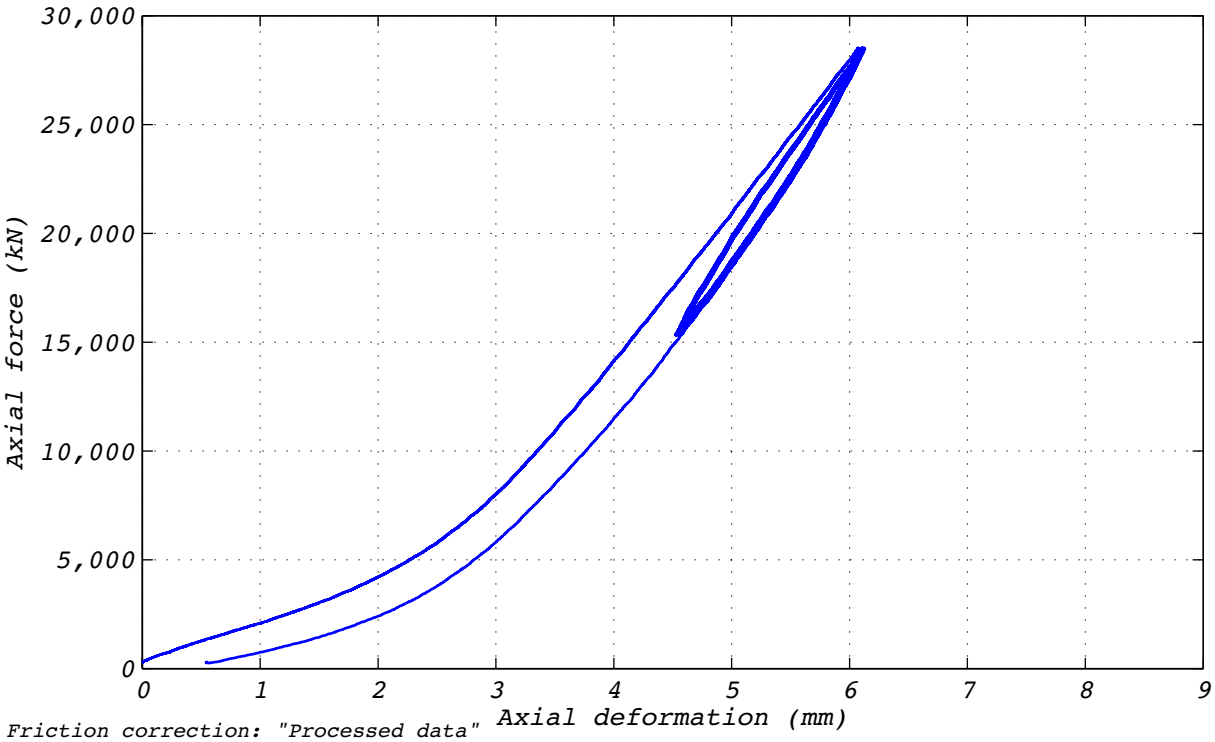

Figure B.4-2 Test run no. 13 hysteresis: Axial (0 mm amplitude and varying axial load).

B.5 TEST RUN 14

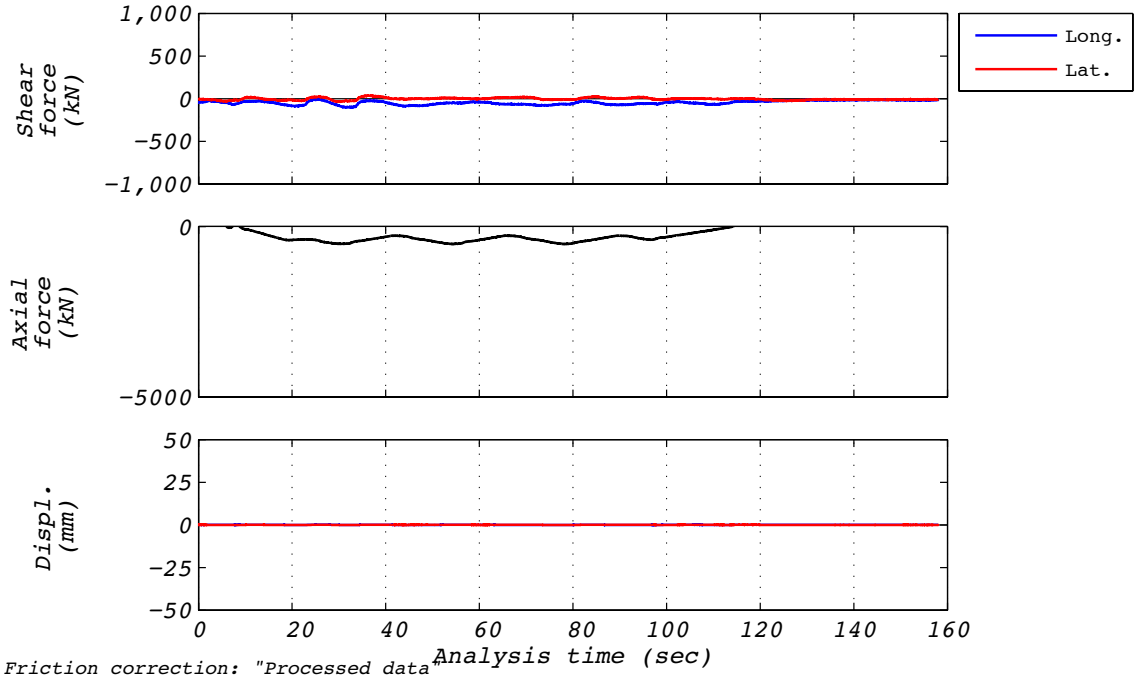

Figure B.5-1 Test run no. 14 time history: Axial (0mm amplitude and tensile axial load).

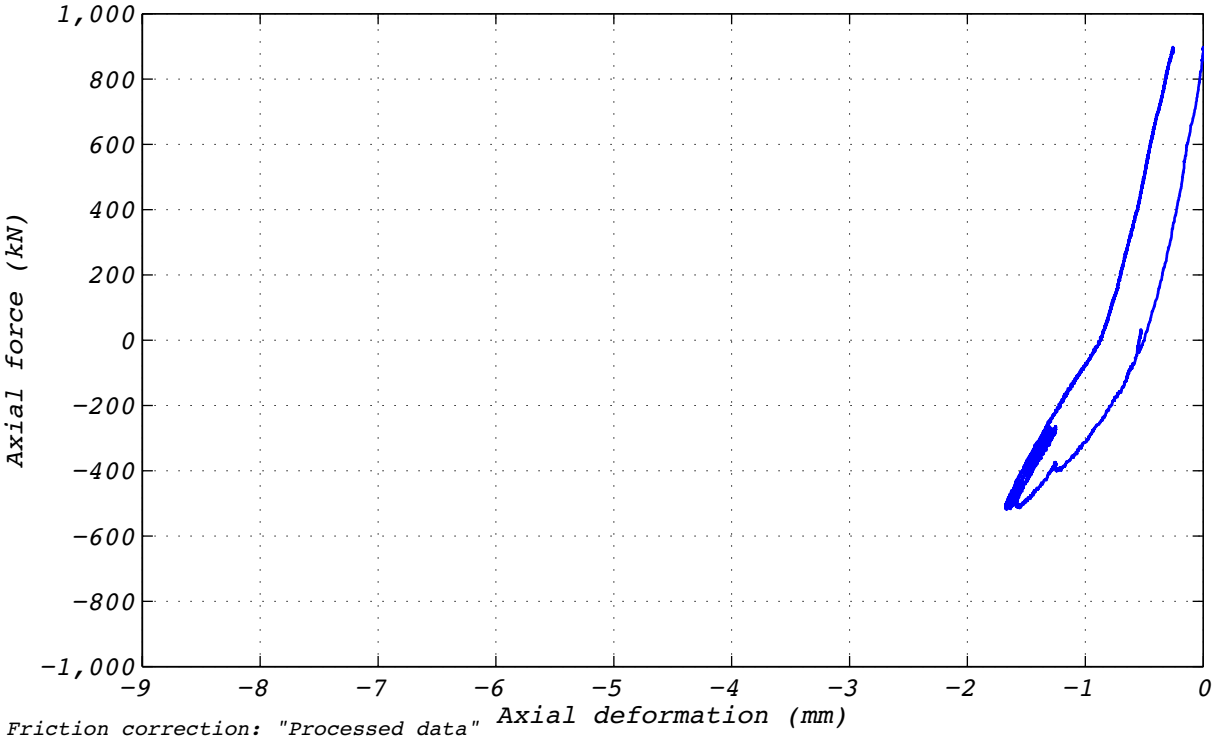

Figure B.5-2 Test run no. 14 hysteresis: Axial (0mm amplitude and tensile axial load).

B.6 TEST RUN 15

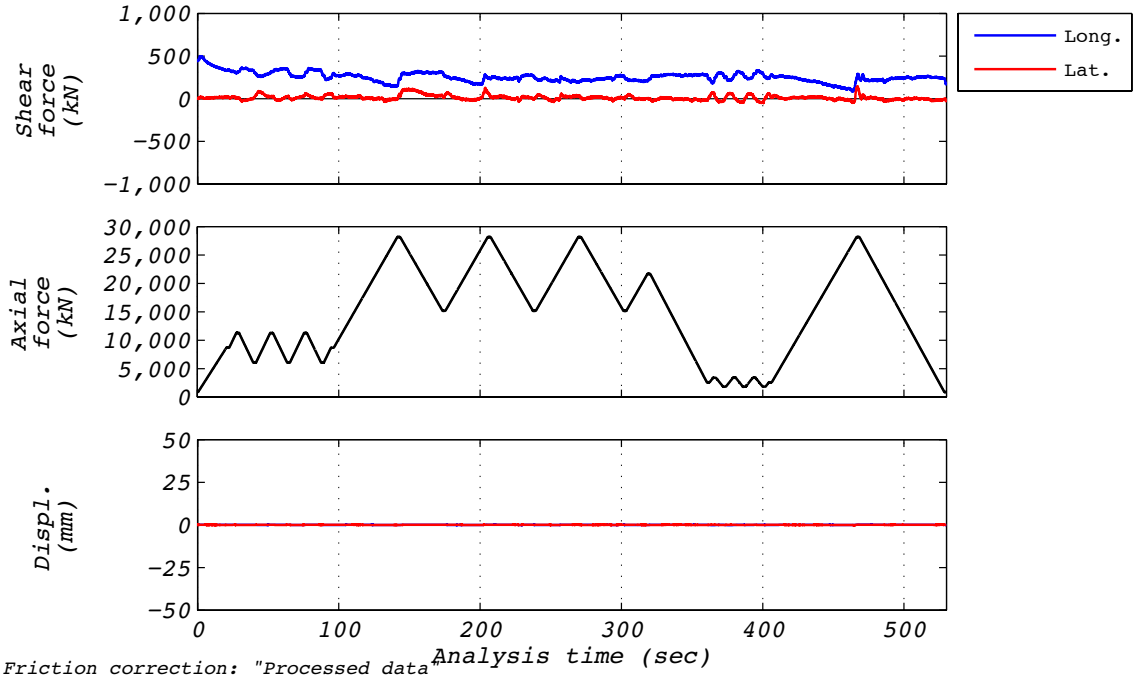

Figure B.6-1 Test run no. 15 time history: Axial (56 mm amplitude and varying axial load).

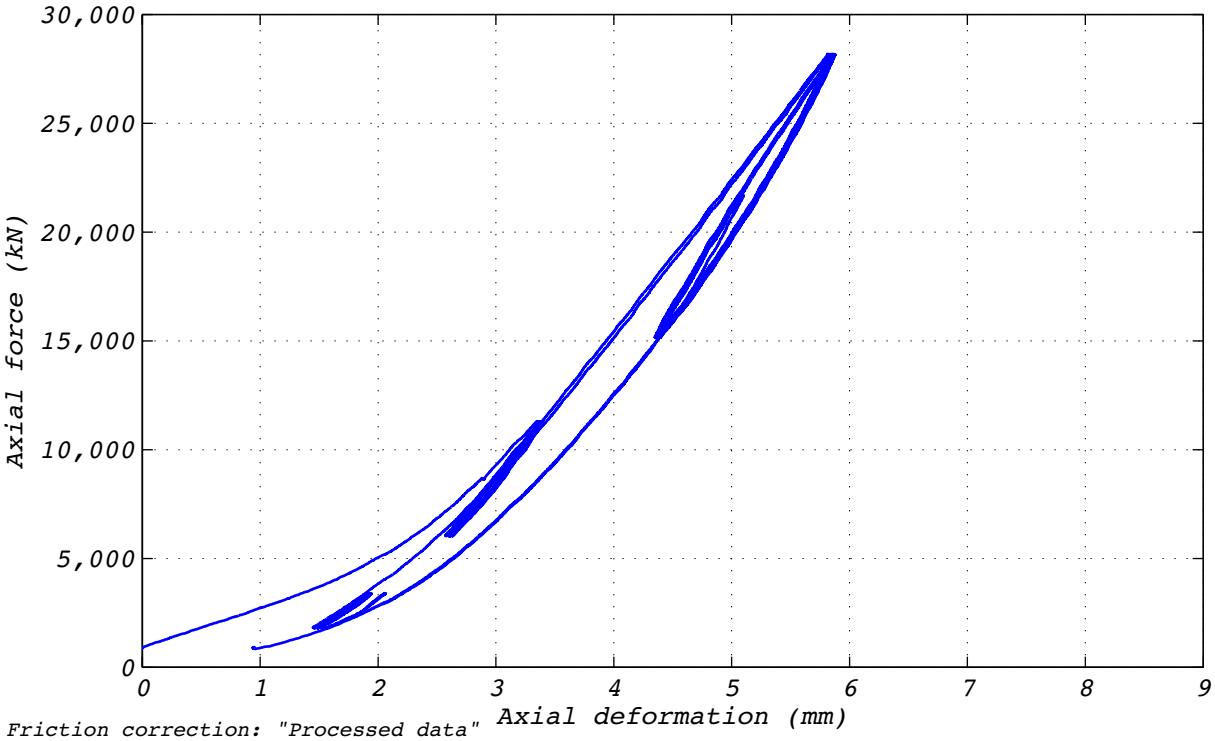

Figure B.6-2 Test run no. 15 hysteresis: Axial (56 mm amplitude and varying axial load).

B.7 TEST RUN 16

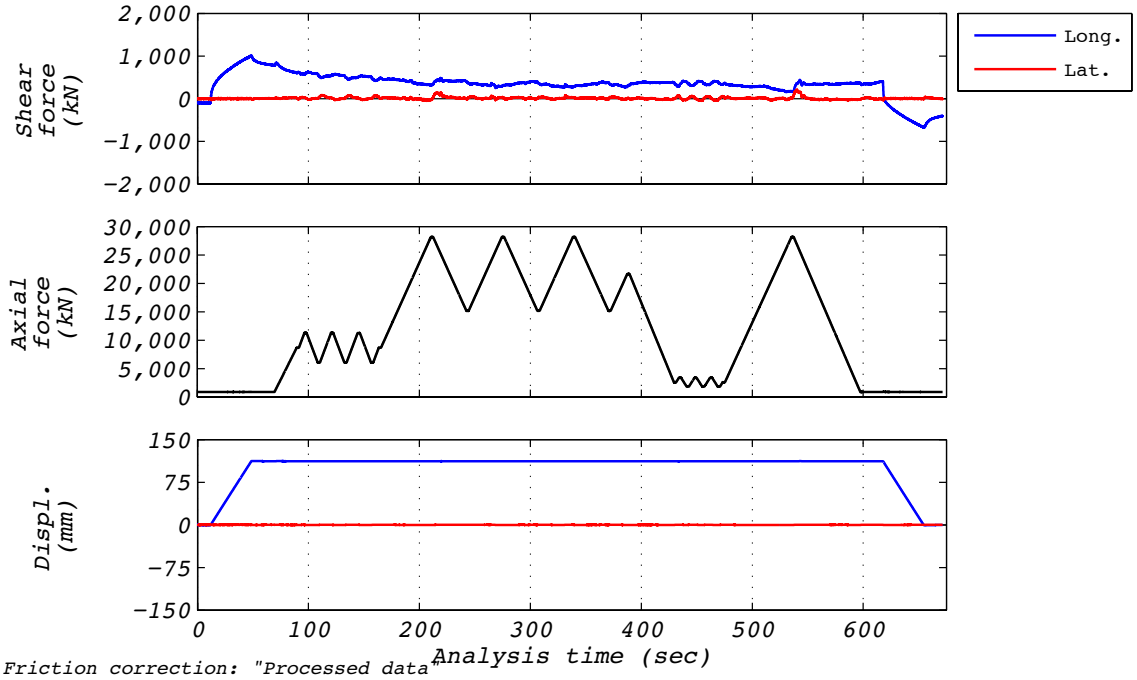

Figure B.7-1 Test run no. 16 time history: Axial (112 mm amplitude and varying axial load).

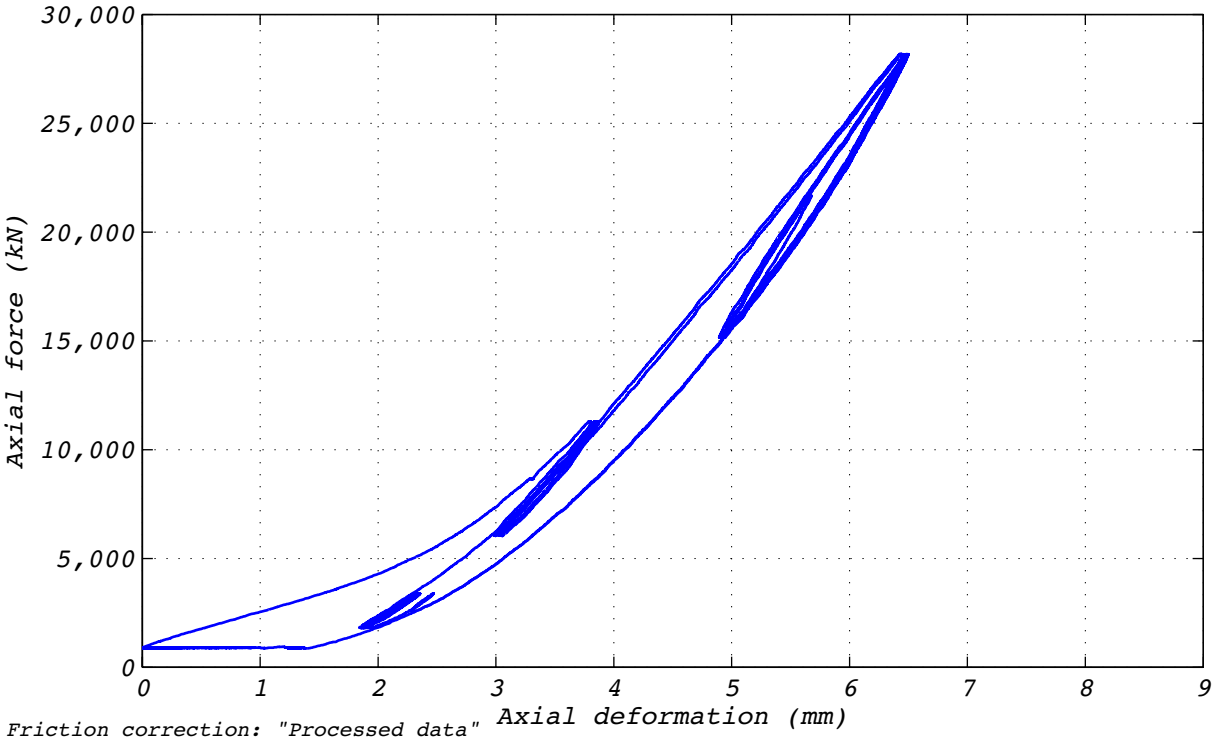

Figure B.7-2 Test run no. 16 hysteresis: Axial (112 mm amplitude and varying axial load).

B.8 TEST RUN 17

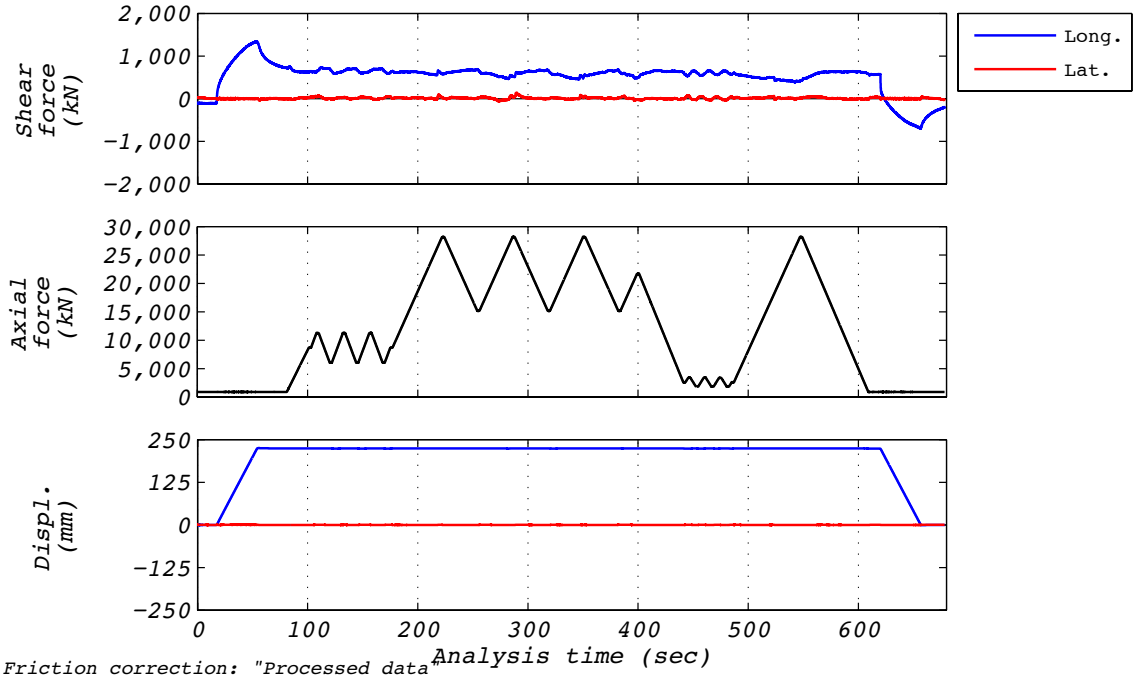

Figure B.8-1 Test run no. 17 time history: Axial (224 mm amplitude and varying axial load).

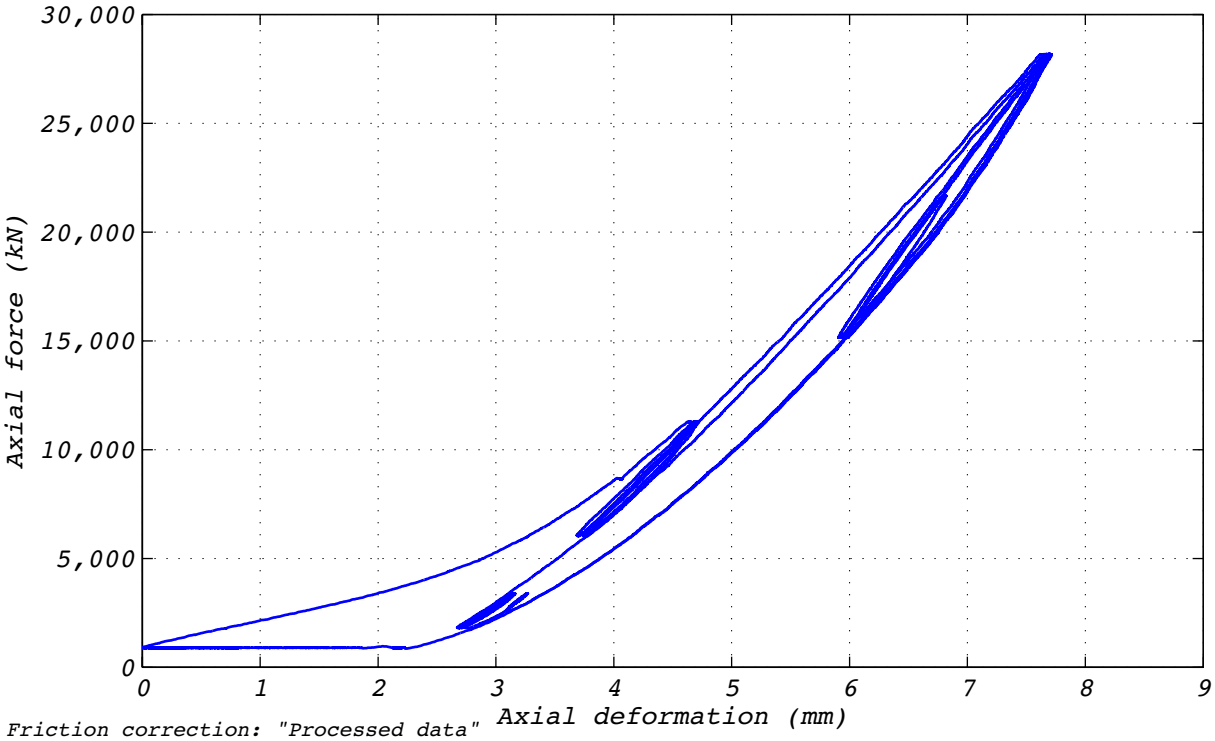

Figure B.8-2 Test run no. 17 hysteresis: Axial (224 mm amplitude and varying axial load).

B.9 TEST RUN 18

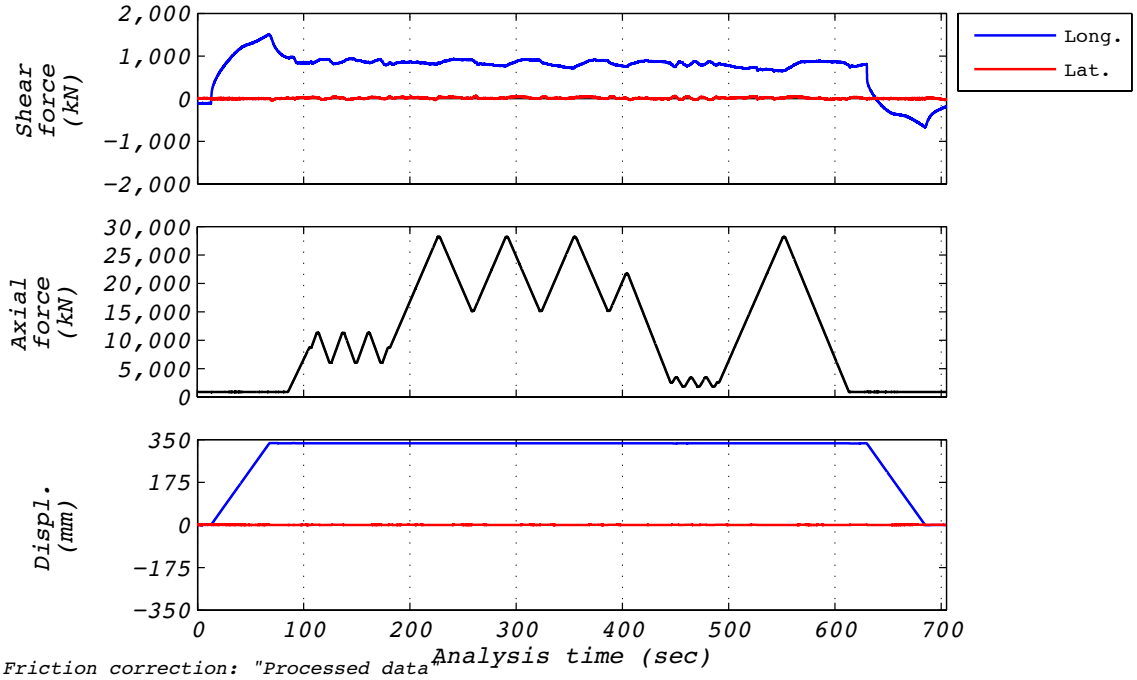

Figure B.9-1 Test run no. 18 time history: Axial (336 mm amplitude and varying axial load).

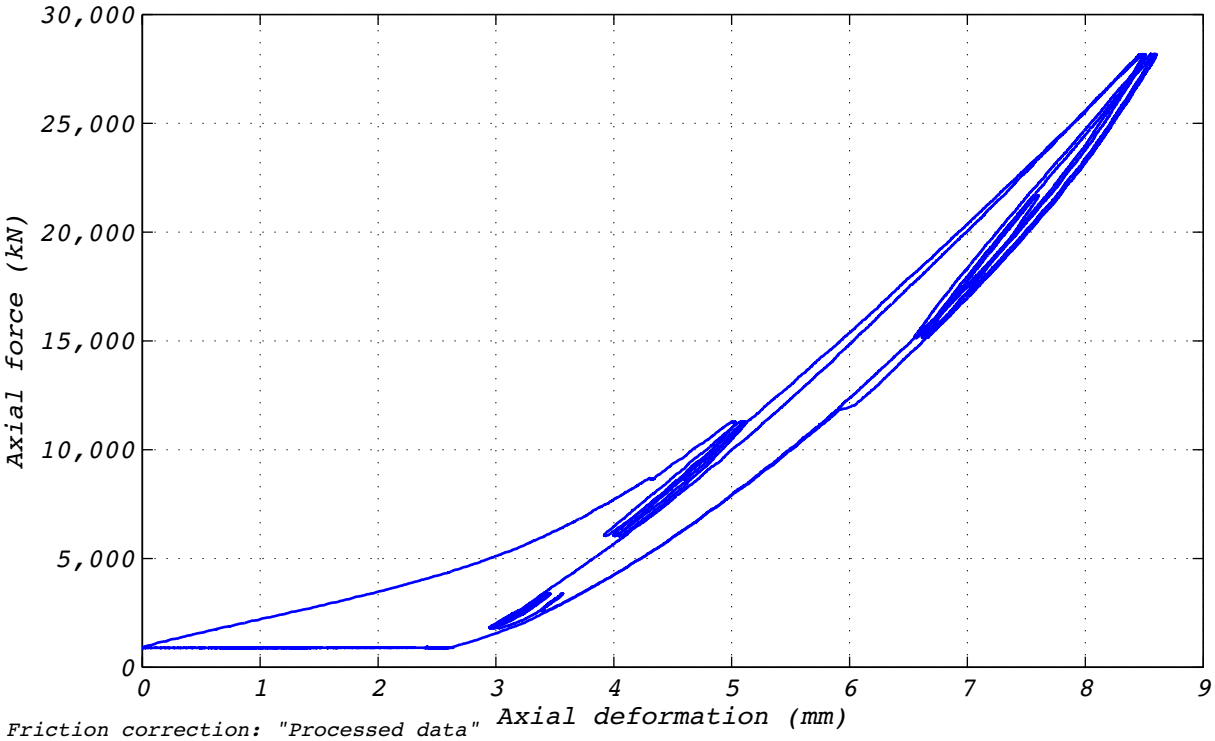

Figure B.9-2 Test run no. 18 hysteresis: Axial (336 mm amplitude and varying axial load).

B.10 TEST RUN 23

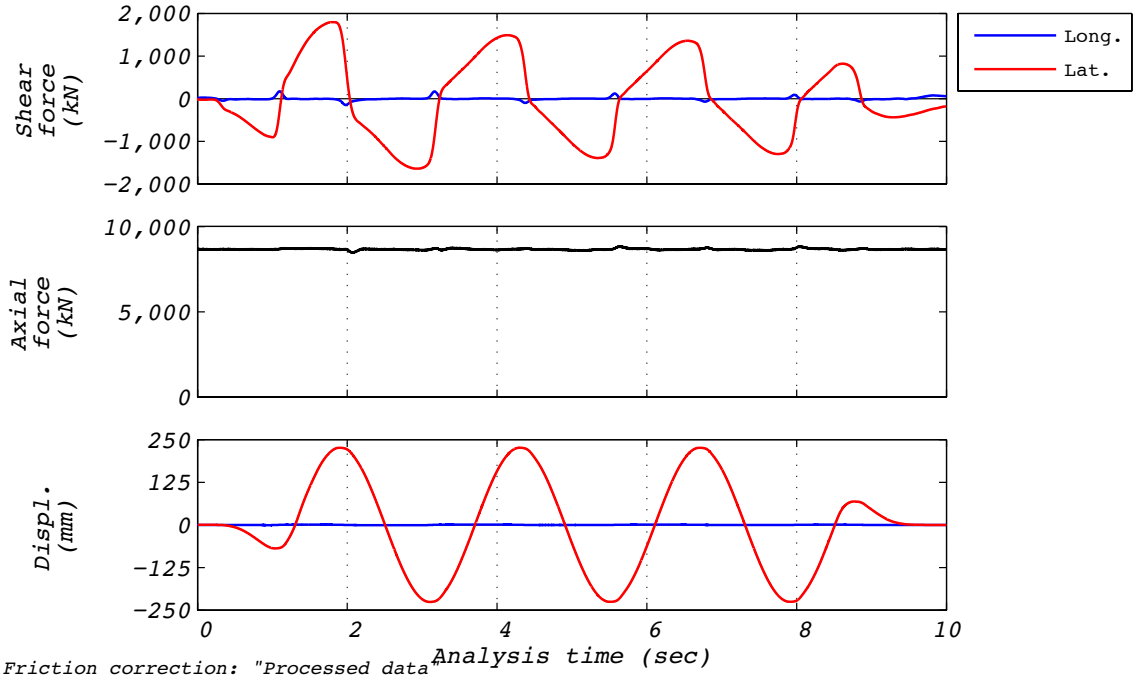

Figure B.10-1 Test run no. 23 time history: Transverse (224 mm amplitude, 8,663 kN axial load, and 586 mm/s velocity).

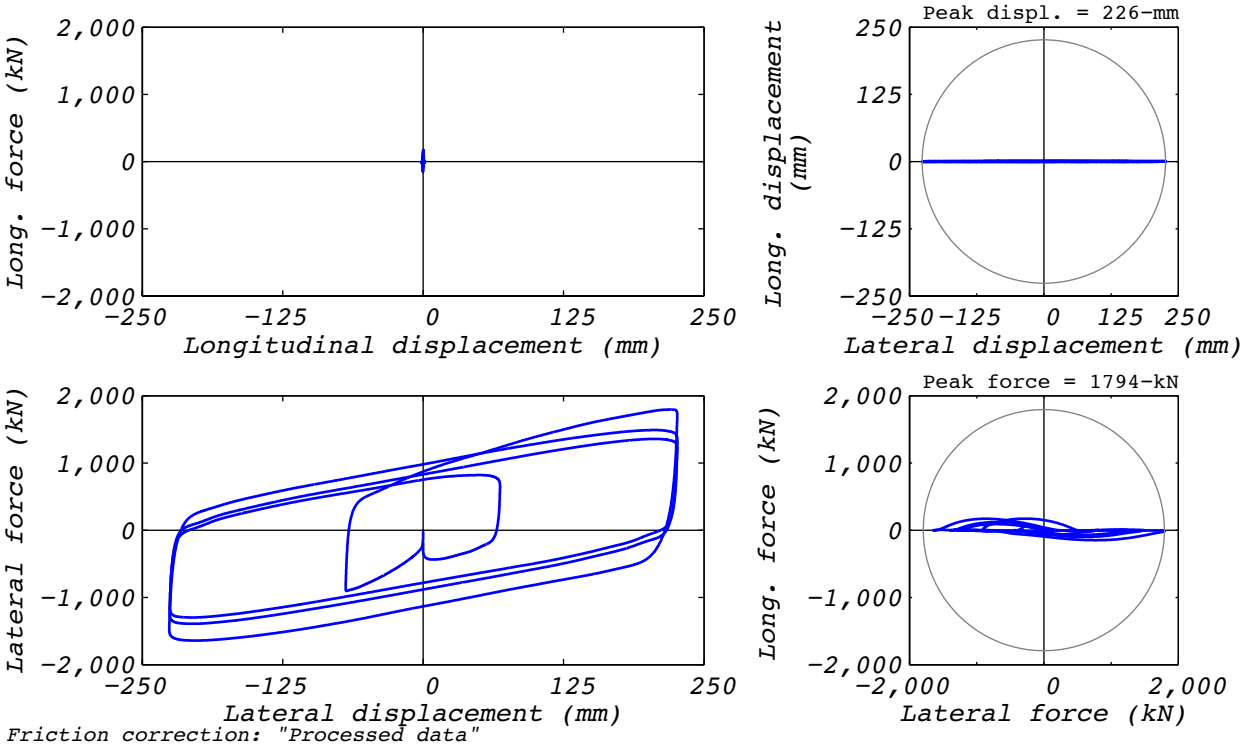

Figure B.10-2 Test run no. 23 hysteresis: Transverse (224 mm amplitude, 8,663 kN axial load, and 586 mm/s velocity).

B.11 TEST RUN 35

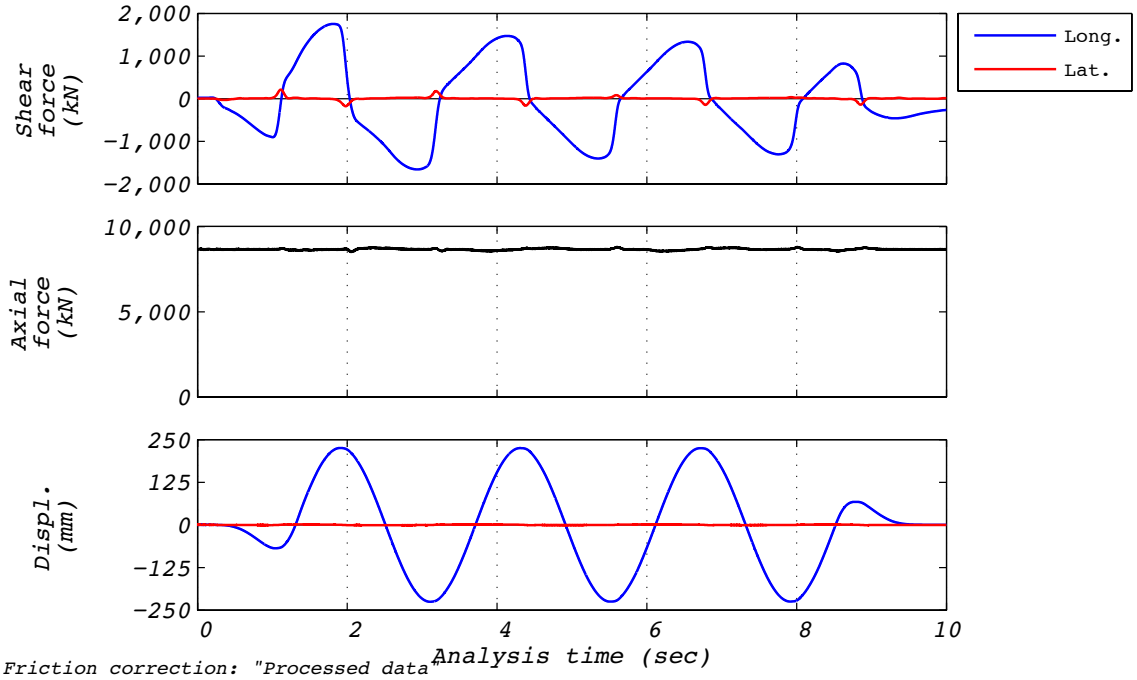

Figure B.11-1 Test run no. 35 time history: Longitudinal (224 mm amplitude, 8,663 kN axial load, and 586 mm/s velocity).

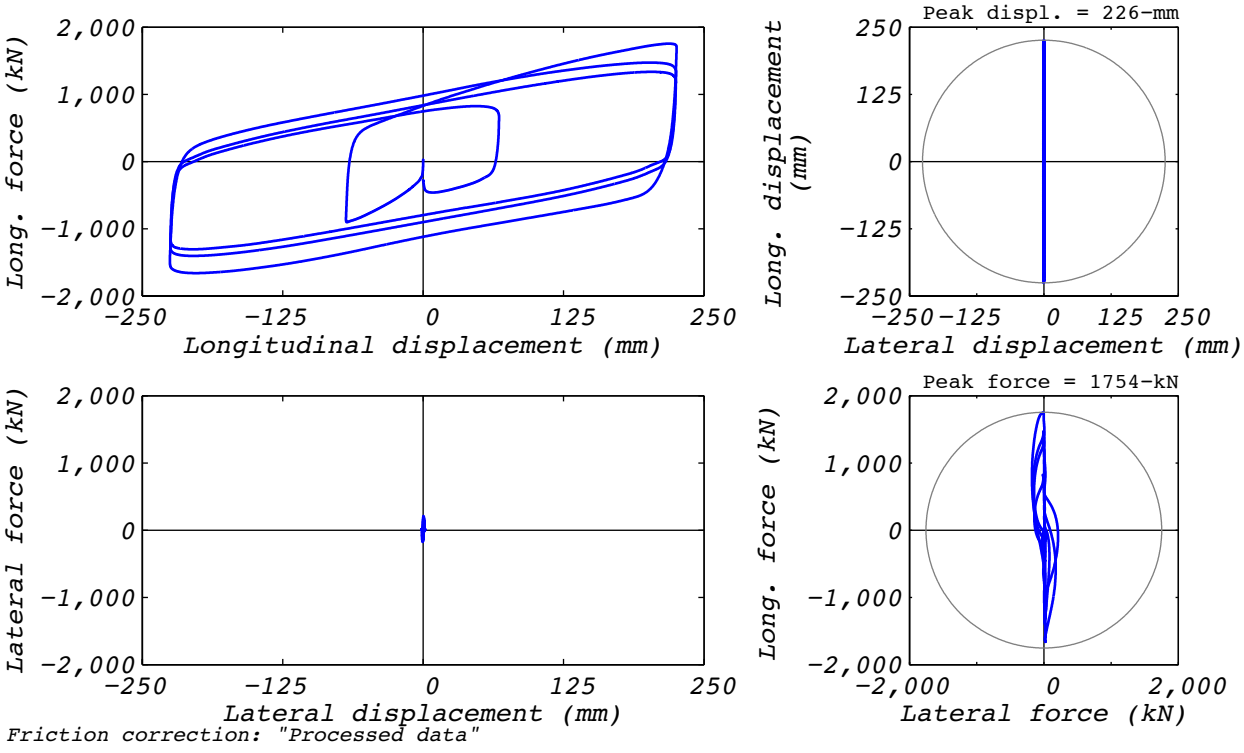

Figure B.11-2 Test run no. 35 hysteresis: Longitudinal (224 mm amplitude, 8,663 kN axial load, and 586 mm/s velocity).

B.12 TEST RUN 41

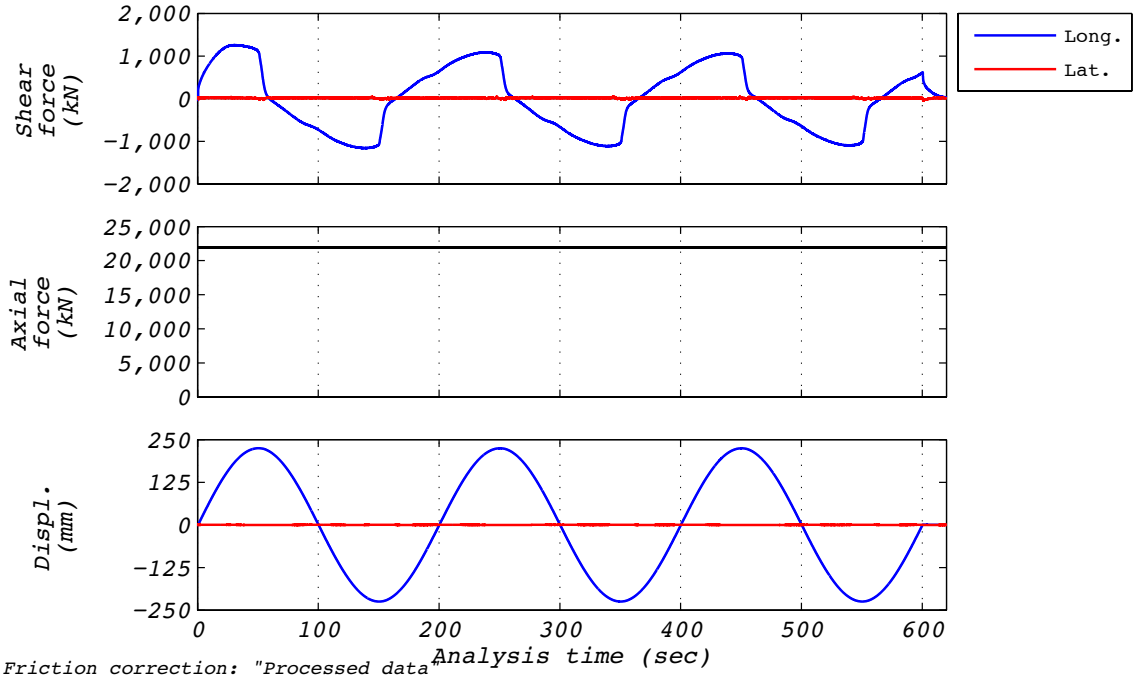

Figure B.12-1 Test run no. 41 time history: Longitudinal (224 mm amplitude, 8,663 kN axial load, and 7 mm/s velocity).

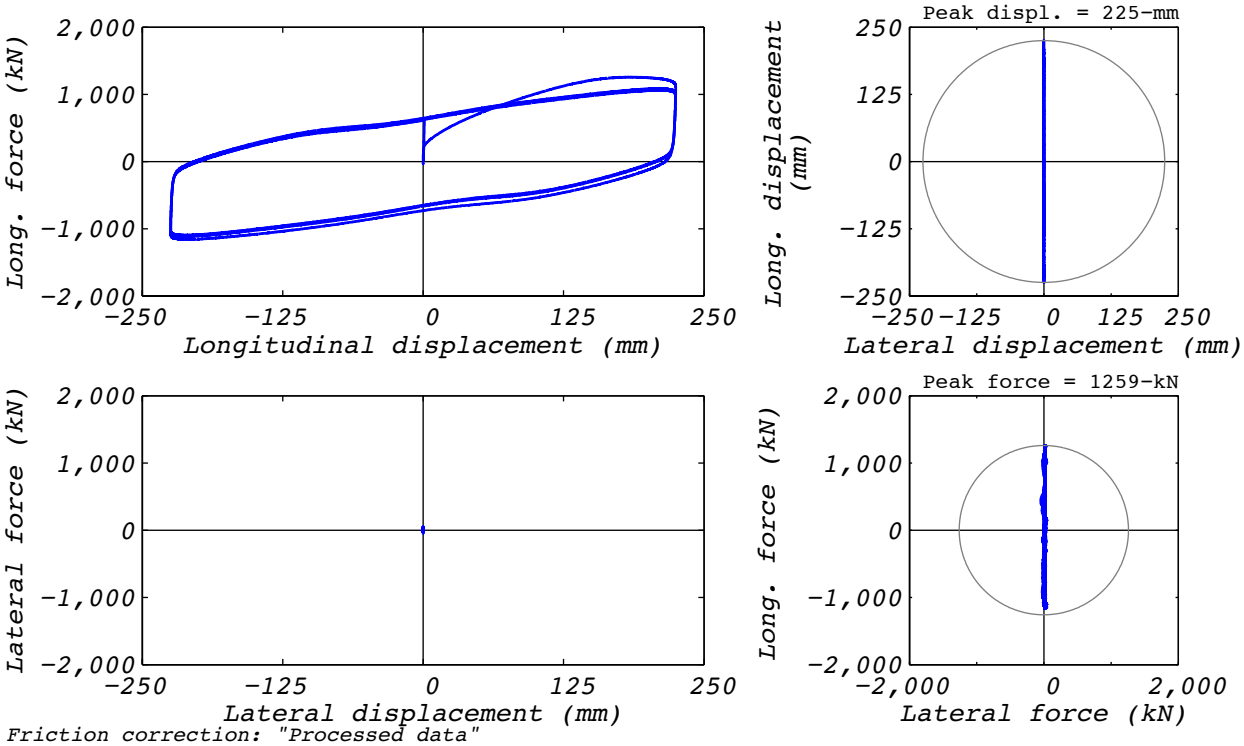

Figure B.12-2 Test run no. 41 hysteresis: Longitudinal (224 mm amplitude, 8,663 kN axial load, and 7 mm/s velocity).

B.13 TEST RUN 51

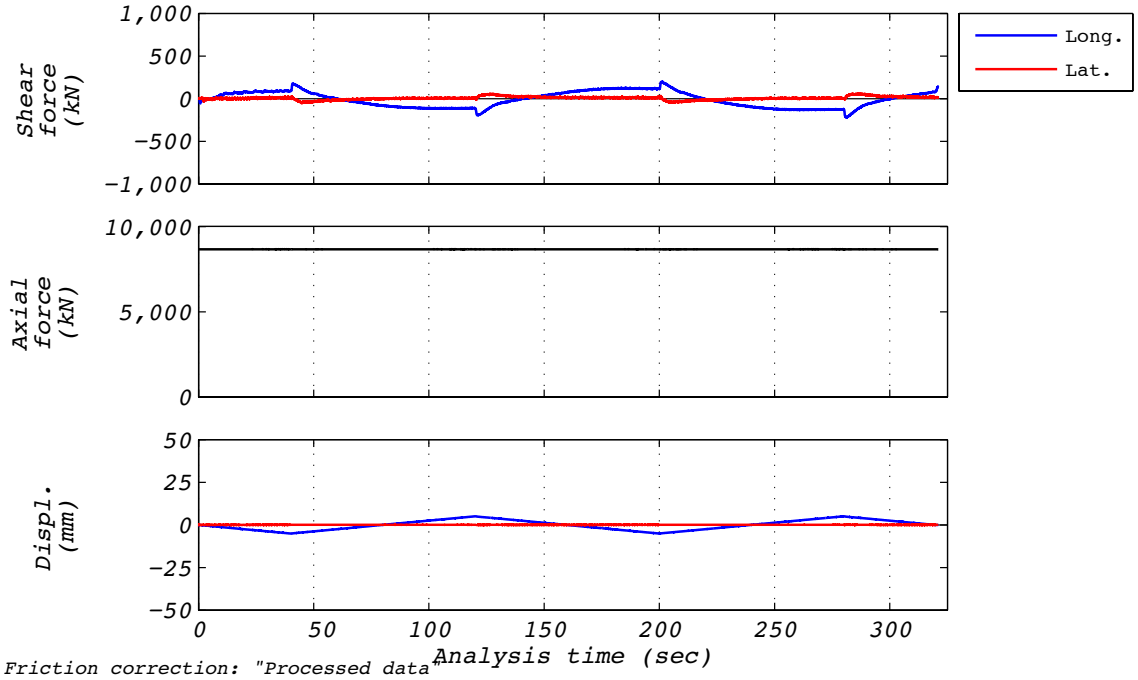

Figure B.13-1 Test run no. 51 time history: Transverse rotation (0 mm amplitude and 8,66 kN axial load).

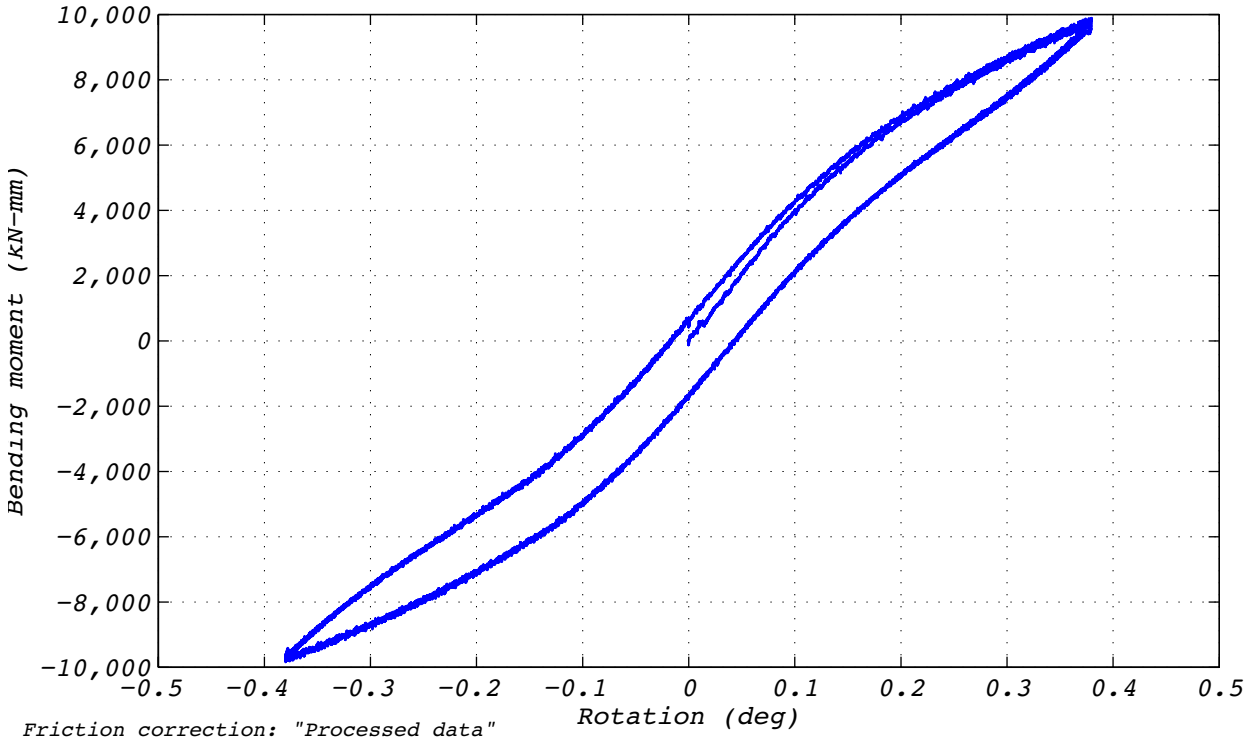

Figure B.13-2 Test run no. 51 hysteresis: Transverse rotation (0 mm amplitude and 8,66 kN axial load).

B.14 TEST RUN 52

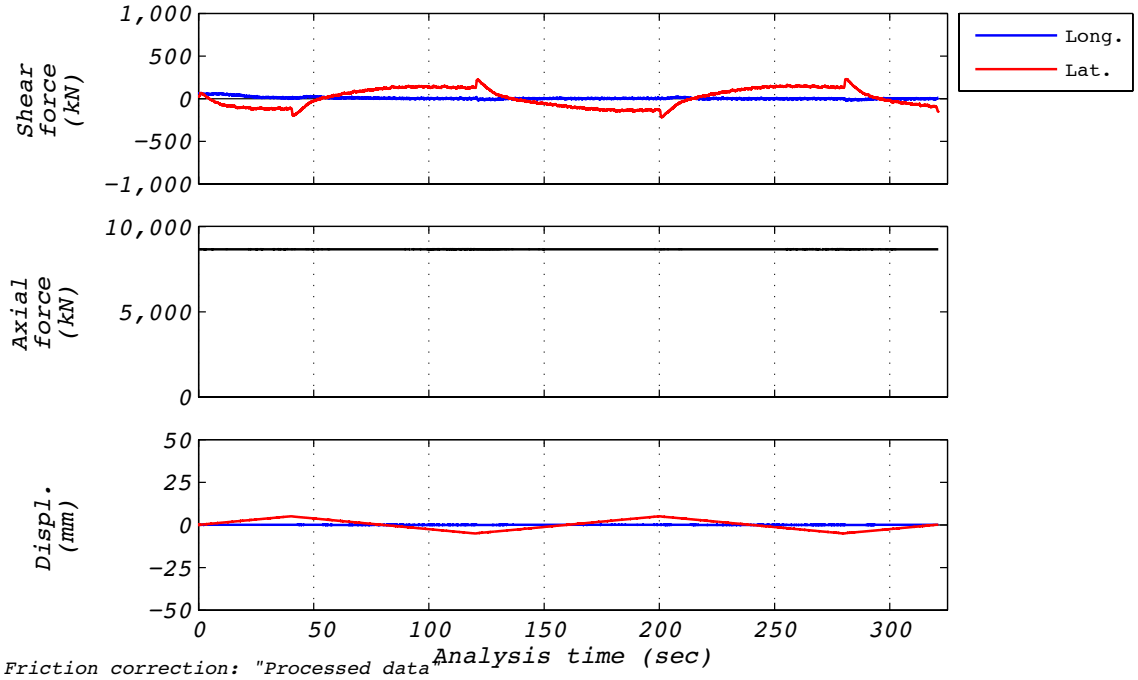

Figure B.14-1 Test run no. 52 time history: Longitudinal rotation (0 mm amplitude and 8,663 kN axial load).

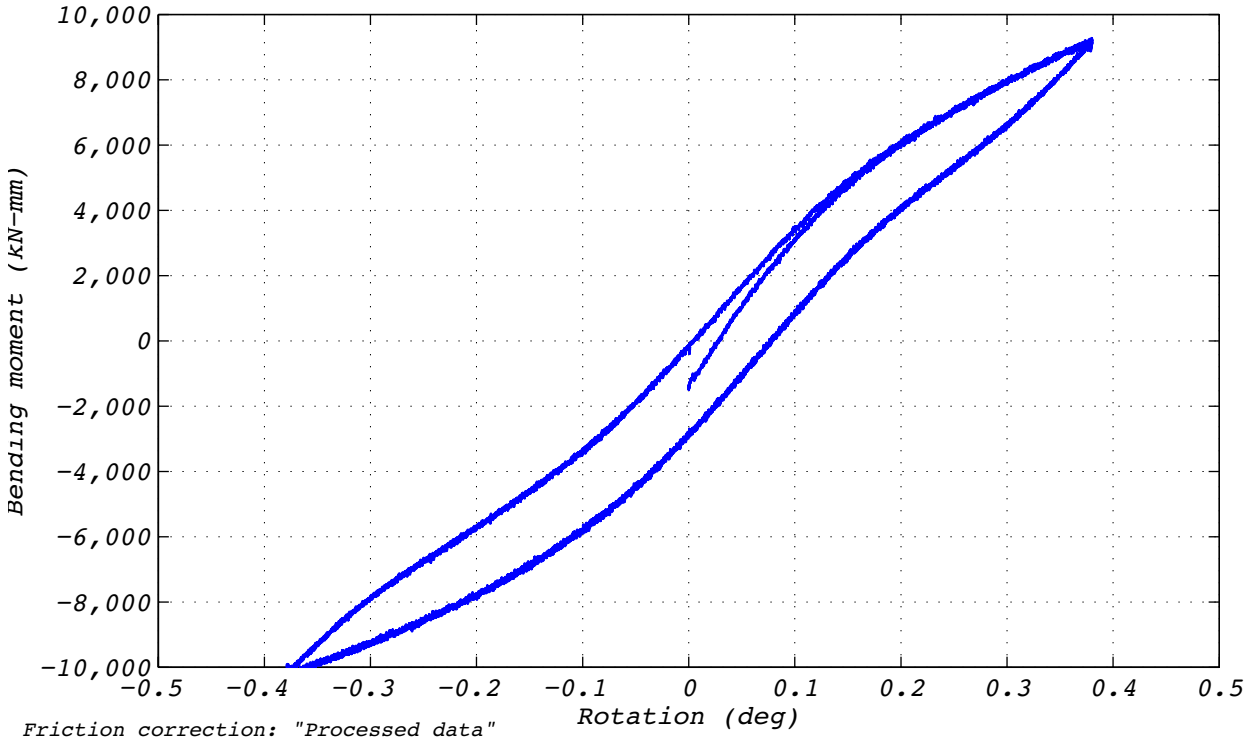

Figure B.14-2 Test run no. 52 hysteresis: Longitudinal rotation (0 mm amplitude and 8,663 kN axial load).

B.15 TEST RUN 53

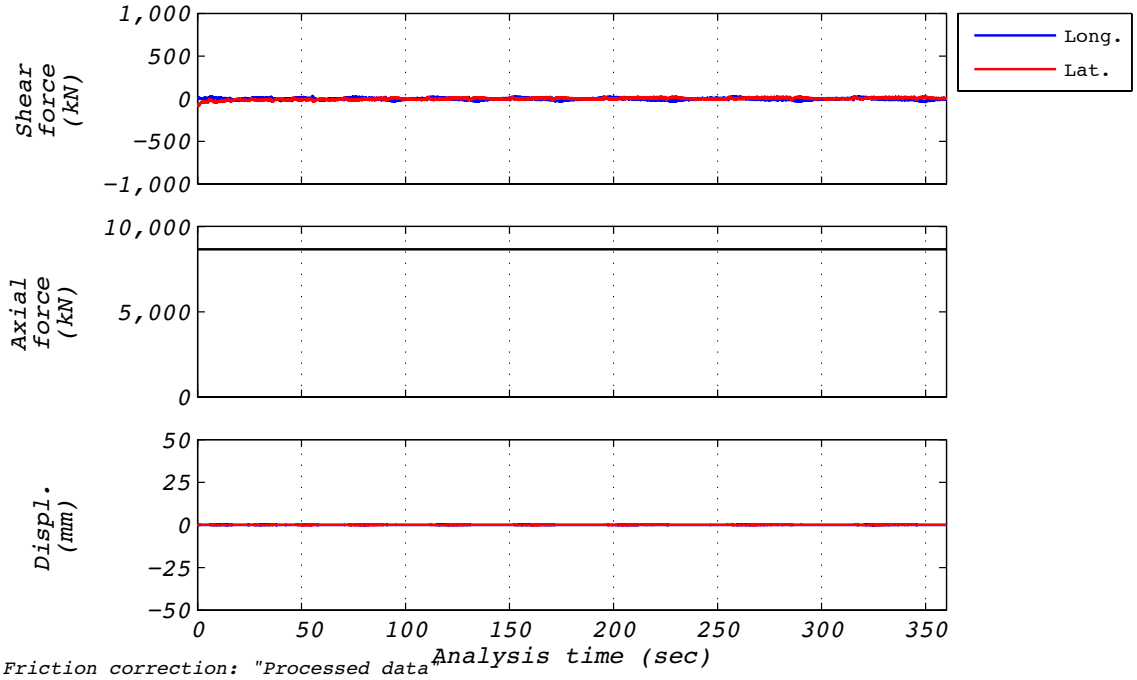

Figure B.15-1 Test run no. 53 time history: Twist (0 mm amplitude and 8,663 kN axial load).

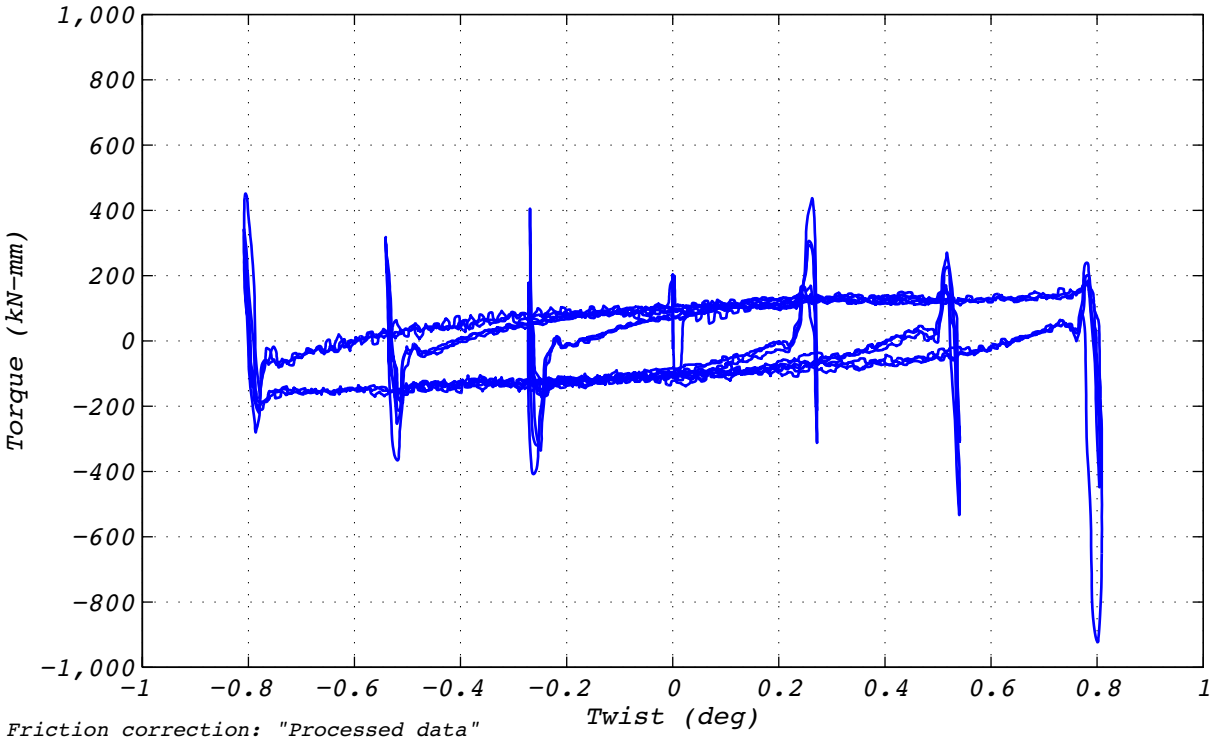

Figure B.15-2 Test run no. 53 hysteresis: Twist (0 mm amplitude and 8,663 kN axial load).

B.16 TEST RUN 54

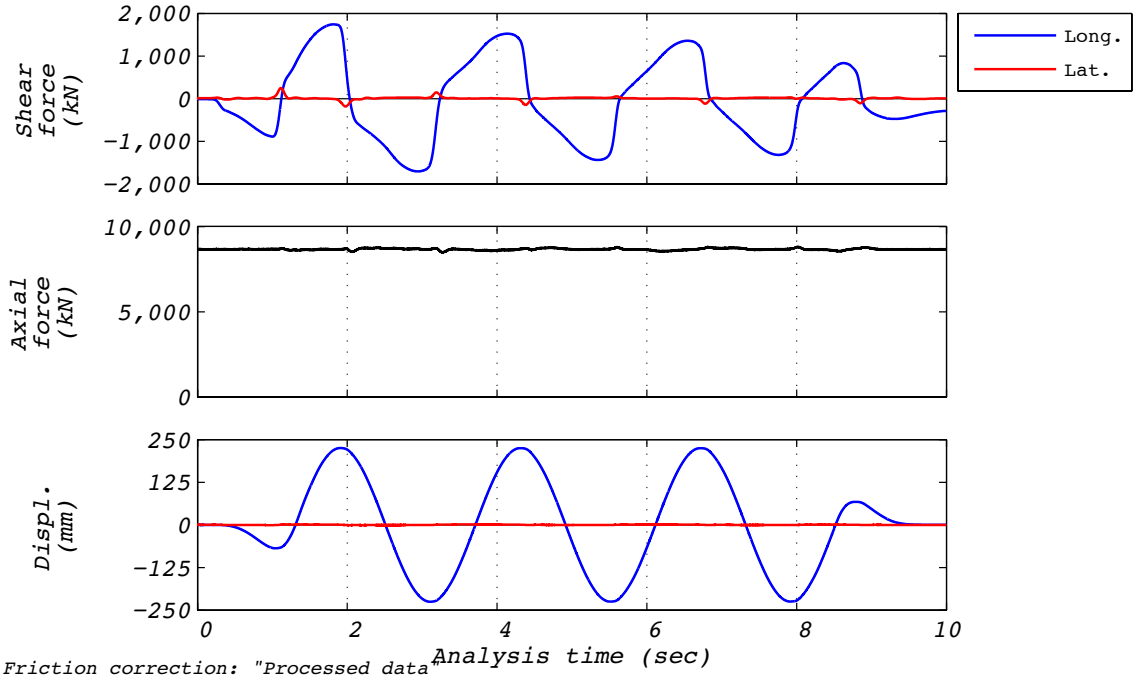

Figure B.16-1 Test run no. 54 time history: Longitudinal (224 mm amplitude, 8,663 kN axial load, and 586 mm/s velocity).

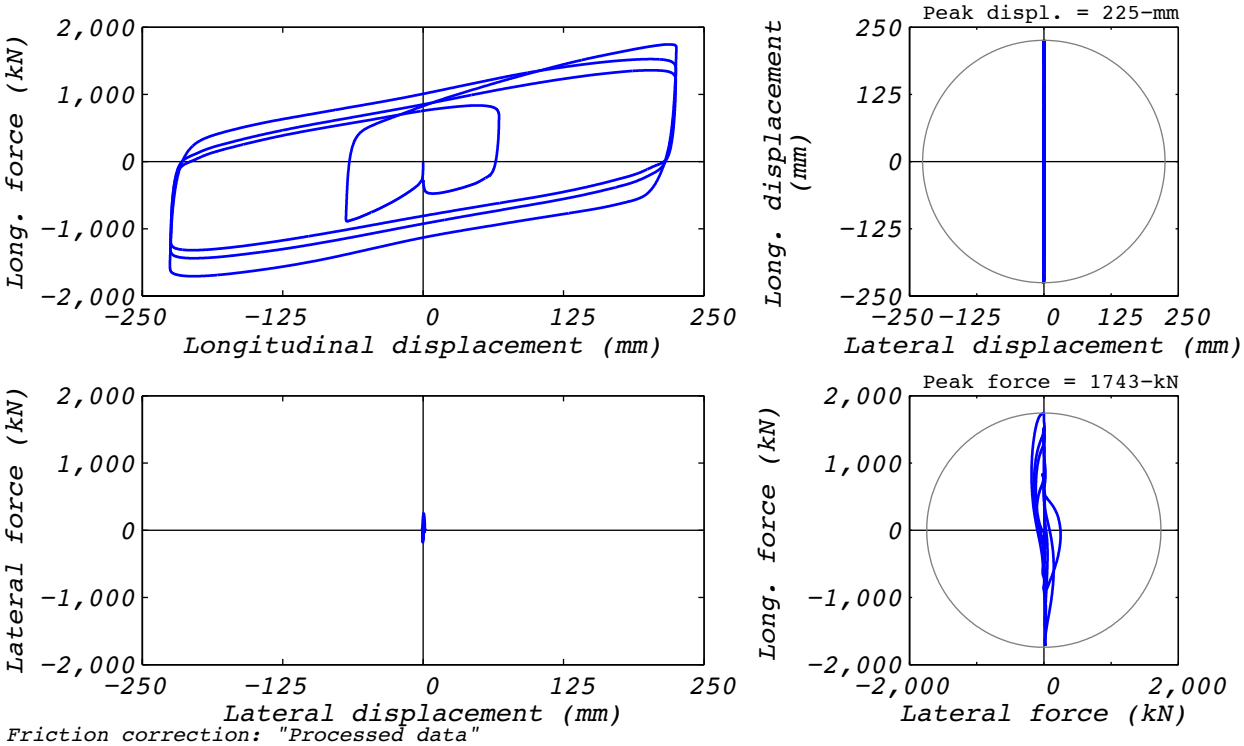

Figure B.16-2 Test run no. 54 hysteresis: Longitudinal (224 mm amplitude, 8,663 kN axial load, and 586 mm/s velocity).

B.17 TEST RUN 56

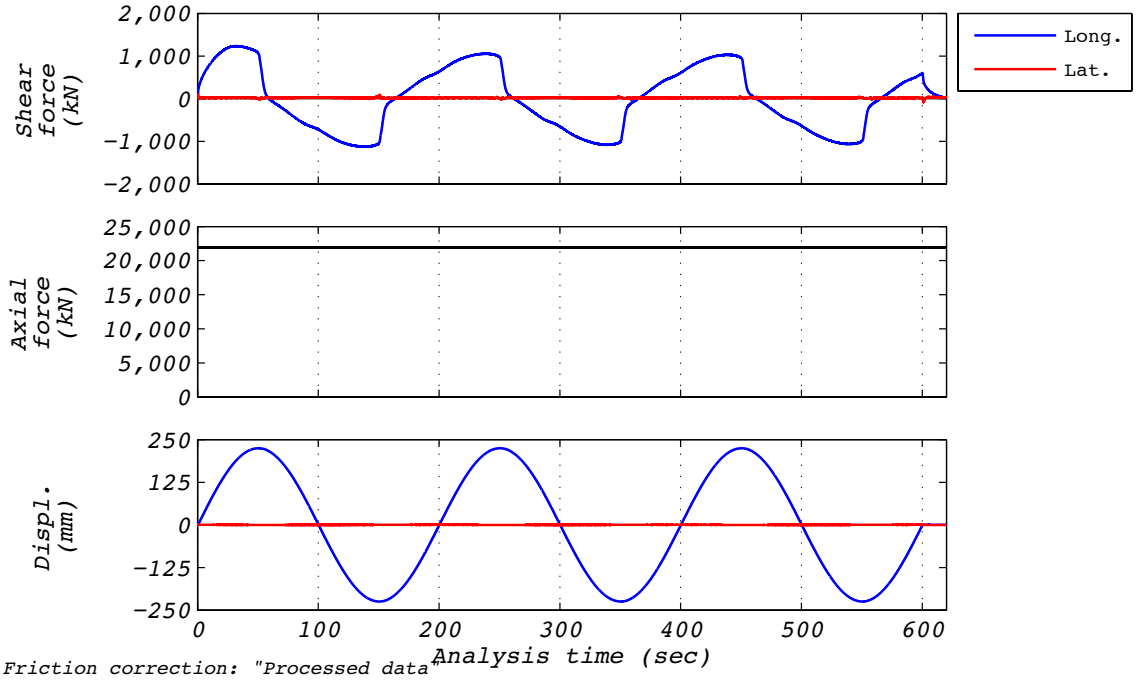

Figure B.17-1 Test run no. 56 time history: Longitudinal (224 mm amplitude, 8,663 kN axial load, and 7 mm/s velocity).

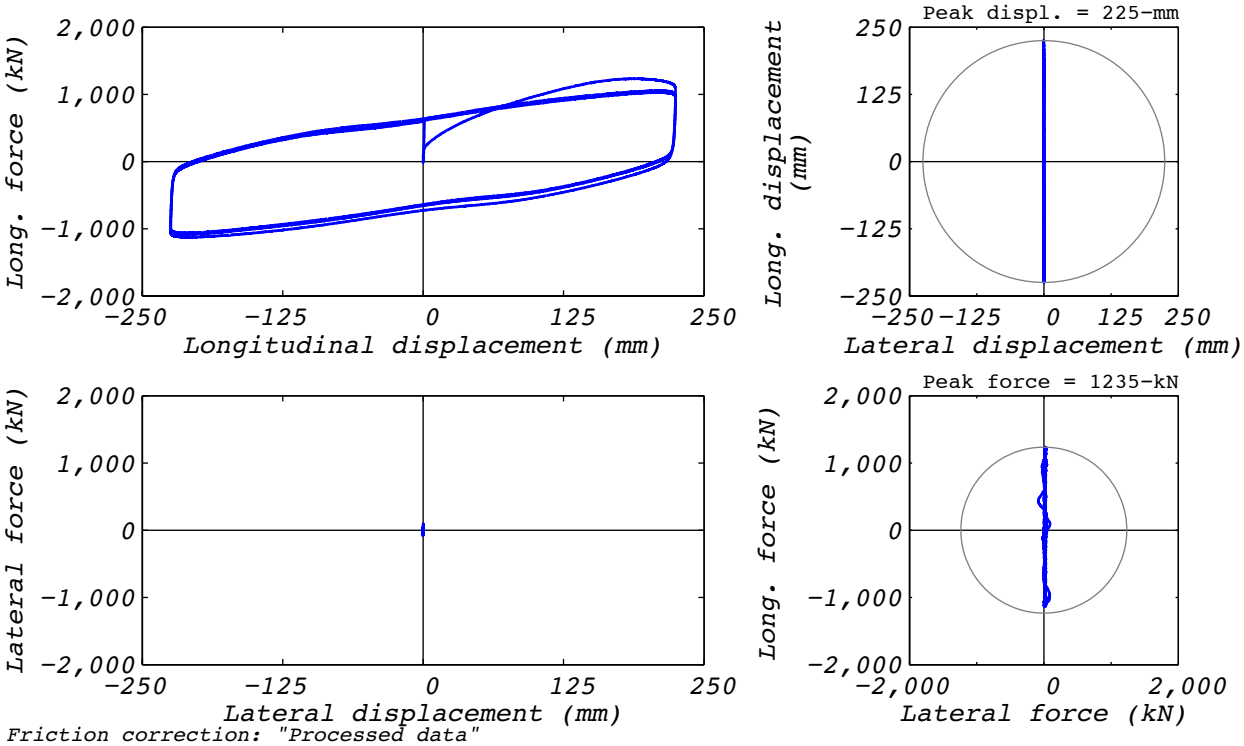

Figure B.17-2 Test run no. 56 hysteresis: Longitudinal (224 mm amplitude, 8,663 kN axial load, and 7 mm/s velocity).

B.18 TEST RUN 57

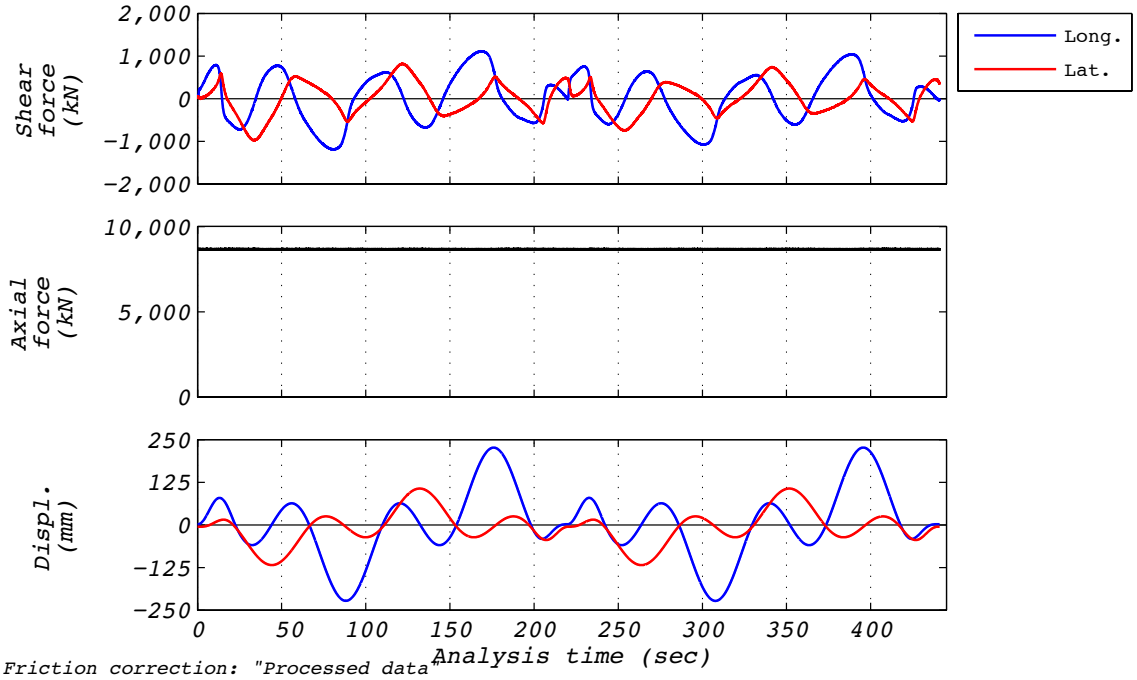

Figure B.18-1 Test run no. 57 time history: Clover leaf orbit (224 mm amplitude, 8,664 kN axial load, and varying velocity).

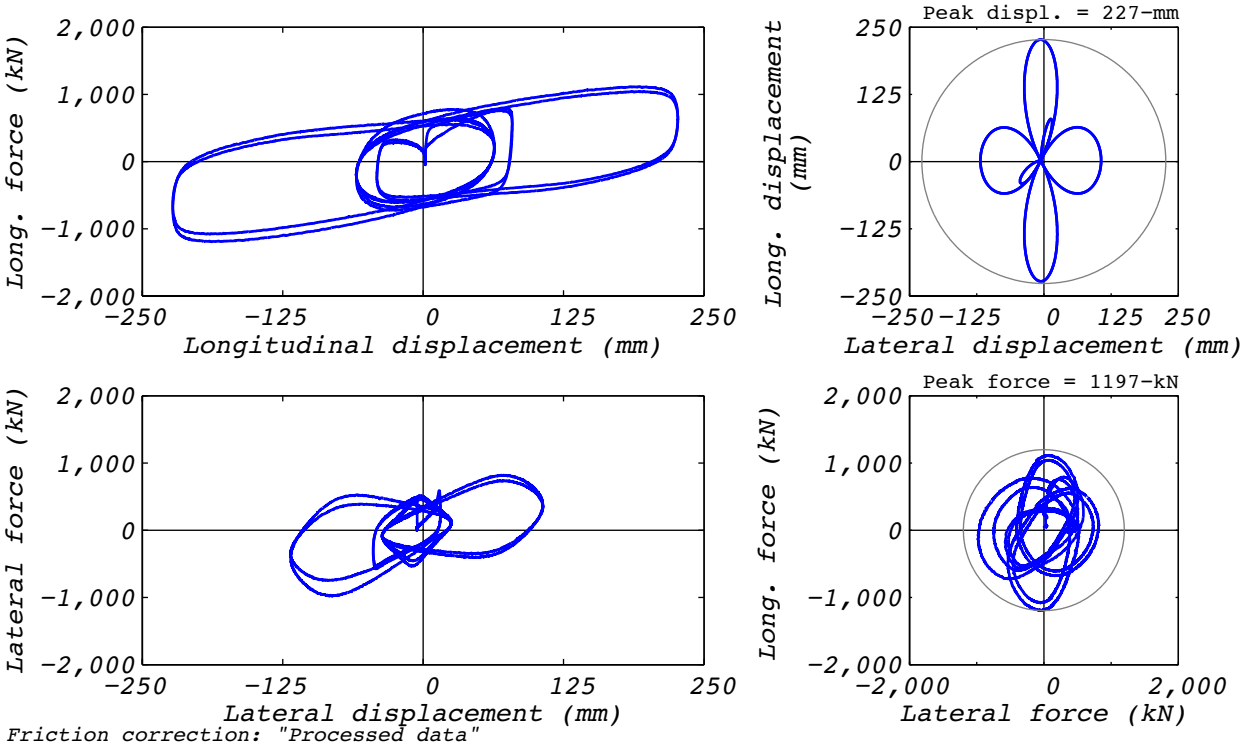

Figure B.18-2 Test run no. 57 hysteresis: Clover leaf orbit (224 mm amplitude, 8,664 kN axial load, and varying velocity).

B.19 TEST RUN 59

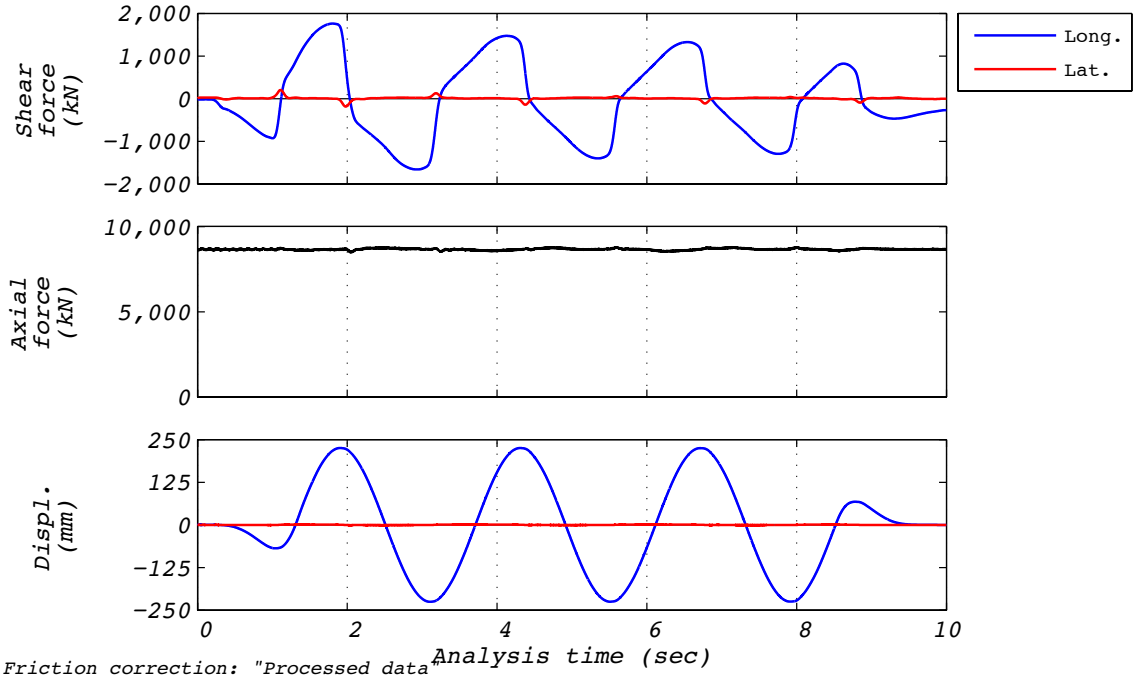

Figure B.19-1 Test run no. 59 time history: Longitudinal (224 mm amplitude, 8,663 kN axial load, and 586 mm/s velocity).

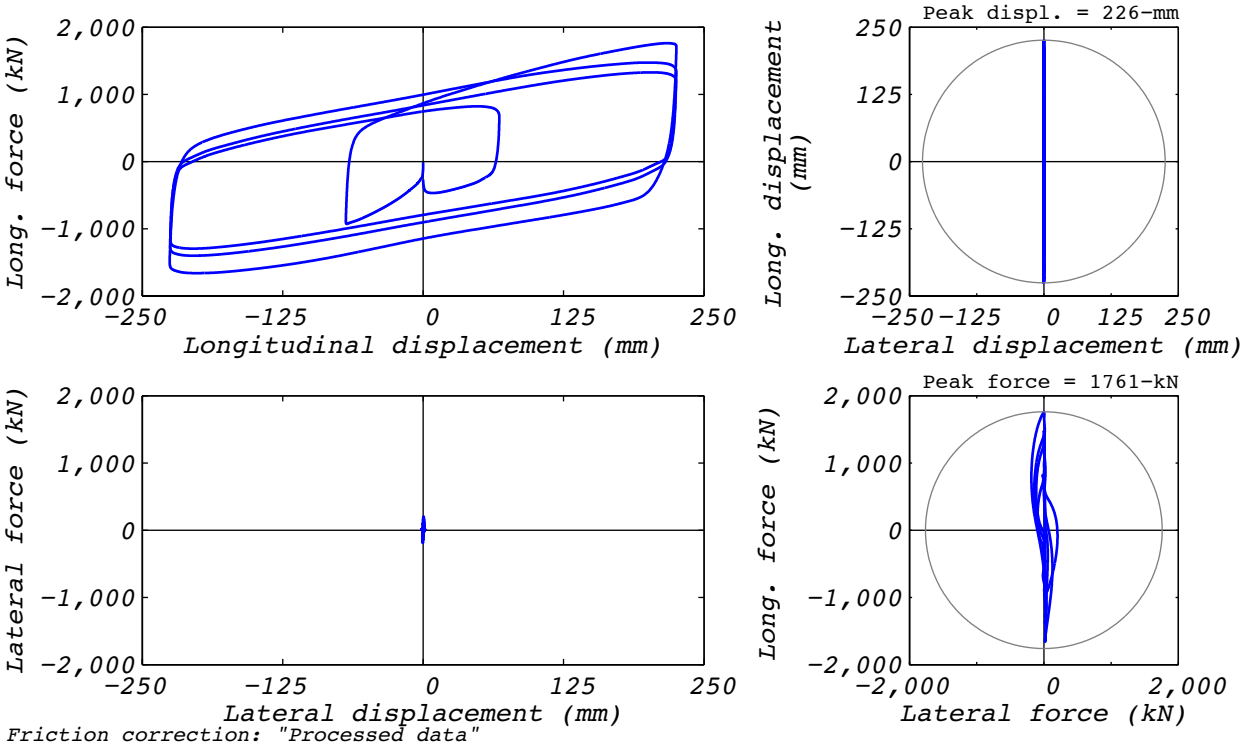

Figure B.19-2 Test run no. 59 hysteresis: Longitudinal (224 mm amplitude, 8,663 kN axial load, and 586 mm/s velocity).

B.20 TEST RUN 62

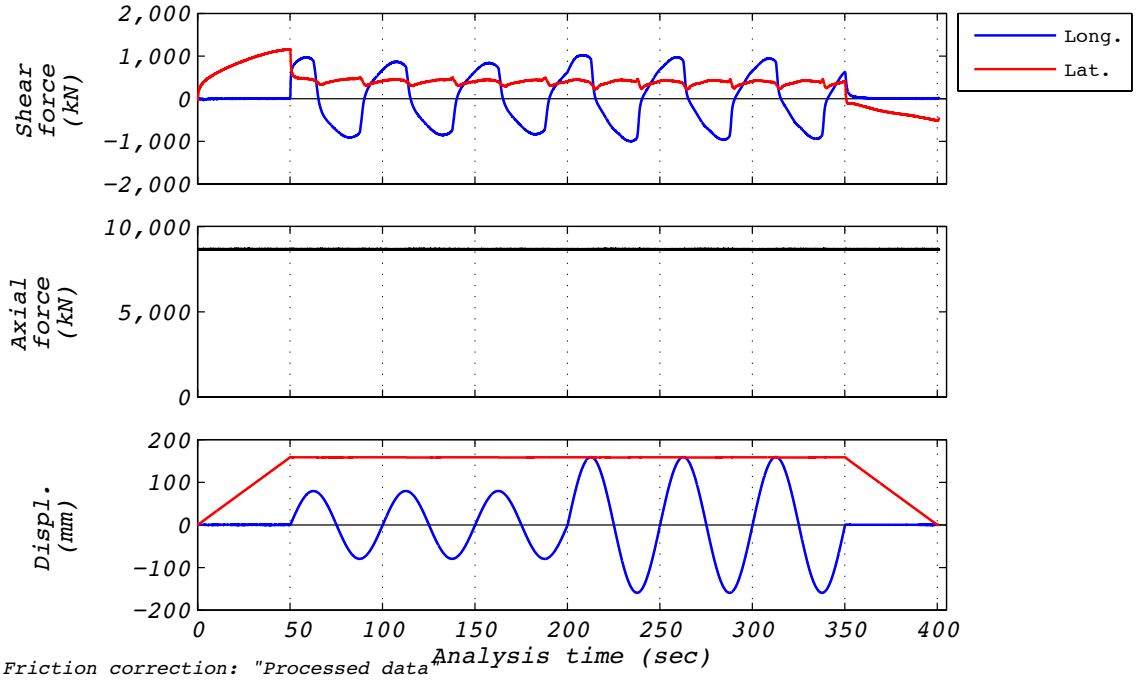

Figure B.20-1 Test run no. 62 time history: Bidirectional (224 mm amplitude, 8,663 kN kN axial load, and 28 mm/s velocity).

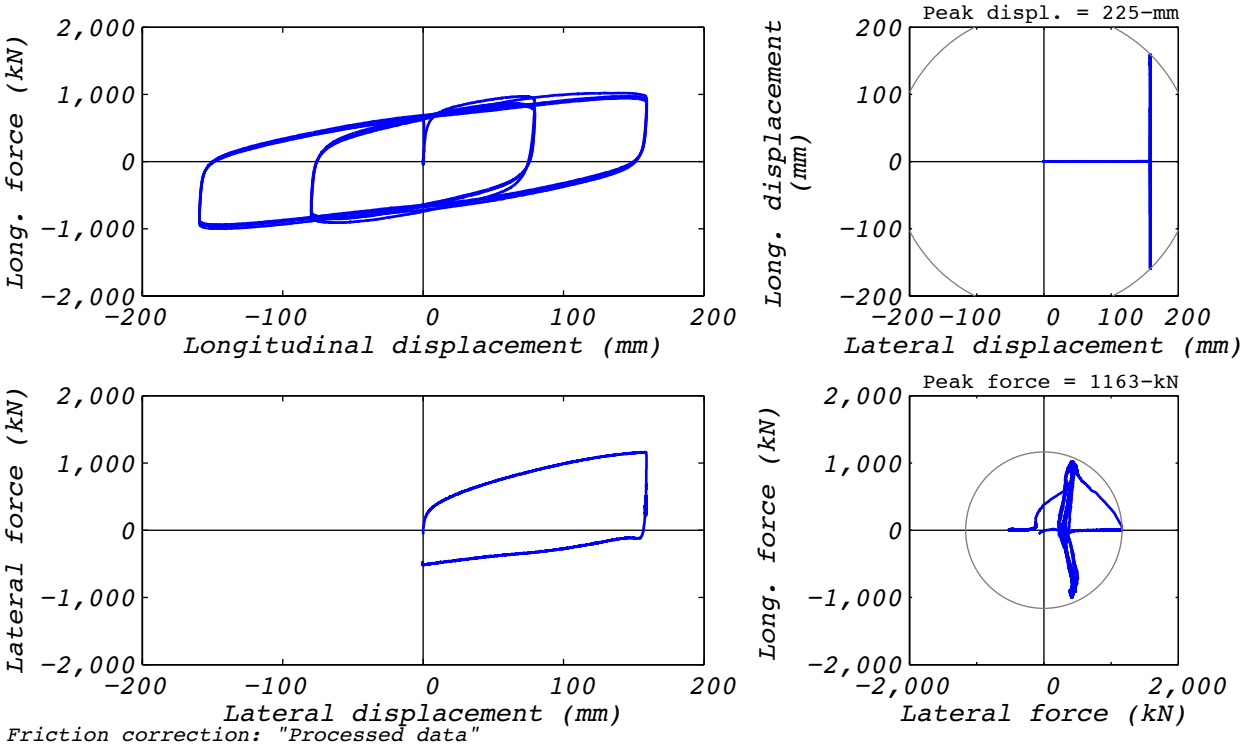

Figure B.20-2 Test run no. 62 hysteresis: Bidirectional (224 mm amplitude, 8,663 kN kN axial load, and 28 mm/s velocity).

B.21 TEST RUN 64

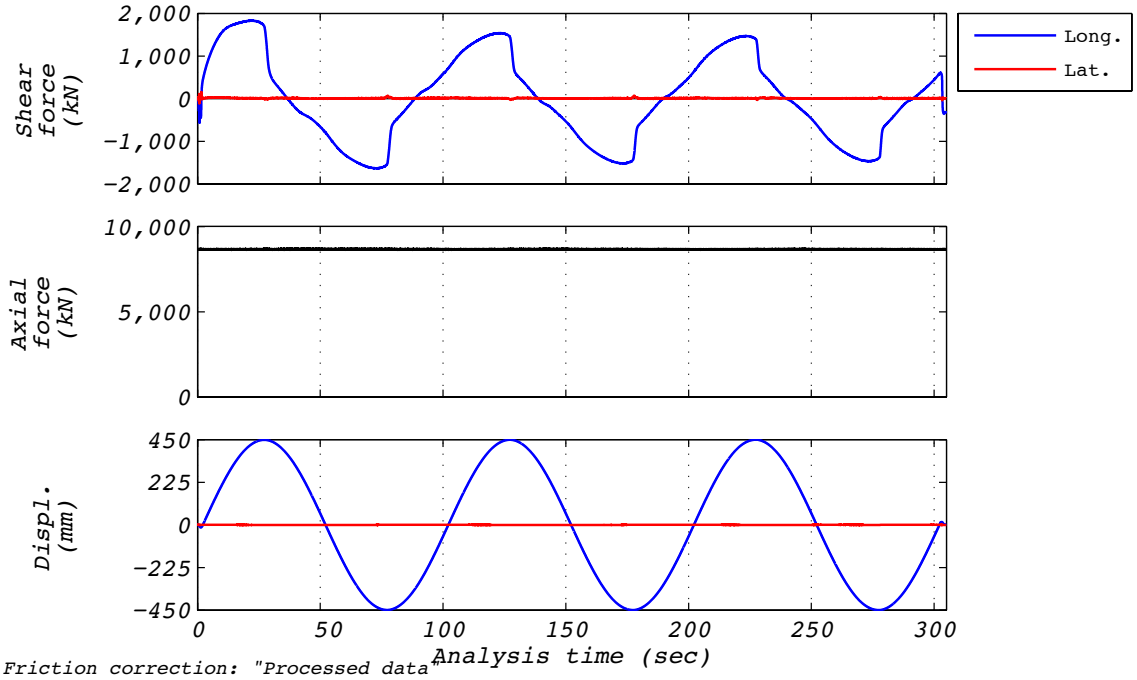

Figure B.21-1 Test run no. 64 time history: Longitudinal (448 mm amplitude, 8,663 kN axial load, and 28 mm/s velocity).

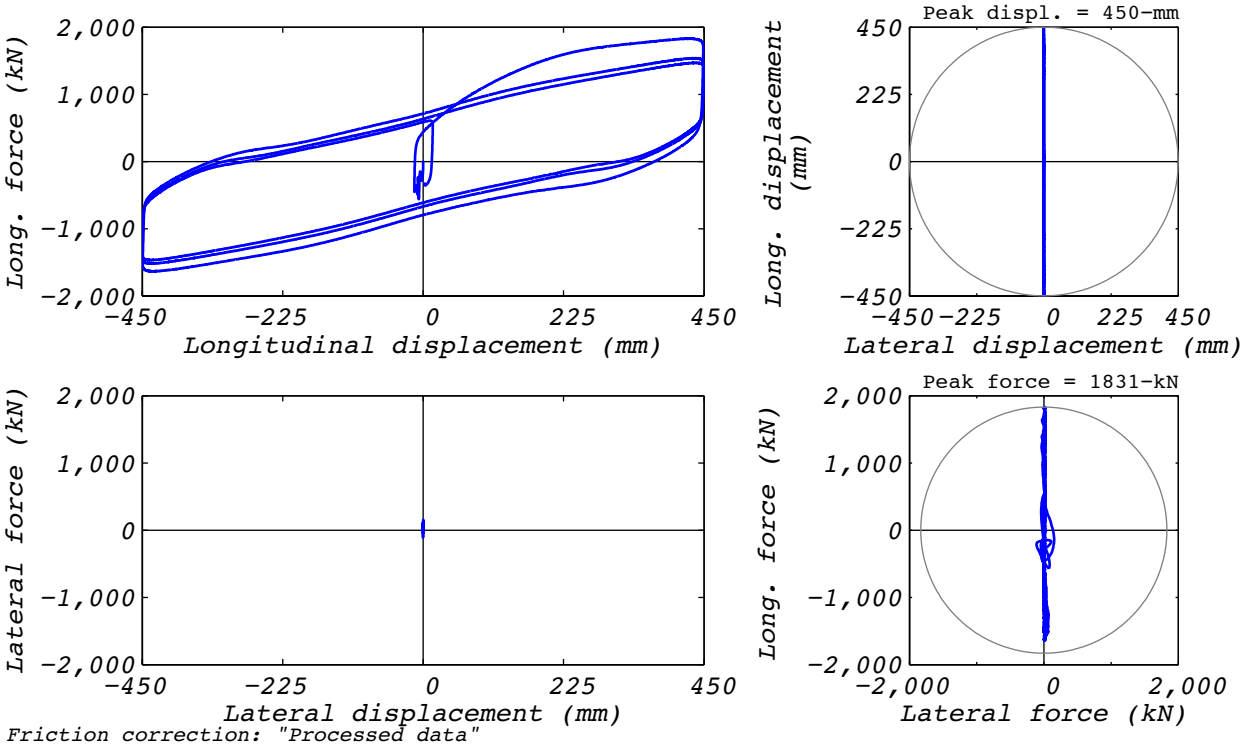

Figure B.21-2 Test run no. 64 hysteresis: Longitudinal (448 mm amplitude, 8,663 kN axial load, and 28 mm/s velocity).

B.22 TEST RUN 65

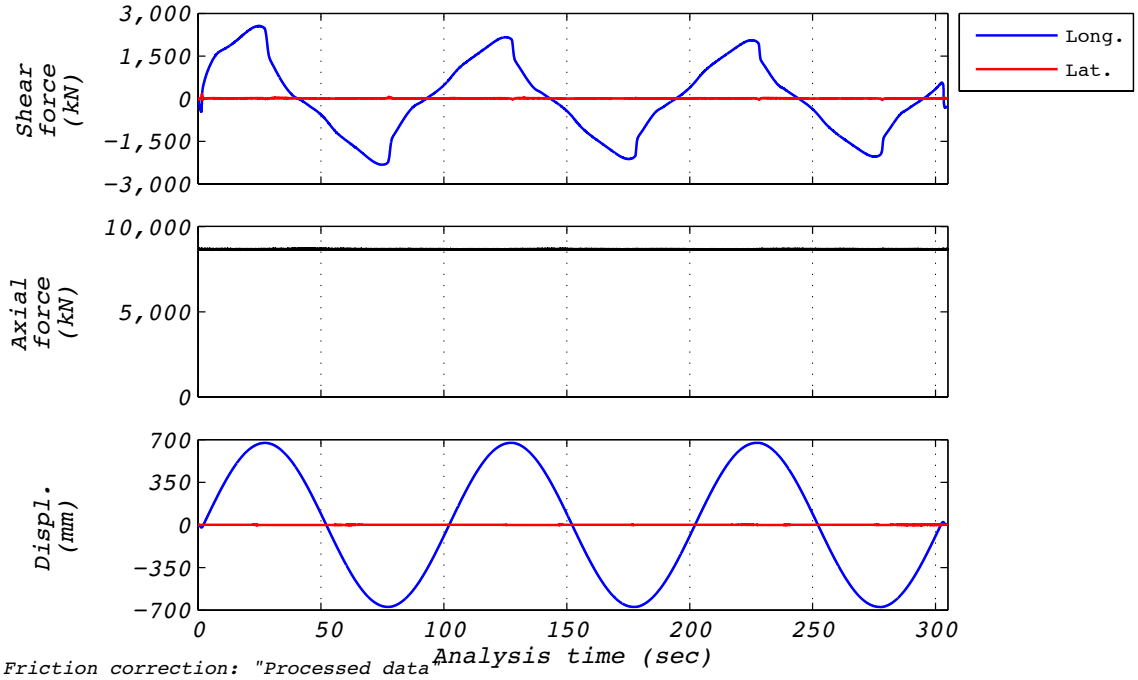

Figure B.22-1 Test run no. 65 time history: Longitudinal (896 mm amplitude, 8,663 kN axial load, and 56 mm/s velocity).

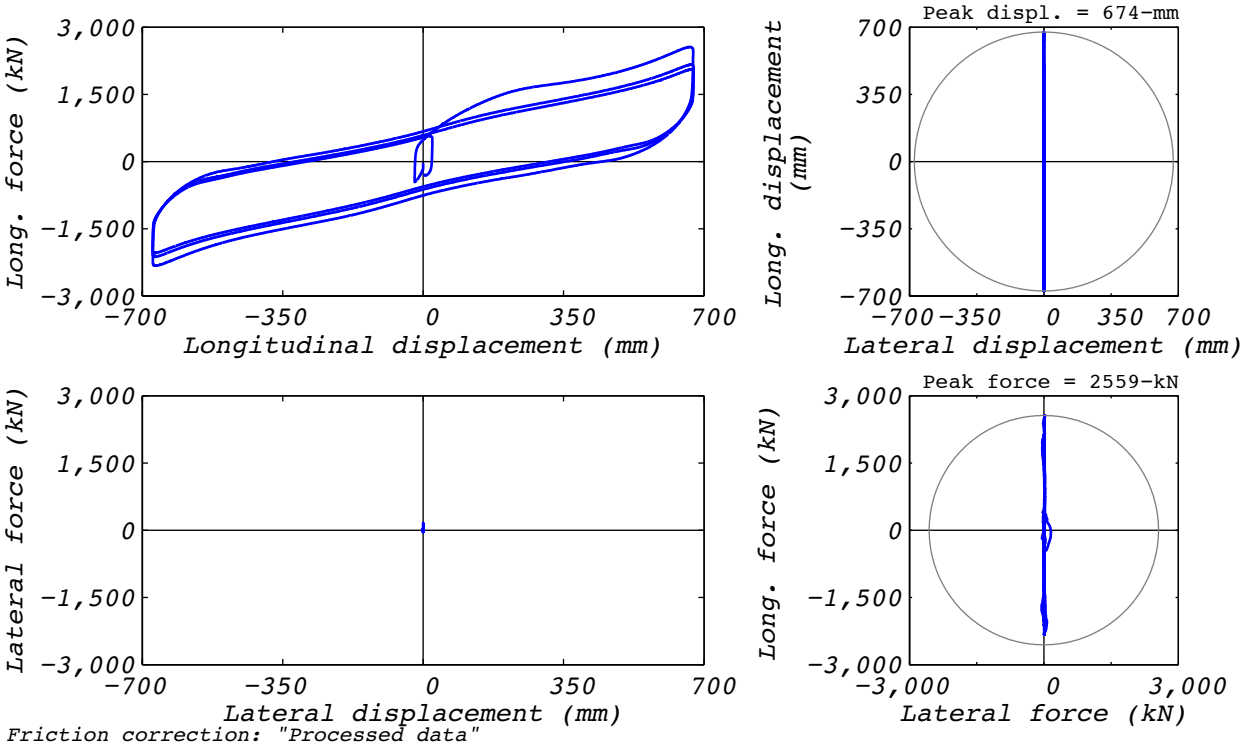

Figure B.22-2 Test run no. 65 hysteresis: Longitudinal (896 mm amplitude, 8,663 kN axial load, and 56 mm/s velocity).

B.23 TEST RUN 66

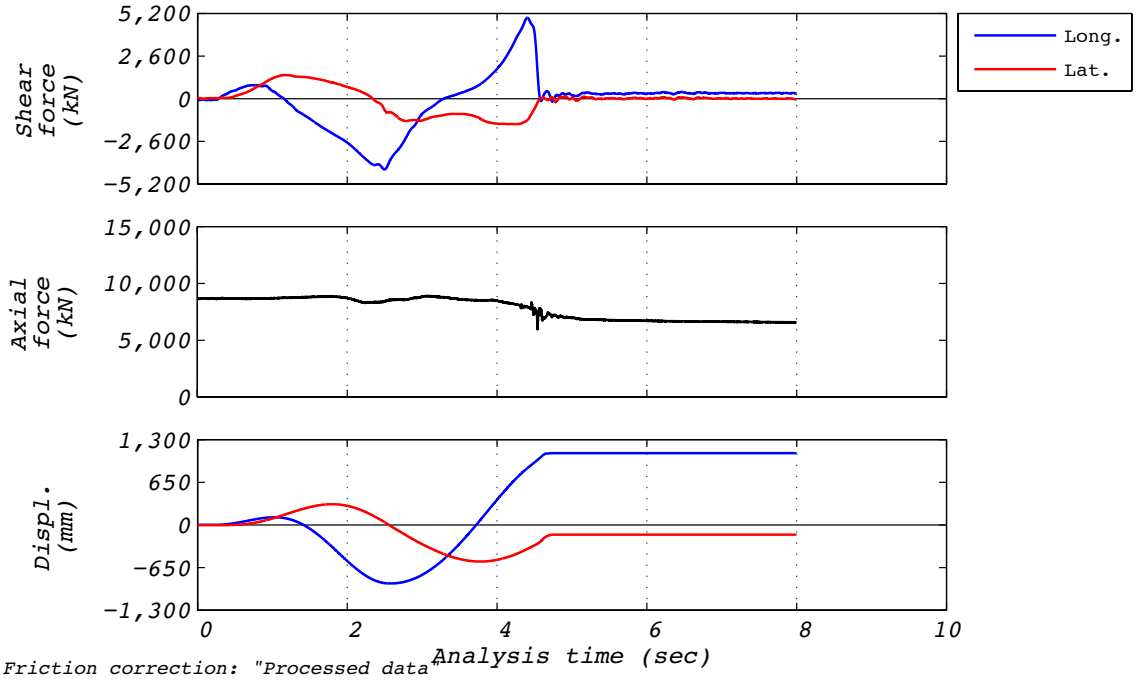

Figure B.23-1 Test run no. 66 time history: Bearing response during failure test (varying amplitude and 8,663 kN axial load).

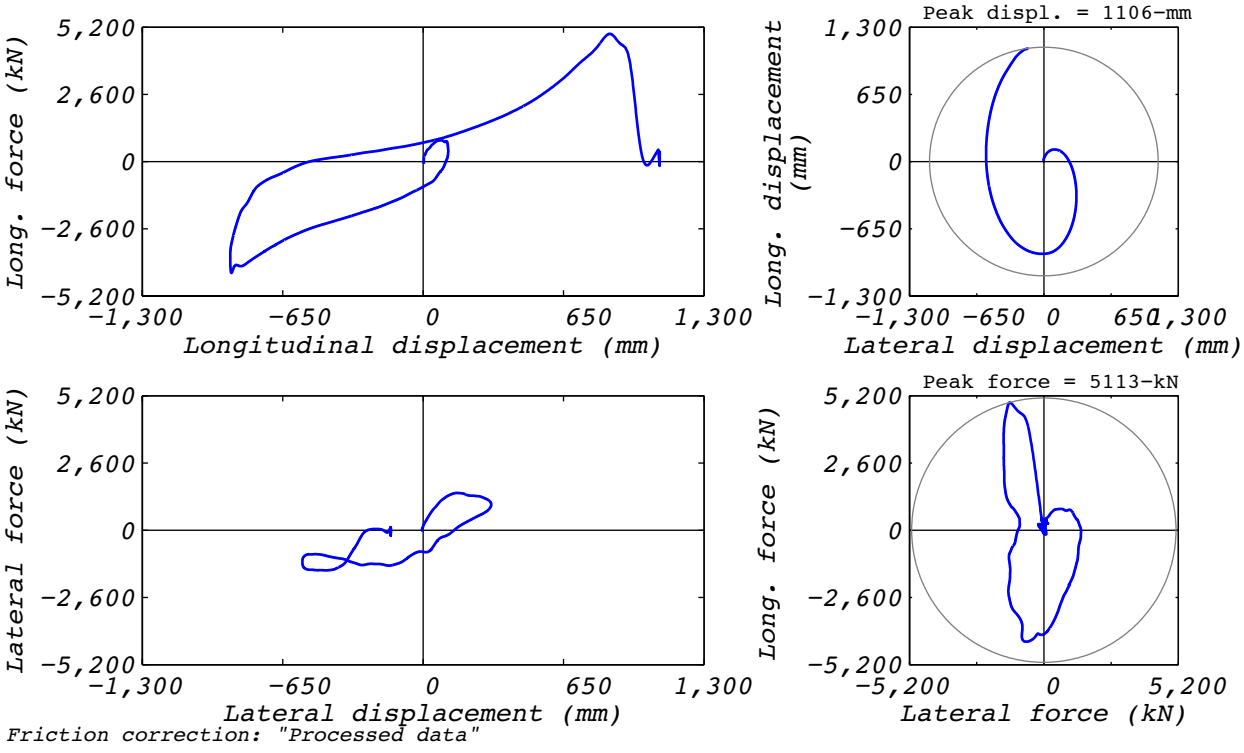

Figure B.23-2 Test run no. 66 hysteresis: Bearing response during failure test (varying amplitude and 8,663 kN axial load).

B.24 TEST RUN 67

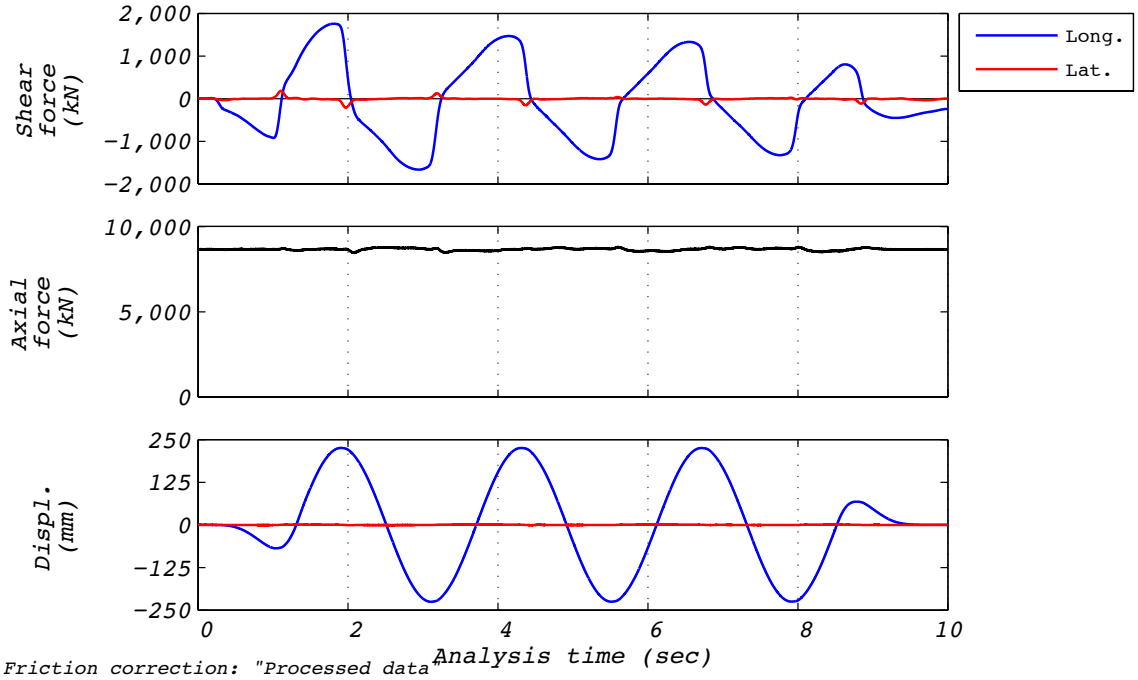

Figure B.24-1 Test run no. 67 time history: Longitudinal (224 mm amplitude, 8,663 kN kN axial load, 586 mm/s velocity).

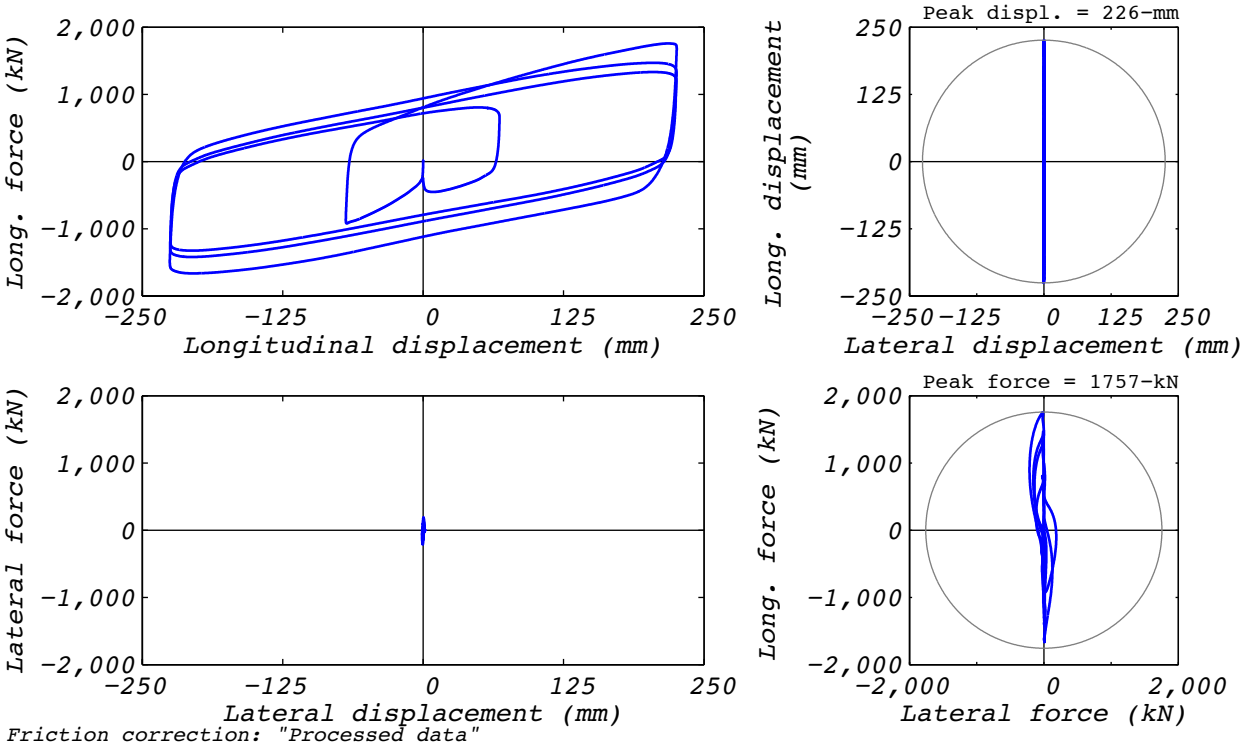

Figure B.24-2 Test run no. 67 hysteresis: Longitudinal (224 mm amplitude, 8,663 kN kN axial load, 586 mm/s velocity).

B.25 TEST RUN 68

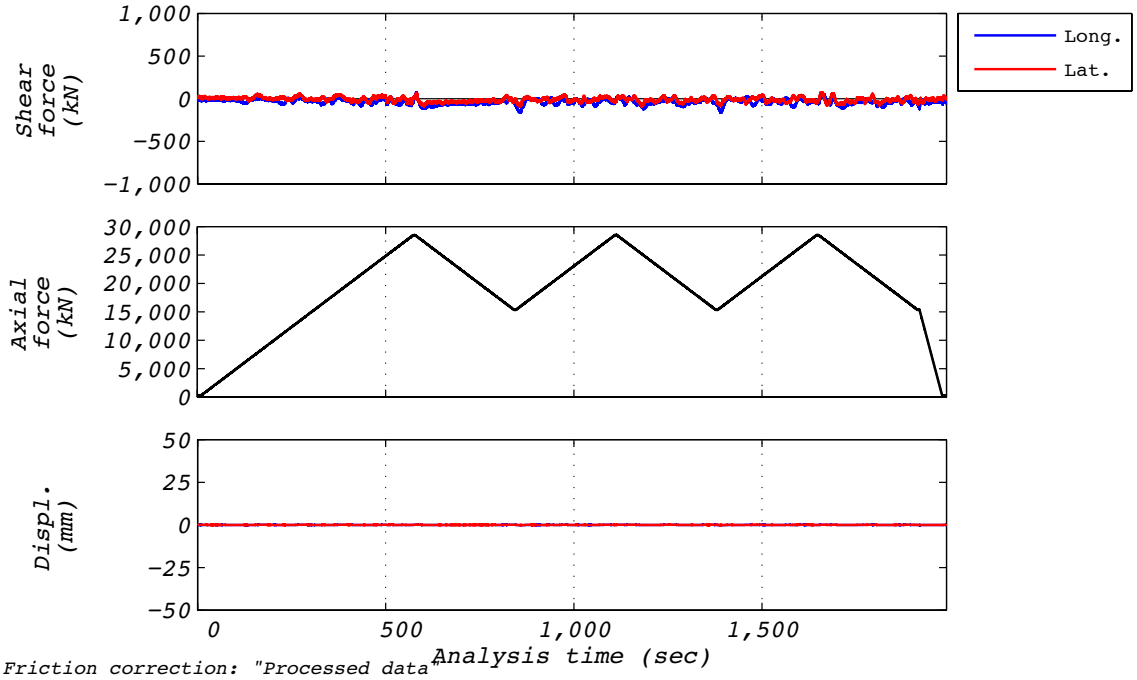

Figure B.25-1 Test run no. 68 time history: Axial (0 mm amplitude, varying axial load).

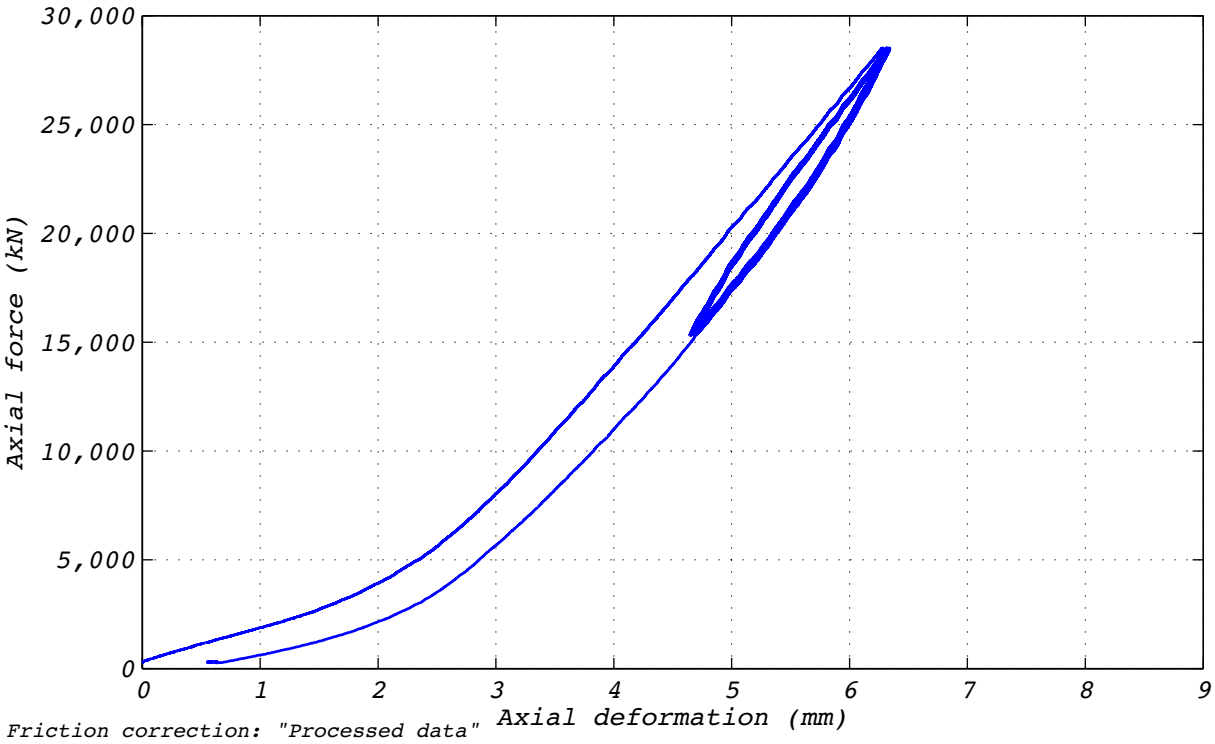

Figure B.25-2 Test run no. 68 hysteresis: Axial (0 mm amplitude, varying axial load).

B.26 TEST RUN 69

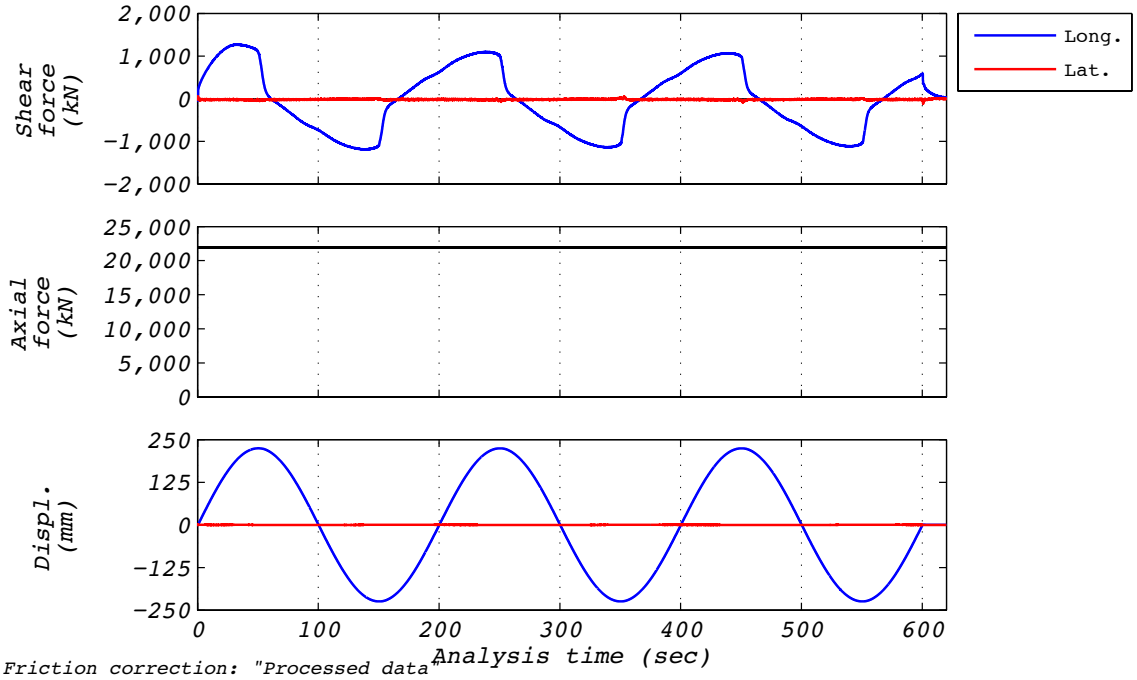

Figure B.26-1 Test run no. 69 time history: Longitudinal (224 mm amplitude, 21,927 kN axial load, and 7 mm/s velocity).

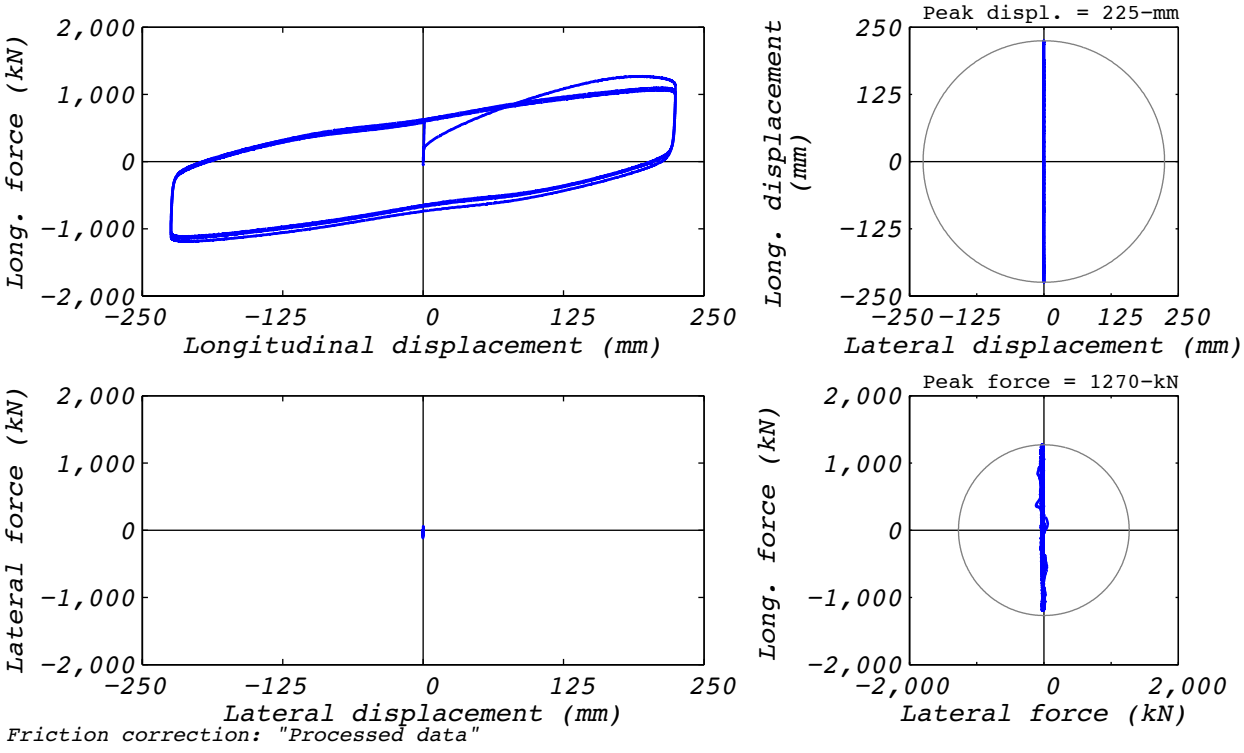

Figure B.26-2 Test run no. 69 hysteresis: Longitudinal (224 mm amplitude, 21,927 kN axial load, and 7 mm/s velocity).

B.27 TEST RUN 70

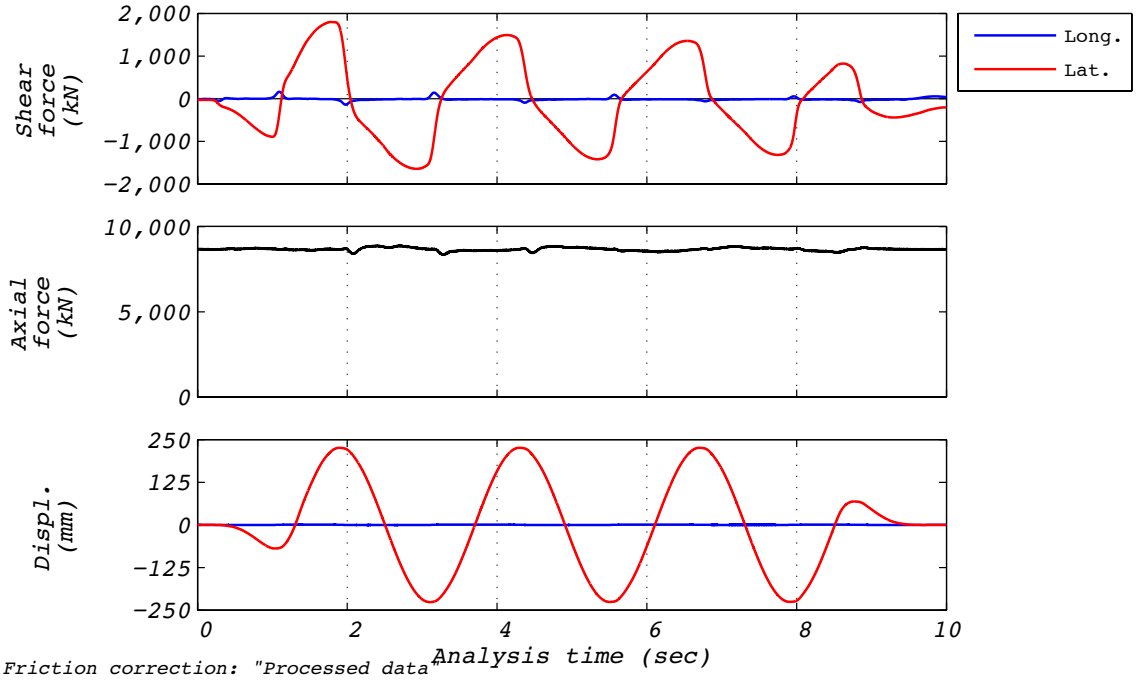

Figure B.27-1 Test run no. 70 time history: Transverse (224 mm amplitude, 8,663 kN axial load, and 586 mm/s velocity).

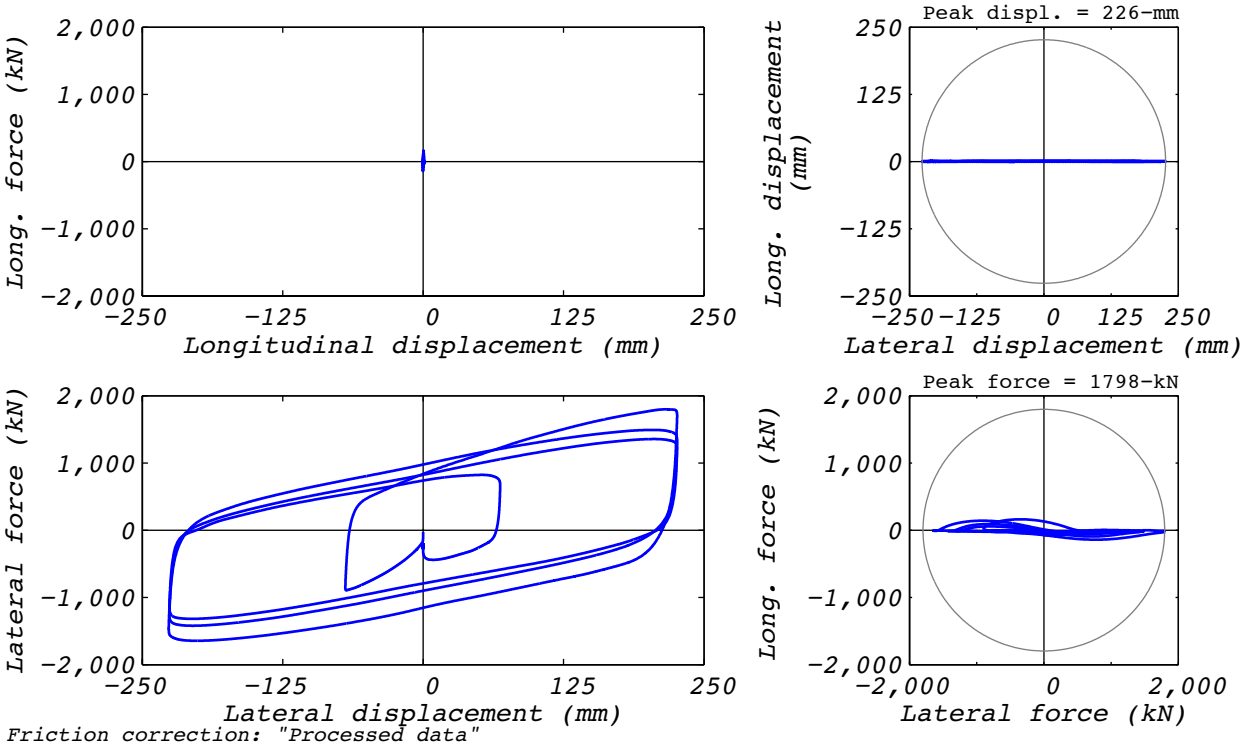

Figure B.27-2 Test run no. 70 hysteresis: Transverse (224 mm amplitude, 8,663 kN axial load, and 586 mm/s velocity).

B.28 TEST RUN 71

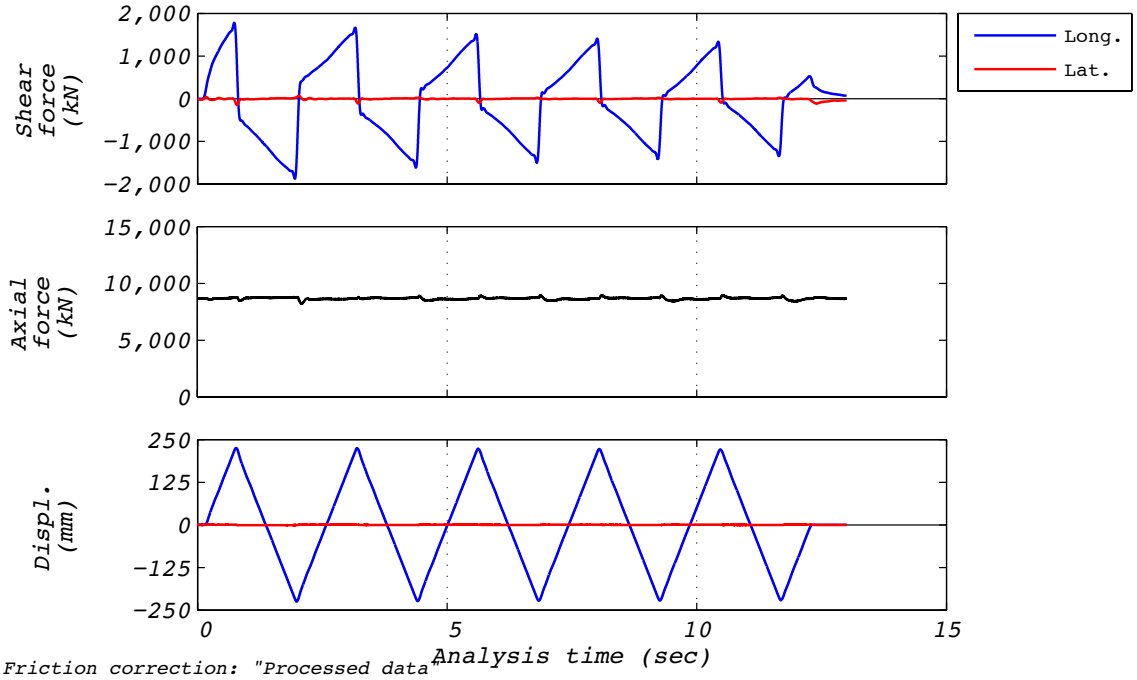

Figure B.28-1 Test run no. 71 time history: Longitudinal (224 mm amplitude, 8,663 kN axial load, and 373 mm/s velocity).

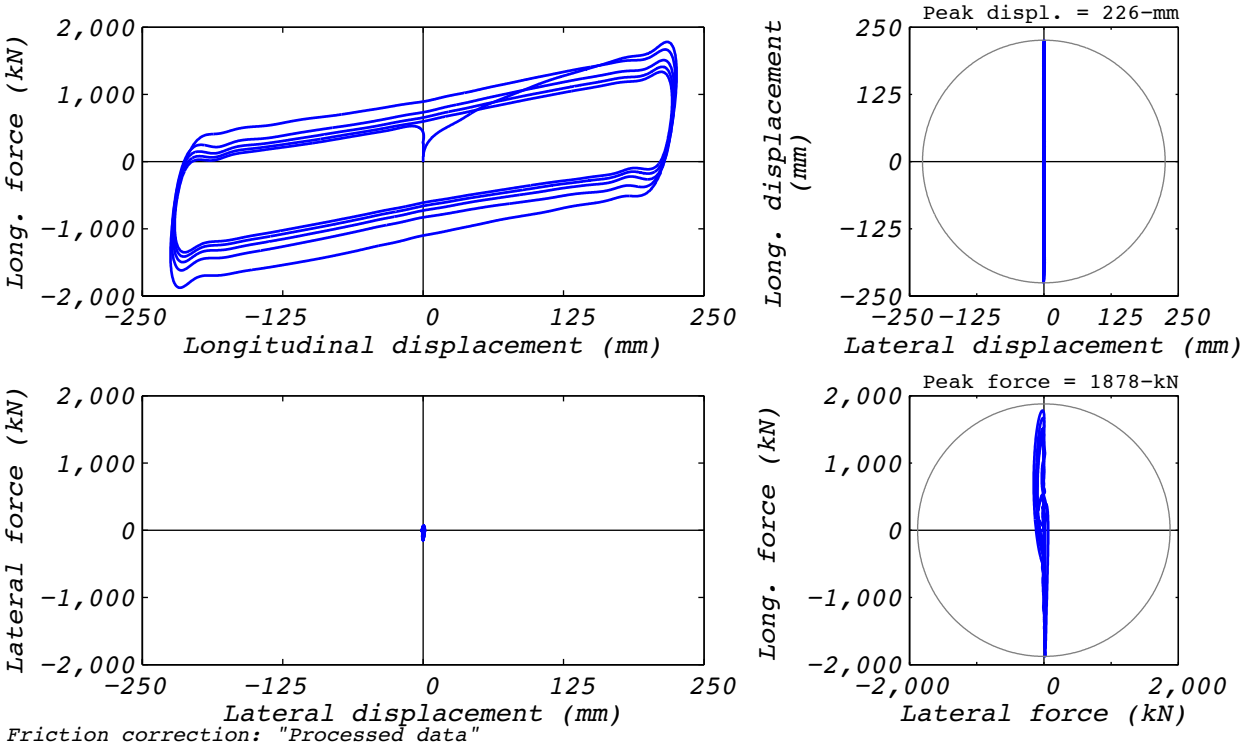

Figure B.28-2 Test run no. 71 hysteresis: Longitudinal (224 mm amplitude, 8,663 kN axial load, and 373 mm/s velocity).

B.29 TEST RUN 72

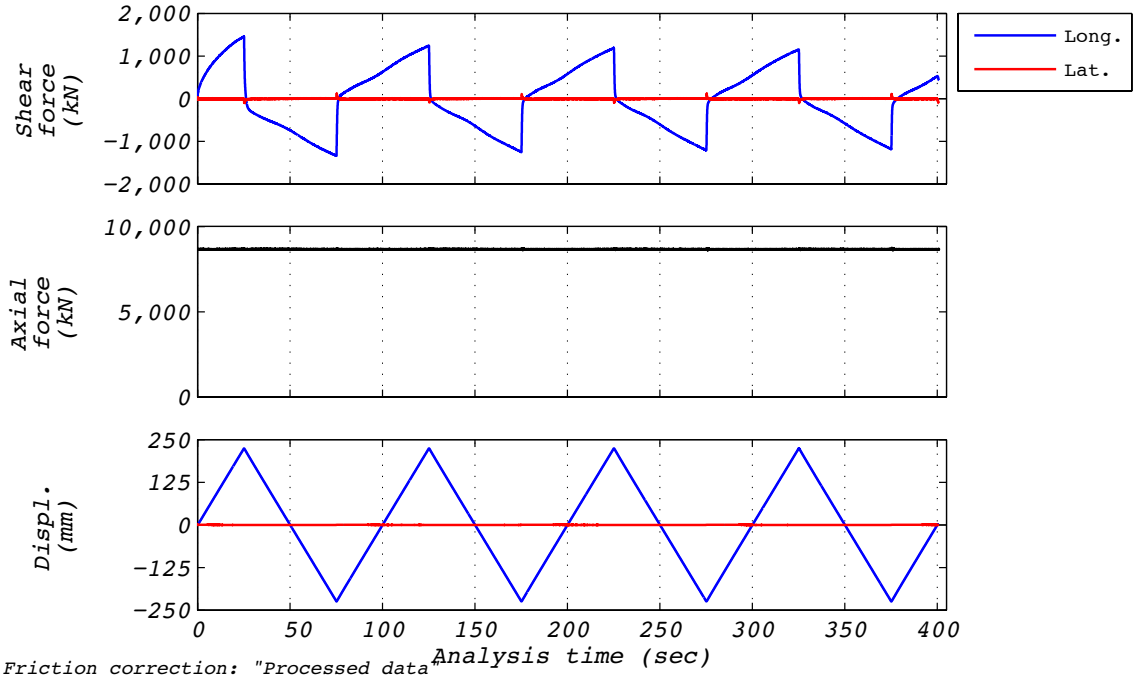

Figure B.29-1 Test run no. 72 time history: Longitudinal (224 mm amplitude, 8,663 kN axial load, and 9 mm/s velocity).

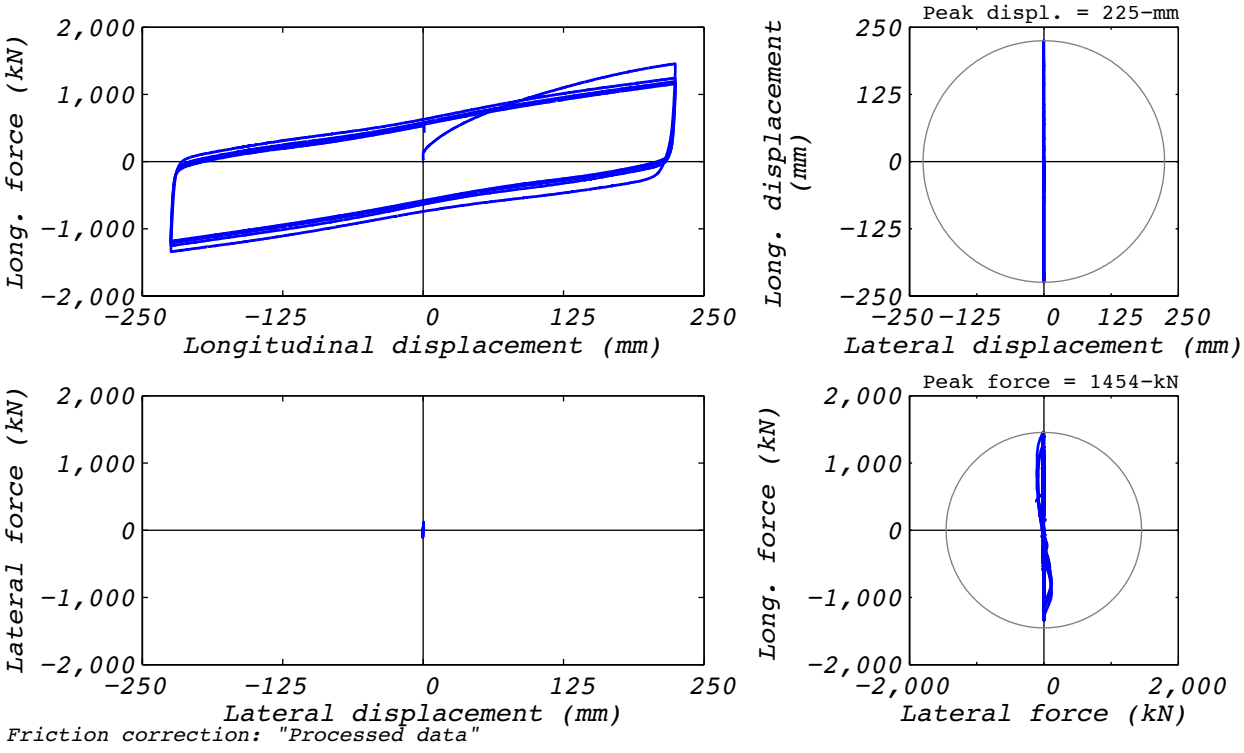

Figure B.29-2 Test run no. 72 hysteresis: Longitudinal (224 mm amplitude, 8,663 kN axial load, and 9 mm/s velocity).

B.30 TEST RUN 73

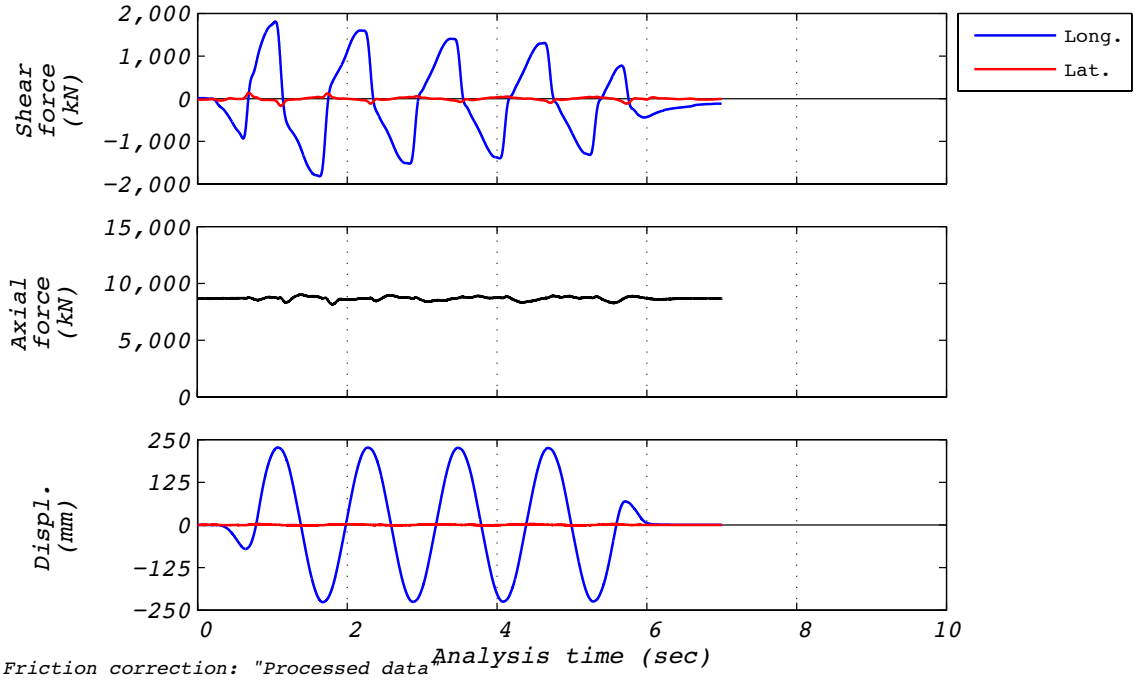

Figure B.30-1 Test run no. 73 time history: Longitudinal (224 mm amplitude, 8,663 kN axial load, and 1,173 mm/s velocity).

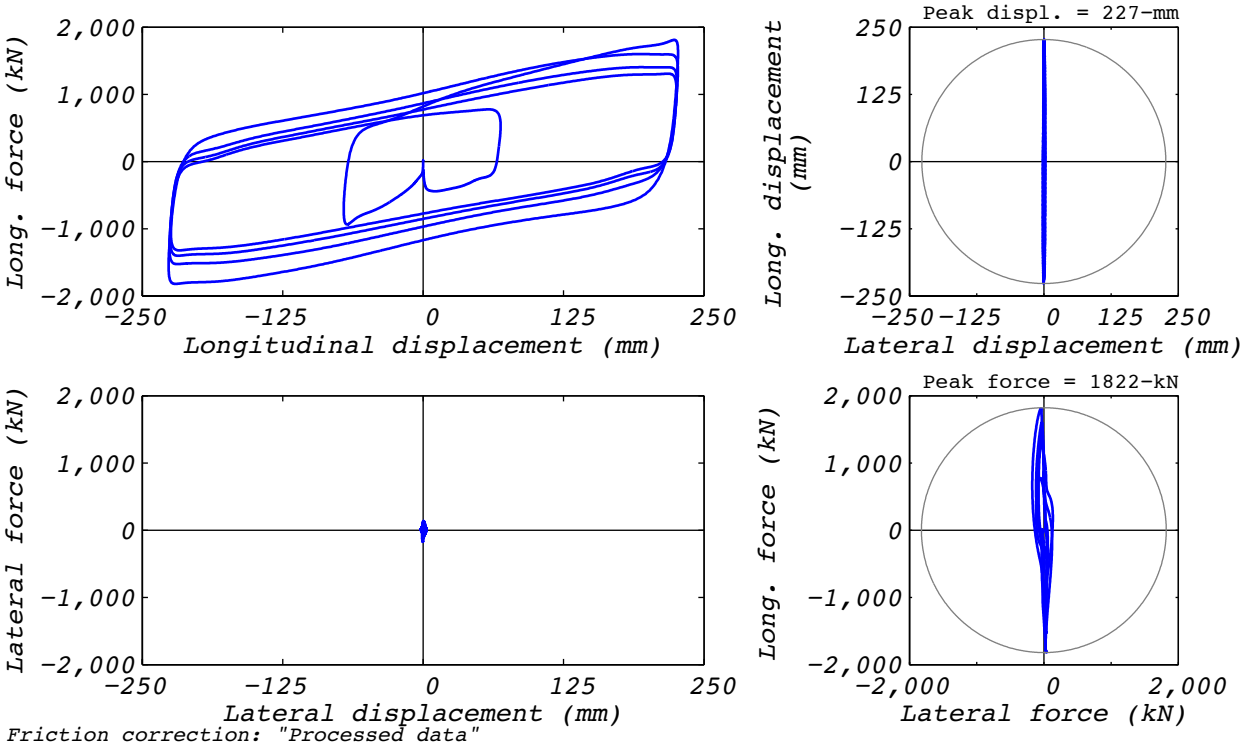

Figure B.30-2 Test run no. 73 hysteresis: Longitudinal (224 mm amplitude, 8,663 kN axial load, and 1,173 mm/s velocity).

B.31 TEST RUN 74

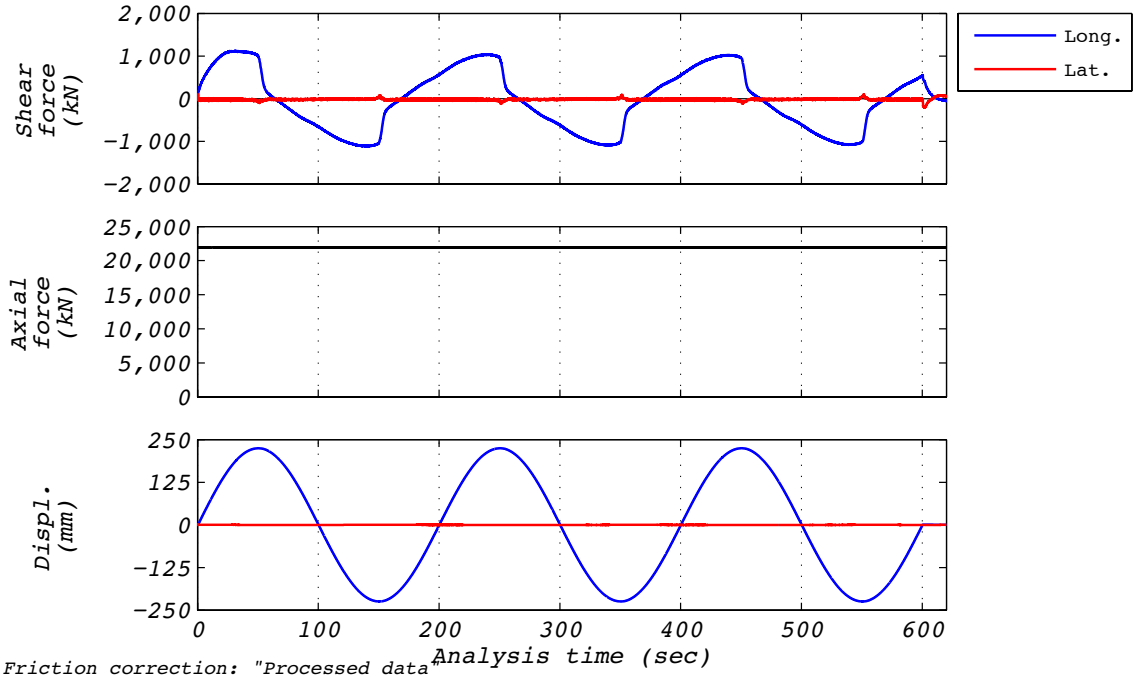

Figure B.31-1 Test run no. 74 time history: Longitudinal (224 mm amplitude, 21,927 kN axial load, and 7 mm/s velocity).

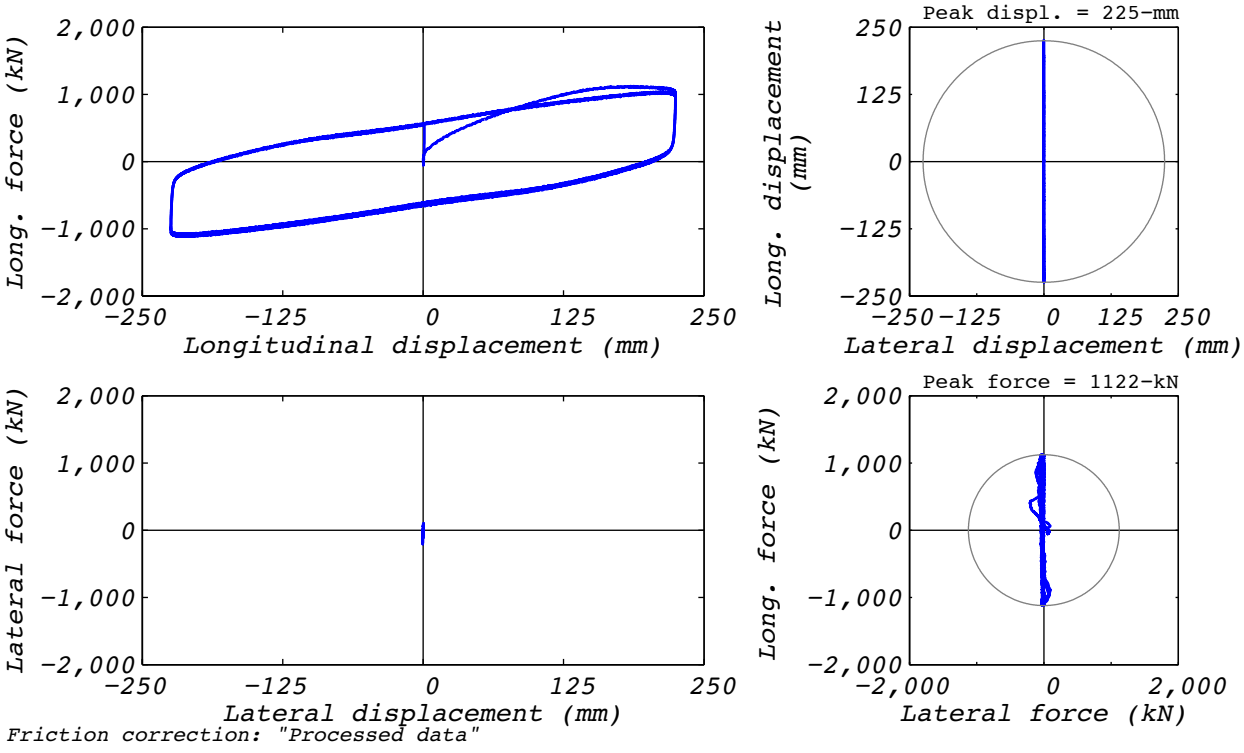

Figure B.31-2 Test run no. 74 hysteresis: Longitudinal (224 mm amplitude, 21,927 kN axial load, and 7 mm/s velocity).

B.32 TEST RUN 75

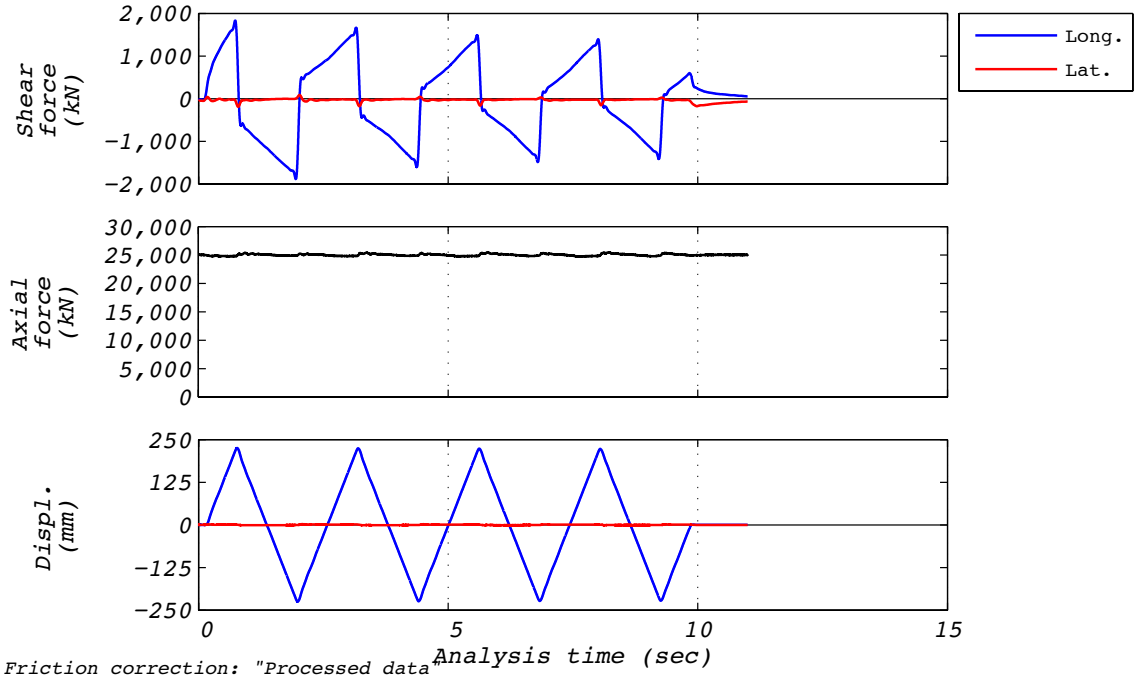

Figure B.32-1 Test run no. 75 time history: Longitudinal (224 mm amplitude, 25,002 kN axial load, and 373 mm/s velocity).

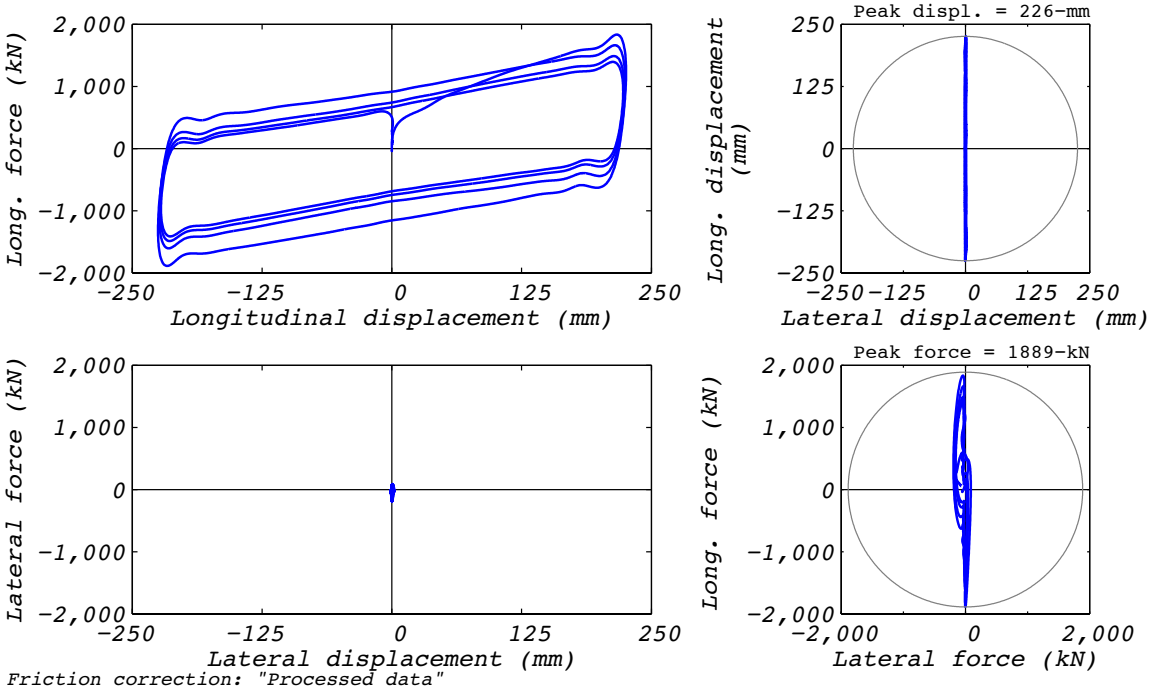

Figure B.32-2 Test run no. 75 hysteresis: Longitudinal (224 mm amplitude, 25,002 kN axial load, and 373 mm/s velocity).

B.33 TEST RUN 76

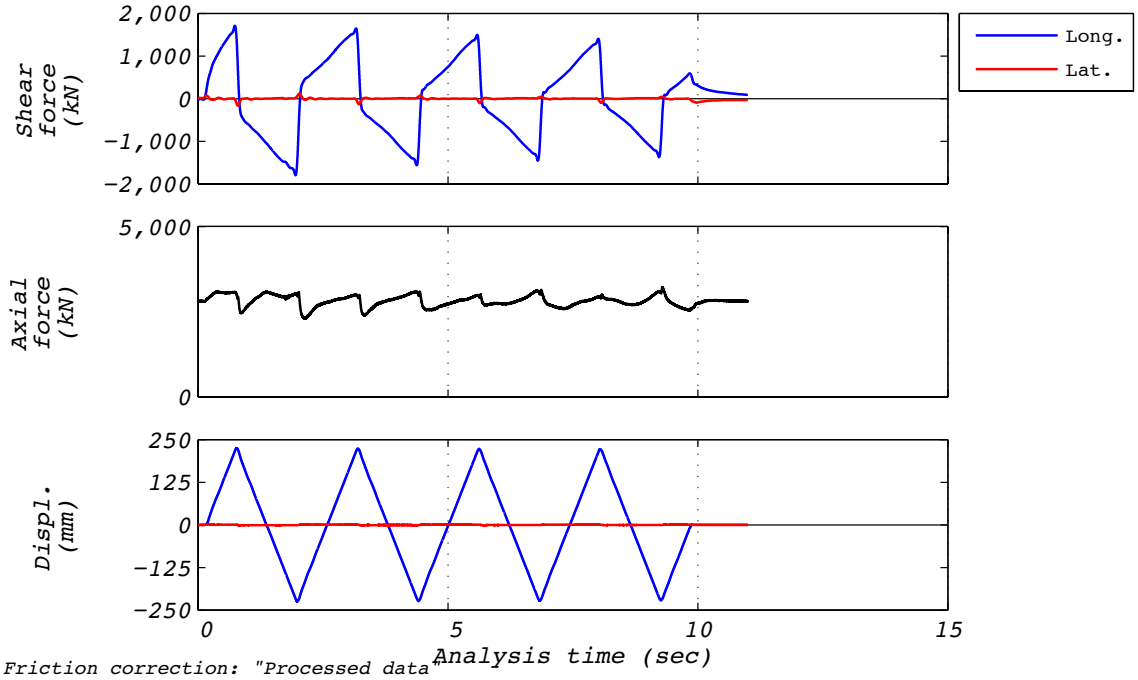

Figure B.33-1 Test run no. 76 time history: Longitudinal (224 mm amplitude, 2,807 kN axial load, and 373 mm/s velocity).

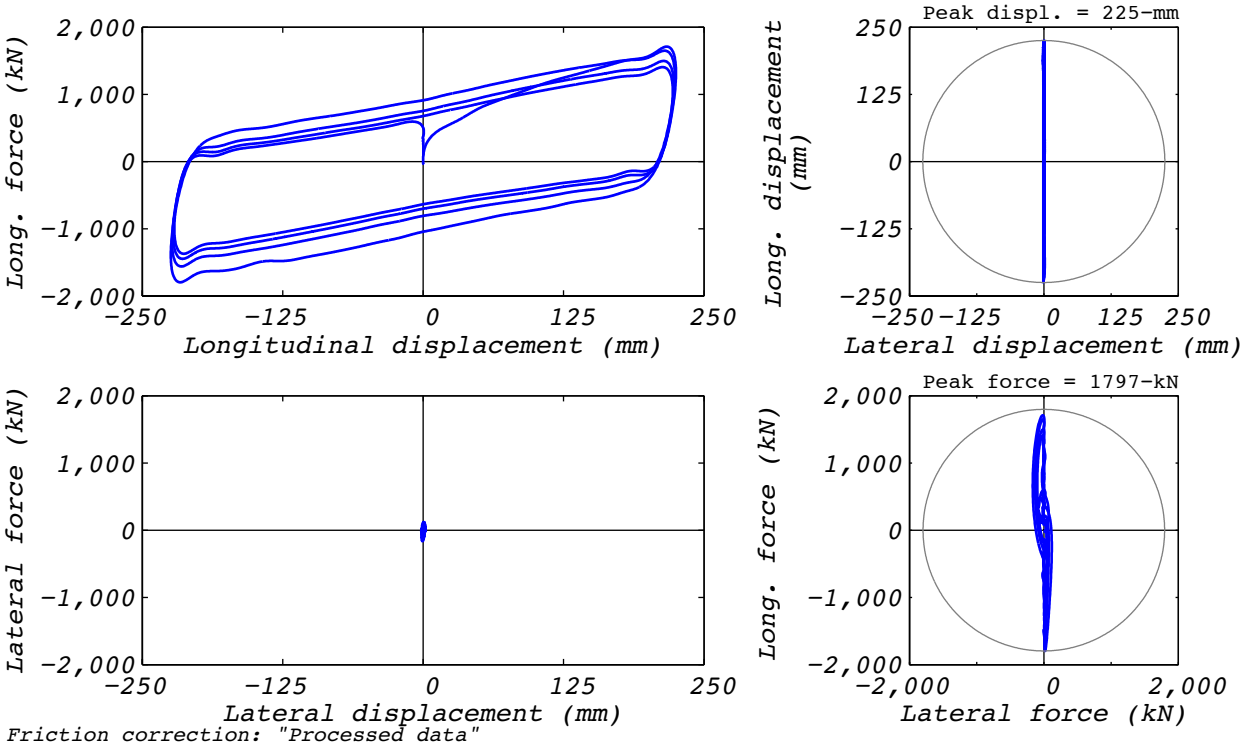

Figure B.33-2 Test run no. 76 hysteresis: Longitudinal (224 mm amplitude, 2,807 kN axial load, and 373 mm/s velocity).

B.34 TEST RUN 81

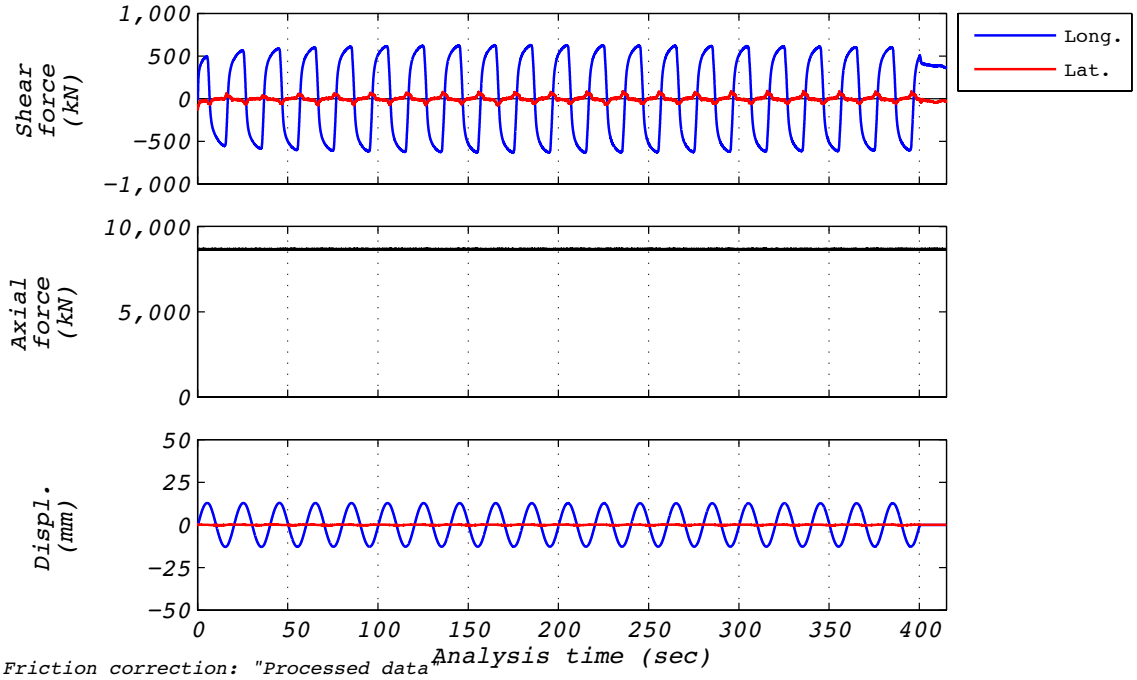

Figure B.34-1 Test run no. 81 time history: Longitudinal (13 mm amplitude, 8,663 kN axial load, and 4 mm/s velocity).

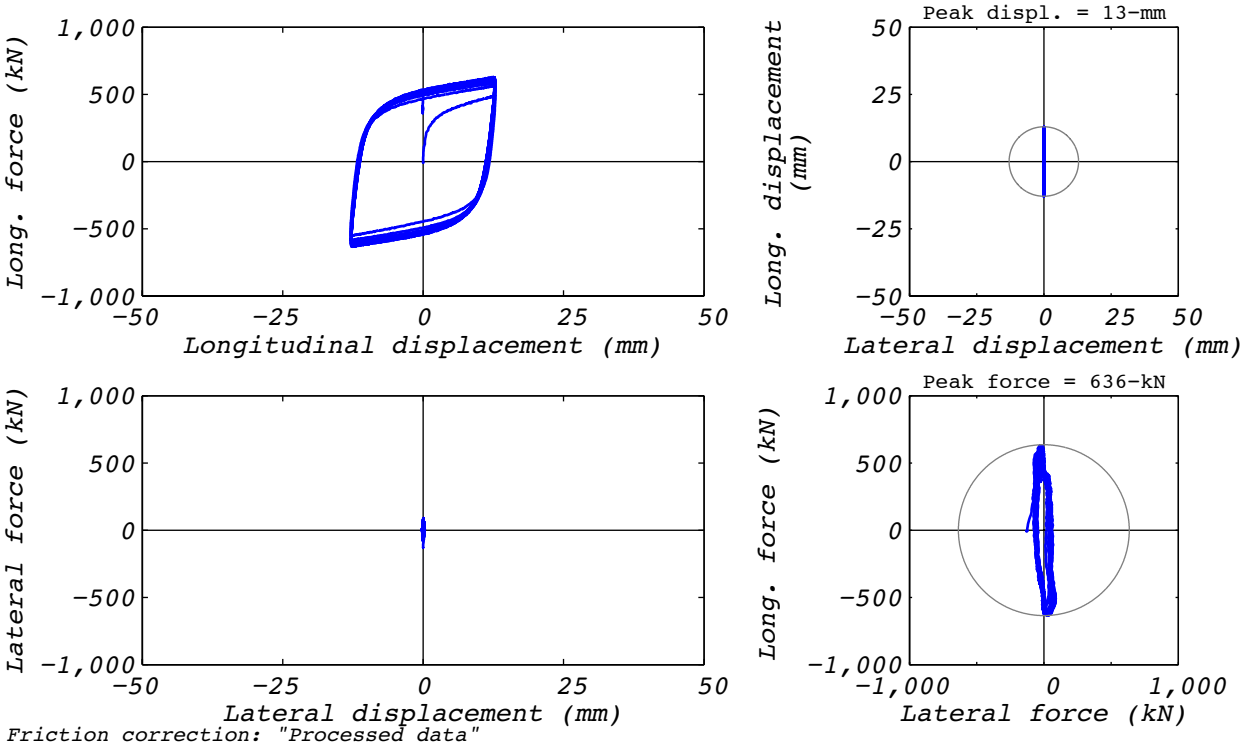

Figure B.34-2 Test run no. 81 hysteresis: Longitudinal (13 mm amplitude, 8,663 kN axial load, and 4 mm/s velocity).

B.35 TEST RUN 87

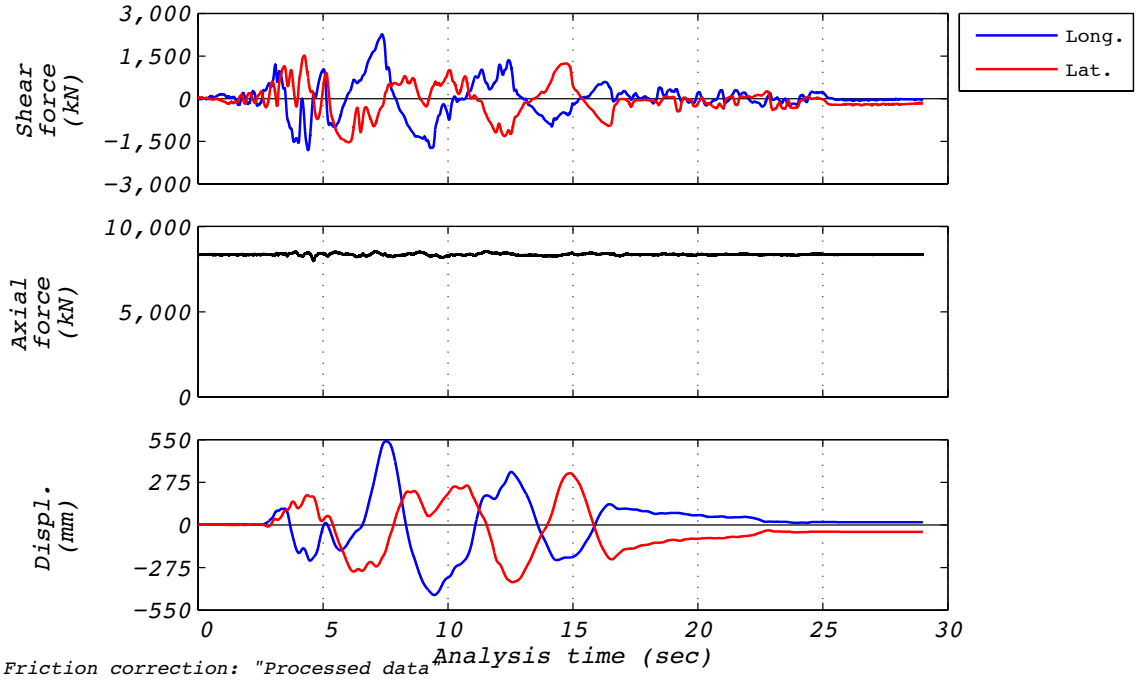

Figure B.35-1 Test run no. 87 time history: Longitudinal (444 mm amplitude, 8,663 kN axial load, and 485 mm/s velocity).

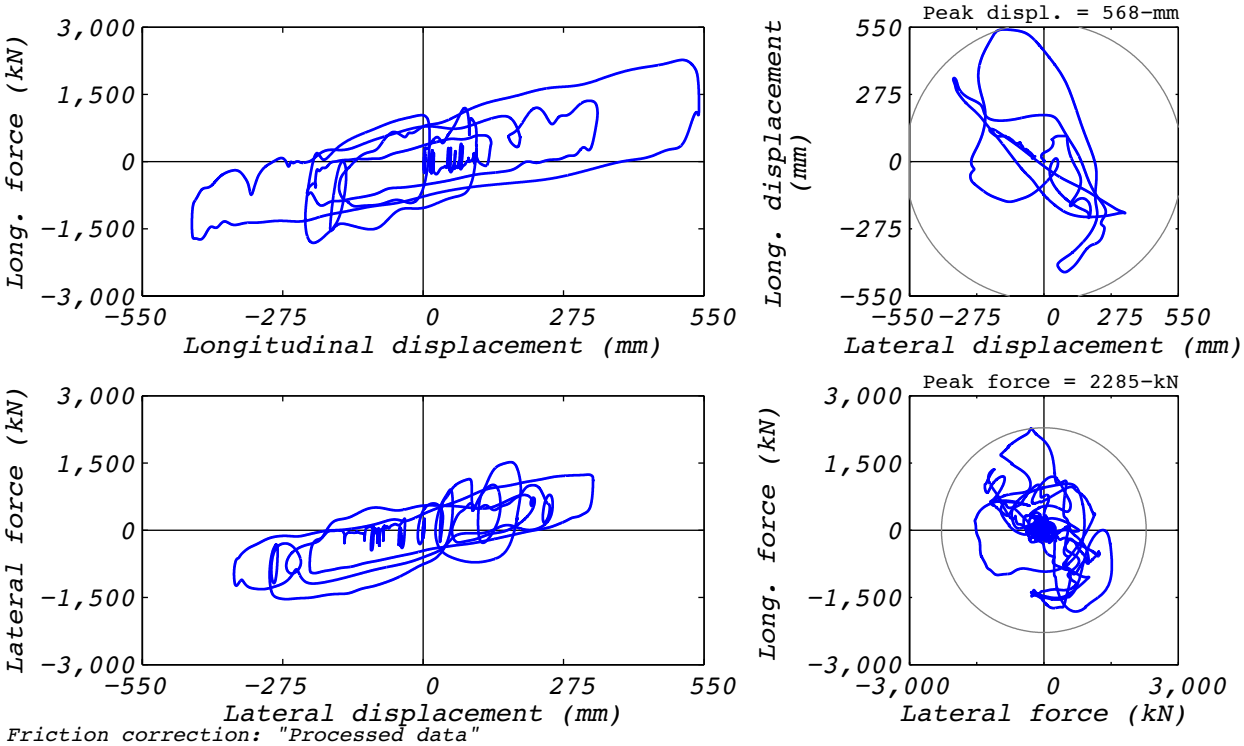

Figure B.35-2 Test run no. 87 hysteresis: Longitudinal (444 mm amplitude, 8,663 kN axial load, and 485 mm/s velocity).

Appendix C: Hybrid Simulation Tests Conducted on Friction Sliding Bearings

Hybrid tests listed in Table C.1 and Table C.2 were performed on the ESCO-RTS friction bearings EQS-1 and EQS-2, respectively. Detailed responses of these tests are shown in sections C.1 through C.24. For select tests, a corresponding analytical estimation was performed and included in this appendix. These are indicated by the letter *A* appending the run number.

Table C.1 Hybrid simulations and analyses conducted on a friction sliding bearing (EQS-1)

Section	Run	Ground motion	Model	Components	Test rate
C.1	17	EUR5	Exp = All	1D	25
C.2	18	EUR5	Exp = All	2D	25
C.3	*18A*	EUR5	Exp = All	2D	-
C.4	19	Displacement from #18	Exp = All	2D	-
C.5	21	NRC2	Exp = All	2D	25
C.6	22	NRC2	Exp = All	1D	25
C.7	23	Displacement from #22	Exp = All	1D	-

Table C.2 Hybrid simulations and analyses conducted on a friction sliding bearing (EQS-2)

Section	Run	Ground motion	Model	Components	Test rate
C.8	43	NRC2	5 groups of bearings (Exp = Center)	2D	5
C.9	44	NRC2	5 groups of bearings (Exp = Center)	3D	15
C.10	46	NRC2	5 groups of bearings (Exp = Center)	3D	18
C.11	47	NRC2	5 groups of bearings (Exp = Center)	3D	20
C.12	48	NRC2	5 groups of bearings (Exp = Corner)	3D	20

Table C.2 (Continued) Hybrid simulations and analyses conducted on a friction sliding bearing (EQS-2)

Section	Run	Ground motion	Model	Components	Test rate
C.13	49	NRC2	5 groups of bearings (Exp = Corner)	3D	20
C.14	50	NRC2	5 groups of bearings (Exp = Corner)	3D	20
C.15	51	NRC2	5 groups of bearings (Exp = Corner)	3D	20
C.16	52	NRC2	Exp = All	1D	5
C.17	*52A*	*NRC2*	*Exp = All*	*1D*	-
C.17	53	EUR5	Exp = All	1D	5
C.19	*53A*	*EUR5*	*Exp = All*	*1D*	-
C.19	54	NRC2	Exp = All	2D	5
C.21	*54A*	*NRC2*	*Exp = All*	*2D*	-
C.21	55	Displacement from #53	Exp = All	1D	-
C.23	57	Displacement from #54	Exp = All	2D	-
C.21	58	NRC10	Exp = All	2D	5

C.1 TEST RUN 17

Test run 17 was a hybrid test of the EUR dispersion appropriate ground motion number 5. The model consisted of a single experimental bearing representing all 527 bearings. Input motions consisted of a single horizontal component and a constant axial load specified as the design axial load of 8,663 kN. The test was executed at a rate 25 times slower than real time to compensate for machine delays. Bearing EQS-1 was used in this test. Figure C.1-1 shows the fidelity achieved in the hybrid test. Figures C.1-2 and C.1-3 contain bearing responses, and Figure C.1-4 depicts the resulting floor response spectra for select locations in two of the isolated structures.

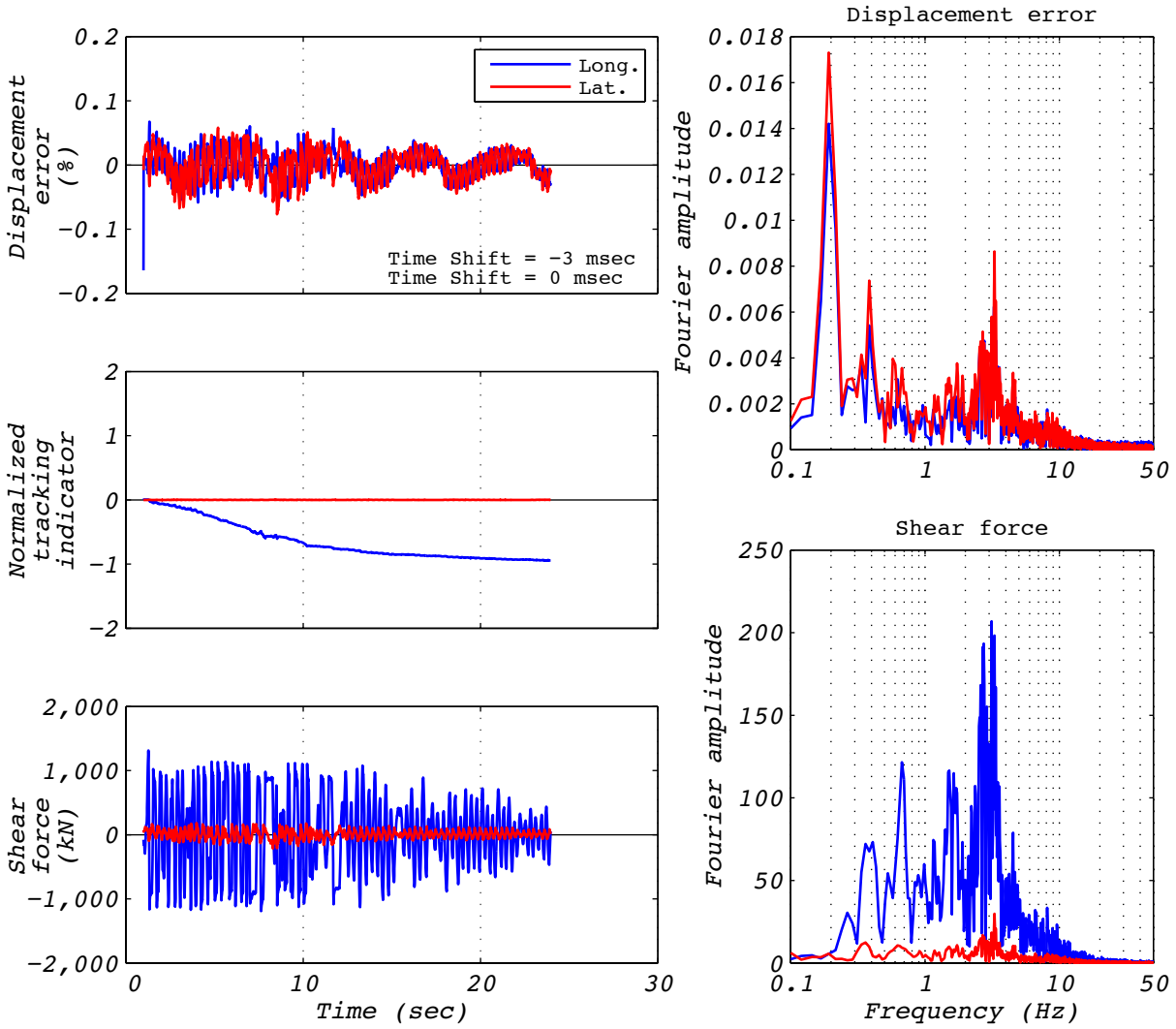

Figure C.1-1 Hybrid test performance metrics for run 17: EUR5, 1D with experimental bearing representing all bearings.

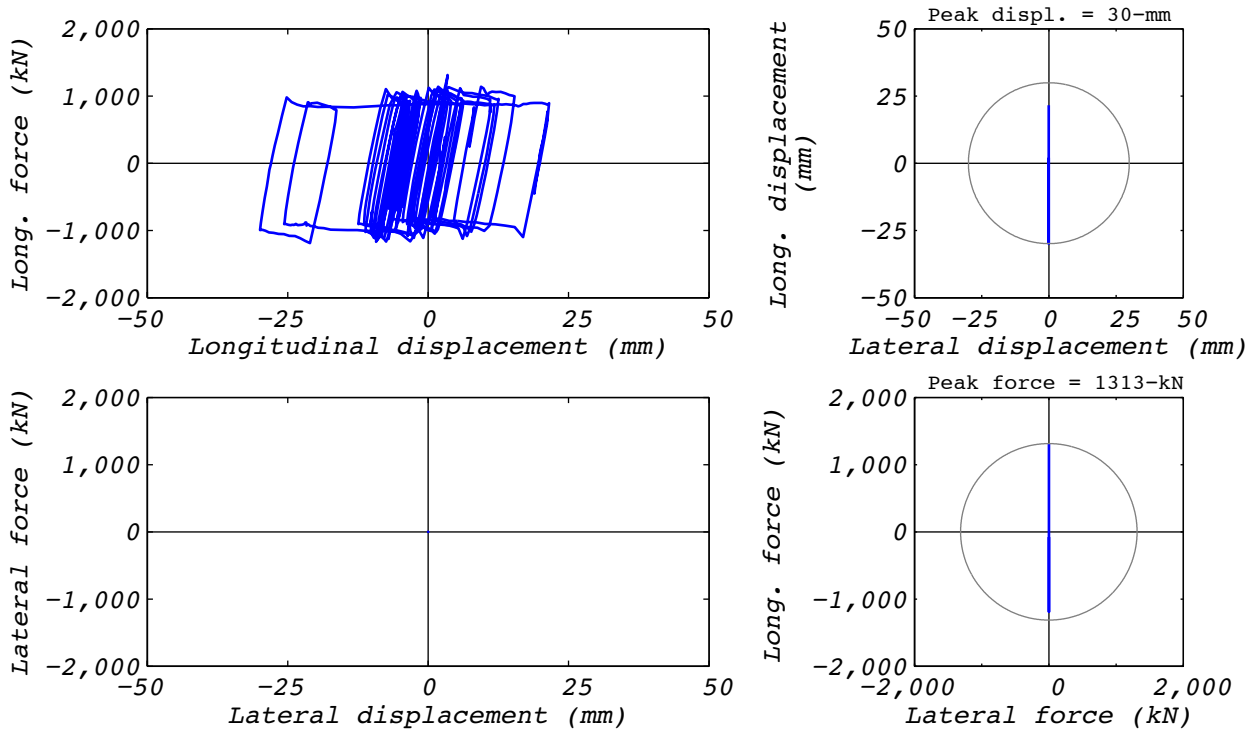

Figure C.1-2 Hybrid test bearing response for run 17: EUR5, 1D with experimental bearing representing all bearings.

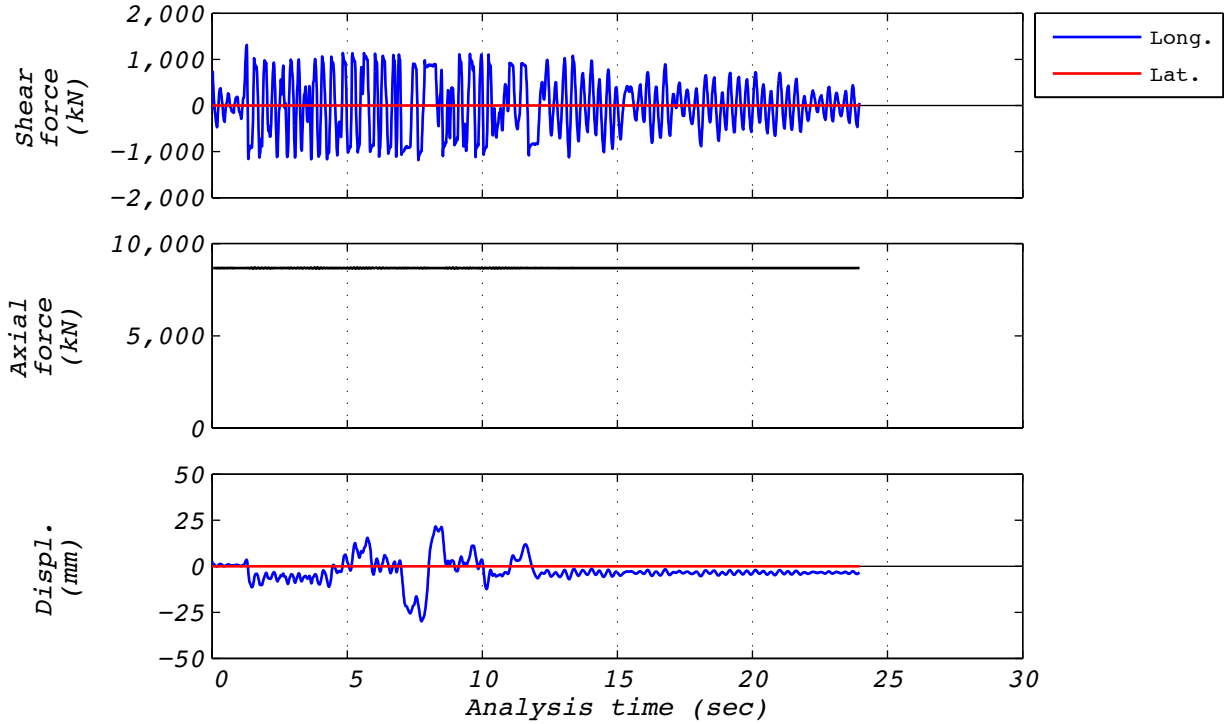

Figure C.1-3 Hybrid test time history responses metrics for run 17: EUR5, 1D with experimental bearing representing all bearings.

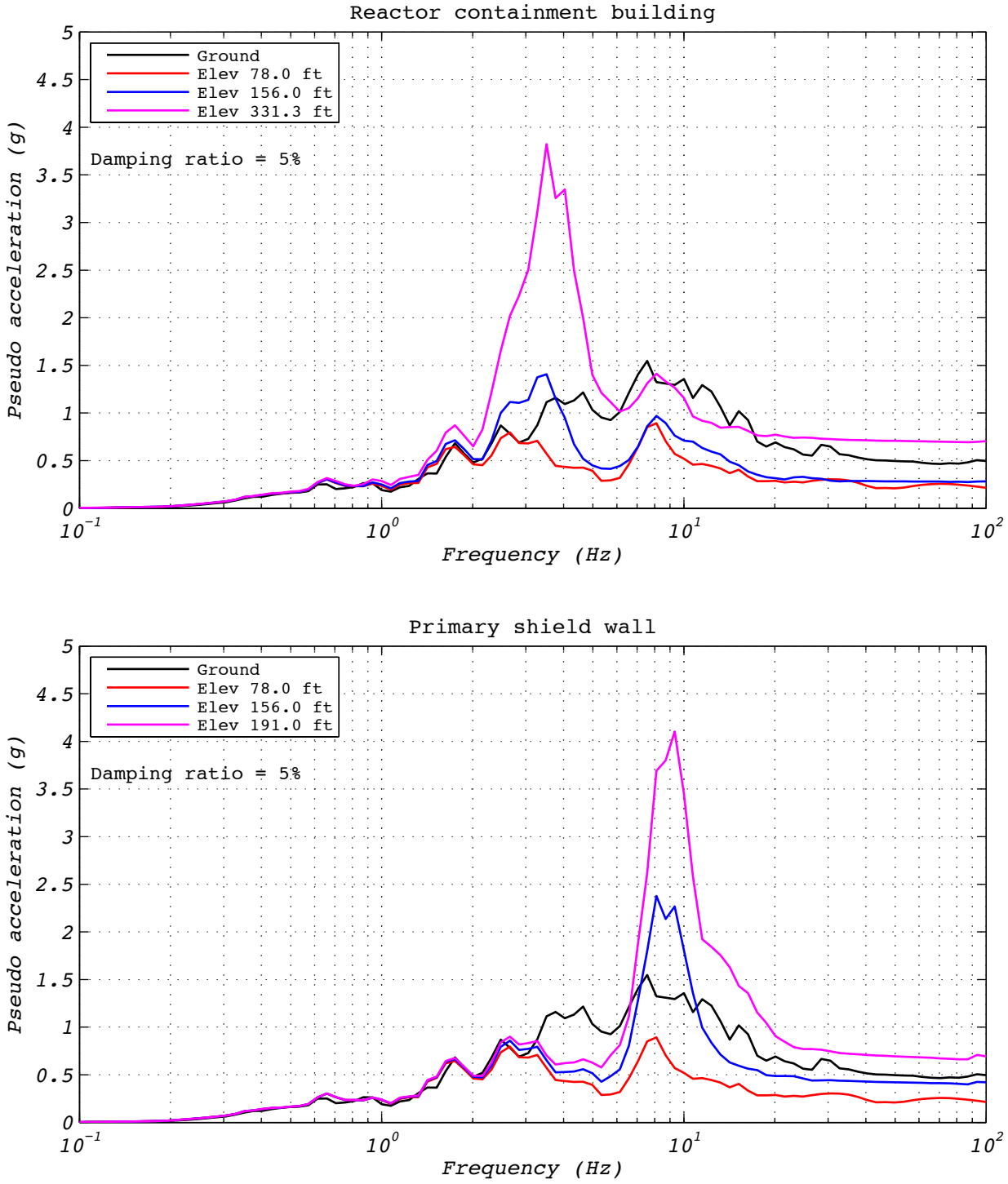

Figure C.1-4 Hybrid test floor spectra for run 17: EUR5, 1D with experimental bearing representing all bearings.

C.2 TEST RUN 18

Test run 18 was a hybrid test of the EUR dispersion appropriate ground motion number 5. The model consisted of a single experimental bearing representing all 527 bearings. Input motions consisted of two horizontal components and a constant axial load specified as the design axial load of 8,663 kN. The test was executed at a rate 25 times slower than real time to compensate for machine delays. Bearing EQS-1 was used in this test. Figure C.2-1 shows the fidelity achieved in the hybrid test. Figures C.2-2 and C.2-3 contain bearing responses, and Figure C.2-4 depicts the resulting floor response spectra for select locations in two of the isolated structures.

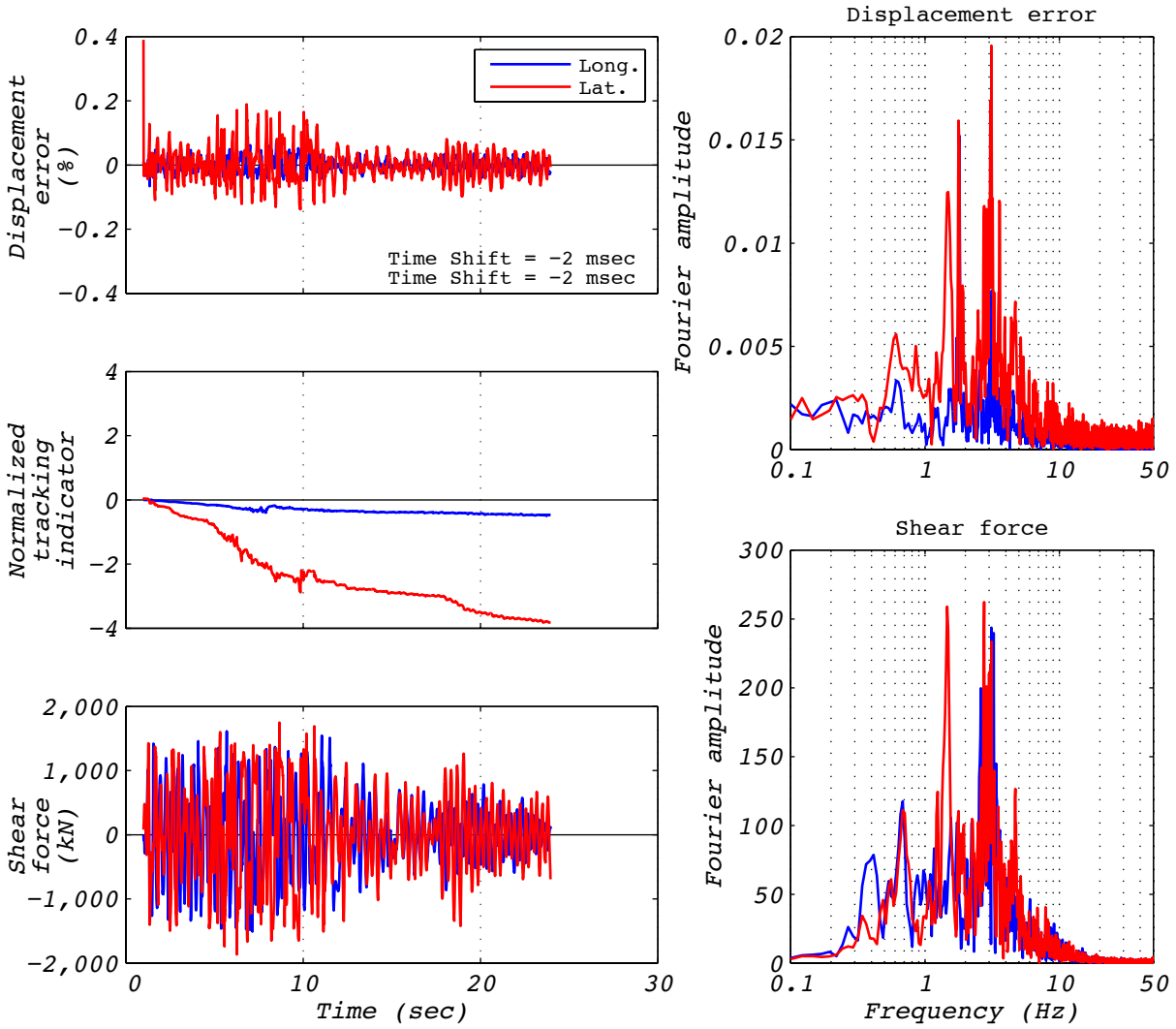

Figure C.2-1 Hybrid test performance metrics for run 18: EUR5, 2D with experimental bearing representing all bearings.

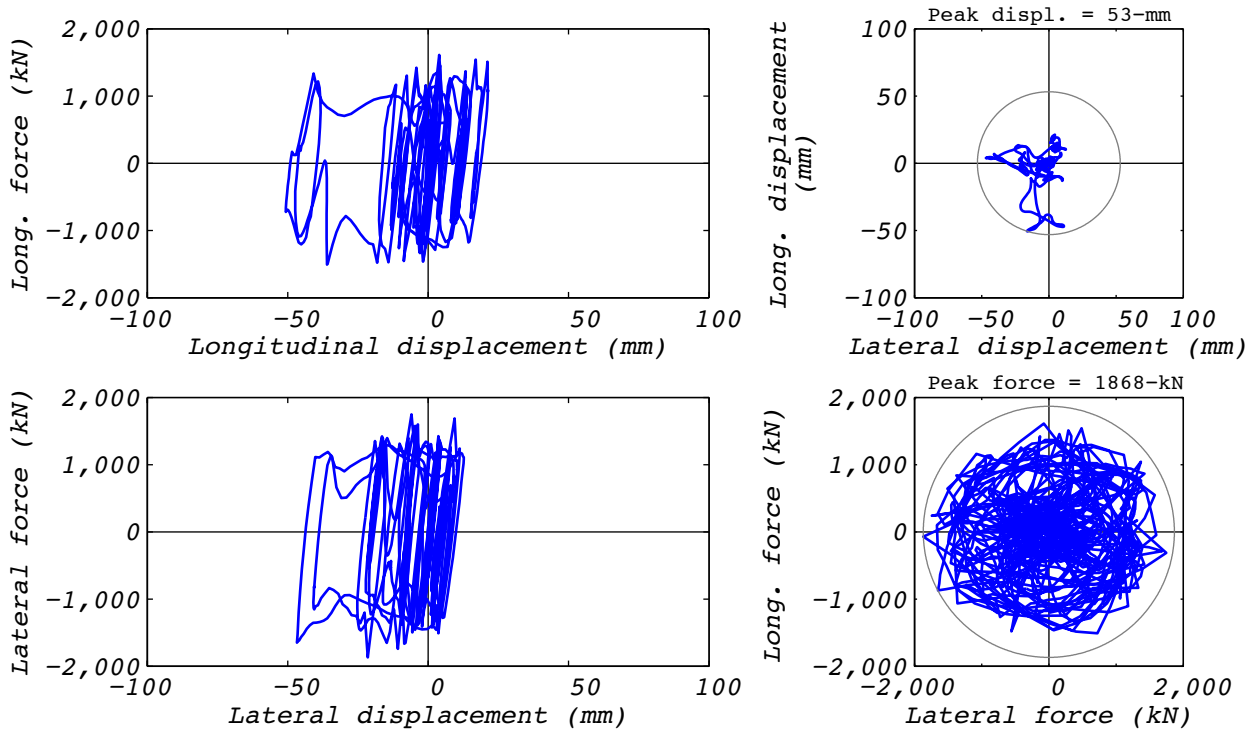

Figure C.2-2 Hybrid test bearing response for run 18: EUR5, 2D with experimental bearing representing all bearings.

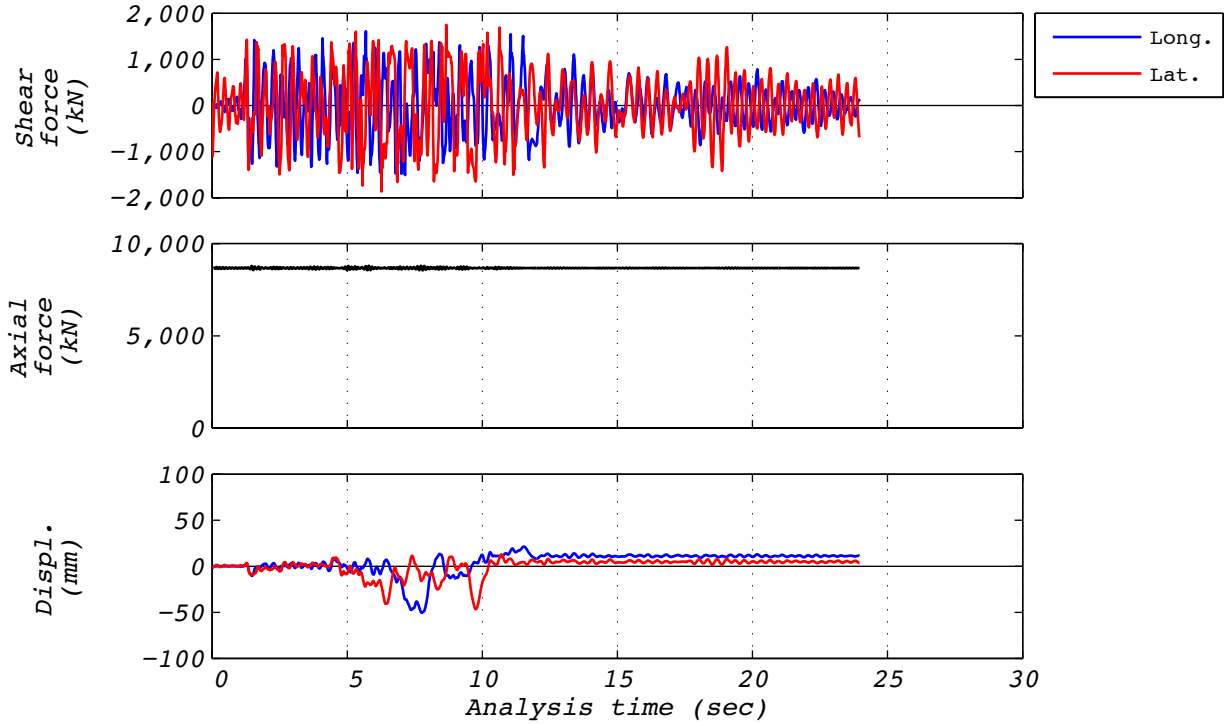

Figure C.2-3 Hybrid test time history responses for run 18: EUR5, 2D with experimental bearing representing all bearings.

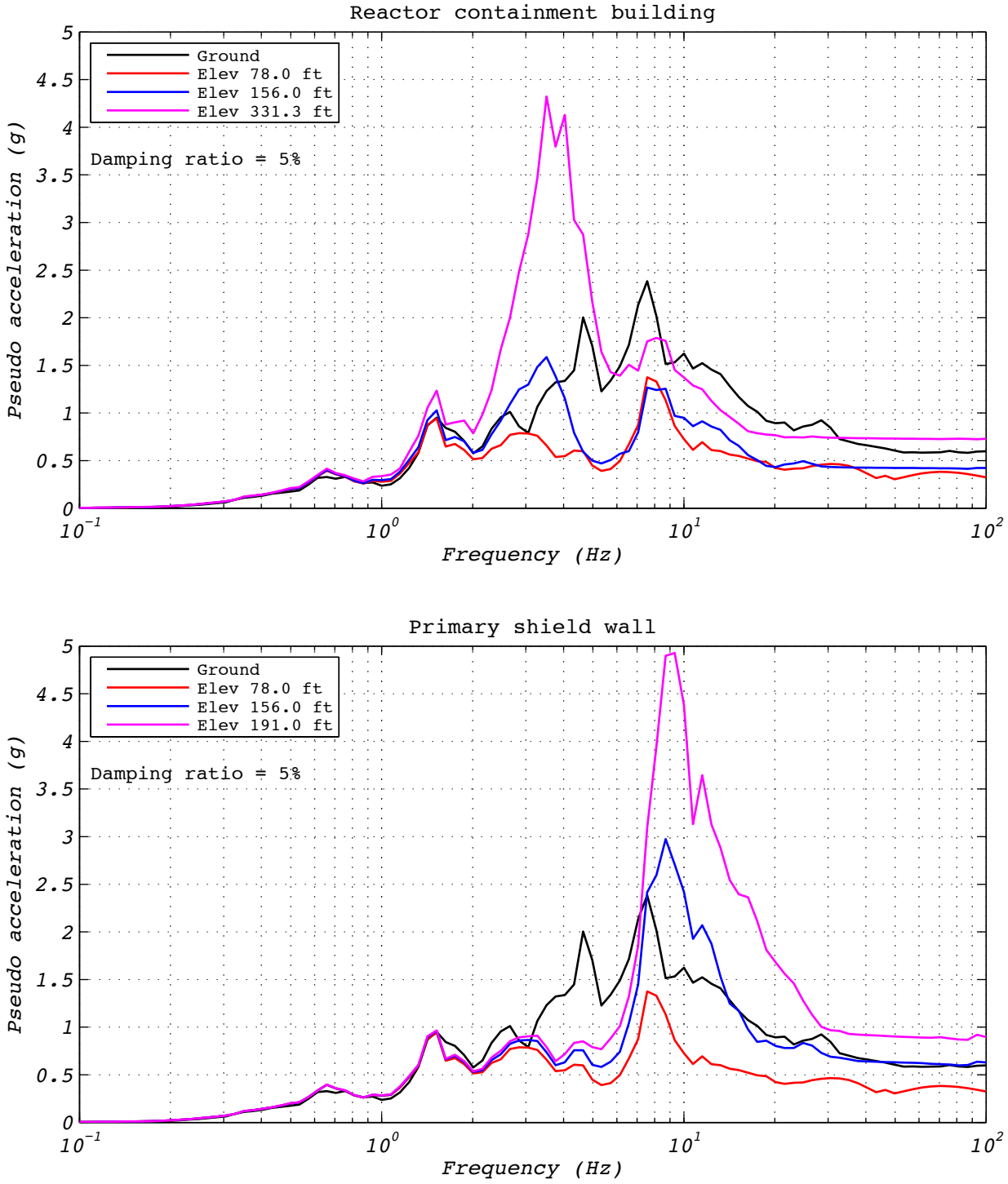

Figure C.2-4 Hybrid test floor spectra for run 18: EUR5, 2D with experimental bearing representing all bearings.

C.3 ANALYSIS RUN 18A

Analysis run 18A was an analytical estimation of the EUR dispersion appropriate ground motion number 5. The model consisted of a single analytical bearing representing all 527 bearings. Input motions consisted of two horizontal components and a constant axial load was specified as the design axial load of 8,663 kN. Bearing EQS-1 was used in this test. Figures C.3-1 and C.3-2 contain analytical bearing responses, and Figure C.3-3 depicts the resulting floor response spectra for select locations in two of the isolated structures.

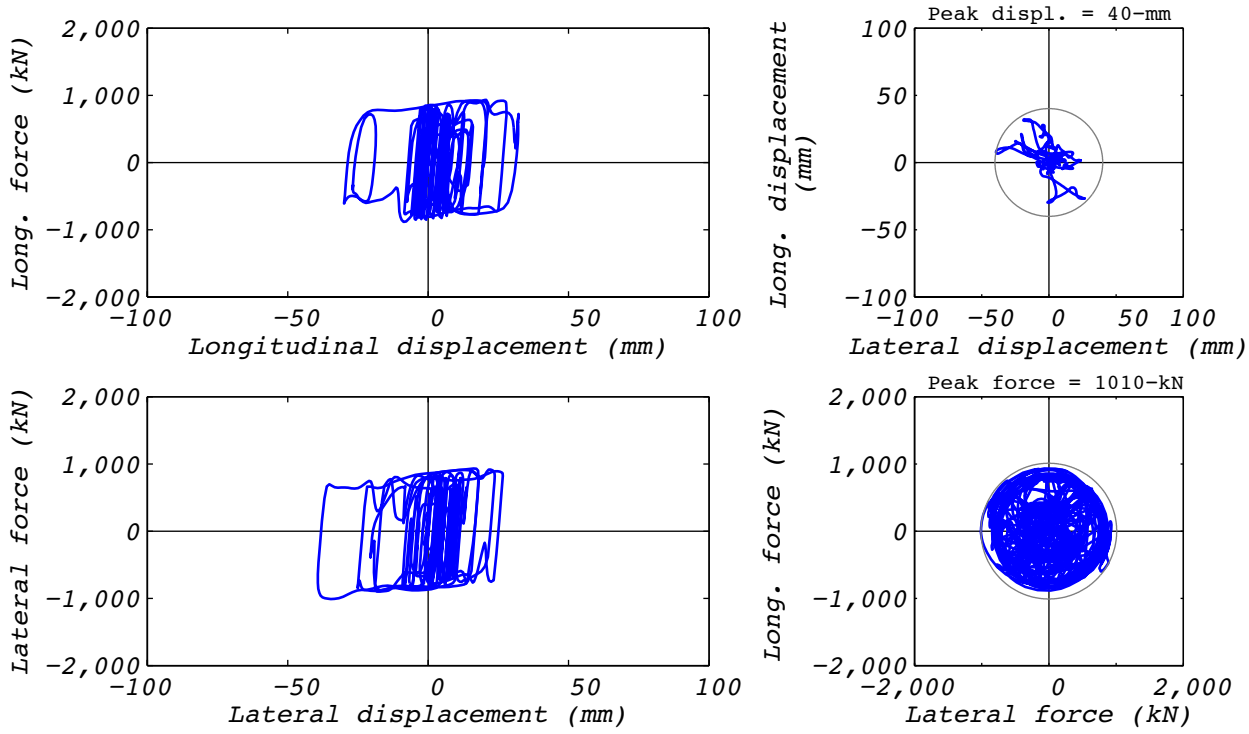

Figure C.3-1 Analytical bearing response for run 18A: EUR5, 2D with a single analytical bearing.

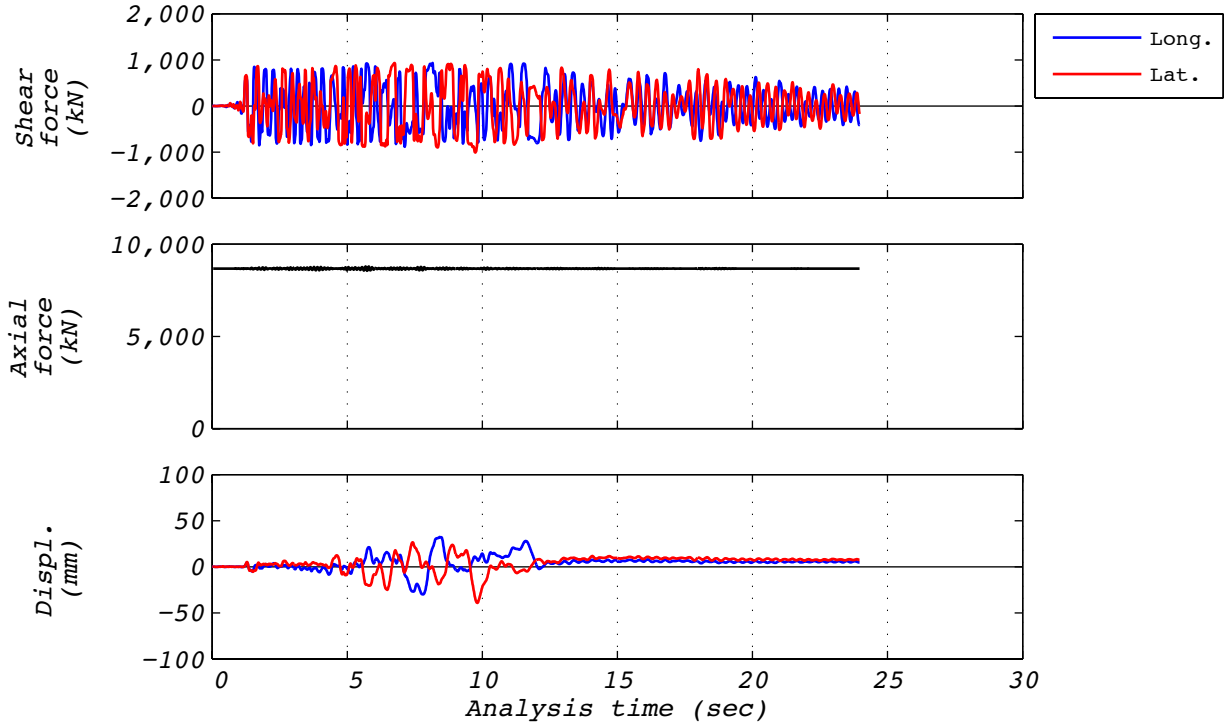

Figure C.3-2 Analytical time history responses for run 18A: EUR5, 2D with a single analytical bearing.

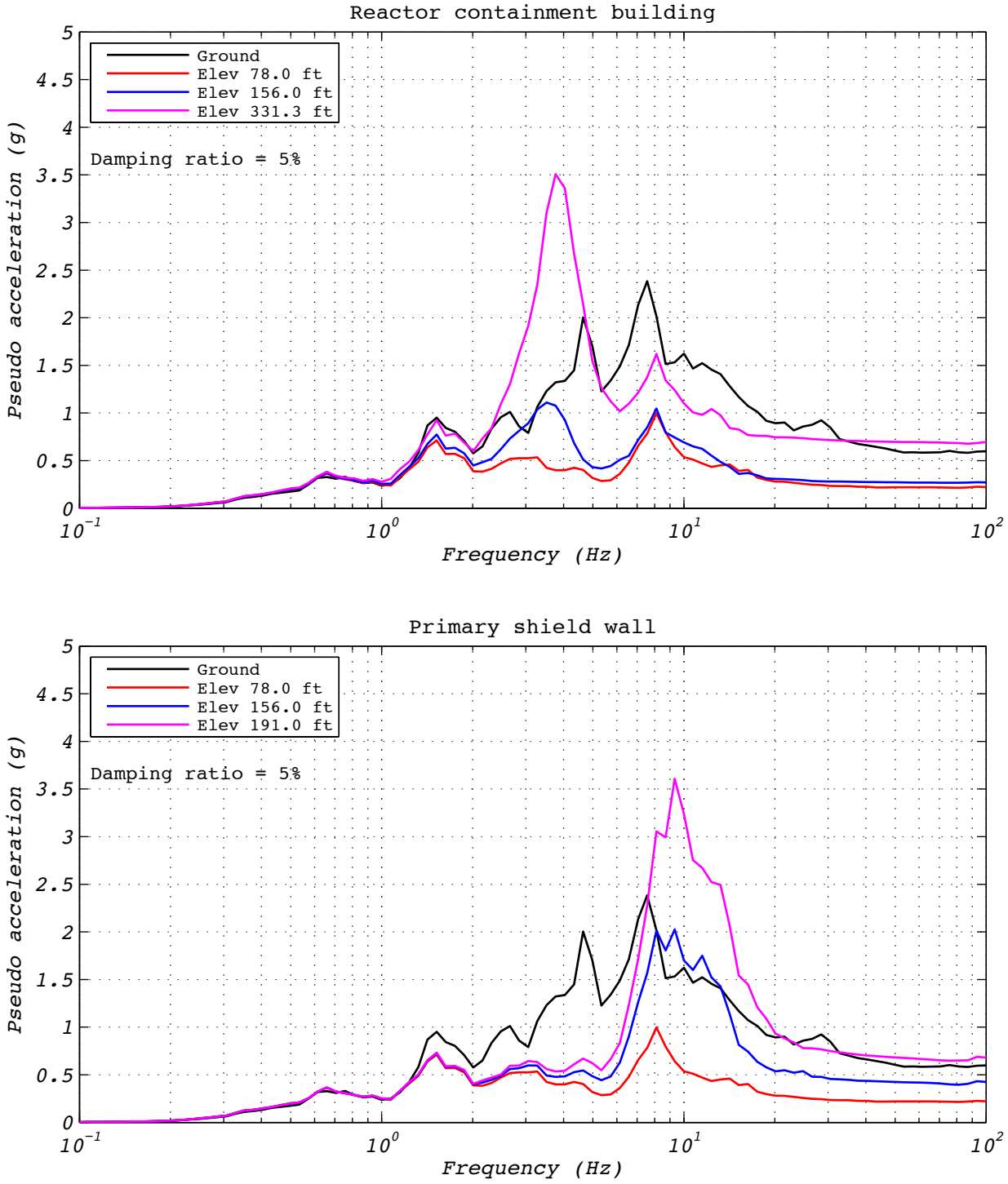

Figure C.3-3 Floor spectra for analytical run 18A: EUR5, 2D with a single analytical bearing.

C.4 DISPLACEMENT RUN 19

Test run 19 was a real-time displacement history recorded from test run 18, which was a hybrid test of the EUR dispersion appropriate ground motion number five. Input motions consisted of two horizontal components and a constant axial load specified as the design axial load of 8,663 kN. The test was executed at a rate real time to investigate loading rate effects. Bearing EQS-1 was used in this test. Figures C.4-1 and C.4-2 contain bearing responses.

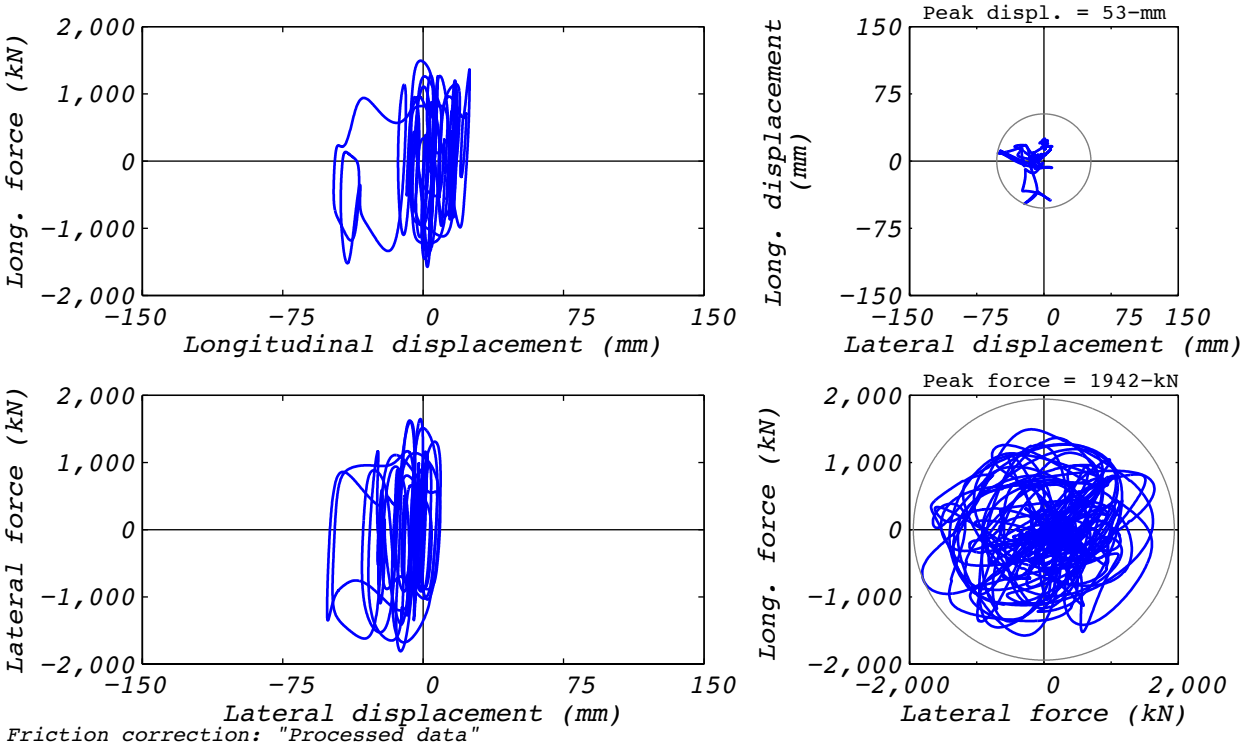

Figure C.4-1 Bearing response for real-time reproduction of hybrid test run 18: EUR5, 2D with experimental bearing representing all bearings.

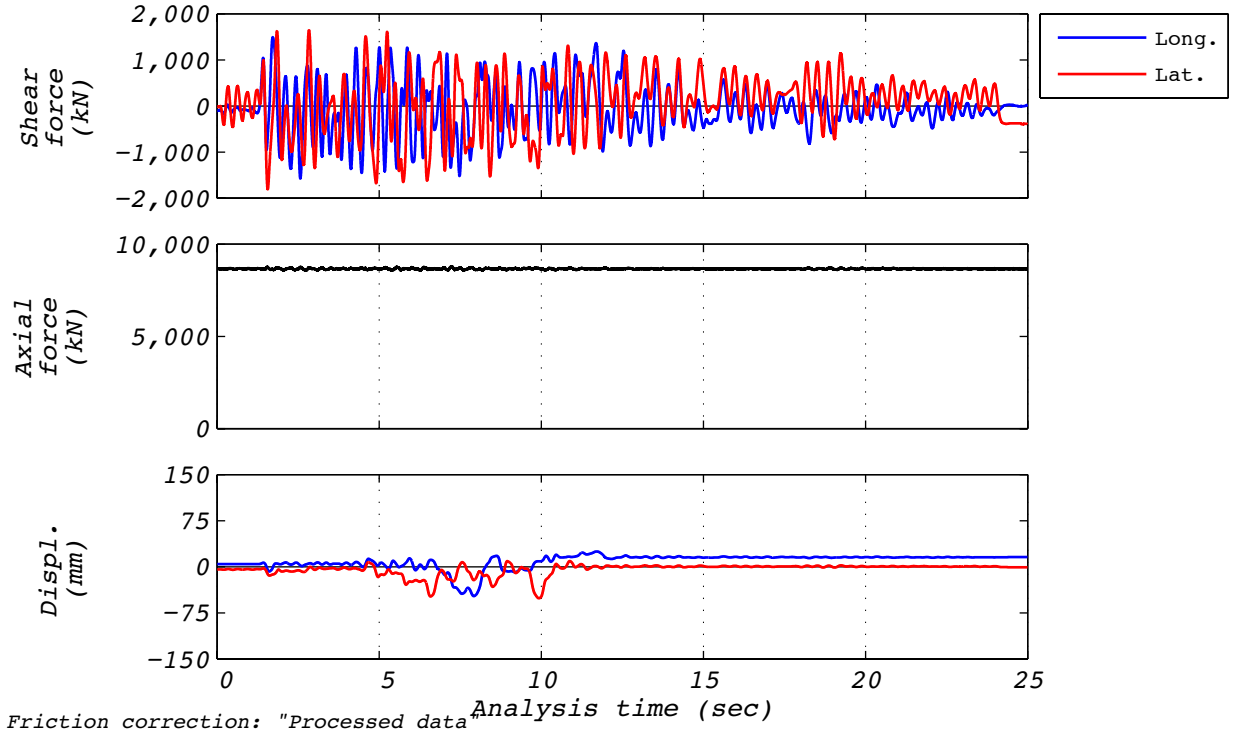

Figure C.4-2 Time history responses for real-time reproduction of hybrid test run 18: EUR5, 2D with experimental bearing representing all bearings.

C.5 TEST RUN 21

Test run 21 was a hybrid test of the NRC dispersion appropriate ground motion number 2. The model consisted of a single experimental bearing representing all 527 bearings. Input motions consisted of two horizontal components and a constant axial load specified as the design axial load of 8,663 kN. The test was executed at a rate 25 times slower than real time to compensate for machine delays. Bearing EQS-1 was used in this test. Figure C.5-1 shows the fidelity achieved in the hybrid test. Figures C.5-2 and C.5-3 contain bearing responses, and Figure C.5-4 depicts the resulting floor response spectra for select locations in two of the isolated structures.

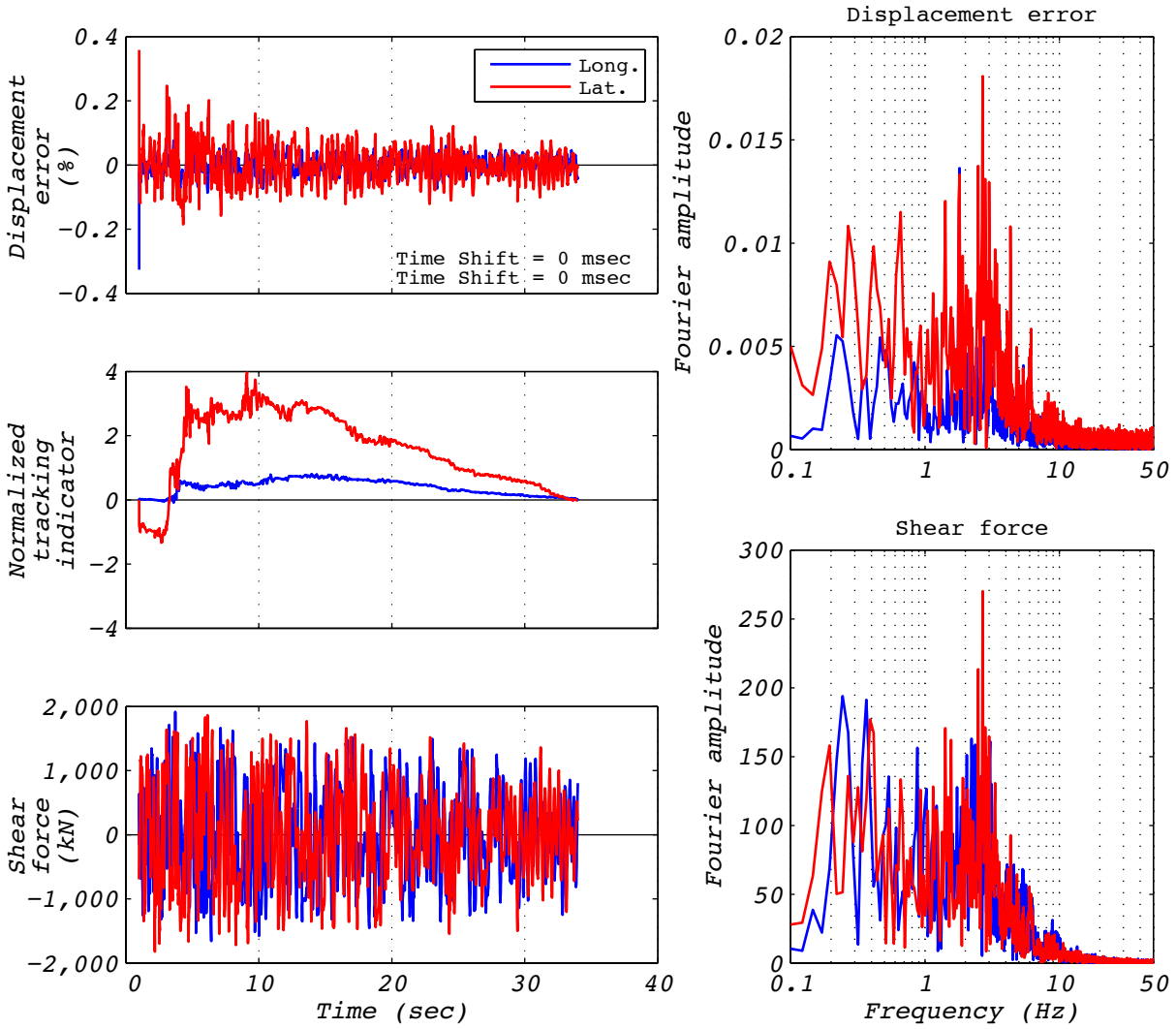

Figure C.5-1 Hybrid test performance metrics for run 21: NRC2, 2D with experimental bearing representing all bearings.

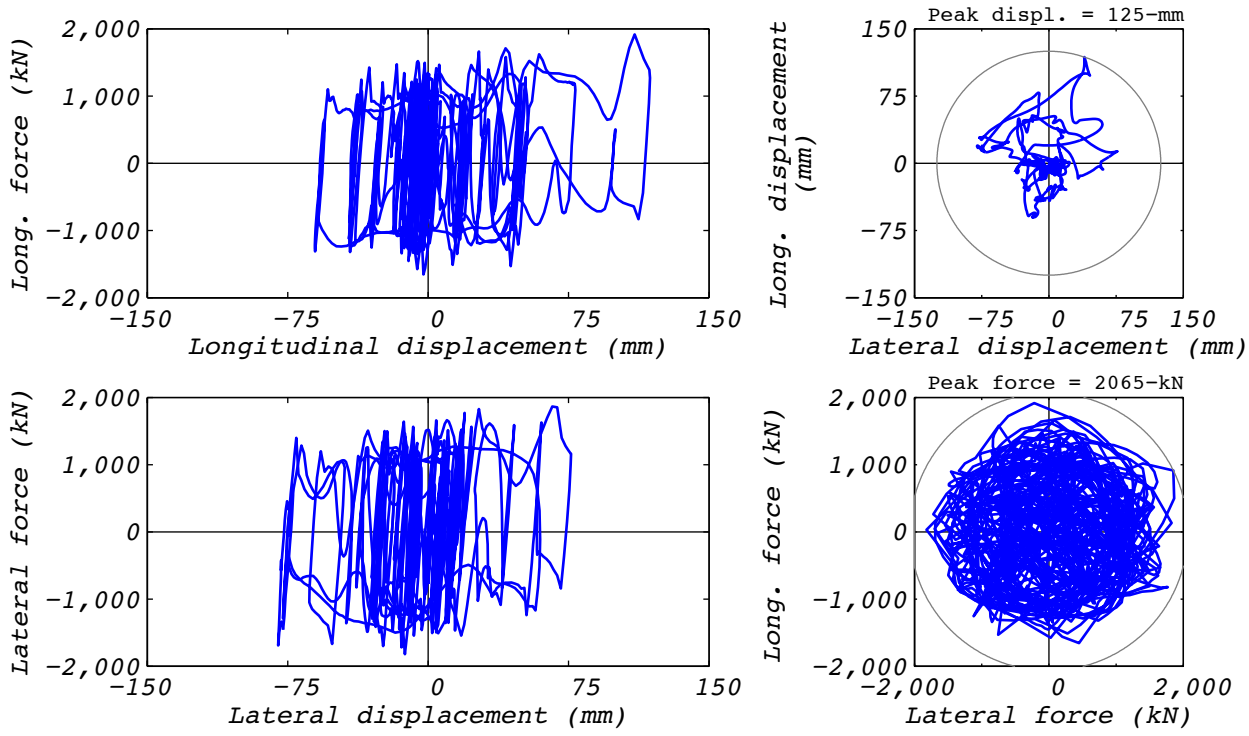

Figure C.5-2 Hybrid test bearing response for run 21: NRC2, 2D with experimental bearing representing all bearings.

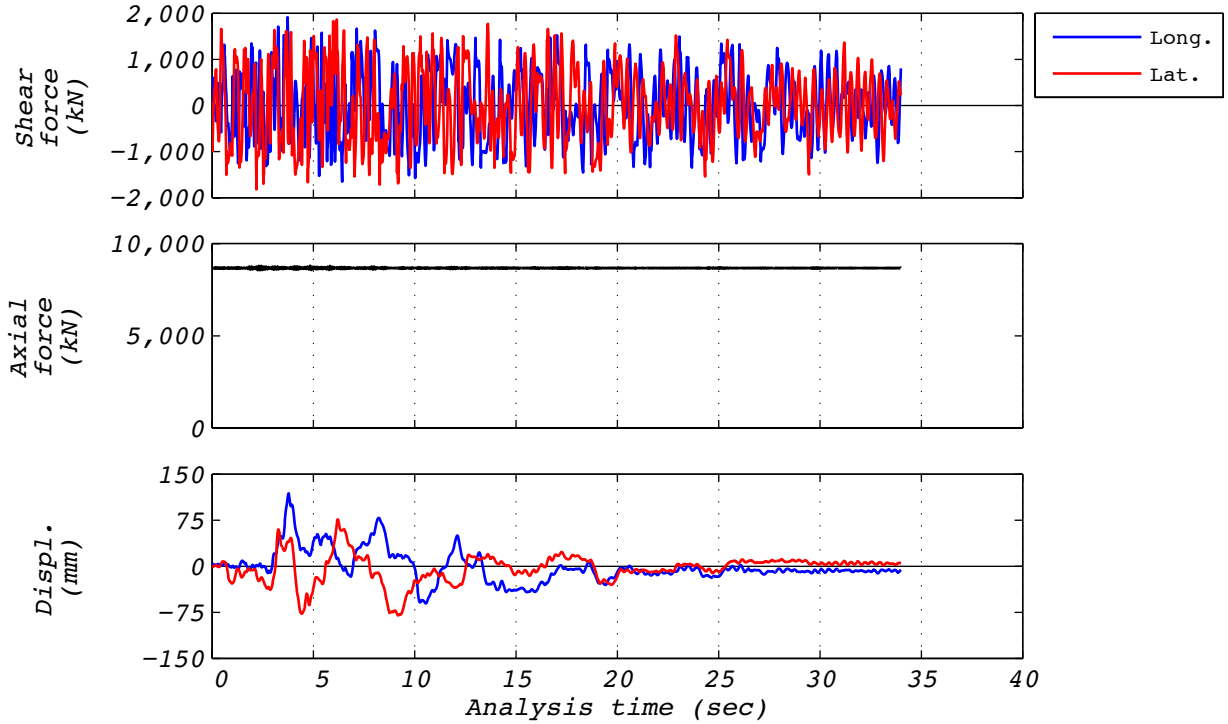

Figure C.5-3 Hybrid test time history responses for run 21 NRC2, 2D with experimental bearing representing all bearings.

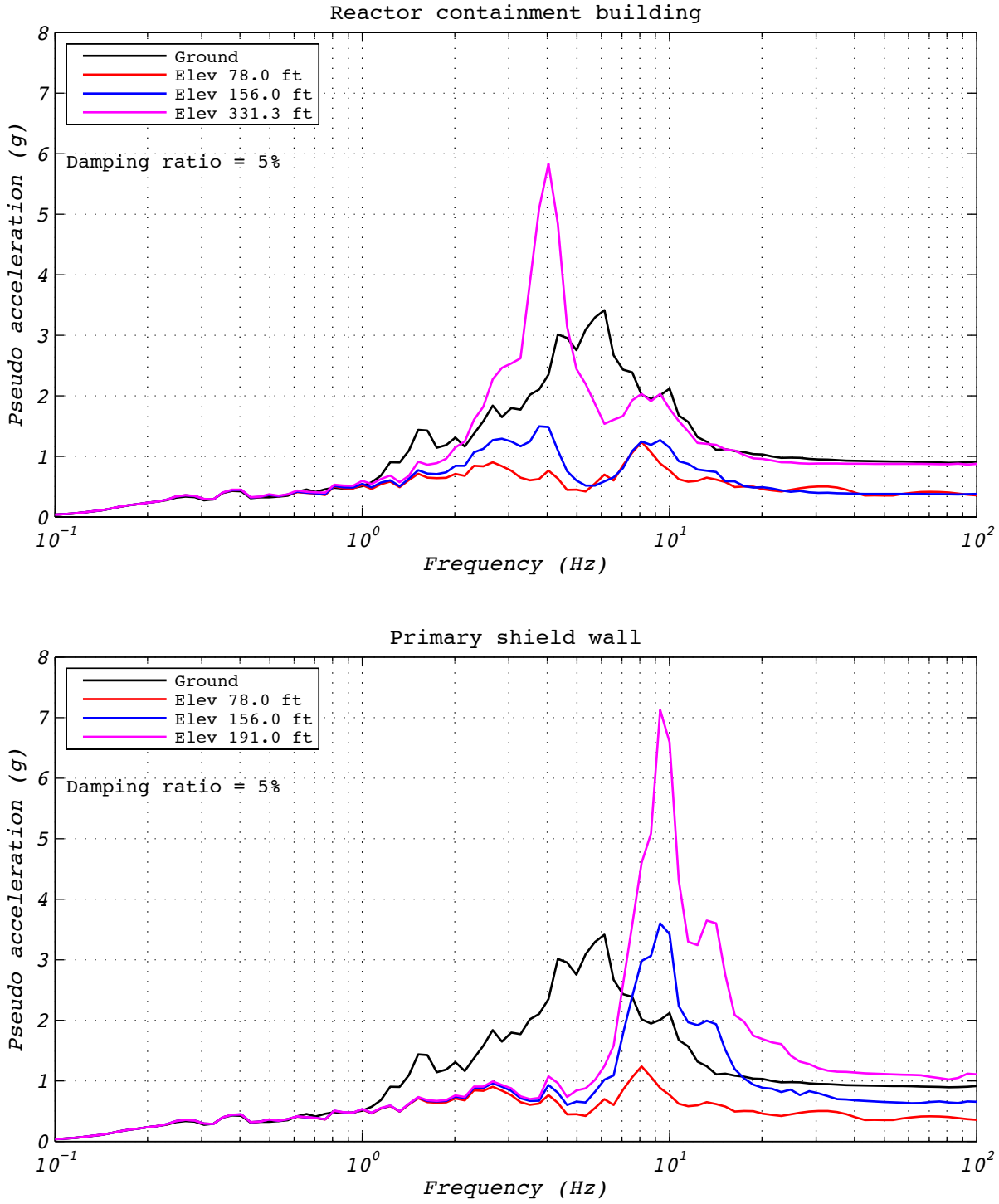

Figure C.5-4 Hybrid test floor spectra for run 21 NRC2, 2D with experimental bearing representing all bearings.

C.6 TEST RUN 22

Test run 22 was a hybrid test of the NRC dispersion appropriate ground motion number 2. The model consisted of a single experimental bearing representing all 527 bearings. Input motions consisted of a single horizontal component and a constant axial load specified as the design axial load of 8,663 kN. The test was executed at a rate 25 times slower than real time to compensate for machine delays. Bearing EQS-1 was used in this test. Figure C.6-1 shows the fidelity achieved in the hybrid test. Figures C.6-2 and C.6-3 contain bearing responses, and Figure C.6-4 depicts the resulting floor response spectra for select locations in two of the isolated structures.

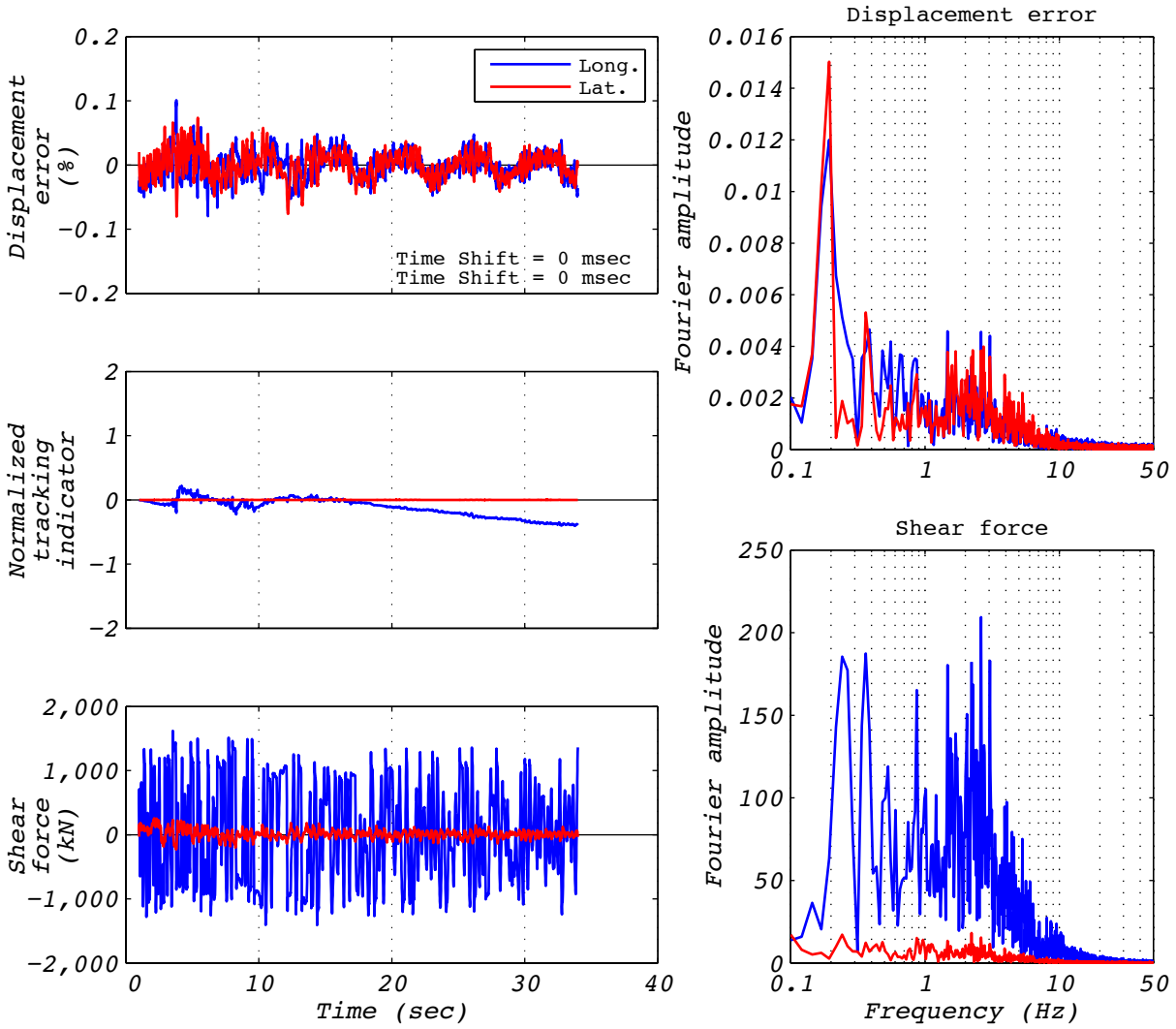

Figure C.6-1 Hybrid test performance metrics for run 22: NRC2, 1D with experimental bearing representing all bearings.

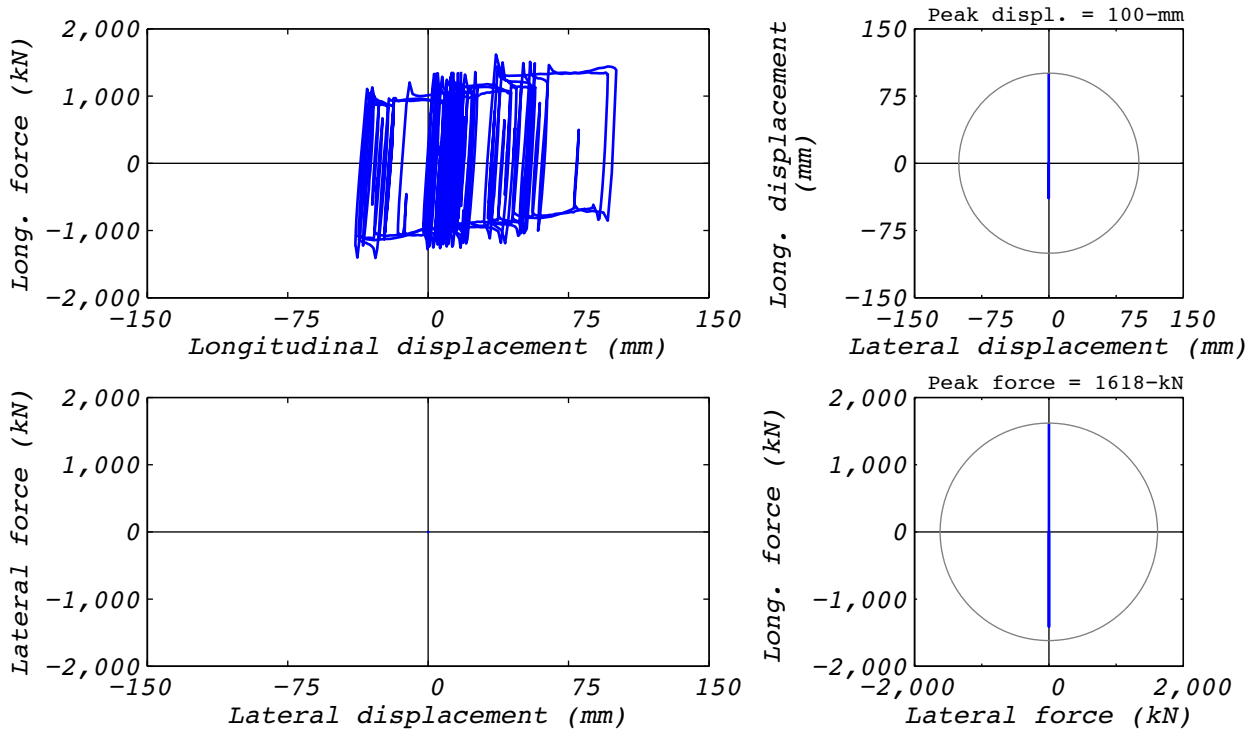

Figure C.6-2 Hybrid test bearing response for run 22: NRC2, 1D with experimental bearing representing all bearings.

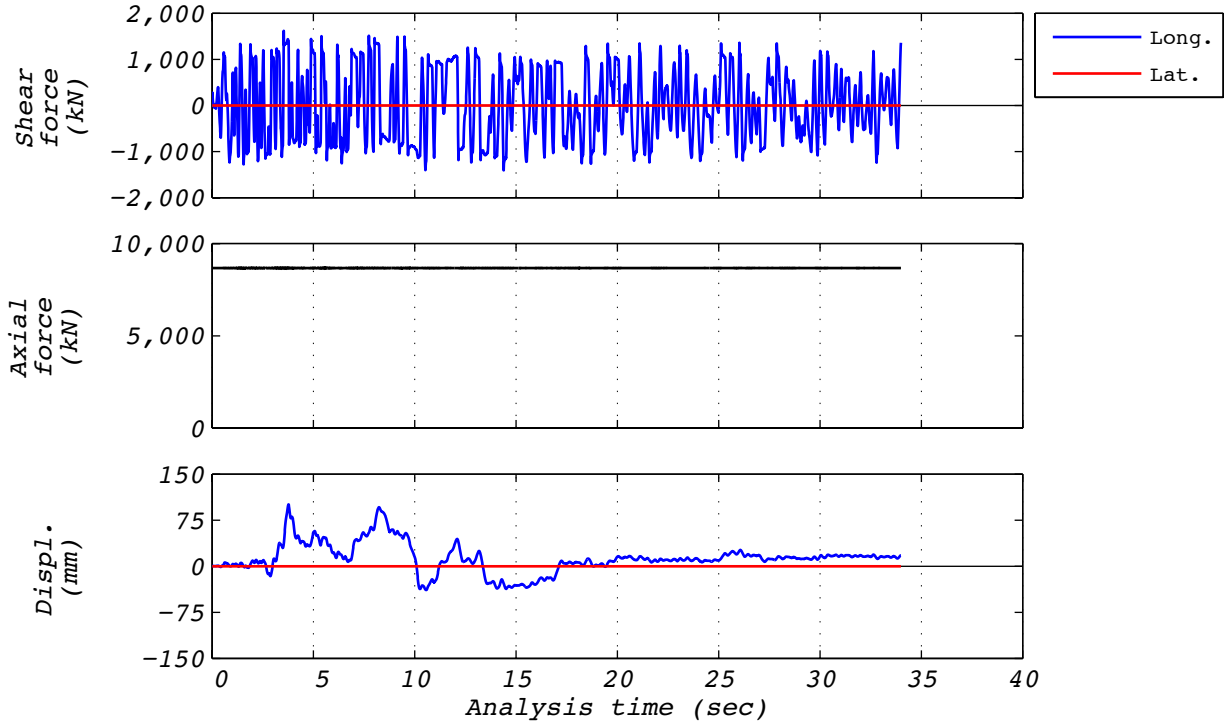

Figure C.6-3 Hybrid test time history responses for run 22: NRC2, 1D with experimental bearing representing all bearings.

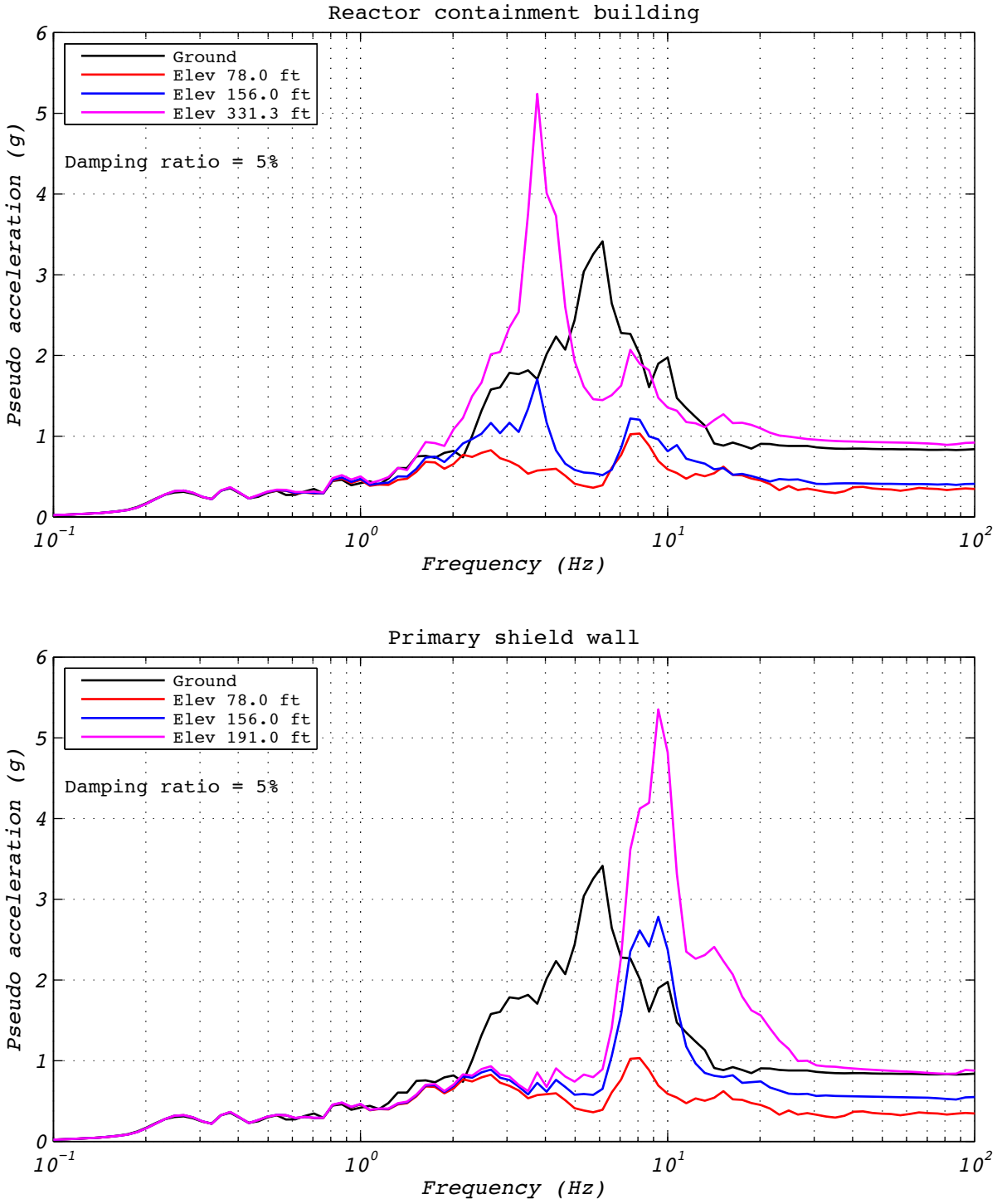

Figure C.6-4 Hybrid test floor spectra for run 22: NRC2, 1D with experimental bearing representing all bearings.

C.7 DISPLACEMENT RUN 23

Test run 23 was a real-time displacement history recorded from test run 22, which was a hybrid test of the NRC dispersion appropriate ground motion number 2. Input motions consisted of a single horizontal component and a constant axial load specified as the design axial load of 8,663 kN. The test was executed at a rate real time to investigate loading rate effects. Bearing EQS-1 was used in this test. Figures C.7-1 and C.7-2 contain bearing responses.

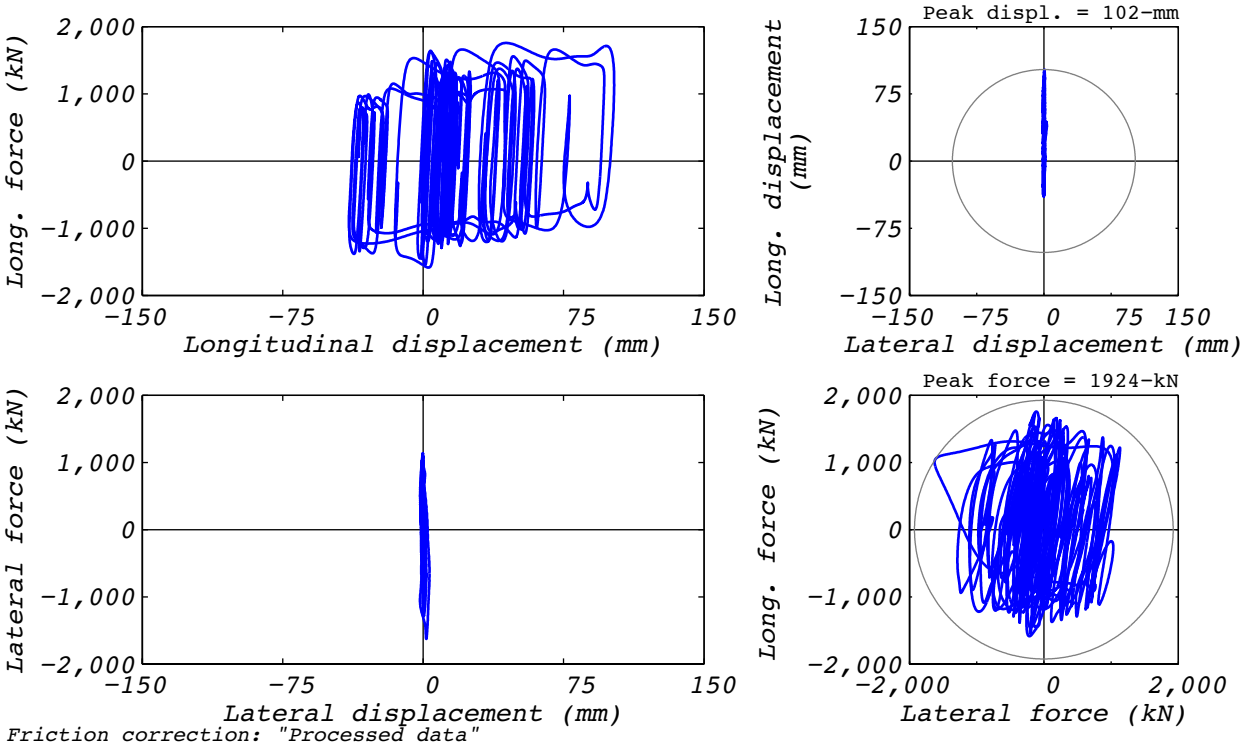

Figure C.7-1 Bearing response for real-time reproduction of hybrid test run 22: NRC2, 1D with experimental bearing representing all bearings.

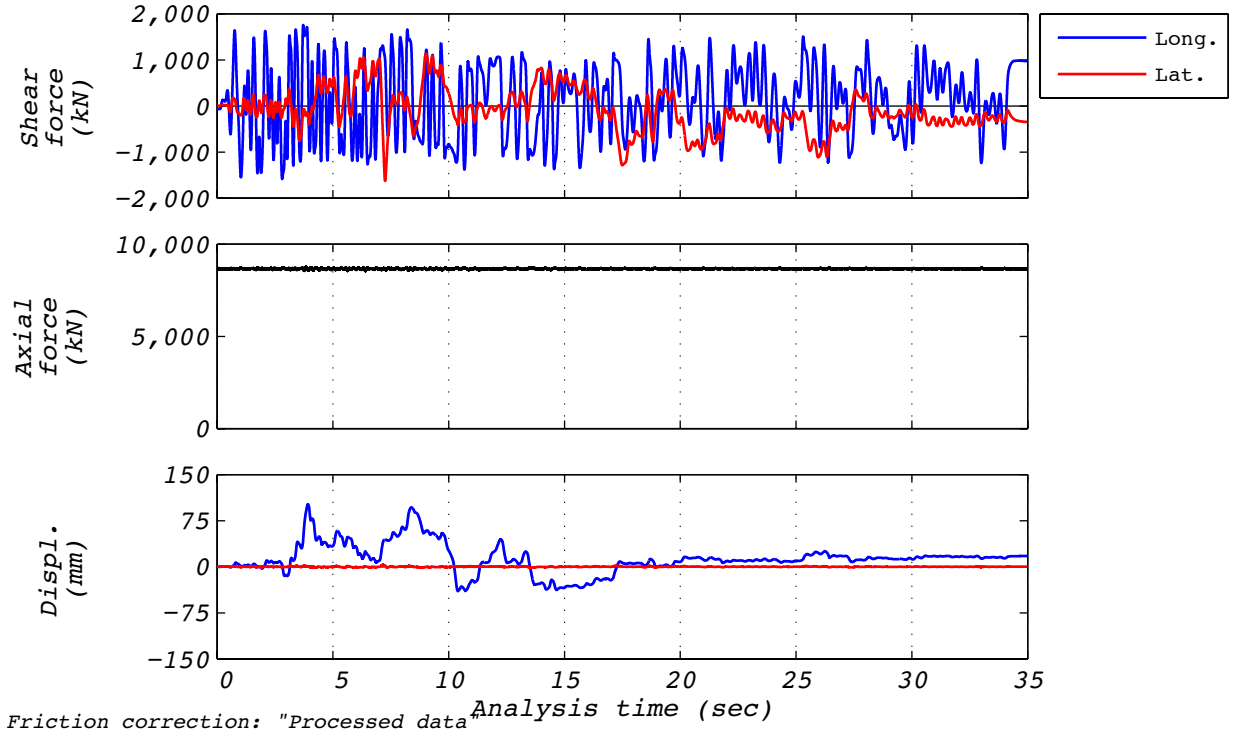

Figure C.7-2 Time history responses for real-time reproduction of hybrid test run 22: NRC2, 1D with experimental bearing representing all bearings.

C.8 TEST RUN 43

Test run 43 was a hybrid test of the NRC dispersion appropriate ground motion number 2. The model consisted of a five groups of bearings. The experimental bearing's group was located in the center of the layout. Input motions consisted of two horizontal components. The vertical component was not applied, but the effects of overturning were included. The initial axial load specified as the design axial load of 8,663 kN. The test was executed at a rate 5 times slower than real time to compensate for machine delays. Bearing EQS-2 was used in this test. Figure C.8-1 shows the fidelity achieved in the hybrid test. Figures C.8-2 and C.8-3 contain bearing responses, and Figure C.8-4 depicts the resulting floor response spectra for select locations in two of the isolated structures.

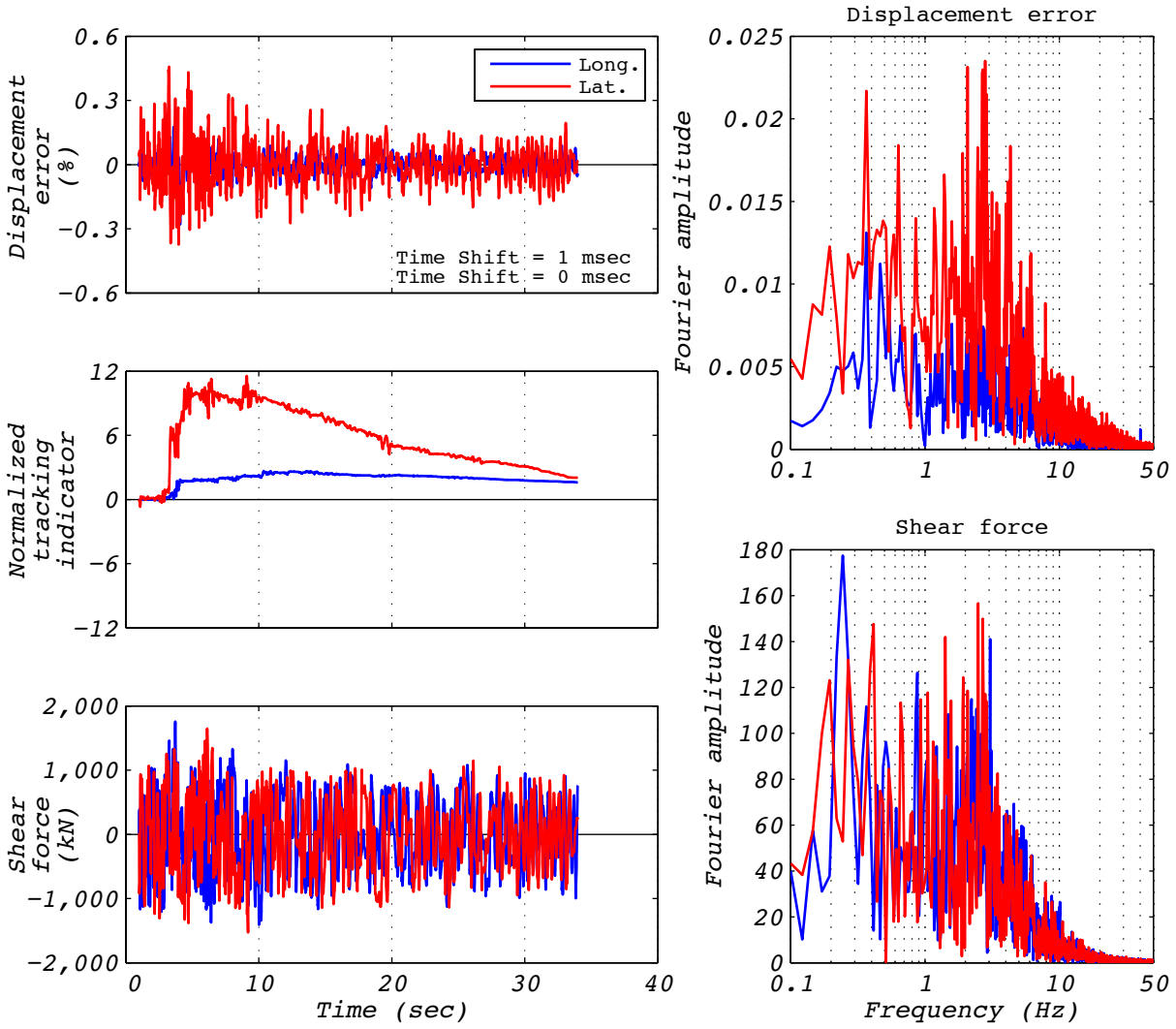

Figure C.8-1 Hybrid test performance metrics for run 43: NRC2, 3D with 5 groups of bearings and the experimental bearing representing the center group.

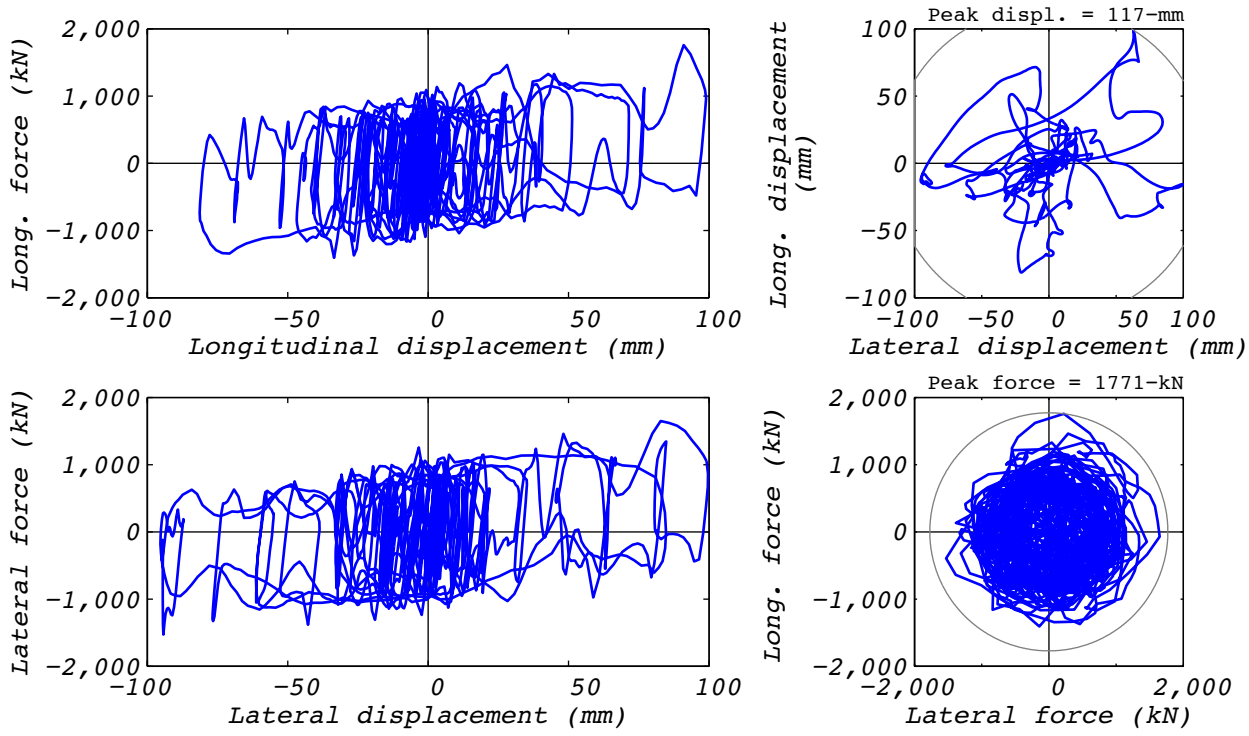

Figure C.8-2 Hybrid test bearing response for run 43: NRC2, 3D with 5 groups of bearings and the experimental bearing representing the center group.

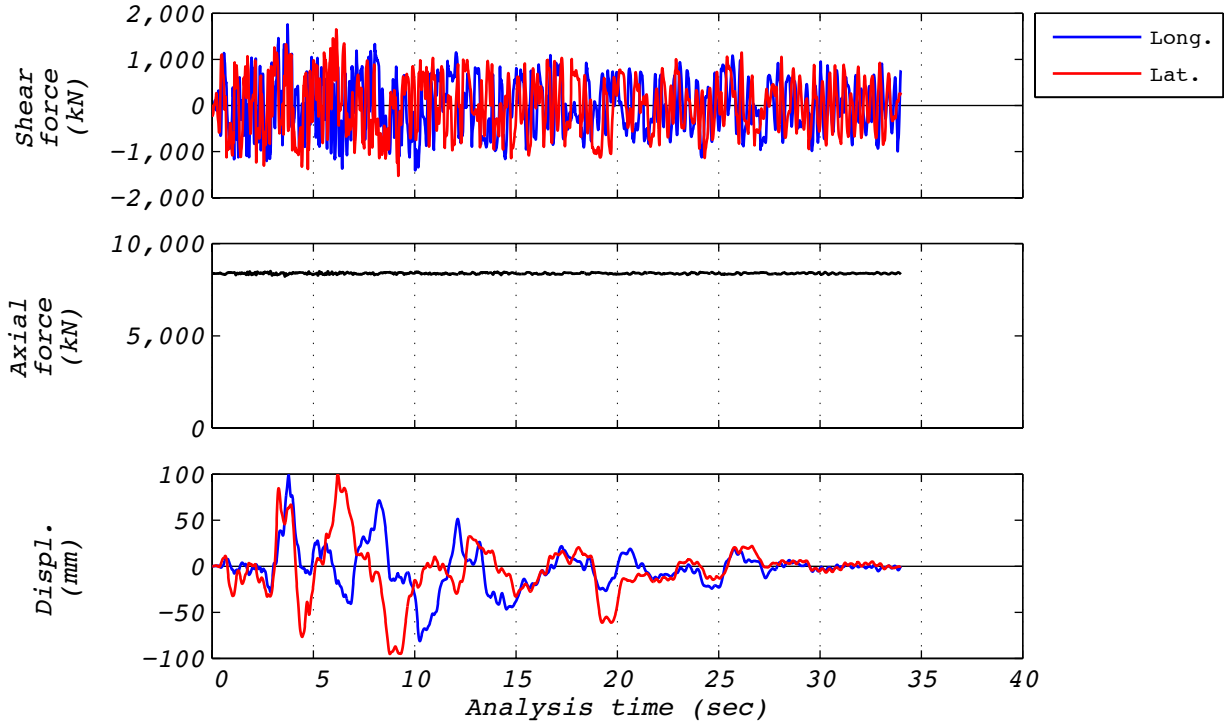

Figure C.8-3 Hybrid test time history responses for run 43: NRC2, 3D with 5 groups of bearings and the experimental bearing representing the center group.

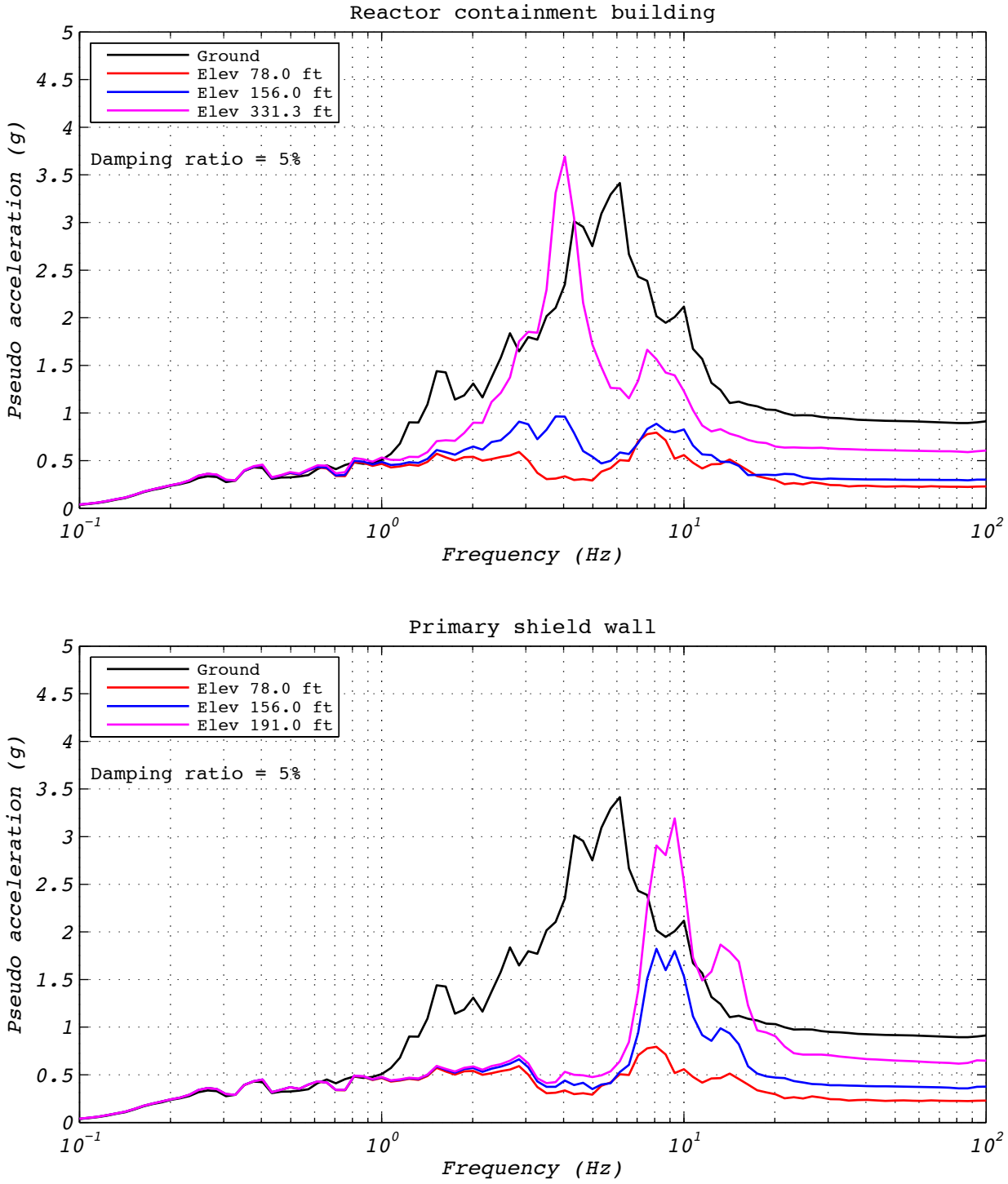

Figure C.8-4 Hybrid test floor spectra for run 43: NRC2, 3D with 5 groups of bearings and the experimental bearing representing the center group.

C.9 DEVELOPMENT RUN 44

Development run 44 was a hybrid test of the NRC dispersion appropriate ground motion number 2. The model consisted of a five groups of bearings. The experimental bearing's group was located in the center of the layout. Input motions consisted of two horizontal components. The vertical component was not applied, but the effects of overturning were included. The initial axial load specified as the design axial load of 8,663 kN. The test was executed at a rate 15 times slower than real time to compensate for machine delays. Bearing EQS-2 was used in this test. Figure C.9-1 shows the fidelity achieved in the hybrid test. Figures C.9-2 and C.9-3 contain bearing responses, and Figure C.9-4 depicts the resulting floor response spectra for select locations in two of the isolated structures.

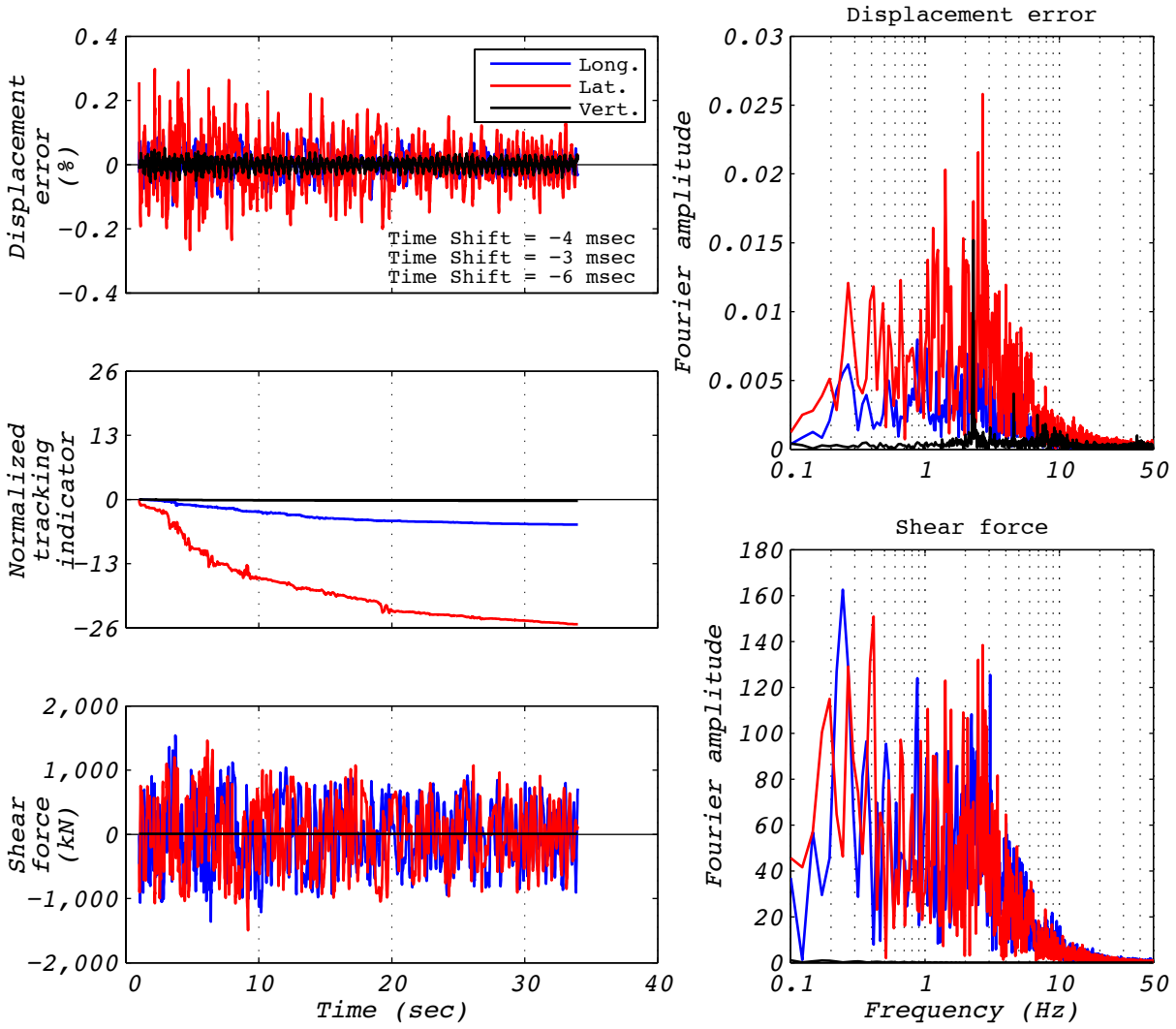

Figure C.9-1 Hybrid test performance metrics for run 44: NRC2, 3D with 5 groups of bearings and the experimental bearing representing the center group.

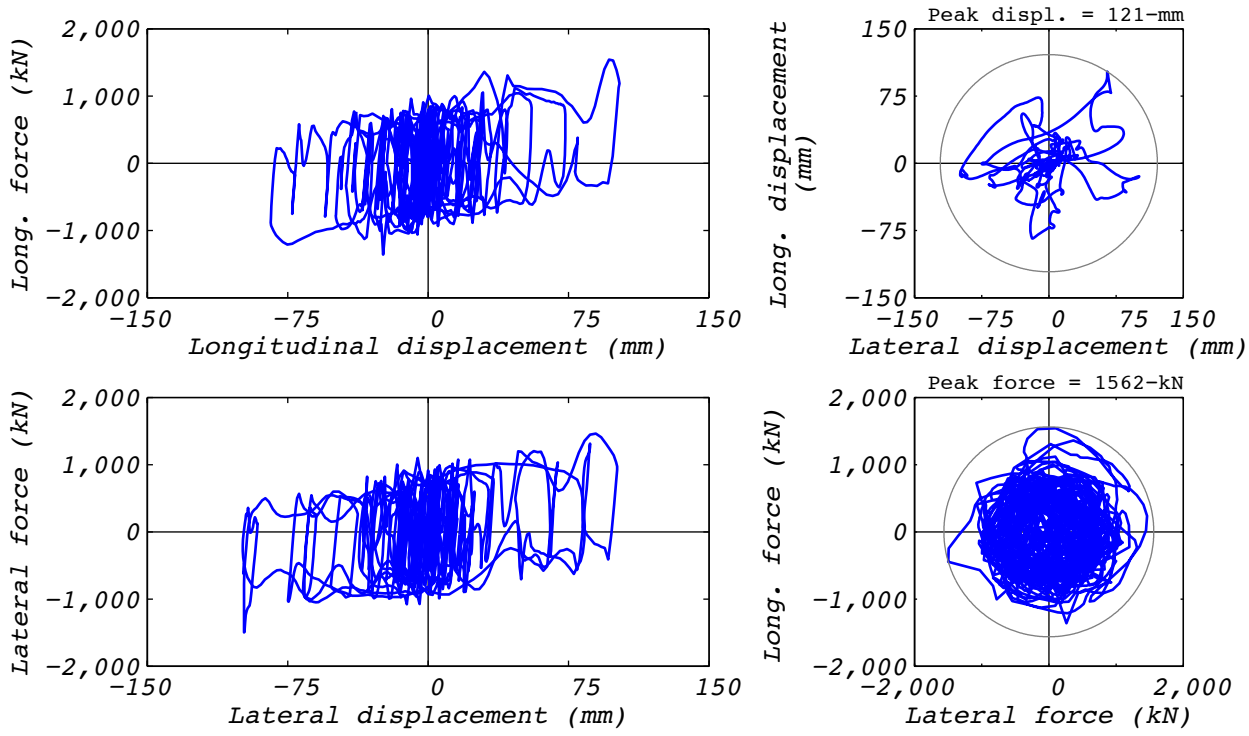

Figure C.9-2 Hybrid test bearing response for run 44: NRC2, 3D with 5 groups of bearings and the experimental bearing representing the center group.

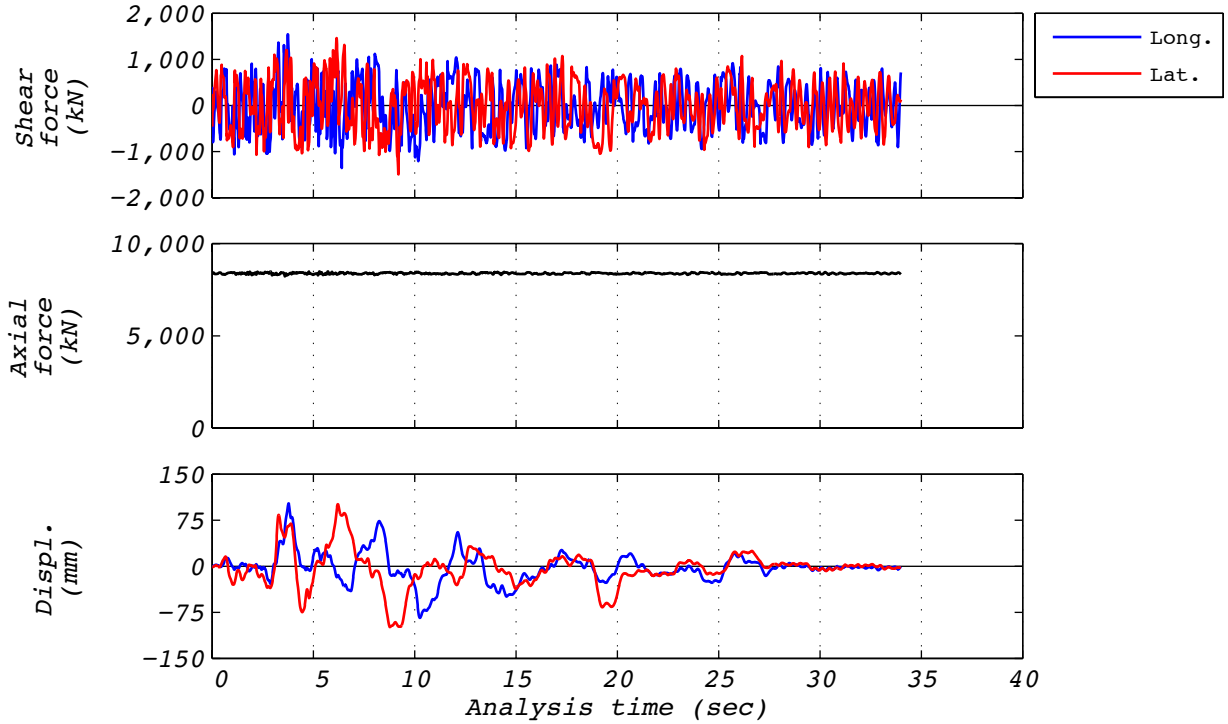

Figure C.9-3 Hybrid test time history responses for run 44: NRC2, 3D with 5 groups of bearings and the experimental bearing representing the center group.

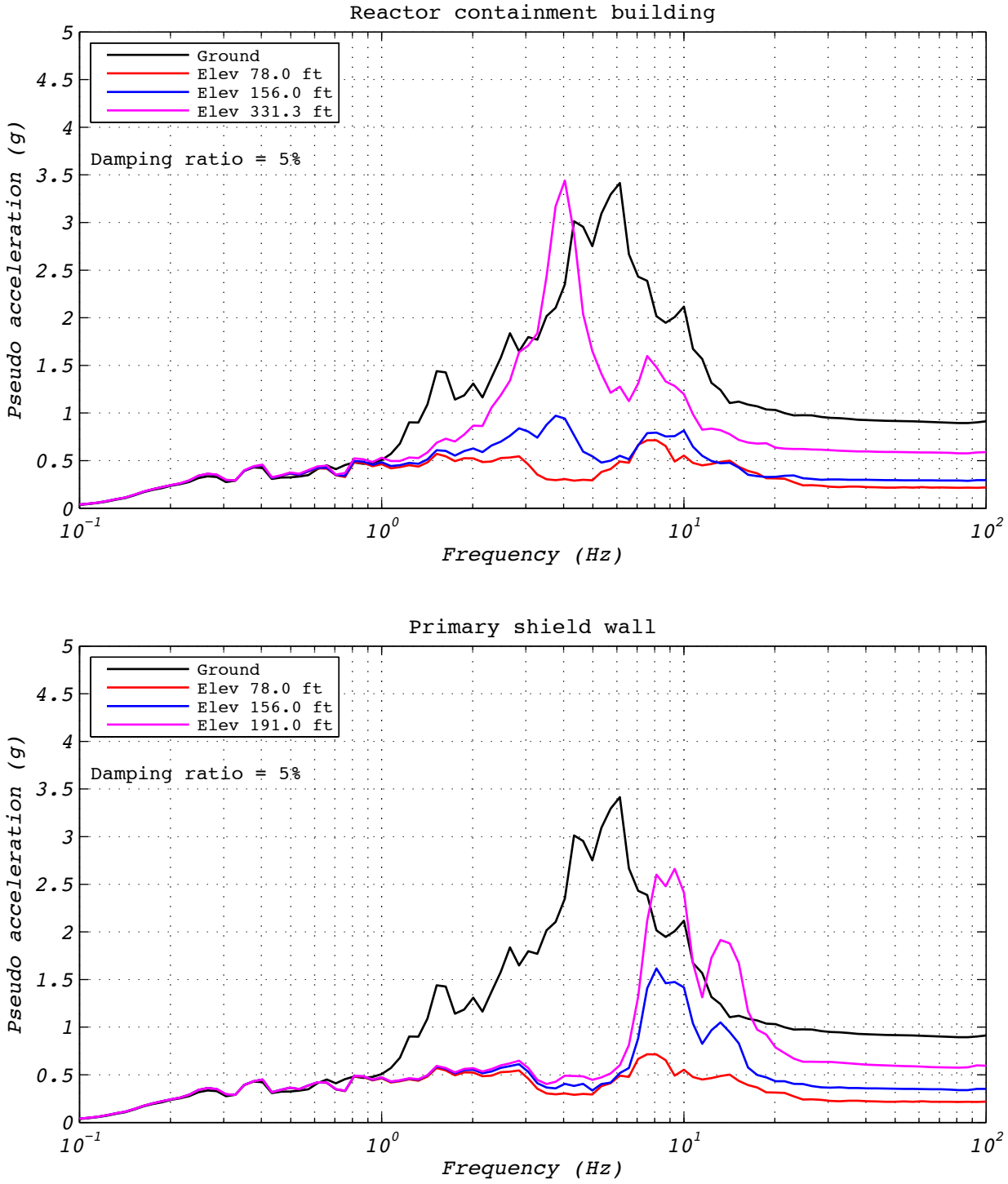

Figure C.9-4 Hybrid test floor spectra for run 44: NRC2, 3D with 5 groups of bearings and the experimental bearing representing the center group.

C.10 DEVELOPMENT RUN 46

Development run 46 was a hybrid test of the NRC dispersion appropriate ground motion number 2. The model consisted of a five groups of bearings. The experimental bearing's group was located in the center of the layout. Input motions consisted of two horizontal components. The vertical component was not applied, but the effects of overturning were included. The initial axial load specified as the design axial load of 8,663 kN. The test was executed at a rate 18 times slower than real time to compensate for machine delays. Bearing EQS-2 was used in this test. Figure C.10-1 shows the fidelity achieved in the hybrid test. Figures C.10-2 and C.10-3 contain bearing responses, and Figure C.10-4 depicts the resulting floor response spectra for select locations in two of the isolated structures.

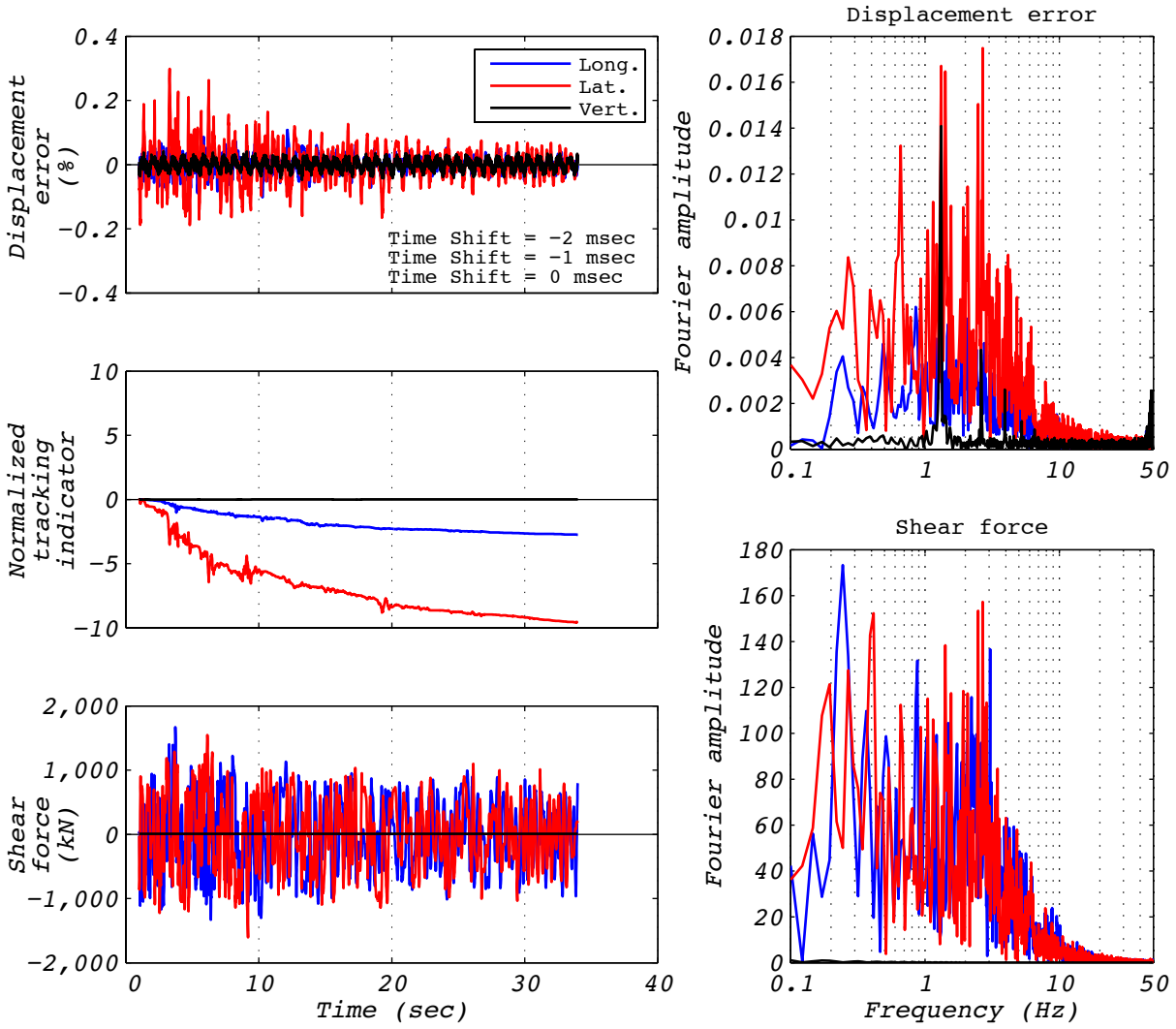

Figure C.10-1 Hybrid test performance metrics for run 46: NRC2, 3D with 5 groups of bearings and the experimental bearing representing the center group.

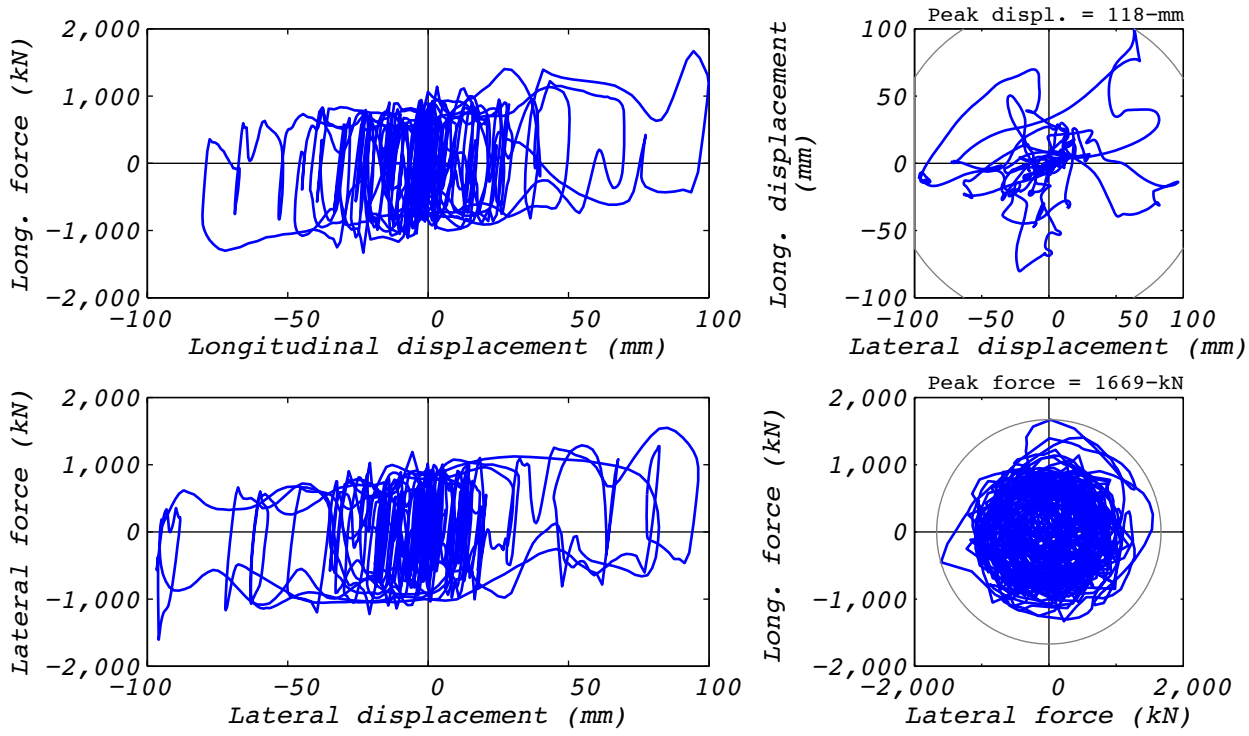

Figure C.10-2 Hybrid test bearing response for run 46: NRC2, 3D with 5 groups of bearings and the experimental bearing representing the center group.

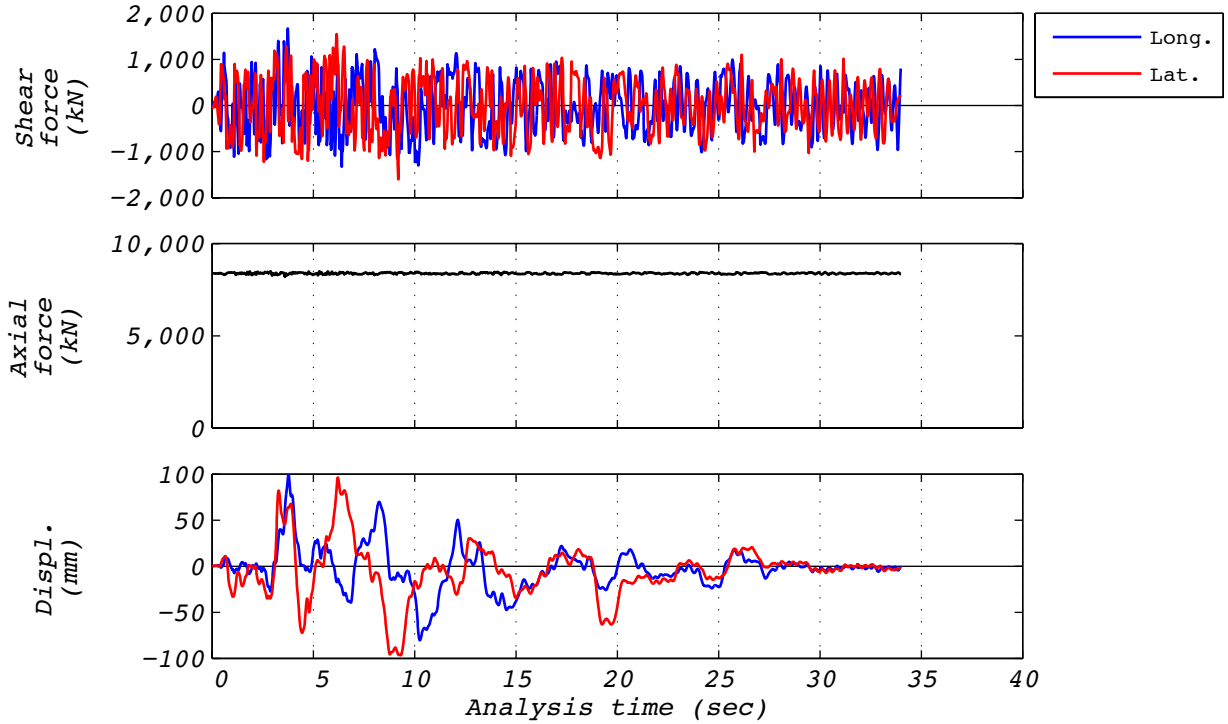

Figure C.10-3 Hybrid test time history responses for run 46: NRC2, 3D with 5 groups of bearings and the experimental bearing representing the center group.

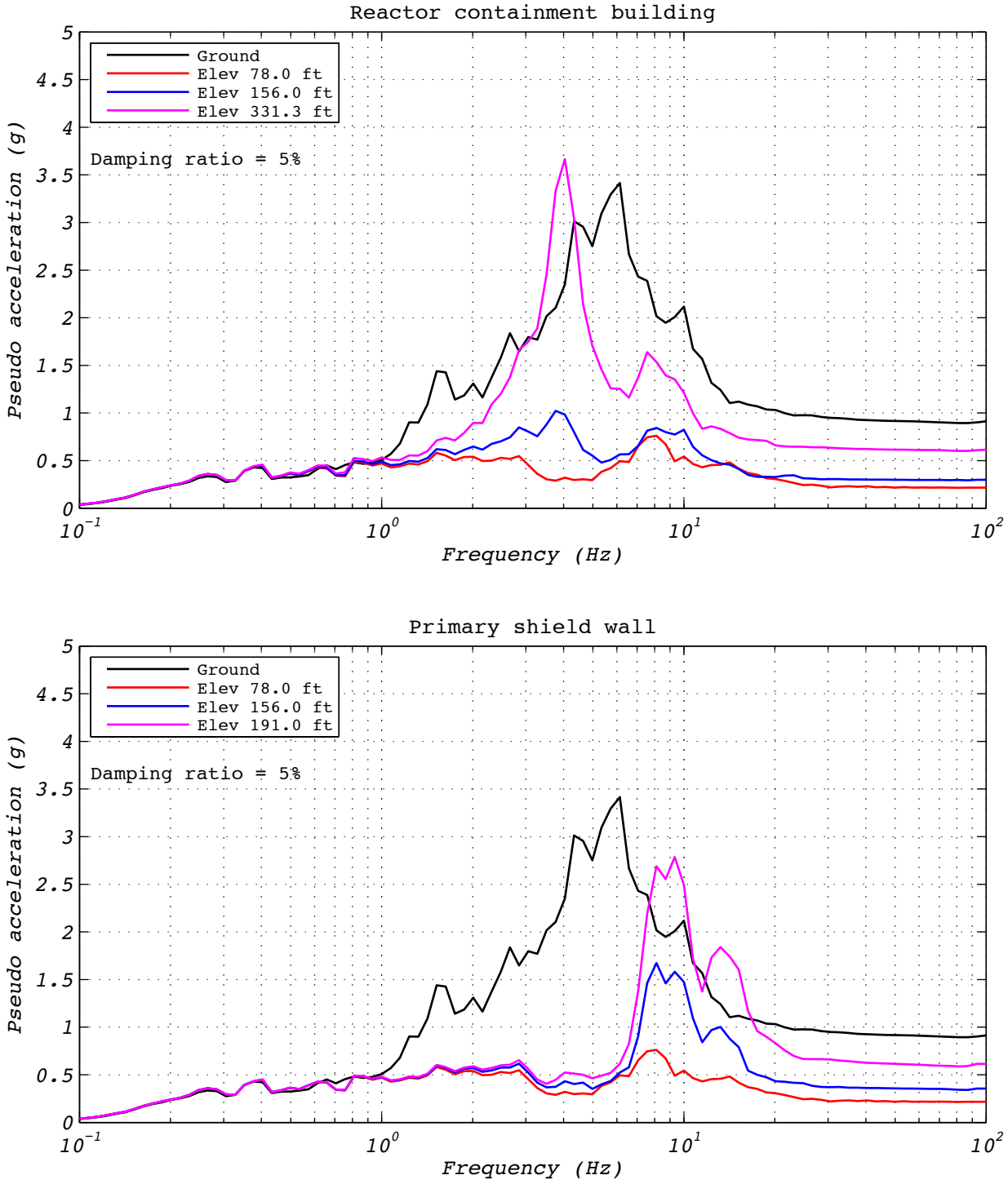

Figure C.10-4 Hybrid test floor spectra for run 46: NRC2, 3D with 5 groups of bearings and the experimental bearing representing the center group.

C.11 TEST RUN 47

Test run 47 was a hybrid test of the NRC dispersion appropriate ground motion number 2. The model consisted of a five groups of bearings. The experimental bearing's group was located in center of the layout. Input motions consisted of two horizontal components. The vertical component was not applied, but the effects of overturning were included. The initial axial load specified as the design axial load of 8,663 kN. The test was executed at a rate 20 times slower than real time to compensate for machine delays. Bearing EQS-2 was used in this test. Figure C.11-1 shows the fidelity achieved in the hybrid test. Figures C.11-2 and C.11-3 contain bearing responses, and Figure C.11-4 depicts the resulting floor response spectra for select locations in two of the isolated structures.

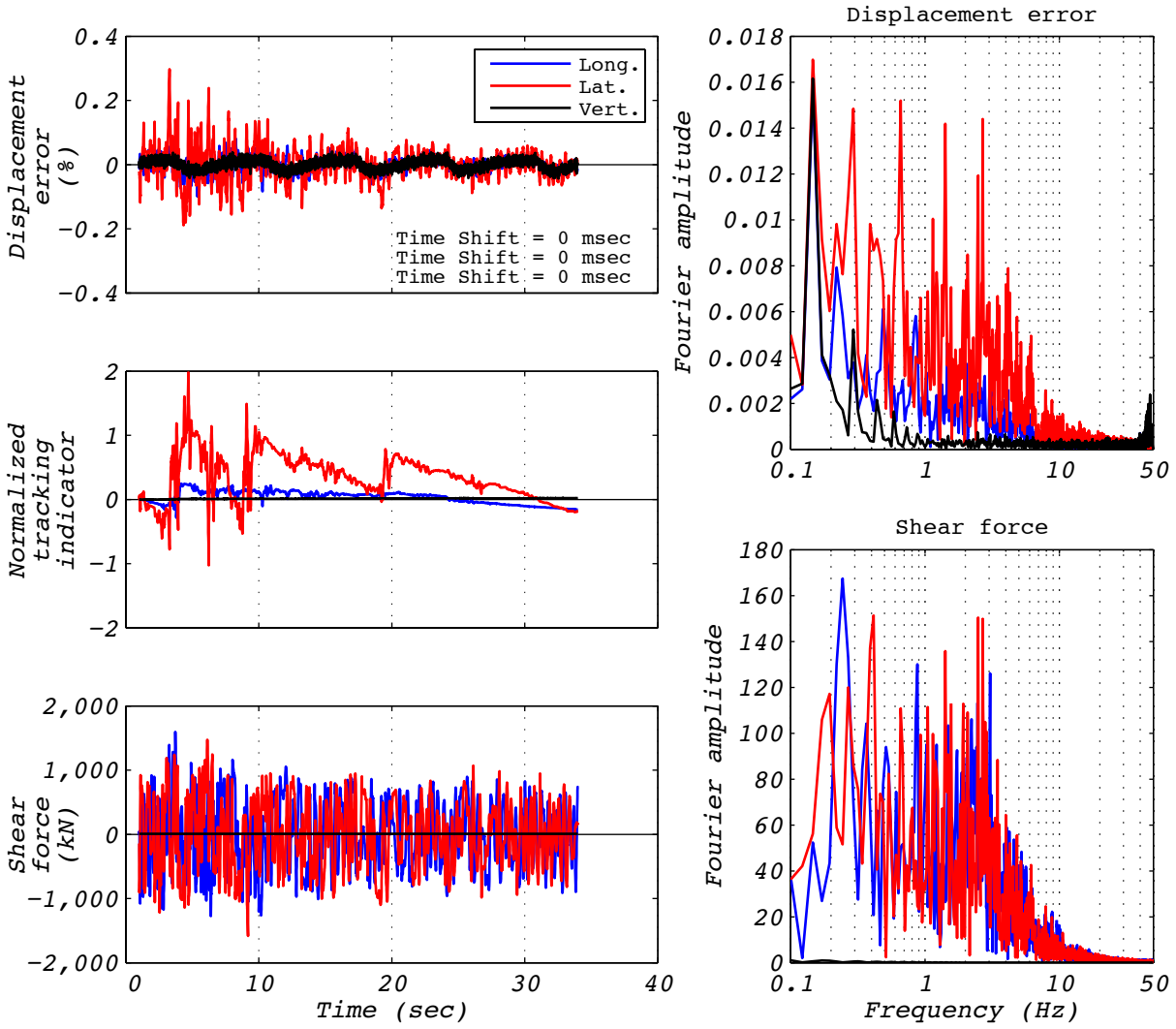

Figure C.11-1 Hybrid test performance metrics for run 47: NRC2, 3D with 5 groups of bearings and the experimental bearing representing the center group.

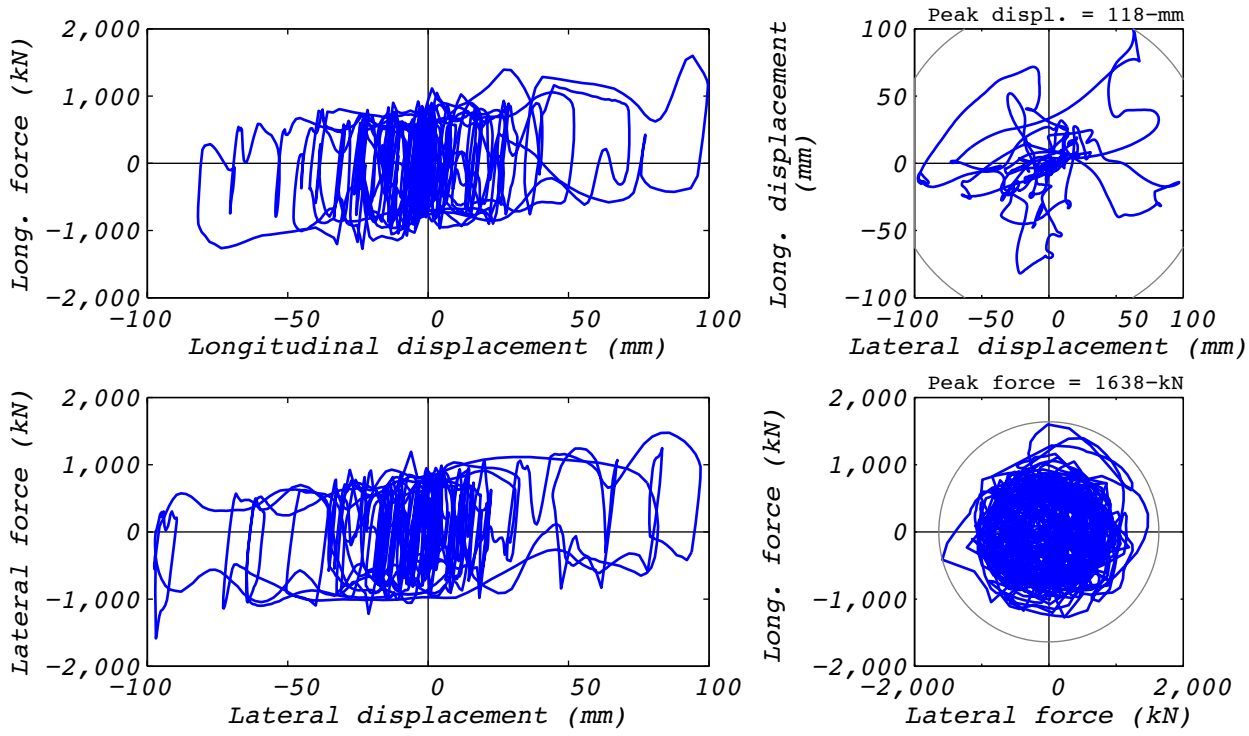

Figure C.11-2 Hybrid test bearing response for run 47: NRC2, 3D with 5 groups of bearings and the experimental bearing representing the center group.

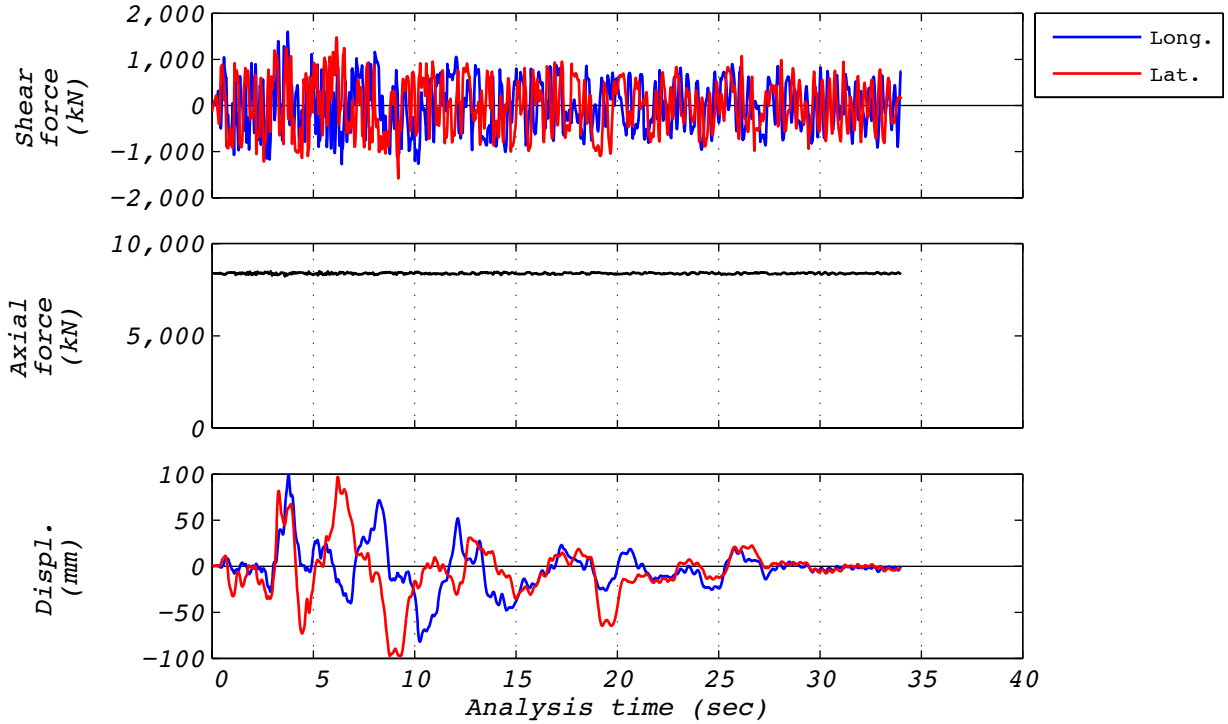

Figure C.11-3 Hybrid test time history responses for run 47: NRC2, 3D with 5 groups of bearings and the experimental bearing representing the center group.

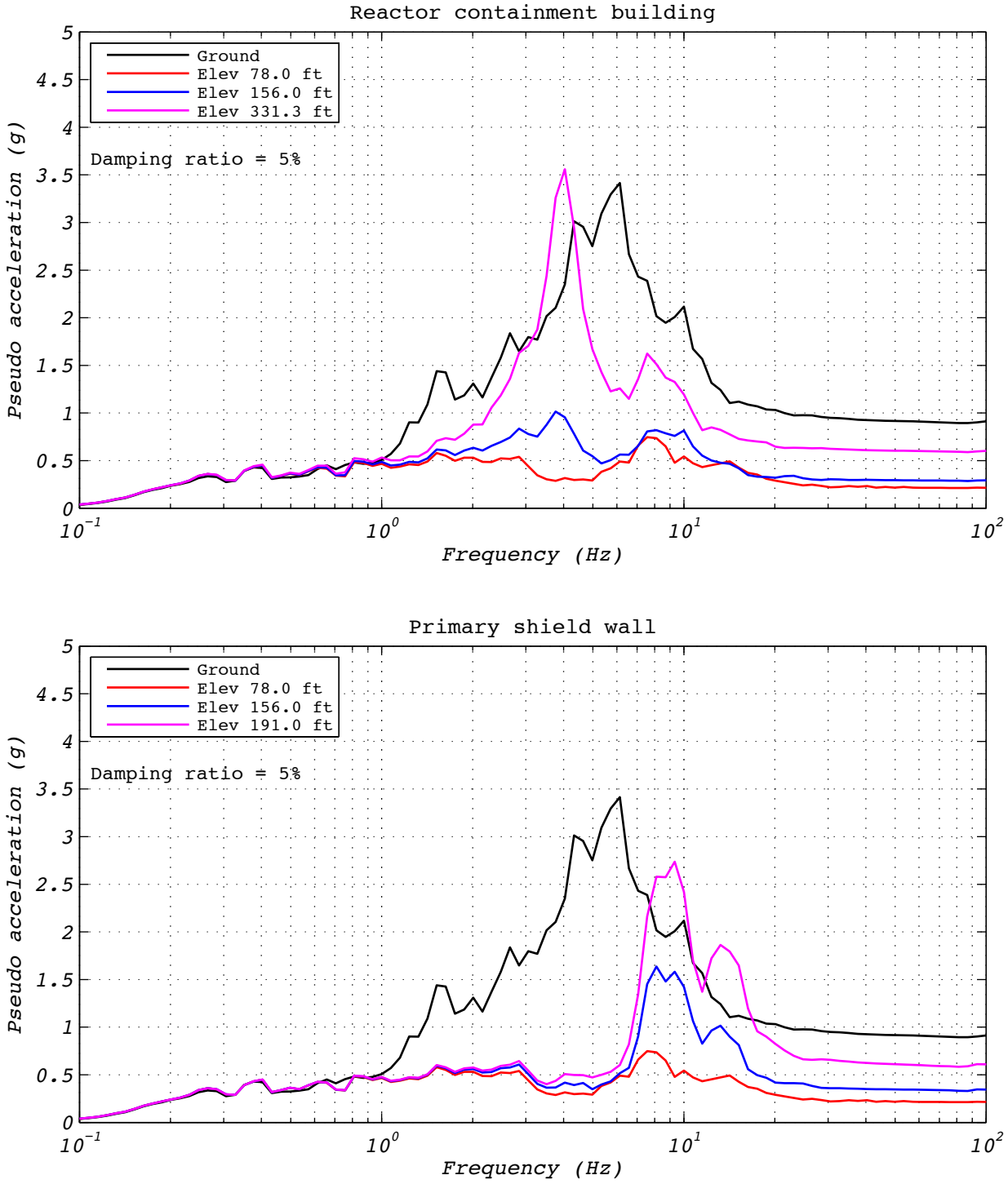

Figure C.11-4 Hybrid test floor spectra for run 47: NRC2, 3D with 5 groups of bearings and the experimental bearing representing the center group.

C.12 DEVELOPMENT RUN 48

Development run 48 was a hybrid test of the NRC dispersion appropriate ground motion number 2. The model consisted of a five groups of bearings. The experimental bearing's group was located in corner number 3 of the layout. Input motions consisted of two horizontal components. The vertical component was not applied, but the effects of overturning were included. The initial axial load specified as the design axial load of 8,663 kN. The test was executed at a rate 20 times slower than real time to compensate for machine delays. Bearing EQS-2 was used in this test. Figure C.12-1 shows the fidelity achieved in the hybrid test. Figures C.12-2 and C.12-3 contain bearing responses, and Figure C.12-4 depicts the resulting floor response spectra for select locations in two of the isolated structures.

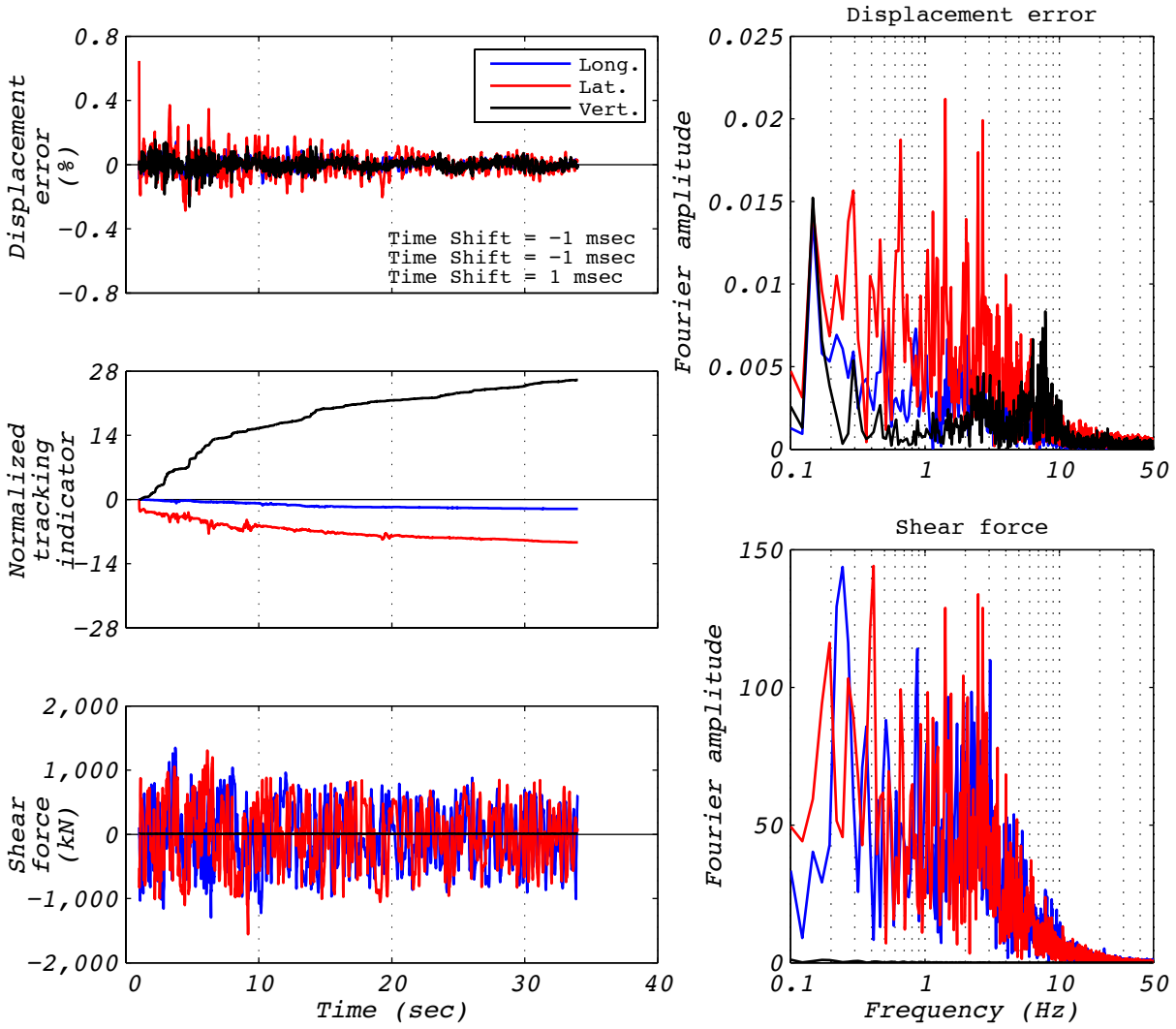

Figure C.12-1 Hybrid test performance metrics for run 48: NRC2, 3D with 5 groups of bearings and the experimental bearing representing the no. 3 corner group.

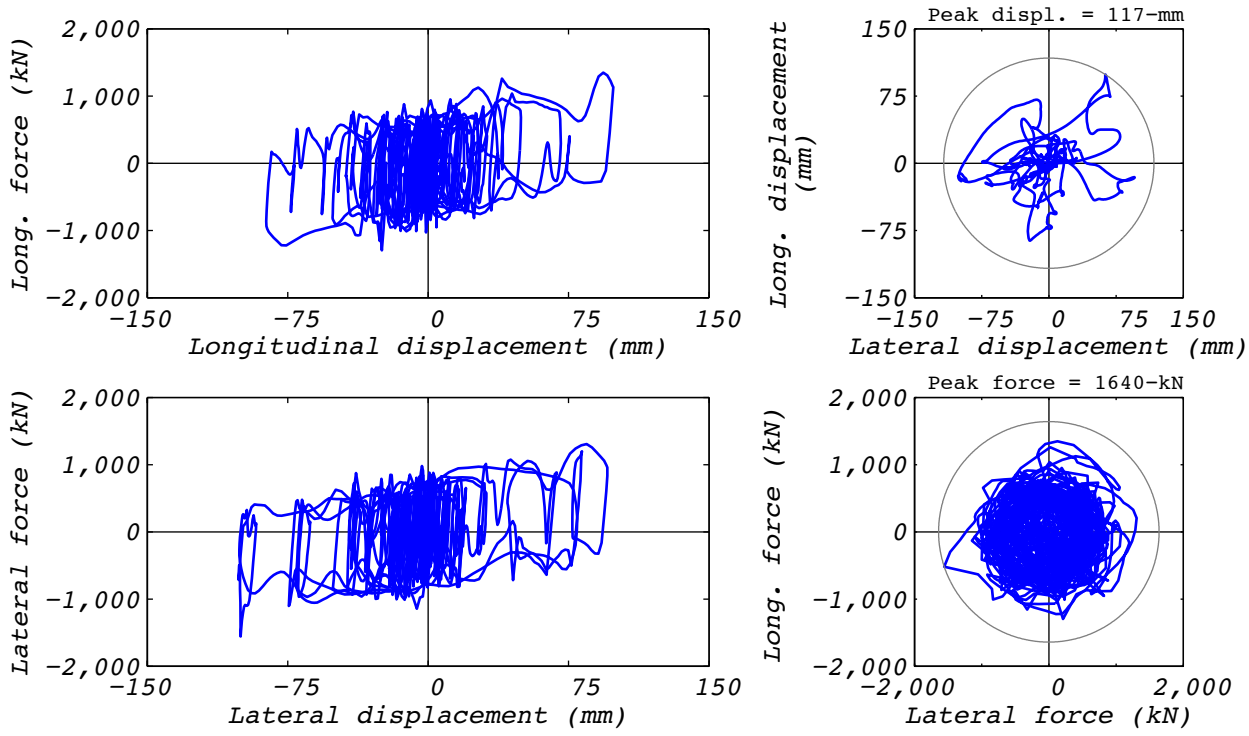

Figure C.12-2 Hybrid test bearing response for run 48: NRC2, 3D with 5 groups and the experimental bearing representing the no. 3 corner group.

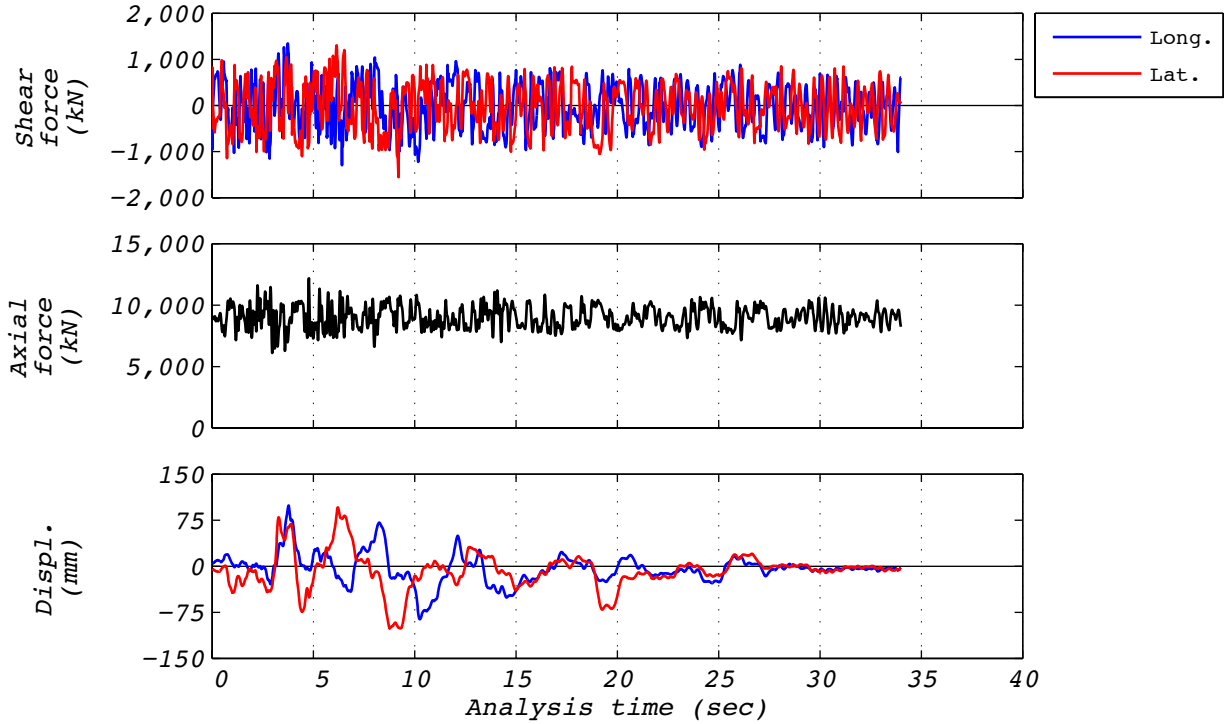

Figure C.12-3 Hybrid test time history responses for run 48: NRC2, 3D with 5 groups and the experimental bearing representing the no. 3 corner group.

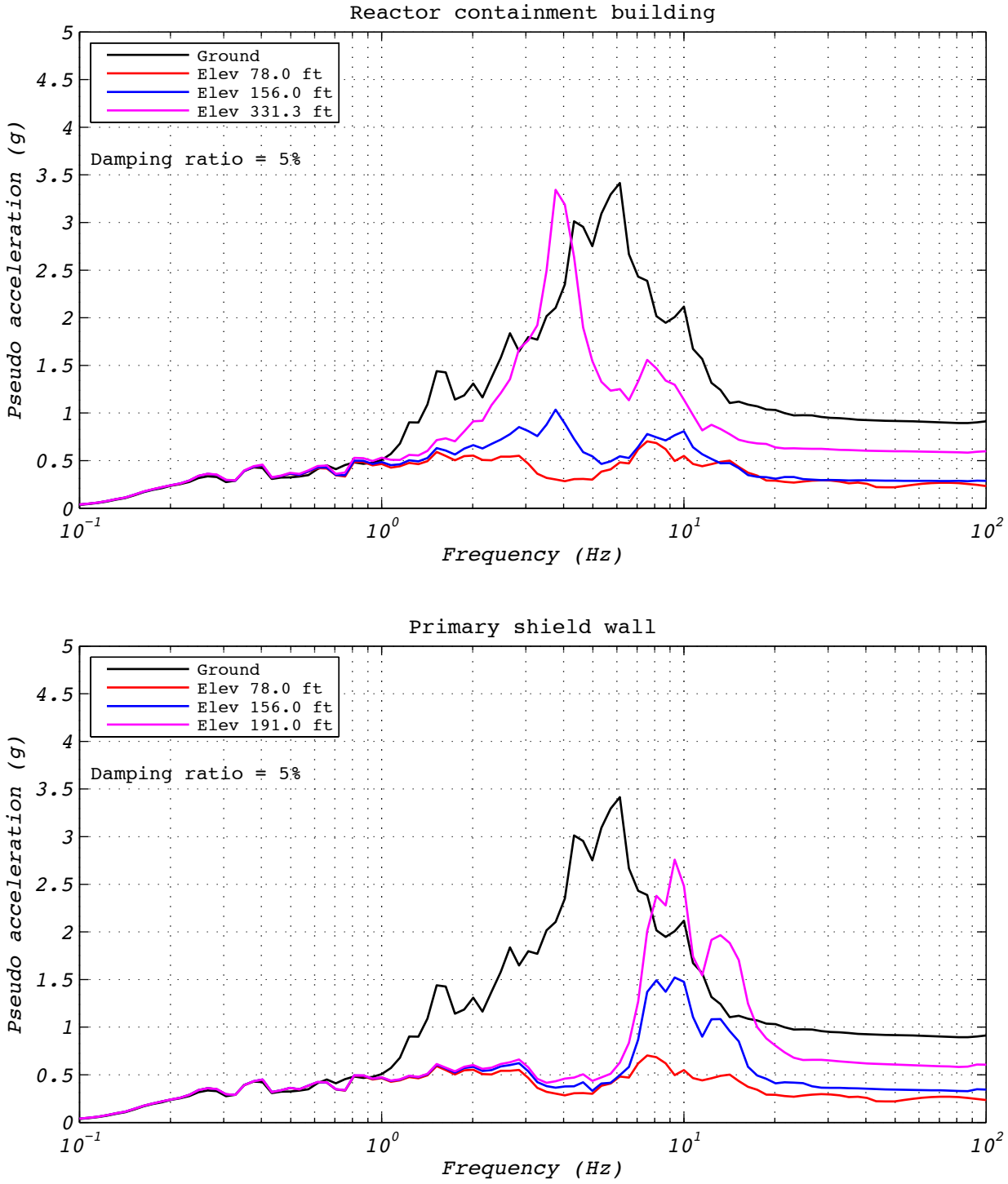

Figure C.12-4 Hybrid test floor spectra for run 48: NRC2, 3D with 5 groups of bearings and the experimental bearing representing the no. 3 corner group.

C.13 DEVELOPMENT RUN 49

Development run 49 was a hybrid test of the NRC dispersion appropriate ground motion number 2. The model consisted of a five groups of bearings. The experimental bearing's group was located in corner number 3 of the layout. Input motions consisted of two horizontal components. The vertical component was not applied, but the effects of overturning were included. The initial axial load specified as the design axial load of 8,663 kN. The test was executed at a rate 20 times slower than real time to compensate for machine delays. Bearing EQS-2 was used in this test. Figure C.13-1 shows the fidelity achieved in the hybrid test. Figures C.13-2 and C.13-3 contain bearing responses, and Figure C.13-4 depicts the resulting floor response spectra for select locations in two of the isolated structures.

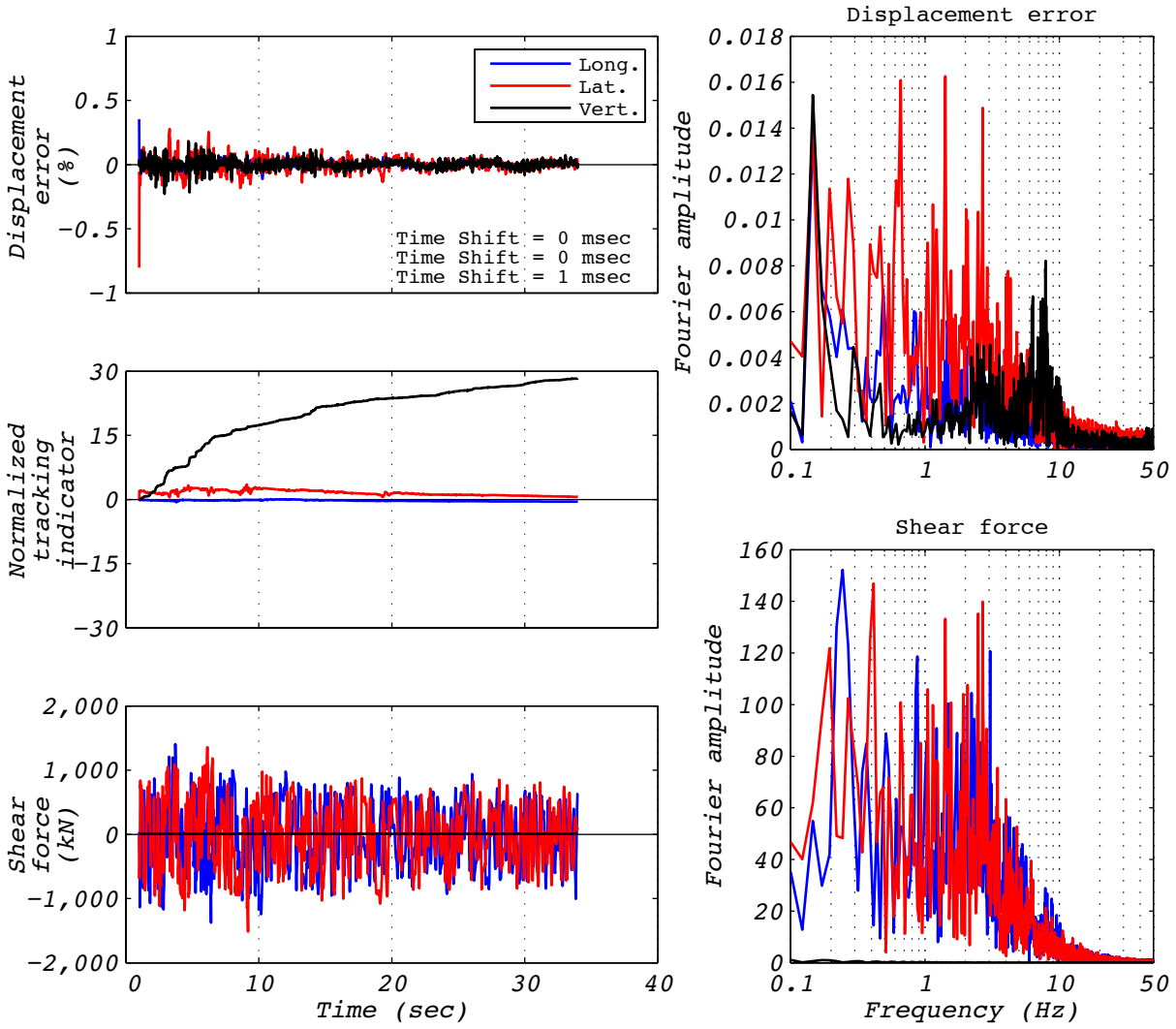

Figure C.13-1 Hybrid test performance metrics for run 49: NRC2, 3D with 5 groups of bearings and the experimental bearing representing the no. 3 corner group.

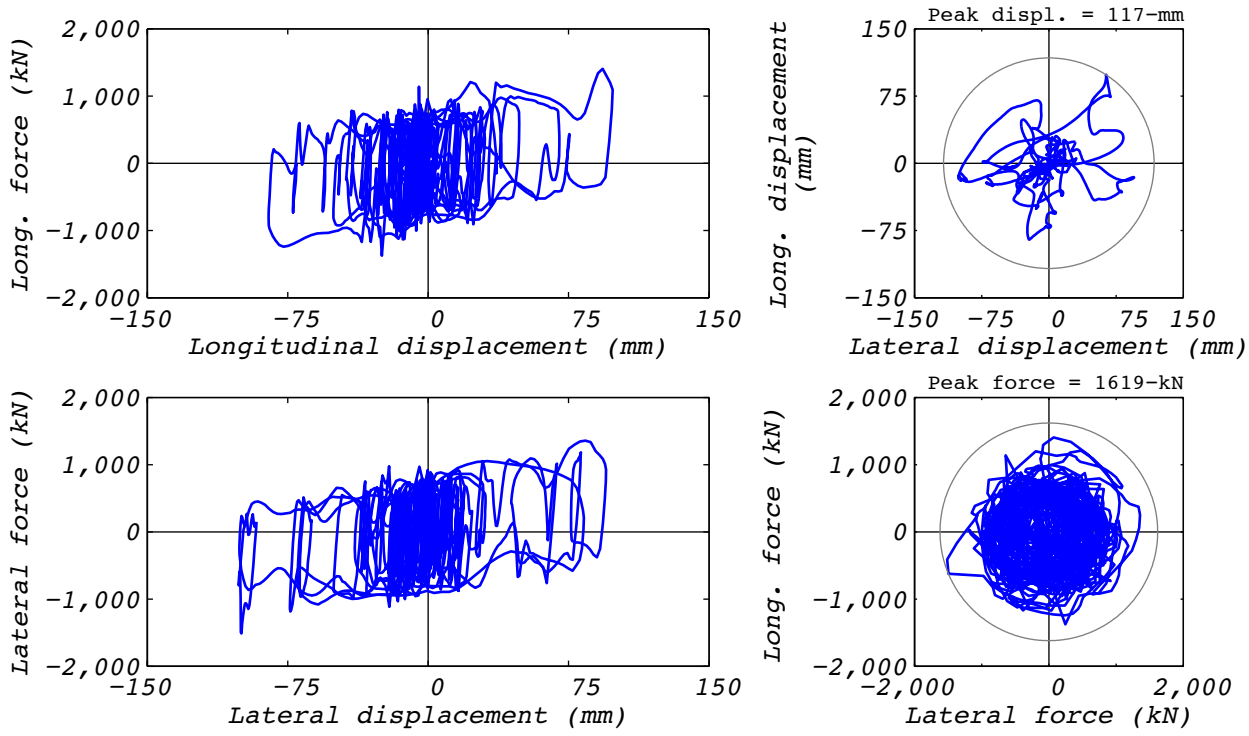

Figure C.13-2 Hybrid test bearing response for run 49: NRC2, 3D with 5 groups and the experimental bearing representing the no. 3 corner group.

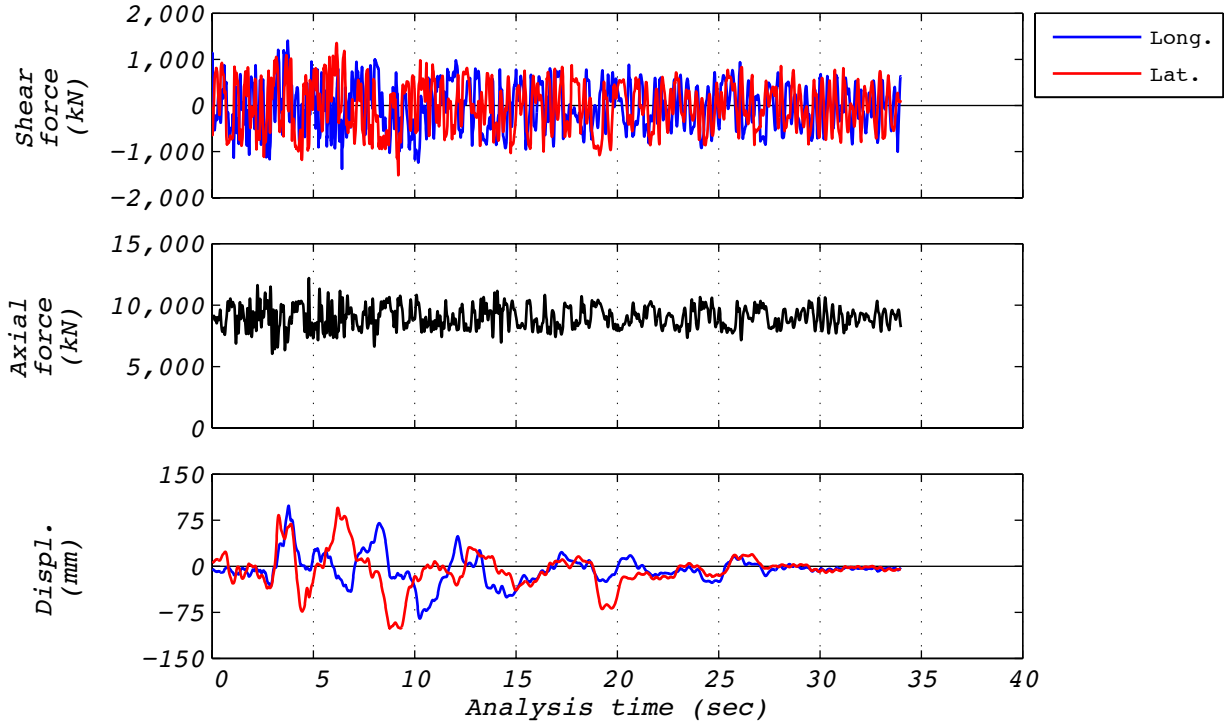

Figure C.13-3 Hybrid test time history responses for run 49: NRC2, 3D with 5 groups and the experimental bearing representing the no. 3 corner group.

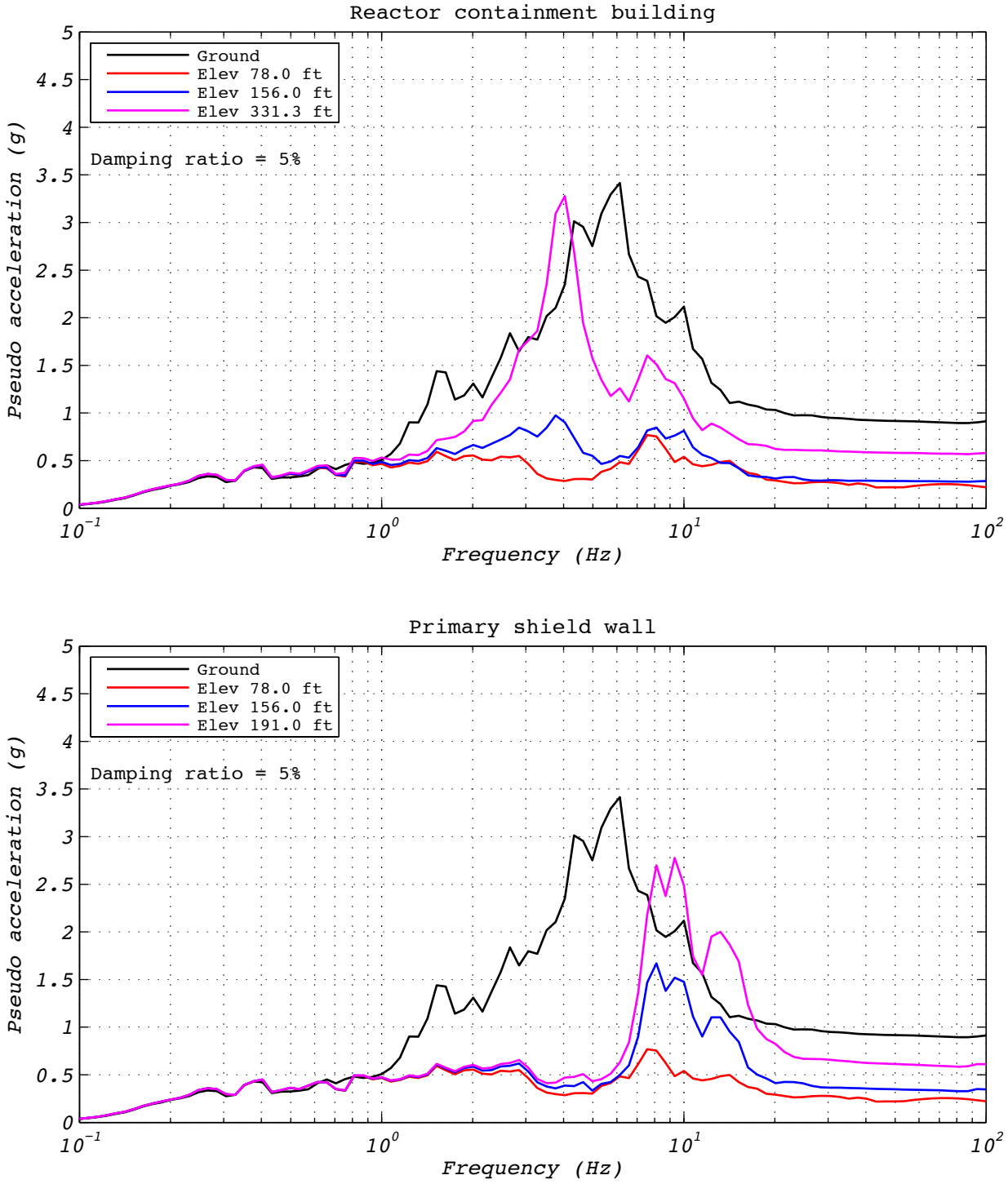

Figure C.13-4 Hybrid test floor spectra for run 49: NRC2, 3D with 5 groups of bearings and the experimental bearing representing the no. 3 corner group.

C.14 TEST RUN 50

Test run 50 was a hybrid test of the NRC dispersion appropriate ground motion number 2. The model consisted of a five groups of bearings. The experimental bearing's group was located in corner number 3 of the layout. Input motions consisted of two horizontal components. The vertical component was not applied, but the effects of overturning were included. The initial axial load specified as the design axial load of 8,663 kN. The test was executed at a rate 20 times slower than real time to compensate for machine delays. Bearing EQS-2 was used in this test. Figure C.14-1 shows the fidelity achieved in the hybrid test. Figures C.14-2 and C.14-3 contain bearing responses, and Figure C.14-4 depicts the resulting floor response spectra for select locations in two of the isolated structures.

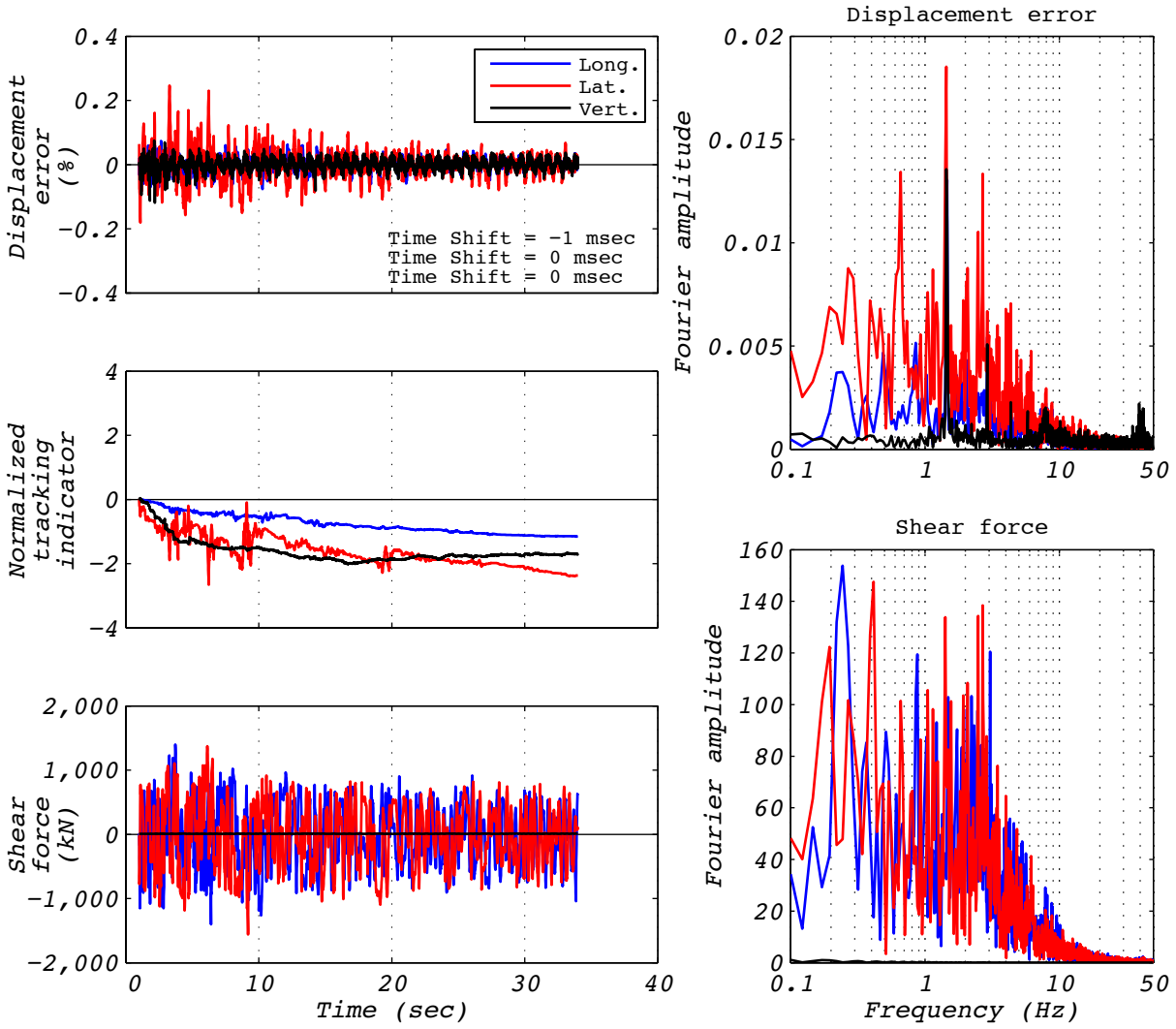

Figure C.14-1 Hybrid test performance metrics for run 50: NRC2, 3D with 5 groups of bearings and the experimental bearing representing the no. 3 corner group.

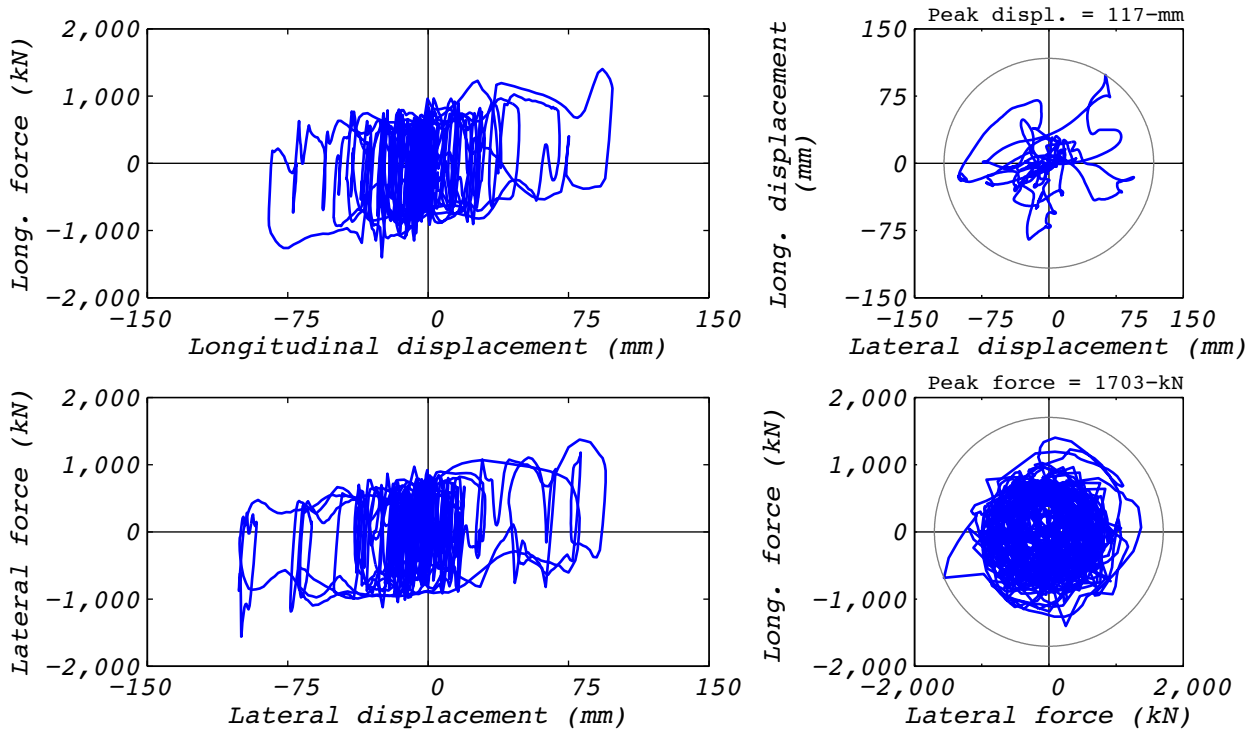

Figure C.14-2 Hybrid test bearing response for run 50: NRC2, 3D with 5 groups and the experimental bearing representing the no. 3 corner group.

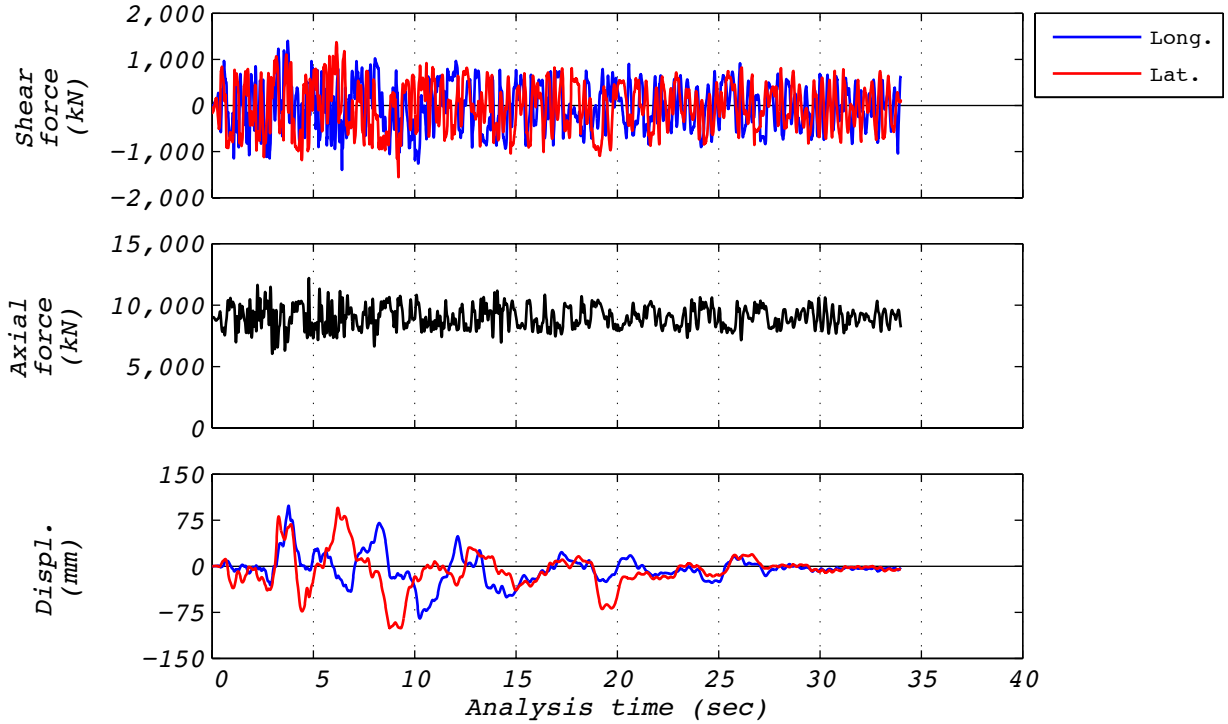

Figure C.14-3 Hybrid test time history responses for run 50: NRC2, 3D with 5 groups and the experimental bearing representing the no. 3 corner group.

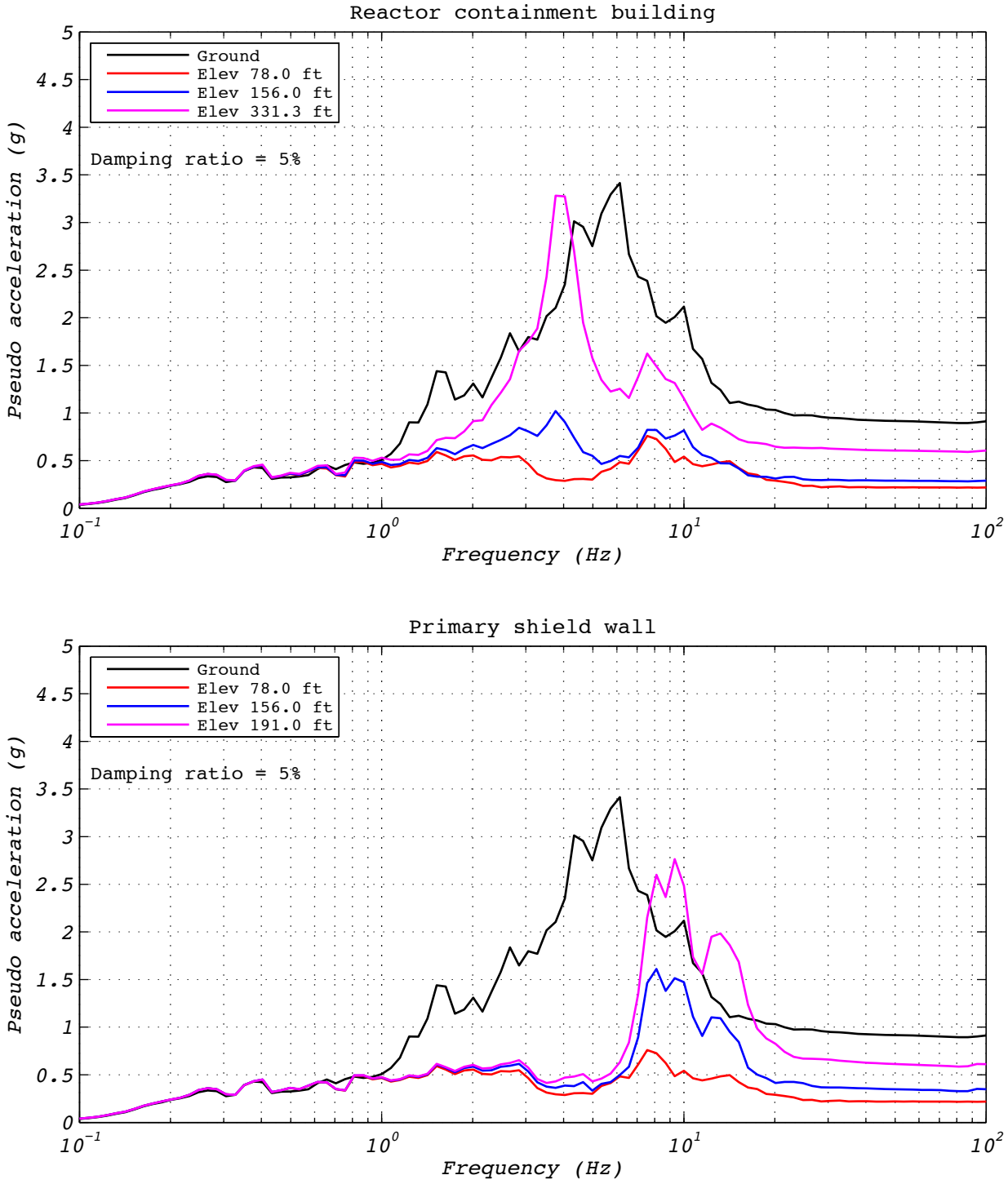

Figure C.14-4 Hybrid test floor spectra for run 50: NRC2, 3D with 5 groups of bearings and the experimental bearing representing the no. 3 corner group.

C.15 TEST RUN 51

Test run 51 was a hybrid test of the NRC dispersion appropriate ground motion number 2. The model consisted of a five groups of bearings. The experimental bearing's group was located in corner number 3 of the layout. Input motions consisted of two horizontal components. The vertical component was not applied, but the effects of overturning were included. The initial axial load specified as the design axial load of 8,663 kN. The test was executed at a rate 20 times slower than real time to compensate for machine delays. Bearing EQS-2 was used in this test. Figure C.15-1 shows the fidelity achieved in the hybrid test. Figures C.15-2 and C.15-3 contain bearing responses, and Figure C.15-4 depicts the resulting floor response spectra for select locations in two of the isolated structures.

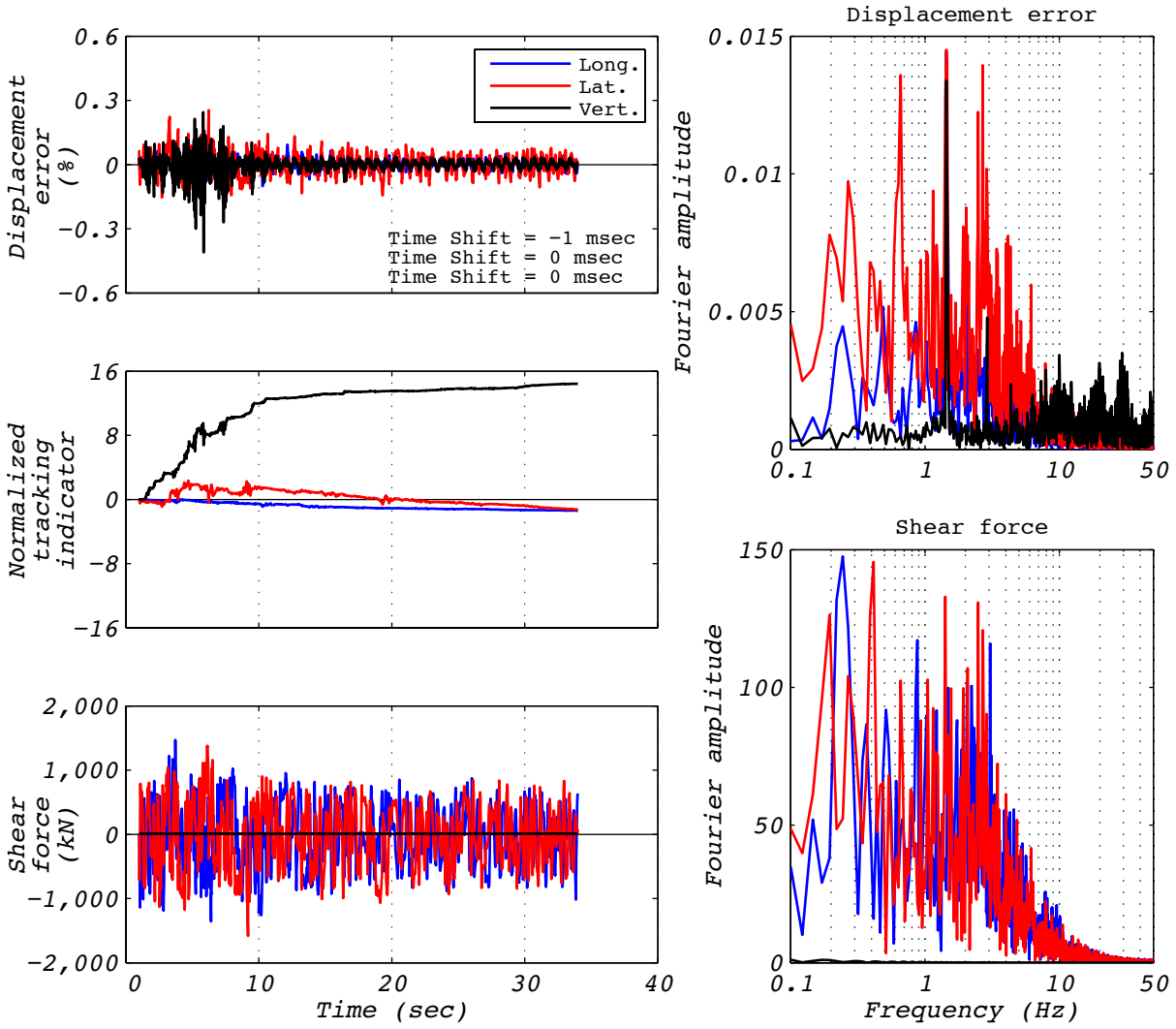

Figure C.15-1 Hybrid test performance metrics for run 51: NRC2, 3D with 5 groups of bearings and the experimental bearing representing the no. 3 corner group.

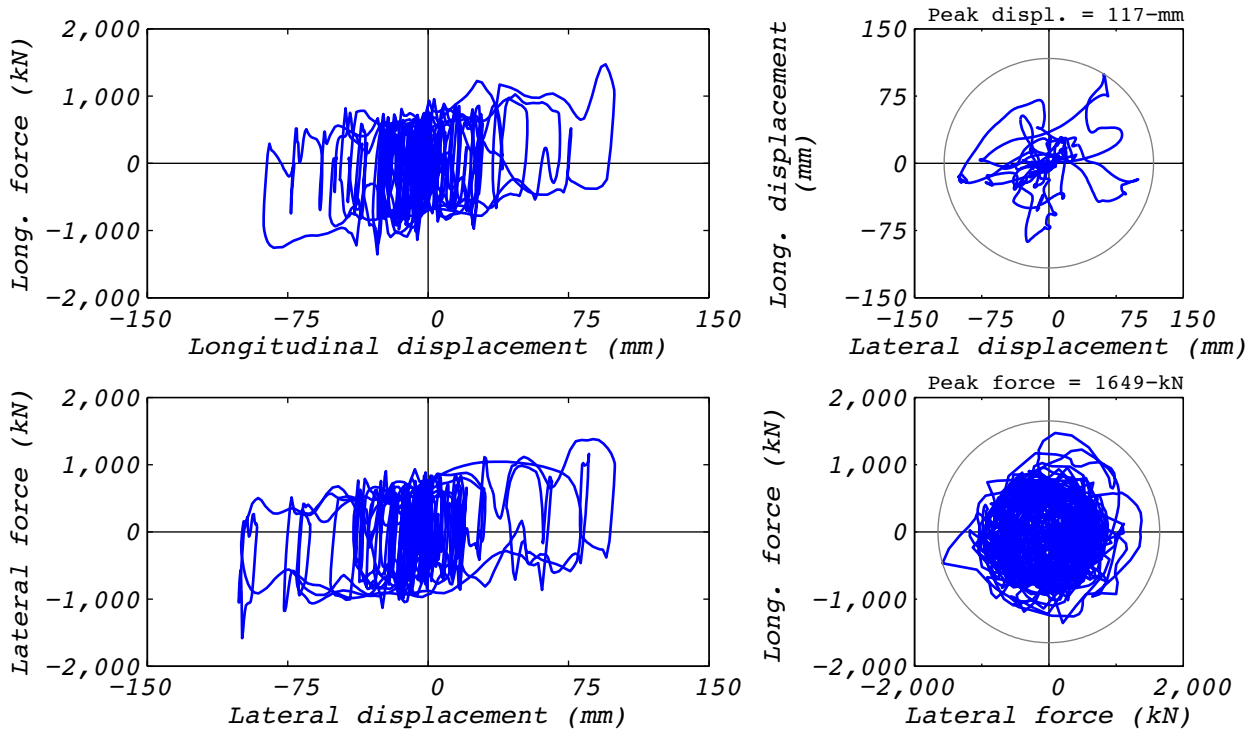

Figure C.15-2 Hybrid test bearing response for run 51: NRC2, 3D with 5 groups and the experimental bearing representing the no. 3 corner group.

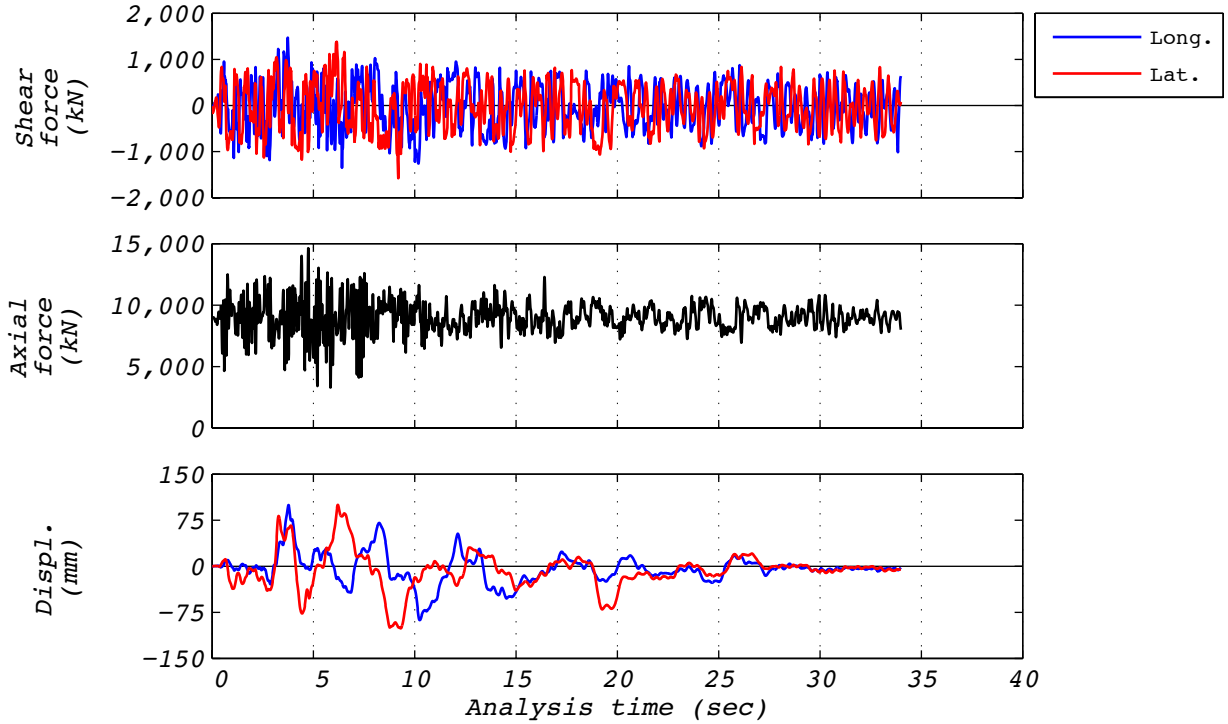

Figure C.15-3 Hybrid test time history responses for run 51: NRC2, 3D with 5 groups and the experimental bearing representing the no. 3 corner group.

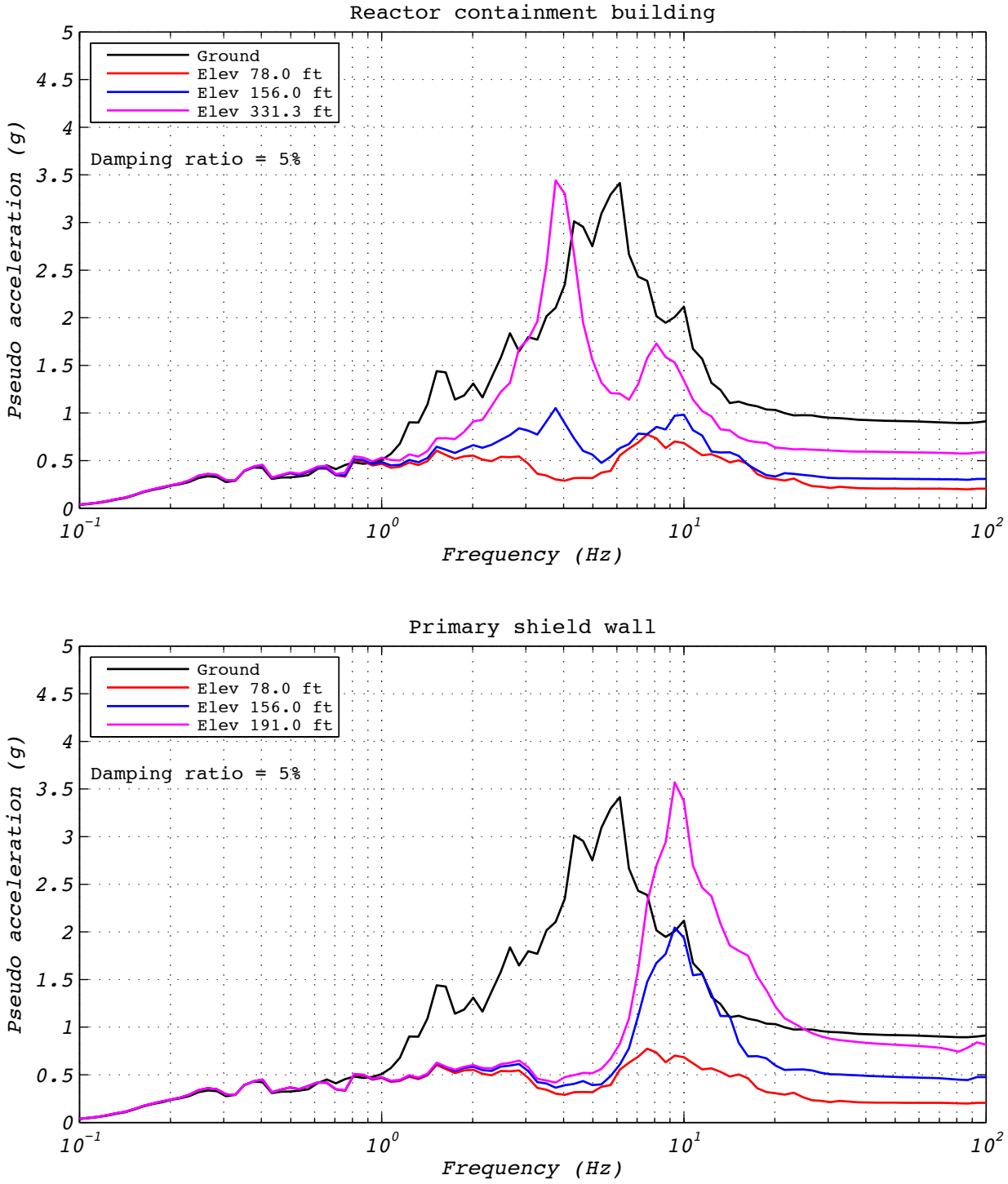

Figure C.15-4 Hybrid test floor spectra for run 51: NRC2, 3D with 5 groups of bearings and the experimental bearing representing the no. 3 corner group.

C.16 TEST RUN 52

Test run 52 was a hybrid test of the NRC dispersion appropriate ground motion number 2. The model consisted of a single experimental bearing representing all 527 bearings. Input motions consisted of a single horizontal component and a constant axial load specified as the design axial load of 8,663 kN. The test was executed at a rate 5 times slower than real time to compensate for machine delays. Bearing EQS-2 was used in this test. Figure C.16-1 shows the fidelity achieved in the hybrid test. Figures C.16-2 and C.16-3 contain bearing responses, and Figure C.16-4 depicts the resulting floor response spectra for select locations in two of the isolated structures.

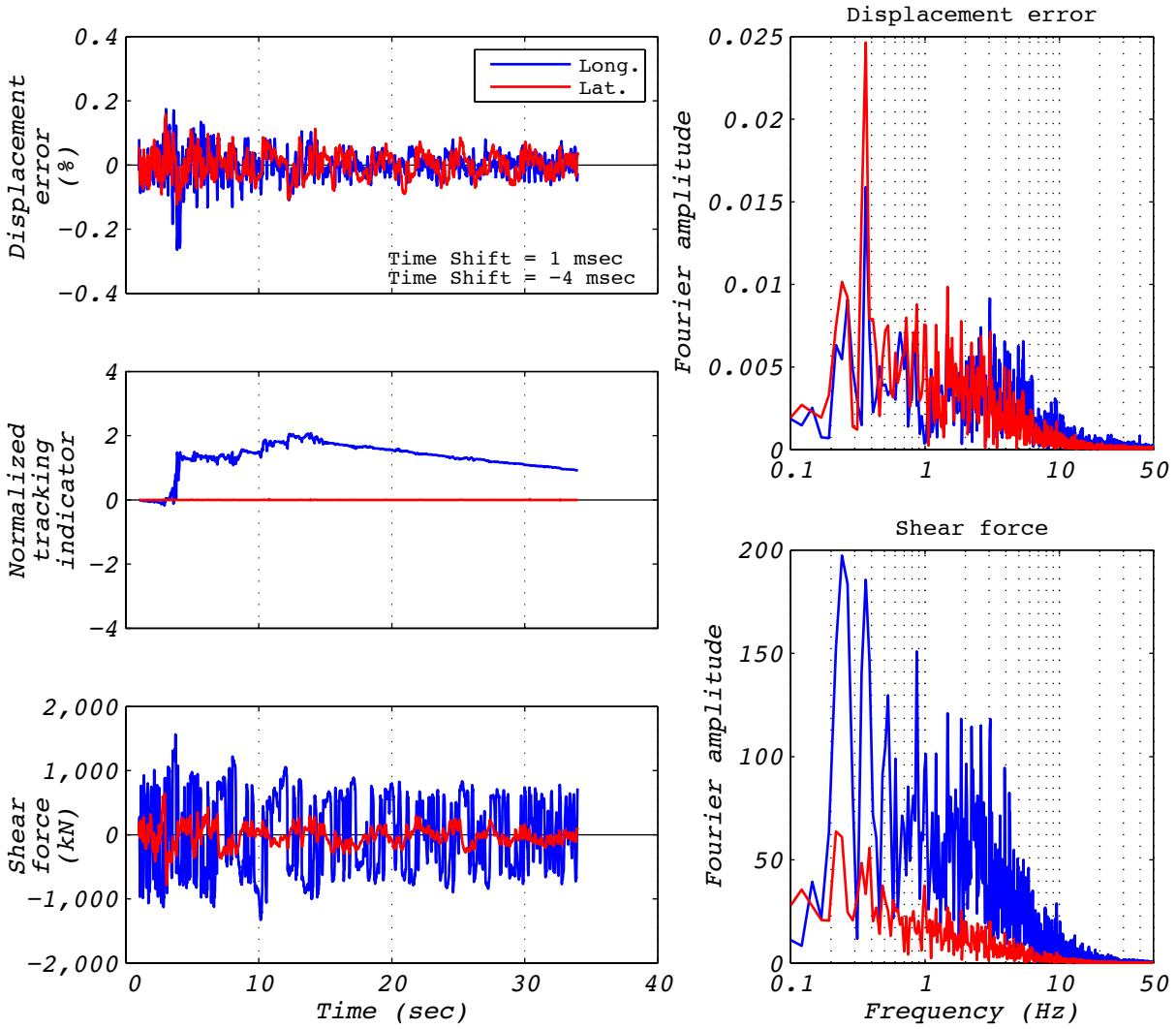

Figure C.16-1 Hybrid test performance metrics for run 52: NRC2, 1D with experimental bearing representing all bearings.

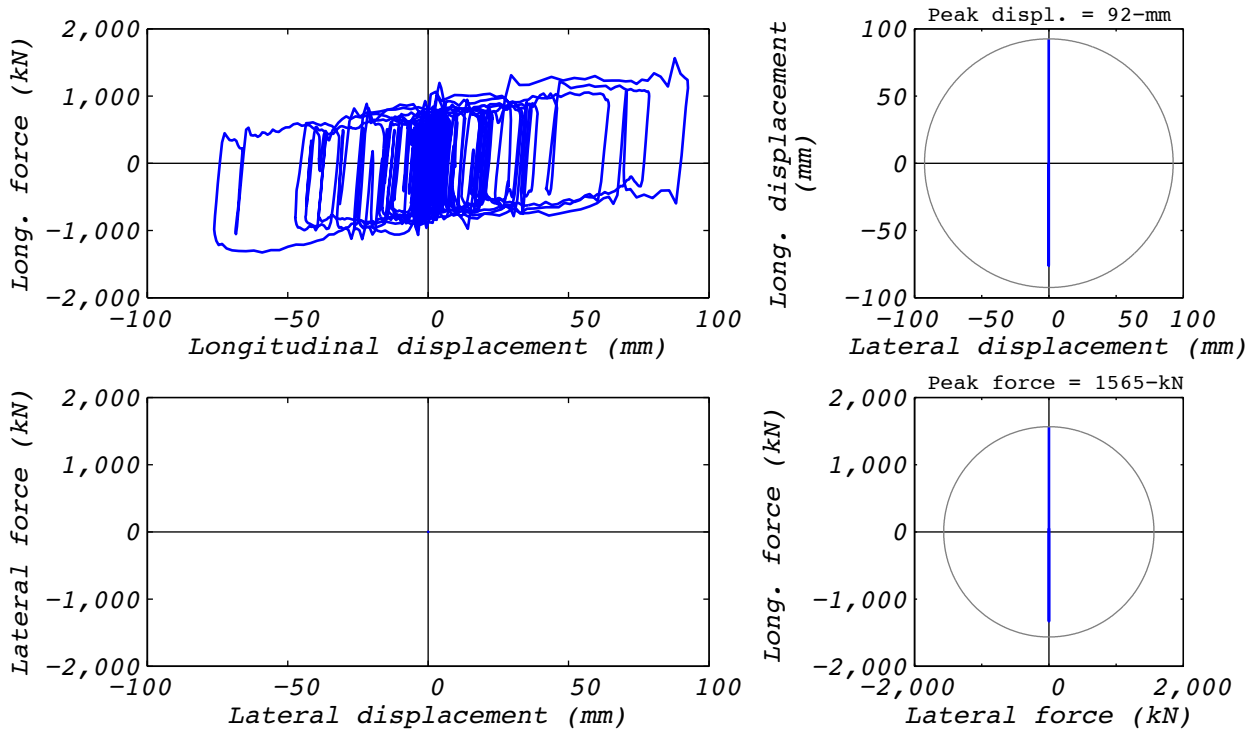

Figure C.16-2 Hybrid test bearing response for run 52: NRC2, 1D with experimental bearing representing all bearings.

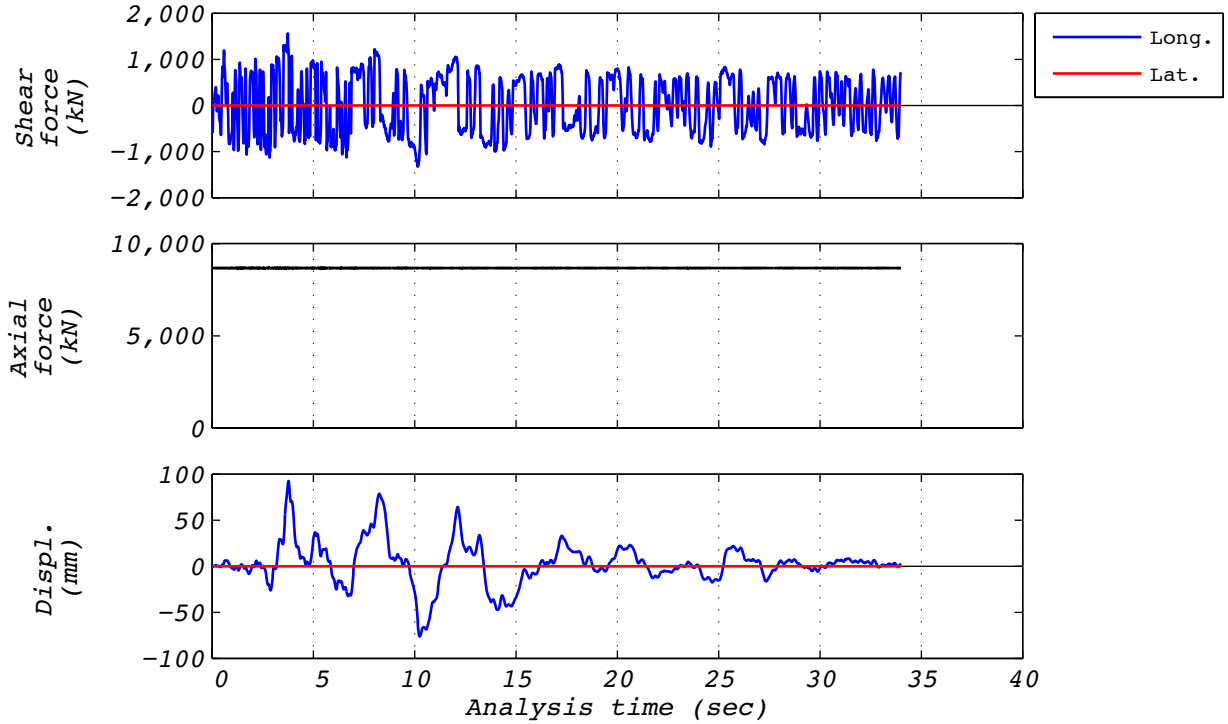

Figure C.16-3 Hybrid test time history responses for run 52: NRC2, 1D with experimental bearing representing all bearings.

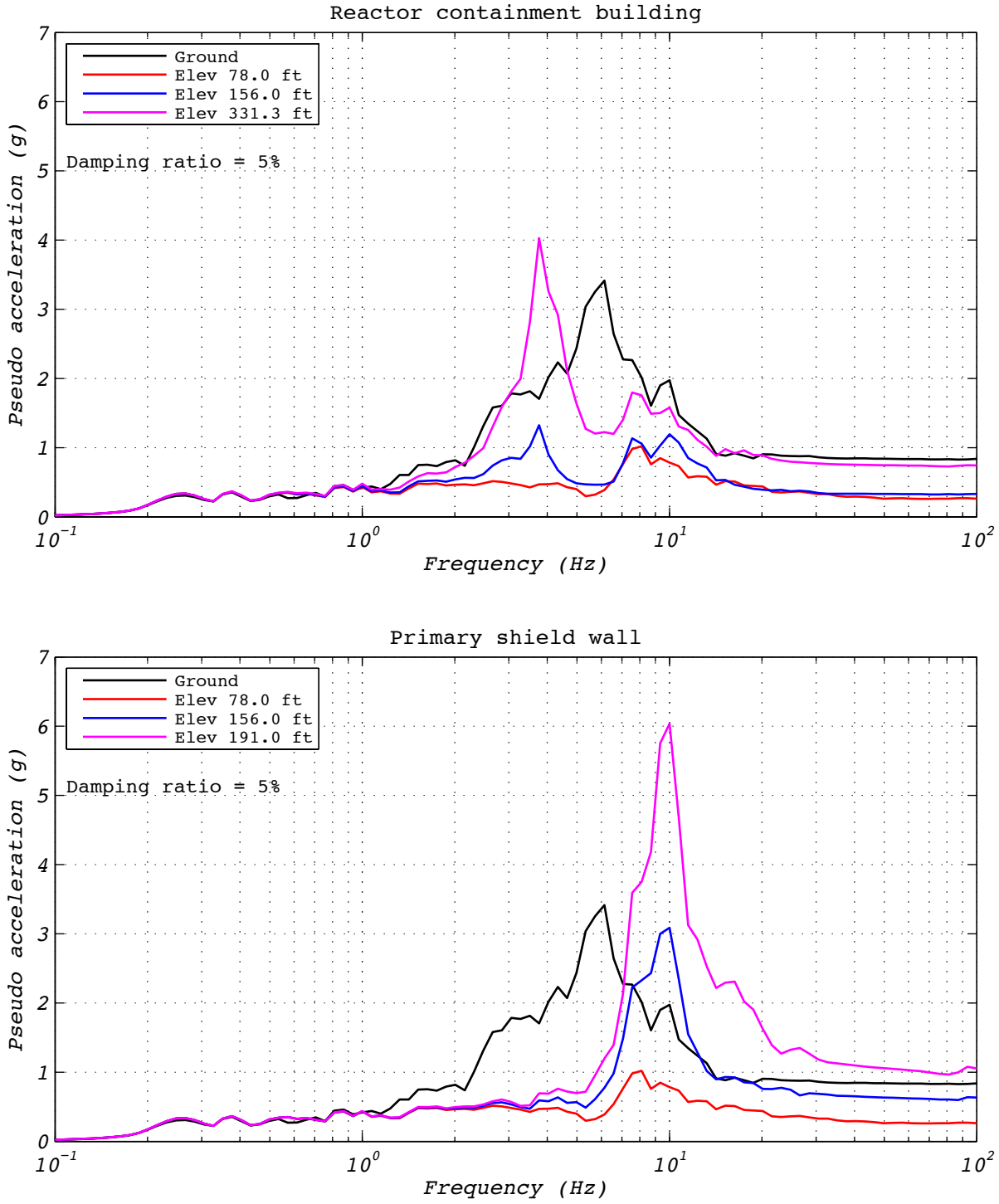

Figure C.16-4 Hybrid test floor spectra for run 52: NRC2, 1D with experimental bearing representing all bearings.

C.17 ANALYSIS RUN 52A

Analysis run 52A was an analytical estimation of the NRC dispersion appropriate ground motion number 2. The model consisted of a single analytical bearing representing all 527 bearings. Input motions consisted of a single horizontal component and a constant axial load was specified as the design axial load of 8,663 kN. Bearing EQS-2 was used in this test. Figures C.17-1 and C.17-2 contain analytical bearing responses, and Figure C.17-3 depicts the resulting floor response spectra for select locations in two of the isolated structures.

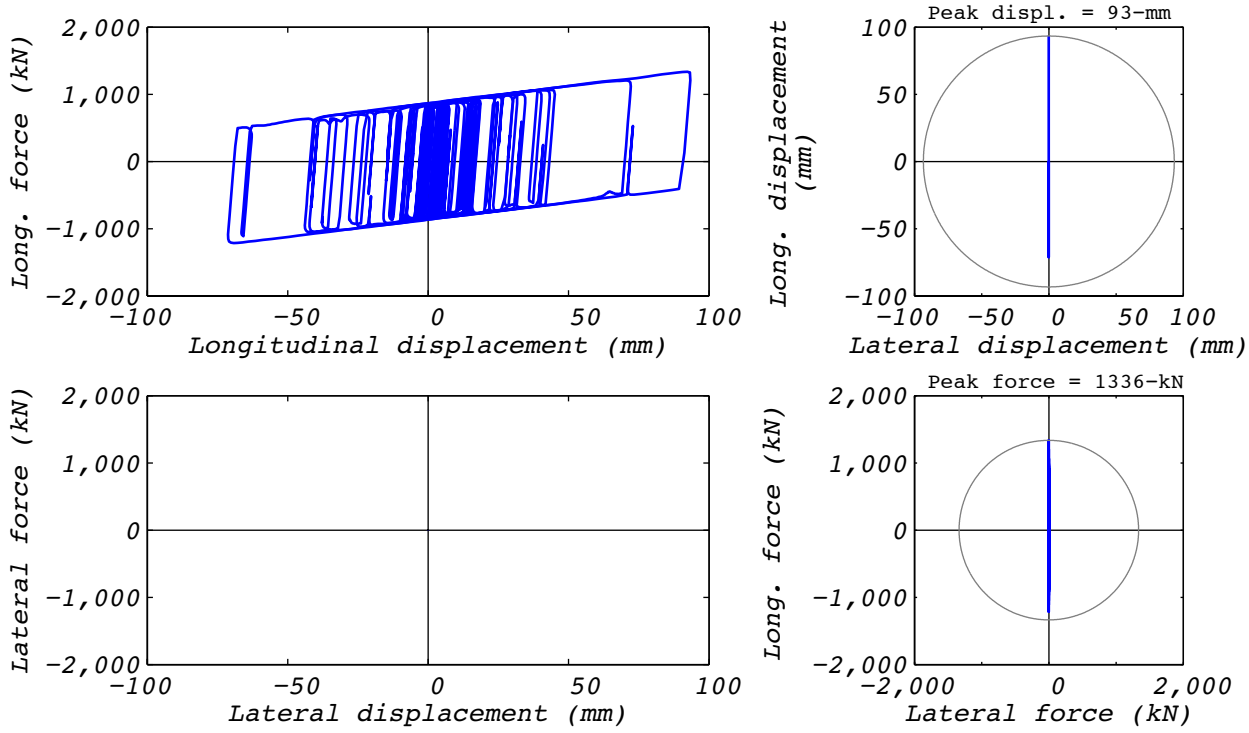

Figure C.17-1 Analytical bearing response for run 52A: NRC2, 1D with a single analytical bearing.

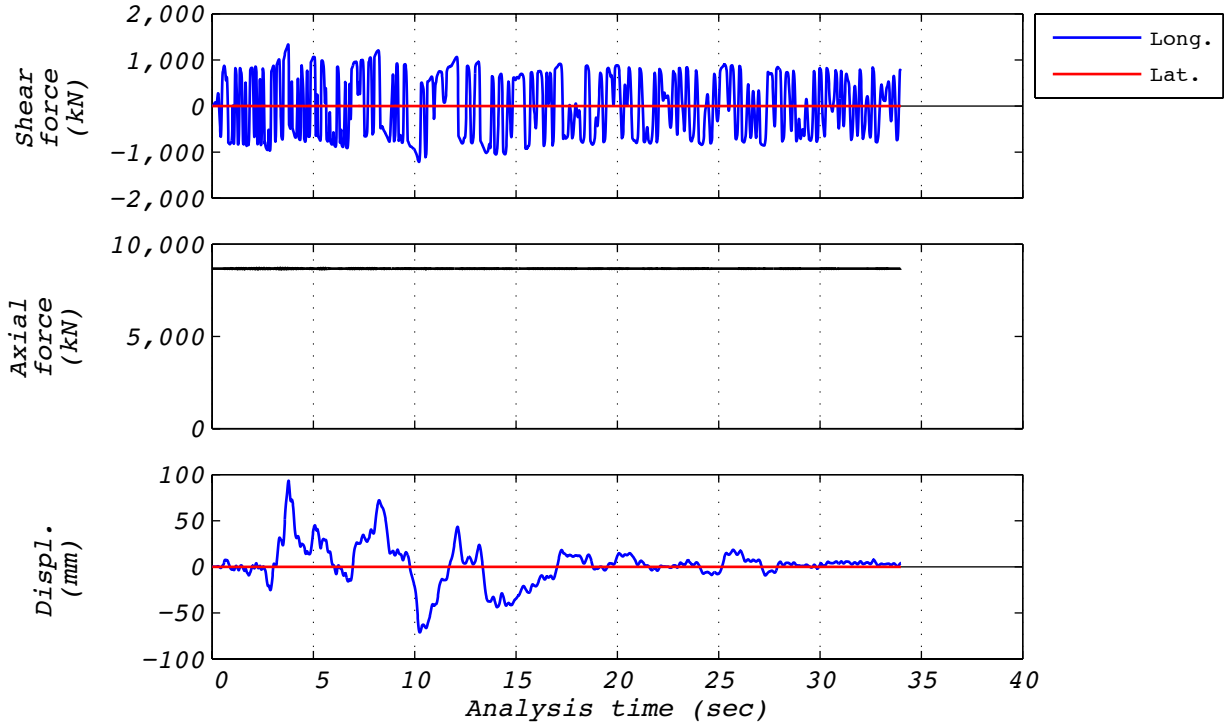

Figure C.17-2 Analytical time history responses for run 52A: NRC2, 1D with a single analytical bearing.

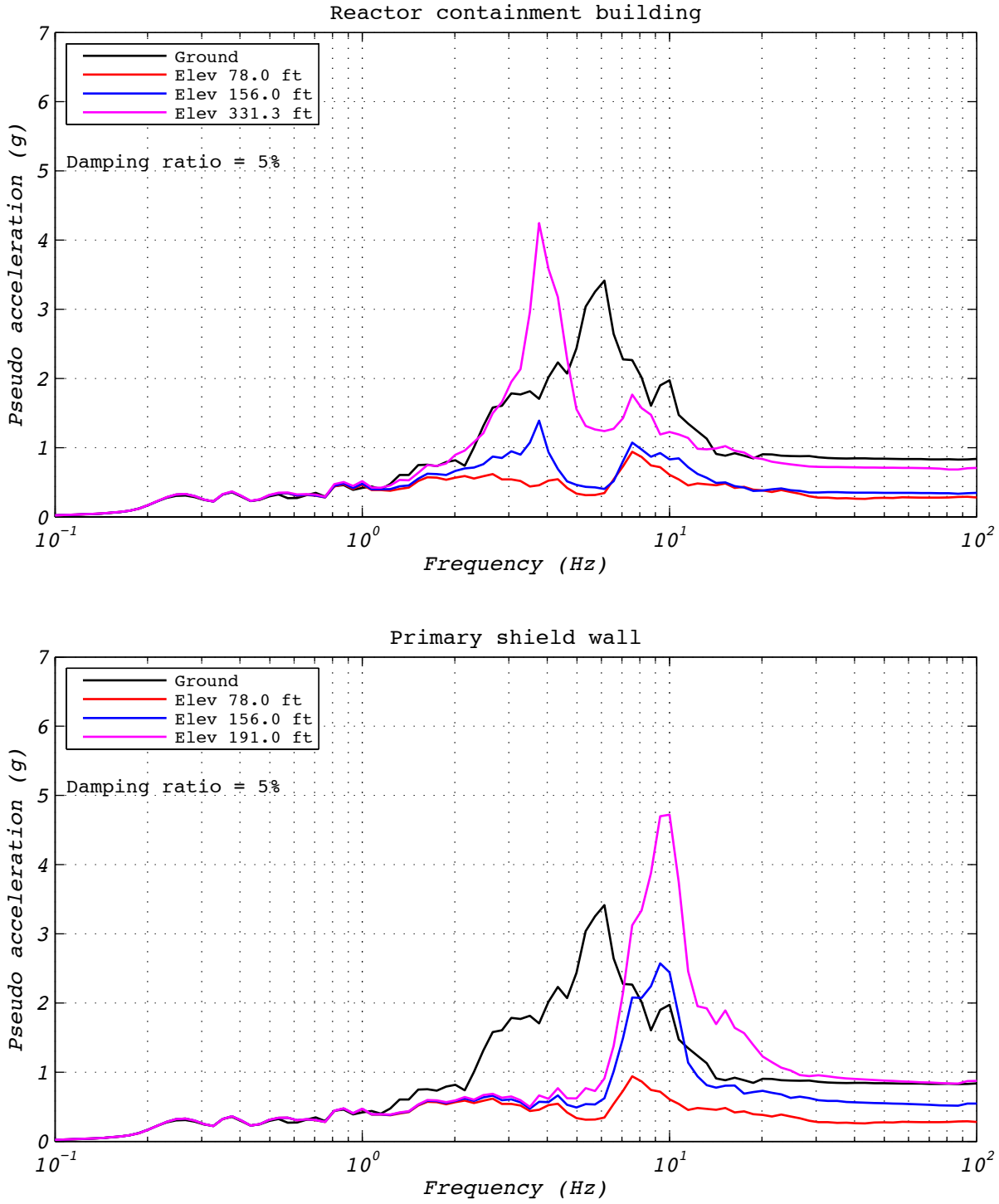

Figure C.17-3 Floor spectra for analytical run 52A: NRC2, 1D with a single analytical bearing.

C.18 TEST RUN 53

Test run 53 was a hybrid test of the EUR dispersion appropriate ground motion number 5. The model consisted of a single experimental bearing representing all 527 bearings. Input motions consisted of a single horizontal component and a constant axial load specified as the design axial load of 8,663 kN. The test was executed at a rate 5 times slower than real time to compensate for machine delays. Bearing EQS-2 was used in this test. Figure C.17-1 shows the fidelity achieved in the hybrid test. Figures C.17-2 and C.17-3 contain bearing responses, and Figure C.17-4 depicts the resulting floor response spectra for select locations in two of the isolated structures.

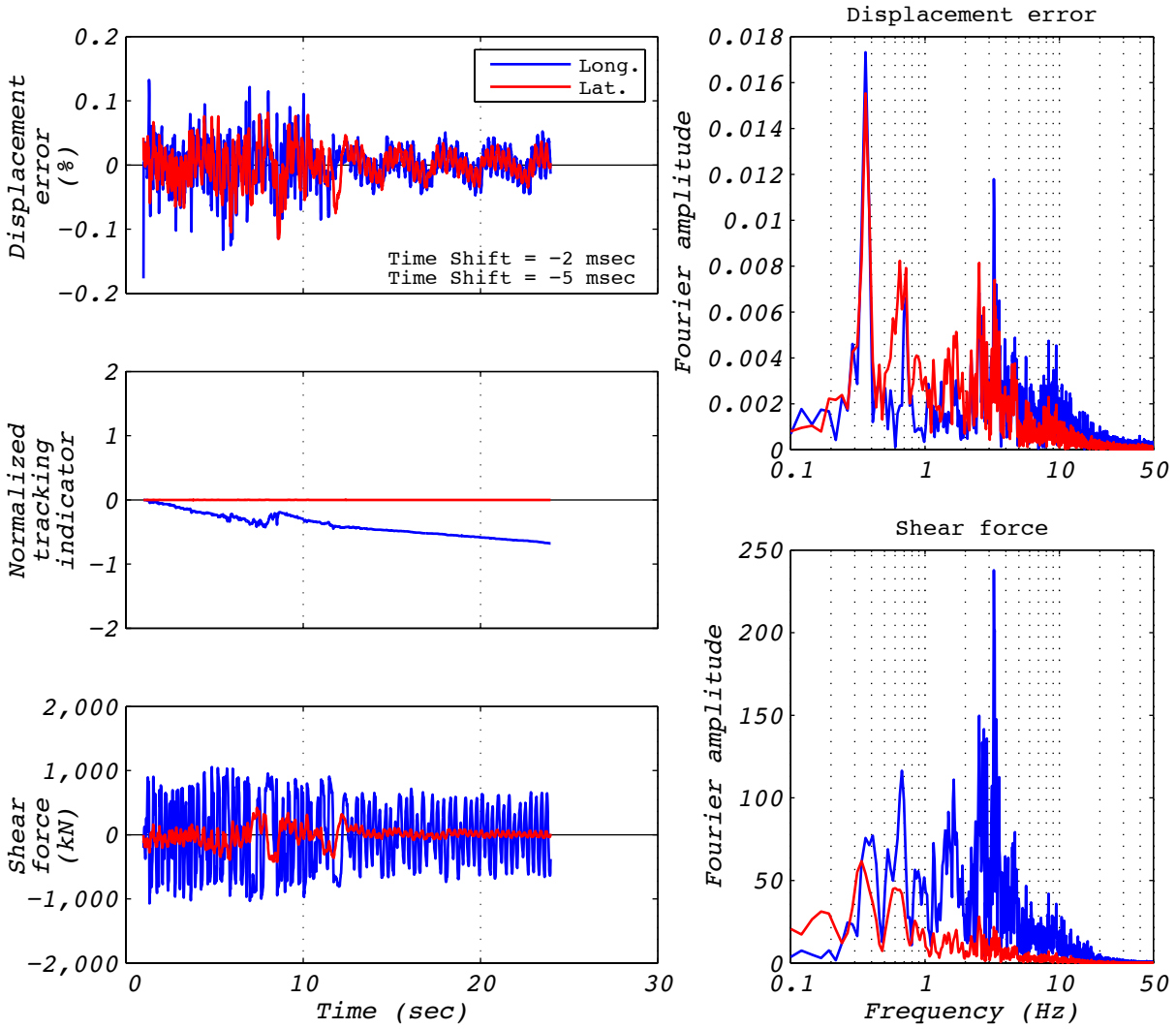

Figure C.18-1 Hybrid test performance metrics for run 53: EUR5, 1D with experimental bearing representing all bearings.

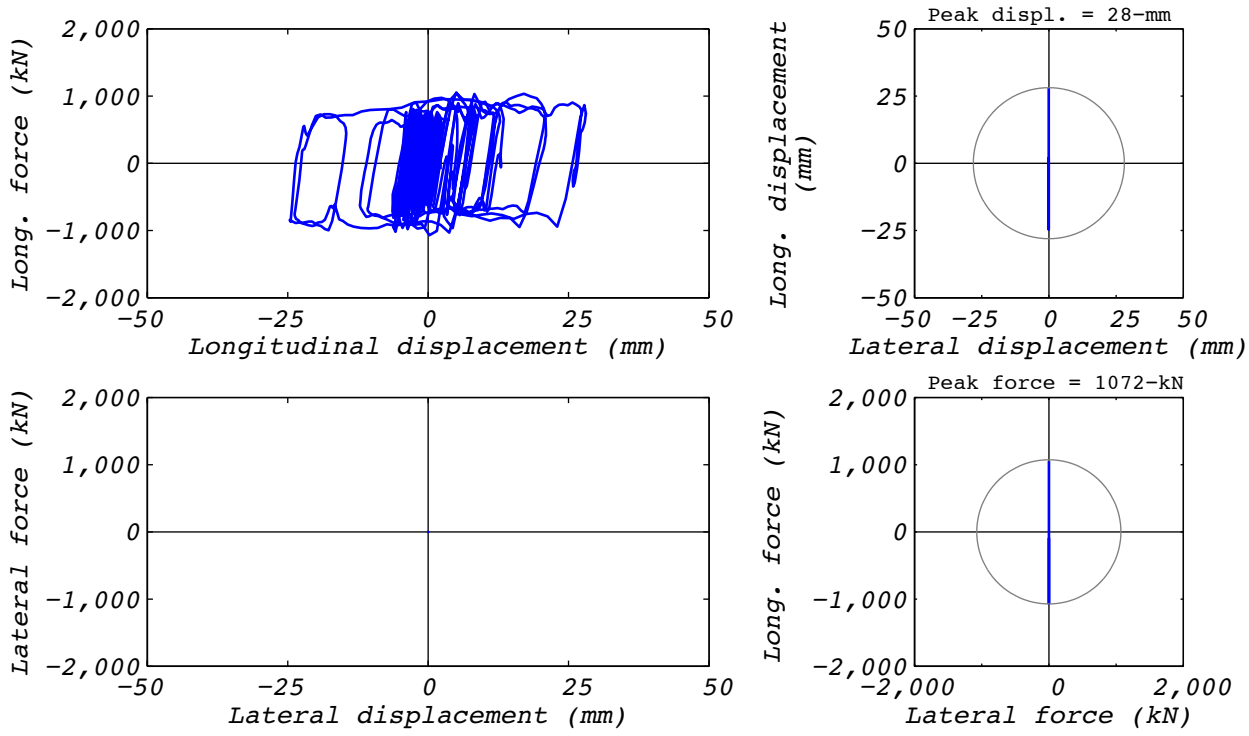

Figure C.18-2 Hybrid test bearing response for run 53: EUR5, 1D with experimental bearing representing all bearings.

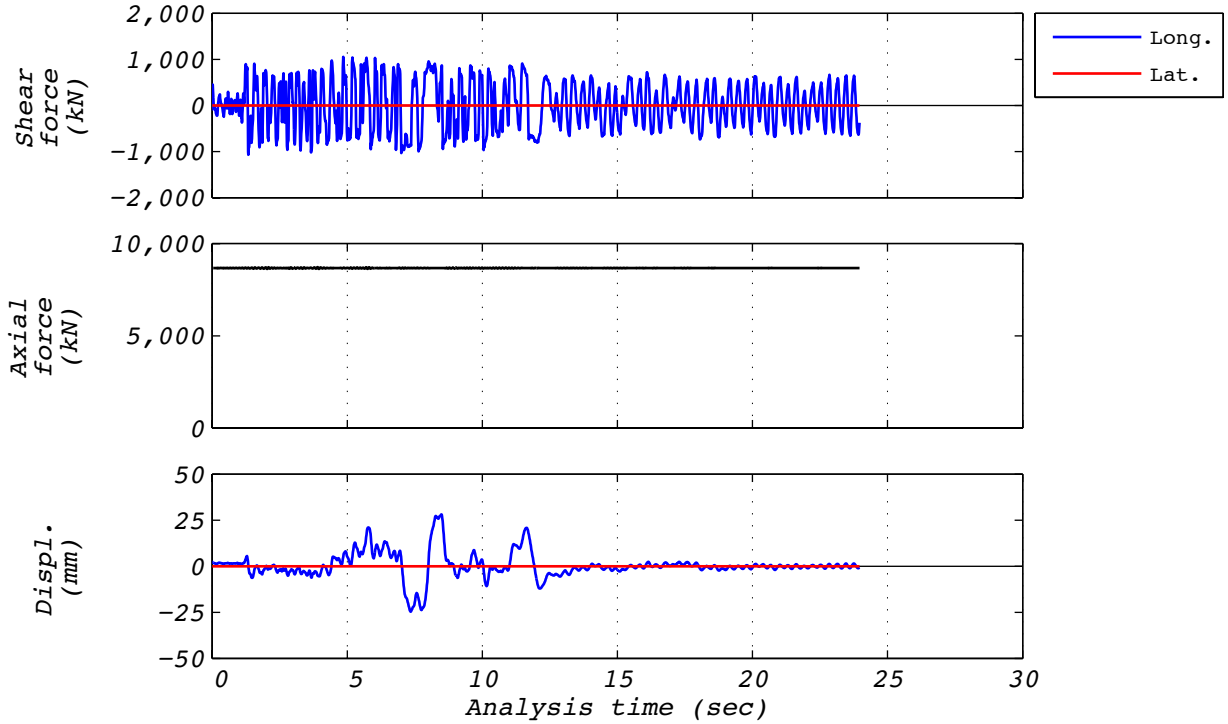

Figure C.18-3 Hybrid test time history responses for run 53: EUR5, 1D with experimental bearing representing all bearings.

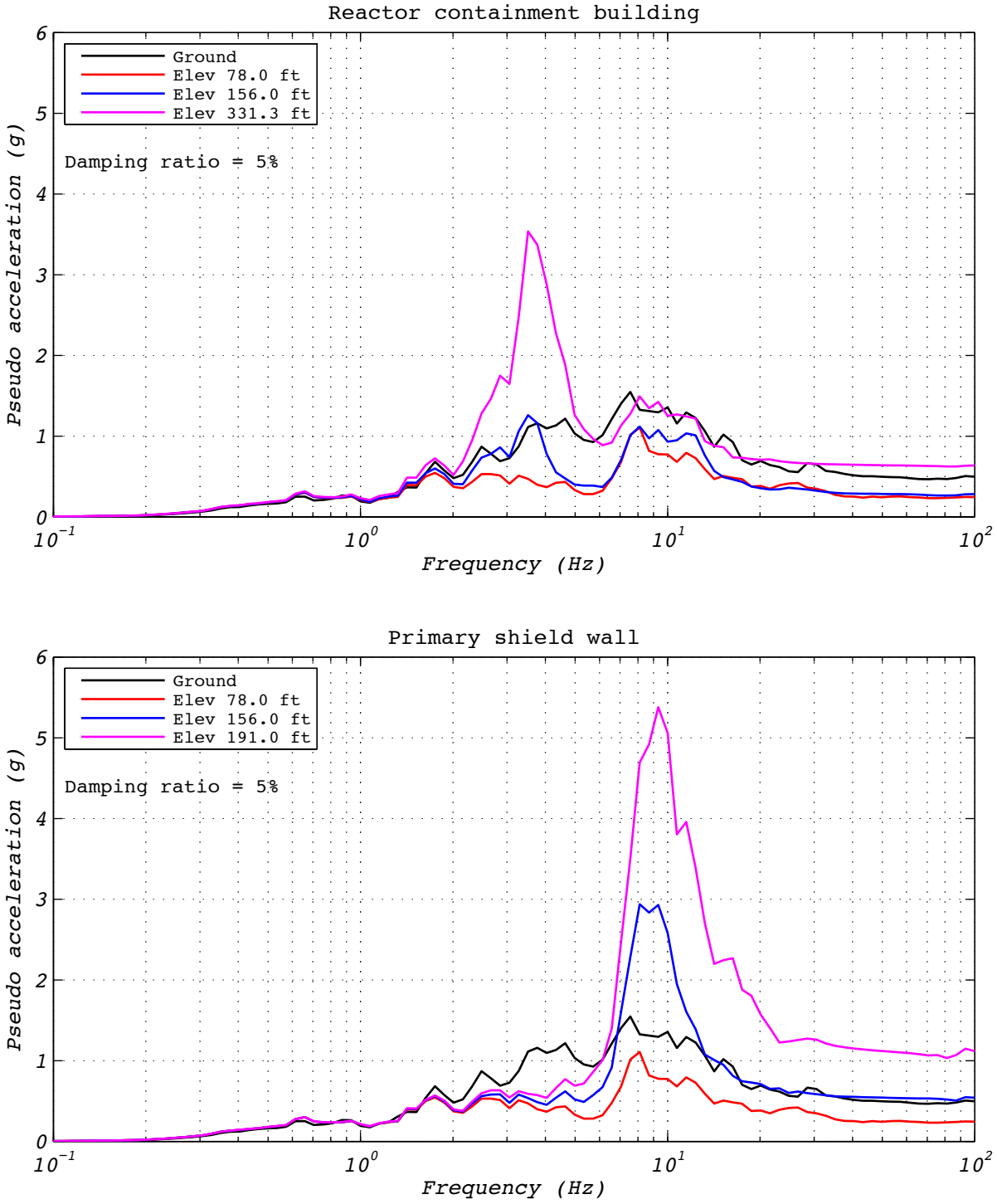

Figure C.18-4 Hybrid test floor spectra for run 53: EUR5, 1D with experimental bearing representing all bearings.

C.19 ANALYSIS RUN 53A

Analysis run 53A was an analytical estimation of the EUR dispersion appropriate ground motion number 5. The model consisted of a single analytical bearing representing all 527 bearings. Input motions consisted of a single horizontal component and a constant axial load was specified as the design axial load of 8,663 kN. Bearing EQS-2 was used in this test. Figures C.19-1 and C.19-2 contain analytical bearing responses, and Figure C.19-3 depicts the resulting floor response spectra for select locations in two of the isolated structures.

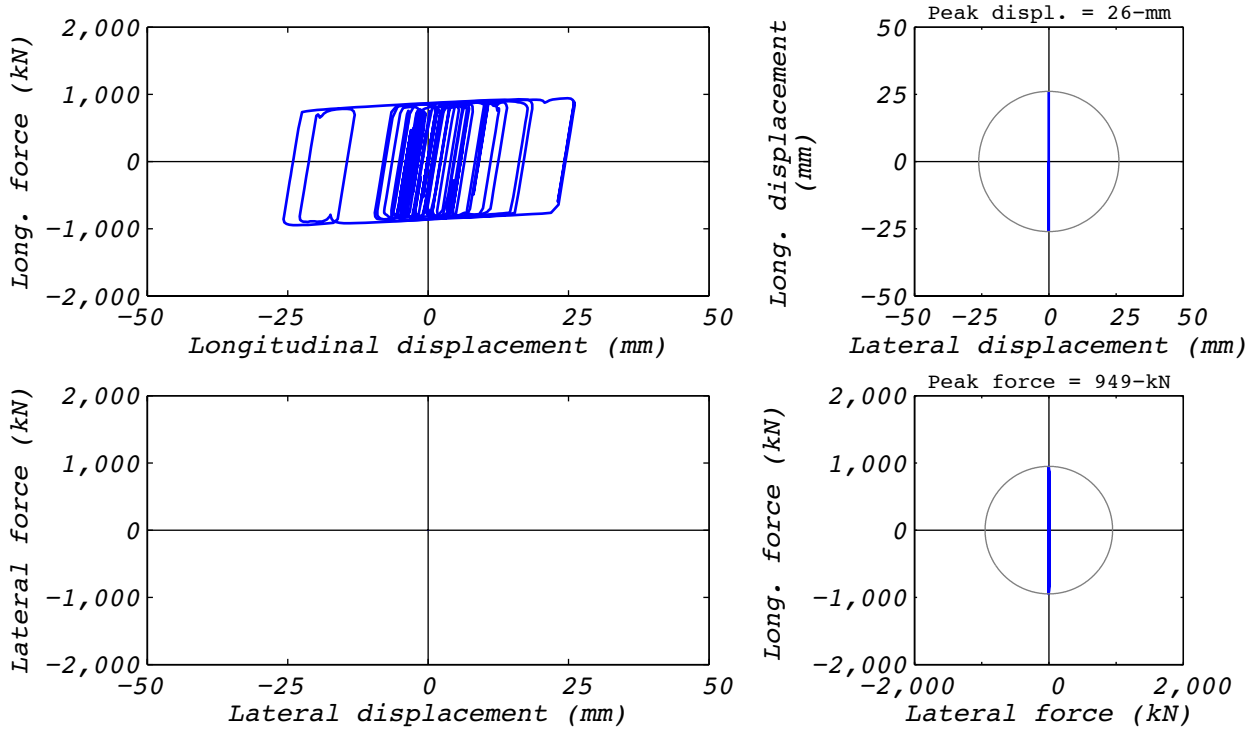

Figure C.19-1 Analytical bearing response for run 53A: EUR5, 1D with a single analytical bearing.

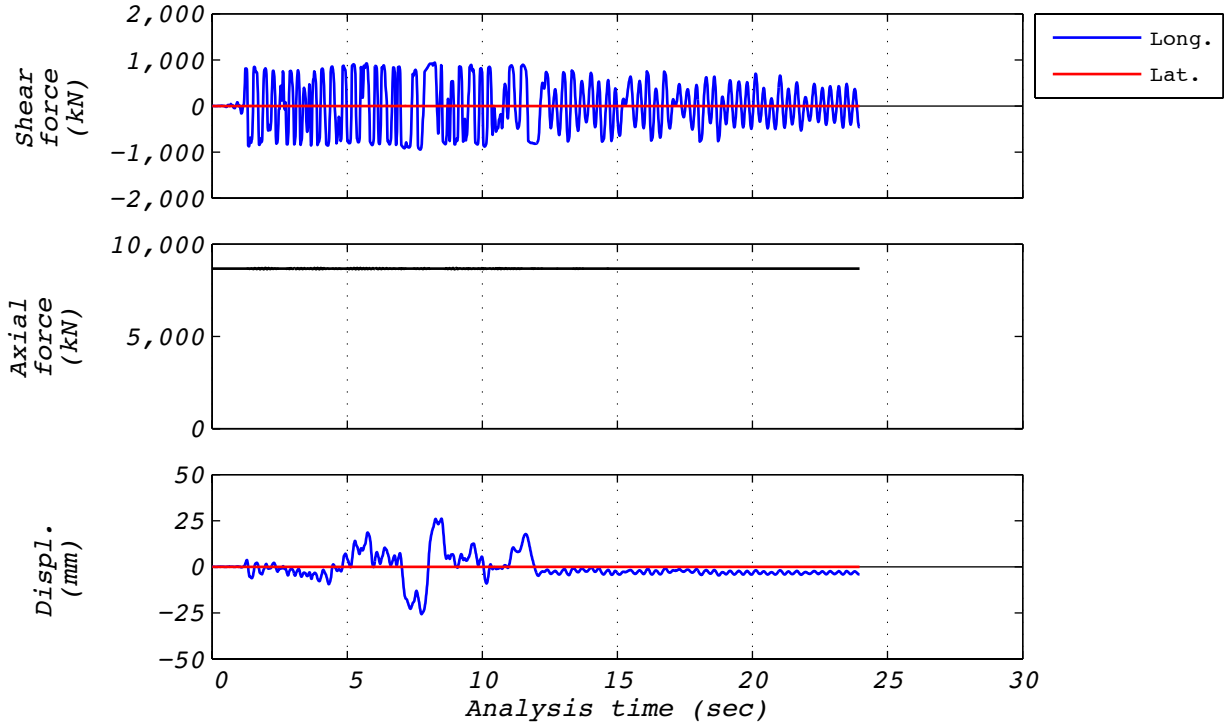

Figure C.19-2 Analytical time history responses for run 53A: EUR5, 1D with a single analytical bearing.

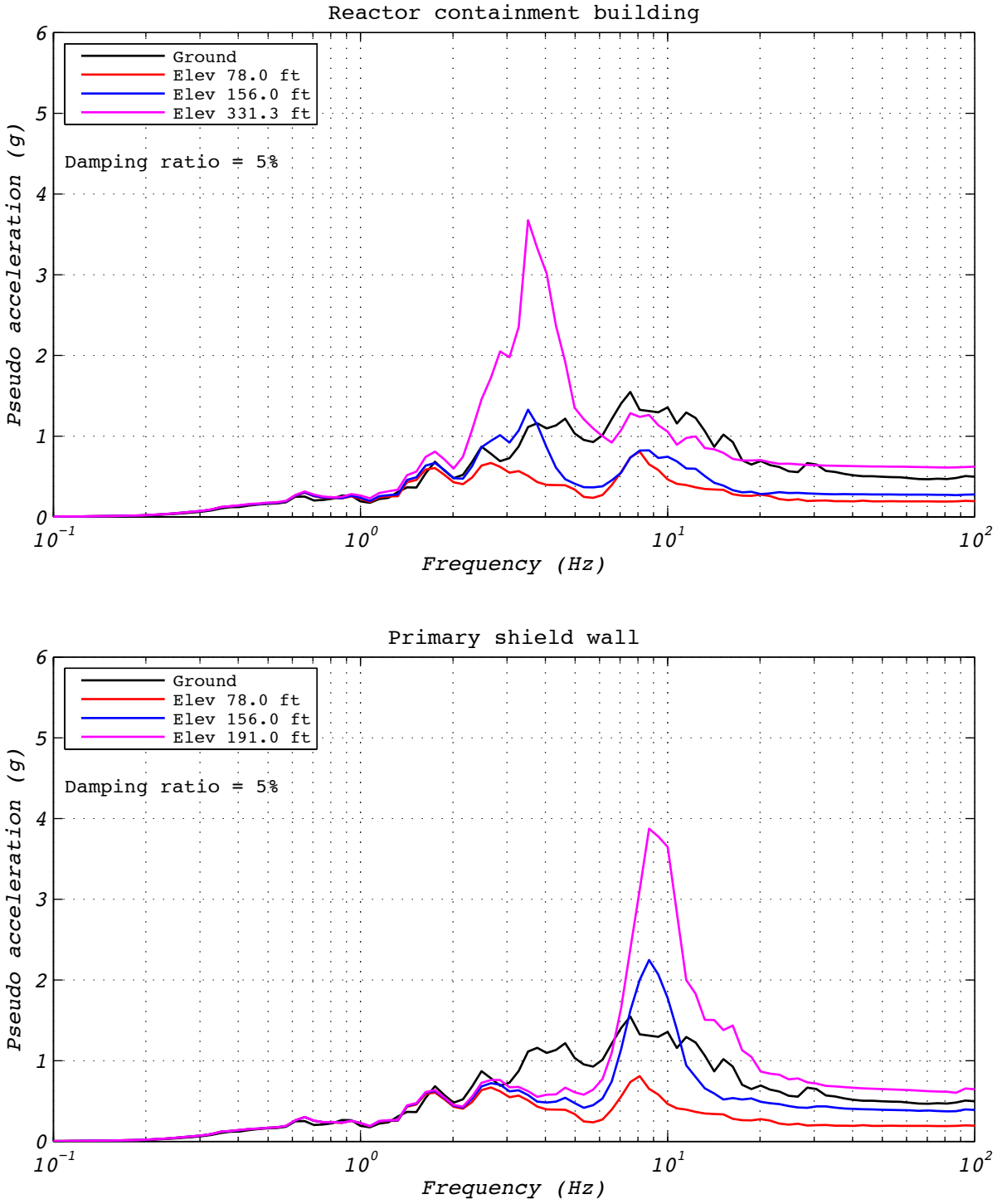

Figure C.19-3 Floor spectra for analytical run 53A: EUR5, 1D with a single analytical bearing.

C.20 TEST RUN 54

Test run 54 was a hybrid test of the NRC dispersion appropriate ground motion number 2. The model consisted of a single experimental bearing representing all 527 bearings. Input motions consisted of two horizontal components and a constant axial load specified as the design axial load of 8,663 kN. The test was executed at a rate 5 times slower than real time to compensate for machine delays. Bearing EQS-2 was used in this test. Figure C.19-1 shows the fidelity achieved in the hybrid test. Figures C.19-2 and C.19-3 contain bearing responses, and Figure C.19-4 depicts the resulting floor response spectra for select locations in two of the isolated structures.

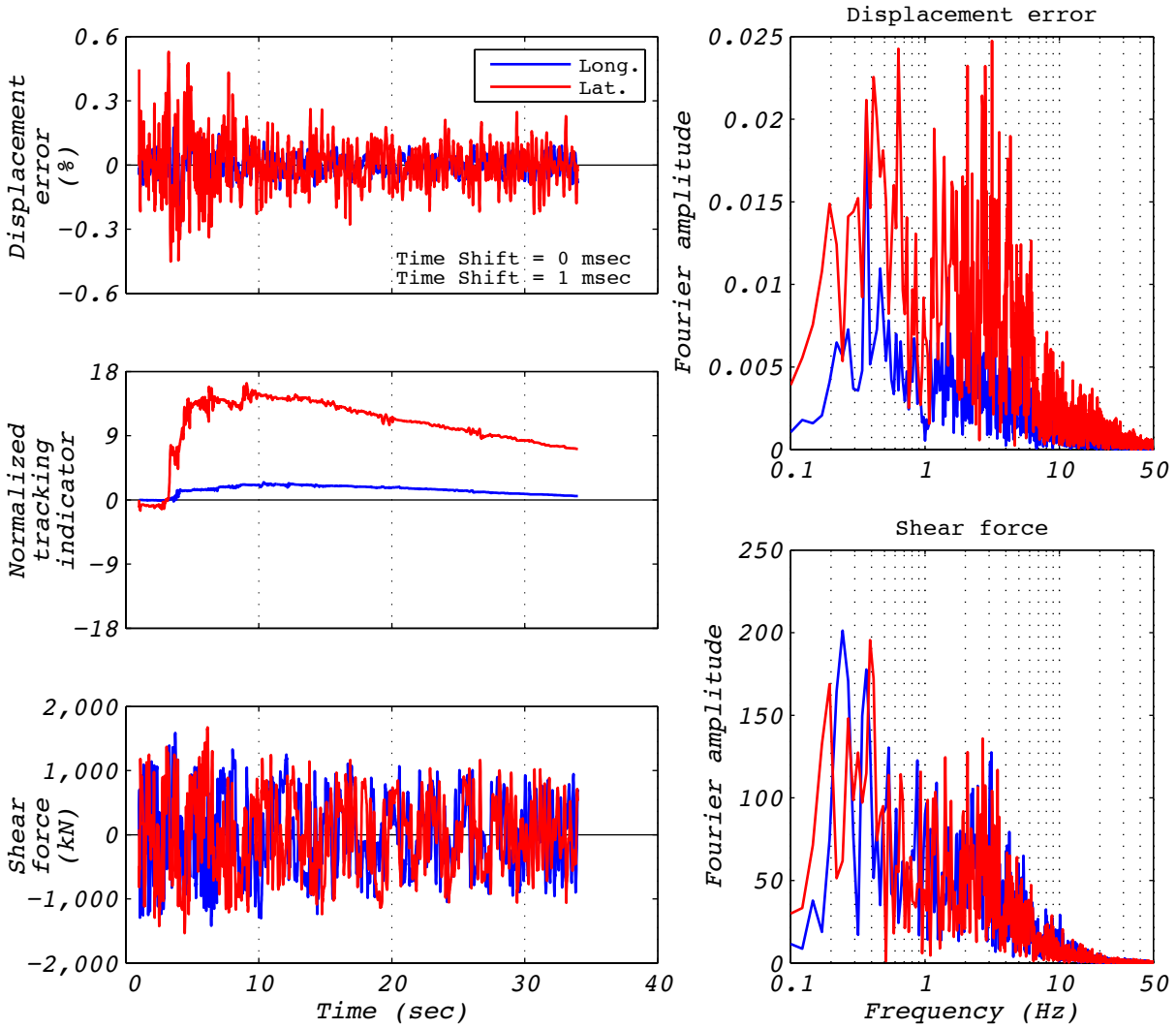

Figure C.20-1 Hybrid test performance metrics for run 54: NRC2, 2D with experimental bearing representing all bearings.

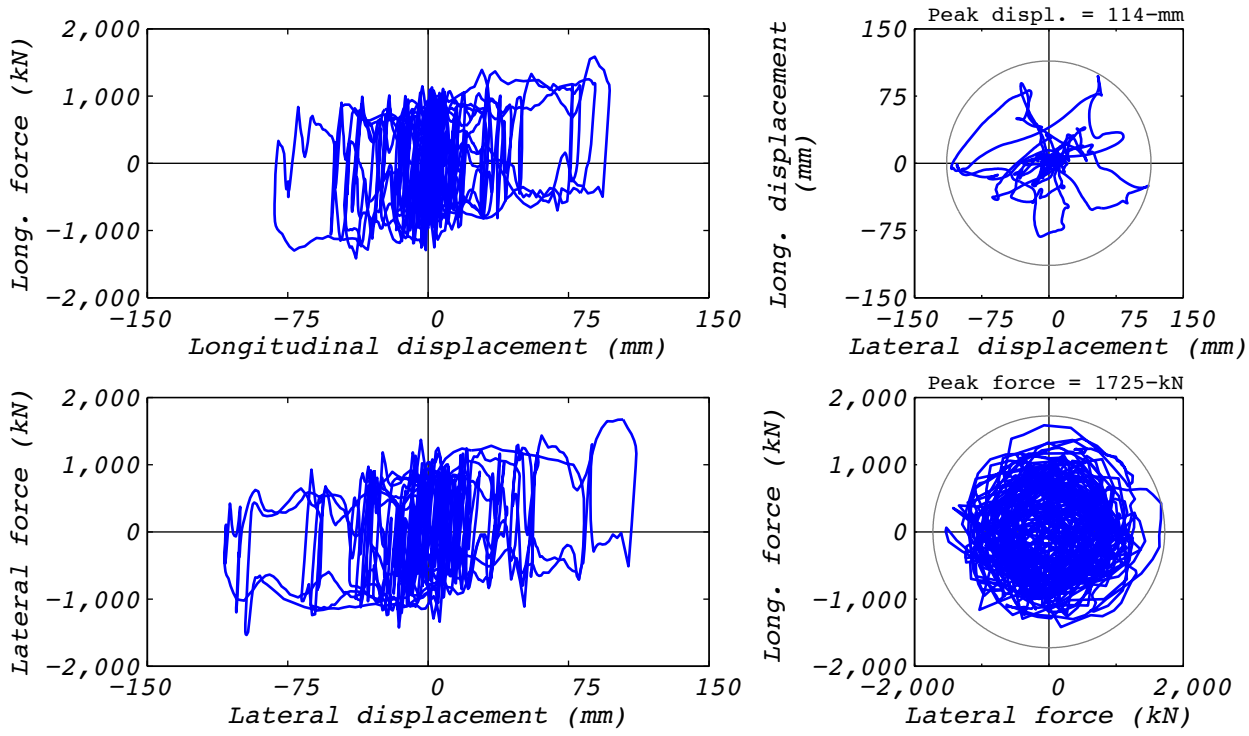

Figure C.20-2 Hybrid test bearing response for run 54: NRC2, 2D with experimental bearing representing all bearings.

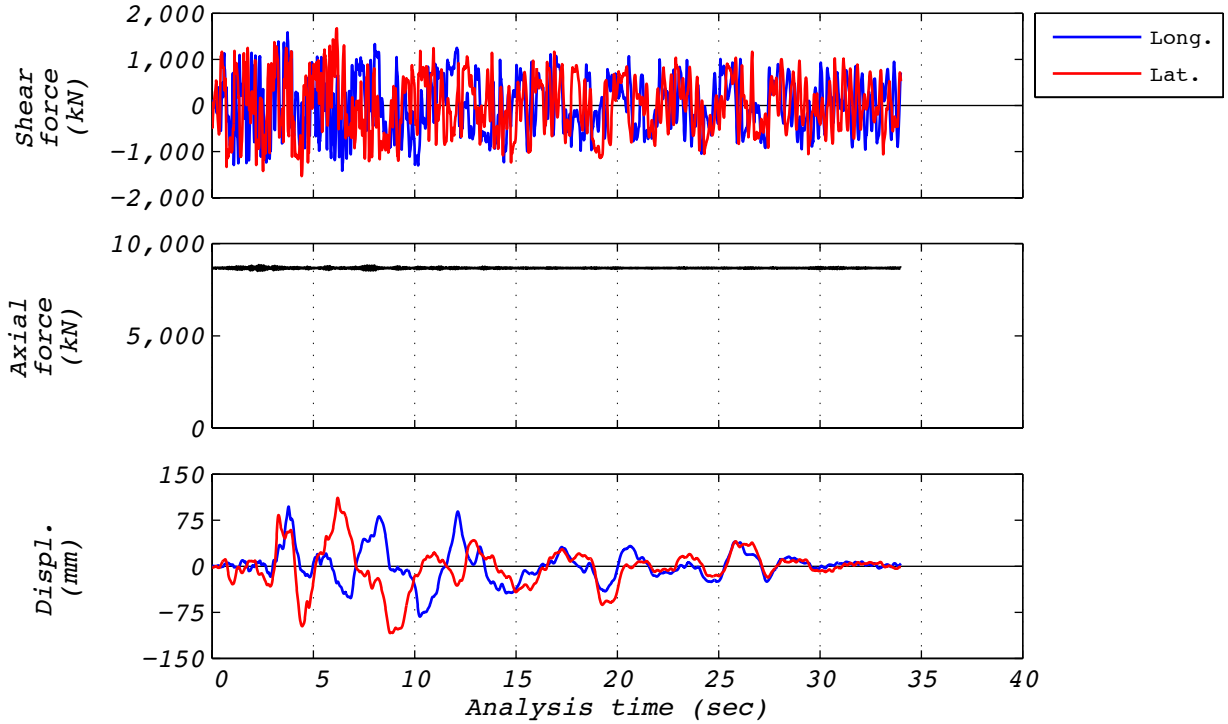

Figure C.20-3 Hybrid test time history responses for run 54: NRC2, 2D with experimental bearing representing all bearings.

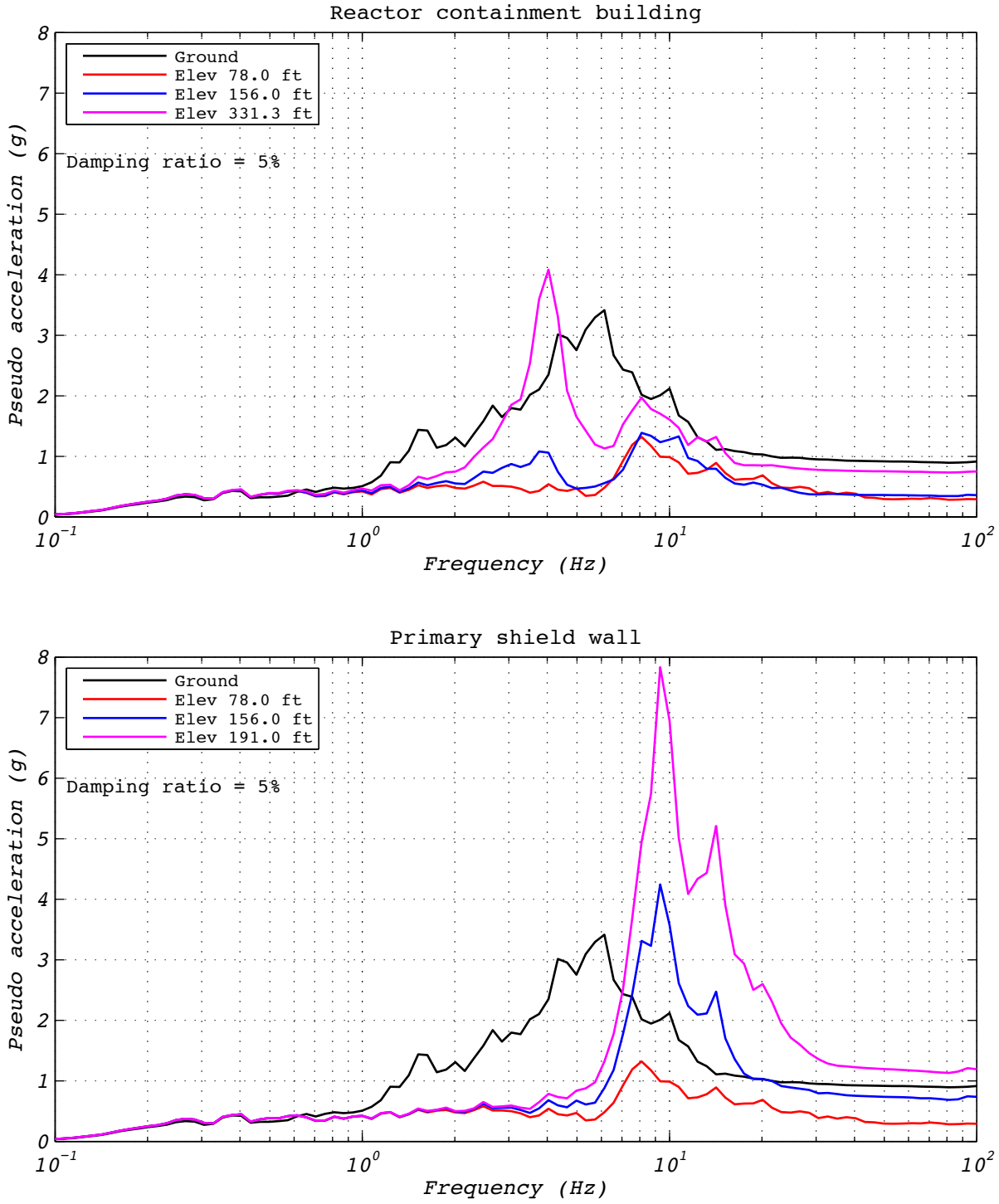

Figure C.20-4 Hybrid test floor spectra for run 54: NRC2, 2D with experimental bearing representing all bearings.

C.21 ANALYSIS RUN 54A

Analysis run 54A was an analytical estimation of the NRC dispersion appropriate ground motion number 2. The model consisted of a single analytical bearing representing all 527 bearings. Input motions consisted of two horizontal components and a constant axial load was specified as the design axial load of 8,663 kN. Bearing EQS-2 was used in this test. Figures -1 and C.2-2 contain analytical bearing responses, and Figure C.2-3 depicts the resulting floor response spectra for select locations in two of the isolated structures.

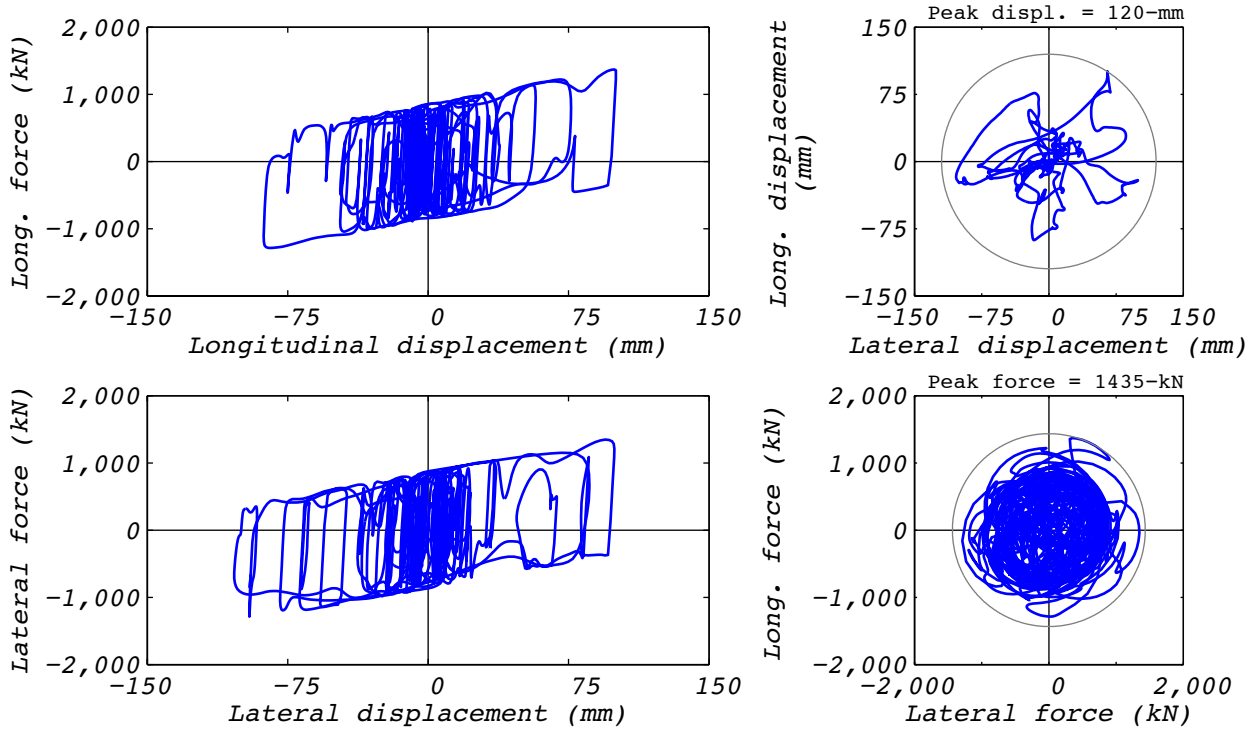

Figure C.21-1 Analytical bearing response for run 54A: NRC2, 2D with a single analytical bearing.

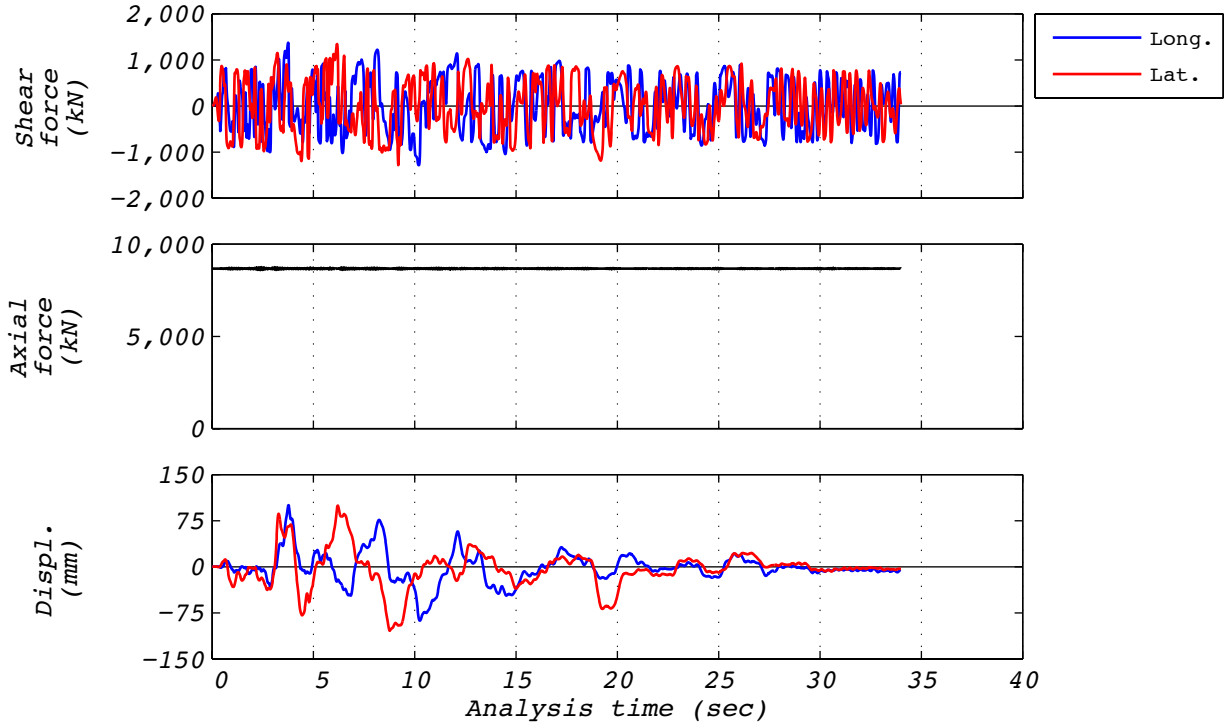

Figure C.21-2 Analytical time history responses for run 54A: NRC2, 2D with a single analytical bearing.

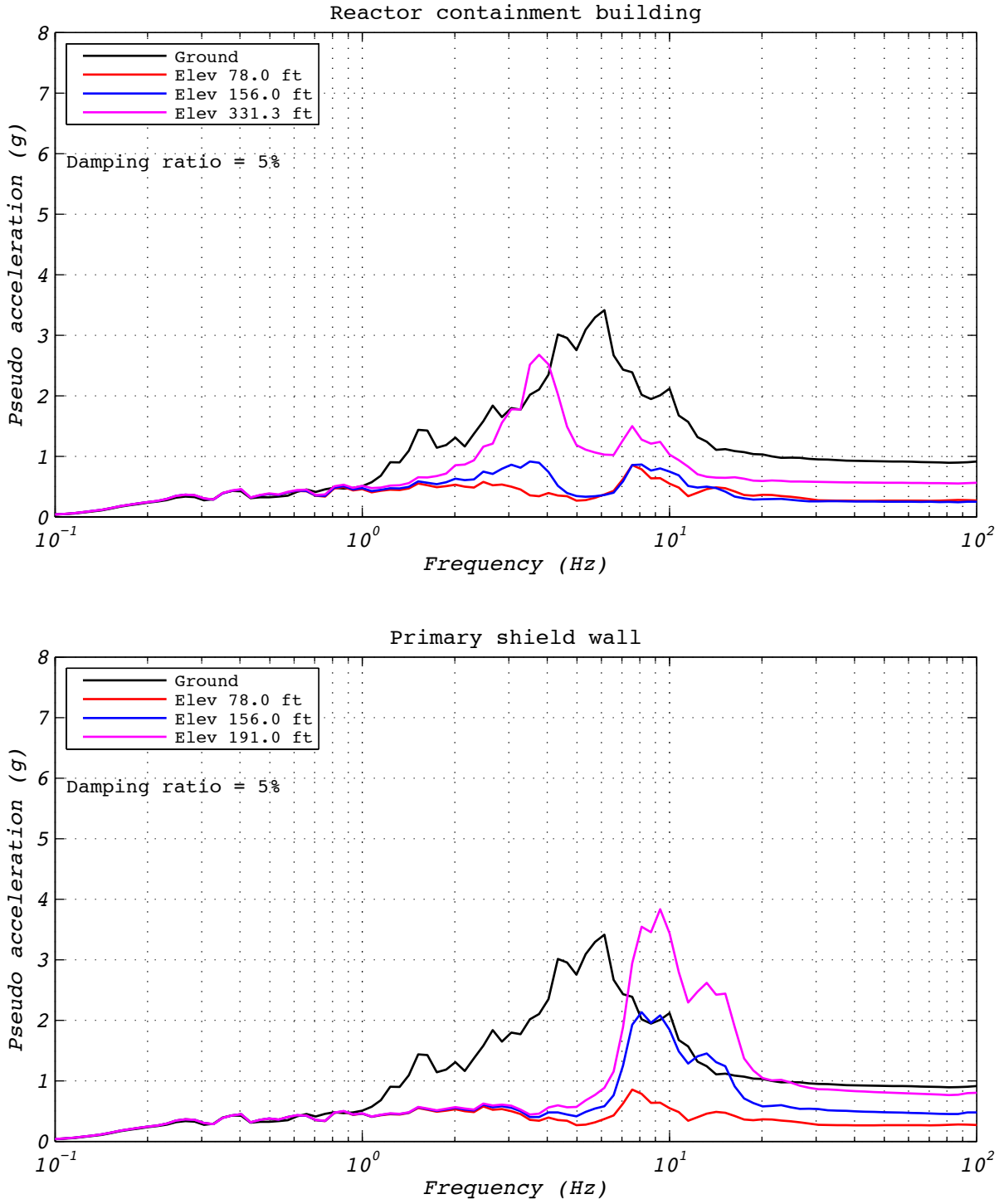

Figure C.21-3 Floor spectra for analytical run 54A: NRC2, 2D with a single analytical bearing.

C.22 DEVELOPMENT RUN 55

Development run 55 was a real-time displacement history recorded from test run 53, which was a hybrid test of the EUR dispersion appropriate ground motion number 5. Input motions consisted of a single horizontal component and a constant axial load specified as the design axial load of 8,663 kN. The test was executed at a rate real time to investigate loading rate effects. Bearing EQS-1 was used in this test. Figures C.21-1 and C.21-2 contain bearing responses.

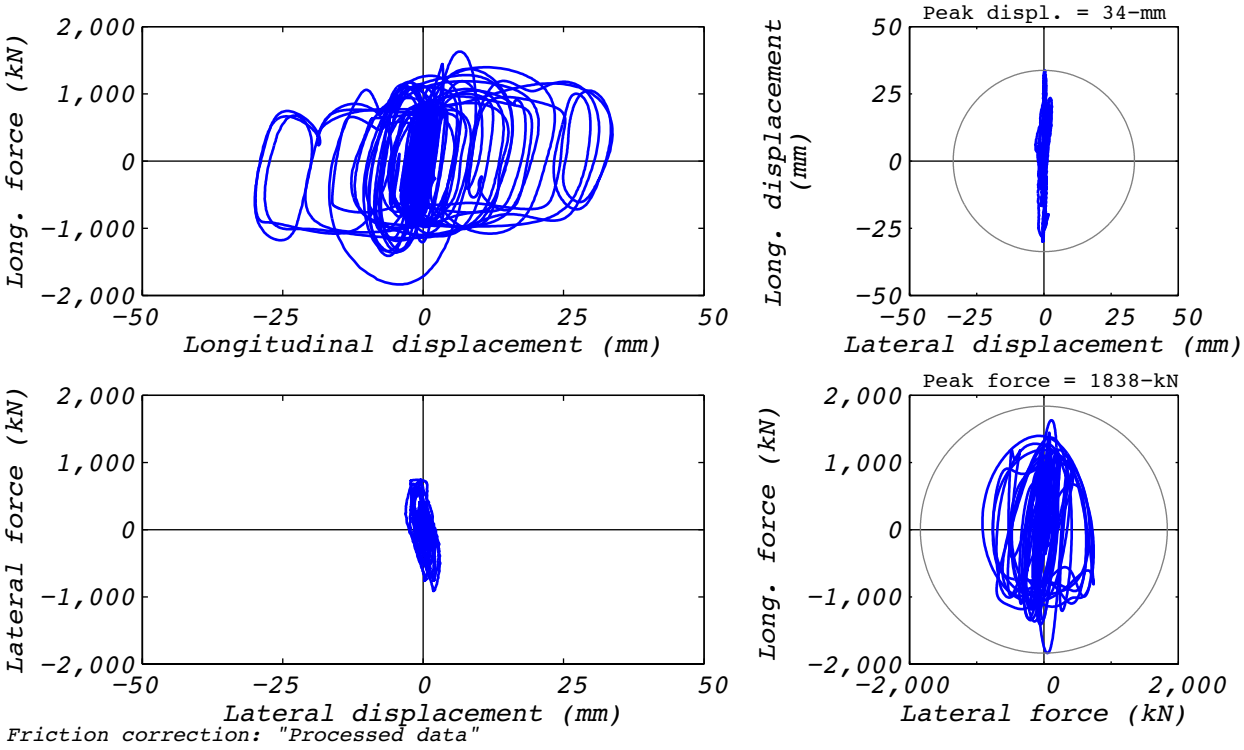

Figure C.22-1 Bearing response for real-time reproduction of hybrid test run 53: EUR5, 1D with experimental bearing representing all bearings.

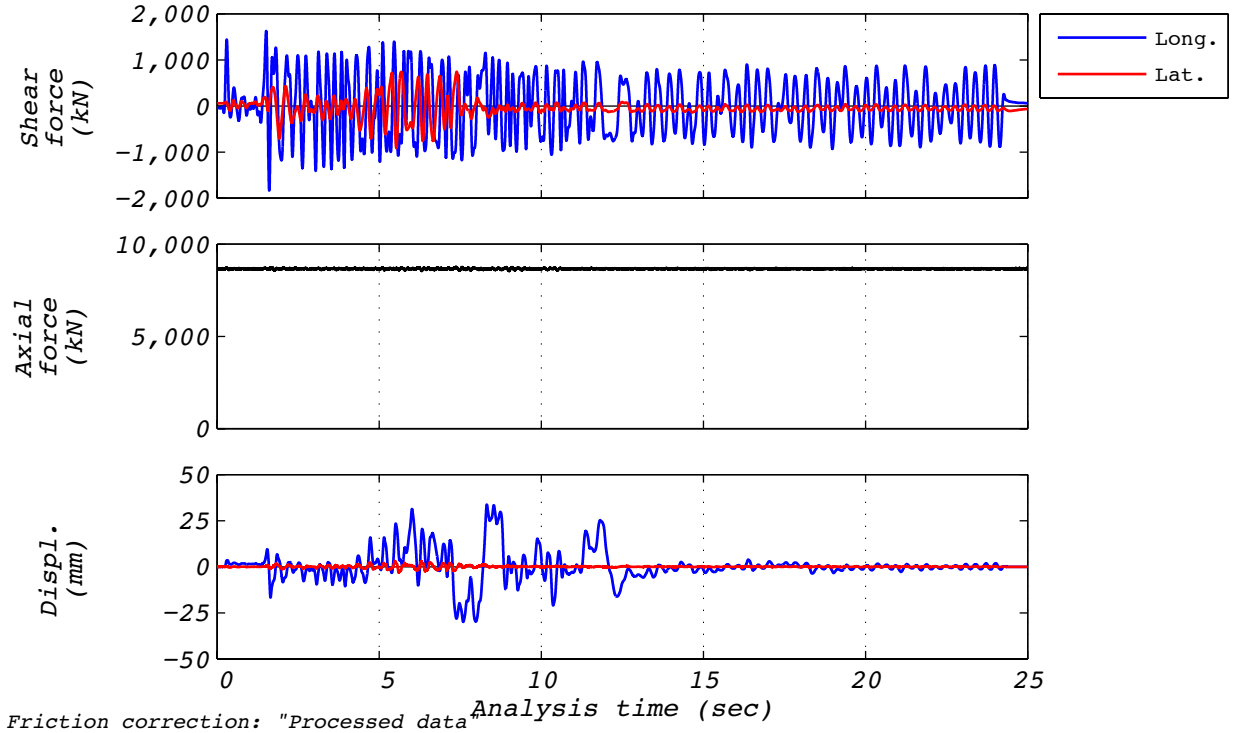

Figure C.22-2 Time history responses for real-time reproduction of hybrid test run 53: EUR5, 1D with experimental bearing representing all bearings.

C.23 DISPLACEMENT RUN 57

Test run 57 was a real-time displacement history recorded from test run 54, which was a hybrid test of the NRC dispersion appropriate ground motion number 2. Input motions consisted of two horizontal components and a constant axial load specified as the design axial load of 8,663 kN. The test was executed at a rate real time to investigate loading rate effects. Bearing EQS-1 was used in this test. Figures C.23-1 and C.23-2 contain bearing responses.

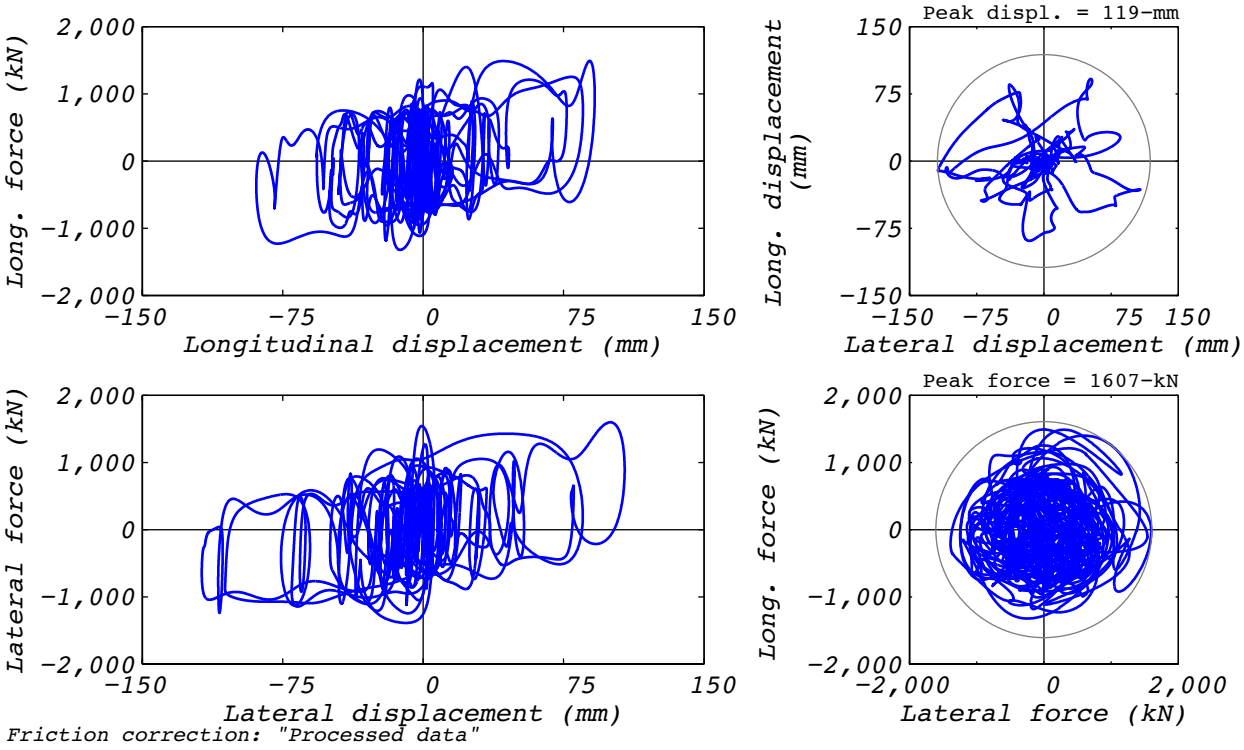

Figure C.23-1 Bearing response for real-time reproduction of hybrid test run 54: NRC2, 2D with experimental bearing representing all bearings.

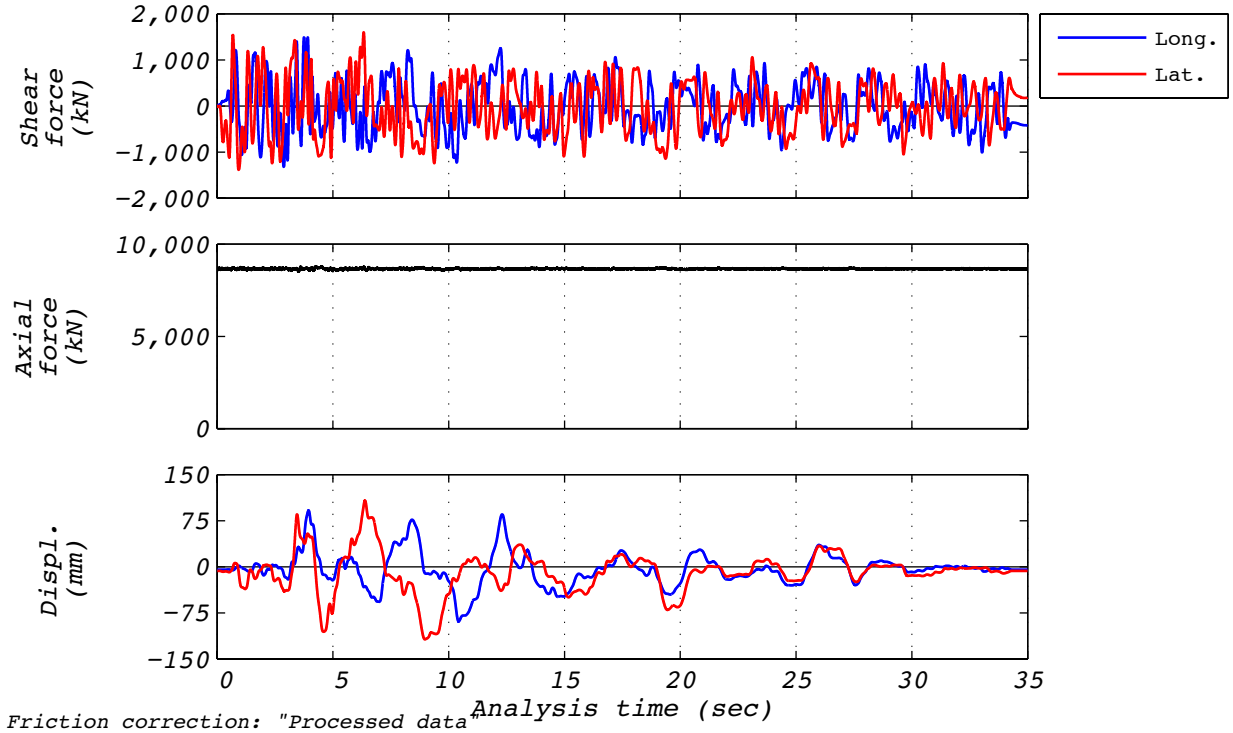

Figure C.23-2 Time history responses for real-time reproduction of hybrid test run 54: NRC2, 2D with experimental bearing representing all bearings.

C.24 TEST RUN 58

Test run 58 was a hybrid test of the NRC dispersion appropriate ground motion number 10. The model consisted of a single experimental bearing representing all 527 bearings. Input motions consisted of two horizontal components and a constant axial load specified as the design axial load of 8,663 kN. The test was executed at a rate 5 times slower than real time to compensate for machine delays. Bearing EQS-2 was used in this test. Figure C.24-1 shows the fidelity achieved in the hybrid test. Figures C.24-2 and C.24-3 contain bearing responses, and Figure C.24-4 depicts the resulting floor response spectra for select locations in two of the isolated structures.

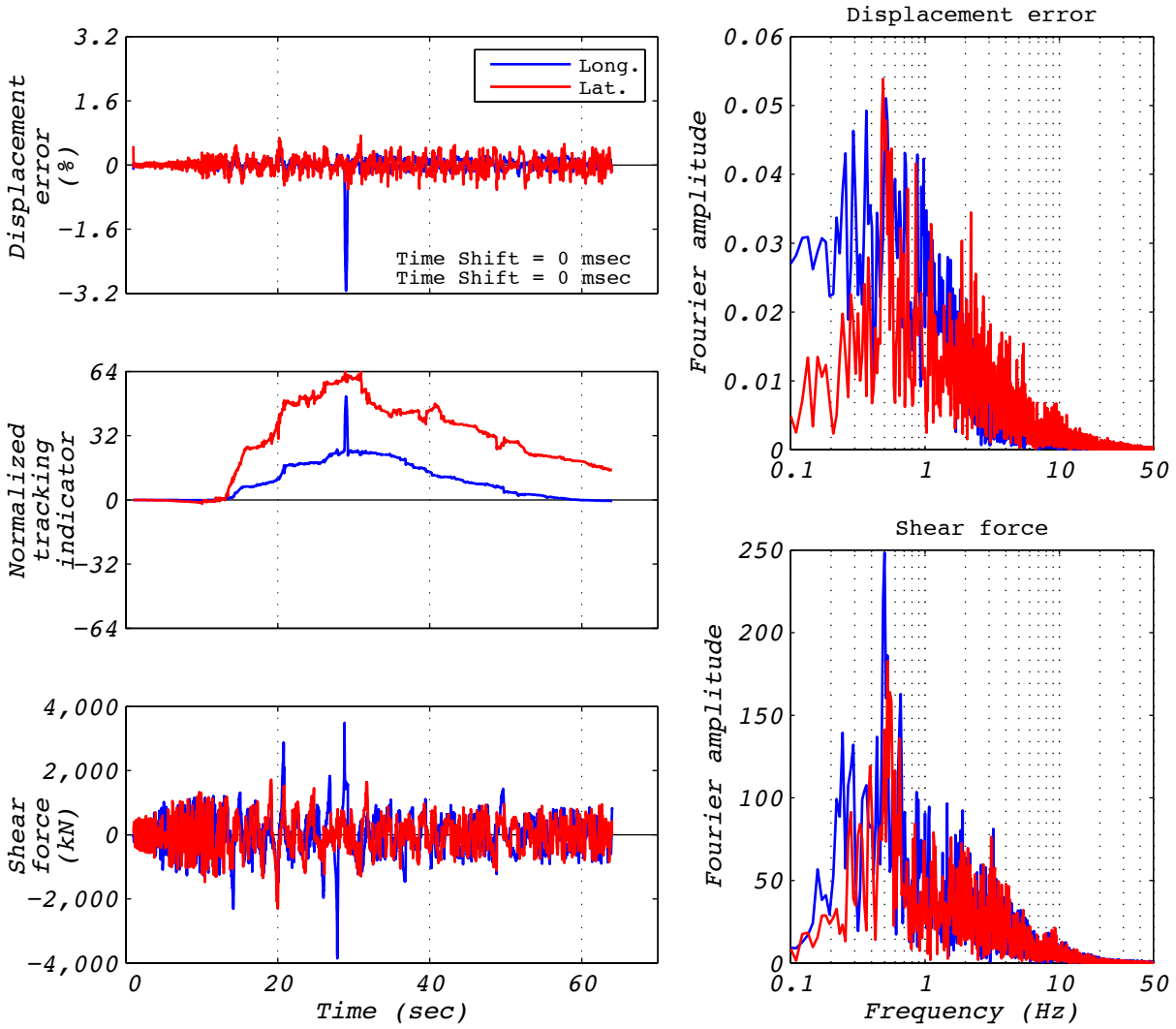

Figure C.24-1 Hybrid test performance metrics for run 58: NRC10, 2D with experimental bearing representing all bearings.

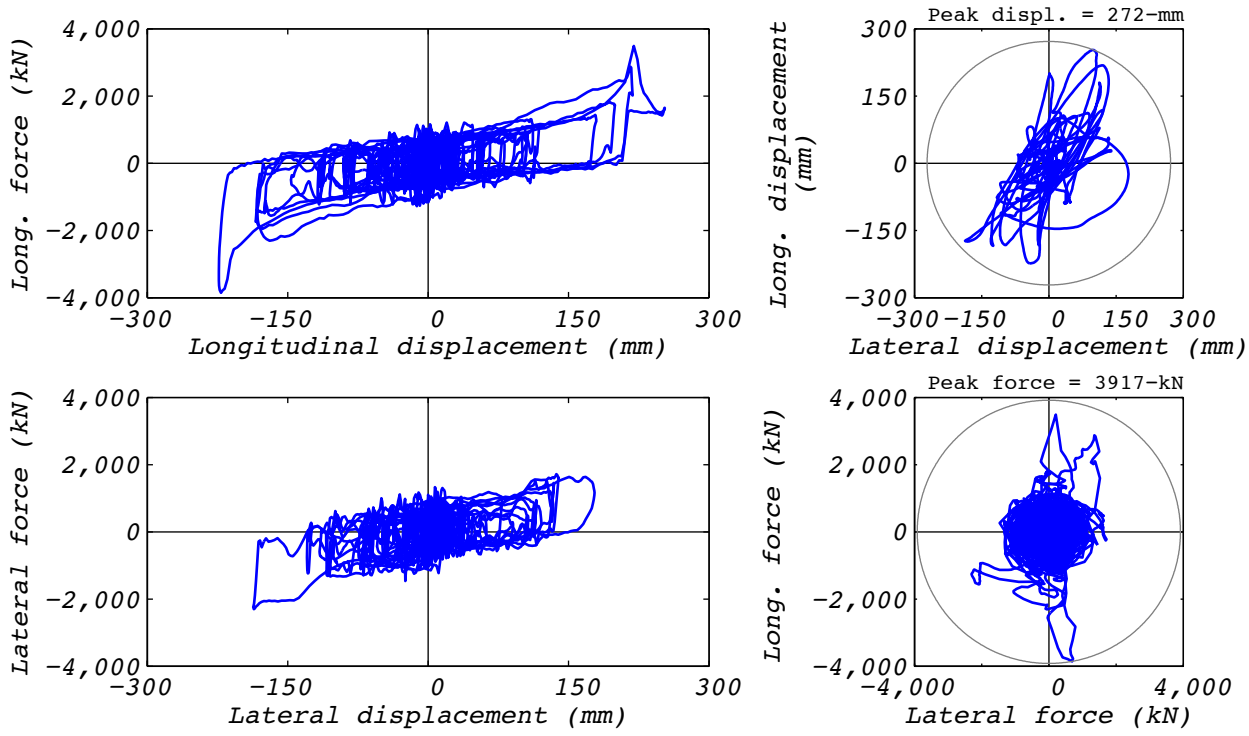

Figure C.24-2 Hybrid test bearing response for run 58: NRC10, 2D with experimental bearing representing all bearings.

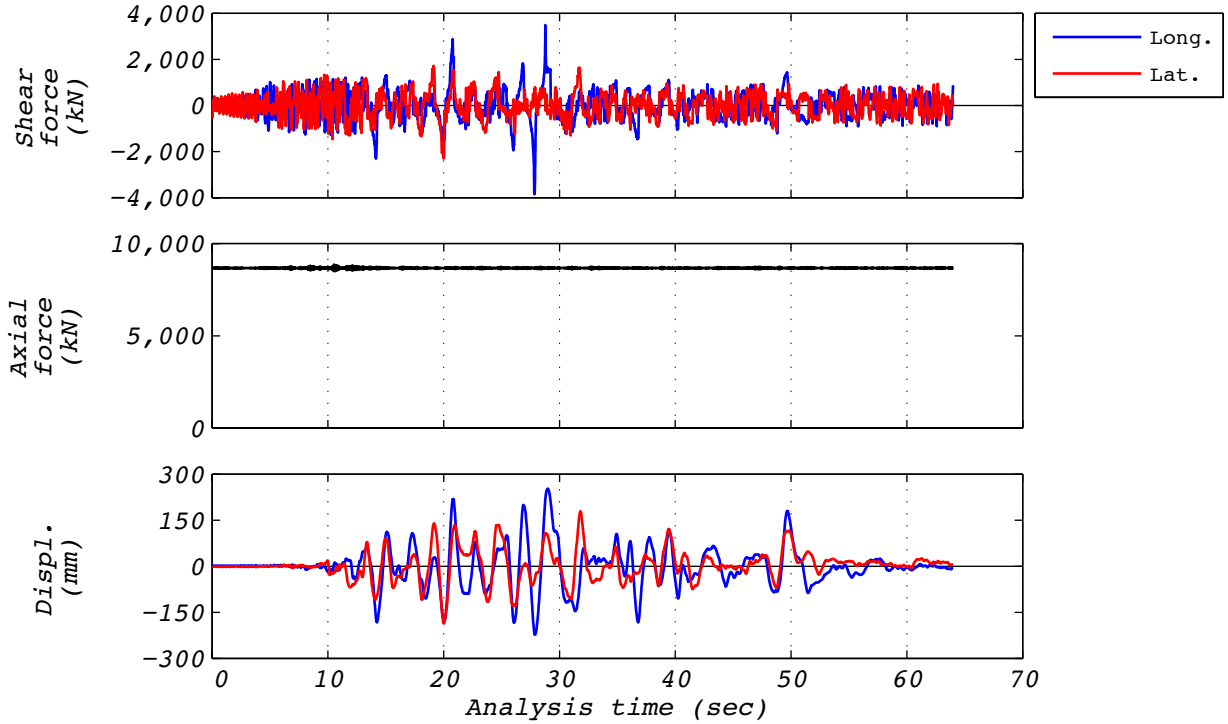

Figure C.24-3 Hybrid test time history responses for run 58: NRC10, 2D with experimental bearing representing all bearings.

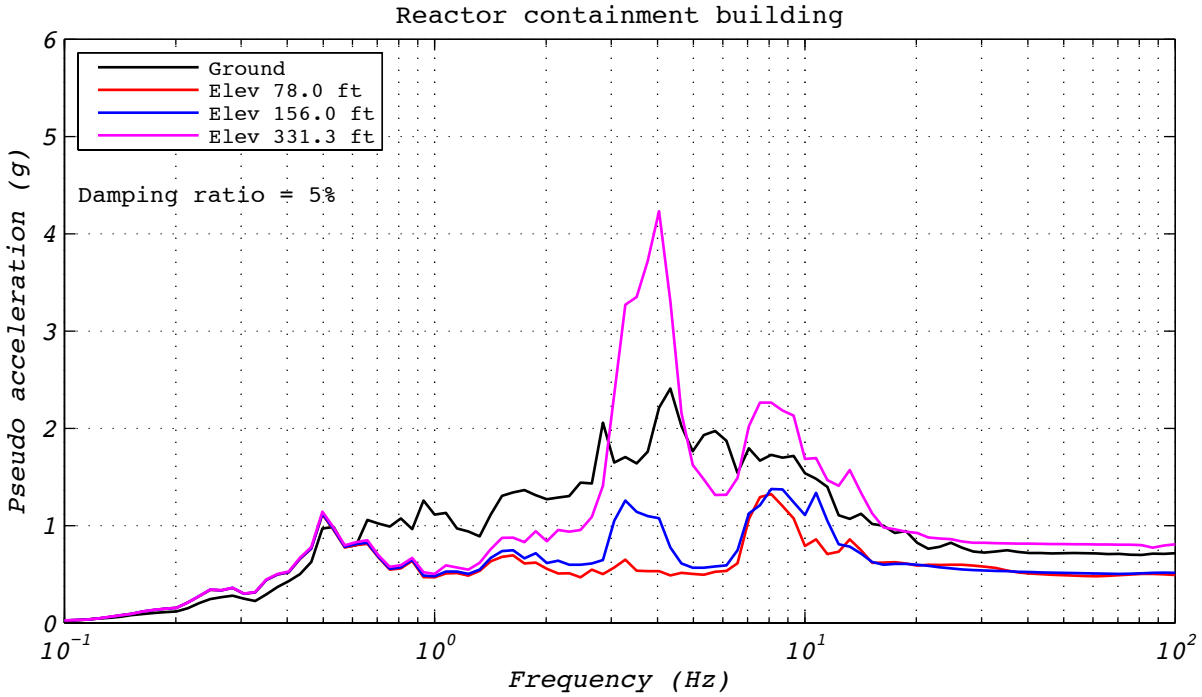

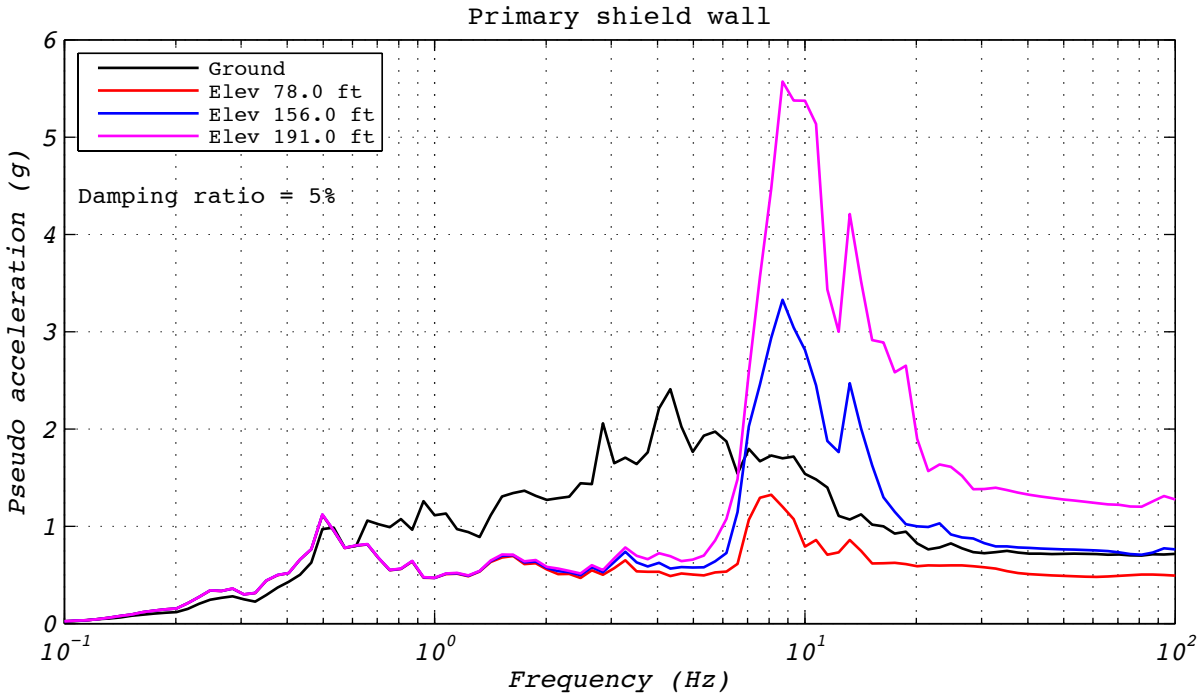

Figure C.24-4 Hybrid test floor spectra for run 58: NRC10, 2D with experimental bearing representing all bearings.

Appendix D: Characterization Tests Conducted on Friction Sliding Bearings

Characterization tests listed in Table D.1 and Table D.2 were performed on the ESCO-RTS bearings EQS-1 and EQS-2, respectively.

Table D.1 Characterization tests conducted on friction slider bearing EQS-1.

Section	Run	Components	Number of cycles	Displ. amplitude* (mm)	Axial load* (kN)	Velocity* (mm/s)	Wave form
D.1	1	Longitudinal	3	120	8,663	410	Sine
D.2	2	Axial	9	0	Varies	-	Ramp & Sine
D.3	3	Axial	9	120	Varies	-	Ramp & Sine
D.4	4	Axial	3	0	Varies	-	Ramp & Sine
D.5	5	Axial	3	0	Varies	-	Ramp & Sine
D.6	6	Trans. Rot.	2	0	8,663	-	Sine
D.7	7	Long. Rot.	2	0	8,663	-	Sine
D.8	8	Twist	9	0	8,663	-	Sine
D.9	9	Longitudinal	6	120	10,000	410	Triangle
D.10	10	Transverse	3	120	8,663	410	Sine
D.11	11	Longitudinal	3	120	0	410	Sine
D.12	12	Longitudinal	6	120	2,500	410	Sine
D.13	13	Longitudinal	6	120	5,000	410	Sine
D.14	14	Longitudinal	6	120	15,000	410	Sine
D.15	15	Longitudinal	6	120	8,663	41	Sine
D.16	16	Longitudinal	6	180	8,663	409	Sine
D.17	20	Longitudinal	3	120	8,663	410	Sine
D.18	24	Longitudinal	6	120	8,663	410	Sine
D.19	25	Longitudinal	3	120	8,663	820	Sine
D.20	26	Longitudinal	6	120	8,663	410	Sine
D.21	27	Longitudinal	3	120	Varies	410	Sine
D.22	28	Bidirectional	4	Varies	8,663	Varies	Time History
D.23	29	Bidirectional	4	Varies	178	Varies	Time History

* Target values

Table D.2 Characterization tests conducted on friction slider bearing EQS-2.

Section	Run	Components	Number of cycles	Displ. amplitude* (mm)	Axial load* (kN)	Velocity* (mm/s)	Wave form
D.24	30	Longitudinal	3	120	8,663	410	Sine
D.25	31	Axial	3	0	Varies	-	Ramp & Sine
D.26	32	Transverse	3	120	8,663	410	Sine
D.28	33	Bidirectional	2	120	8,663	Varies	Sine
D.28	34	Longitudinal	-	120	8,663	Varies	Sine
D.29	35	Longitudinal	24.5	Varies	8,663	Varies	Sine
D.30	36	Longitudinal	20	13	8,663	4	Sine
D.31	59	Longitudinal	3	120	8,663	410	Sine
D.32	60	Transverse	3	120	8,663	410	Sine

* Target values

D.1 TEST RUN 1

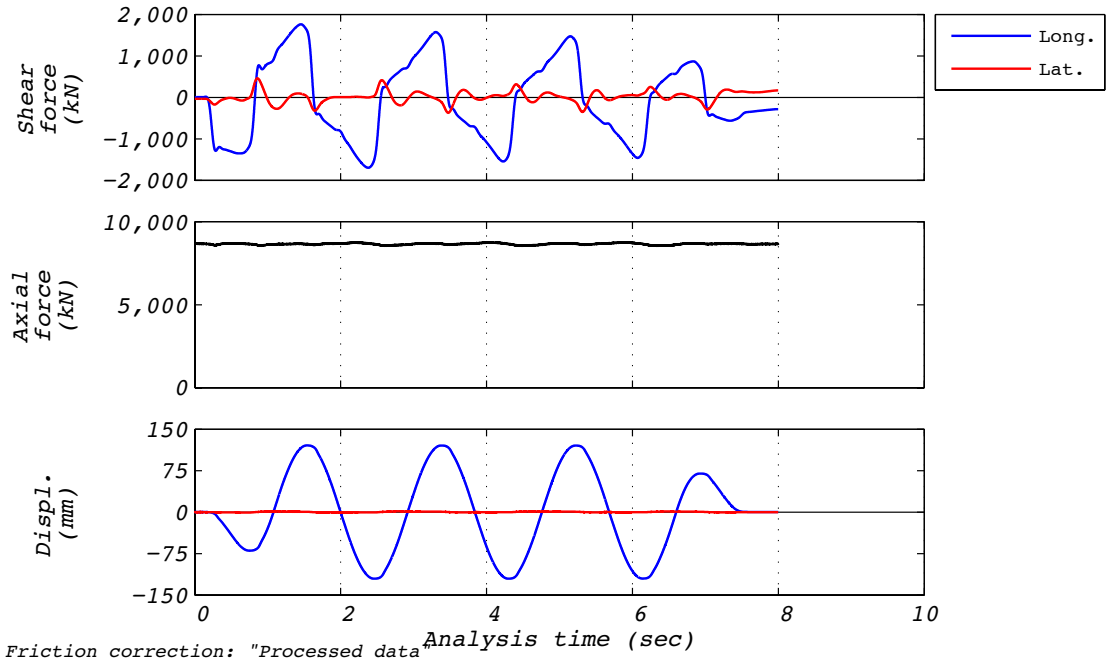

Figure D.1-1 Test run no. 1 time history: Longitudinal (120 mm amplitude, 8,663 kN axial load, and 410 mm/s velocity).

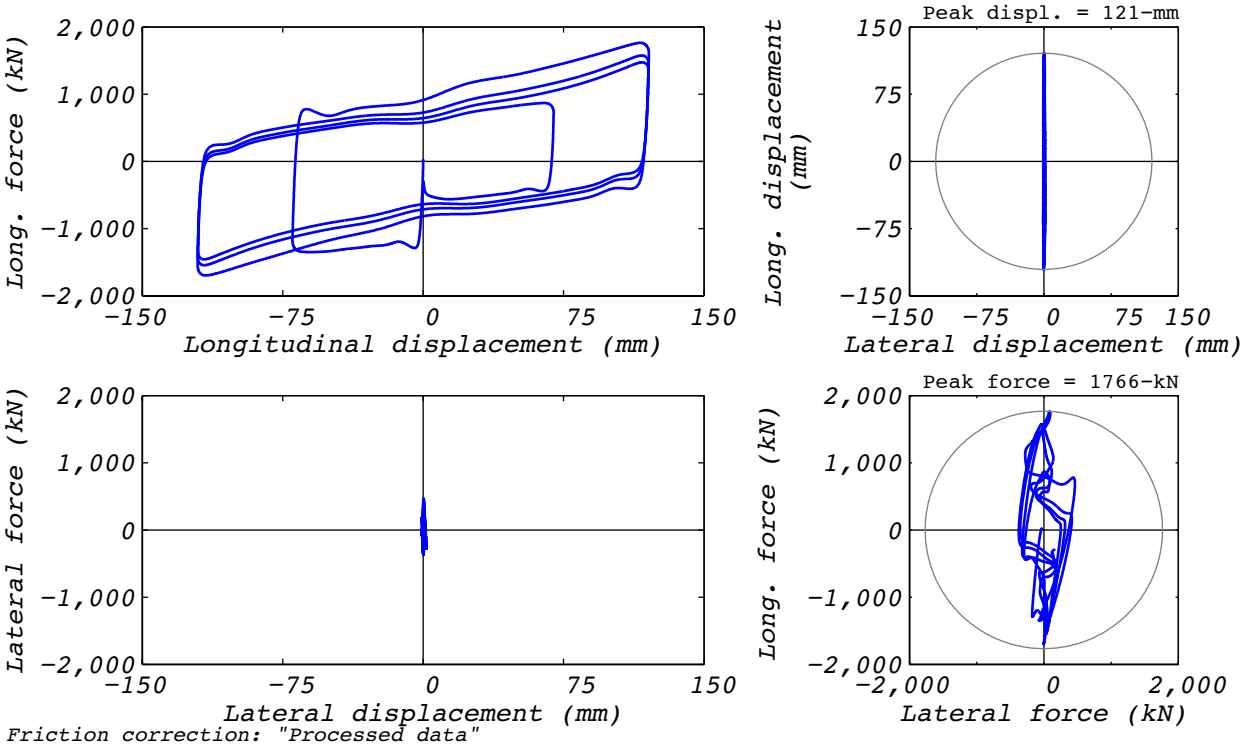

Figure D.1-2 Test run no. 1 hysteresis: Longitudinal (120 mm amplitude, 8,663 kN axial load, and 410 mm/s velocity).

D.2 TEST RUN 2

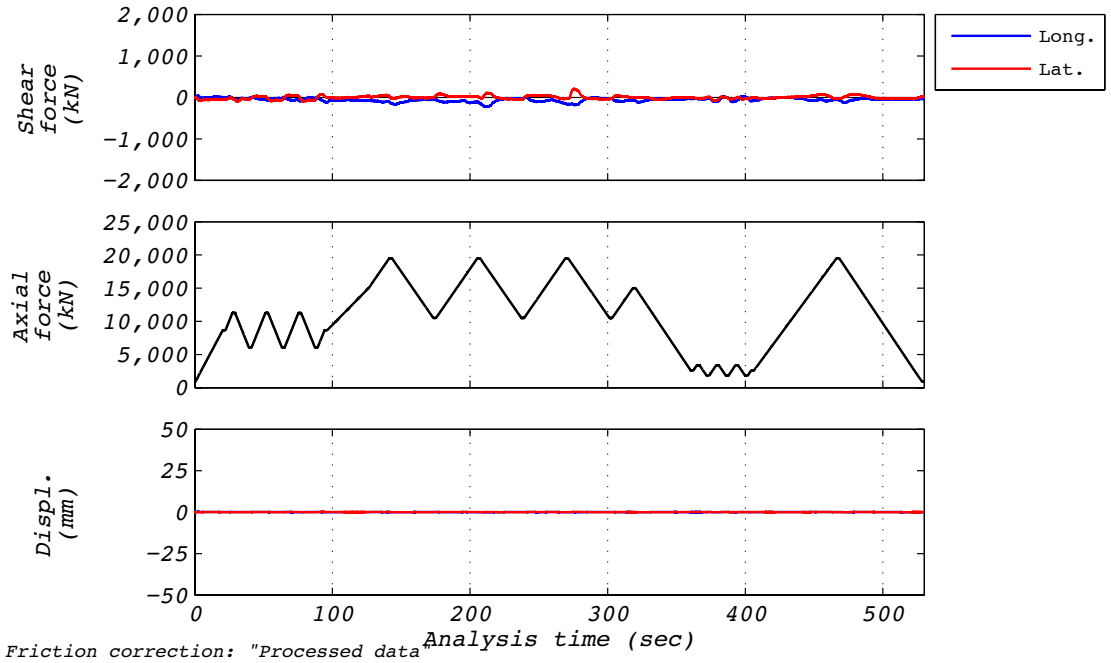

Figure D.2-1 Test run no. 2 time history: Axial (0 mm displacement and varying axial load).

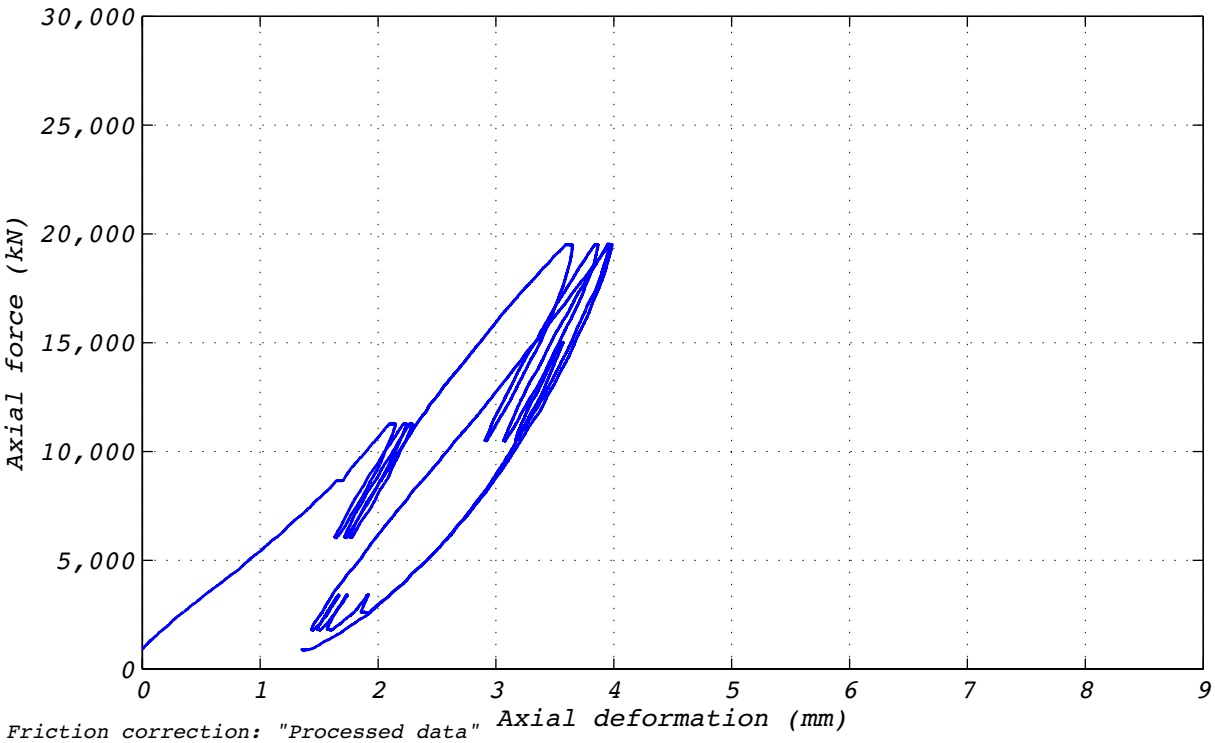

Figure D.2-2 Test run no. 2 hysteresis: Axial (0 mm displacement and varying axial load).

D.3 TEST RUN 3

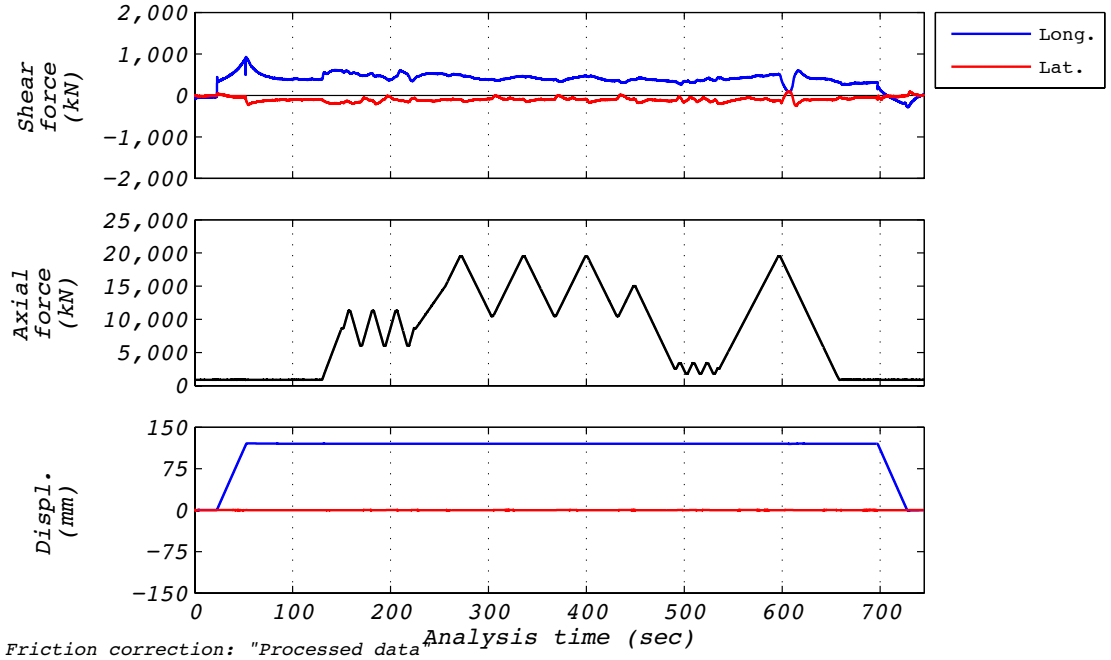

Figure D.3-1 Test run no. 3 time history: Axial (120 mm displacement and varying axial load).

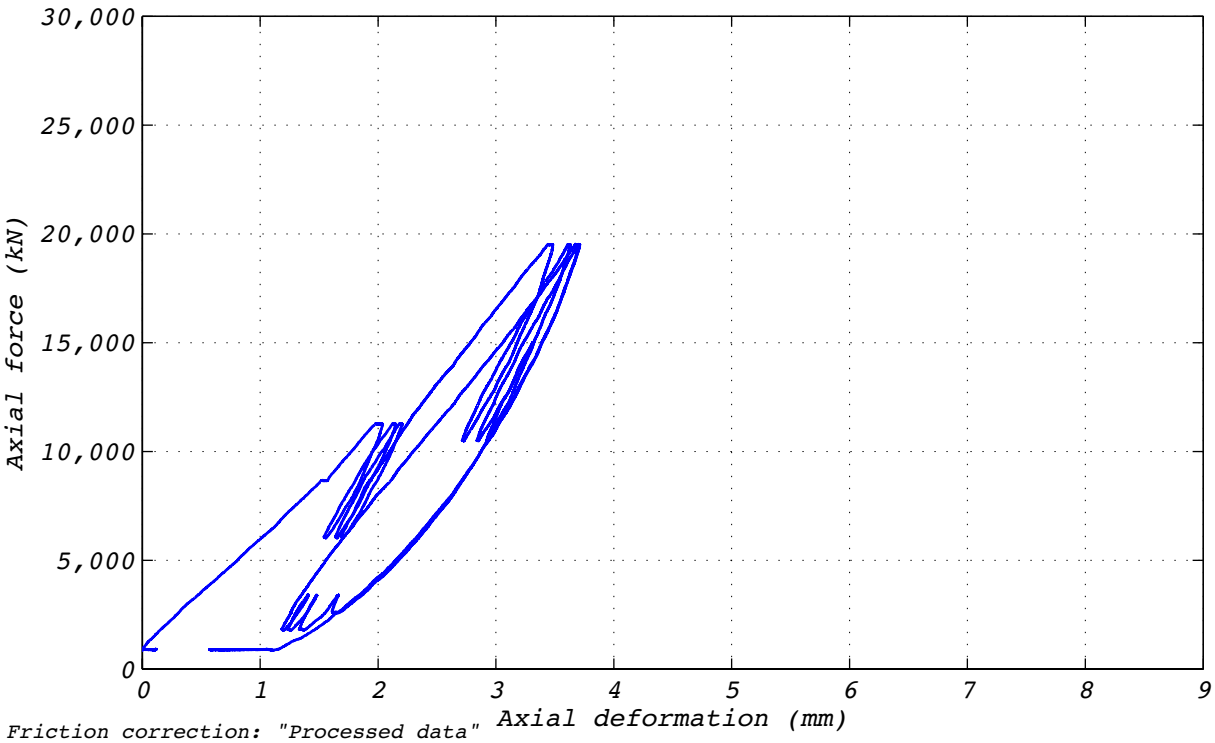

Figure D.3-2 Test run no. 3 hysteresis: Axial (120 mm displacement and varying axial load).

D.4 TEST RUN 4

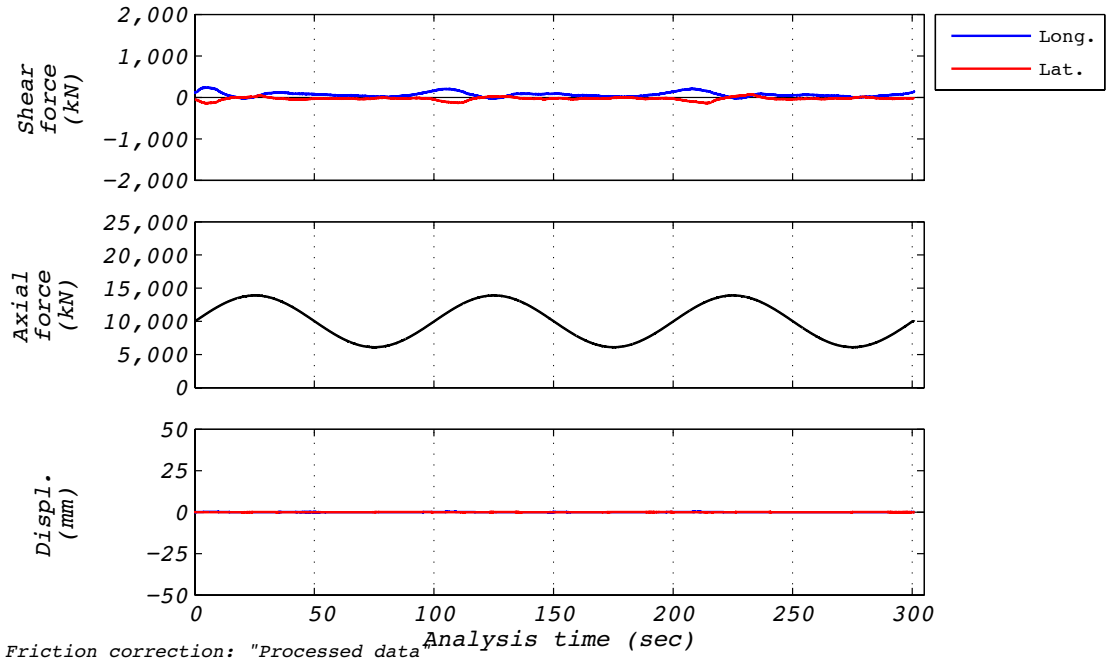

Figure D.4-1 Test run no. 4 time history: Axial (0 mm displacement and varying axial load).

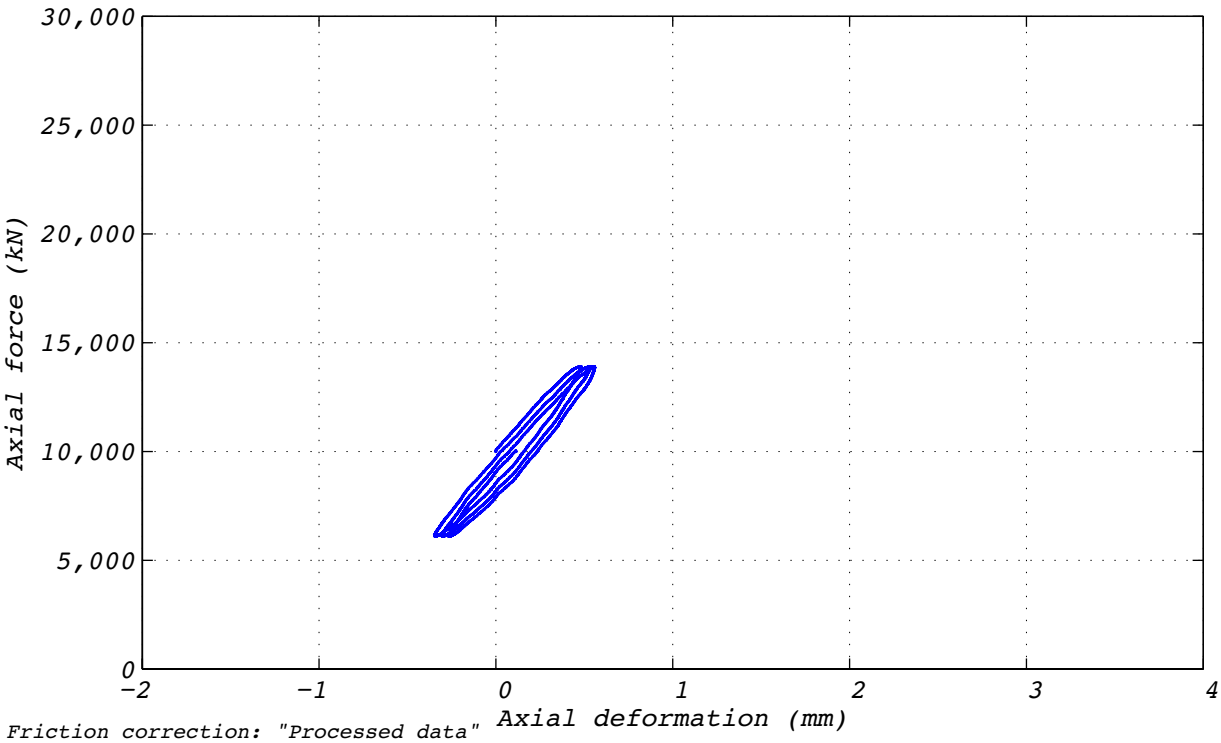

Figure D.4-2 Test run no. 4 hysteresis: Axial (0 mm displacement and varying axial load).

D.5 TEST RUN 5

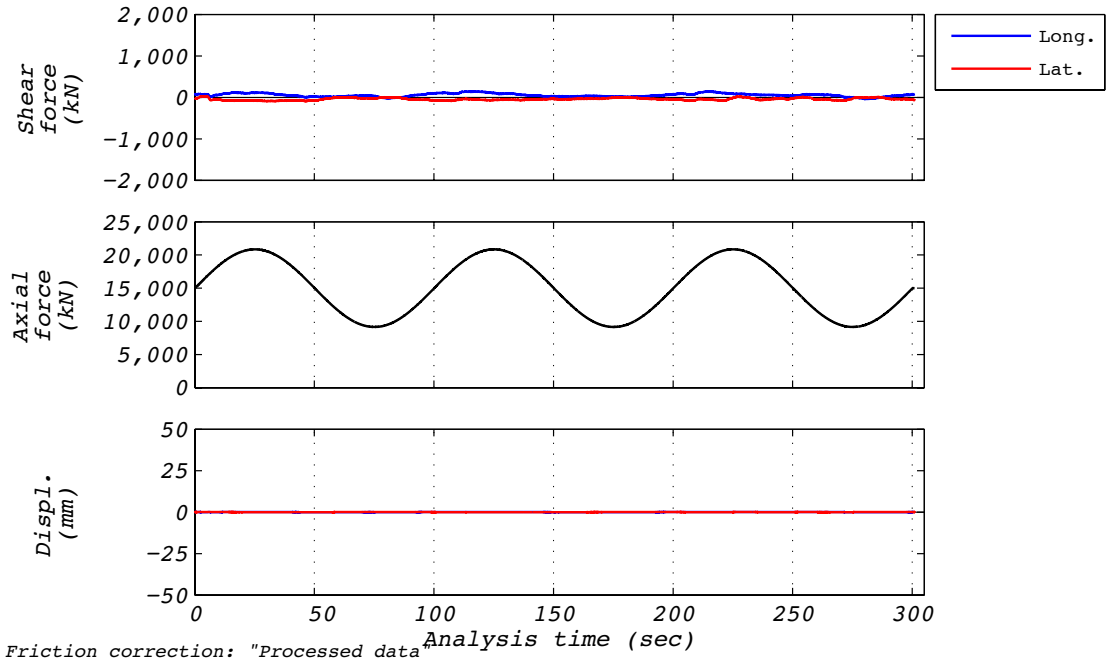

Figure D.5-1 Test run no. 5 time history: Axial (0 mm displacement and varying axial load).

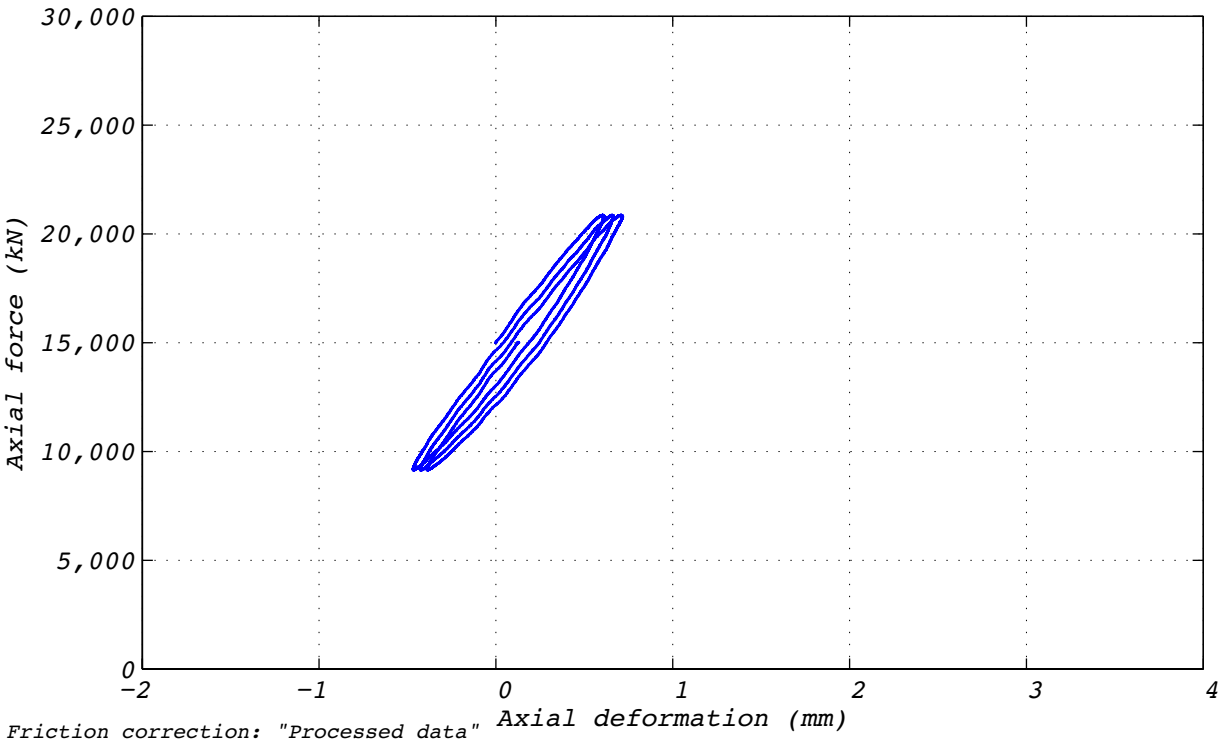

Figure D.5-2 Test run no. 5 hysteresis: Axial (0 mm displacement and varying axial load).

D.6 TEST RUN 6

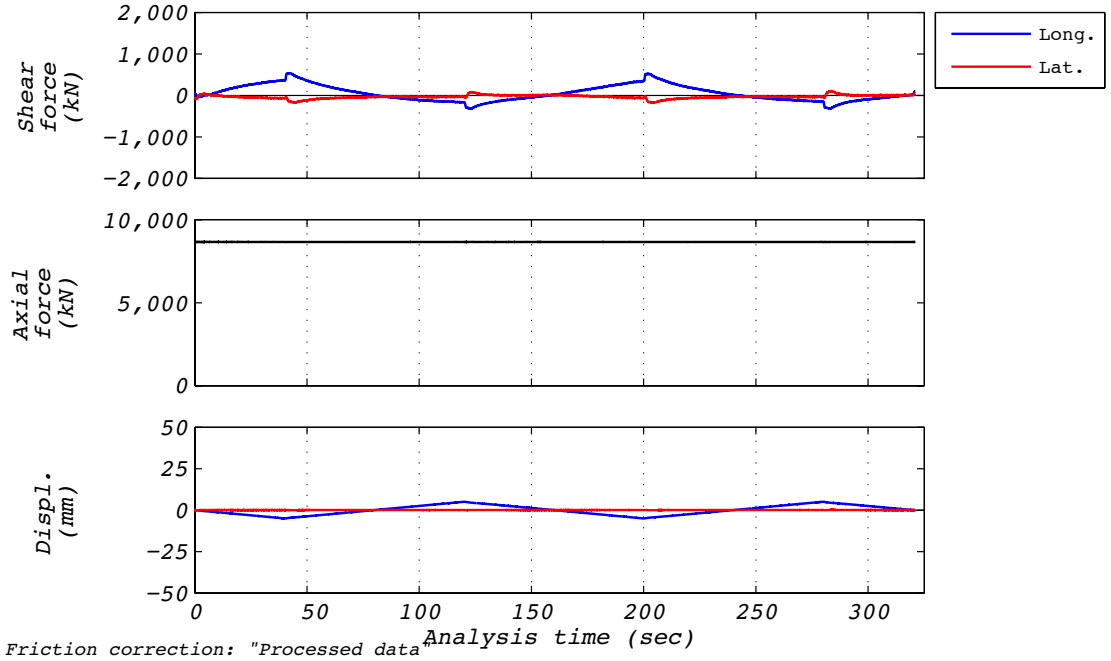

Figure D.6-1 Test run no. 6 time history: Transverse rotation (0 mm displacement and 8,663 kN axial load).

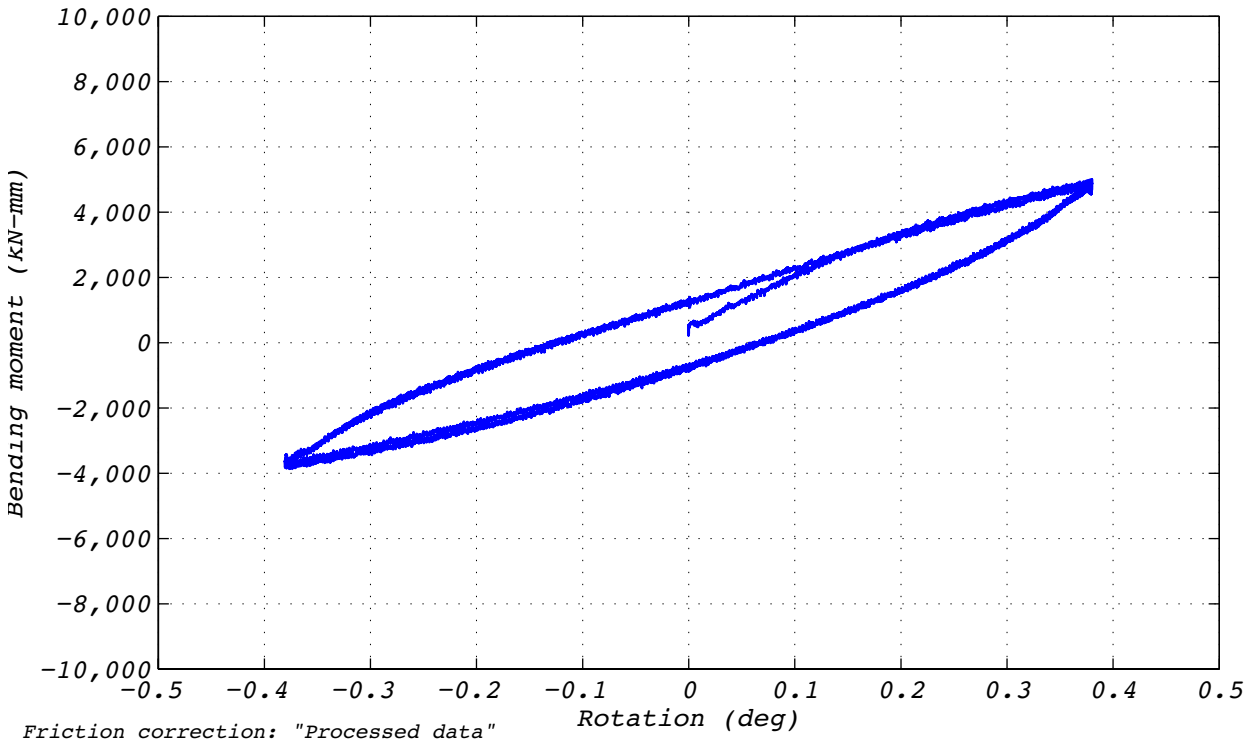

Figure D.6-2 Test run no. 6 hysteresis: Transverse rotation (0 mm displacement and 8,663 kN axial load).

D.7 TEST RUN 7

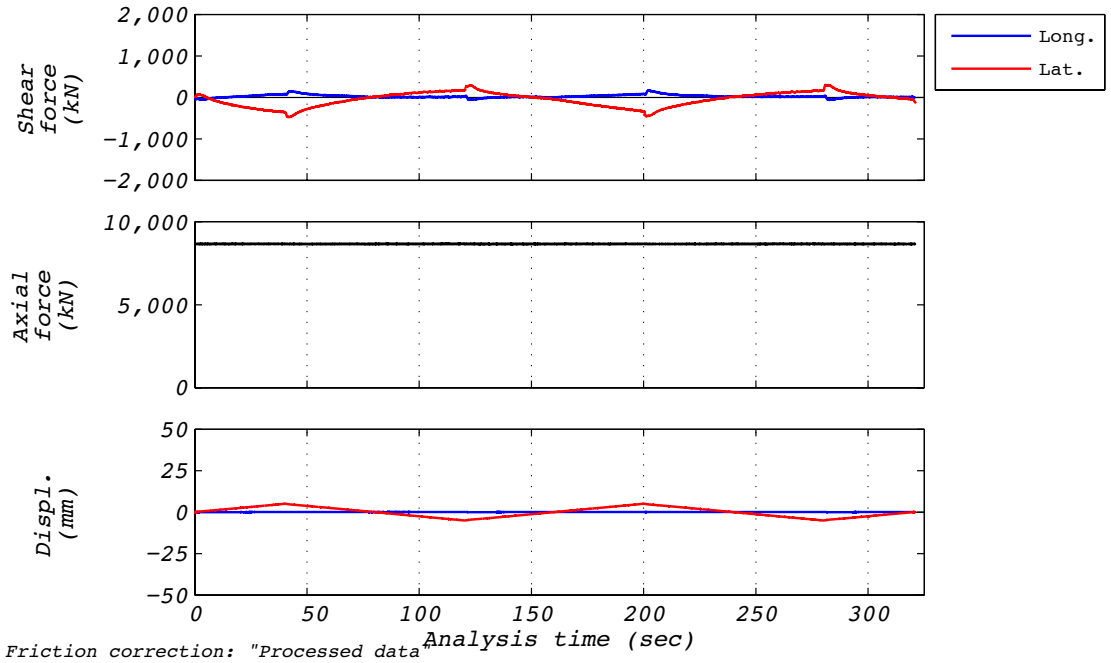

Figure D.7-1 Test run no. 7 time history: Longitudinal rotation (0 mm displacement and 8,663 kN axial load).

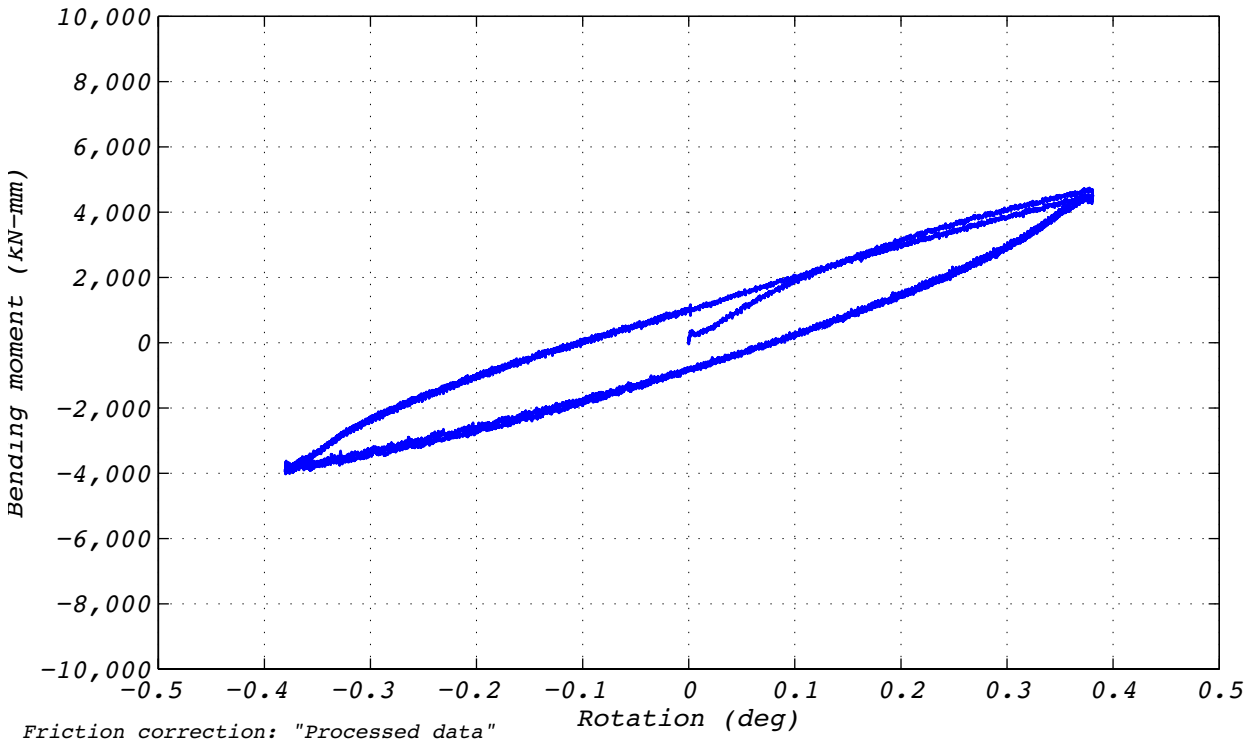

Figure D.7-2 Test run no. 7 hysteresis: Longitudinal rotation (0 mm displacement and 8,663 kN axial load).

D.8 TEST RUN 8

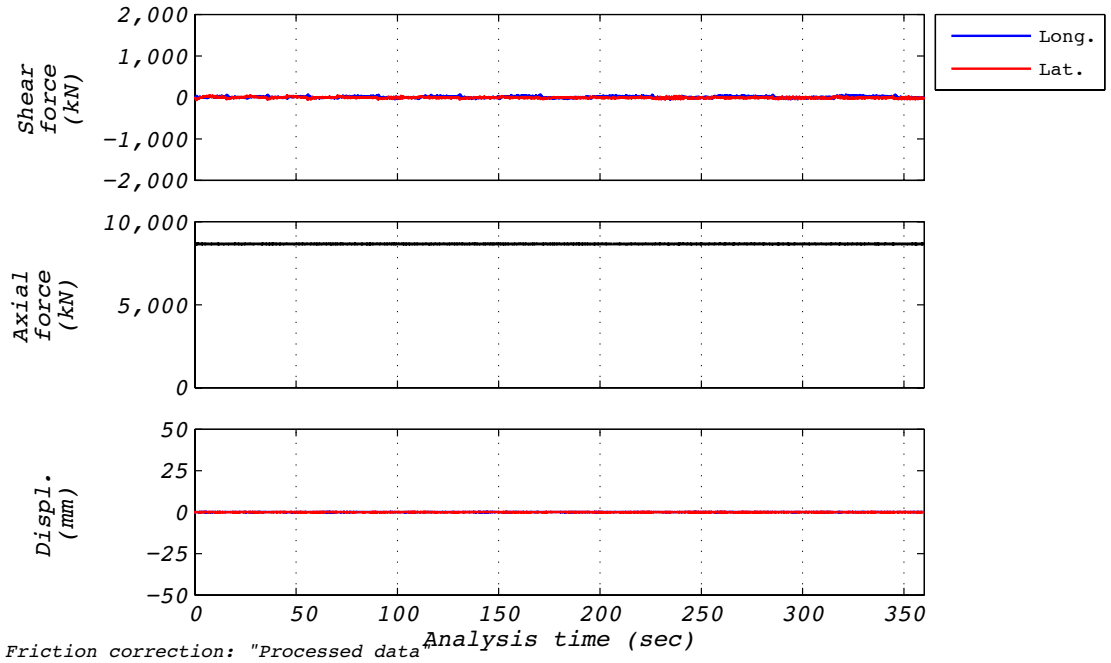

Figure D.8-1 Test run no. 8 time history: Twist (0 mm displacement and 8,663 kN axial load).

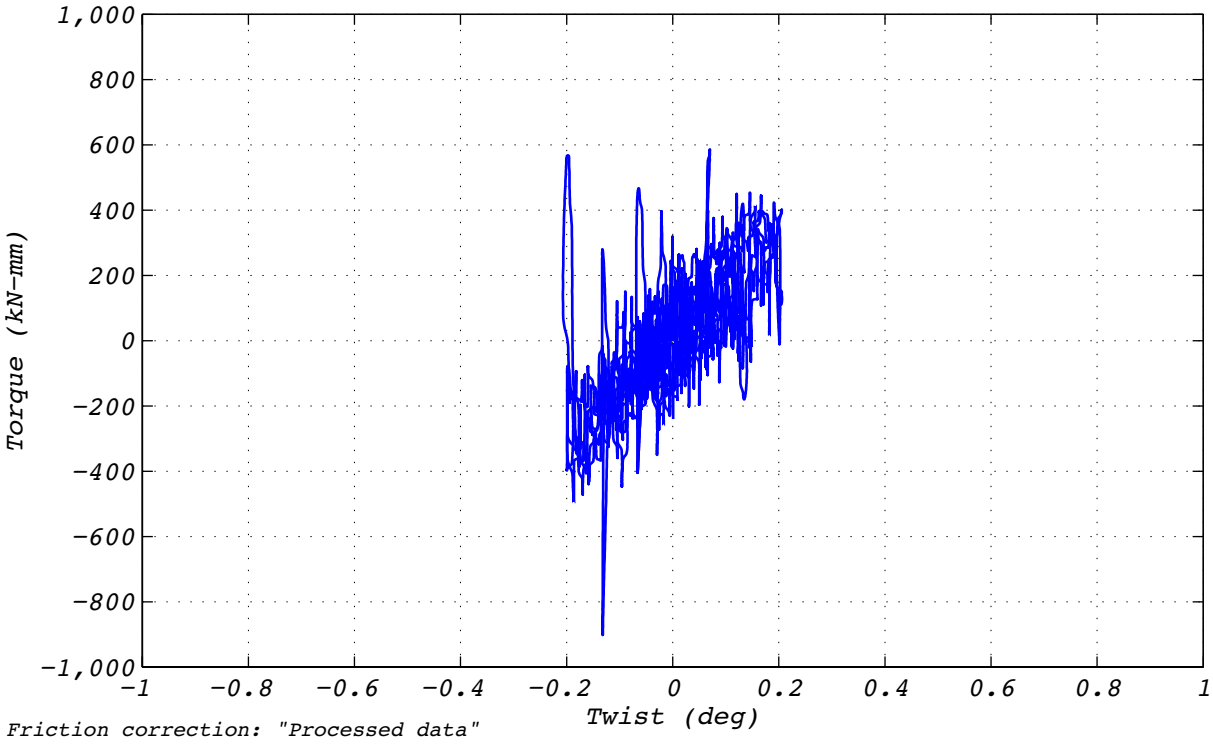

Figure D.8-2 Test run no. 8 hysteresis: Twist (0 mm displacement and 8,663 kN axial load).

D.9 TEST RUN 9

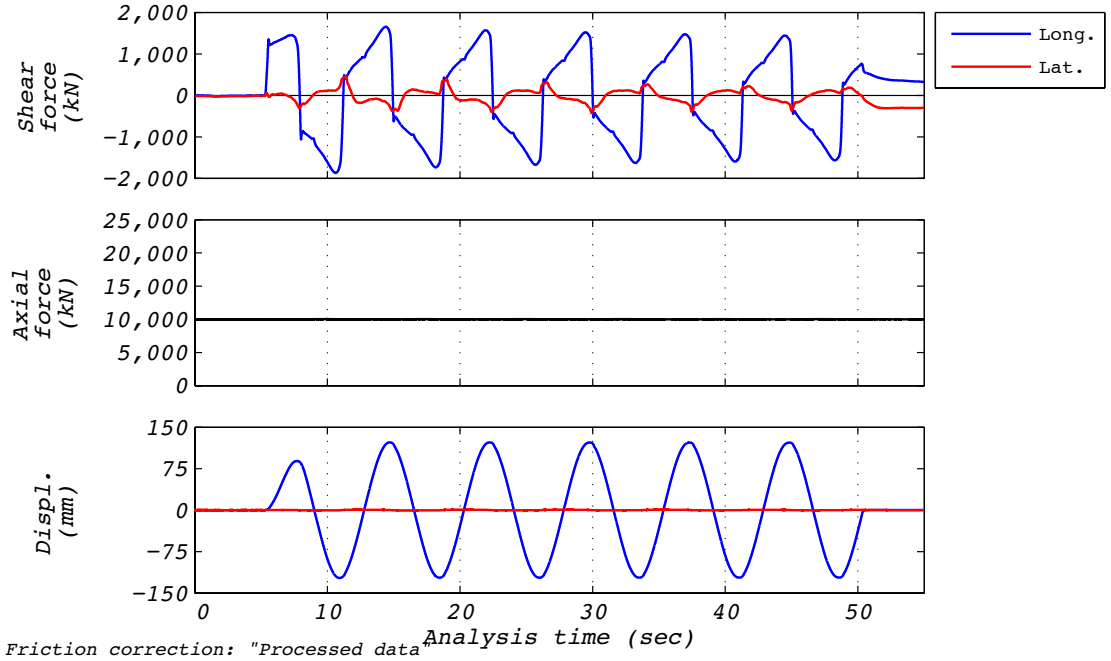

Figure D.9-1 Test run no. 9 time history: Longitudinal (120 mm amplitude, 10,000 kN kN axial load, and 410 mm/s velocity).

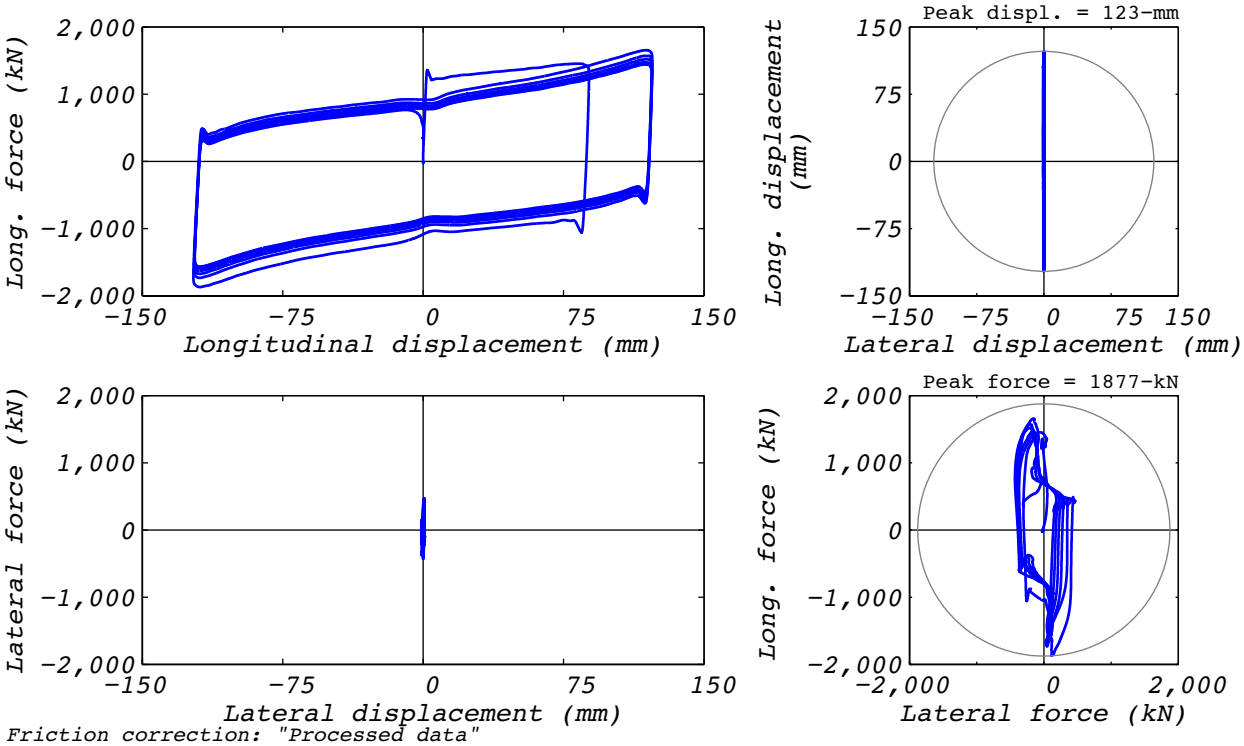

Figure D.9-2 Test run no. 9 hysteresis: Longitudinal (120 mm amplitude, 10,000 kN kN axial load, and 410 mm/s velocity).

D.10 TEST RUN 10

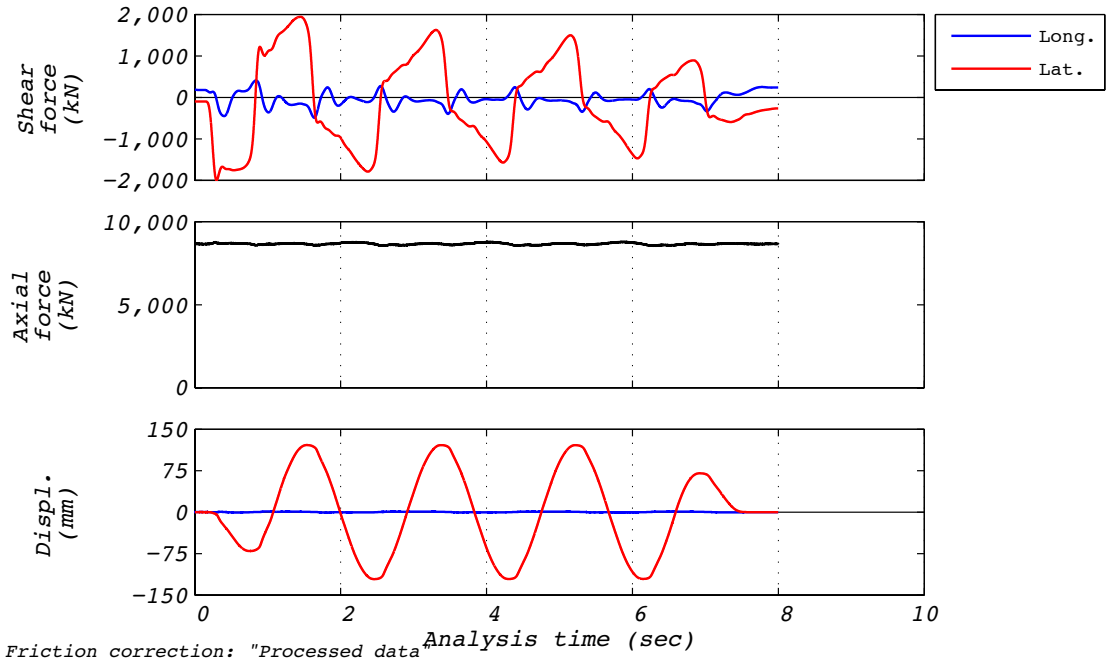

Figure D.10-1 Test run no. 10 time history: Transverse (120 mm amplitude, 8,663 kN kN axial load, and 410 mm/s velocity).

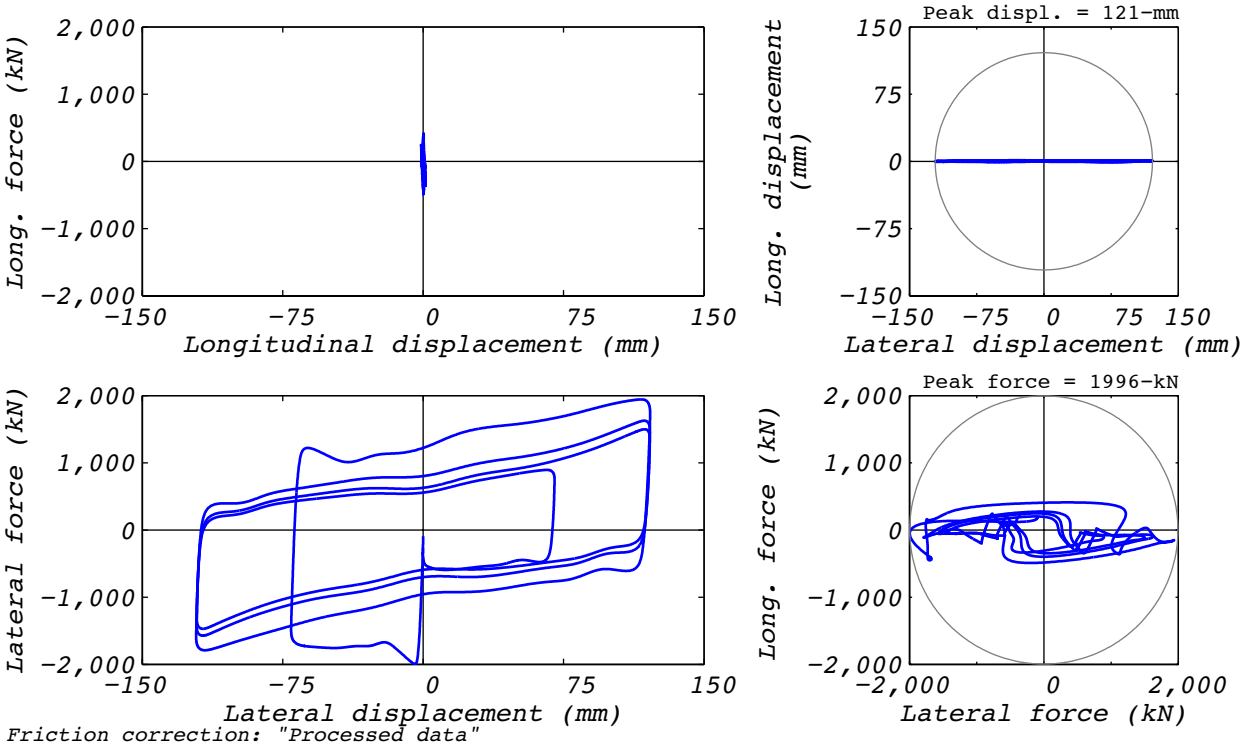

Figure D.10-2 Test run no. 10 hysteresis: Transverse (120 mm amplitude, 8,663 kN kN axial load, and 410 mm/s velocity).

D.11 TEST RUN 11

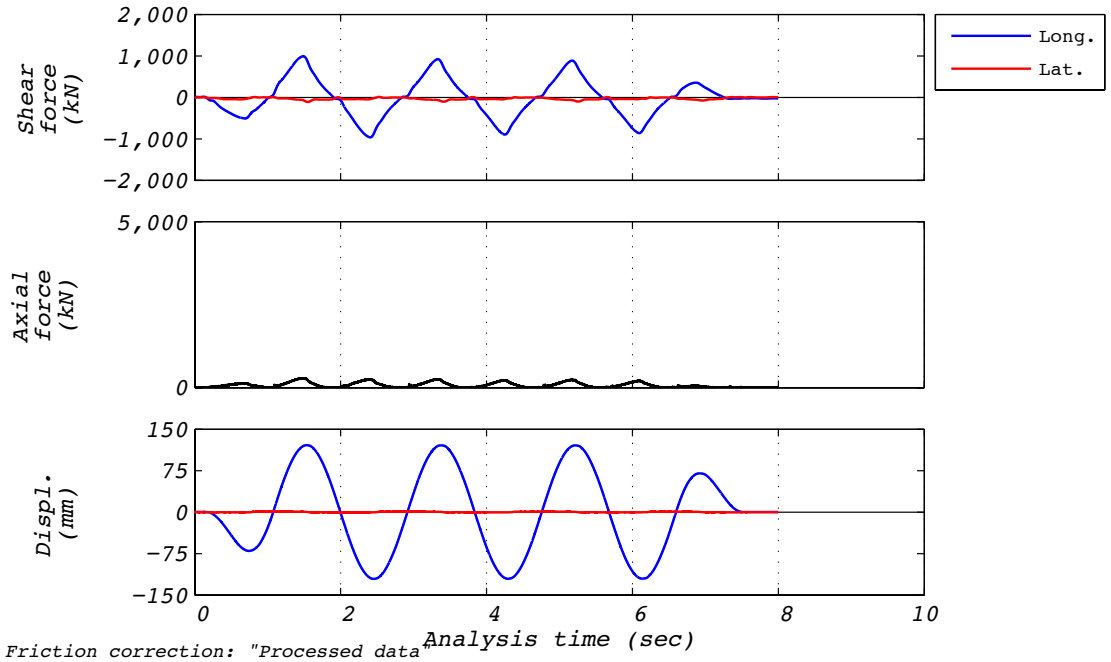

Figure D.11-1 Test run no. 11 time history: Longitudinal (120 mm amplitude, 0 kN axial load, and 410 mm/s velocity).

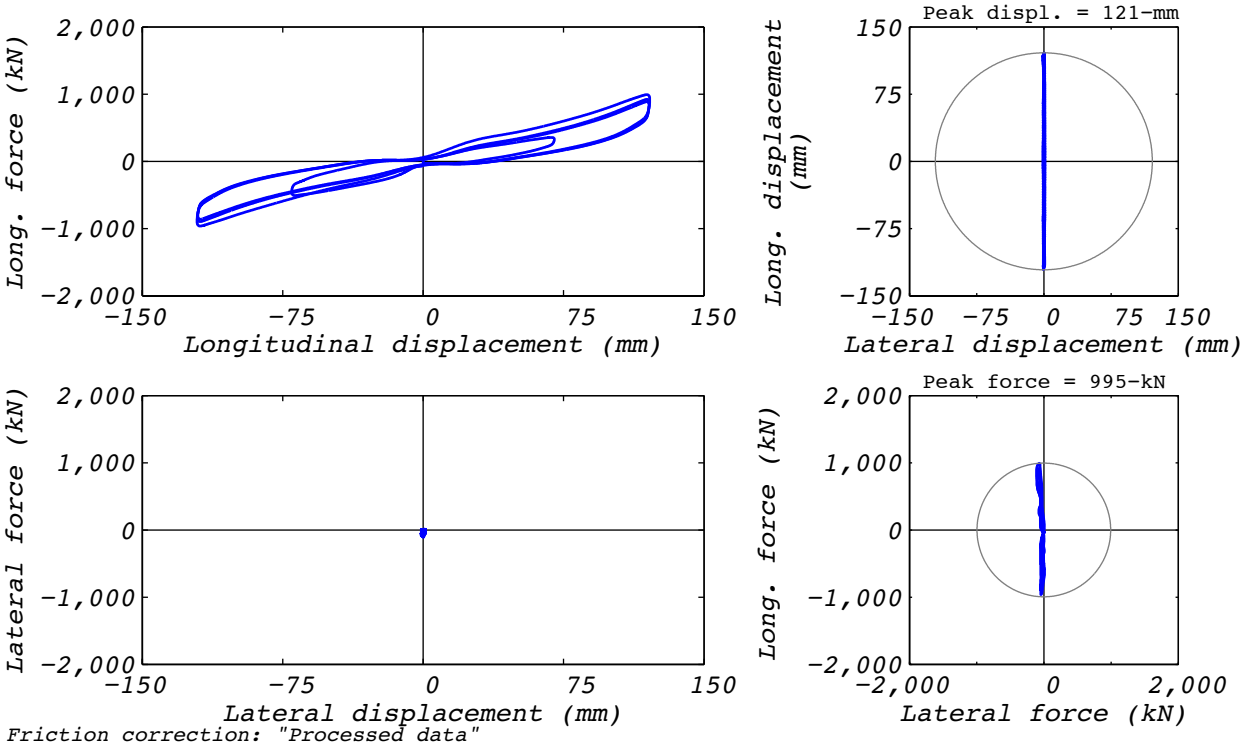

Figure D.11-2 Test run no. 11 hysteresis: Longitudinal (120 mm amplitude, 0 kN axial load, and 410 mm/s velocity).

D.12 TEST RUN 12

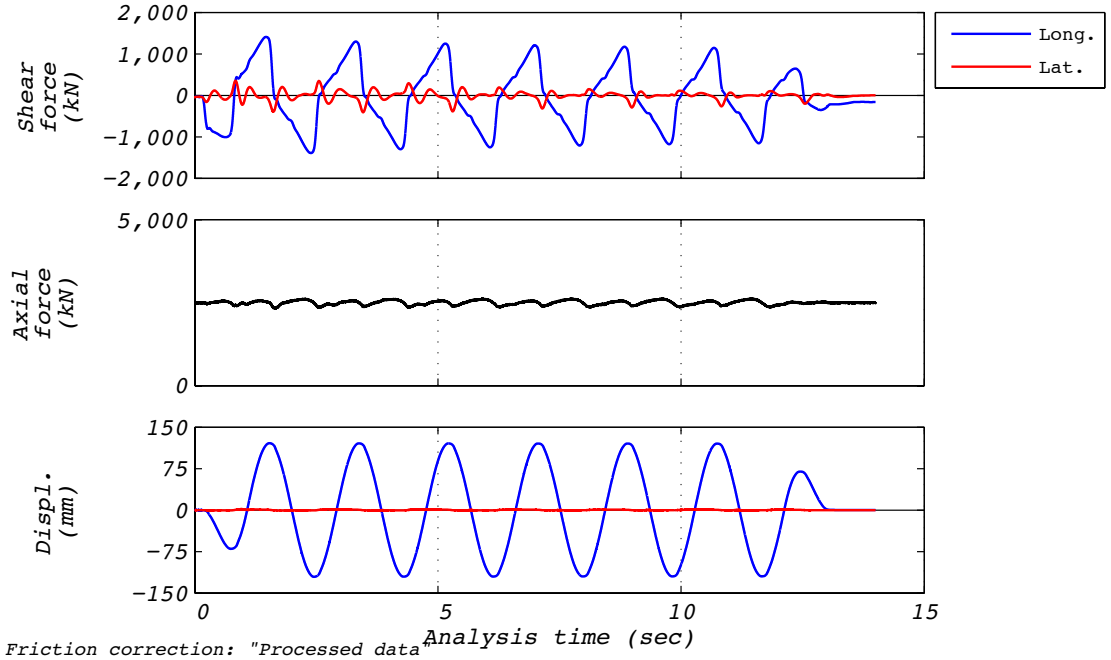

Figure D.12-1 Test run no. 12 time history: Longitudinal (120 mm amplitude, 2,500 kN axial load, and 410 mm/s velocity).

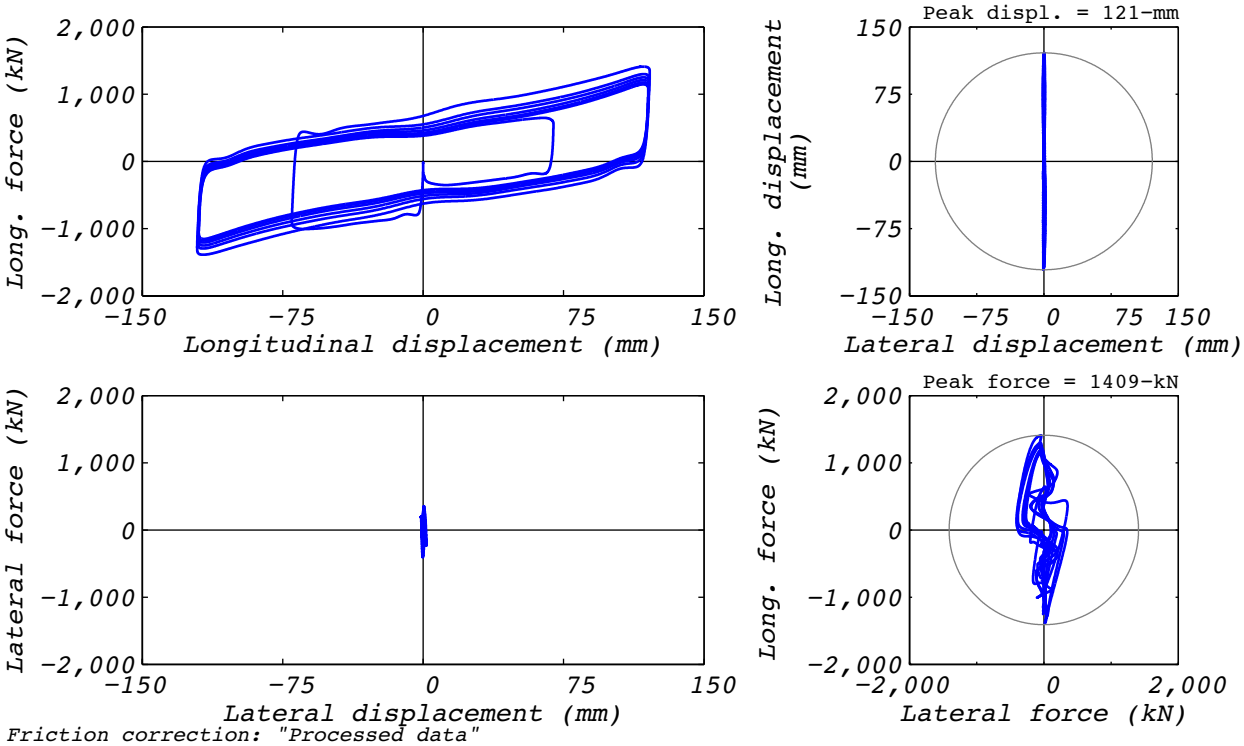

Figure D.12-2 Test run no. 12 hysteresis: Longitudinal (120 mm amplitude, 2,500 kN axial load, and 410 mm/s velocity).

D.13 TEST RUN 13

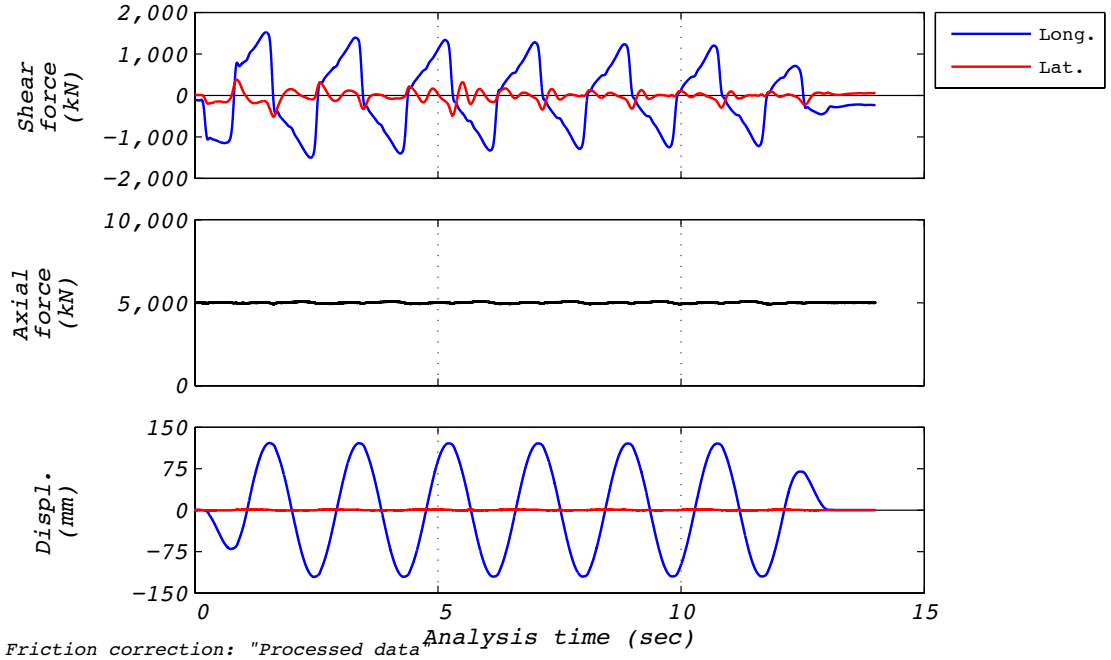

Figure D.13-1 Test run no. 13 time history: Longitudinal (120 mm amplitude, 5,000 kN axial load, and 410 mm/s velocity).

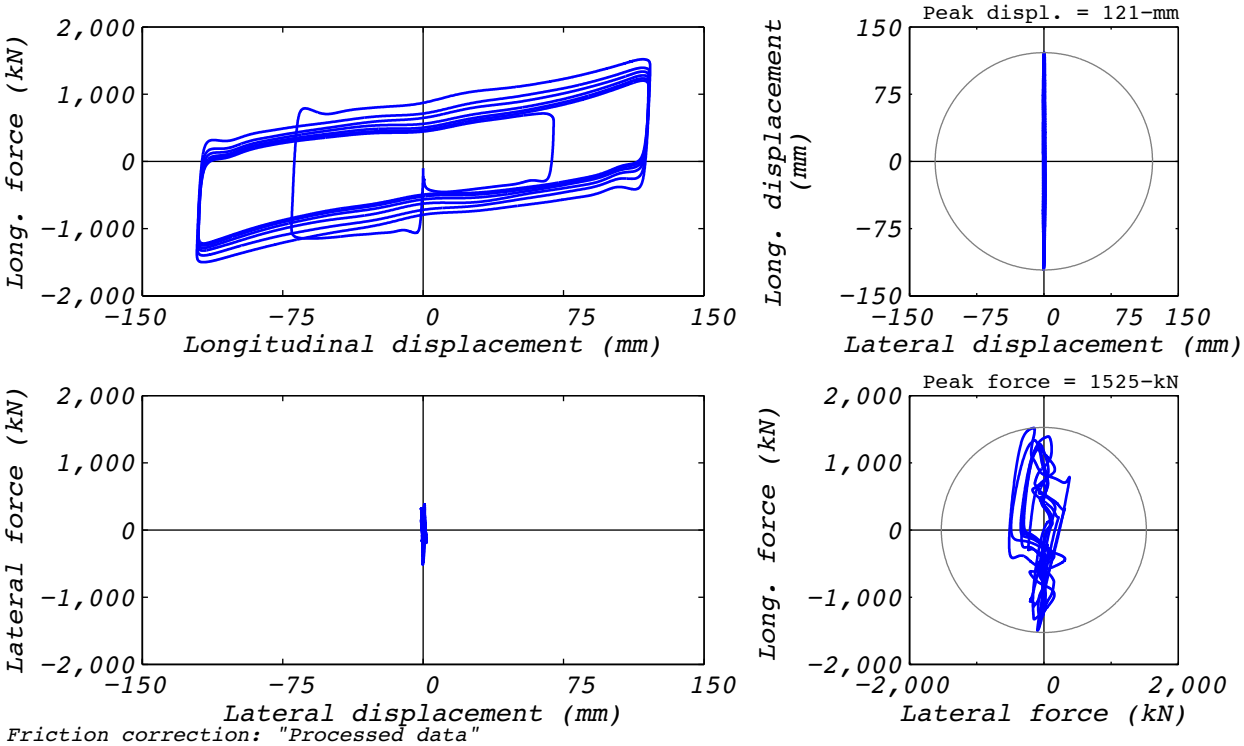

Figure D.13-2 Test run no. 13 hysteresis: Longitudinal (120 mm amplitude, 5,000 kN axial load, and 410 mm/s velocity).

D.14 TEST RUN 14

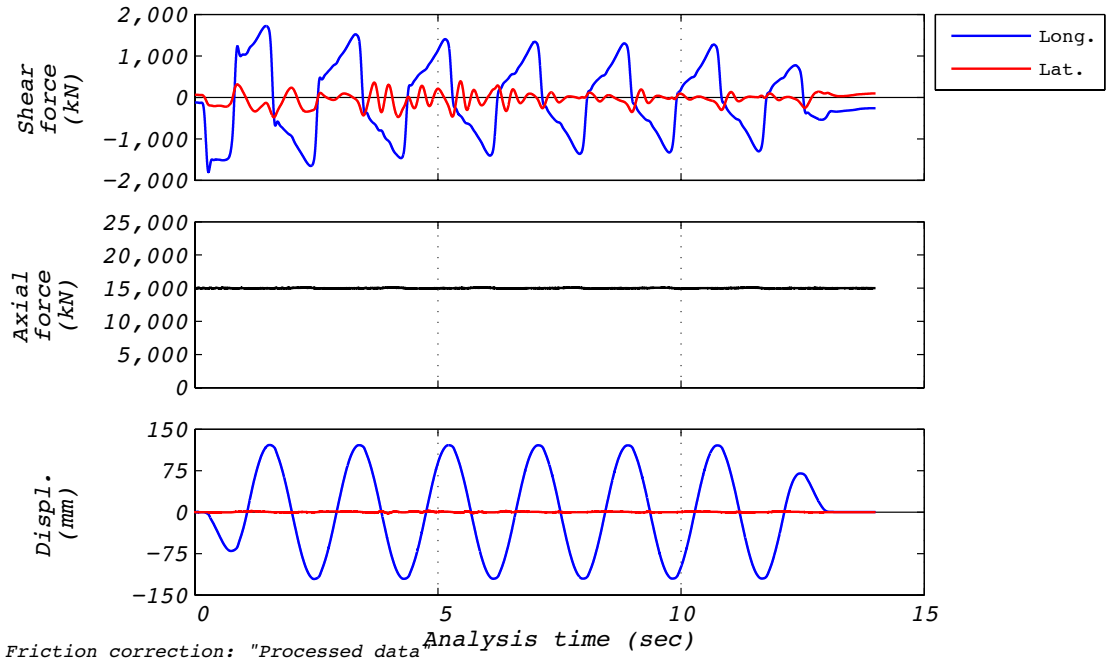

Figure D.14-1 Test run no. 14 time history: Longitudinal (120 mm amplitude, 15,000 kN axial load, and 410 mm/s velocity).

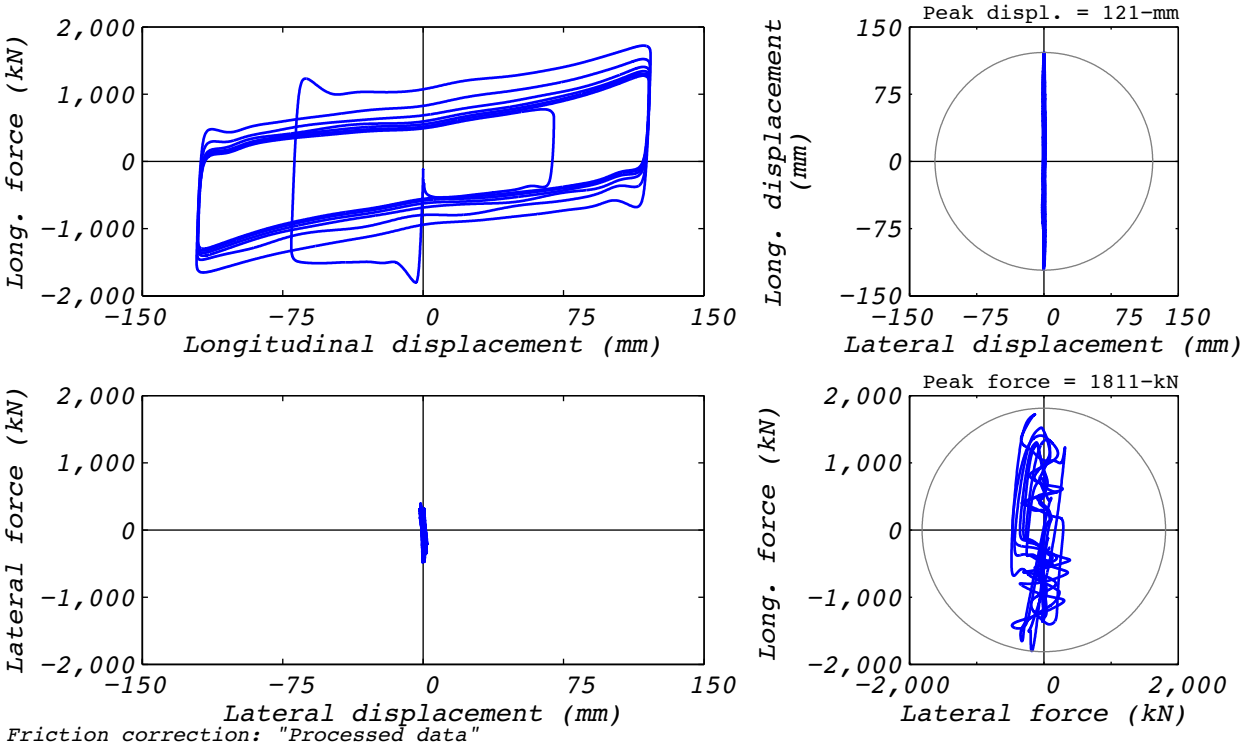

Figure D.14-2 Test run no. 14 hysteresis: Longitudinal (120 mm amplitude, 15,000 kN axial load, and 410 mm/s velocity).

D.15 TEST RUN 15

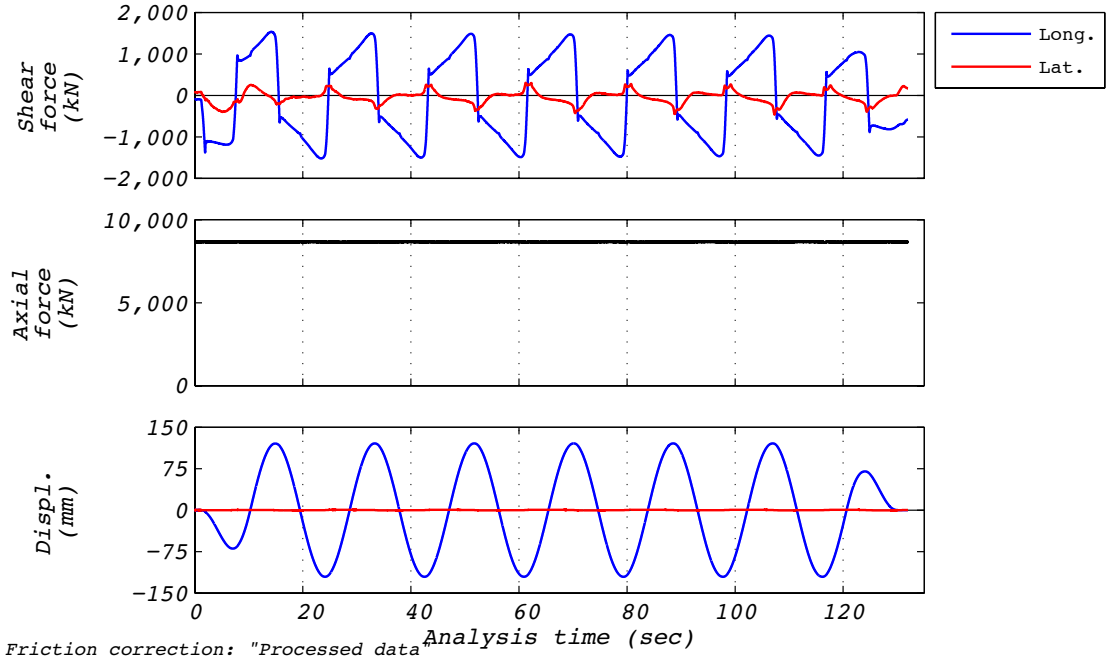

Figure D.15-1 Test run no. 15 time history: Longitudinal (120 mm amplitude, 8,663 kN axial load, and 41 mm/s velocity).

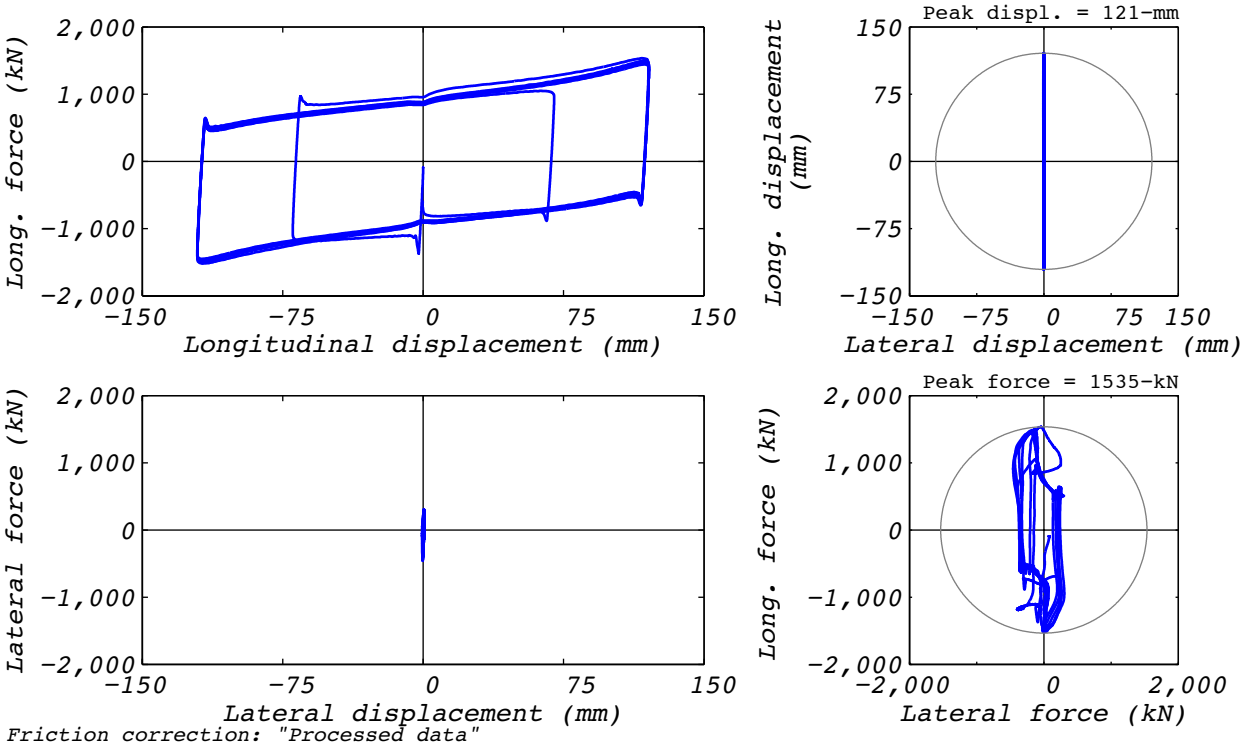

Figure D.15-2 Test run no. 15 hysteresis: Longitudinal (120 mm amplitude, 8,663 kN axial load, and 41 mm/s velocity).

D.16 TEST RUN 16

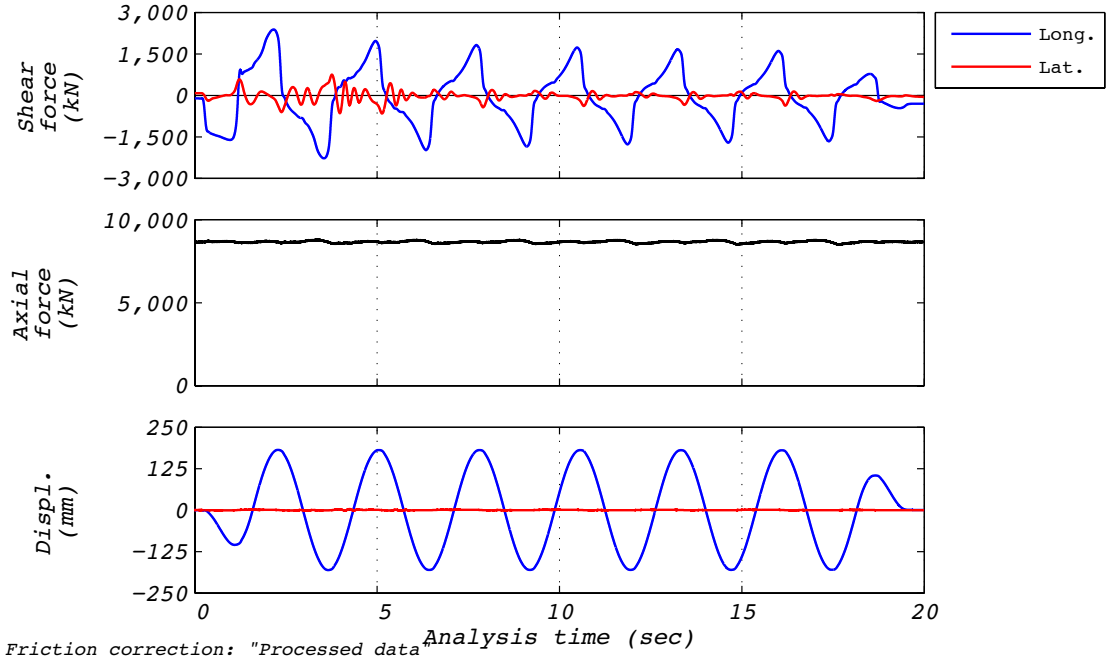

Figure D.16-1 Test run no. 16 time history: Longitudinal (180 mm amplitude, 8,663 kN axial load, and 409 mm/s velocity).

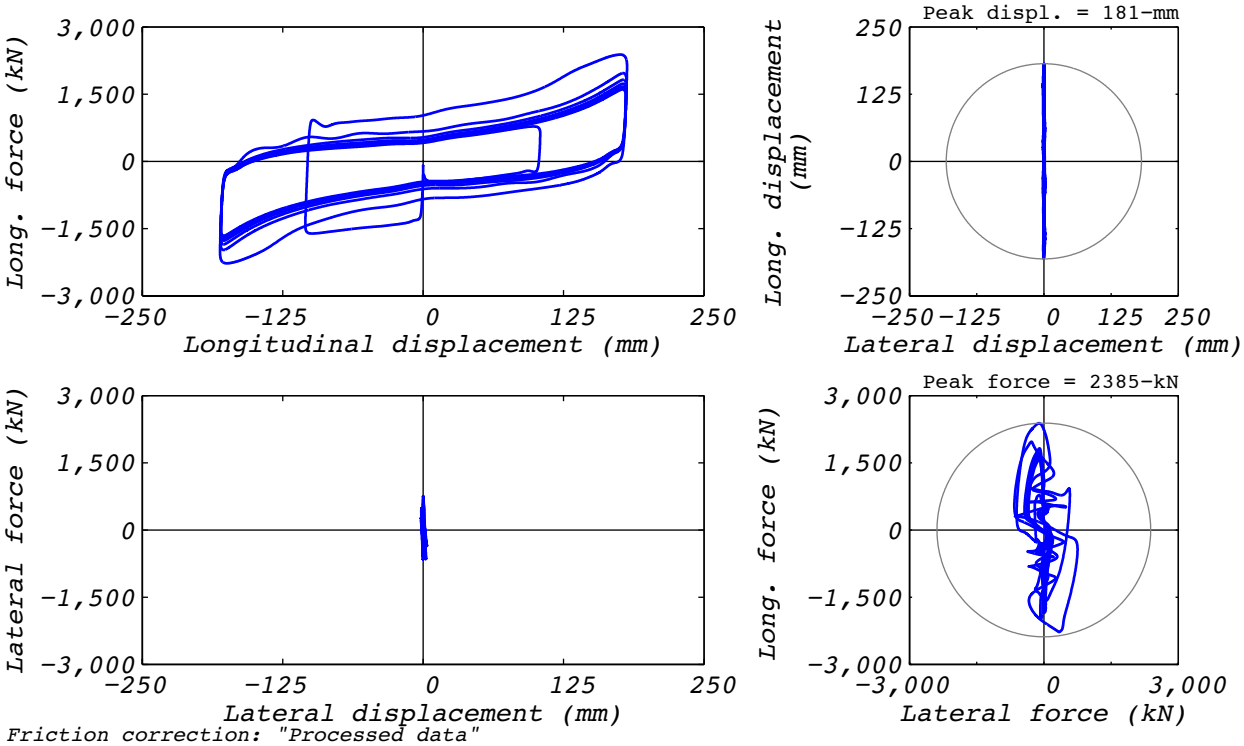

Figure D.16-2 Test run no. 16 hysteresis: Longitudinal (180 mm amplitude, 8,663 kN axial load, and 409 mm/s velocity).

D.17 TEST RUN 20

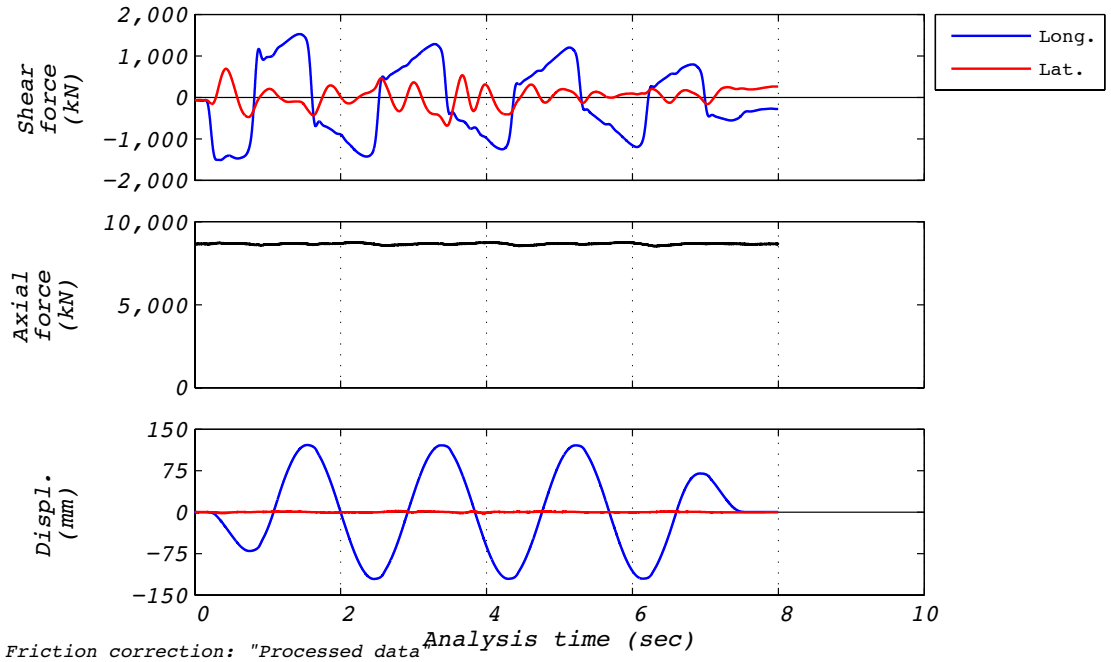

Figure D.17-1 Test run no. 20 time history: Longitudinal (120 mm amplitude, 8,663 kN axial load, and 410 mm/s velocity).

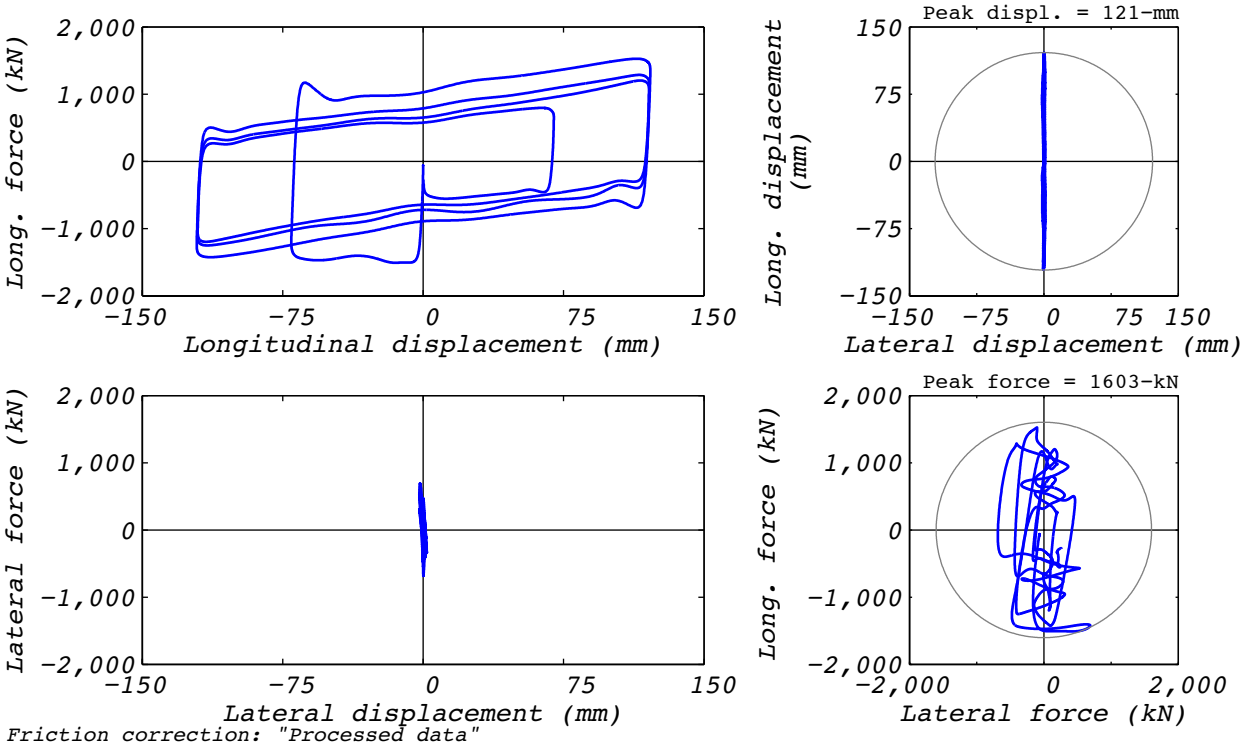

Figure D.17-2 Test run no. 20 hysteresis: Longitudinal (120 mm amplitude, 8,663 kN axial load, and 410 mm/s velocity).

D.18 TEST RUN 24

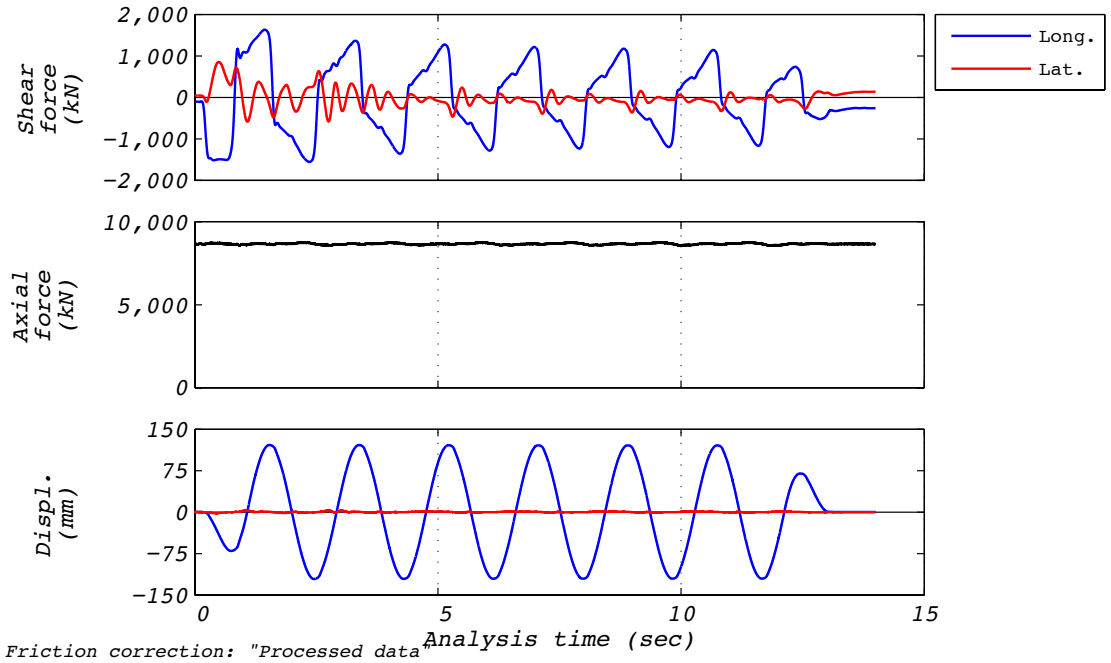

Figure D.18-1 Test run no. 24 time history: Longitudinal (120 mm amplitude, 8,663 kN axial load, and 410 mm/s velocity).

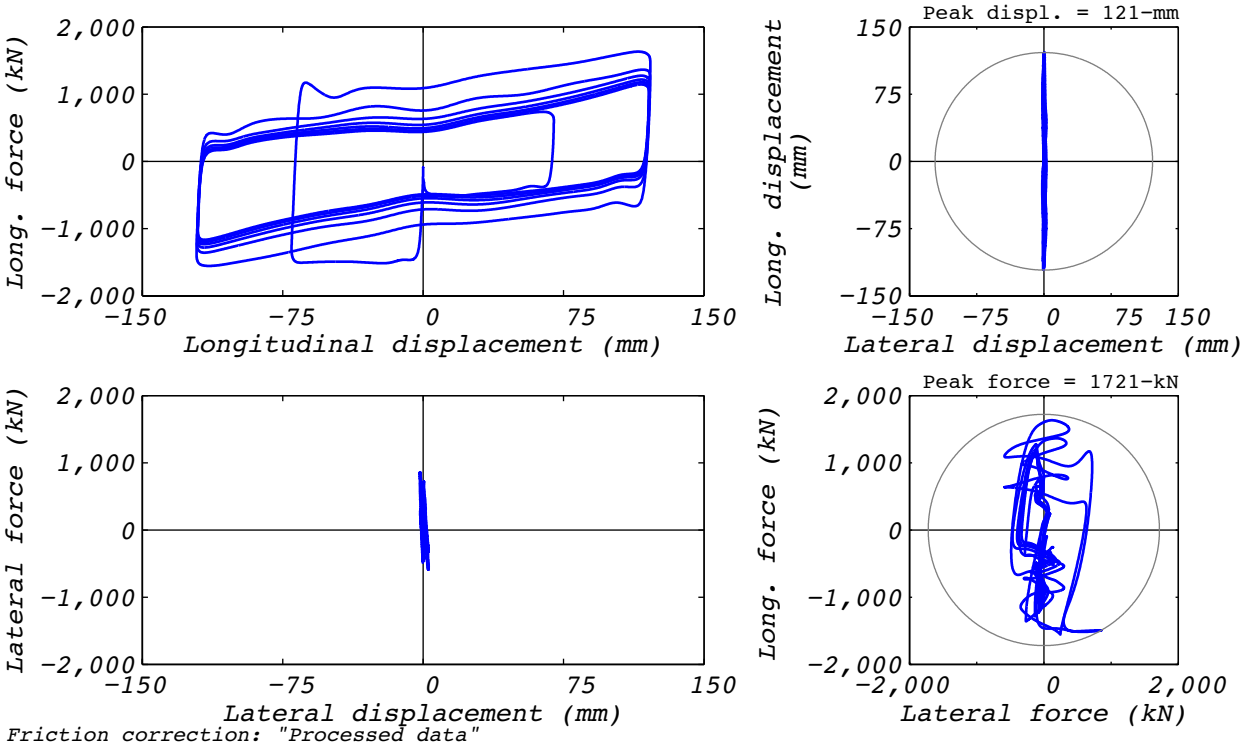

Figure D.18-2 Test run no. 24 hysteresis: Longitudinal (120 mm amplitude, 8,663 kN axial load, and 410 mm/s velocity).

D.19 TEST RUN 25

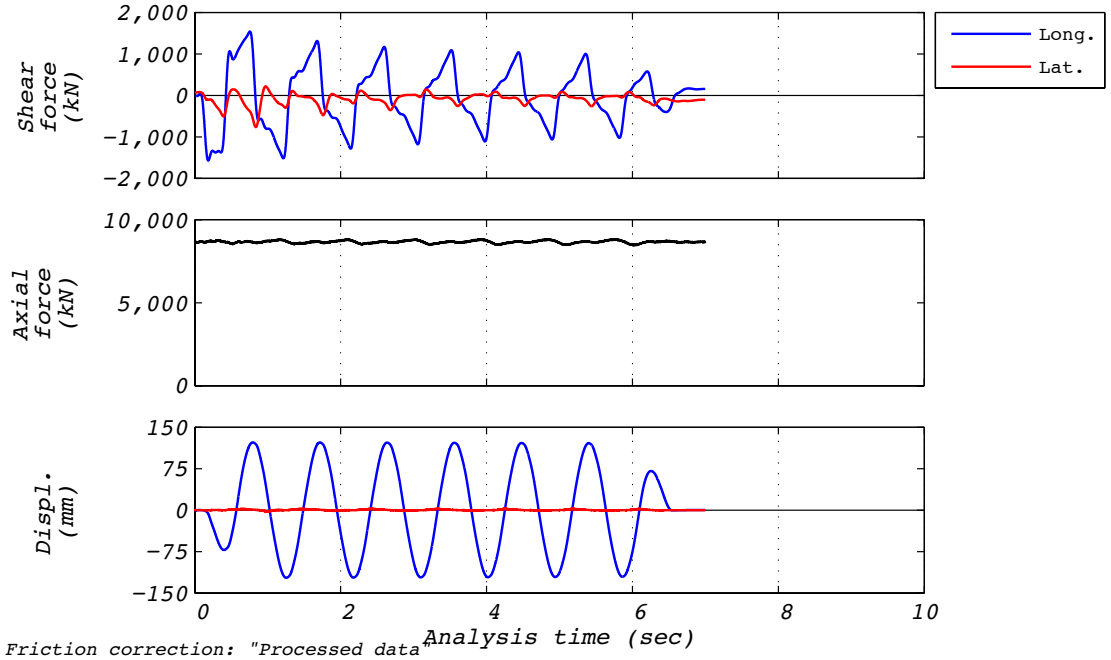

Figure D.19-1 Test run no. 25 time history: Longitudinal (120 mm amplitude, 8,663 kN axial load, and 820 mm/s velocity).

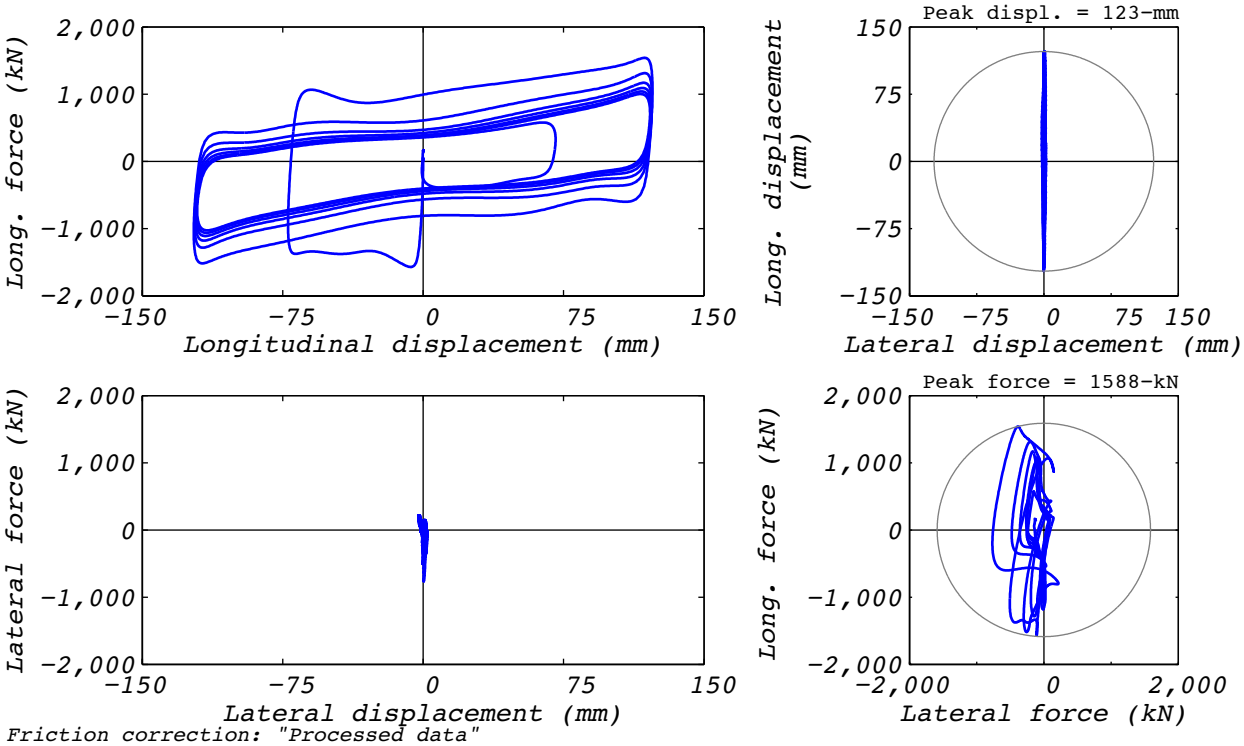

Figure D.19-2 Test run no. 25 hysteresis: Longitudinal (120 mm amplitude, 8,663 kN axial load, and 820 mm/s velocity).

D.20 TEST RUN 26

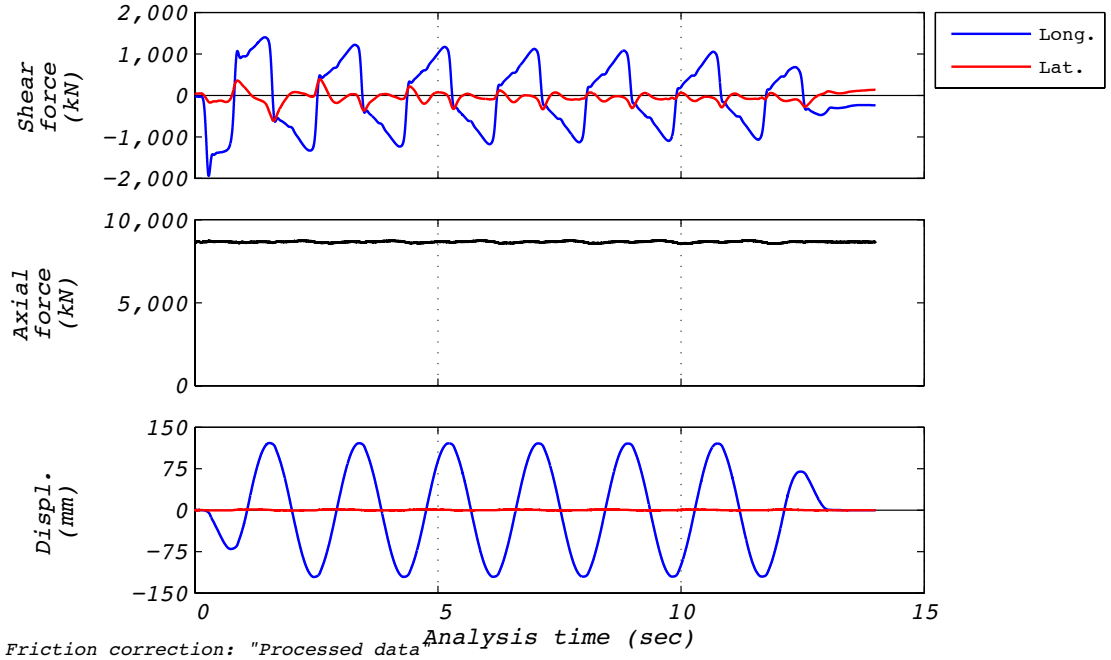

Figure D.20-1 Test run no. 26 time history: Longitudinal (120 mm amplitude, 8,663 kN axial load, and 410 mm/s velocity).

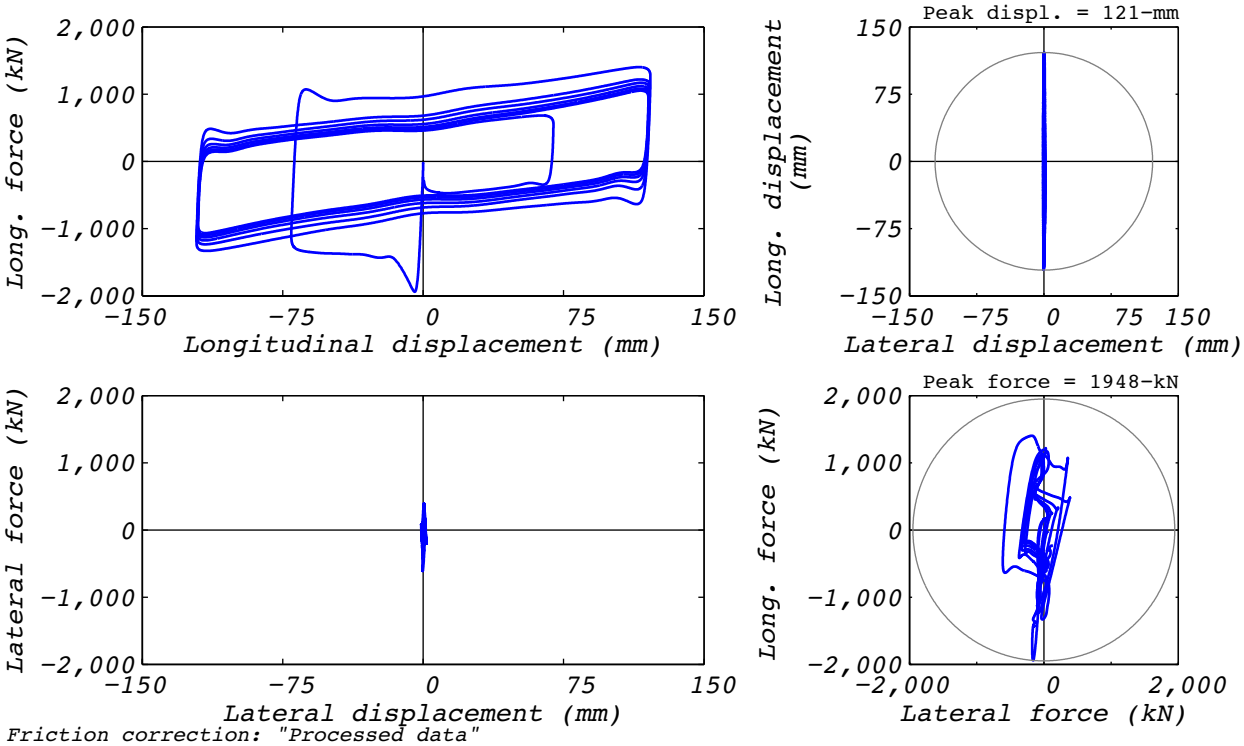

Figure D.20-2 Test run no. 26 hysteresis: Longitudinal (120 mm amplitude, 8,663 kN axial load, and 410 mm/s velocity).

D.21 TEST RUN 27

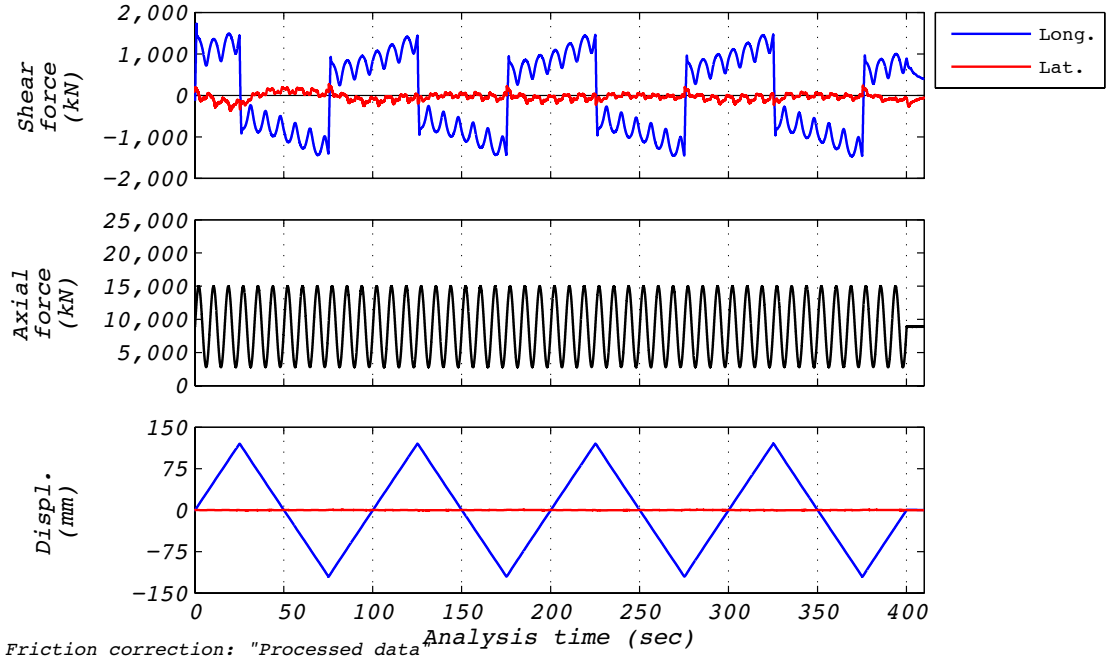

Figure D.21-1 Test run no. 27 time history: Longitudinal (120 mm amplitude, varying axial load, and 410 mm/s velocity).

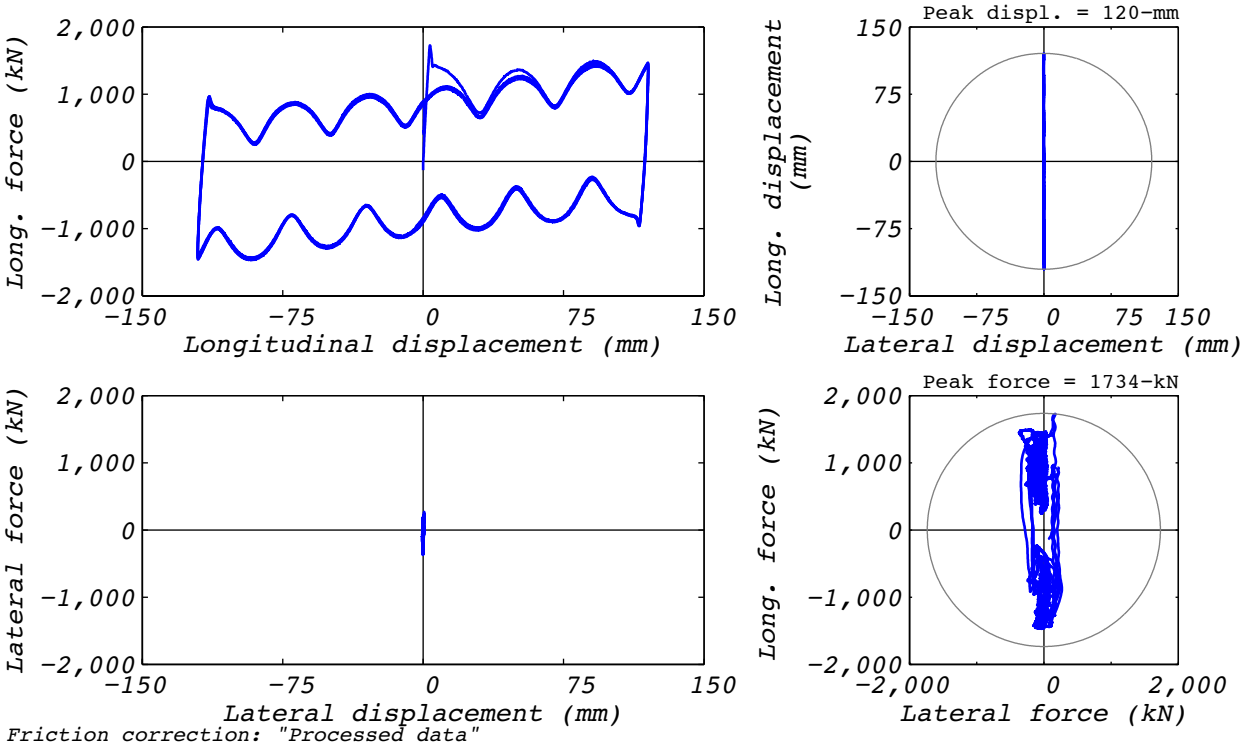

Figure D.21-2 Test run no. 27 hysteresis: Longitudinal (120 mm amplitude, varying axial load, and 410 mm/s velocity).

D.22 TEST RUN 28

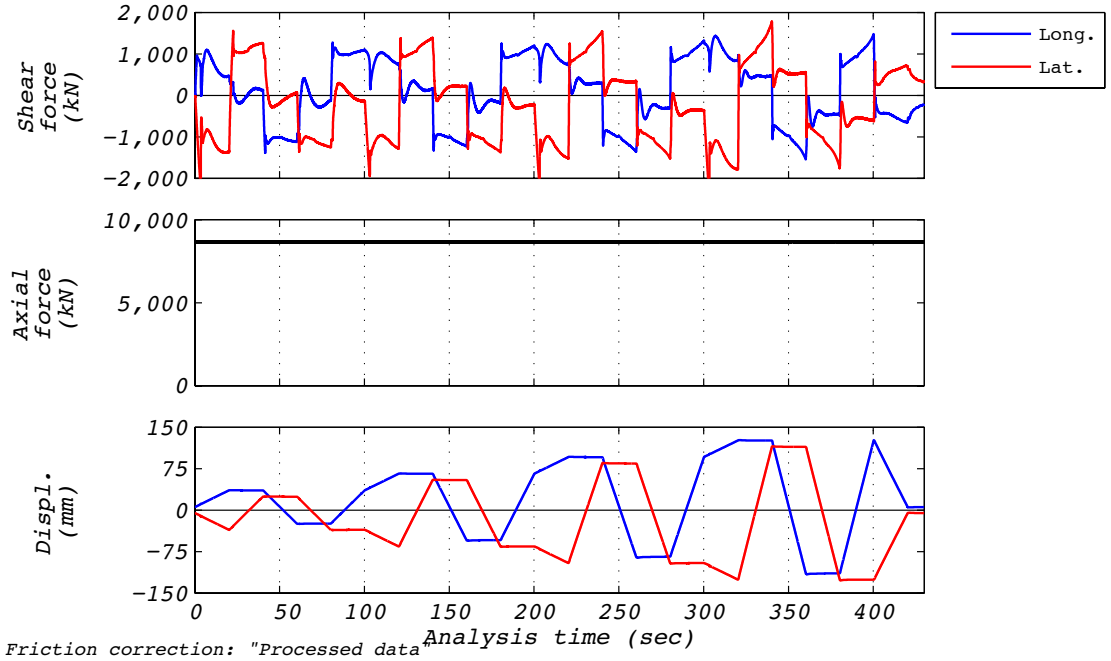

Figure D.22-1 Test run no. 28 time history: Square orbit (Varying amplitude, 8,663 kN axial load, and varying velocity).

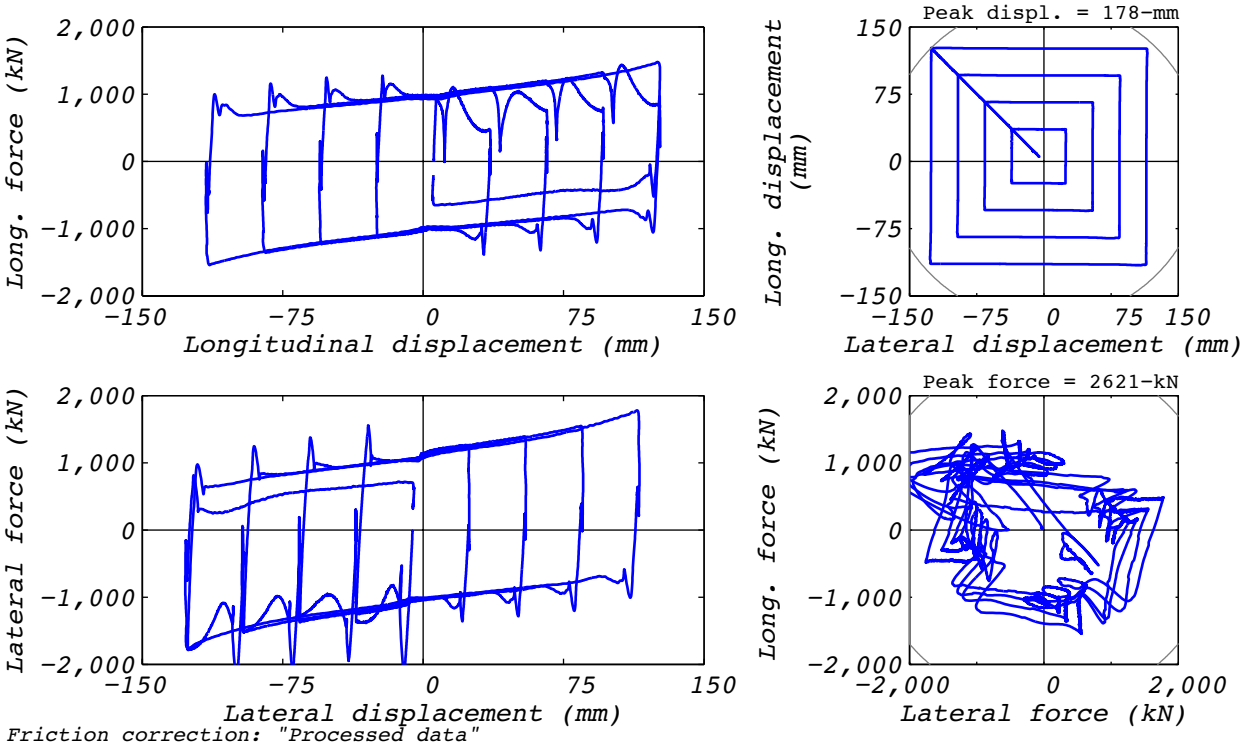

Figure D.22-2 Test run no. 28 hysteresis: Square orbit (Varying amplitude, 8,663 kN axial load, and varying velocity).

D.23 TEST RUN 29

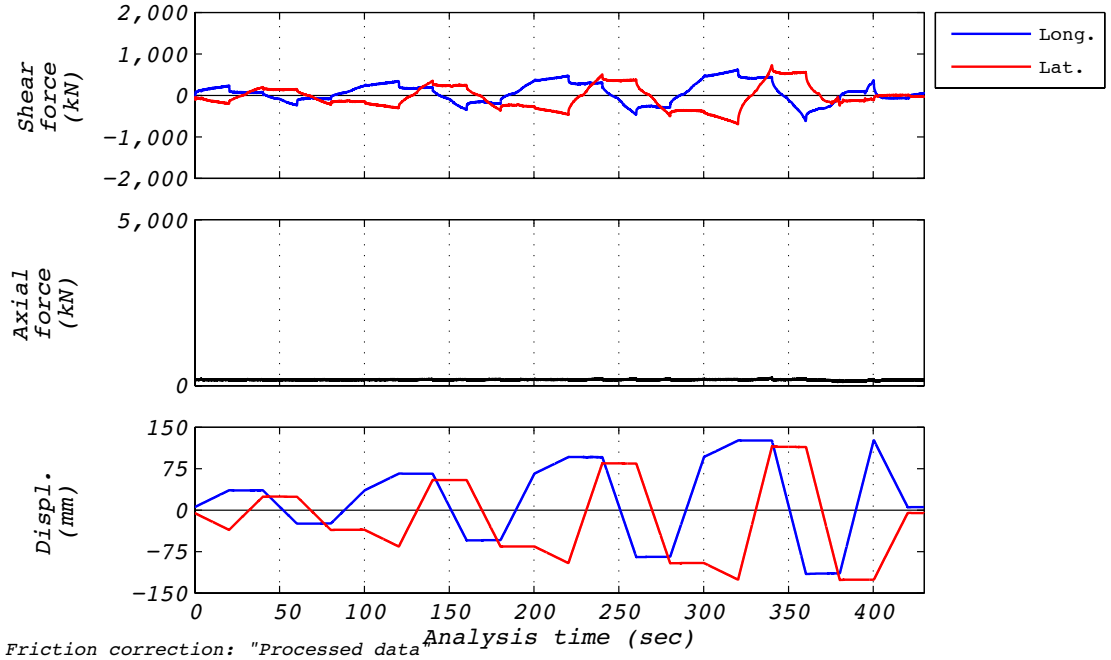

Figure D.23-1 Test run no. 29 time history: Square orbit (Varying amplitude, 178 kN axial load, and varying velocity).

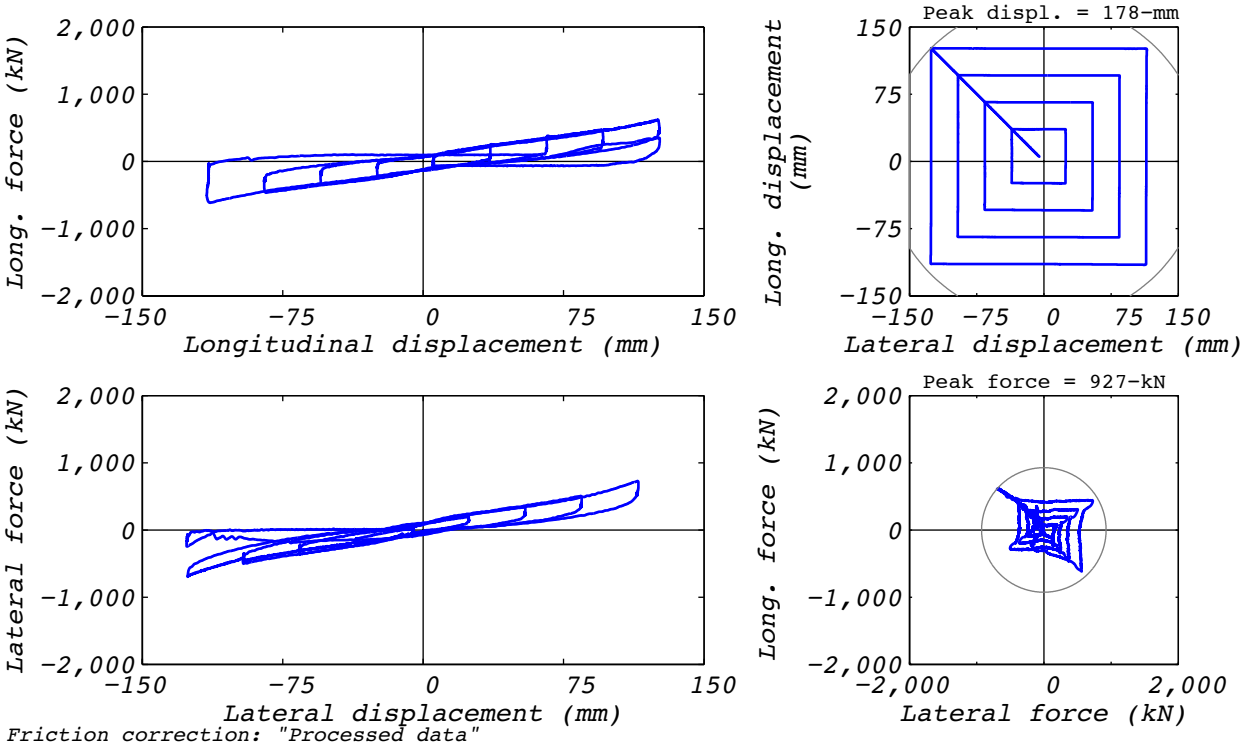

Figure D.23-2 Test run no. 29 hysteresis: Square orbit (Varying amplitude, 178 kN axial load, and varying velocity).

D.24 TEST RUN 30

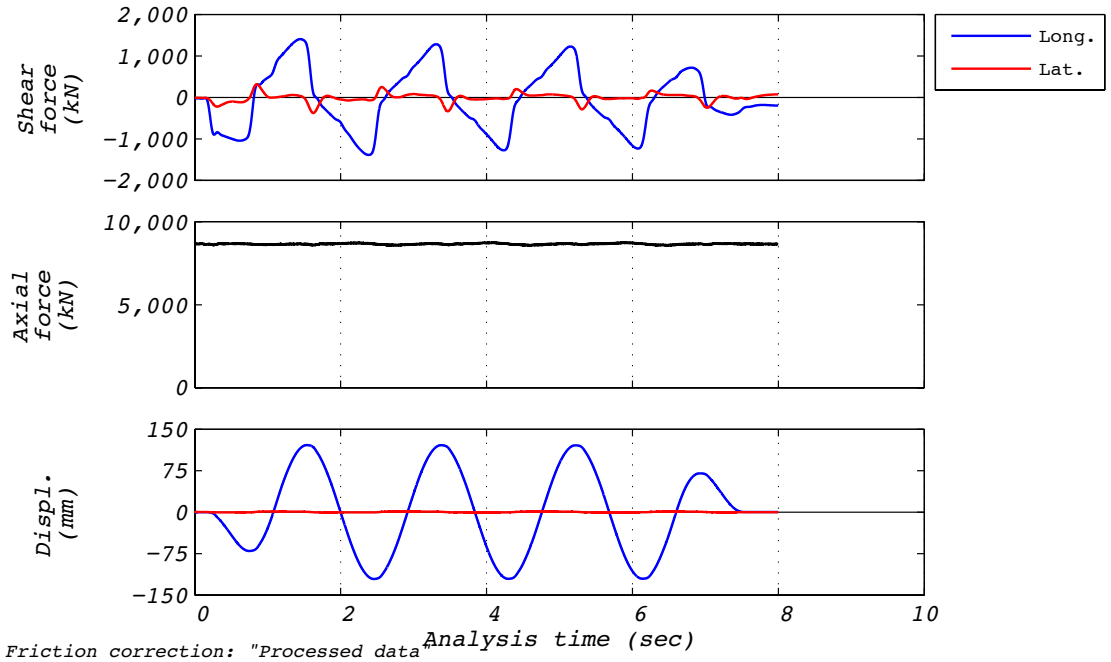

Figure D.24-1 Test run no. 30 time history: Longitudinal (120 mm amplitude, 8,663 kN axial load, and 410 mm/s velocity).

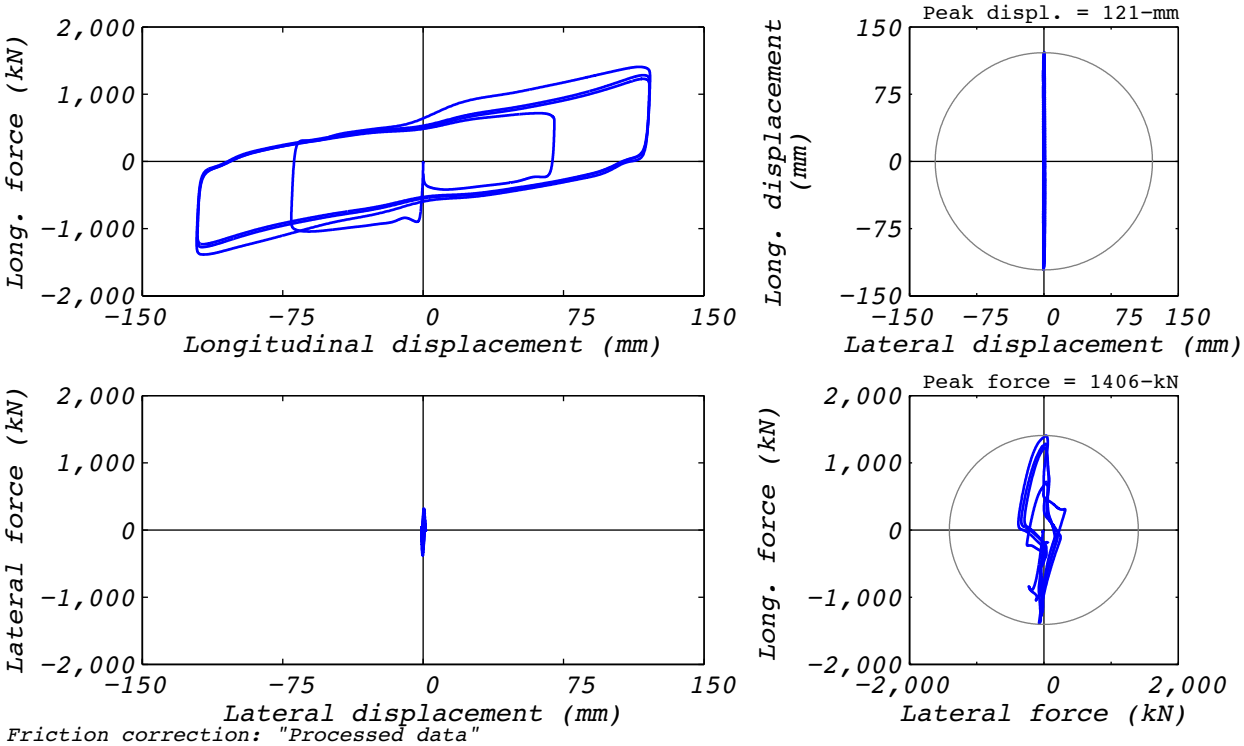

Figure D.24-2 Test run no. 30 hysteresis: Longitudinal (120 mm amplitude, 8,663 kN axial load, and 410 mm/s velocity).

D.25 TEST RUN 31

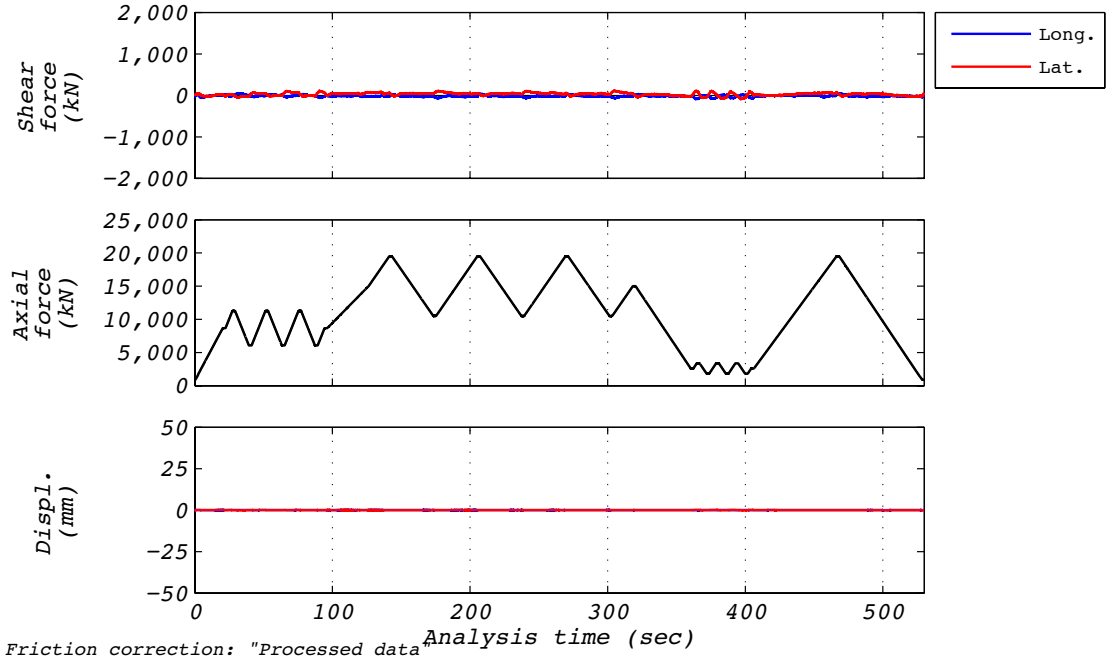

Figure D.25-1 Test run no. 31 time history: Axial (0 mm amplitude and varying axial load).

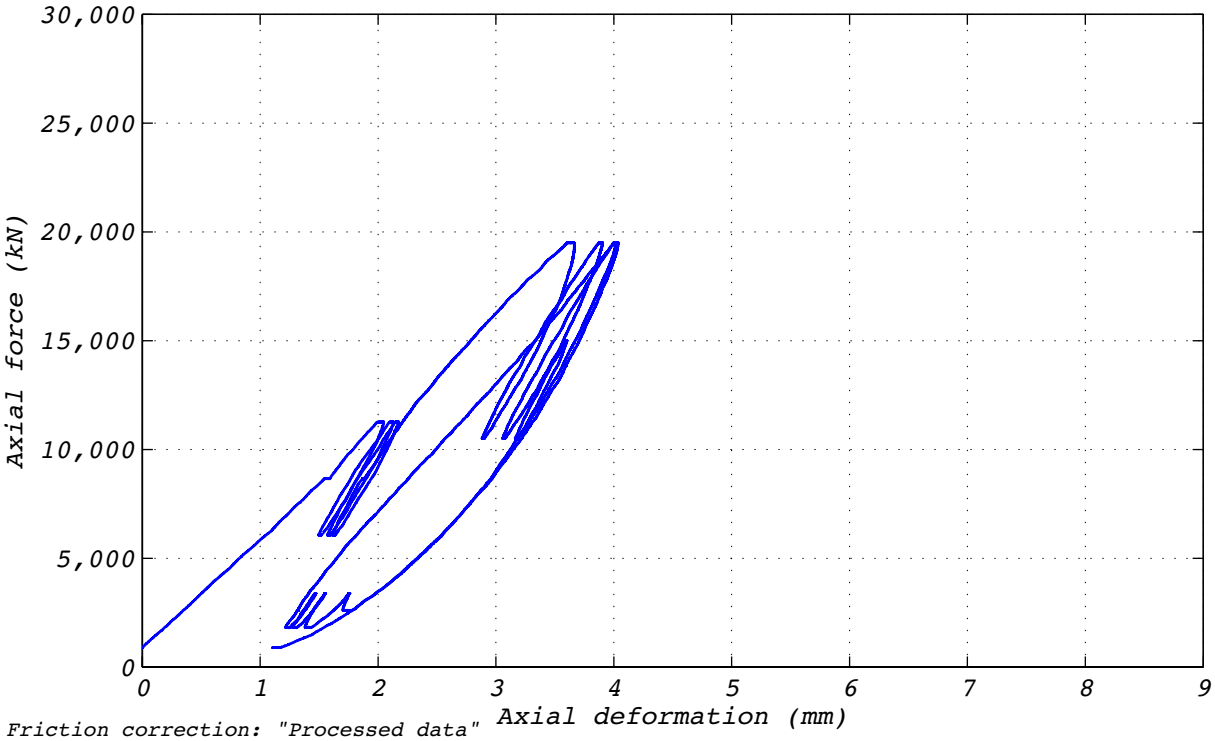

Figure D.25-2 Test run no. 31 hysteresis: Axial (0 mm amplitude and varying axial load).

D.26 TEST RUN 32

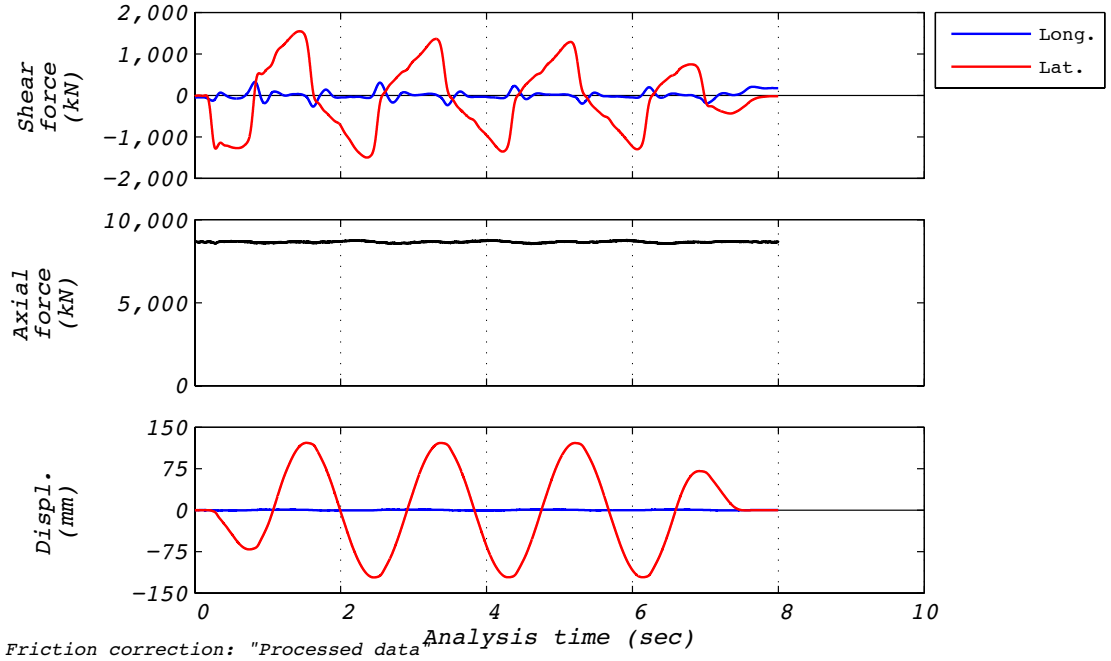

Figure D.26-1 Test run no. 32 time history: Transverse (120 mm amplitude, 8,663 kN axial load, and 410 mm/s velocity).

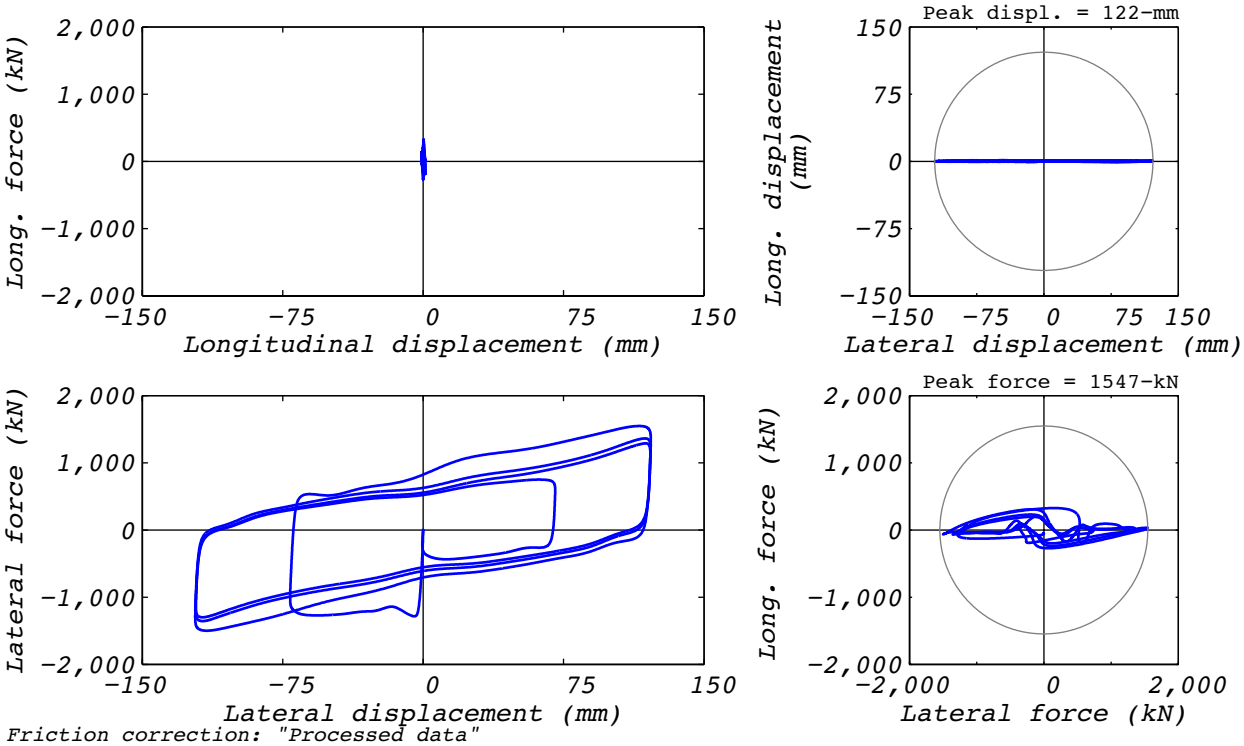

Figure D.26-2 Test run no. 32 hysteresis: Transverse (120 mm amplitude, 8,663 kN axial load, and 410 mm/s velocity).

D.27 TEST RUN 33

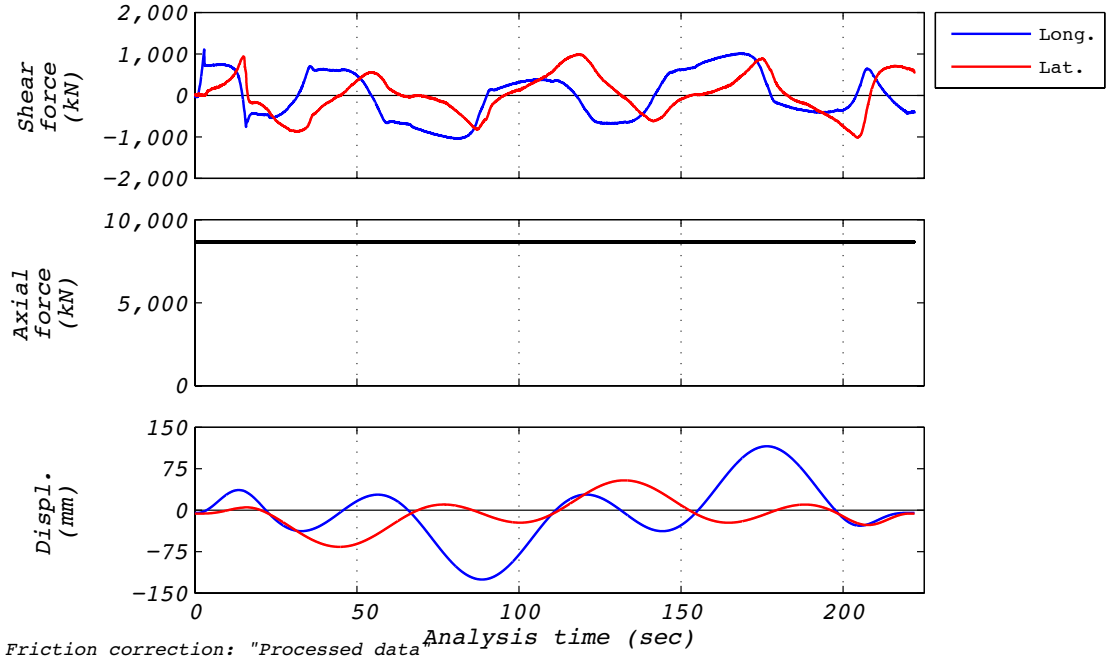

Figure D.27-1 Test run no. 33 time history: Clover leaf orbit (120 mm amplitude, 8,663 kN axial load, and varying velocity).

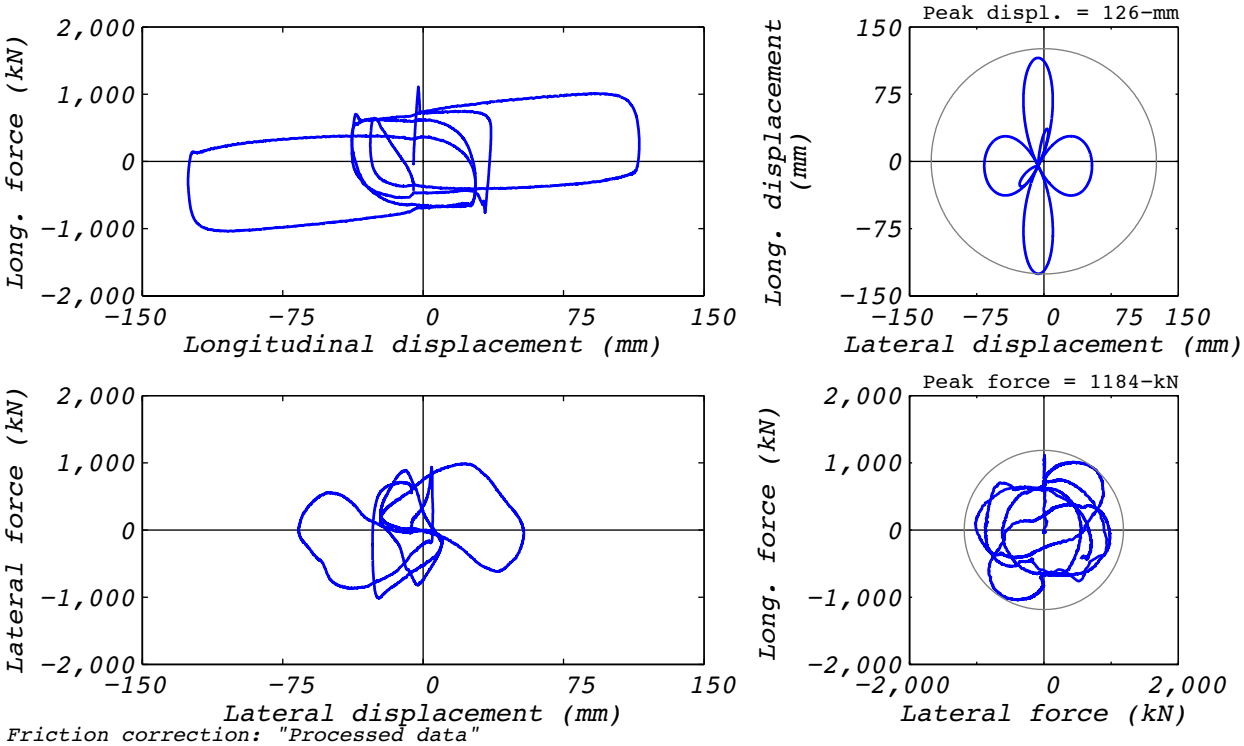

Figure D.27-2 Test run no. 33 hysteresis: Clover leaf orbit (120 mm amplitude, 8,663 kN axial load, and varying velocity).

D.28 TEST RUN 34

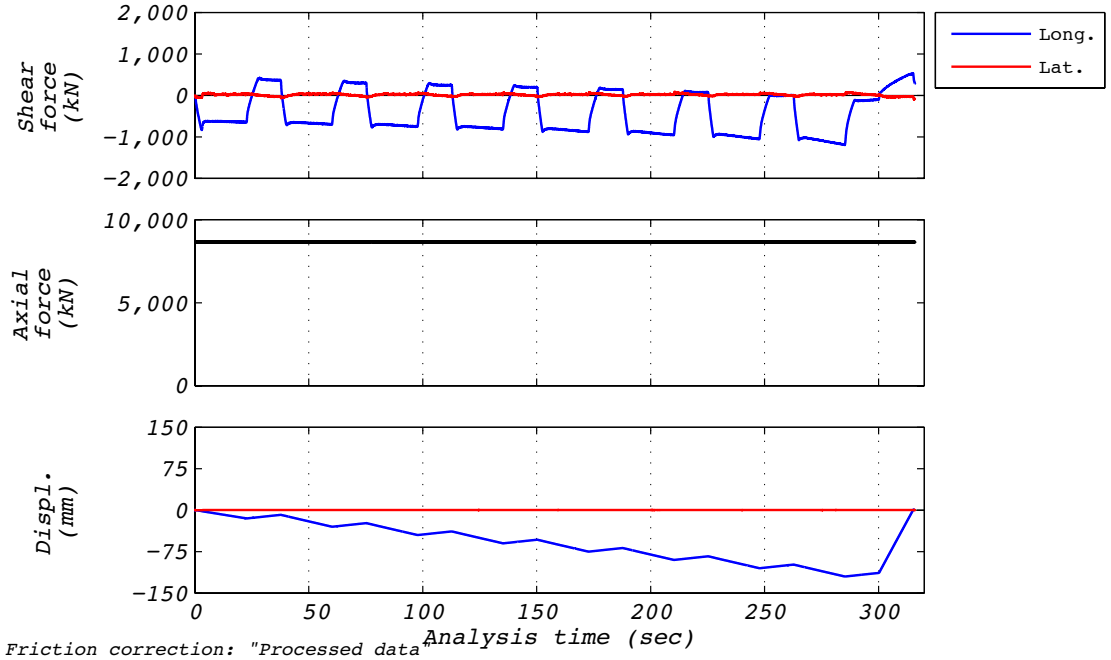

Figure D.28-1 Test run no. 34 time history: Longitudinal (120 mm amplitude, 8,663 kN axial load).

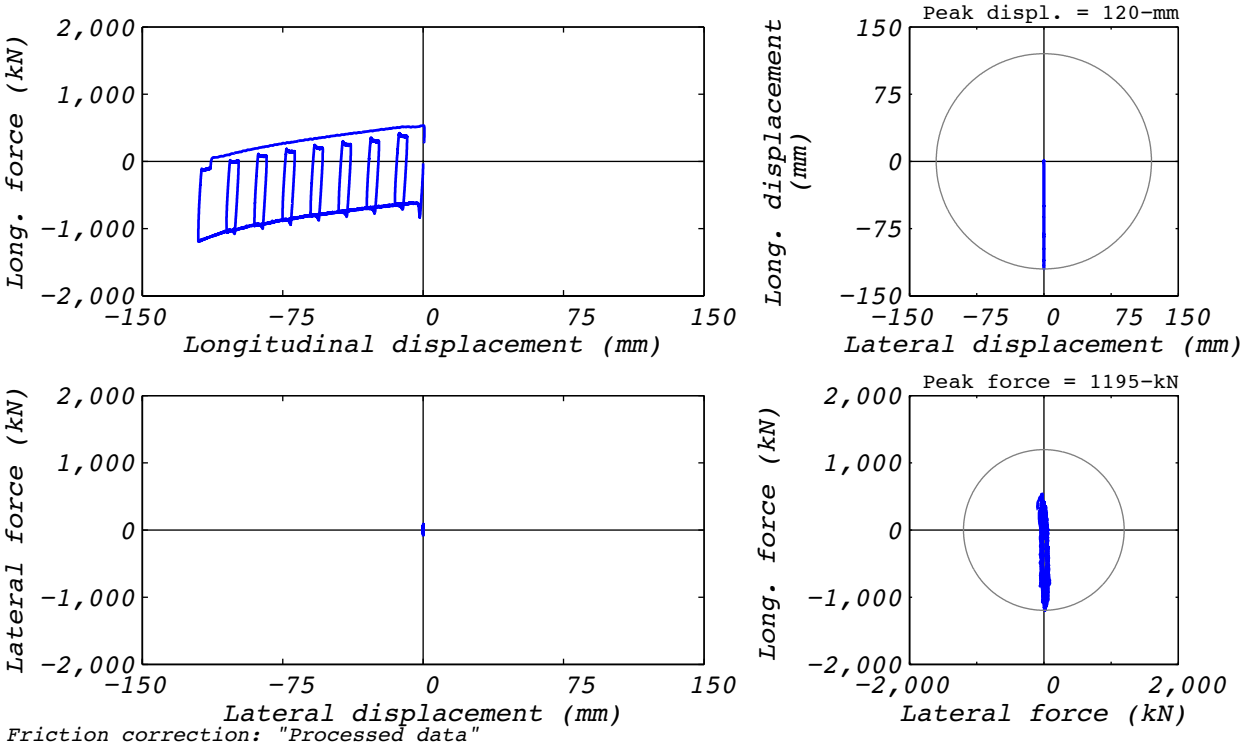

Figure D.28-2 Test run no. 34 hysteresis: Longitudinal (120 mm amplitude, 8,663 kN axial load).

D.29 TEST RUN 35

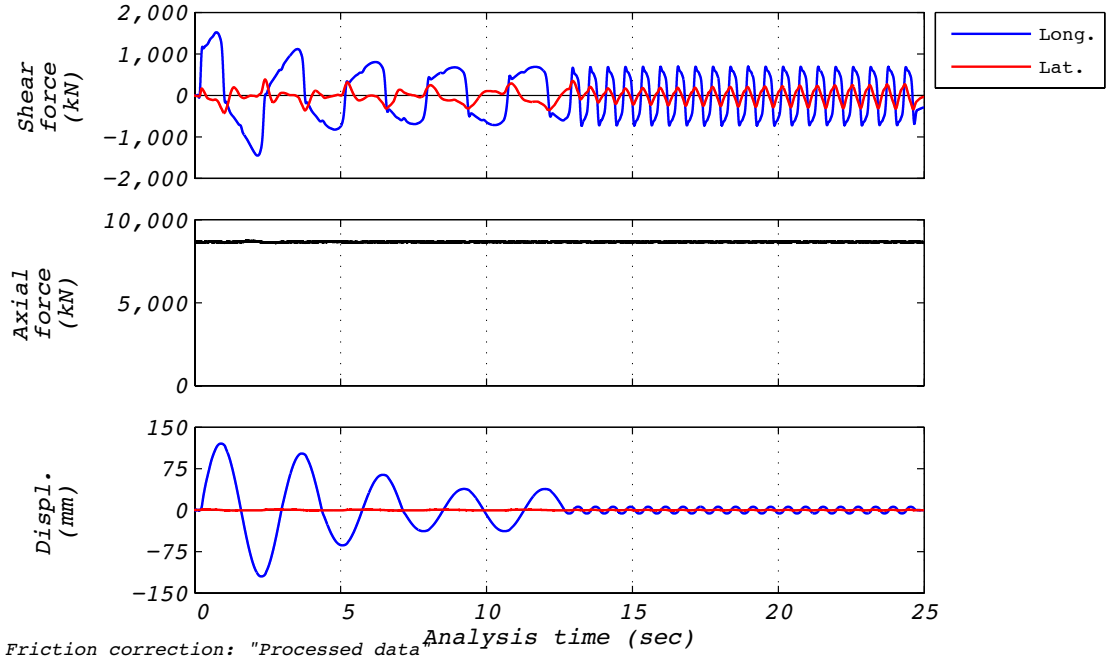

Figure D.29-1 Test run no. 35 time history: Longitudinal (varying amplitude, 8,663 kN axial load, and varying frequency).

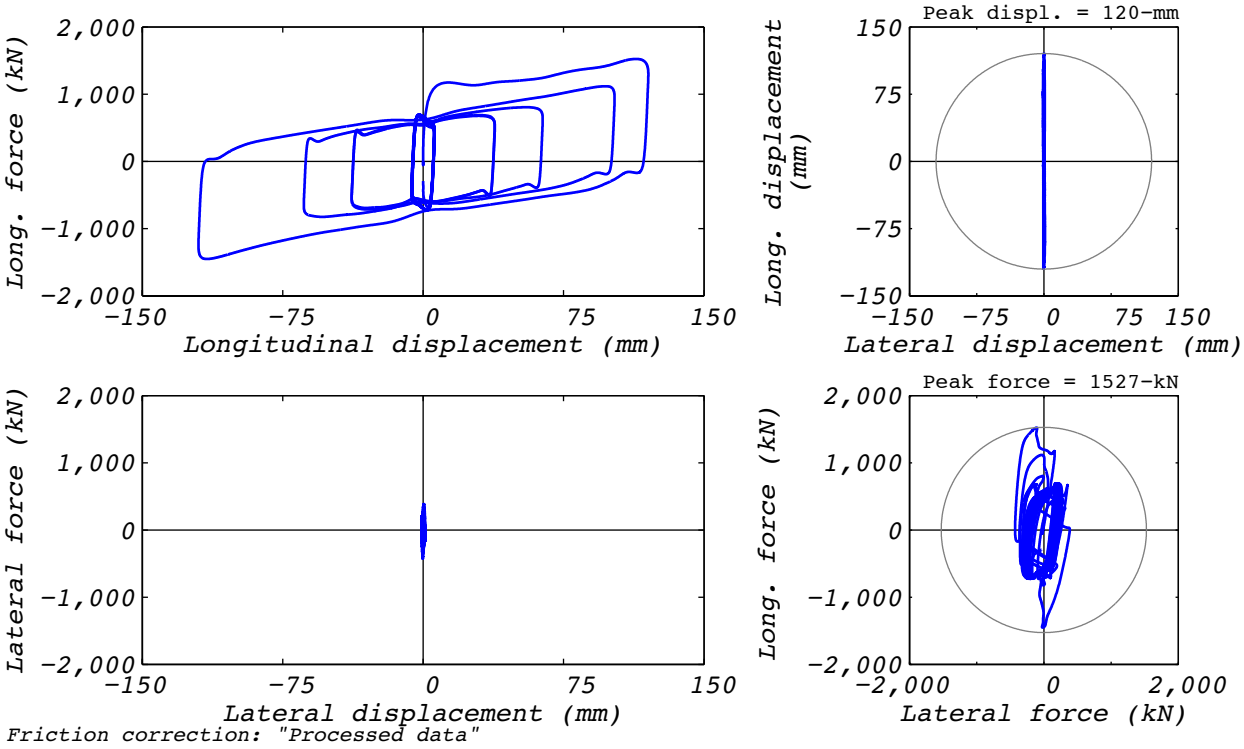

Figure D.29-2 Test run no. 35 hysteresis: Longitudinal (varying amplitude, 8,663 kN axial load, and varying frequency).

D.30 TEST RUN 36

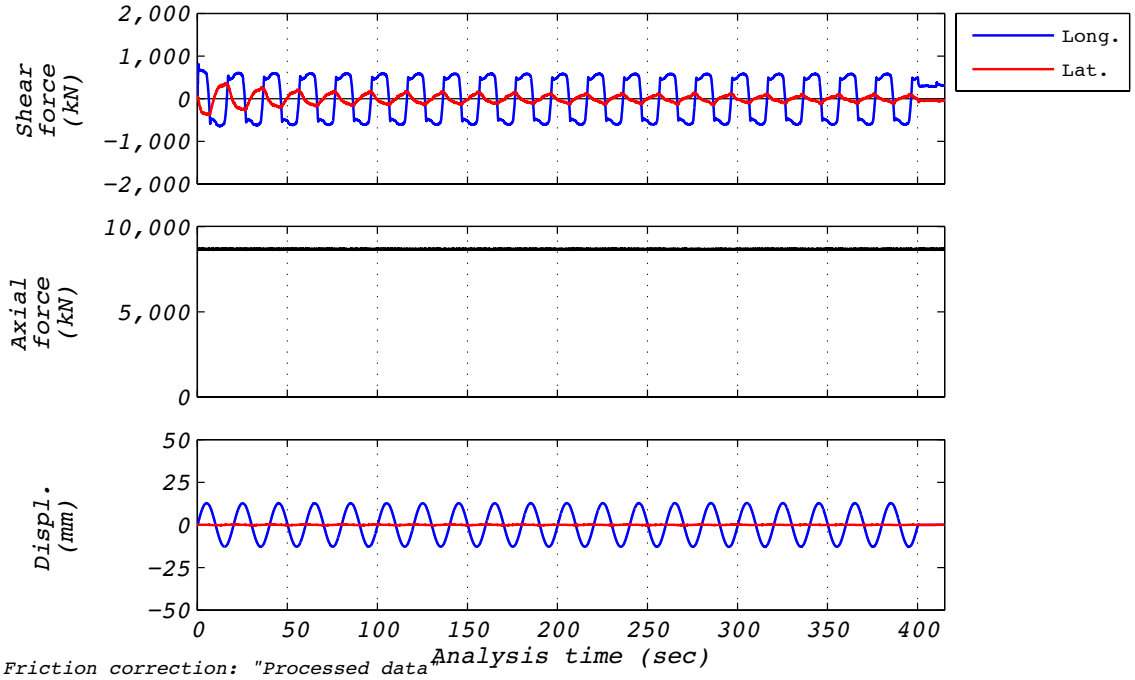

Figure D.30-1 Test run no. 36 time history: Longitudinal (13 mm amplitude, 8,663 kN axial load, and 4 mm/s velocity).

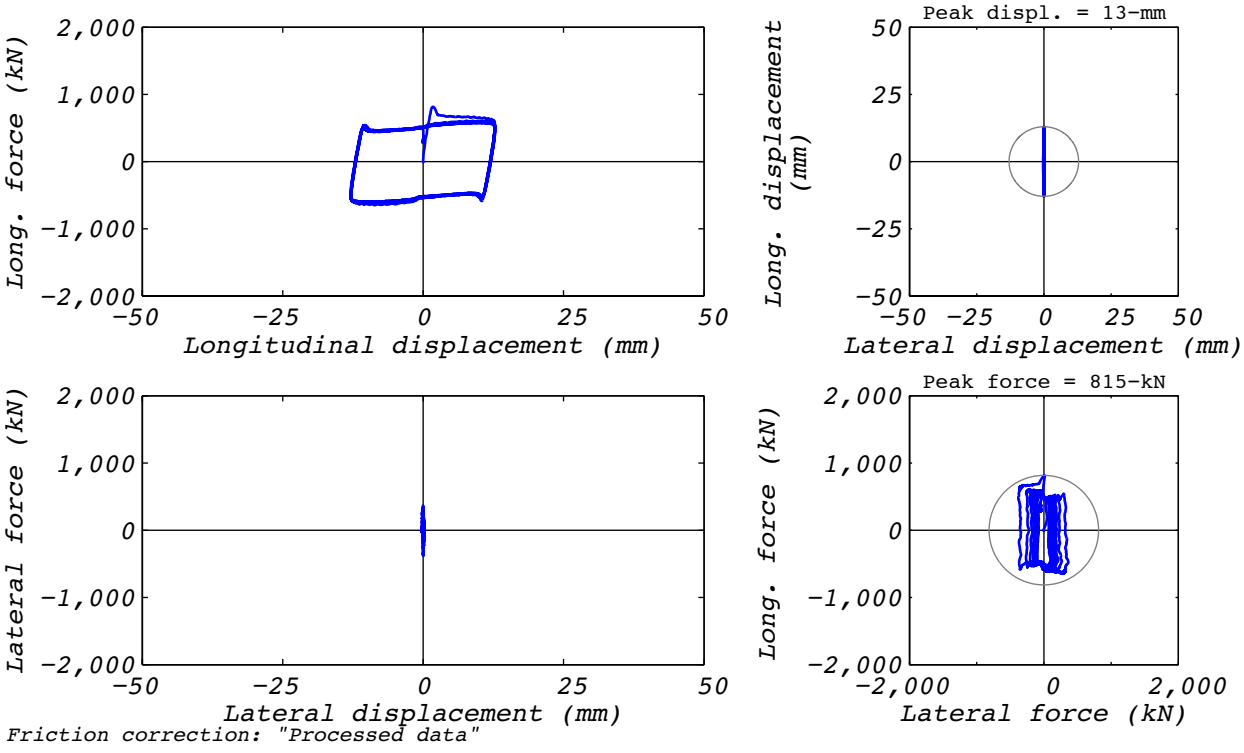

Figure D.30-2 Test run no. 36 hysteresis: Longitudinal (13 mm amplitude, 8,663 kN axial load, and 4 mm/s velocity).

D.31 TEST RUN 59

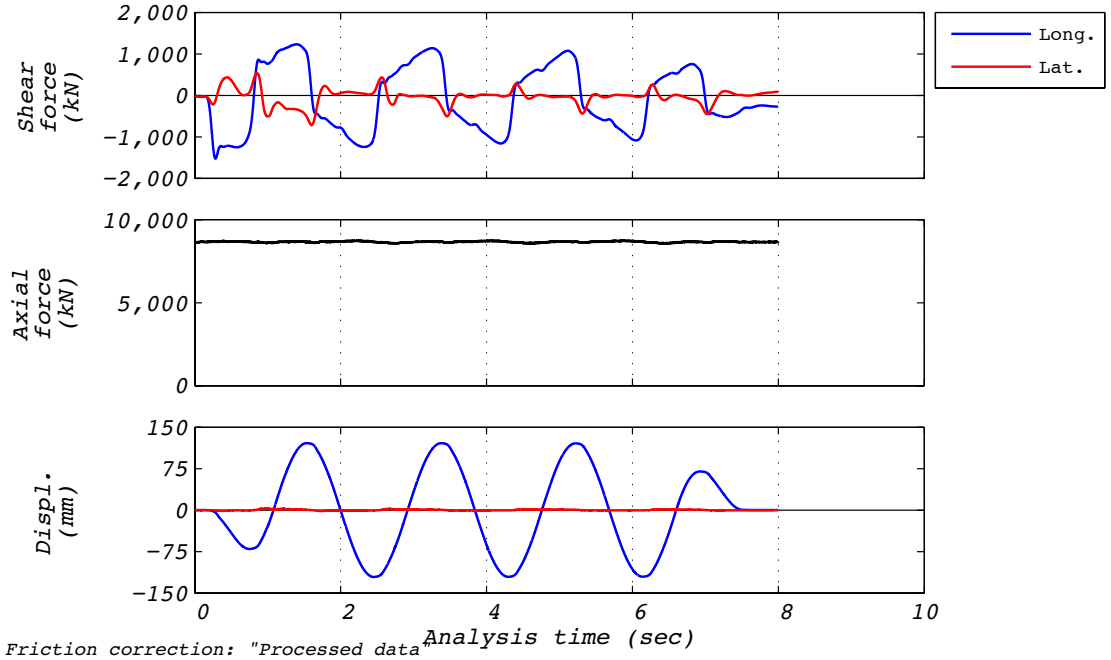

Figure D.31-1 Test run no. 59 time history: Longitudinal (120 mm amplitude, 8,663 kN axial load, and 410 mm/s velocity).

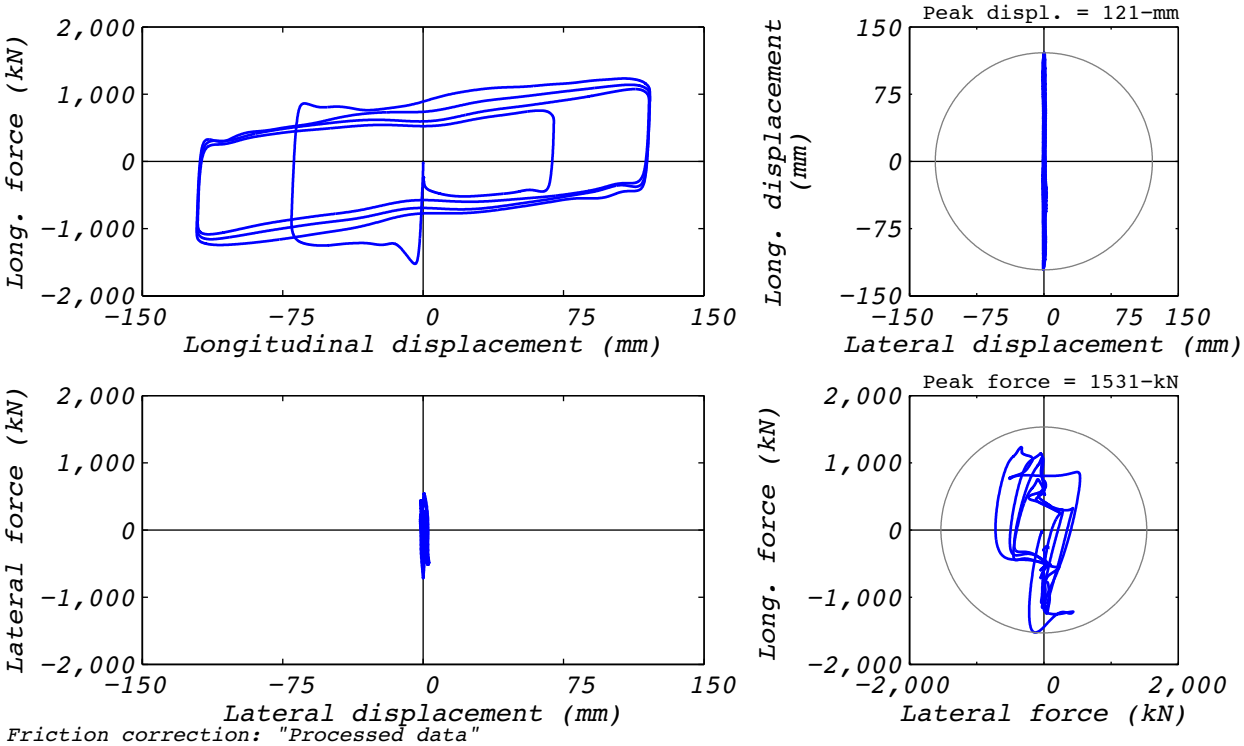

Figure D.31-2 Test run no. 59 hysteresis: Longitudinal (120 mm amplitude, 8,663 kN axial load, and 410 mm/s velocity).

D.32 TEST RUN 60

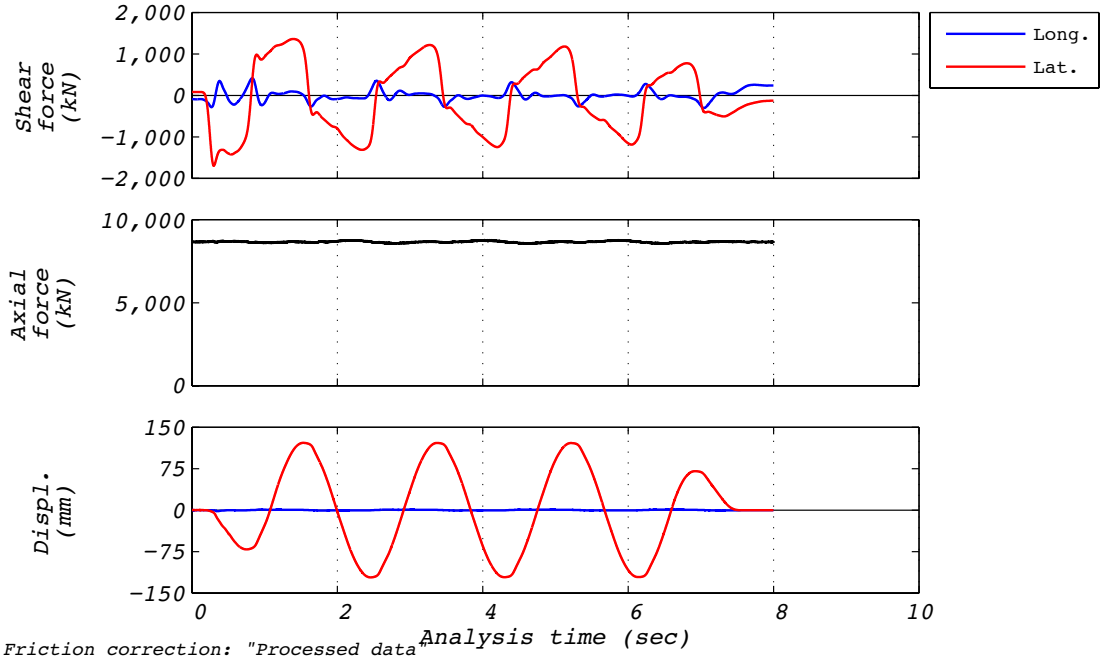

Figure D.32-1 Test run no. 60 time history: Transverse (120 mm amplitude, 8,663 kN axial load, and 410 mm/s velocity).

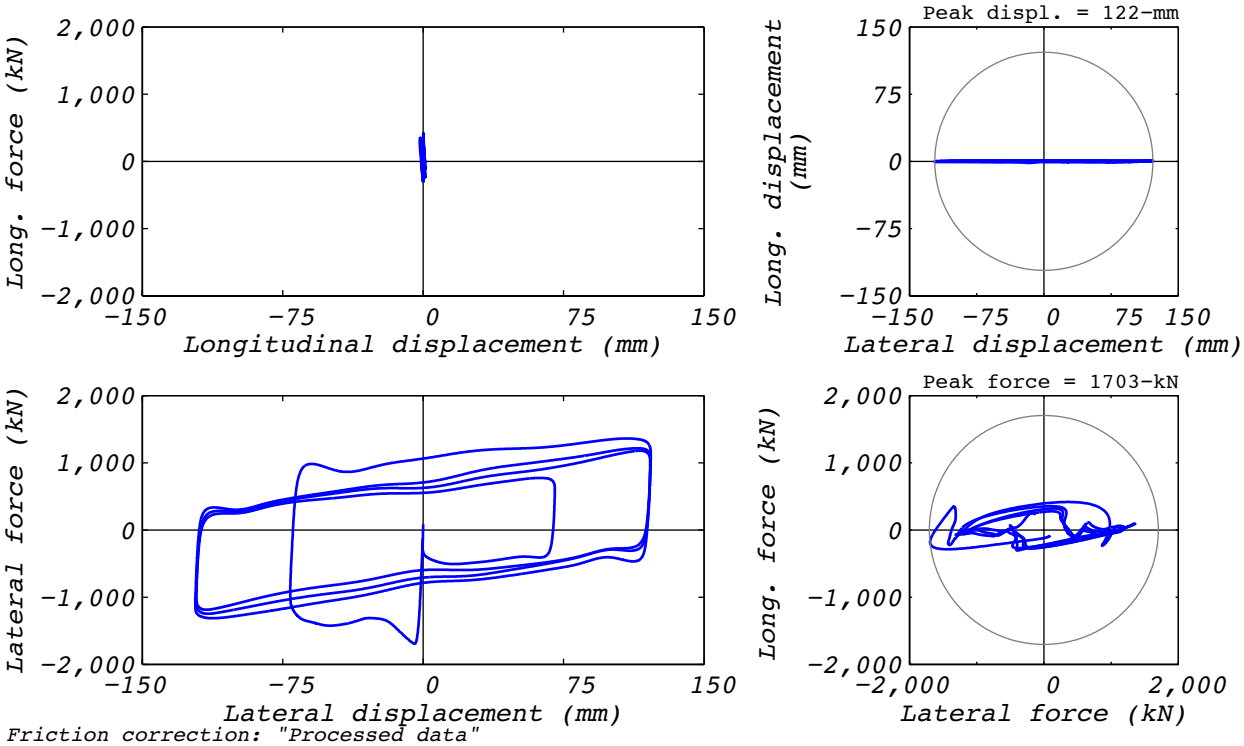

Figure D.32-2 Test run no. 60 hysteresis: Transverse (120 mm amplitude, 8,663 kN axial load, and 410 mm/s velocity).

PEER REPORTS

PEER reports are available as a free PDF download from http://peer.berkeley.edu/publications/peer_reports_complete.html. Printed hard copies of PEER reports can be ordered directly from our printer by following the instructions at http://peer.berkeley.edu/publications/peer_reports.html. For other related questions about the PEER Report Series, contact the Pacific Earthquake Engineering Research Center, 325 Davis Hall mail code 1792, Berkeley, CA 94720. Tel.: (510) 642-3437; Fax: (510) 665-1655; Email: peer_editor@berkeley.edu

PEER 2015/05 *Hybrid Simulation of Seismic Isolation Systems Applied to an APR-1400 Nuclear Power Plant.* Andreas H. Schellenberg, Alireza Sarebanha, Matthew J. Schoettler, Gilberto Mosqueda, Gianmario Benzoni, and Stephen A. Mahin. April 2015.

PEER 2015/04 *NGA-East: Median Ground-Motion Models for the Central and Eastern North America Region.* April 2015.

PEER 2015/03 *Single Series Solution for the Rectangular Fiber-Reinforced Elastomeric Isolator Compression Modulus.* James M. Kelly and Niel C. Van Engelen. March 2015.

PEER 2015/02 *A Full-Scale, Single-Column Bridge Bent Tested by Shake-Table Excitation.* Matthew J. Schoettler, José I. Restrepo, Gabriele Guerrini, David E. Duck, and Francesco Carrea. March 2015.

PEER 2015/01 *Concrete Column Blind Prediction Contest 2010: Outcomes and Observations.* Vesna Terzic, Matthew J. Schoettler, José I. Restrepo, and Stephen A Mahin. March 2015.

PEER 2014/20 *Stochastic Modeling and Simulation of Near-Fault Ground Motions for Performance-Based Earthquake Engineering.* Mayssa Dabaghi and Armen Der Kiureghian. December 2014.

PEER 2014/19 *Seismic Response of a Hybrid Fiber-Reinforced Concrete Bridge Column Detailed for Accelerated Bridge Construction.* Wilson Nguyen, William Trono, Marios Panagiotou, and Claudia P. Ostertag. December 2014.

PEER 2014/18 *Three-Dimensional Beam-Truss Model for Reinforced Concrete Walls and Slabs Subjected to Cyclic Static or Dynamic Loading.* Yuan Lu, Marios Panagiotou, and Ioannis Koutromanos. December 2014.

PEER 2014/17 *PEER NGA-East Database.* Christine A. Goulet, Tadahiro Kishida, Timothy D. Ancheta, Chris H. Cramer, Robert B. Darragh, Walter J. Silva, Youssef M.A. Hashash, Joseph Harmon, Jonathan P. Stewart, Katie E. Wooddell, and Robert R. Youngs. October 2014.

PEER 2014/16 *Guidelines for Performing Hazard-Consistent One-Dimensional Ground Response Analysis for Ground Motion Prediction.* Jonathan P. Stewart, Kioumars Afshari, and Youssef M.A. Hashash. October 2014.

PEER 2014/15 *NGA-East Regionalization Report: Comparison of Four Crustal Regions within Central and Eastern North America using Waveform Modeling and 5%-Damped Pseudo-Spectral Acceleration Response.* Jennifer Dreiling, Marius P. Isken, Walter D. Mooney, Martin C. Chapman, and Richard W. Godbee. October 2014.

PEER 2014/14 *Scaling Relations between Seismic Moment and Rupture Area of Earthquakes in Stable Continental Regions*. Paul Somerville. August 2014.

PEER 2014/13 *PEER Preliminary Notes and Observations on the August 24, 2014, South Napa Earthquake*. Grace S. Kang (Editor), Stephen A. Mahin (Editors). September 2014.

PEER 2014/12 *Reference-Rock Site Conditions for Central and Eastern North America: Part II – Attenuation (Kappa) Definition*. Kenneth W. Campbell, Youssef M.A. Hashash, Byungmin Kim, Albert R. Kottke, Ellen M. Rathje, Walter J. Silva, and Jonathan P. Stewart. August 2014.

PEER 2014/11 *Reference-Rock Site Conditions for Central and Eastern North America: Part I - Velocity Definition*. Youssef M.A. Hashash, Albert R. Kottke, Jonathan P. Stewart, Kenneth W. Campbell, Byungmin Kim, Ellen M. Rathje, Walter J. Silva, Sissy Nikolaou, and Cheryl Moss. August 2014.

PEER 2014/10 *Evaluation of Collapse and Non-Collapse of Parallel Bridges Affected by Liquefaction and Lateral Spreading*. Benjamin Turner, Scott J. Brandenberg, and Jonathan P. Stewart. August 2014.

PEER 2014/09 *PEER Arizona Strong-Motion Database and GMPEs Evaluation*. Tadahiro Kishida, Robert E. Kayen, Olga-Joan Ktenidou, Walter J. Silva, Robert B. Darragh, and Jennie Watson-Lamprey. June 2014.

PEER 2014/08 *Unbonded Pretensioned Bridge Columns with Rocking Detail*. Jeffrey A. Schaefer, Bryan Kennedy, Marc O. Eberhard, John F. Stanton. June 2014.

PEER 2014/07 *Northridge 20 Symposium Summary Report: Impacts, Outcomes, and Next Steps*. May 2014.

PEER 2014/06 *Report of the Tenth Planning Meeting of NEES/E-Defense Collaborative Research on Earthquake Engineering*. December 2013.

PEER 2014/05 *Seismic Velocity Site Characterization of Thirty-One Chilean Seismometer Stations by Spectral Analysis of Surface Wave Dispersion.* Robert Kayen, Brad D. Carkin, Skye Corbet, Camilo Pinilla, Allan Ng, Edward Gorbis, and Christine Truong. April 2014.

PEER 2014/04 *Effect of Vertical Acceleration on Shear Strength of Reinforced Concrete Columns.* Hyerin Lee and Khalid M. Mosalam. April 2014.

PEER 2014/03 *Retest of Thirty-Year-Old Neoprene Isolation Bearings.* James M. Kelly and Niel C. Van Engelen. March 2014.

PEER 2014/02 *Theoretical Development of Hybrid Simulation Applied to Plate Structures.* Ahmed A. Bakhaty, Khalid M. Mosalam, and Sanjay Govindjee. January 2014.

PEER 2014/01 *Performance-Based Seismic Assessment of Skewed Bridges.* Peyman Kaviani, Farzin Zareian, and Ertugrul Taciroglu. January 2014.

PEER 2013/26 *Urban Earthquake Engineering. Proceedings of the U.S.-Iran Seismic Workshop.* December 2013.

PEER 2013/25 *Earthquake Engineering for Resilient Communities: 2013 PEER Internship Program Research Report Collection.* Heidi Tremayne (Editor), Stephen A. Mahin (Editor), Jorge Archbold Monterossa, Matt Brosman, Shelly Dean, Katherine deLaveaga, Curtis Fong, Donovan Holder, Rakeeb Khan, Elizabeth Jachens, David Lam, Daniela Martinez Lopez, Mara Minner, Geffen Oren, Julia Pavicic, Melissa Quinonez, Lorena Rodriguez, Sean Salazar, Kelli Slaven, Vivian Steyert, Jenny Taing, and Salvador Tena. December 2013.

PEER 2013/24 *NGA-West2 Ground Motion Prediction Equations for Vertical Ground Motions.* September 2013.

PEER 2013/23 *Coordinated Planning and Preparedness for Fire Following Major Earthquakes.* Charles Scawthorn. November 2013.

PEER 2013/22 *GEM-PEER Task 3 Project: Selection of a Global Set of Ground Motion Prediction Equations.* Jonathan P. Stewart, John Douglas, Mohammad B. Javanbarg, Carola Di Alessandro, Yousef Bozorgnia, Norman A. Abrahamson, David M. Boore, Kenneth W. Campbell, Elise Delavaud, Mustafa Erdik and Peter J. Stafford. December 2013.

PEER 2013/21 *Seismic Design and Performance of Bridges with Columns on Rocking Foundations.* Grigorios Antonellis and Marios Panagiotou. September 2013.

PEER 2013/20 *Experimental and Analytical Studies on the Seismic Behavior of Conventional and Hybrid Braced Frames.* Jiun-Wei Lai and Stephen A. Mahin. September 2013.

PEER 2013/19 *Toward Resilient Communities: A Performance-Based Engineering Framework for Design and Evaluation of the Built Environment.* Michael William Mieler, Bozidar Stojadinovic, Robert J. Budnitz, Stephen A. Mahin and Mary C. Comerio. September 2013.

PEER 2013/18 *Identification of Site Parameters that Improve Predictions of Site Amplification.* Ellen M. Rathje and Sara Navidi. July 2013.

PEER 2013/17 *Response Spectrum Analysis of Concrete Gravity Dams Including Dam-Water-Foundation Interaction.* Arnkjell Løkke and Anil K. Chopra. July 2013.

PEER 2013/16 *Effect of hoop reinforcement spacing on the cyclic response of large reinforced concrete special moment frame beams.* Marios Panagiotou, Tea Visnjic, Grigorios Antonellis, Panagiotis Galanis, and Jack P. Moehle. June 2013.

PEER 2013/15 *A Probabilistic Framework to Include the Effects of Near-Fault Directivity in Seismic Hazard Assessment.* Shrey Kumar Shahi, Jack W. Baker. October 2013.

PEER 2013/14 *Hanging-Wall Scaling using Finite-Fault Simulations.* Jennifer L. Donahue and Norman A. Abrahamson. September 2013.

PEER 2013/13 *Semi-Empirical Nonlinear Site Amplification and its Application in NEHRP Site Factors.* Jonathan P. Stewart and Emel Seyhan. November 2013.

PEER 2013/12 *Nonlinear Horizontal Site Response for the NGA-West2 Project.* Ronnie Kamai, Norman A. Abramson, Walter J. Silva. May 2013.

PEER 2013/11 *Epistemic Uncertainty for NGA-West2 Models.* Linda Al Atik and Robert R. Youngs. May 2013.

PEER 2013/10 *NGA-West 2 Models for Ground-Motion Directionality.* Shrey K. Shahi and Jack W. Baker. May 2013.

PEER 2013/09 *Final Report of the NGA-West2 Directivity Working Group.* Paul Spudich, Jeffrey R. Bayless, Jack W. Baker, Brian S.J. Chiou, Badie Rowshandel, Shrey Shahi, and Paul Somerville. May 2013.

PEER 2013/08 *NGA-West2 Model for Estimating Average Horizontal Values of Pseudo-Absolute Spectral Accelerations Generated by Crustal Earthquakes.* I. M. Idriss. May 2013.

PEER 2013/07 *Update of the Chiou and Youngs NGA Ground Motion Model for Average Horizontal Component of Peak Ground Motion and Response Spectra.* Brian Chiou and Robert Youngs. May 2013.

PEER 2013/06 *NGA-West2 Campbell-Bozorgnia Ground Motion Model for the Horizontal Components of PGA, PGV, and 5%-Damped Elastic Pseudo-Acceleration Response Spectra for Periods Ranging from 0.01 to 10 sec.* Kenneth W. Campbell and Yousef Bozorgnia. May 2013.

PEER 2013/05 *NGA-West 2 Equations for Predicting Response Spectral Accelerations for Shallow Crustal Earthquakes.* David M. Boore, Jonathan P. Stewart, Emel Seyhan, Gail M. Atkinson. May 2013.

PEER 2013/04 *Update of the AS08 Ground-Motion Prediction Equations Based on the NGA-West2 Data Set.* Norman Abrahamson, Walter Silva, and Ronnie Kamai. May 2013.

PEER 2013/03 *PEER NGA-West2 Database.* Timothy D. Ancheta, Robert B. Darragh, Jonathan P. Stewart, Emel Seyhan, Walter J. Silva, Brian S.J. Chiou, Katie E. Wooddell, Robert W. Graves, Albert R. Kottke, David M. Boore, Tadahiro Kishida, and Jennifer L. Donahue. May 2013.

PEER 2013/02 *Hybrid Simulation of the Seismic Response of Squat Reinforced Concrete Shear Walls.* Catherine A. Whyte and Bozidar Stojadinovic. May 2013.

PEER 2013/01 *Housing Recovery in Chile: A Qualitative Mid-program Review.* Mary C. Comerio. February 2013.

PEER 2012/08 *Guidelines for Estimation of Shear Wave Velocity.* Bernard R. Wair, Jason T. DeJong, and Thomas Shantz. December 2012.

PEER 2012/07 *Earthquake Engineering for Resilient Communities: 2012 PEER Internship Program Research Report Collection.* Heidi Tremayne (Editor), Stephen A. Mahin (Editor), Collin Anderson, Dustin Cook, Michael Erceg, Carlos Esparza, Jose Jimenez, Dorian Krausz, Andrew Lo, Stephanie Lopez, Nicole McCurdy, Paul Shipman, Alexander Strum, Eduardo Vega. December 2012.

PEER 2012/06 *Fragilities for Precarious Rocks at Yucca Mountain.* Matthew D. Purvance, Rasool Anooshehpoor, and James N. Brune. December 2012.

PEER 2012/05 *Development of Simplified Analysis Procedure for Piles in Laterally Spreading Layered Soils.* Christopher R. McGann, Pedro Arduino, and Peter Mackenzie–Helnwein. December 2012.

PEER 2012/04 *Unbonded Pre-Tensioned Columns for Bridges in Seismic Regions.* Phillip M. Davis, Todd M. Janes, Marc O. Eberhard, and John F. Stanton. December 2012.

PEER 2012/03 *Experimental and Analytical Studies on Reinforced Concrete Buildings with Seismically Vulnerable Beam-Column Joints.* Sangjoon Park and Khalid M. Mosalam. October 2012.

PEER 2012/02 *Seismic Performance of Reinforced Concrete Bridges Allowed to Uplift during Multi-Directional Excitation.* Andres Oscar Espinoza and Stephen A. Mahin. July 2012.

PEER 2012/01 *Spectral Damping Scaling Factors for Shallow Crustal Earthquakes in Active Tectonic Regions.* Sanaz Rezaeian, Yousef Bozorgnia, I. M. Idriss, Kenneth Campbell, Norman Abrahamson, and Walter Silva. July 2012.

PEER 2011/10 *Earthquake Engineering for Resilient Communities: 2011 PEER Internship Program Research Report Collection.* Eds. Heidi Faison and Stephen A. Mahin. December 2011.

PEER 2011/09 *Calibration of Semi-Stochastic Procedure for Simulating High-Frequency Ground Motions.* Jonathan P. Stewart, Emel Seyhan, and Robert W. Graves. December 2011.

PEER 2011/08 *Water Supply in regard to Fire Following Earthquake.* Charles Scawthorn. November 2011.

PEER 2011/07 *Seismic Risk Management in Urban Areas. Proceedings of a U.S.-Iran-Turkey Seismic Workshop.* September 2011.

PEER 2011/06 *The Use of Base Isolation Systems to Achieve Complex Seismic Performance Objectives.* Troy A. Morgan and Stephen A. Mahin. July 2011.

PEER 2011/05 *Case Studies of the Seismic Performance of Tall Buildings Designed by Alternative Means.* Task 12 Report for the Tall Buildings Initiative. Jack Moehle, Yousef Bozorgnia, Nirmal Jayaram, Pierson Jones, Mohsen Rahnama, Nilesh Shome, Zeynep Tuna, John Wallace, Tony Yang, and Farzin Zareian. July 2011.

PEER 2011/04 *Recommended Design Practice for Pile Foundations in Laterally Spreading Ground.* Scott A. Ashford, Ross W. Boulanger, and Scott J. Brandenberg. June 2011.

PEER 2011/03 *New Ground Motion Selection Procedures and Selected Motions for the PEER Transportation Research Program.* Jack W. Baker, Ting Lin, Shrey K. Shahi, and Nirmal Jayaram. March 2011.

PEER 2011/02 *A Bayesian Network Methodology for Infrastructure Seismic Risk Assessment and Decision Support.* Michelle T. Bensi, Armen Der Kiureghian, and Daniel Straub. March 2011.

PEER 2011/01 *Demand Fragility Surfaces for Bridges in Liquefied and Laterally Spreading Ground.* Scott J. Brandenberg, Jian Zhang, Pirooz Kashighandi, Yili Huo, and Minxing Zhao. March 2011.

PEER 2010/05 *Guidelines for Performance-Based Seismic Design of Tall Buildings.* Developed by the Tall Buildings Initiative. November 2010.

PEER 2010/04 *Application Guide for the Design of Flexible and Rigid Bus Connections between Substation Equipment Subjected to Earthquakes.* Jean-Bernard Dastous and Armen Der Kiureghian. September 2010.

PEER 2010/03 *Shear Wave Velocity as a Statistical Function of Standard Penetration Test Resistance and Vertical Effective Stress at Caltrans Bridge Sites.* Scott J. Brandenberg, Naresh Bellana, and Thomas Shantz. June 2010.

PEER 2010/02 *Stochastic Modeling and Simulation of Ground Motions for Performance-Based Earthquake Engineering.* Sanaz Rezaeian and Armen Der Kiureghian. June 2010.

PEER 2010/01 *Structural Response and Cost Characterization of Bridge Construction Using Seismic Performance Enhancement Strategies.* Ady Aviram, Božidar Stojadinović, Gustavo J. Parra-Montesinos, and Kevin R. Mackie. March 2010.

PEER 2009/03 *The Integration of Experimental and Simulation Data in the Study of Reinforced Concrete Bridge Systems Including Soil-Foundation-Structure Interaction.* Matthew Dryden and Gregory L. Fenves. November 2009.

PEER 2009/02 *Improving Earthquake Mitigation through Innovations and Applications in Seismic Science, Engineering, Communication, and Response. Proceedings of a U.S.-Iran Seismic Workshop.* October 2009.

PEER 2009/01 *Evaluation of Ground Motion Selection and Modification Methods: Predicting Median Interstory Drift Response of Buildings.* Curt B. Haselton, Ed. June 2009.

PEER 2008/10 *Technical Manual for Strata.* Albert R. Kottke and Ellen M. Rathje. February 2009.

PEER 2008/09 *NGA Model for Average Horizontal Component of Peak Ground Motion and Response Spectra.* Brian S.-J. Chiou and Robert R. Youngs. November 2008.

PEER 2008/08 *Toward Earthquake-Resistant Design of Concentrically Braced Steel Structures.* Patxi Uriz and Stephen A. Mahin. November 2008.

PEER 2008/07 *Using OpenSees for Performance-Based Evaluation of Bridges on Liquefiable Soils.* Stephen L. Kramer, Pedro Arduino, and HyungSuk Shin. November 2008.

PEER 2008/06 *Shaking Table Tests and Numerical Investigation of Self-Centering Reinforced Concrete Bridge Columns.* Hyung IL Jeong, Junichi Sakai, and Stephen A. Mahin. September 2008.

PEER 2008/05 *Performance-Based Earthquake Engineering Design Evaluation Procedure for Bridge Foundations Undergoing Liquefaction-Induced Lateral Ground Displacement.* Christian A. Ledezma and Jonathan D. Bray. August 2008.

PEER 2008/04 *Benchmarking of Nonlinear Geotechnical Ground Response Analysis Procedures.* Jonathan P. Stewart, Annie On-Lei Kwok, Yousseff M. A. Hashash, Neven Matasovic, Robert Pyke, Zhiliang Wang, and Zhaohui Yang. August 2008.

PEER 2008/03 *Guidelines for Nonlinear Analysis of Bridge Structures in California.* Ady Aviram, Kevin R. Mackie, and Božidar Stojadinović. August 2008.

PEER 2008/02 *Treatment of Uncertainties in Seismic-Risk Analysis of Transportation Systems.* Evangelos Stergiou and Anne S. Kiremidjian. July 2008.

PEER 2008/01 *Seismic Performance Objectives for Tall Buildings.* William T. Holmes, Charles Kircher, William Petak, and Nabih Youssef. August 2008.

PEER 2007/12 *An Assessment to Benchmark the Seismic Performance of a Code-Conforming Reinforced Concrete Moment-Frame Building.* Curt Haselton, Christine A. Goulet, Judith Mitrani-Reiser, James L. Beck, Gregory G. Deierlein, Keith A. Porter, Jonathan P. Stewart, and Ertugrul Taciroglu. August 2008.

PEER 2007/11 *Bar Buckling in Reinforced Concrete Bridge Columns.* Wayne A. Brown, Dawn E. Lehman, and John F. Stanton. February 2008.

PEER 2007/10 *Computational Modeling of Progressive Collapse in Reinforced Concrete Frame Structures.* Mohamed M. Talaat and Khalid M. Mosalam. May 2008.

PEER 2007/09 *Integrated Probabilistic Performance-Based Evaluation of Benchmark Reinforced Concrete Bridges.* Kevin R. Mackie, John-Michael Wong, and Božidar Stojadinović. January 2008.

PEER 2007/08 *Assessing Seismic Collapse Safety of Modern Reinforced Concrete Moment-Frame Buildings.* Curt B. Haselton and Gregory G. Deierlein. February 2008.

PEER 2007/07 *Performance Modeling Strategies for Modern Reinforced Concrete Bridge Columns.* Michael P. Berry and Marc O. Eberhard. April 2008.

PEER 2007/06 *Development of Improved Procedures for Seismic Design of Buried and Partially Buried Structures.* Linda Al Atik and Nicholas Sitar. June 2007.

PEER 2007/05 *Uncertainty and Correlation in Seismic Risk Assessment of Transportation Systems.* Renee G. Lee and Anne S. Kiremidjian. July 2007.

PEER 2007/04 *Numerical Models for Analysis and Performance-Based Design of Shallow Foundations Subjected to Seismic Loading.* Sivapalan Gajan, Tara C. Hutchinson, Bruce L. Kutter, Prishati Raychowdhury, José A. Ugalde, and Jonathan P. Stewart. May 2008.

PEER 2007/03 *Beam-Column Element Model Calibrated for Predicting Flexural Response Leading to Global Collapse of RC Frame Buildings.* Curt B. Haselton, Abbie B. Liel, Sarah Taylor Lange, and Gregory G. Deierlein. May 2008.

PEER 2007/02 *Campbell-Bozorgnia NGA Ground Motion Relations for the Geometric Mean Horizontal Component of Peak and Spectral Ground Motion Parameters.* Kenneth W. Campbell and Yousef Bozorgnia. May 2007.

PEER 2007/01 *Boore-Atkinson NGA Ground Motion Relations for the Geometric Mean Horizontal Component of Peak and Spectral Ground Motion Parameters.* David M. Boore and Gail M. Atkinson. May. May 2007.

PEER 2006/12 *Societal Implications of Performance-Based Earthquake Engineering.* Peter J. May. May 2007.

PEER 2006/11 *Probabilistic Seismic Demand Analysis Using Advanced Ground Motion Intensity Measures, Attenuation Relationships, and Near-Fault Effects.* Polsak Tothong and C. Allin Cornell. March 2007.

PEER 2006/10 *Application of the PEER PBEE Methodology to the I-880 Viaduct.* Sashi Kunnath. February 2007.

PEER 2006/09 *Quantifying Economic Losses from Travel Forgone Following a Large Metropolitan Earthquake.* James Moore, Sungbin Cho, Yue Yue Fan, and Stuart Werner. November 2006.

PEER 2006/08 *Vector-Valued Ground Motion Intensity Measures for Probabilistic Seismic Demand Analysis*. Jack W. Baker and C. Allin Cornell. October 2006.

PEER 2006/07 *Analytical Modeling of Reinforced Concrete Walls for Predicting Flexural and Coupled–Shear-Flexural Responses*. Kutay Orakcal, Leonardo M. Massone, and John W. Wallace. October 2006.

PEER 2006/06 *Nonlinear Analysis of a Soil-Drilled Pier System under Static and Dynamic Axial Loading.* Gang Wang and Nicholas Sitar. November 2006.

PEER 2006/05 *Advanced Seismic Assessment Guidelines.* Paolo Bazzurro, C. Allin Cornell, Charles Menun, Maziar Motahari, and Nicolas Luco. September 2006.

PEER 2006/04 *Probabilistic Seismic Evaluation of Reinforced Concrete Structural Components and Systems.* Tae Hyung Lee and Khalid M. Mosalam. August 2006.

PEER 2006/03 *Performance of Lifelines Subjected to Lateral Spreading.* Scott A. Ashford and Teerawut Juirnarongrit. July 2006.

PEER 2006/02 *Pacific Earthquake Engineering Research Center Highway Demonstration Project.* Anne Kiremidjian, James Moore, Yue Yue Fan, Nesrin Basoz, Ozgur Yazali, and Meredith Williams. April 2006.

PEER 2006/01 *Bracing Berkeley. A Guide to Seismic Safety on the UC Berkeley Campus.* Mary C. Comerio, Stephen Tobriner, and Ariane Fehrenkamp. January 2006.

PEER 2005/16 *Seismic Response and Reliability of Electrical Substation Equipment and Systems.* Junho Song, Armen Der Kiureghian, and Jerome L. Sackman. April 2006.

PEER 2005/15 *CPT-Based Probabilistic Assessment of Seismic Soil Liquefaction Initiation.* R. E. S. Moss, R. B. Seed, R. E. Kayen, J. P. Stewart, and A. Der Kiureghian. April 2006.

PEER 2005/14 *Workshop on Modeling of Nonlinear Cyclic Load-Deformation Behavior of Shallow Foundations.* Bruce L. Kutter, Geoffrey Martin, Tara Hutchinson, Chad Harden, Sivapalan Gajan, and Justin Phalen. March 2006.

PEER 2005/13 *Stochastic Characterization and Decision Bases under Time-Dependent Aftershock Risk in Performance-Based Earthquake Engineering.* Gee Liek Yeo and C. Allin Cornell. July 2005.

PEER 2005/12 *PEER Testbed Study on a Laboratory Building: Exercising Seismic Performance Assessment.* Mary C. Comerio, editor. November 2005.

PEER 2005/11 *Van Nuys Hotel Building Testbed Report: Exercising Seismic Performance Assessment.* Helmut Krawinkler, editor. October 2005.

PEER 2005/10 *First NEES/E-Defense Workshop on Collapse Simulation of Reinforced Concrete Building Structures.* September 2005.

PEER 2005/09 *Test Applications of Advanced Seismic Assessment Guidelines.* Joe Maffei, Karl Telleen, Danya Mohr, William Holmes, and Yuki Nakayama. August 2006.

PEER 2005/08 *Damage Accumulation in Lightly Confined Reinforced Concrete Bridge Columns.* R. Tyler Ranf, Jared M. Nelson, Zach Price, Marc O. Eberhard, and John F. Stanton. April 2006.

PEER 2005/07 *Experimental and Analytical Studies on the Seismic Response of Freestanding and Anchored Laboratory Equipment.* Dimitrios Konstantinidis and Nicos Makris. January 2005.

PEER 2005/06 *Global Collapse of Frame Structures under Seismic Excitations*. Luis F. Ibarra and Helmut Krawinkler. September 2005.

PEER 2005//05 *Performance Characterization of Bench- and Shelf-Mounted Equipment.* Samit Ray Chaudhuri and Tara C. Hutchinson. May 2006.

PEER 2005/04 *Numerical Modeling of the Nonlinear Cyclic Response of Shallow Foundations.* Chad Harden, Tara Hutchinson, Geoffrey R. Martin, and Bruce L. Kutter. August 2005.

PEER 2005/03 *A Taxonomy of Building Components for Performance-Based Earthquake Engineering.* Keith A. Porter. September 2005.

PEER 2005/02 *Fragility Basis for California Highway Overpass Bridge Seismic Decision Making*. Kevin R. Mackie and Božidar Stojadinović. June 2005.

PEER 2005/01 *Empirical Characterization of Site Conditions on Strong Ground Motion.* Jonathan P. Stewart, Yoojoong Choi, and Robert W. Graves. June 2005.

PEER 2004/09 *Electrical Substation Equipment Interaction: Experimental Rigid Conductor Studies.* Christopher Stearns and André Filiatrault. February 2005.

PEER 2004/08 *Seismic Qualification and Fragility Testing of Line Break 550-kV Disconnect Switches.* Shakhzod M. Takhirov, Gregory L. Fenves, and Eric Fujisaki. January 2005.

PEER 2004/07 *Ground Motions for Earthquake Simulator Qualification of Electrical Substation Equipment.* Shakhzod M. Takhirov, Gregory L. Fenves, Eric Fujisaki, and Don Clyde. January 2005.

PEER 2004/06 *Performance-Based Regulation and Regulatory Regimes.* Peter J. May and Chris Koski. September 2004.

PEER 2004/05 *Performance-Based Seismic Design Concepts and Implementation: Proceedings of an International Workshop.* Peter Fajfar and Helmut Krawinkler, editors. September 2004.

PEER 2004/04 *Seismic Performance of an Instrumented Tilt-up Wall Building.* James C. Anderson and Vitelmo V. Bertero. July 2004.

PEER 2004/03 *Evaluation and Application of Concrete Tilt-up Assessment Methodologies.* Timothy Graf and James O. Malley. October 2004.

PEER 2004/02 *Analytical Investigations of New Methods for Reducing Residual Displacements of Reinforced Concrete Bridge Columns.* Junichi Sakai and Stephen A. Mahin. August 2004.

PEER 2004/01 *Seismic Performance of Masonry Buildings and Design Implications.* Kerri Anne Taeko Tokoro, James C. Anderson, and Vitelmo V. Bertero. February 2004.

PEER 2003/18 *Performance Models for Flexural Damage in Reinforced Concrete Columns.* Michael Berry and Marc Eberhard. August 2003.

PEER 2003/17 *Predicting Earthquake Damage in Older Reinforced Concrete Beam-Column Joints.* Catherine Pagni and Laura Lowes. October 2004.

PEER 2003/16 *Seismic Demands for Performance-Based Design of Bridges.* Kevin Mackie and Božidar Stojadinović. August 2003.

PEER 2003/15 *Seismic Demands for Nondeteriorating Frame Structures and Their Dependence on Ground Motions.* Ricardo Antonio Medina and Helmut Krawinkler. May 2004.

PEER 2003/14 *Finite Element Reliability and Sensitivity Methods for Performance-Based Earthquake Engineering.* Terje Haukaas and Armen Der Kiureghian. April 2004.

PEER 2003/13 *Effects of Connection Hysteretic Degradation on the Seismic Behavior of Steel Moment-Resisting Frames.* Janise E. Rodgers and Stephen A. Mahin. March 2004.

PEER 2003/12 *Implementation Manual for the Seismic Protection of Laboratory Contents: Format and Case Studies.* William T. Holmes and Mary C. Comerio. October 2003.

PEER 2003/11 *Fifth U.S.-Japan Workshop on Performance-Based Earthquake Engineering Methodology for Reinforced Concrete Building Structures.* February 2004.

PEER 2003/10 *A Beam-Column Joint Model for Simulating the Earthquake Response of Reinforced Concrete Frames.* Laura N. Lowes, Nilanjan Mitra, and Arash Altoontash. February 2004.

PEER 2003/09 *Sequencing Repairs after an Earthquake: An Economic Approach.* Marco Casari and Simon J. Wilkie. April 2004.

PEER 2003/08 *A Technical Framework for Probability-Based Demand and Capacity Factor Design (DCFD) Seismic Formats*. Fatemeh Jalayer and C. Allin Cornell. November 2003.

PEER 2003/07 *Uncertainty Specification and Propagation for Loss Estimation Using FOSM Methods.* Jack W. Baker and C. Allin Cornell. September 2003.

PEER 2003/06 *Performance of Circular Reinforced Concrete Bridge Columns under Bidirectional Earthquake Loading*. Mahmoud M. Hachem, Stephen A. Mahin, and Jack P. Moehle. February 2003.

PEER 2003/05 *Response Assessment for Building-Specific Loss Estimation.* Eduardo Miranda and Shahram Taghavi. September 2003.

PEER 2003/04 *Experimental Assessment of Columns with Short Lap Splices Subjected to Cyclic Loads*. Murat Melek, John W. Wallace, and Joel Conte. April 2003.

PEER 2003/03 *Probabilistic Response Assessment for Building-Specific Loss Estimation.* Eduardo Miranda and Hesameddin Aslani. September 2003.

PEER 2003/02 *Software Framework for Collaborative Development of Nonlinear Dynamic Analysis Program.* Jun Peng and Kincho H. Law. September 2003.

PEER 2003/01 *Shake Table Tests and Analytical Studies on the Gravity Load Collapse of Reinforced Concrete Frames.* Kenneth John Elwood and Jack P. Moehle. November 2003.

PEER 2002/24 *Performance of Beam to Column Bridge Joints Subjected to a Large Velocity Pulse.* Natalie Gibson, André Filiatrault, and Scott A. Ashford. April 2002.

PEER 2002/23 *Effects of Large Velocity Pulses on Reinforced Concrete Bridge Columns.* Greg L. Orozco and Scott A. Ashford. April 2002.

PEER 2002/22 *Characterization of Large Velocity Pulses for Laboratory Testing.* Kenneth E. Cox and Scott A. Ashford. April 2002.

PEER 2002/21 *Fourth U.S.-Japan Workshop on Performance-Based Earthquake Engineering Methodology for Reinforced Concrete Building Structures*. December 2002.

PEER 2002/20 *Barriers to Adoption and Implementation of PBEE Innovations.* Peter J. May. August 2002.

PEER 2002/19 *Economic-Engineered Integrated Models for Earthquakes: Socioeconomic Impacts.* Peter Gordon, James E. Moore II, and Harry W. Richardson. July 2002.

PEER 2002/18 *Assessment of Reinforced Concrete Building Exterior Joints with Substandard Details.* Chris P. Pantelides, Jon Hansen, Justin Nadauld, and Lawrence D. Reaveley. May 2002.

PEER 2002/17 *Structural Characterization and Seismic Response Analysis of a Highway Overcrossing Equipped with Elastomeric Bearings and Fluid Dampers: A Case Study*. Nicos Makris and Jian Zhang. November 2002.

PEER 2002/16 *Estimation of Uncertainty in Geotechnical Properties for Performance-Based Earthquake Engineering.* Allen L. Jones, Steven L. Kramer, and Pedro Arduino. December 2002.

PEER 2002/15 *Seismic Behavior of Bridge Columns Subjected to Various Loading Patterns.* Asadollah Esmaeily-Gh. and Yan Xiao. December 2002.

PEER 2002/14 *Inelastic Seismic Response of Extended Pile Shaft Supported Bridge Structures.* T.C. Hutchinson, R.W. Boulanger, Y.H. Chai, and I.M. Idriss. December 2002.

PEER 2002/13 *Probabilistic Models and Fragility Estimates for Bridge Components and Systems.* Paolo Gardoni, Armen Der Kiureghian, and Khalid M. Mosalam. June 2002.

PEER 2002/12 *Effects of Fault Dip and Slip Rake on Near-Source Ground Motions: Why Chi-Chi Was a Relatively Mild M7.6 Earthquake*. Brad T. Aagaard, John F. Hall, and Thomas H. Heaton. December 2002.

PEER 2002/11 *Analytical and Experimental Study of Fiber-Reinforced Strip Isolators*. James M. Kelly and Shakhzod M. Takhirov. September 2002.

PEER 2002/10 *Centrifuge Modeling of Settlement and Lateral Spreading with Comparisons to Numerical Analyses***.** Sivapalan Gajan and Bruce L. Kutter. January 2003.

PEER 2002/09 *Documentation and Analysis of Field Case Histories of Seismic Compression during the 1994 Northridge, California, Earthquake*. Jonathan P. Stewart, Patrick M. Smith, Daniel H. Whang, and Jonathan D. Bray. October 2002.

PEER 2002/08 *Component Testing, Stability Analysis and Characterization of Buckling-Restrained Unbonded Braces™.* Cameron Black, Nicos Makris, and Ian Aiken. September 2002.

PEER 2002/07 *Seismic Performance of Pile-Wharf Connections.* Charles W. Roeder, Robert Graff, Jennifer Soderstrom, and Jun Han Yoo. December 2001.

PEER 2002/06 *The Use of Benefit-Cost Analysis for Evaluation of Performance-Based Earthquake Engineering Decisions*. Richard O. Zerbe and Anthony Falit-Baiamonte. September 2001.

PEER 2002/05 *Guidelines, Specifications, and Seismic Performance Characterization of Nonstructural Building Components and Equipment*. André Filiatrault, Constantin Christopoulos, and Christopher Stearns. September 2001.

PEER 2002/04 *Consortium of Organizations for Strong-Motion Observation Systems and the Pacific Earthquake Engineering Research Center Lifelines Program: Invited Workshop on Archiving and Web Dissemination of Geotechnical Data, 4–5 October 2001*. September 2002.

PEER 2002/03 *Investigation of Sensitivity of Building Loss Estimates to Major Uncertain Variables for the Van Nuys Testbed.* Keith A. Porter, James L. Beck, and Rustem V. Shaikhutdinov. August 2002.

PEER 2002/02 *The Third U.S.-Japan Workshop on Performance-Based Earthquake Engineering Methodology for Reinforced Concrete Building Structures*. July 2002.

PEER 2002/01 *Nonstructural Loss Estimation: The UC Berkeley Case Study.* Mary C. Comerio and John C. Stallmeyer. December 2001.

PEER 2001/16 *Statistics of SDF-System Estimate of Roof Displacement for Pushover Analysis of Buildings.* Anil K. Chopra, Rakesh K. Goel, and Chatpan Chintanapakdee. December 2001.

PEER 2001/15 *Damage to Bridges during the 2001 Nisqually Earthquake.* R. Tyler Ranf, Marc O. Eberhard, and Michael P. Berry. November 2001.

PEER 2001/14 *Rocking Response of Equipment Anchored to a Base Foundation.* Nicos Makris and Cameron J. Black. September 2001.

PEER 2001/13 *Modeling Soil Liquefaction Hazards for Performance-Based Earthquake Engineering.* Steven L. Kramer and Ahmed-W. Elgamal. February 2001.

PEER 2001/12 *Development of Geotechnical Capabilities in OpenSees.* Boris Jeremić. September 2001.

PEER 2001/11 *Analytical and Experimental Study of Fiber-Reinforced Elastomeric Isolators*. James M. Kelly and Shakhzod M. Takhirov. September 2001.

PEER 2001/10 *Amplification Factors for Spectral Acceleration in Active Regions.* Jonathan P. Stewart, Andrew H. Liu, Yoojoong Choi, and Mehmet B. Baturay. December 2001.

PEER 2001/09 *Ground Motion Evaluation Procedures for Performance-Based Design.* Jonathan P. Stewart, Shyh-Jeng Chiou, Jonathan D. Bray, Robert W. Graves, Paul G. Somerville, and Norman A. Abrahamson. September 2001.

PEER 2001/08 *Experimental and Computational Evaluation of Reinforced Concrete Bridge Beam-Column Connections for Seismic Performance*. Clay J. Naito, Jack P. Moehle, and Khalid M. Mosalam. November 2001.

PEER 2001/07 *The Rocking Spectrum and the Shortcomings of Design Guidelines.* Nicos Makris and Dimitrios Konstantinidis. August 2001.

PEER 2001/06 *Development of an Electrical Substation Equipment Performance Database for Evaluation of Equipment Fragilities*. Thalia Agnanos. April 1999.

PEER 2001/05 *Stiffness Analysis of Fiber-Reinforced Elastomeric Isolators.* Hsiang-Chuan Tsai and James M. Kelly. May 2001.

PEER 2001/04 *Organizational and Societal Considerations for Performance-Based Earthquake Engineering.* Peter J. May. April 2001.

PEER 2001/03 *A Modal Pushover Analysis Procedure to Estimate Seismic Demands for Buildings: Theory and Preliminary Evaluation.* Anil K. Chopra and Rakesh K. Goel. January 2001.

PEER 2001/02 *Seismic Response Analysis of Highway Overcrossings Including Soil-Structure Interaction.* Jian Zhang and Nicos Makris. March 2001.

PEER 2001/01 *Experimental Study of Large Seismic Steel Beam-to-Column Connections.* Egor P. Popov and Shakhzod M. Takhirov. November 2000.

PEER 2000/10 *The Second U.S.-Japan Workshop on Performance-Based Earthquake Engineering Methodology for Reinforced Concrete Building Structures.* March 2000.

PEER 2000/09 *Structural Engineering Reconnaissance of the August 17, 1999 Earthquake: Kocaeli (Izmit), Turkey.* Halil Sezen, Kenneth J. Elwood, Andrew S. Whittaker, Khalid Mosalam, John J. Wallace, and John F. Stanton. December 2000.

PEER 2000/08 *Behavior of Reinforced Concrete Bridge Columns Having Varying Aspect Ratios and Varying Lengths of Confinement.* Anthony J. Calderone, Dawn E. Lehman, and Jack P. Moehle. January 2001.

PEER 2000/07 *Cover-Plate and Flange-Plate Reinforced Steel Moment-Resisting Connections.* Taejin Kim, Andrew S. Whittaker, Amir S. Gilani, Vitelmo V. Bertero, and Shakhzod M. Takhirov. September 2000.

PEER 2000/06 *Seismic Evaluation and Analysis of 230-kV Disconnect Switches.* Amir S. J. Gilani, Andrew S. Whittaker, Gregory L. Fenves, Chun-Hao Chen, Henry Ho, and Eric Fujisaki. July 2000.

PEER 2000/05 *Performance-Based Evaluation of Exterior Reinforced Concrete Building Joints for Seismic Excitation.* Chandra Clyde, Chris P. Pantelides, and Lawrence D. Reaveley. July 2000.

PEER 2000/04 *An Evaluation of Seismic Energy Demand: An Attenuation Approach.* Chung-Che Chou and Chia-Ming Uang. July 1999.

PEER 2000/03 *Framing Earthquake Retrofitting Decisions: The Case of Hillside Homes in Los Angeles.* Detlof von Winterfeldt, Nels Roselund, and Alicia Kitsuse. March 2000.

PEER 2000/02 *U.S.-Japan Workshop on the Effects of Near-Field Earthquake Shaking.* Andrew Whittaker, ed. July 2000.

PEER 2000/01 *Further Studies on Seismic Interaction in Interconnected Electrical Substation Equipment.* Armen Der Kiureghian, Kee-Jeung Hong, and Jerome L. Sackman. November 1999.

PEER 1999/14 *Seismic Evaluation and Retrofit of 230-kV Porcelain Transformer Bushings*. Amir S. Gilani, Andrew S. Whittaker, Gregory L. Fenves, and Eric Fujisaki. December 1999.

PEER 1999/13 *Building Vulnerability Studies: Modeling and Evaluation of Tilt-up and Steel Reinforced Concrete Buildings.* John W. Wallace, Jonathan P. Stewart, and Andrew S. Whittaker, editors. December 1999.

PEER 1999/12 *Rehabilitation of Nonductile RC Frame Building Using Encasement Plates and Energy-Dissipating Devices.* Mehrdad Sasani, Vitelmo V. Bertero, James C. Anderson. December 1999.

PEER 1999/11 *Performance Evaluation Database for Concrete Bridge Components and Systems under Simulated Seismic Loads.* Yael D. Hose and Frieder Seible. November 1999.

PEER 1999/10 *U.S.-Japan Workshop on Performance-Based Earthquake Engineering Methodology for Reinforced Concrete Building Structures.* December 1999.

PEER 1999/09 *Performance Improvement of Long Period Building Structures Subjected to Severe Pulse-Type Ground Motions*. James C. Anderson, Vitelmo V. Bertero, and Raul Bertero. October 1999.

PEER 1999/08 *Envelopes for Seismic Response Vectors.* Charles Menun and Armen Der Kiureghian. July 1999.

PEER 1999/07 *Documentation of Strengths and Weaknesses of Current Computer Analysis Methods for Seismic Performance of Reinforced Concrete Members.* William F. Cofer. November 1999.

PEER 1999/06 *Rocking Response and Overturning of Anchored Equipment under Seismic Excitations.* Nicos Makris and Jian Zhang. November 1999.

PEER 1999/05 *Seismic Evaluation of 550 kV Porcelain Transformer Bushings.* Amir S. Gilani, Andrew S. Whittaker, Gregory L. Fenves, and Eric Fujisaki. October 1999.

PEER 1999/04 *Adoption and Enforcement of Earthquake Risk-Reduction Measures.* Peter J. May, Raymond J. Burby, T. Jens Feeley, and Robert Wood.

PEER 1999/03 *Task 3 Characterization of Site Response General Site Categories*. Adrian Rodriguez-Marek, Jonathan D. Bray, and Norman Abrahamson. February 1999.

PEER 1999/02 *Capacity-Demand-Diagram Methods for Estimating Seismic Deformation of Inelastic Structures: SDF Systems*. Anil K. Chopra and Rakesh Goel. April 1999.

PEER 1999/01 *Interaction in Interconnected Electrical Substation Equipment Subjected to Earthquake Ground Motions.* Armen Der Kiureghian, Jerome L. Sackman, and Kee-Jeung Hong. February 1999.

PEER 1998/08 *Behavior and Failure Analysis of a Multiple-Frame Highway Bridge in the 1994 Northridge Earthquake*. Gregory L. Fenves and Michael Ellery. December 1998.

PEER 1998/07 *Empirical Evaluation of Inertial Soil-Structure Interaction Effects.* Jonathan P. Stewart, Raymond B. Seed, and Gregory L. Fenves. November 1998.

PEER 1998/06 *Effect of Damping Mechanisms on the Response of Seismic Isolated Structures.* Nicos Makris and Shih-Po Chang. November 1998.

PEER 1998/05 *Rocking Response and Overturning of Equipment under Horizontal Pulse-Type Motions.* Nicos Makris and Yiannis Roussos. October 1998.

PEER 1998/04 *Pacific Earthquake Engineering Research Invitational Workshop Proceedings, May 14–15, 1998: Defining the Links between Planning, Policy Analysis, Economics and Earthquake Engineering.* Mary Comerio and Peter Gordon. September 1998.

PEER 1998/03 *Repair/Upgrade Procedures for Welded Beam to Column Connections.* James C. Anderson and Xiaojing Duan. May 1998.

PEER 1998/02 *Seismic Evaluation of 196 kV Porcelain Transformer Bushings.* Amir S. Gilani, Juan W. Chavez, Gregory L. Fenves, and Andrew S. Whittaker. May 1998.

PEER 1998/01 *Seismic Performance of Well-Confined Concrete Bridge Columns.* Dawn E. Lehman and Jack P. Moehle. December 2000.

ONLINE PEER REPORTS

The following PEER reports are available by Internet only at http://peer.berkeley.edu/publications/peer_reports_complete.html.

PEER 2012/103 *Performance-Based Seismic Demand Assessment of Concentrically Braced Steel Frame Buildings.* Chui-Hsin Chen and Stephen A. Mahin. December 2012.

PEER 2012/102 *Procedure to Restart an Interrupted Hybrid Simulation: Addendum to PEER Report 2010/103.* Vesna Terzic and Bozidar Stojadinovic. October 2012.

PEER 2012/101 *Mechanics of Fiber Reinforced Bearings.* James M. Kelly and Andrea Calabrese. February 2012.

PEER 2011/107 *Nonlinear Site Response and Seismic Compression at Vertical Array Strongly Shaken by 2007 Niigata-ken Chuetsu-oki Earthquake.* Eric Yee, Jonathan P. Stewart, and Kohji Tokimatsu. December 2011.

PEER 2011/106 *Self Compacting Hybrid Fiber Reinforced Concrete Composites for Bridge Columns.* Pardeep Kumar, Gabriel Jen, William Trono, Marios Panagiotou, and Claudia Ostertag. September 2011.

PEER 2011/105 *Stochastic Dynamic Analysis of Bridges Subjected to Spacially Varying Ground Motions.* Katerina Konakli and Armen Der Kiureghian. August 2011.

PEER 2011/104 *Design and Instrumentation of the 2010 E-Defense Four-Story Reinforced Concrete and Post-Tensioned Concrete Buildings.* Takuya Nagae, Kenichi Tahara, Taizo Matsumori, Hitoshi Shiohara, Toshimi Kabeyasawa, Susumu Kono, Minehiro Nishiyama (Japanese Research Team) and John Wallace, Wassim Ghannoum, Jack Moehle, Richard Sause, Wesley Keller, Zeynep Tuna (U.S. Research Team). June 2011.

PEER 2011/103 *In-Situ Monitoring of the Force Output of Fluid Dampers: Experimental Investigation.* Dimitrios Konstantinidis, James M. Kelly, and Nicos Makris. April 2011.

PEER 2011/102 *Ground-motion prediction equations 1964 - 2010.* John Douglas. April 2011.

PEER 2011/101 *Report of the Eighth Planning Meeting of NEES/E-Defense Collaborative Research on Earthquake Engineering.* Convened by the Hyogo Earthquake Engineering Research Center (NIED), NEES Consortium, Inc. February 2011.

PEER 2010/111 *Modeling and Acceptance Criteria for Seismic Design and Analysis of Tall Buildings.* Task 7 Report for the Tall Buildings Initiative - Published jointly by the Applied Technology Council. October 2010.

PEER 2010/110 *Seismic Performance Assessment and Probabilistic Repair Cost Analysis of Precast Concrete Cladding Systems for Multistory Buildlings.* Jeffrey P. Hunt and Božidar Stojadinovic. November 2010.

PEER 2010/109 *Report of the Seventh Joint Planning Meeting of NEES/E-Defense Collaboration on Earthquake Engineering. Held at the E-Defense, Miki, and Shin-Kobe, Japan, September 18–19, 2009.* August 2010.

PEER 2010/108 *Probabilistic Tsunami Hazard in California.* Hong Kie Thio, Paul Somerville, and Jascha Polet, preparers. October 2010.

PEER 2010/107 *Performance and Reliability of Exposed Column Base Plate Connections for Steel Moment-Resisting Frames.* Ady Aviram, Božidar Stojadinovic, and Armen Der Kiureghian. August 2010.

PEER 2010/106 *Verification of Probabilistic Seismic Hazard Analysis Computer Programs.* Patricia Thomas, Ivan Wong, and Norman Abrahamson. May 2010.

PEER 2010/105 *Structural Engineering Reconnaissance of the April 6, 2009, Abruzzo, Italy, Earthquake, and Lessons Learned.* M. Selim Günay and Khalid M. Mosalam. April 2010.

PEER 2010/104 *Simulating the Inelastic Seismic Behavior of Steel Braced Frames, Including the Effects of Low-Cycle Fatigue.* Yuli Huang and Stephen A. Mahin. April 2010.

PEER 2010/103 *Post-Earthquake Traffic Capacity of Modern Bridges in California.* Vesna Terzic and Božidar Stojadinović. March 2010.

PEER 2010/102 *Analysis of Cumulative Absolute Velocity (CAV) and JMA Instrumental Seismic Intensity (I_{JMA}) Using the PEER–NGA Strong Motion Database.* Kenneth W. Campbell and Yousef Bozorgnia. February 2010.

PEER 2010/101 *Rocking Response of Bridges on Shallow Foundations.* Jose A. Ugalde, Bruce L. Kutter, and Boris Jeremic. April 2010.

PEER 2009/109 *Simulation and Performance-Based Earthquake Engineering Assessment of Self-Centering Post-Tensioned Concrete Bridge Systems.* Won K. Lee and Sarah L. Billington. December 2009.

PEER 2009/108 *PEER Lifelines Geotechnical Virtual Data Center.* J. Carl Stepp, Daniel J. Ponti, Loren L. Turner, Jennifer N. Swift, Sean Devlin, Yang Zhu, Jean Benoit, and John Bobbitt. September 2009.

PEER 2009/107 *Experimental and Computational Evaluation of Current and Innovative In-Span Hinge Details in Reinforced Concrete Box-Girder Bridges: Part 2: Post-Test Analysis and Design Recommendations.* Matias A. Hube and Khalid M. Mosalam. December 2009.

PEER 2009/106 *Shear Strength Models of Exterior Beam-Column Joints without Transverse Reinforcement.* Sangjoon Park and Khalid M. Mosalam. November 2009.

PEER 2009/105 *Reduced Uncertainty of Ground Motion Prediction Equations through Bayesian Variance Analysis.* Robb Eric S. Moss. November 2009.

PEER 2009/104 *Advanced Implementation of Hybrid Simulation.* Andreas H. Schellenberg, Stephen A. Mahin, Gregory L. Fenves. November 2009.

PEER 2009/103 *Performance Evaluation of Innovative Steel Braced Frames.* T. Y. Yang, Jack P. Moehle, and Božidar Stojadinovic. August 2009.

PEER 2009/102 *Reinvestigation of Liquefaction and Nonliquefaction Case Histories from the 1976 Tangshan Earthquake.* Robb Eric Moss, Robert E. Kayen, Liyuan Tong, Songyu Liu, Guojun Cai, and Jiaer Wu. August 2009.

PEER 2009/101 *Report of the First Joint Planning Meeting for the Second Phase of NEES/E-Defense Collaborative Research on Earthquake Engineering.* Stephen A. Mahin et al. July 2009.

PEER 2008/104 *Experimental and Analytical Study of the Seismic Performance of Retaining Structures.* Linda Al Atik and Nicholas Sitar. January 2009.

PEER 2008/103 *Experimental and Computational Evaluation of Current and Innovative In-Span Hinge Details in Reinforced Concrete Box-Girder Bridges. Part 1: Experimental Findings and Pre-Test Analysis.* Matias A. Hube and Khalid M. Mosalam. January 2009.

PEER 2008/102 *Modeling of Unreinforced Masonry Infill Walls Considering In-Plane and Out-of-Plane Interaction.* Stephen Kadysiewski and Khalid M. Mosalam. January 2009.

PEER 2008/101 *Seismic Performance Objectives for Tall Buildings.* William T. Holmes, Charles Kircher, William Petak, and Nabih Youssef. August 2008.

PEER 2007/101 *Generalized Hybrid Simulation Framework for Structural Systems Subjected to Seismic Loading.* Tarek Elkhoraibi and Khalid M. Mosalam. July 2007.

PEER 2007/100 *Seismic Evaluation of Reinforced Concrete Buildings Including Effects of Masonry Infill Walls.* Alidad Hashemi and Khalid M. Mosalam. July 2007.

The Pacific Earthquake Engineering Research Center (PEER) is a multi-institutional research and education center with headquarters at the University of California, Berkeley. Investigators from over 20 universities, several consulting companies, and researchers at various state and federal government agencies contribute to research programs focused on performance-based earthquake engineering.

These research programs aim to identify and reduce the risks from major earthquakes to life safety and to the economy by including research in a wide variety of disciplines including structural and geotechnical engineering, geology/seismology, lifelines, transportation, architecture, economics, risk management, and public policy.

PEER is supported by federal, state, local, and regional agencies, together with industry partners.

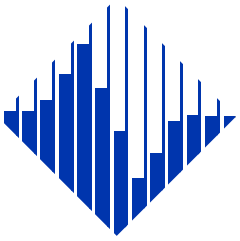

PEER Core Institutions:
University of California, Berkeley (Lead Institution)
California Institute of Technology
Oregon State University
Stanford University
University of California, Davis
University of California, Irvine
University of California, Los Angeles
University of California, San Diego
University of Southern California
University of Washington

PEER reports can be ordered at http://peer.berkeley.edu/publications/peer_reports.html or by contacting

Pacific Earthquake Engineering Research Center
University of California, Berkeley
325 Davis Hall, mail code 1792
Berkeley, CA 94720-1792
Tel: 510-642-3437
Fax: 510-642-1655
Email: peer_editor@berkeley.edu

ISSN 1547-0587X